AD NUMBER

AD855718

LIMITATION CHANGES

TO:

Approved for public release; distribution is unlimited.

FROM:

Distribution authorized to U.S. Gov't. agencies and their contractors; Critical Technology; MAR 1969. Other requests shall be referred to U.S. Army Aviation Materiel Laboratories, Fort Eustis, VA. This document contains export-controlled technical data.

AUTHORITY

USAAMRDL ltr, Mar 1976

AD

USAAVLABS TECHNICAL REPORT 68-38B

RADIAL OUTFLOW COMPRESSOR COMPONENT DEVELOPMENT

VOLUME II

PHASE II - DESIGN, FABRICATION, AND TEST OF AN EXPERIMENTAL COMPRESSOR

By

John R. Erwin

Nickolas G. Vitale

March 1969

U. S. ARMY AVIATION MATERIEL LABORATORIES
FORT EUSTIS, VIRGINIA

CONTRACT DA 44-177-AMC-180(T)

GENERAL ELECTRIC COMPANY
CINCINNATI, OHIO

Disclaimers

The findings in this report are not to be construed as an official Department of the Army position unless so designated by other authorized documents.

When Government drawings, specifications, or other data are used for any purpose other than in connection with a definitely related Government procurement operation, the United States Government thereby incurs no responsibility nor any obligation whatsoever; and the fact that the Government may have formulated, furnished, or in any way supplied the said drawings, specifications, or other data is not to be regarded by implication or otherwise as in any manner licensing the holder or any other person or corporation, or conveying any rights or permission, to manufacture, use, or sell any patented invention that may in any way be related thereto.

Trade names cited in this report do not constitute an official endorsement or approval of the use of such commercial hardware or software.

Disposition Instructions

Destroy this report when no longer needed. Do not return it to the originator.

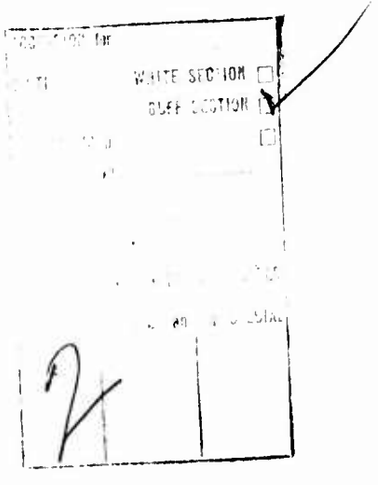

DEPARTMENT OF THE ARMY
U. S. ARMY AVIATION MATERIEL LABORATORIES
FORT EUSTIS, VIRGINIA 23604

This report has been reviewed by the U. S. Army Aviation Materiel Laboratories and is considered to be technically sound.

The design of the radial outflow compressor, tested in Phase II of the program, was based on the research completed in Phase I. The data and information contained herein will be used to determine the final configuration to be tested and demonstrated in Phase III.

Task 1G121401D14413
Contract DA 44-177-AMC-180(T)
USAAVLABS Technical Report 68-38B
March 1969

RADIAL OUTFLOW COMPRESSOR COMPONENT DEVELOPMENT

Volume II

Phase II - Design, Fabrication, and Test
of an Experimental Compressor

by

John R. Erwin

Nickolas G. Vitale

Prepared by

General Electric Company
Cincinnati, Ohio

for

U. S. ARMY AVIATION MATERIEL LABORATORIES
FORT EUSTIS, VIRGINIA

SUMMARY

This report describes the second phase of an investigation to develop a small, high-pressure-ratio radial outflow compressor (ROC). The first phase included aerodynamic and mechanical analyses, aerodynamic cascade tests, low-speed compressor tests, mechanical bench tests, machining, fabrication, and design studies which led to the configuration of a high-speed compressor. The second phase consisted of developmental testing of the high-speed compressor and further low-speed compressor testing to guide the design of an improved compressor.

Significant improvements in compressor performance and operating range were achieved by (1) eliminating the inlet guide vane system, (2) including a circular inlet turning vane, (3) enlarging the exit scroll, (4) using new rotor blades, and (5) employing the subsonic stator vanes. In combination, these modifications resulted in compressor rotor performance that provides strong encouragement that efficient high-pressure-ratio compressors of the radial outflow type can be developed.

FOREWORD

Under United States Army Contract DA-177-AMC-180(T), the Flight Propulsion Division of the General Electric Company in Cincinnati, Ohio, is conducting a program to advance and demonstrate high-pressure-ratio compressor technology for small gas turbine engines. The investigation concerning the analysis, design, construction, and testing of a Radial Outflow Compressor (ROC) is presented in three volumes, each volume generally describing one of the three phases of the program. Volume I presents the ROC design philosophy, mechanical analysis and bench test results, inlet system and rotating wall vaneless diffuser studies using a low-speed compressor, the design and supersonic cascade tests of the rotor blade sections, and high-speed transonic and supersonic cascade tests of single row and tandem row stator vanes. The design of the high-speed compressor test vehicle used in the Phase II and III investigations was also presented in Volume I.

Volume II describes the Phase II investigation including the aerodynamic and mechanical design of the high-speed rotor and the stator system. The experiments conducted consisted of testing 6 major buildups (A through F) of the compressor. A number of aerodynamic, mechanical, and operation problems were encountered during testing of the new compressor using a new test vehicle. During Buildup F, encouraging rotor performance was obtained at 70 percent speed, with a maximum rotor efficiency of 92.1 percent recorded at a rotor exit total pressure ratio of 3.97, and a rotor exit static pressure ratio of 1.97. This performance was accomplished by elimination of the inlet guide vanes, the use of a circular inlet vane, the Phase III rotor blades, and the subsonic stators. Analysis of the rotating wall vaneless diffuser was described and further low-speed compressor test results were presented. The rotating diffuser configuration selected for the Phase III rotor was also presented in Volume II.

Volume III describes the Phase III investigation of 3 major buildups (A through C) of the high-speed compressor. Buildup A was intended to provide direct comparison of the Phase III rotor performance with the best performance obtained with the Phase II rotor during Buildup F. The circular inlet vane was not used in Buildup A (Phase III) because the rotor inlet curvature was more gradual and it was hoped that the assembly, balancing, and installation difficulties inherent with the circular inlet vane could be avoided. Operating problems with the bellmouth liner used to form the air path into the new rotor were encountered. Fracture of the liner occurred at low speed. Continued operation of the compressor was obtained by machining the liner back to eliminate interference with the rotor. Although an unsatisfactory rotor entrance condition existed, some aerodynamic and mechanical data were obtained. A satisfactory inlet was constructed by modifying the bellmouth with a liner composed of pyrolytic graphite and glass fibers bonded with phenolic resin.

For the final test phases, the circular inlet vane was used, the rotor strain gages and leads were removed, and the supersonic stator vanes were installed upstream of the subsonic stators. An improved seal was employed upstream of the rotor for Buildup B. Buildup C was similar to Buildup B except that reduced seal clearance was established, reduced rotor to casing offset (cold, nonrotating) was used, and greater capacity to remove flow from the forward cavity was provided. A systematic series of stator vane settings was tested during Buildup C at speeds up to 100 percent.

The manager of the Small Gas Turbine Engine Compressor Technology Program is J. R. Erwin, and the principal contributing engineers are N. C. Vitale, R. G. Giffin, E. L. Timperman, C. H. Gay, and R. E. Troeger. Volume I was compiled and edited by Mr. D. V. Robinett. The assistance and consultations provided by Dr. D. C. Prince, Jr. and Dr. L. H. Smith, both of the General Electric Company, are gratefully acknowledged, as are the services of Dr. G. F. Wislicenus of Pennsylvania State University, who served as consultant on the program. Mr. LeRoy H. Hubert is Project Engineer for this program on behalf of the U.S. Army.

TABLE OF CONTENTS

	Page
SUMMARY	iii
FOREWORD	v
LIST OF ILLUSTRATIONS	vi
LIST OF TABLES	xxvi
LIST OF SYMBOLS	xxvii
ANALYTICAL INVESTIGATIONS	1
MECHANICAL INVESTIGATIONS	44
LOW-SPEED COMPRESSOR INVESTIGATIONS	113
EXPERIMENTAL INVESTIGATION OF THE HIGH-SPEED COMPRESSOR	189
PHASE III COMPRESSOR DESIGN	343
DISCUSSION	358
CONCLUSIONS	364
RECOMMENDATIONS	365
REFERENCES	366
APPENDIXES	
I Compressor Map Calculations	367
II ROC Rotor and Stator Case Displacements	371
III ROC Rotor Instrumentation	374
IV Component Test - Belleville Washer Preload	382
V ROC Test Phases II and III Failure Areas and Safety Items	385
VI Data Analysis Methods	390
VII Evaluation of Lebow Liquid Cooled Slip Ring	407
VIII ROC Scroll Collector Flow Limits	412
IX ROC Rotor Instrumentation for Buildup D	414
X Material Inspection of Phase III ROC Blades	420
XI Static Pressure Fluctuations	421
XII Summary of Test Runs	425
DISTRIBUTION	427

LIST OF ILLUSTRATIONS

Figure		Page
1	Variations in Inlet System Contours Used in Calculating Modified Inlet	2
2	Calculated Mach Numbers Through Compressor Inlet for Profile Number 1	3
3	Mach Number Distribution Over the Inner Surface of Profile Number 1 With 0, 15, and 30 Degrees Swirl . . .	4
4	Flow Angle Distribution Over the Inner Surface for Profile Number 1 With 15, 30, and 45 Degrees Swirl. . .	5
5	Axial Velocity Distribution Over the Inner Surface of Profile Number 1 With 0, 15, 30, and 45 Degrees Swirl .	7
6	Calculated Mach Numbers Through Compressor Inlet for Profile Number 2	8
7	Calculated Mach Numbers Through Compressor Inlet for Profile Number 3	9
8	Mach Number Distribution Over the Inner Surface of Profile Number 3 With 0, 15, 30, 45, and 60 Degrees Swirl	11
9	Mach Number Distribution Over the Outer Surface of Profile Number 3 With 0, 15, 30, and 60 Degrees Swirl	12
10	Flow Angle Distribution Over the Inner Surface of Profile Number 3 With 0, 15, 30, 45, and 60 Degrees Swirl	13
11	Radial Pressure Gradient Calculated for the Free Stream and for the Boundary Layer for Supersonic Flow	17
12	Radial Pressure Gradient Calculated for the Free Stream and for the Boundary Layer for Supersonic Flow	18
13	Radial Static Pressure Gradient Normalized by Relative Dynamic Pressure x $\cos\theta$	20
14	Effective Radial Static Pressure Gradient Normalized by Relative Dynamic Pressure x $\cos\theta$.	21

Figure		Page
15	Radial Static Pressure Gradient Normalized by Relative Dynamic Pressure x $\cos^2 \theta$	22
16	Effective Radial Static Pressure Gradient Normalized by Relative Dynamic Pressure x $\cos^2 \theta$	23
17	Potential Rotating Vaneless Diffuser Passage Contours Compared With Original	25
18	Comparison of Diffuser Loading Parameter for Original Contour and Contour Number 3 at 60 Percent Speed	26
19	Comparison of Diffuser Loading Parameter G_1/r_2 for Original, Contour Number 2, and Contour Number 3 at 100 Percent Speed	27
20	Comparison of Original and Contour Number 5 of Rotating Vaneless Diffuser Passage	30
21	Comparison of Diffuser Loading Parameter G_1/r_2 for Original Contour and Contour Number 5 at 60 Percent Speed	31
22	Comparison of Diffuser Loading Parameter G_1/r_2 for Original Contour and Contour Number 5 at 100 Percent Speed	32
23	Comparison of Diffuser Loading Parameter G_2/r_2 for Original Contour and Contour Number 5 at 60 Percent Speed	33
24	Comparison of Diffuser Loading Parameter G_2/r_2 for Original Contour and Contour Number 5 at 100 Percent Speed	34
25	Predicted Rotor Total Pressure Ratio Versus Airflow With -18.4 Degrees Counter-Preswirl Entering the Rotor Blades	35
26	Predicted Rotor Total Pressure Ratio Versus Airflow With 0 Degrees Swirl Entering the Rotor Blades	36
27	Predicted Rotor Total Pressure Ratio Versus Airflow for Swirl Angle of 31.1 Degrees Entering Rotor Blades	37
28	Predicted Rotor Exit Static Pressure Ratio Versus Airflow for -18.4 Degrees Counter-Swirl Entering Rotor Blades	38

Figure		Page
29	Predicted Rotor Exit Static Pressure Ratio Versus Airflow for 0 Degrees Swirl Entering Rotor Blades	39
30	Predicted Rotor Static Pressure Ratio Versus Airflow With 31.1 Degrees Preswirl Entering Rotor Blades	40
31	Estimated Rotor Efficiency Versus Airflow for -18.4 Degrees Counter-Preswirl Entering Rotor Blades	41
32	Estimated Rotor Efficiency Versus Airflow for 0 Degrees Swirl Entering Rotor Blades	42
33	Estimated Rotor Efficiency Versus Airflow for 31.1 Degrees Preswirl Entering Rotor Blades	43
34	Stress Distribution on ROC Disc at 100 Percent Speed	45
35	Deflection Distribution on ROC Disc at 100 Percent Speed	46
36	Stress Distribution on ROC Shroud at 100 Percent Speed	47
37	Deflection Distribution on ROC Shroud at 100 Percent Speed	48
38	Supersonic Stator Load Distribution	52
39	Deflected ROC Supersonic Stator Cascade	53
40	Diametral and Circumferential Vibration Modes of a Thin Disc	54
41	Representation of the Rotating Shroud and the Models Used to Synthesize Rotating Shroud Computer Program	57
42	ROC Shroud Campbell Diagram (Blade Side)	59
43	ROC Shroud Campbell Diagram (Seal Side).	60
44	Instrumented Rotor Blade Mounted in Simulated Disc and Shroud for Experimental Vibration Analysis	62
45	Overall View of Bench Setup for Experimental Analysis of Rotor Blade Vibration	63
46	Setup (1) for Frequencies and Modes Investigation	66

Figure		Page
47	Setup (2) for Vibratory Deflections and Stress Investigation	67
48	Close-up View of Setup Number 1 Showing Electronic Pickup Used to Detect Rotating Shroud Vibrations	68
49	Overall View of Bench Setup for Experimental Analysis of Rotating Vibration Patterns (Setup Number 2)	69
50	Details of Excitation Mechanism and Deflection Measurement Apparatus	70
51	Close-up View of Rotating Shroud Mounted on the Fixture With the Shaker Used for Setup Number 2	71
52	Setup Used to Calibrate the Proximeter Which is Shown Mounted Adjacent to the Rim of the Rotating Shroud	72
53	Shroud (Blade Side) Strain Gage Location	73
54	Shroud (Seal Side) Strain Gage Locations	74
55	Schematic Shapes of the Principal Shroud Modes.	79
56	Shroud Sand Pattern Pictures.	80
57	Cos 2θ Mode Shroud Stress Distribution (Blade Side)	81
58	Cos 3θ Radial Stress Distribution in Shroud (Blade Side)	82
59	Cos 4θ Radial Stress Distribution in Shroud (Blade Side)	83
60	Cos 2θ Radial Stress Distribution in Shroud (Seal Side)	84
61	Cos 3θ Radial Stress Distribution in Shroud (Seal Side)	85
62	Radial Stress Distribution in Shroud (Seal Side) for Cos 4θ Vibration Mode	86
63	Blade Side Stress Displacement Curve for Axial Motions of the Shroud Rim for Cos 2θ Vibration Mode	87
64	Blade Side Stress Displacement Curve for Axial Motions of the Shroud Rim for Cos 3θ Vibration Mode	88

Figure		Page
65	Blade Side Stress Displacement Curve for Axial Motions of the Shroud Rim for Cos 4θ Vibration Mode.	89
66	Seal Side Stress Displacement Curve for Axial Motions of the Shroud Rim for Cos 2θ Vibration Mode.	90
67	Seal Side Stress Displacement Curve for Axial Motions of the Shroud Rim for Cos 3θ Vibration Mode	91
68	Seal Side Stress Displacement Curve for Axial Motions of the Shroud Rim for Cos 4θ Vibration Mode	92
69	Bently Probe Calibration Test Setup	95
70	Bently Detector Driver and Probe	96
71	Effect of Probe-to-Part Gap on DC Output Voltage Under Steady-State Conditions With and Without Heating	98
72	AC Output Voltage - Vibratory Amplitude Relationship of Bently Probe for a Steady-State Gap of 0.090 Inch With and Without Heating	99
73	Temperature Effects on Output Voltage Curve for a Steady-State Gap of 0.090 Inch	100
74	Variation of AC Output Voltage With Gap Width for Bently Probe	101
75	AC Output Voltage Versus Bently Probe Gap for Several Vibratory Amplitudes	102
76	Vibration Test Setup for Supersonic Stator Vane	104
77	Supersonic Stator Strain Gage Locations	105
78	ROC Supersonic Stator Vane Mode Shapes	108
79	Variation of Deflection With Applied Torque From Belleville Washer Load Tests	110
80	Variation of Bolt Tension With Applied Torque From Belleville Washer Load Tests	111
81	Variation of Bolt Tension With Washer Deflection From Belleville Washer Load Tests	112

Figure		Page
82	Variation in the Aerodynamic Loading Coefficient G_1 With Radius for Various Flow Coefficients	118
83	Effect of Suction on the Aerodynamic Loading Coefficient G_1 in the Low-Speed Vaneless Diffuser for ϕ = 1.0	120
84	Effect of Rotational Speed on the Aerodynamic Loading Parameter G_1 With Suction for ϕ = 1.0	121
85	Comparison of the Aerodynamic Loading Parameter G_1 for the Low-Speed ROC at 3 Flow Coefficients in the High-Speed ROC	122
86	Low-Speed ROC as Modified for the Porous Wall Diffuser Tests	125
87	Details of the Suction Chamber Used to Control the Flow Through the Porous Wall	127
88	Calculated Streamline Patterns in Rotating Vaneless Diffuser of Low-Speed ROC for 2 Values of Flow Coefficient With Maximum Suction	130
89	Static Pressure Distribution in the Rotating Vaneless Diffuser of the Low-Speed ROC for Flow Coefficient 0.6 and Several Suction Quantities	131
90	Static Pressure Distribution in the Rotating Vaneless Diffuser of the Low-Speed ROC for Flow Coefficient 1.0 and Several Suction Quantities	132
91	Values of the Aerodynamic Loading Coefficient G_1 on the Rotating Disc Wall of the Vaneless Diffuser for Various Values of Suction Quantity Z, ϕ = 0.6.	133
92	Values of the Aerodynamic Loading Coefficient G_1 on the Rotating Disc Wall of the Vaneless Diffuser for Various Values of Suction Quantity Z, ϕ = 1.0	134
93	Comparison of the Aerodynamic Loading Coefficient G_1 in the Low-Speed ROC With the High-Speed ROC at 30 and 100 Percent Speed.	135
94	Meridional Streamlines in a Rotating Vaneless Diffuser in the Presence of an Assumed Separation Bubble.	136
95	Comparison of the Static Pressure Distribution in the Rotating Vaneless Diffuer With and Without a Separation Bubble	137

Figure		Page
96	Low-Speed Rotor With 1 Wall of the Rotating Diffuser Removed	139
97	Porous Surface and Bleed Chambers Used With the Low-Speed Rotor	140
98	Porous Wall Showing Location of Static Pressure Orifices, Fixed Probe Positions, and Openings for Traversing Probes	141
99	Assembly of Low-Speed ROC Modified With Porous Wall and Bleed System.	142
100	Side View of Modified Low-Speed Compressor	143
101	Carpet Plot of Diffuser Loading Parameter G_1 as a Function of Flow Coefficient and Suction Coefficient.	144
102	Low-Speed ROC Flow Angle and Total Pressure Distribution for Run Number 3, Reading Number 6	145
103	Low-Speed ROC Flow Angle and Total Pressure Distribution for Run Number 7, Reading Number 9	146
104	Low-Speed ROC Flow Angle and Total Pressure Distribution for Run Number 7, Reading Number 12	147
105	Details of Teflon Seals Installed in Low-Speed Compressor Between Rotor and Blade Chambers	149
106	Low-Speed ROC Flow Angle and Total Pressure Distribution for Run Number 8, Reading Number 1	150
107	Low-Speed ROC Flow Angle and Total Pressure Distribution for Run Number 8, Reading Number 4	151
108	Low-Speed ROC Flow Angle and Total Pressure Distribution for Run Number 9, Reading Number 1	152
109	Low-Speed ROC Flow Angle and Total Pressure Distribution for Run Number 9, Reading Number 5	153
110	Low-Speed ROC Flow Angle and Total Pressure Distribution for Run Number 20, Reading Number 1	154
111	Low-Speed ROC Flow Angle and Total Pressure Distribution for Run Number 20, Reading Number 2	155

Figure		Page
112	Low-Speed ROC Flow Angle and Total Pressure Distribution for Run Number 20, Reading Number 3	156
113	Velocity Diagram for Low-Speed ROC	158
114	Distribution of Absolute Velocity at Rotor Blade Trailing Edge for Various Suction Quantities for the Low-Speed ROC	159
115	Distribution of Relative Velocity of Rotor Blade Trailing Edge for Various Suction Quantities for the Low-Speed ROC	160
116	Distribution of Relative Tangential Velocity of Rotor Blade Trailing Edge for Various Suction Quantities for the Low-Speed ROC	161
117	Distribution of Radial Velocity for Rotor Blade Trailing Edge for Various Suction Quantities for the Low-Speed ROC	162
118	Distribution of Relative Exit Flow Angle at Rotor Blade Trailing Edge for Various Suction Quantities for the Low-Speed ROC.	163
119	Distribution of Efficiency at Rotor Blade Trailing Edge for Various Suction Quantities for Low-Speed ROC	164
120	Distribution of Loss Coefficient at Rotor Blade Trailing Edge for Various Suction Quantities for Low-Speed ROC	165
121	Circular Inlet Vane Used in Low-Speed ROC	167
122	Fiber Glass Circular Vane Used in Inlet of Low-Speed Compressor	168
123	Distribution of Velocity Ratio Over the Outer Surface A-B on the Low-Speed ROC Inlet	169
124	Distribution of Velocity Ratio Over Splitter Surfaces C-D Mounted in Low-Speed ROC Inlet.	170
125	Distribution of Velocity Ratio Over Inner Surface of Low-Speed ROC Inlet	171
126	Distribution of Absolute Exit Velocity at Rotor Blade Trailing Edge for Various Suction Quantities for Low-Speed ROC.	173

Figure		Page
127	Distribution of Relative Exit Velocity at Rotor Blade Trailing Edge for Various Suction Quantities for Low-Speed ROC	174
128	Distribution of Relative Tangential Velocity at Rotor Blade Trailing Edge for Various Suction Quantities for Low-Speed ROC	175
129	Distribution of Radial Exit Velocity at Rotor Blade Trailing Edge for Various Suction Quantities for Low-Speed ROC	176
130	Distribution of Relative Exit Flow Angle at Rotor Blade Trailing Edge for Various Suction Quantities for Low-Speed ROC	177
131	Distribution of Efficiency at Rotor Blade Trailing Edge for Various Suction Quantities for Low-Speed ROC	178
132	Distribution of Loss Coefficient at Rotor Blade Trailing Edge for Various Suction Quantities for Low-Speed ROC	179
133	Low-Speed ROC Flow Angle and Total Pressure Distribution for Run Number 27, Reading Number 2, With Inlet Vane	180
134	Low-Speed ROC Flow Angle and Total Pressure Distribution for Run Number 27, Reading Number 3, With Inlet Vane	181
135	Low-Speed ROC Flow Angle and Total Pressure Distribution for Run Number 27, Reading Number 6, With Inlet Vane	182
136	Low-Speed ROC Flow Angle and Total Pressure Distribution for Run Number 32, Reading Number 3, With Inlet Vane	183
137	Low-Speed ROC Flow Angle and Total Pressure Distribution for Run Number 32, Reading Number 7, With Inlet Vane	184
138	Low-Speed ROC Flow Angle and Total Pressure Distribution for Run Number 32, Reading Number 8, With Inlet Vane	185

Figure		Page
139	Low-Speed ROC Flow Angle and Total Pressure Distribution for Run Number 31, Reading Number 2, With Inlet Vane	186
140	Low-Speed ROC Flow Angle and Total Pressure Distribution for Run Number 31, Reading Number 6, With Inlet Vane	187
141	Low-Speed ROC Flow Angle and Total Pressure Distribution for Run Number 31, Reading Number 7, With Inlet Vane	188
142	Main Frame for Supporting High-Speed Test Vehicle	190
143	Casing for Mounting High-Speed Gear and Test Vehicle	191
144	High-Speed Gearbox and Gears	192
145	Housing for Supporting High-Speed Main Bearing Shaft	193
146	Front View of Bearing Housings Including Seal Plates	194
147	Miscellaneous Seals and Spacers Used With the High-Speed ROC	195
148	Assembly of Rotor Shaft and Bearings for High-Speed ROC	196
149	Motor, Reduction Gear, Pivotal Mounting, Drive Screw and Bracket for Actuating Supersonic Stator Blades	197
150	Downstream View of Inlet Guide Vane Assembly	198
151	Upstream View of Inlet Guide Vane Assembly.	199
152	External View of Forward Compressor Stator Casing	200
153	Internal View of Forward Compressor Stator Casing	201
154	Compressor Exit Ducts and Elbows	202
155	Assembly of Rotor Disc and Rotating Centerbody Mounted on the Balancing Machine	204
156	Trial Assembly of Alternate Long Shank and Short Pin Rotor Blades in Rotor Disc	205
157	Close-up of Long Shank Rotor Blade Seated in Rotor Disc.	206

Figure		Page
158	Preliminary Assembly of Rotor Disc Blades and Centerbody	207
159	High-Speed ROC Rotor Prior to Assembly of Rotating Shroud	208
160	Inlet Side of Assembled Rotor	209
161	Exit of Assembled Rotor	210
162	View of Assembled Rotor and Shaft	211
163	High-Speed Test Vehicle Installed in Cell	212
164	Stator Casing Showing Location of Traverse Instrumentation Installed in Test Cell	213
165	Sketch of High-Speed ROC Illustrating Location of Instrumentation Stations	227
166	High-Speed ROC and Nomenclature of Various Parts	228
167	Details of Yaw and Total Pressure Probe Used in High-Speed ROC	229
168	Details of 5-Element Temperature Rake Used in High-Speed ROC	230
169	Probe Actuator - Typical of Those Used in High-Speed ROC Investigation	231
170	Assembly of High-Speed ROC Prior to Tests of Buildup A	233
171	Comparison of Test Results With Predicted Performance for Run Number 2, Buildup A	237
172	Traverses of Flow Angle and Total Pressure for Run Number 2, Reading Number 18, at Rotor Exit (Station 3) at 33 Percent Speed	238
173	Comparison of Operating Line Obtained During Run Number 3 of Buildup A With Predicted Performance	239
174	Rotor Blade Leading Edges Showing FOD Encountered During Tests of Buildup A - Sector 1	241

Figure		Page
175	Rotor Blade Leading Edges Showing FOD Encountered During Tests of Buildup A - Sector 2	242
176	Reworked Rotor Blade Leading Edges in Sector 1	244
177	Total Pressure Ratio Versus Mass Flow for Run Number 4 (Buildup B)	245
178	Static Pressure Ratio Versus Mass Flow for Run Number 4 (Buildup B)	246
179	Total Temperature Ratio Versus Mass Flow for Run Number 4 (Buildup B)	247
180	Total Pressure Ratio Versus Mass Flow for Run Number 5 (Buildup B)	249
181	Static Pressure Ratio Versus Mass Flow for Run Number 5 (Buildup B)	250
182	Total Temperature Ratio Versus Mass Flow for Run Number 5 (Buildup B)	251
183	Total Pressure Ratio Versus Mass Flow for Run Number 6 (Buildup B) Without Stators	252
184	Static Pressure Ratio Versus Mass Flow for Run Number 6 (Buildup B)	253
185	Total Temperature Ratio Versus Mass Flow for Run Number 6 (Buildup B)	254
186	Rotor Exit Flow Angle Versus Mass Flow for Run Number 6 (Buildup B) Without Stators	255
187	Preliminary Assembly of Supersonic Stator Vanes in Forward Compressor Stator Casing	257
188	Supersonic Stator Vanes Including 1 of the 2 Vanes Having Strain Gages	258
189	Total Pressure Rake and Static Pressure Orifice Locations Adjacent to Supersonic Stators	259
190	Cobra Probe Containing Total Pressure and Yaw Tubes Located Downstream of the Supersonic Stator Vanes	260
191	Total Temperature Rake Located in Subsonic Stator Spindle	261

Figure		Page
192	Total Pressure Ratio Versus Mass Flow for Run Number 7 (Buildup C) With Supersonic Stators	262
193	Static Pressure Ratio Versus Mass Flow for Run Number 7 (Buildup C) With Supersonic Stators	263
194	Total Temperature Versus Mass Flow for Run Number 7 (Buildup C) With Supersonic Stators	264
195	Total Pressure Ratio Versus Mass Flow for Run Number 8 (Buildup C) With Supersonic Stators	268
196	Static Pressure Ratio Versus Mass Flow for Run Number 8 (Buildup C) With Supersonic Stators	269
197	Total Temperature Versus Mass Flow for Run Number 8 (Buildup C) With Supersonic Stators	270
198	Phase II Rotor Sharp Shroud Showing Dust Patterns Observed After Testing Buildup C	272
199	Dust Patterns on Rotor Shroud Adjacent to Rotor Blades	273
200	Dust Patterns on Rotor Blades and Disc Following Tests of Buildup C	275
201	Patterns Left on Rotor Blades - White Particles are Teflon Originating from the Forward Seal	276
202	Dust and Teflon Particle Patterns on Convex Surface of Rotor Blades Following Test of Buildup C	277
203	Dust Patterns on Rotor Disc Following Tests During Buildup C	279
204	Modified Inlets Used in Buildup D (Upper Drawing) and Buildup F (Lower Drawing)	280
205	Assembly of High-Speed Compressor Prior to Test of Buildup D	282
206	Close-up of Open Inlet Used in Buildup D	283
207	Assembly of Compressor for Test of Buildup D After Installation of Inlet Screen	284
208	Total Pressure Ratio Versus Mass Flow for Run Numbers 10 and 11 (Buildup D) With Open Inlet	285

Figure		Page
209	Static Pressure Ratio Versus Mass Flow for Run Numbers 10 and 11 (Buildup D) With Open Inlet	286
210	Total Temperature Versus Mass Flow for Run Numbers 10 and 11 (Buildup D) With Open Inlet	287
211	Reworked Scroll Collector in the Upstream Compressor Stator Casing	290
212	Total Pressure Tubes Installed on Leading Edge of Supersonic Stator Vane	291
213	Total Pressure Ratio Versus Mass Flow for Run Numbers 12 and 13 (Buildup E) With Open Inlet	292
214	Static Pressure Ratio Versus Mass Flow for Run Numbers 12 and 13 (Buildup E) With Open Inlet	293
215	Total Temperature Ratio Versus Mass Flow for Run Numbers 12 and 13 (Buildup E) With Open Inlet	294
216	Rotor and Circular Inlet Vane Tested as Buildup F	297
217	Side View of Circular Vane Used in Buildup F	298
218	Comparison of Phase II and Phase III Rotor Blade Sections	299
219	Preliminary Assembly of New (Phase III) Rotor Blades and Strain Gage Leads Prior to Testing Buildup F	300
220	Assembly of Compressor Rotor and Circular Inlet Vane Mounted in Balancing Machine	301
221	Circular Turning Vane Installed in Inlet of High-Speed Compressor	302
222	Total Pressure Ratio Versus Mass Flow for Run Numbers 15 and 16 (Buildup F).	304
223	Static Pressure Ratio Versus Mass Flow for Run Numbers 15 and 16 (Buildup F)	305
224	Total Temperature Ratio Versus Mass Flow for Run Numbers 15 and 16 (Buildup F)	306

Figure		Page
225	Rotor Efficiency Versus Mass Flow for Run Numbers 15 and 16 (Buildup F).	307
226	Predicted Total Pressure Ratio Versus Mass Flow for ROC Rotor Without Inlet Guide Vanes	309
227	Total Pressure Ratio Versus Mass Flow for Buildup F	314
228	Rotor Efficiency Versus Mass Flow for Buildup F	315
229	High-Speed ROC Flow Angle and Total Pressure Traverses for Run Number 17, Reading Number 48, With Circular Inlet Vane at 65 Degrees Position	316
230	High-Speed ROC Flow Angle and Total Pressure Traverses for Run Number 17, Reading Number 48, With Circular Inlet Vane at 135 Degrees Position.	317
231	High-Speed ROC Flow Angle and Total Pressure Traverses for Run Number 17, Reading Number 49, With Circular Inlet Vane at 65 Degrees Position	318
232	High-Speed ROC Flow Angle and Total Pressure Traverses for Run Number 17, Reading Number 49, With Circular Inlet Vane at 135 Degrees Position.	319
233	High-Speed ROC Flow Angle and Total Pressure Traverses for Run Number 17, Reading Number 51, With Circular Inlet Vane at 65 Degrees Position	320
234	High-Speed ROC Flow Angle and Total Pressure Traverses for Run Number 17, Reading Number 51, With Circular Inlet Vane at 135 Degrees Position.	321
235	High-Speed ROC Flow Angle and Total Pressure Traverses for Run Number 17, Reading Number 52, With Circular Inlet Vane at 65 Degrees Position	322
236	High-Speed ROC Flow Angle and Total Pressure Traverses for Run Number 17, Reading Number 52, With Circular Inlet Vane at 135 Degrees Position.	323
237	Soot Patterns on the Rotating Shroud Following Buildup F, Phase II Investigation.	326
238	Soot Patterns on the Rotor Blades and Rotating Shroud Following Buildup F, Phase II Investigation	327

Figure		Page
239	Soot Patterns on Rotor Disc Showing Variations Downstream of Strain Gage Leads	328
240	Soot Patterns on the Rotor Disc Following Buildup F, Phase II Investigation.	329
241	Stator Casing Illustrating Stator Vane, Instrumentation and Scroll Configuration for Buildup F, Phase II Investigation	330
242	Close-up View of Scroll Splitter Lip, Subsonic Stators, and Cobra Probe for Buildup F, Phase II Investigation	331
243	Teflon Seal Illustrating Warpage Which Occurred During Run Numbers 15 and 16, Buildup F, Phase II Investigation.	332
244	Side View of Teflon Seal Following Run Numbers 15 and 16, Buildup F, Phase II Investigation	333
245	Internal View of Forward Compressor Casing Following Phase II Investigation.	334
246	External View of Forward Compressor Casing Following Phase II Investigation.	335
247	Internal View of Main Bearing Housing Following Phase II Investigation	336
248	External View of Main Bearing Housing Following Phase II Investigation - Ring Gear Position for Operating Supersonic Stators	337
249	Overall View of Long Shank Rotor Blade Following Run Number 18 of Buildup F.	338
250	Detail of Soot Pattern Near Leading Edge on Concave Surface of Rotor Blade.	339
251	Soot Pattern Near Trailing Edge on Concave Surface of Rotor Blade	340
252	Convex Surface of Rotor Blade Following Run Number 18, Buildup F, Phase II Investigation	341
253	Remains of Teflon Seal Following Run Number 18, Buildup F, Phase II Investigation.	342

Figure		Page
254	Variation of Diffuser Width With Radius for Contour Number 17	344
255	Distribution of the Diffuser Loading Parameter G_2/r_2 for Contour Number 17 at 100 Percent Speed With Design Inlet Swirl Angle at -18.4 Degrees.	345
256	Distribution of the Diffuser Loading Parameter G_1/r_2 for Contour Number 6 at 100 Percent Speed With Design Inlet Swirl Angle of -18.4 Degrees.	347
257	Distribution of the Diffuser Loading Parameter G_2/r_2 for Contour Number 6 at 100 Percent Speed With Design Inlet Swirl Angle of -18.4 Degrees.	348
258	Variation of Diffuser Width With Radius for Contour Numbers 5E, 6, and 7.	349
259	Distribution of the Diffuser Loading Parameter G_2/r_2 for Contour Number 5E at 100 Percent Speed With Design Inlet Swirl Angle at -18.4 Degrees.	350
260	Distribution of the Diffuser Loading Parameter G_2/r_2 for Contour Number 7 at 100 Percent Speed With Design Inlet Swirl Angle at -18.4 Degrees.	351
261	Configuration of the Rotor and Adjacent Parts for Buildup A of Phase III.	353
262	Flow Area and Mach Number Distribution for Original Phase II and Proposed Phase III ROC Inlet	354
263	Configuration of ROC for Phase III.	357
264	Calculated Net Terminal and Dynamic Displacement of the High-Speed ROC Shroud and Disc.	372
265	Calculated Relative Displacement of High-Speed ROC Rotor to Stator Case.	373
266	Strain Gage Locations Used on Concave Surface of Rotor Blades of High-Speed ROC.	378
267	Strain Gage Locations Used on Convex Surface of Rotor Blades of High-Speed ROC.	379

Figure		Page
268	Strain Gage Location Used on Concave and Convex Surfaces of Rotor Blade of High-Speed ROC (for Bench Tests Only)	380
269	Circumferential Distribution of Strain Gages and Thermocouples Used in Buildup A of the High-Speed ROC	381
270	Location of Strain Gages on Rotating Shroud of High-Speed ROC	417
271	Strain Gage Location and Lead Path to Shroud Strain Gage on Convex Surface of High-Speed ROC Rotor Blade (for Buildup D Only)	418
272	Circumferential Location of Thermocouples and Total Blades Having Shroud Strain Gage Leads.	419
273	Oscilloscope Traces Obtained From High Frequency Response Static Pressure Crystals With Timing Trace Shown at Bottom.	423
274	Oscilloscope Traces Obtained From High Frequency Response Static Pressure Crystals With Timing Trace Shown at Bottom.	424

LIST OF TABLES

Table		Page
I	Maximum Blade Stresses.	50
II	Blade Side Shroud Vibration - Natural Frequencies	56
III	Final Shroud Vibration - Natural Frequencies.	56
IV	Stress Distribution at Resonance on Ti-6Al-4V ROC Blades.	64
V	Shroud Vibratory Modes.	77
VI	Shroud Strain Gage Readings	78
VII	Supersonic Stator Vane Strain Distribution.	107
VIII	Sensitivity Check on Aerodynamic Efficiency Calculation	218
IX	Sensitivity Check on Mechanical Efficiency Calculation	219
X	Review of Computational Capabilities.	221
XI	ROC Station Definition.	223
XII	ROC Research Instrumentation - Phase II	224
XIII	Switching for Strain Gages for Slip Ring Hookup	376
XIV	ROC Blades - Location List.	377
XV	Summary of Test Runs.	425

LIST OF SYMBOLS

A	area, $feet^2$
AR	aspect ratio
a	speed of sound, feet/second
C_p	specific heat at constant pressure, Btu/lb/^oF
C_P	static pressure rise coefficient
C_{Peff}	effective static pressure rise coefficient
C_v	specific heat at constant volume, Btu/lb/^oF
D	diameter, inches
d	distortion
F	force, pounds
f	frequency, cps
G_1	$r_2 \frac{(dp_s/dr)_{FS} - (dp_s/dr)_{BL}}{1/2\ \rho\ V_{Rel}^2\ Cos\ \theta}$, diffuser loading parameter
G_2	$r_2 \frac{(dp_s/dr)_{FS} - (dp_s/dr)_{BL}}{1/2\ \rho\ V_{Rel}^2\ Cos^2\ \theta}$, diffuser loading parameter
g	gravitational constant, $feet/second^2$
H	enthalpy, Btu/lb
h	passage height (width), inches
i	incidence angle, degrees
J	Joule's mechanical equivalent of heat, 778 foot-pound/Btu
K	coefficient
M	Mach number
N	rotating speed, rpm (N = 34,650 rpm at 100 percent speed)

N_R	Reynolds number
P	pressure, pounds/inch^2
PV4	plenum upstream of rotor
R	radius ratio (when used with subscripts)
R	gas constant, ft-lb/lb/^oF
r	radius, inches
s_p	pitch, inches
T	temperature, degrees Rankine
U	tangential velocity, feet/second
V	absolute velocity, feet/second
W	relative velocity, feet/second
w	flow rate, pounds/second
X	weighting function
Z	suction flow parameter

α	angle between radial line and absolute velocity, degrees
β	angle between radial line and relative velocity, degrees
β^*	angle between radial line and rotor blade mean line, degrees
Γ	net wall slope
γ	ratio of specific heats, (C_p/C_v)
Δ	increment
η	efficiency
θ	temperature ratio, T/T_{std}
θ	angle between radial line and absolute velocity, degrees
θ_s	angle between blade surface tangent and the local radius, degrees
ρ	density, pounds/feet^3
σ	stress, psi
Σ	summation
τ	torque, feet-pounds
ϕ	flow coefficient, (V_r/U)
Φ	flow direction with respect to $\bar{R}$, degrees
Ψ	work coefficient
ω	angular velocity, radians/second
$\bar{\omega}$	loss coefficient, $\left(\frac{P_{t1} - P_{t2}}{P_{t1} - P_{s1}}\right)$

Subscripts

o thru 9	refer to stations as defined in Figure 165
A	aerodynamic
BL	boundary layer
c	compressible
cir	circumferential
corr	correction
d	diffuser
des	design
f	flow restriction
FS	free stream
lc	enthalpy
i	isentropic
inc	incompressible
ind	indicated
j	element
L	loss
l	leakage
M	mechanical
m	mass weighted
P	pressure
p	polytropic
Rel	relative
r	component in radial direction
S	shroud

s	static
sh	shock
std	standard
s.b.	solid body
T	temperature calibration
t	total
u	component in tangential direction
v	venturi
X	station

BLANK PAGE

ANALYTICAL INVESTIGATIONS

INLETS FOR THE HIGH-SPEED COMPRESSOR

Because of the possibility of unsatisfactory inlet flow into the high-speed rotor with the original design, further analysis of this design and of 2 modifications has been conducted; also, a new inlet bellmouth was ordered without struts and centerbody so that the rotor could be tested with a simple inlet if necessary.

The original inlet passage contour (1) is shown in Figure 1. Two modifications to the inner contour (2 and 3) are also shown. The first modification (2) is confined to the rotating centerbody. The second modification is somewhat more extensive and requires a contour change on the stationary inner housing upstream of the rotor.

Original Inlet Contour

The Mach number distribution over the original design contours without inlet swirl as a function of axial distance is presented in Figure 2. A rapid deceleration of the flow on the inner surface is calculated between stations 2.5 and 4.0. A pressure coefficient of 0.59 is predicted to occur. These calculations employed a compressible flow flux plotting program which has been used in early inlet system calculations presented in the Phase I report (Reference 1). This program does not include the effects of tangential flow velocities. Another program, Compressor Axisymmetric Flow Determination (CAFD), capable of accepting tangential fluid velocities was used to calculate the inlet system flow velocities and directions with inlet guide vanes imparting swirl to the air. The information required as input to this latter program is somewhat different from that required for the flux plot program, and some minor differences in results were obtained for the zero swirl conditions which either program can calculate. For example, the static pressure rise coefficient calculated for the flow over the inner contour for zero swirl shown in Figure 3 is 0.656 using the CAFD program.

The effect of 15 and 30 degrees inlet swirl angle on the Mach number distribution over the inner contour is shown in Figure 3. For 15 degrees swirl angle, the decrease in Mach number between axial stations 3 and 4 is significantly reduced. For 30 degrees inlet swirl angle, an acceleration of the flow downstream of station 3 is calculated. Due to the low value of the minimum radius on the inner contour of the high-speed inlet, the flow attains a very high swirl angle in this region over the inner surface. As shown in Figure 4, for only 15 degrees of inlet swirl angle, the flow angle reaches a value of 54.4 degrees at the 5.25 station. For higher inlet swirl angles, the local value reached at this station is correspondingly higher.

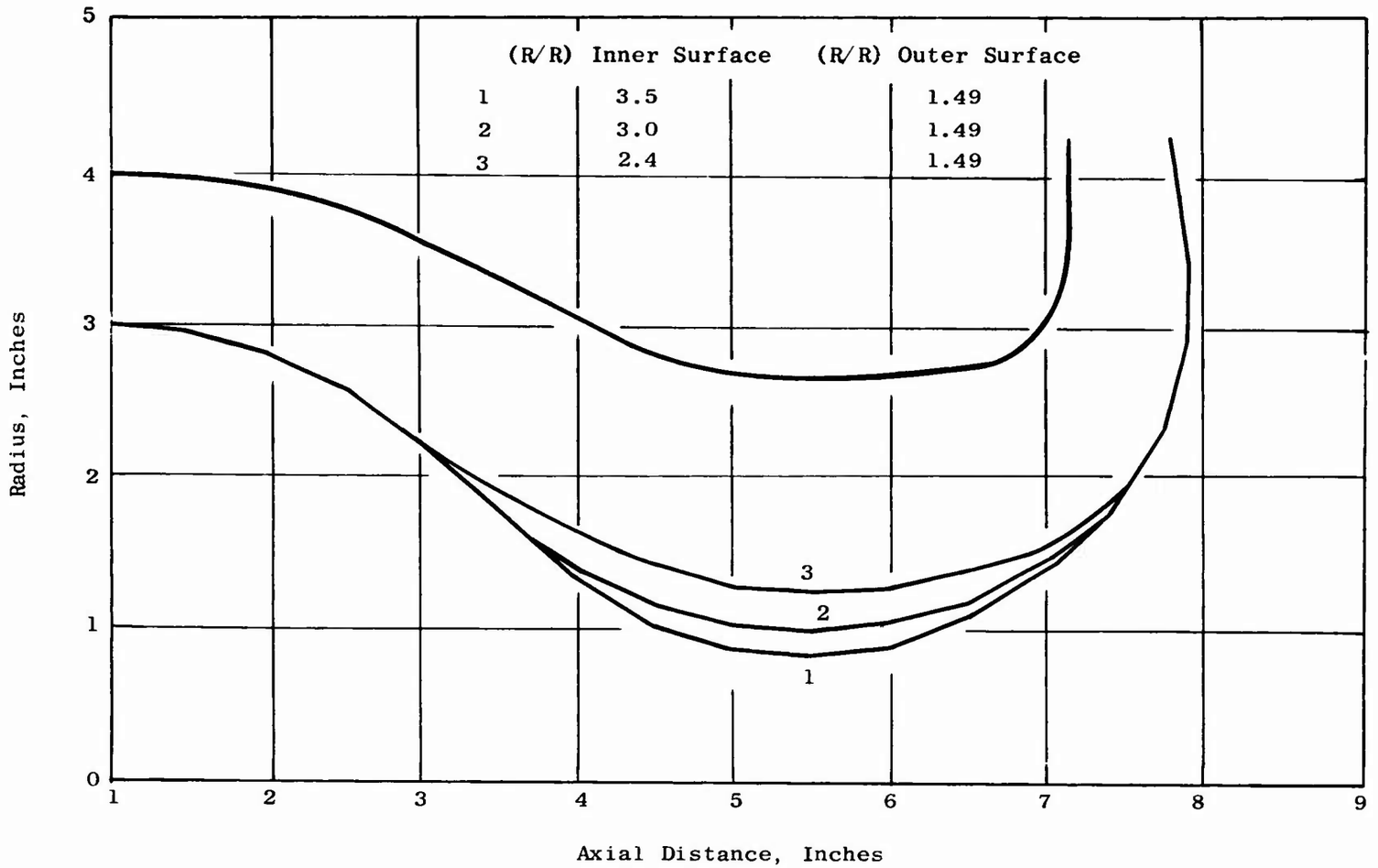

Figure 1. Variations in Inlet System Contours Used in Calculating Modified Inlet.

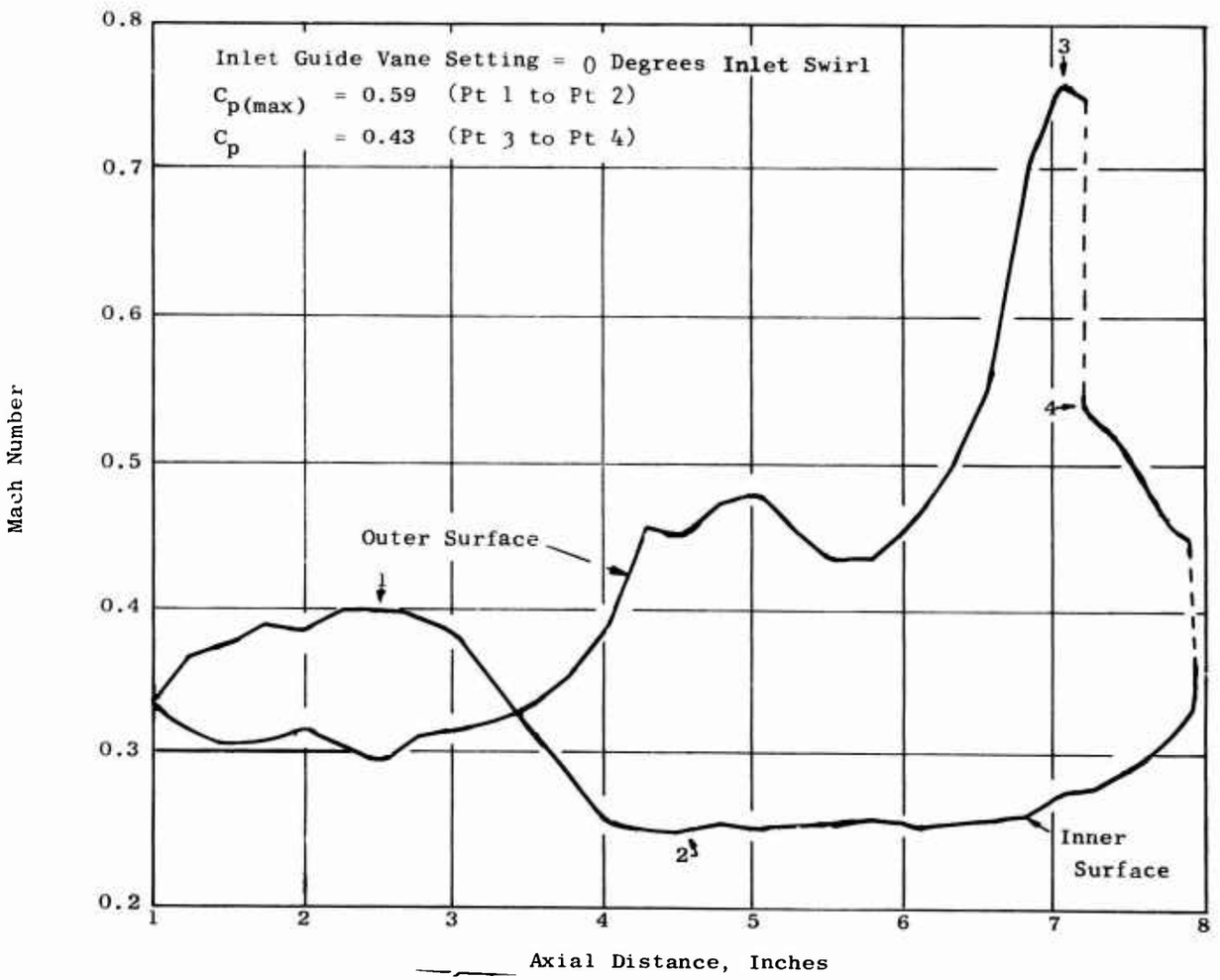

Figure 2. Calculated Mach Numbers Through Compressor Inlet for Profile No. 1.

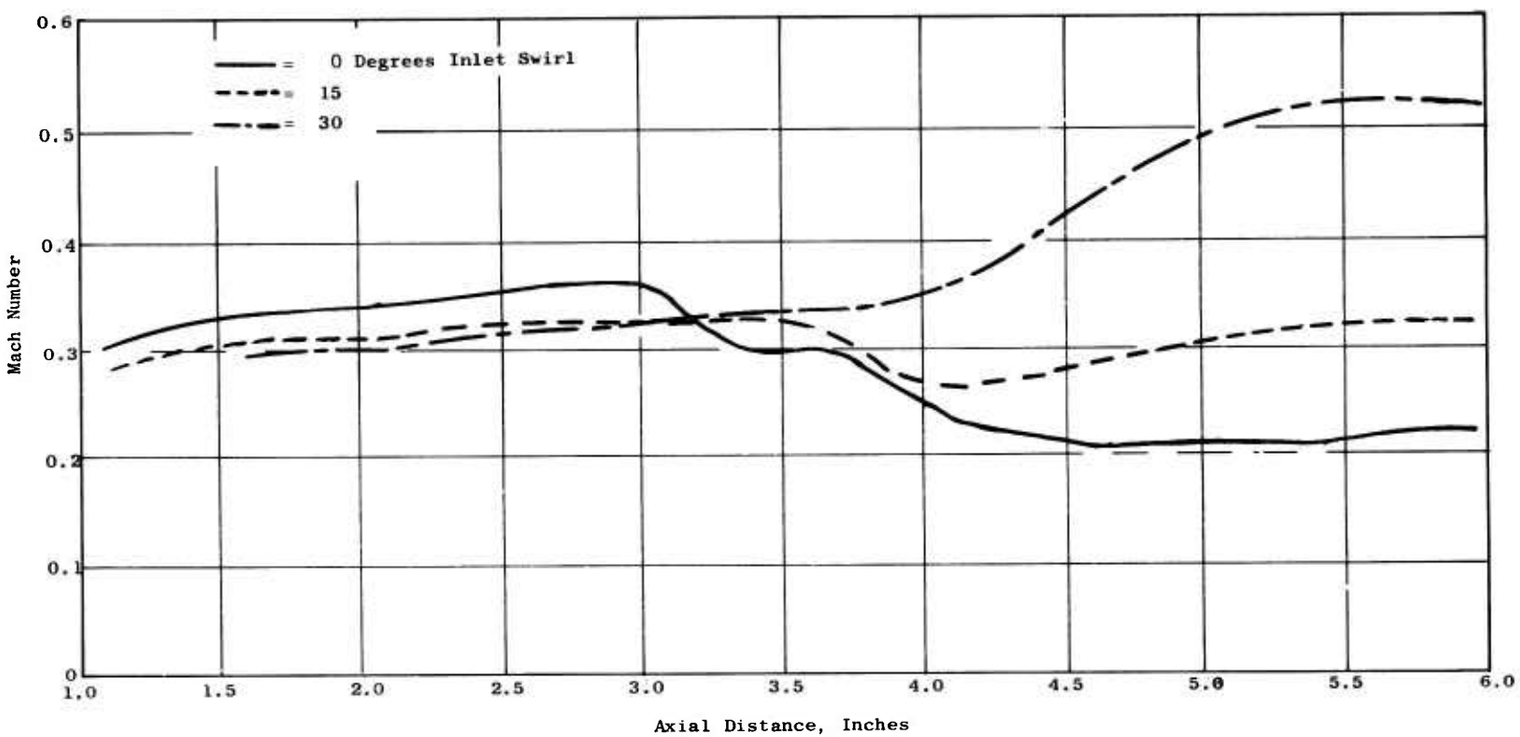

Figure 3. Mach Number Distribution Over the Inner Surface of Profile No. 1 With 0, 15, and 30 Degrees Swirl.

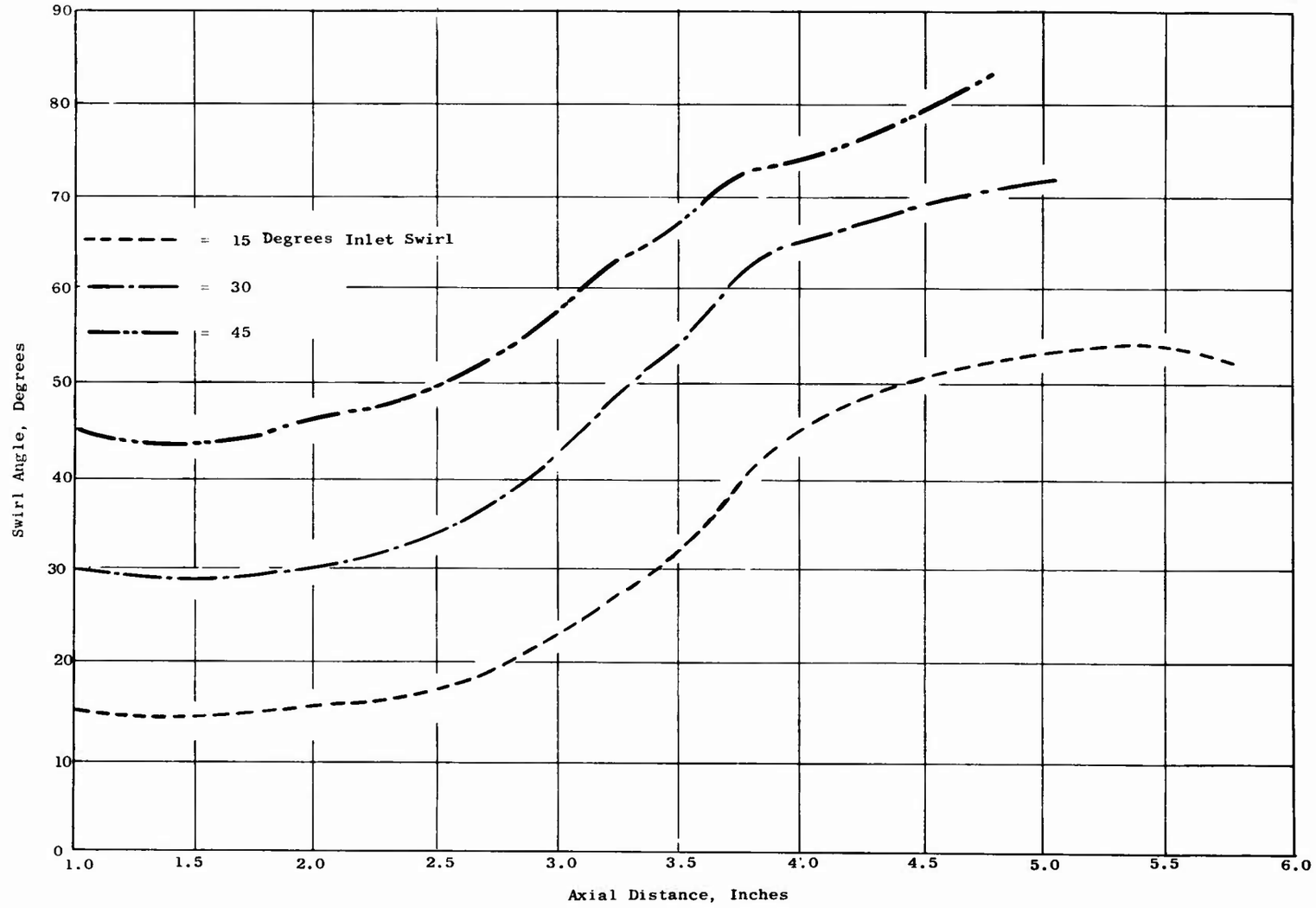

Figure 4. Flow Angle Distribution Over the Inner Surface for Profile No. 1 With 15, 30, and 45 Degrees Swirl.

The CAFD program also calculates the axial velocity component, and these results are presented in Figure 5. This figure indicates that a significant decrease in the axial component of velocity occurs for all inlet swirl angles even though the total component of velocity does not decrease as much for 15 degrees of swirl as for zero swirl; it may increase, as in the case of 30 degrees of swirl shown in Figure 3. The axial component of velocity decreases for 15 degrees of inlet swirl angle from a maximum of 317 feet per second (fps) at station 1.6 to a minimum of 179 fps at station 4.0. The significance of this reduction in axial velocity is not clear, but it may account for the high losses observed in the high-speed ROC. For higher swirl angles, an even larger decrease in axial velocity is calculated. In fact, for the 45-degree inlet angle case, the program broke down, since an axial velocity value approaching zero apparently resulted.

The validity of using an artificial static pressure rise coefficient based on the axial component of velocity (particularly in a case where a static pressure drop actually occurs) is of course questionable and is not presented herein, although high adverse values can be calculated on this basis. For positive swirl angles, the centerbody surface is rotating in the same direction as the tangential component velocity, and beyond the 5.5-inch station, the effect of centrifugal force on the boundary layer particles will be to propel them in the downstream direction. These latter 2 facts give reason to think that the high-speed inlet may be satisfactory; but at the same time, the decrease in the axial component of velocity provides an explanation of why the inlet may show unsatisfactory inlet velocity profiles even though the actual static pressure distribution may have only a moderate static pressure rise, or in the case of the 30 degrees and greater swirl, a falling static pressure.

Inlet Contour Number 2

The Mach number distribution over both the inner and outer contours of the modified high-speed inlet Profile Number 2 calculated by the flux plot program is shown in Figure 6. The reduction in Mach number over the inner contour which occurs between stations 2.5 and 4.0 results in a static pressure rise coefficient of 0.51 which is somewhat reduced below the comparative value (0.59) for the original design of this high-speed inlet. Some improvement of the inlet flow profile entering the rotor blades would be expected if Modification Number 2 is employed in the high-speed inlet system.

Inlet Contour Number 3

The somewhat more extensive modification to the high-speed inlet described as Profile Number 3 is used in the calculated results shown in Figures 7, 8, and 9. In Figure 7, the Mach number distribution calculated using the flux plot program indicates only a small amount of diffusion between stations 2.5 and 4 for this modification to the inlet. The static pressure rise coefficient calculated for the flow up to this point is 0.222.

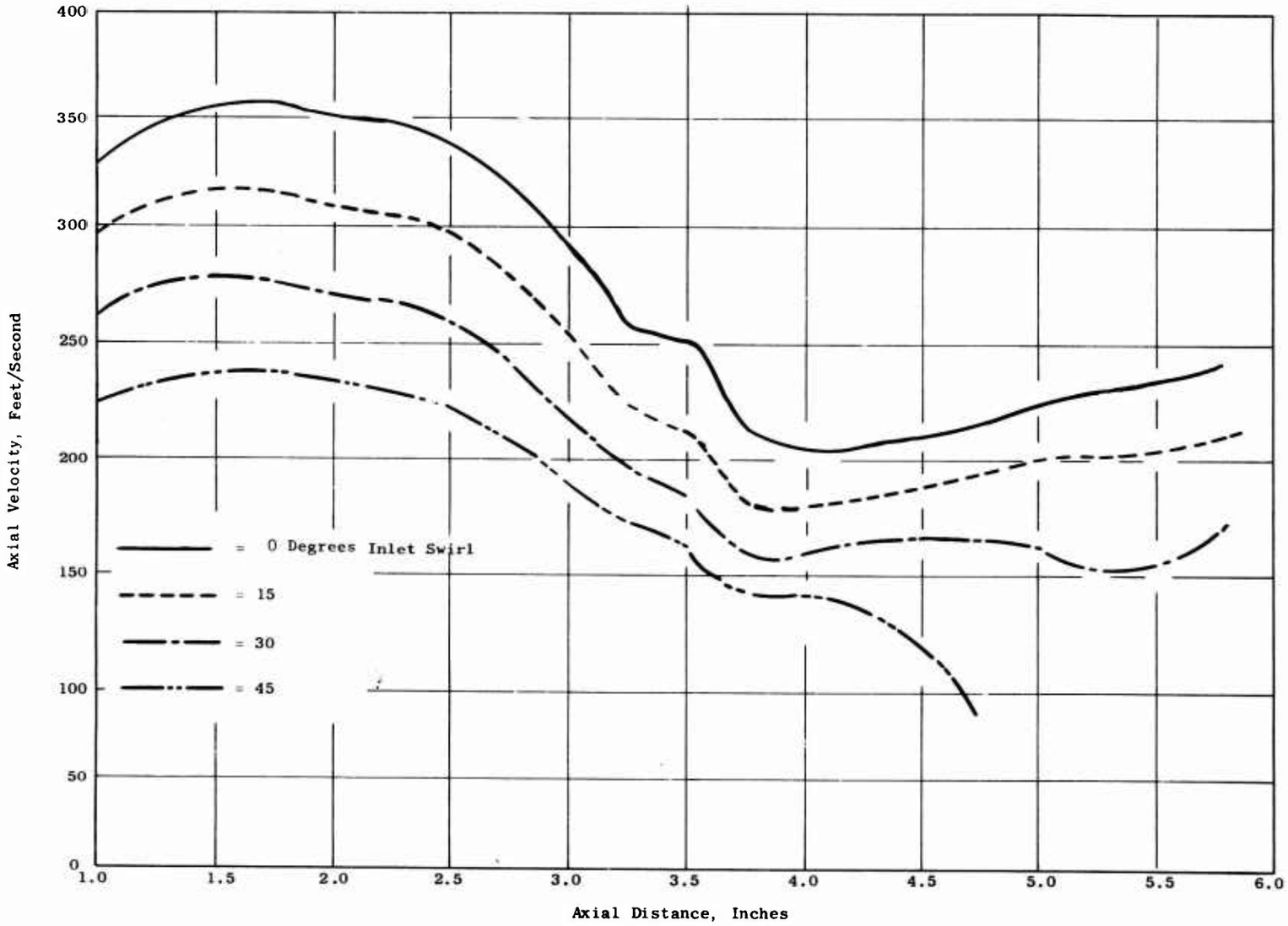

Figure 5. Axial Velocity Distribution Over the Inner Surface of Profile No. 1 With 0, 15, 30, and 45 Degrees Swirl.

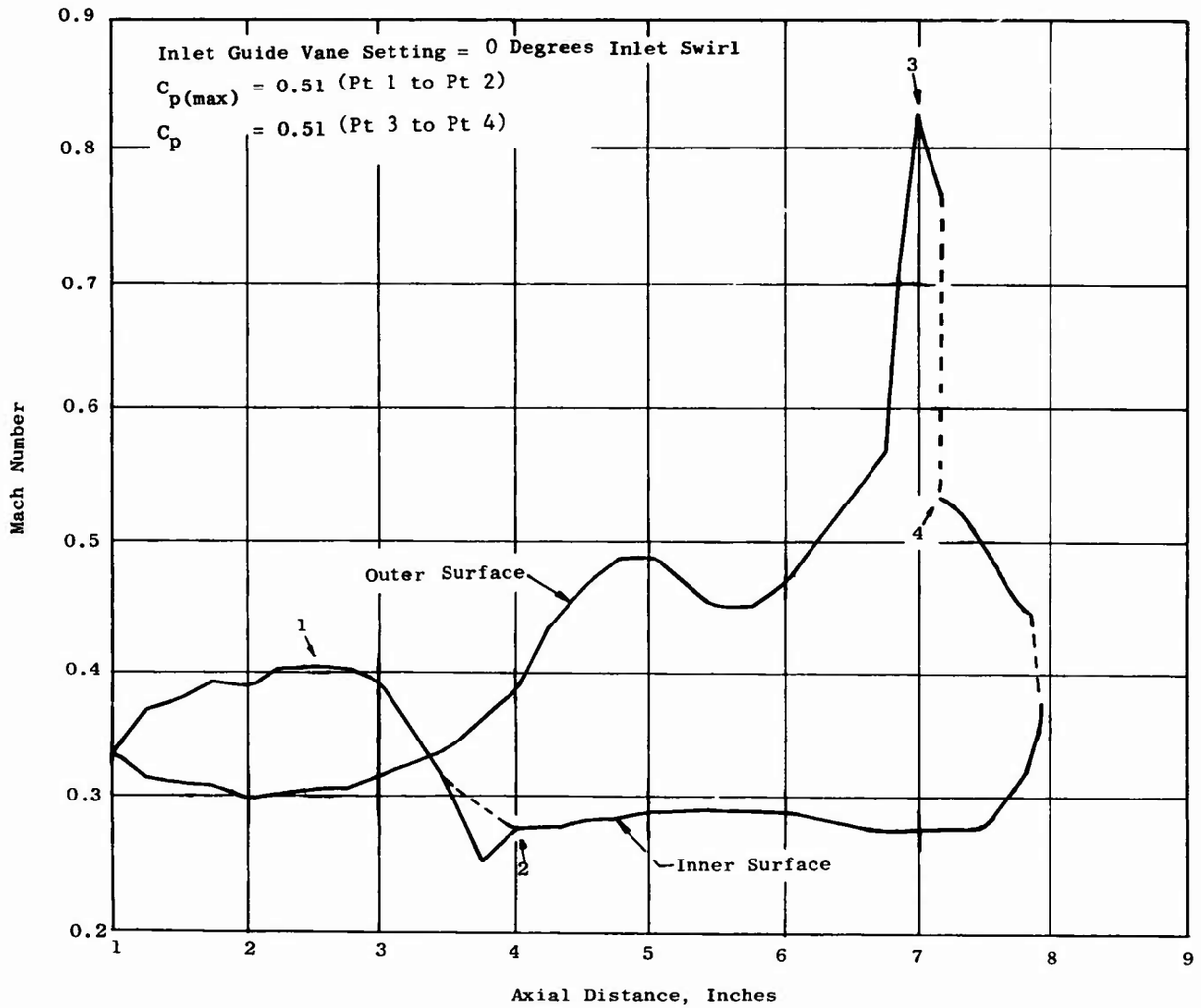

Figure 6. Calculated Mach Numbers Through Compressor Inlet for Profile No. 2.

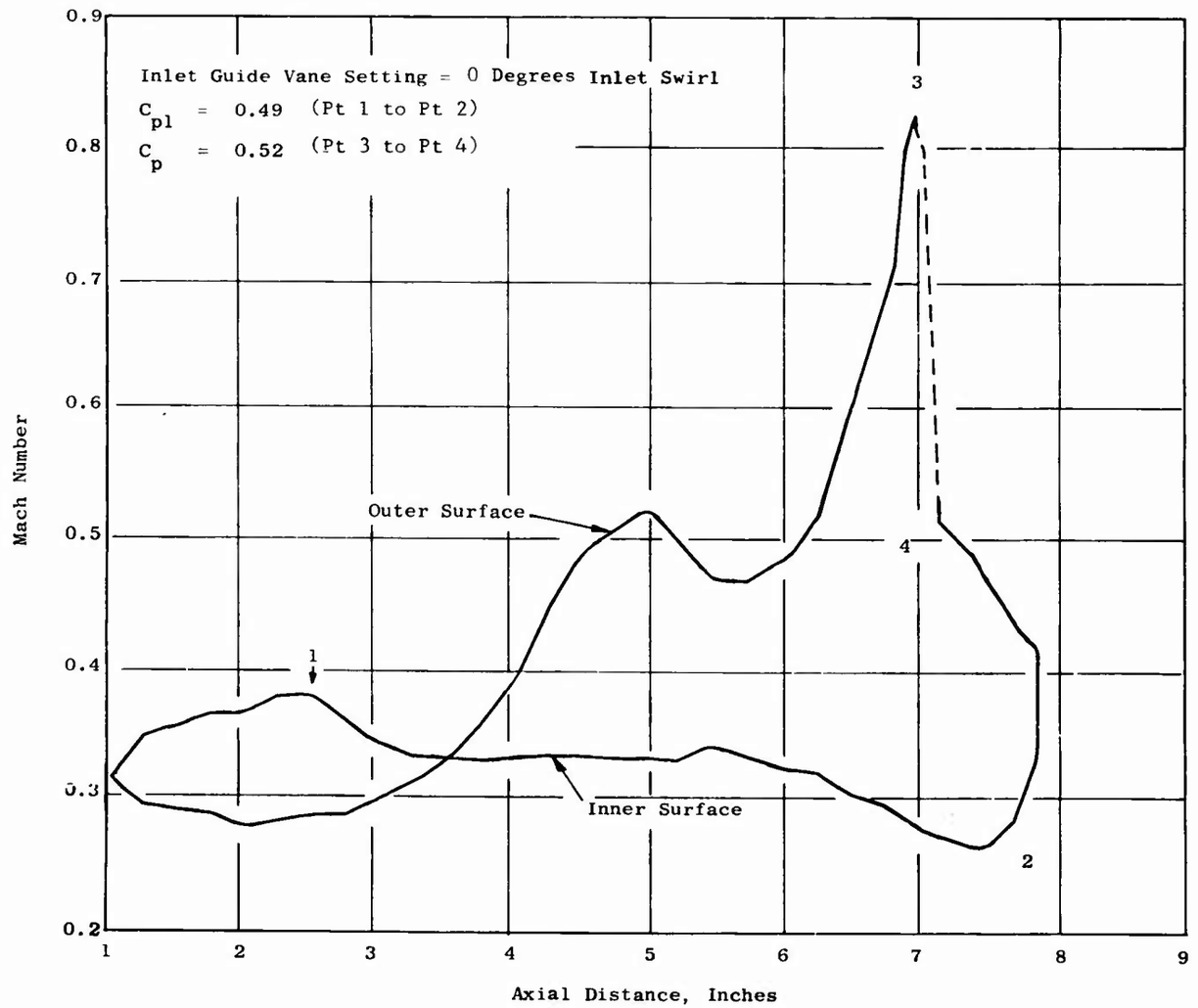

Figure 7. Calculated Mach Numbers Through Compressor Inlet for Profile No. 3.

Further diffusion occurs between stations 5.5 and 7.5; however, the value calculated between stations 2.5 and 7.5 is 0.49. Although this static pressure coefficient is of significant magnitude, it will be noted that most of this diffusion occurs in the outward turn portion of the inner profile; over this portion, the centrifugal force effects on the boundary layer are beneficial.

Comparative calculations for the inlet swirl angles of 0, 15, 30, 45, and 60 degrees are shown in Figure 8 over the inner contour of the flowpath and in Figure 9 over the outer contour of the flowpath. The effect of the tangential velocity imparted by the inlet guide vanes is to reduce the diffusion which occurred over the inner contour for the condition without inlet swirl. Therefore, the effect of swirl is to increase the Mach number over the inner surface and, as is seen in Figure 9, to decrease the Mach number that occurs over the outer contour of the inlet flow passage. Another important effect of inlet Profile Number 3 is to reduce the maximum value of swirl angle that occurs over the inner inlet flowpath as illustrated in Figure 10. For example, with 15 degrees of inlet guide vane turning, the maximum value that occurs at station 5.0 is 33 degrees compared to the maximum value of 54.4 degrees which was calculated at station 5.25 for the original design (Contour Number 1) high-speed inlet flowpath. Unfortunately, the CAFD program cannot accept radial flow or nearly radial flow. This condition occurs with these inlet systems as the flow approaches the rotor blades. It was necessary to end the calculations at a station significantly upstream of the rotor blades, and station 5.75 was chosen as the end point of this calculation. There is little question but that the low Mach number calculated for Profile Number 3 at station 7.5 would be increased when a swirl velocity is imposed on the flow in the inlet, and that the overall static pressure rise coefficient would be significantly reduced.

A tentative explanation for the differences observed in the performance of the radial inflow and axial flow inlet guide vane system can now be postulated.

Although the radial inflow and the axial flow inlet guide vane systems are quite different in physical arrangement, the flow conditions for a given inlet swirl angle are probably similar. A significant difference is the increase in the axial velocity that occurs in the axial flow system downstream of the inlet guide vanes as the flow passes over the convex inner contour. The radial inflow system does not have convex curvature on the inner surface contour and therefore should exhibit lower maximum values of axial velocity and a significantly lower static pressure rise coefficient (or ratio of maximum to minimum axial velocity, if this ratio is a critical parameter.

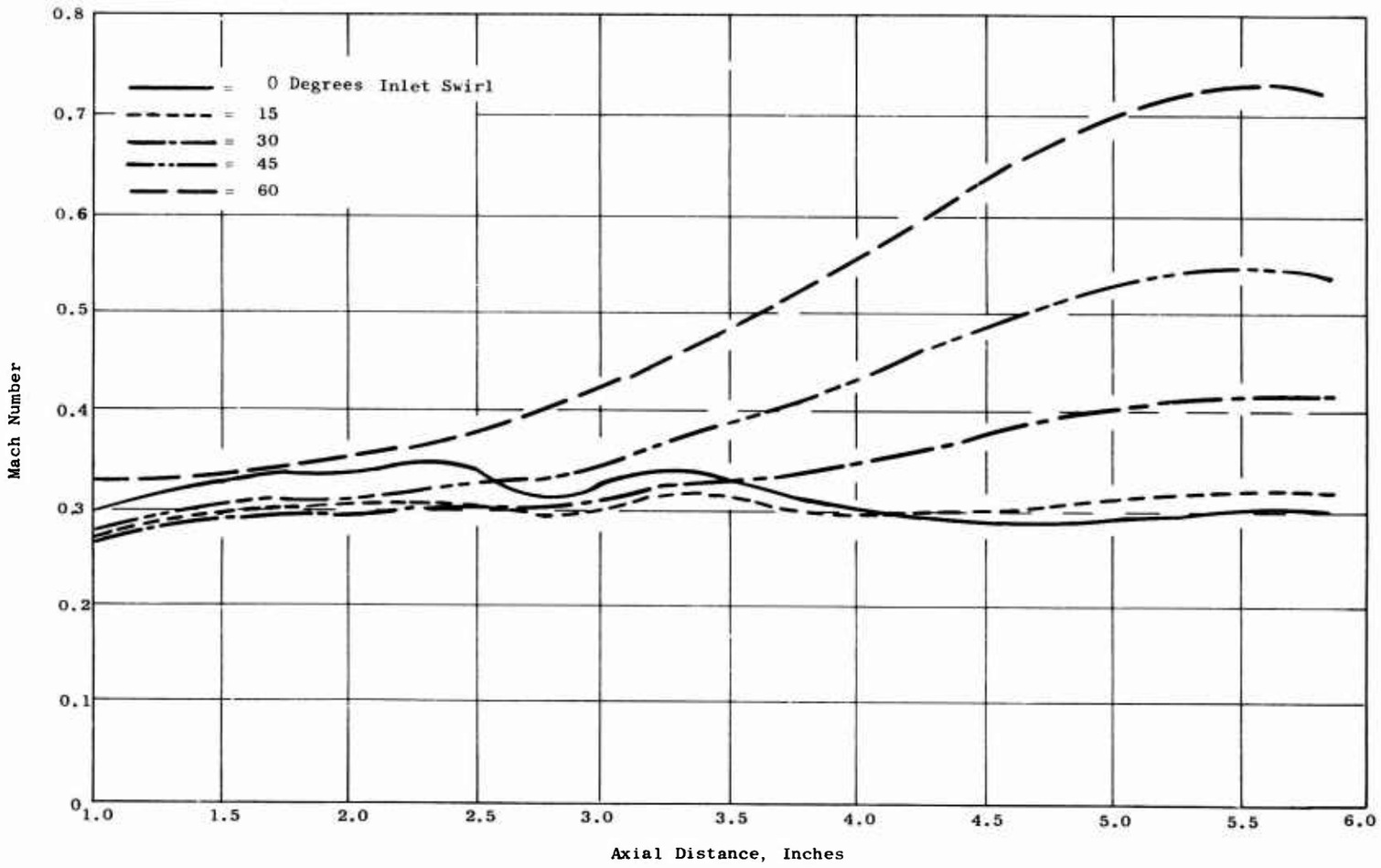

Figure 8. Mach Number Distribution Over the Inner Surface of Profile No. 3 With 0, 15, 30, 45, and 60 Degrees Swirl.

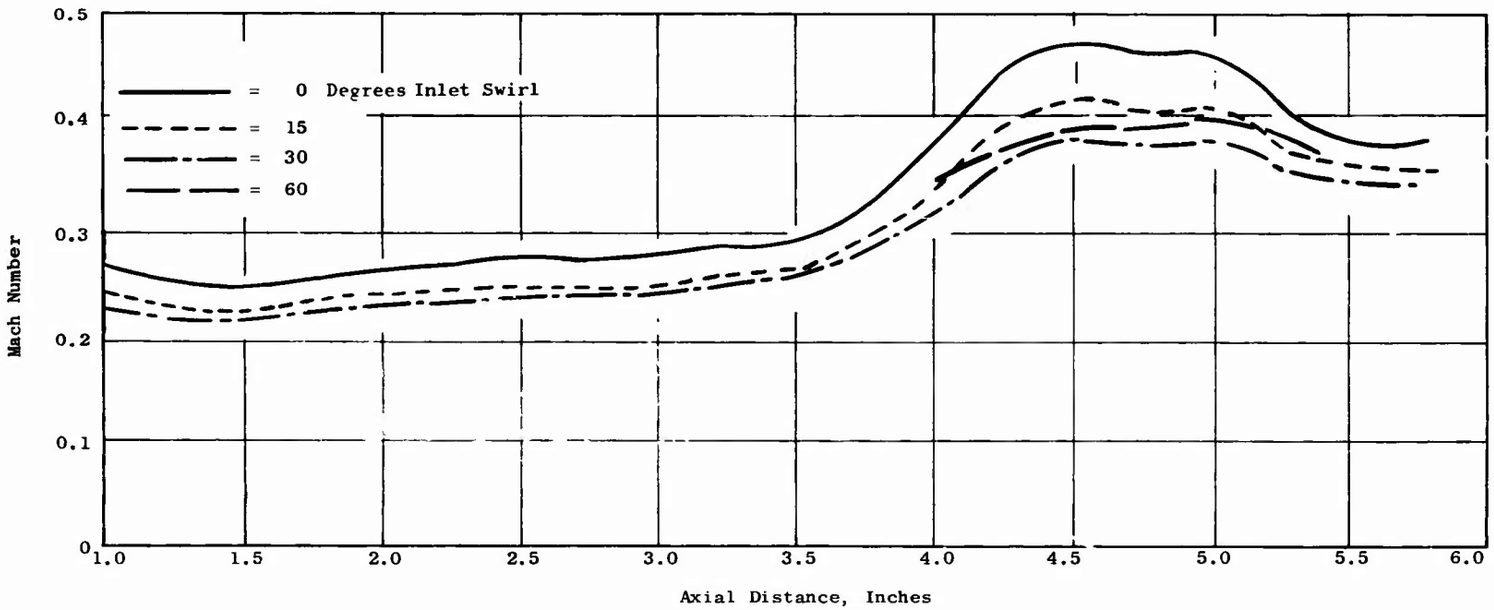

Figure 9. Mach Number Distribution Over the Outer Surface of Profile No. 3 With 0, 15, 30, and 60 Degrees Swirl.

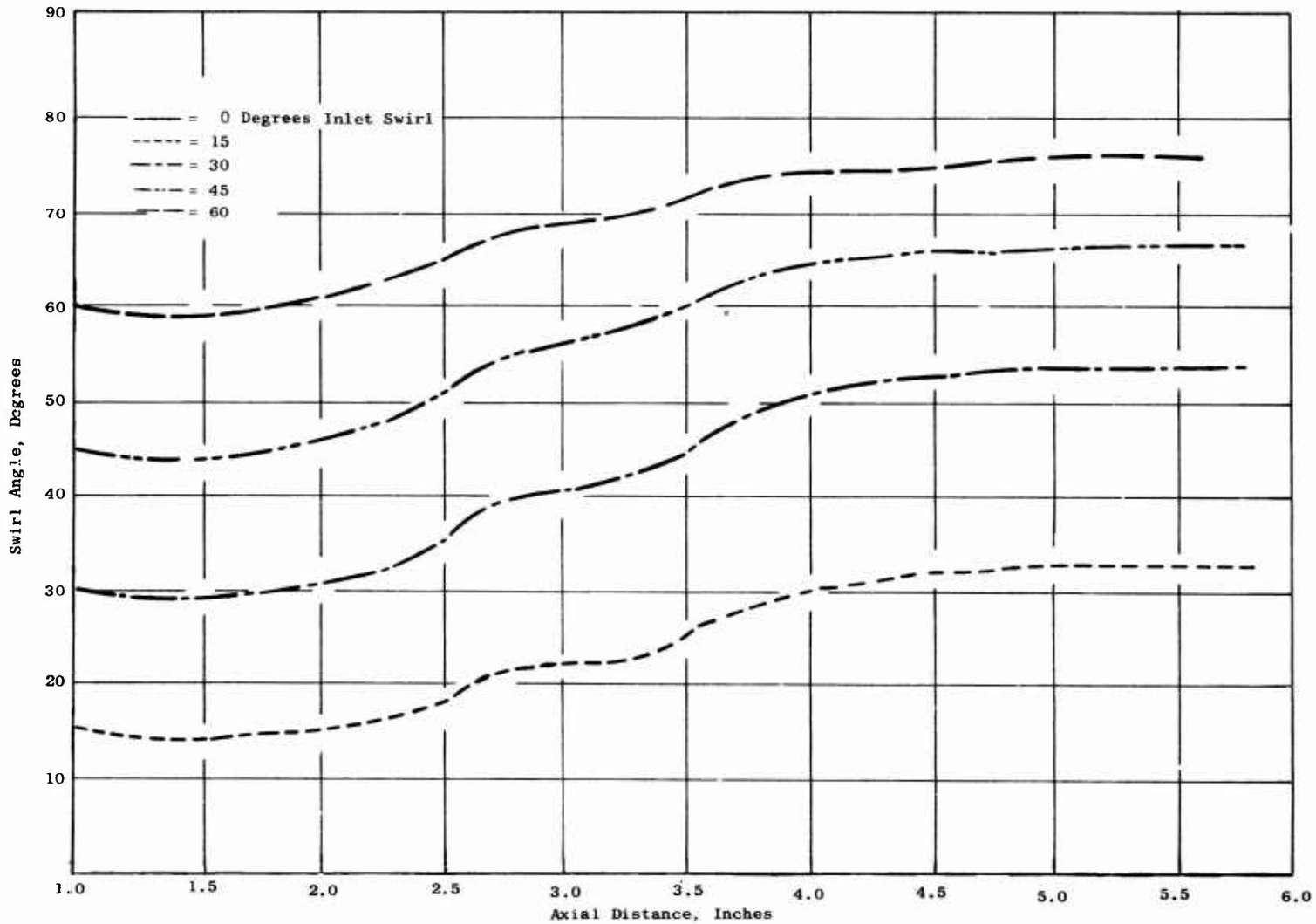

Figure 10. Flow Angle Distribution Over the Inner Surface of Profile No. 3 With 0, 15, 30, 45, and 60 Degrees Swirl.

ROC ROTOR BLADE DESIGN

A basic difference between radial flow and axial flow turbomachinery is that in axial flow design it is generally possible to make direct use of cascade data, whereas in radial flow design such is not the case. The reason for this is that in radial flow turbomachinery, the Coriolis and centripetal accelerations predominate over the flow deflection effects. A major design intent of the ROC is to employ low radius ratio, high turning impulse blade sections to make cascade experience at least indirectly applicable.

Preliminary investigations indicated that the rotational effects are still strong enough to require some method of transformation between the cascade and the compressor. Fortunately, the blades are fully supersonic at the design point and have an axial span, so that the method of characteristics is applicable. The characteristic equations were modified to account for the fact that the blade coordinate system rotates, and the resulting equations were programmed in the Method of Characteristics Program (MOC). The equation and program represent a transformation tool; unfortunately, they do not represent a transformation technique. For this purpose, 2 design models were available.

1) The one-dimensional compressor analysis which accounted for blade losses and blockage effects.

2) The two-dimensional cascade blade analysis which had neither losses nor blockage.

One possible approach to the design problem would be to eliminate the losses from the one-dimensional analysis and to obtain from this calculation the lossless work input (force) per blade. Using the ideal two-dimensional cascade calculation of Mach number versus chord as a guide, an ideal Mach number versus chord specification should, when converted to surface pressures and integrated, yield a force per blade consistent with the lossless one-dimensional calculation. This distribution could then be run through MOC to provide a blade passage contour. It should be expected that this contour, when converted into a blade, would close properly at the trailing edge. However, after sufficient trial and error, the modification necessary to close the blade should not be large. This approach is relatively simple and straightforward, and since the design model is lossless, it is completely consistent with the blade analysis method. However, the blade so designed may not be acceptable in the real flow case because of excessively thin leading and trailing edges. In addition, this method does not allow more than an indirect control over the blade surface Mach number distribution.

An alternate method intended to alleviate the above defects would be to calculate the force per blade required from the one-dimensional performance calculation with losses. Then, again using the two-dimensional

blade as a guide, a Mach number versus chord distribution could be generated which is equivalent to this force per blade. This distribution would then be used to generate a blade contour in the MOC program. However, in this instance, the program input and output would be modified to include loss and blockage effects. This input modification might consist of a simple increase in the rate of spanwise wall contraction (to account for wall boundary layer blockage) and a modified value of γ (to account for any distributed wave losses). In this case, the computed profile shape should be sufficiently open at the trailing edge to allow the actual profile to be constructed by subtraction of the estimated wall boundary layers. Since this approach strains the analysis capability by including lumped real flow effects, it would not be a straightforward technique.

In both design methods described above, the final specification of the blade trailing edge can be made by hand. There are basically two methods of doing this:

1) Simply bring the blade to a close with the proper mean metal angle (corrected for blockage effects).

2) Fair the trailing edge into a best-guess trailing edge streamline (similarly corrected).

The latter method should give a more lightly loaded trailing edge.

Due to lack of time, neither method was used in the actual ROC blade design. Instead, the cascade blade Mach number distribution was simply reproduced in the rotor design (no losses) and the trailing edge was closed as per item 1 above. Although the work input is of proper magnitude, the Mach number distribution is not closed at the trailing edge. In general, this has two adverse effects:

1) A violent adjustment in the form of shocks and expansion waves is called for at the trailing edge to match suction and pressure surface discharge pressures (in the real flow cases, such as adjustment would be modified by the boundary layer).

2) An increase in downstream losses occurs due to mixing.

A comparison between the one-dimensional calculations with and without losses is given below:

	Losses	No Losses
P/P, atm	2.45	2.75
P_{s3}, atm	0.571	0.464
M_{2R}	1.61	1.82
T, deg	646	722
F_B, lb	5.27	5.89

The Mach number distribution which was used to define the initial 85-90 percent of the ROC rotor blade had a total calculated ideal work input of 5.80 pounds per blade.

Despite the fact that the trailing edge was slightly modified in closing the blade profile and that the real flow effects will have a pronounced effect on the actual blade behavior, it was felt that the open Mach number distribution could be a source of trouble. In addition, due to manufacturing limitation, both the leading and trailing edges of the blade were cut back, hence reducing the physical chord. In order to allow the trailing edge flow more opportunity to adjust and at the same time to reestablish the physical chord length of the Phase III rotor blade, the trailing edges have been extended. These extended chord blades have been used in Buildup F of the Phase II investigation (see section on High-Speed Compressor).

ANALYSIS OF VANELESS DIFFUSER HAVING ROTATING WALLS

The purpose of the vaneless diffuser is to raise the static pressure of the flow from a subatmospheric value at the rotor blade exit to several atmospheres at the rotor exit. Since the pressure rise takes place in a short radial distance, 2.2 inches, the radial static pressure gradient is expected to be quite large. Figure 11 is a plot of the calculated static pressure gradient as a function of radius for the free stream and for the boundary layer at corrected speeds of from 30 to 80 percent. Maximum values of static pressure gradient greater than 1 atmosphere per inch are calculated to occur at the rotor blade trailing edge radius of 4.3 inches. The gradient decreases rapidly toward the rotor exit, and at 80 percent speed is 0.55 at the rotor exit radius of 6.5 inches.

The static pressure gradient that is experienced by air particles in the boundary layer rotating at the speed of the wheel is a beneficial effect. Calculated values for the various rotational speeds from 30 to 80 percent are shown in Figure 11 (subsonic rotor blade exit Mach number) and in Figure 12 (supersonic rotor blade exit Mach number) as dashed lines. The static pressure gradient of the boundary layer is small at the rotor blade

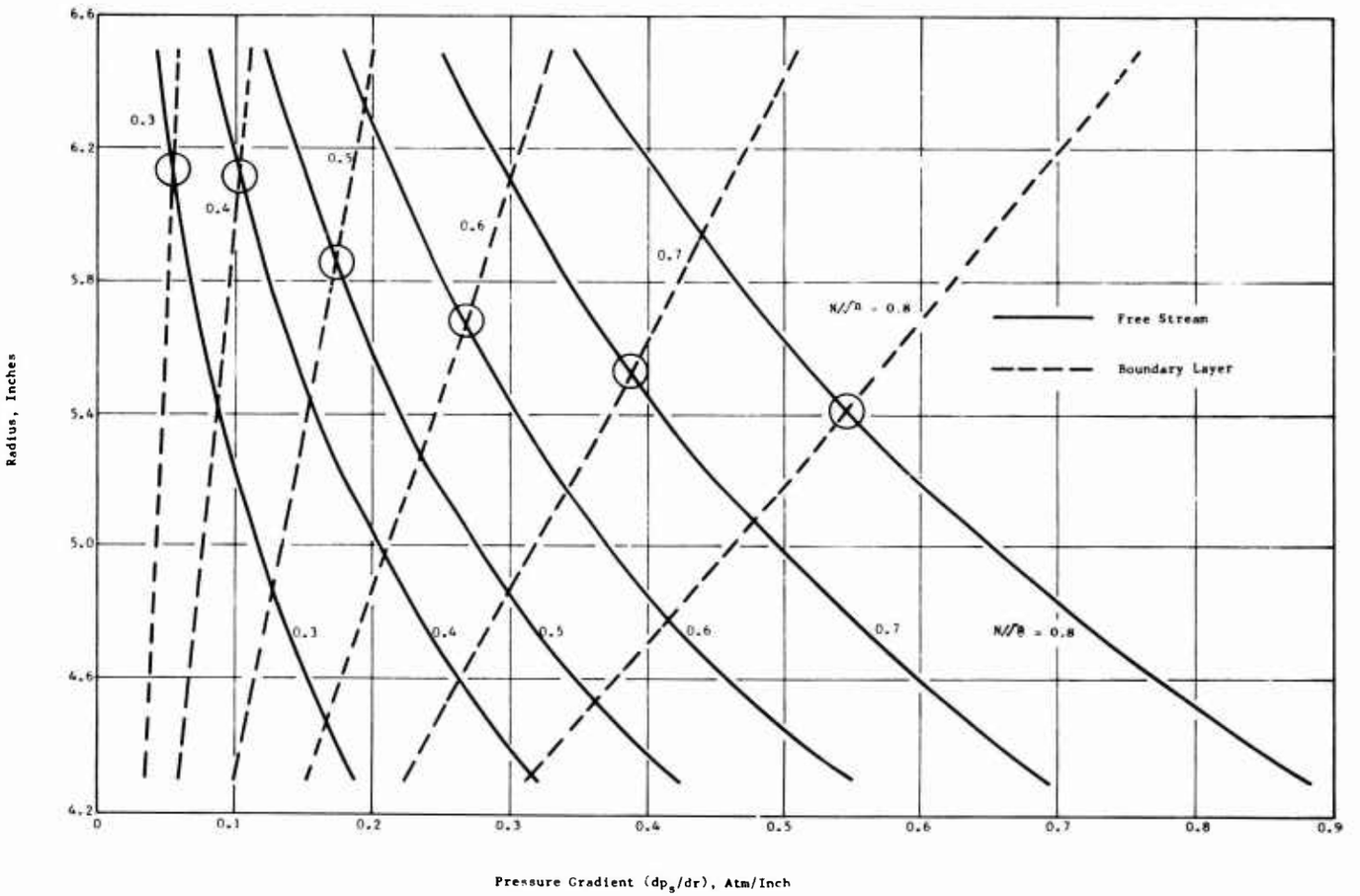

Figure 11. Radial Pressure Gradient Calculated for the Free Stream and for the Boundary Layer for Subsonic Flow.

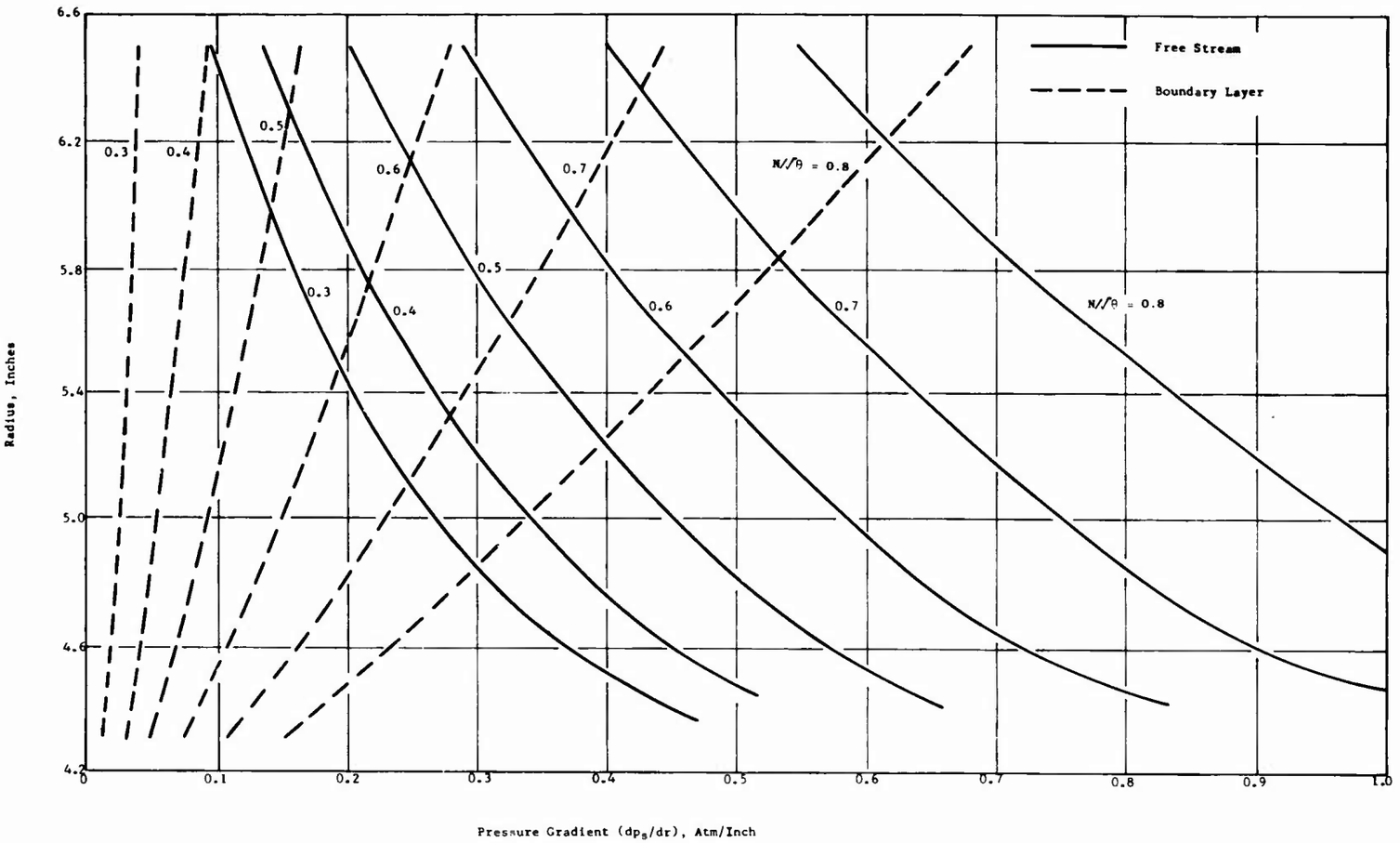

Figure 12. Radial Pressure Gradient Calculated for the Free Stream and for the Boundary Layer for Supersonic Flow.

trailing edge, about 0.15 atmosphere per inch. At larger radii this gradient is significant, reaching a value of 0.68 at the rotor exit, which is larger than the calculated free stream static pressure gradient at that radius. The difference between the free stream and the boundary layer static pressure gradient, normalized by a suitable local dynamic pressure, is believed to be a measure of the aerodynamic loading. It is not yet clear, however, what the most significant normalizing parameter should be nor what the limiting value of the normalized static pressure gradient (or its integral) will be. Further discussion of this problem is presented in "General Analysis of Low-Speed Rotating Diffuser Research" on page 116.

Only the radial component of the dynamic pressure is believed to be effective in resisting the tendency of the radial static pressure gradient to drive the boundary layer inward. Figure 13 is a plot of the free stream and boundary layer static pressure gradient divided by the classical dynamic pressure times the Cos of the angle θ between the relative velocity and the radial direction. Values are given for 30 percent and 100 percent speeds. Since the difference between the free stream and boundary layer static pressure gradients is important, this difference is plotted in Figure 14 using the same normalizing parameter used in Figure 13. This figure indicates that aerodynamic loading is much more severe for the 100 percent speed case than for the 30 percent speed case, and that the loading is severe over the inner half of the rotating wall vaneless diffuser at full speed.

If the radial velocity is the significant parameter, then the effective radial static pressure gradient should be divided by a dynamic pressure times $\text{Cos}^2\ \theta$. This relationship is plotted in Figure 15, and the difference between the free stream and the boundary layer values is plotted in Figure 16. Using this aerodynamic loading coefficient, the most severe condition occurs at a radius of about 4.85 inches. Although the value of the loading coefficient decreases rapidly with increasing radius from this point, the value corresponding to the maximum calculated at 60 percent speed is not reached until a radius of 5.5 inches has been reached. In tests of Buildup A through E, serious departure of ROC rotor performance from calculated values did not occur until speeds greater than 60 percent were tested (see High-Speed Compressor section).

Similar values for the radial pressure gradients in free stream and boundary layer and their differences have been calculated using the difference between relative total pressure and static pressure as the normalizing parameter. The effects of employing Cos θ and $\text{Cos}^2\ \theta$ in the denominator are generally similar to those using $1/2\ \rho\ V^2_{Rel}$ as the normalizing factor.

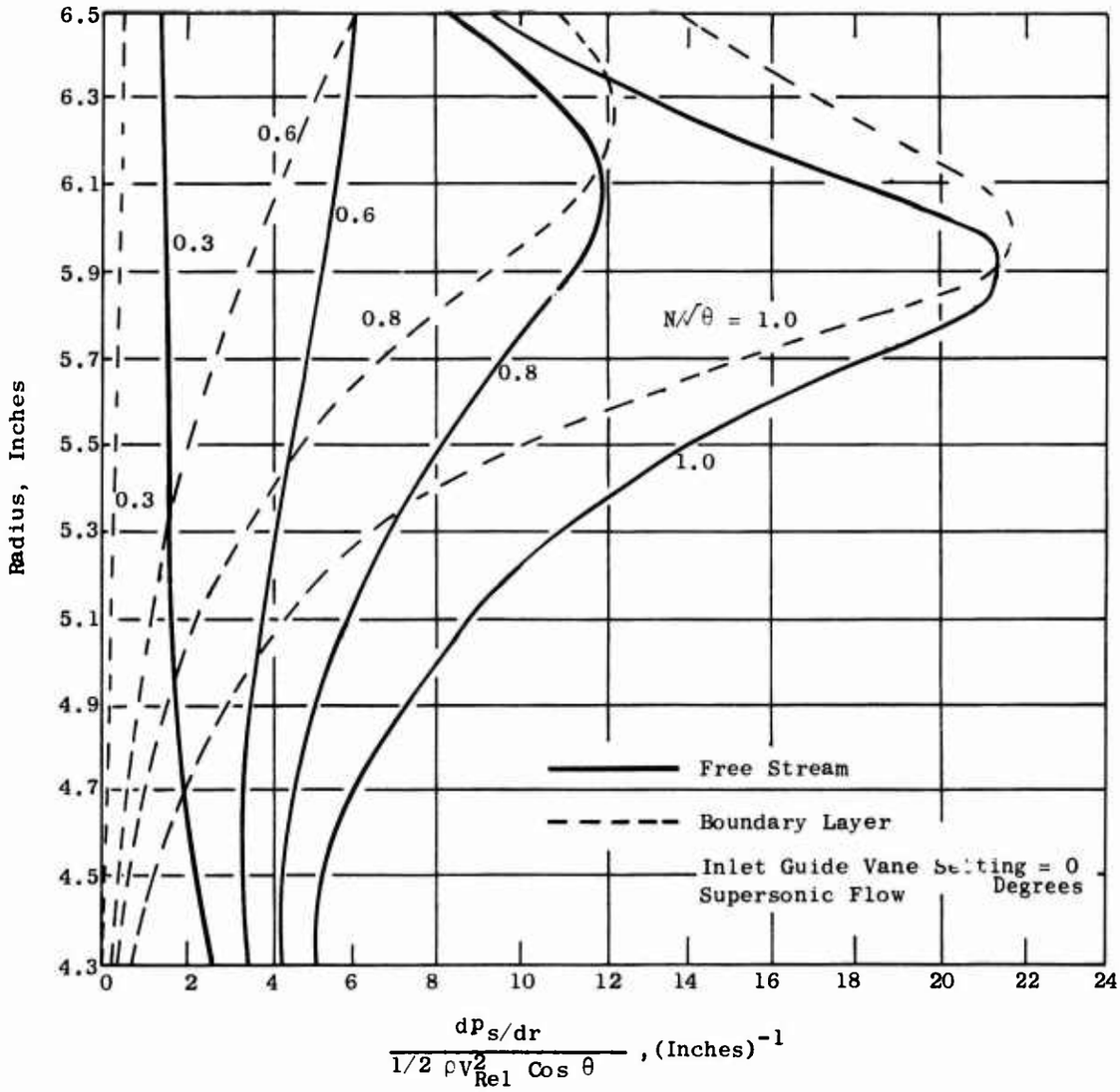

Figure 13. Radial Static Pressure Gradient Normalized by Relative Dynamic Pressure x Cos θ.

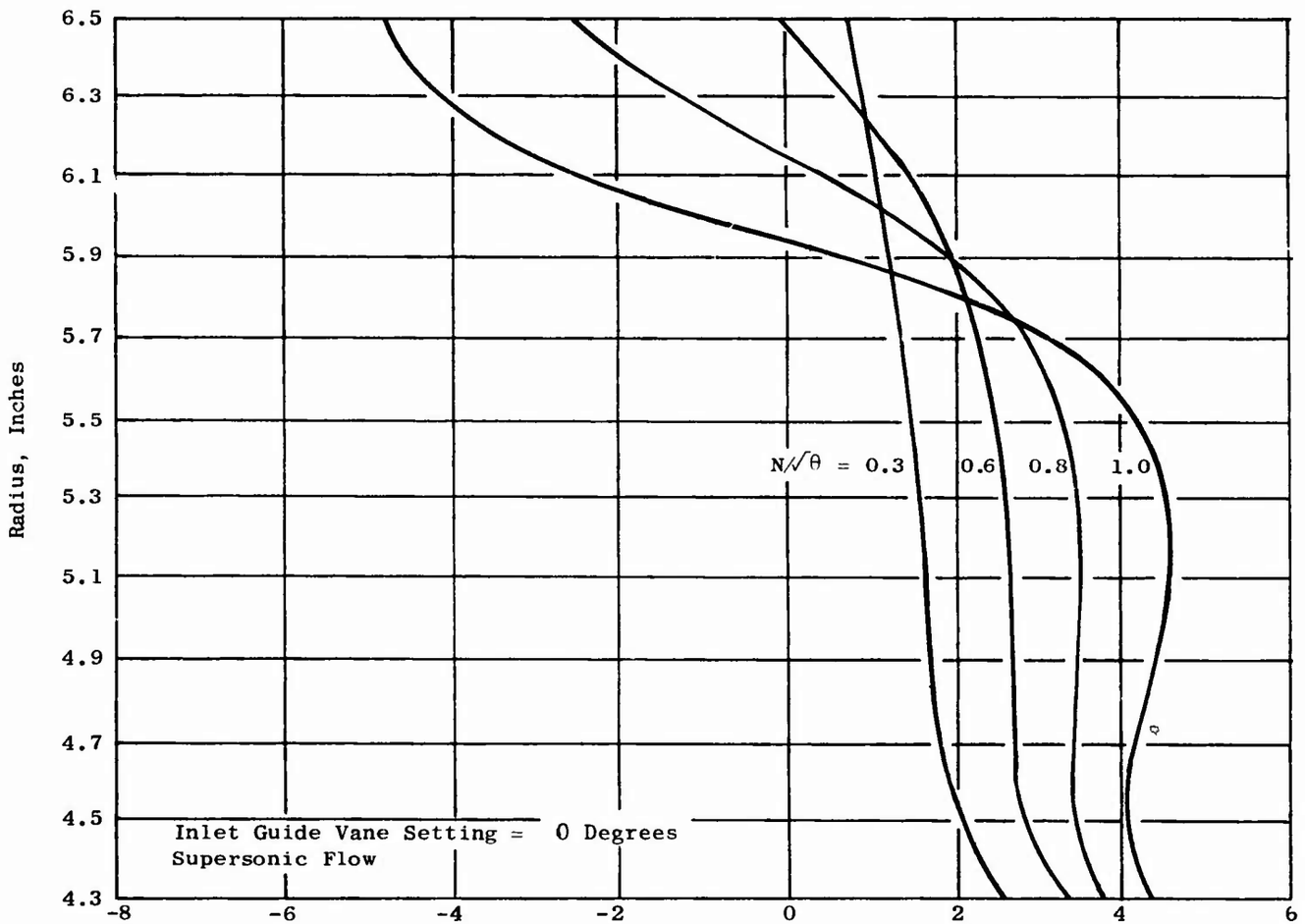

$$\frac{G_1}{r_2} = \frac{(dp_s/dr)_{FS} - (dp_s/dr)_{BL}}{1/2\ \rho\ V_{Rel}^2\ \cos\ \theta}$$

Figure 14. Effective Radial Static Pressure Gradient Normalized by Relative Dynamic Pressure x Cos θ.

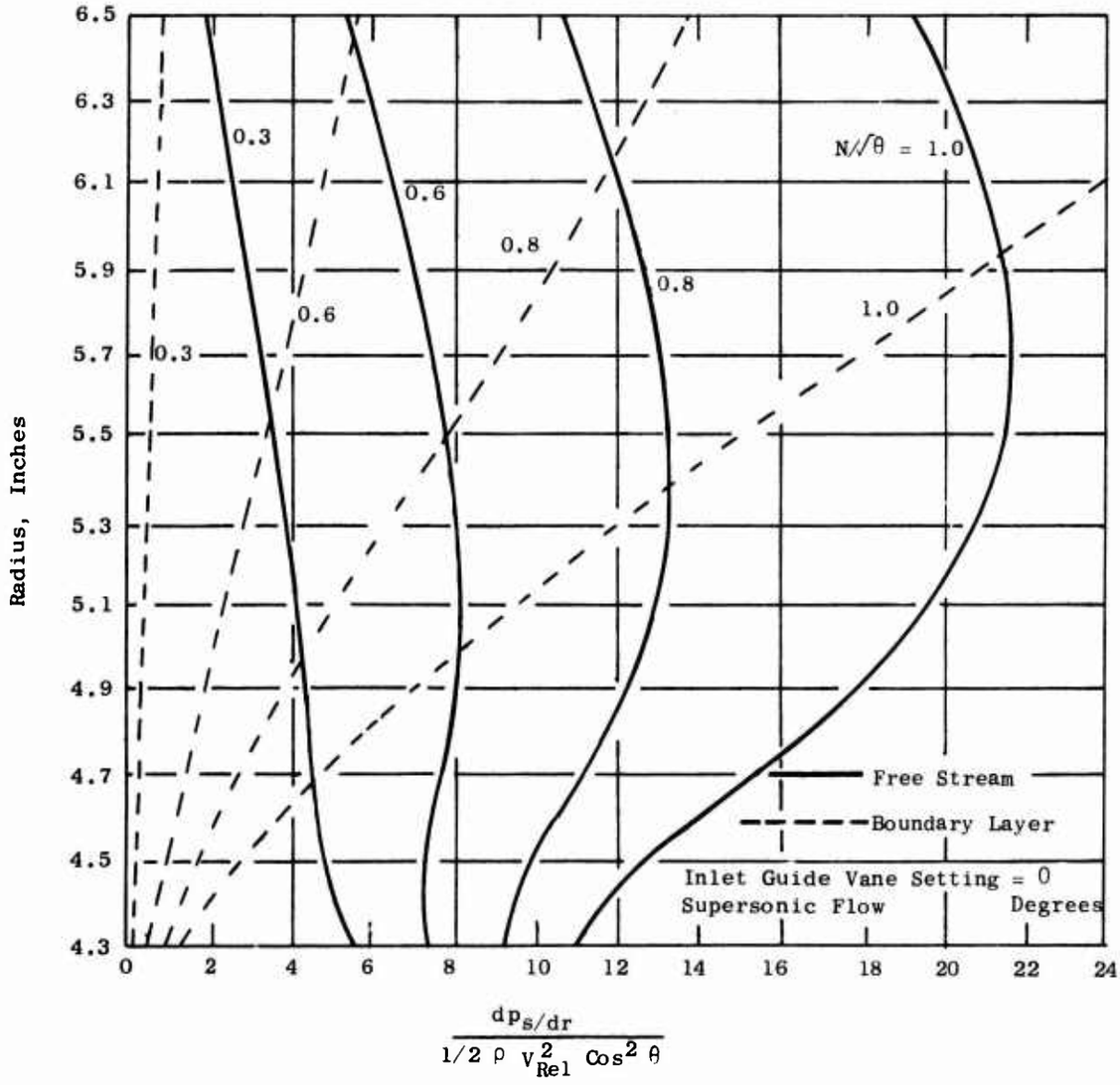

Figure 15. Radial Static Pressure Gradient Normalized by Relative Dynamic Pressure x $\cos^2 \theta$.

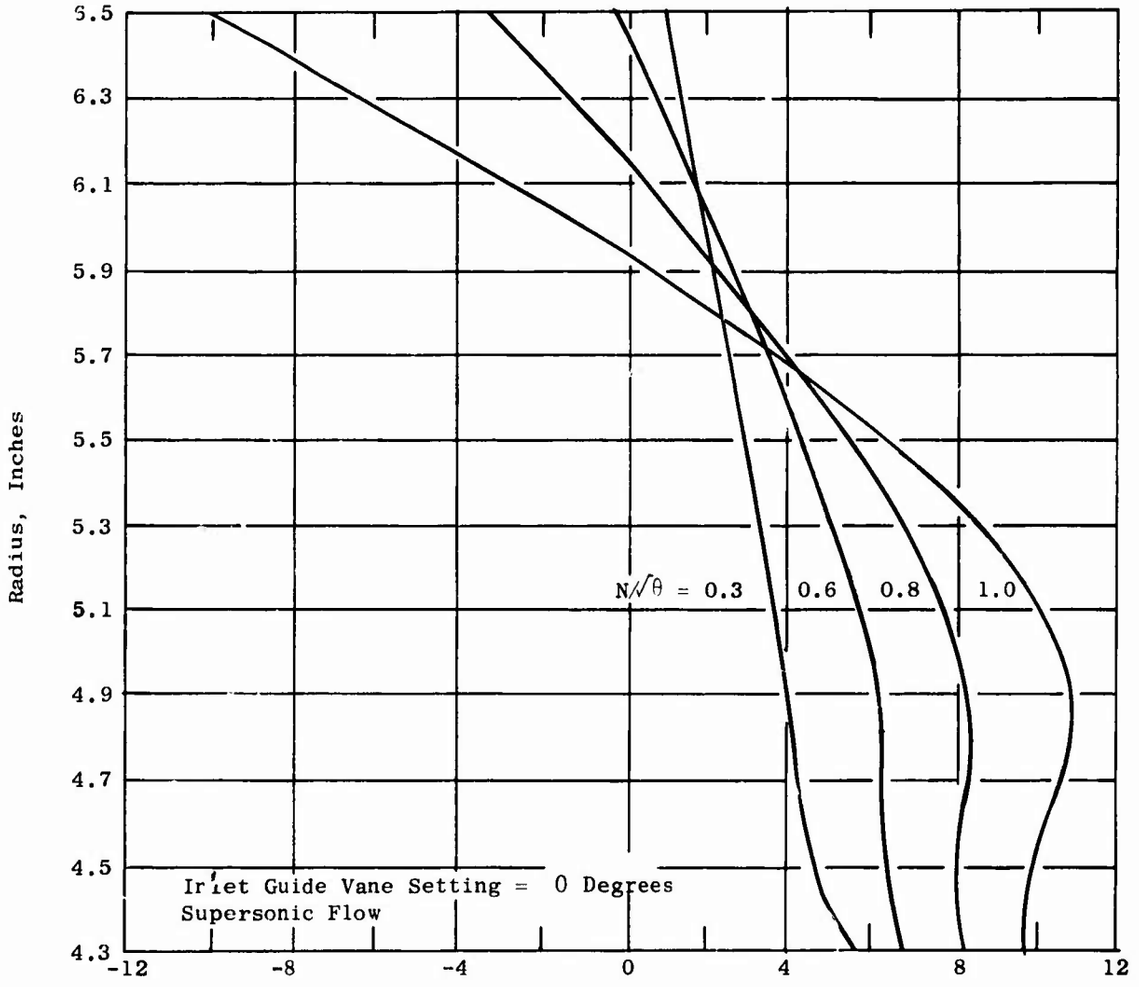

$$\frac{G_2}{r_2} = \frac{(dp_s/dr)_{FS} - (dp_s/dr)_{BL}}{1/2\ \rho\ V_{Rel}^2\ \cos^2\ \theta}$$

Figure 16. Effective Radial Static Pressure Gradient Normalized by Relative Dynamic Pressure x $\cos^2\ \theta$.

ANALYSIS OF MODIFIED ROTATING VANELESS DIFFUSERS

Major progress has been made in the analysis of the effective pressure coefficients calculated to exist within the rotating vaneless diffuser. Although sufficient information for selecting the best parameter to use as a load limit guide is not available, the parameter used on the accompanying figures exhibits the trends expected. The parameter plotted has the difference between the static pressure gradient in the free stream minus that in the boundary layer as the numerator, and the relative dynamic pressure times the Cos of the relative flow angle θ measured from the radial direction as the denominator. The search for improved parameters will continue and will include using the $\cos^2 \theta$ in the denominator. This parameter will show the same general trends but will indicate that the loading is concentrated in the inboard section of the diffuser. This appears to be more in line with observations of high-speed rotors (see section on High-Speed Compressor).

Figure 17 shows diffuser width variations (as a function of radius of the rotating vaneless diffuser) which have been studied and the original contour. To some extent, the contours shown represent the full range of possible width variations. The original contour was probably too heavily loaded in the inner regions, and Contour Number 4 was calculated to choke at the 4.9-inch radius at 60 percent speed and zero inlet guide vane turning.

High speed compressor tests (see section on High-Speed Compressor) have indicated relatively good correlation between predicted and experimental results at speeds up to 60 percent. Figure 18 indicates that at 60 percent speed, a value of the effective static pressure coefficient of about 3.0 is calculated to exist for either subsonic or supersonic flow leaving the rotor blades. This value can therefore be considered as a loading limit for the rotating vaneless diffuser.

At full speed and with inlet guide vanes set for zero turning (Figure 19), the original contour shows values of this coefficient above 4.0 for both subsonic and supersonic solutions. Contour Number 2 shows reduced values but exceeds 3.0 for supersonic rotor blade exit flow in the mid-region of the diffuser. Contour Number 3 indicates values below 3.0 at all radii, with the exception of the very beginning of the diffuser. An intermediate contour between numbers 2 and 3 will probably be the optimum shape on the basis of the loading parameter presented herein.

The original rotating vaneless diffuser pressure gradients have been calculated using the relative dynamic pressure times $\cos^2 \theta$. Results for 30, 60, 80, and 100 percent speed are presented in Figure 16 for zero inlet guide vane turning. As anticipated, the use of this parameter indicates that the aerodynamic loading is concentrated in the inner region of the diffuser. Again assuming that 60 percent speed was the dividing line between acceptable and unacceptable rotor performance, a value of this parameter of 6.4 can be considered limiting.

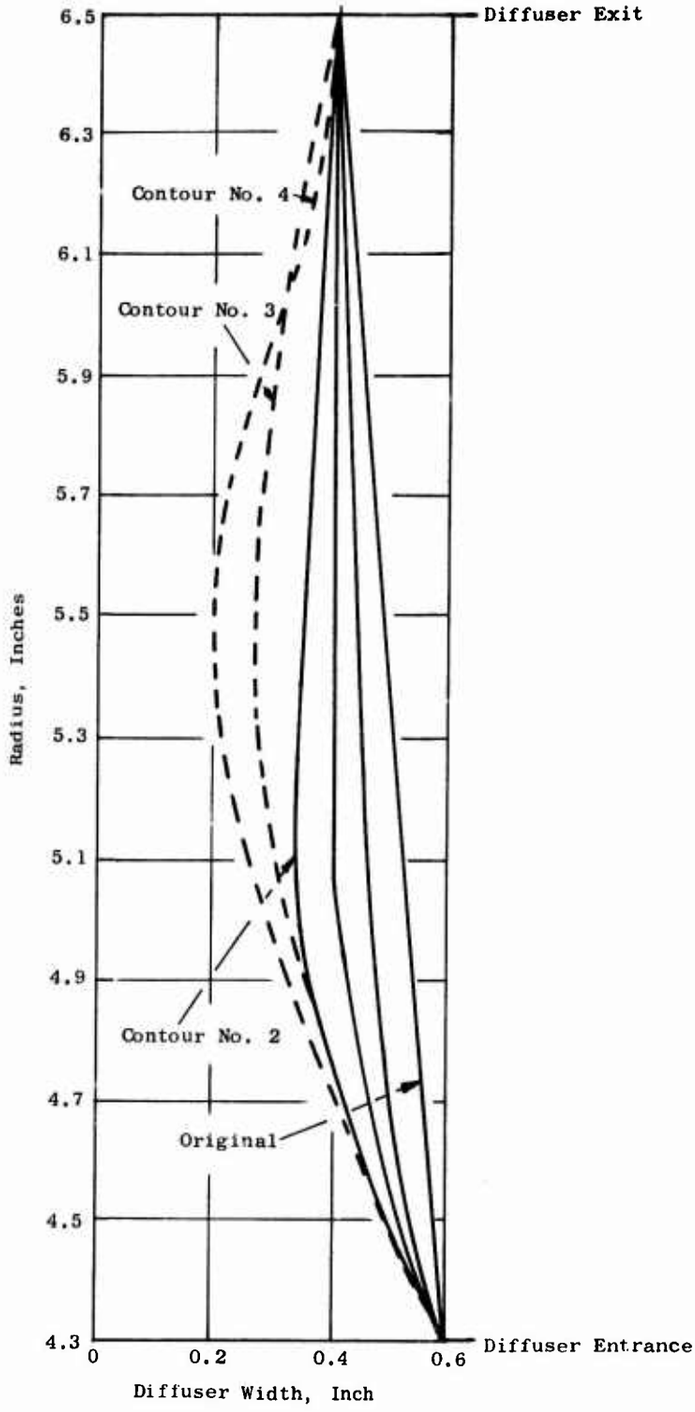

Figure 17. Potential Rotating Vaneless Diffuser Passage Contours Compared With Original.

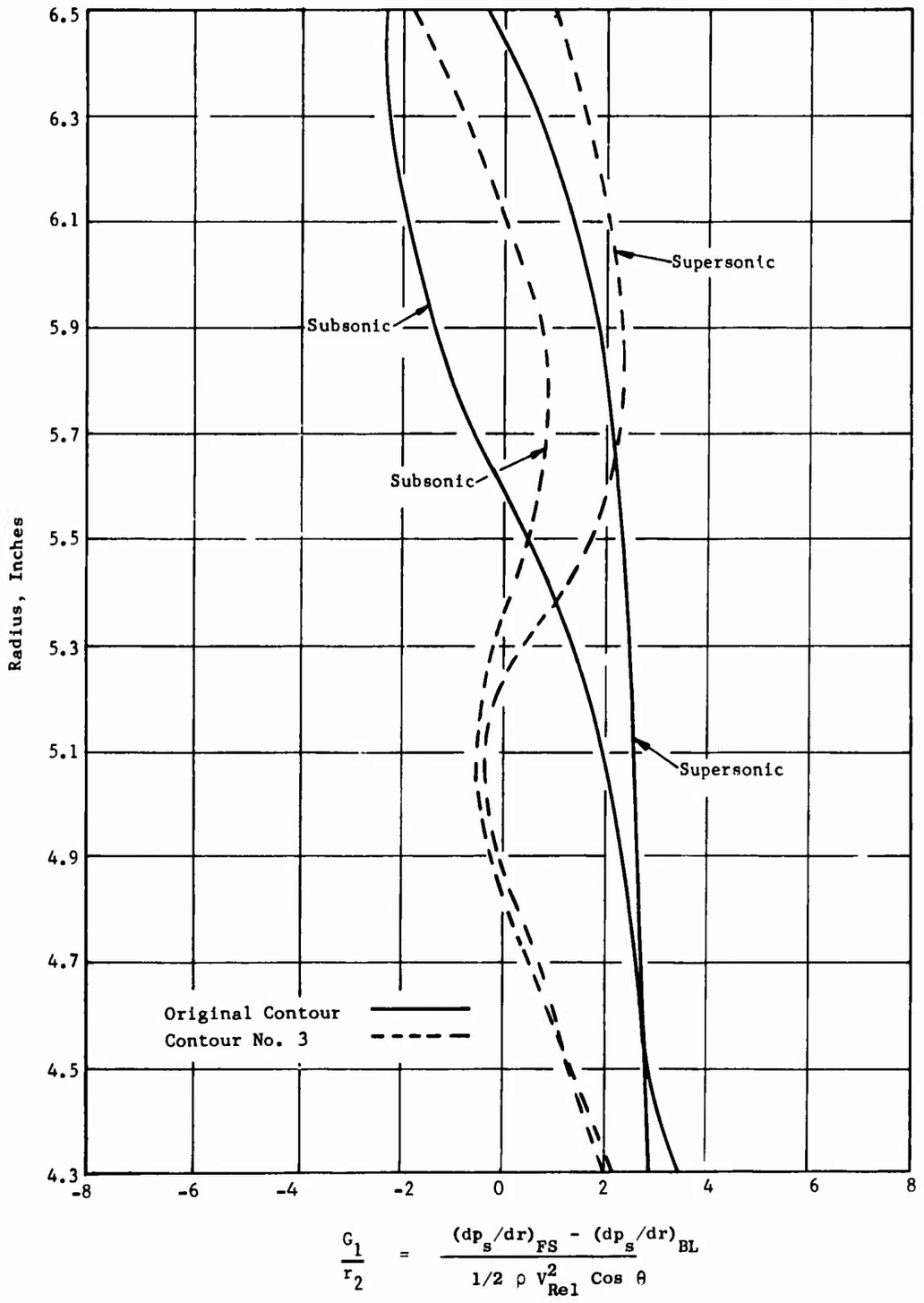

Figure 18. Comparison of Diffuser Loading Parameter for Original Contour and Contour No. 3 at 60 Percent Speed.

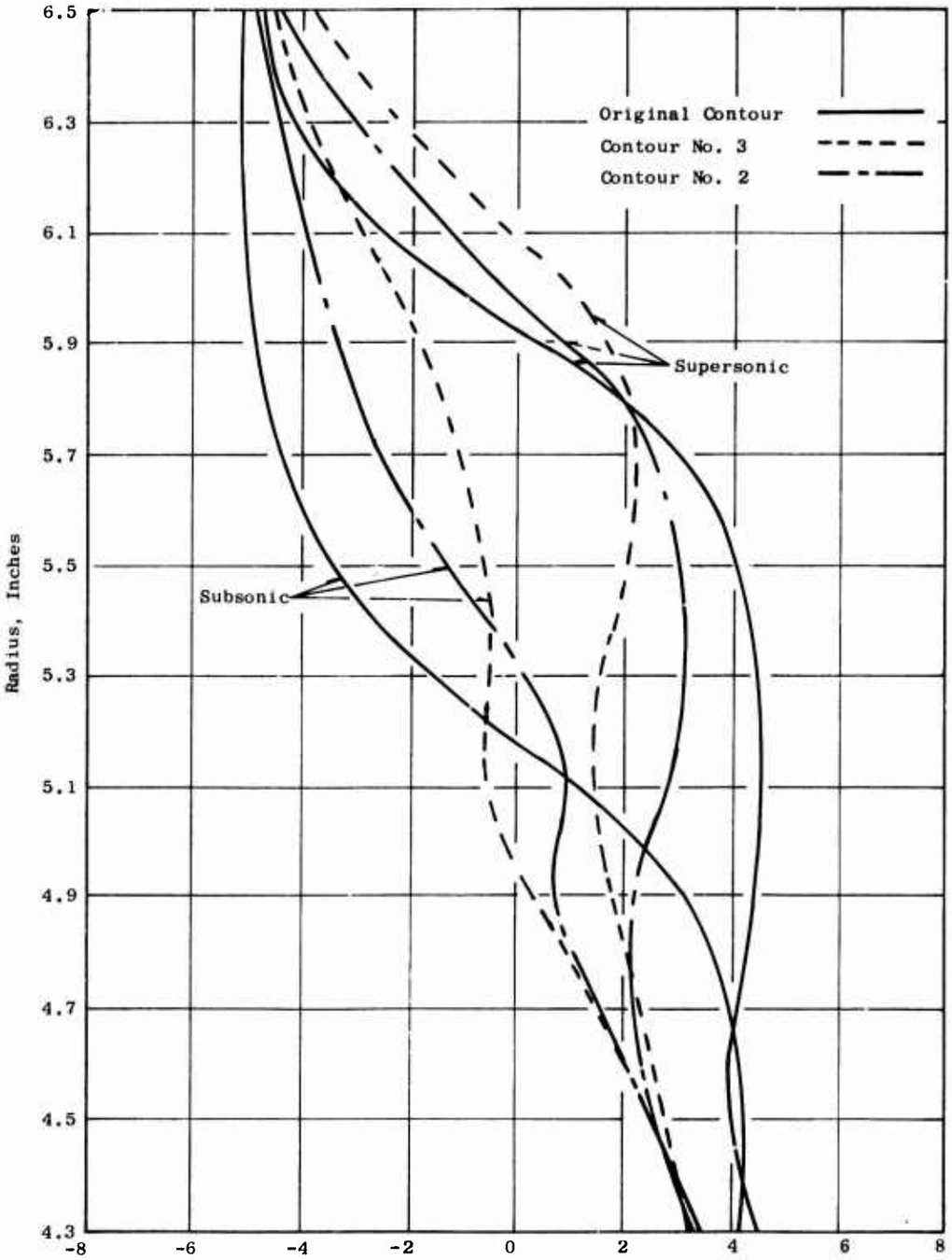

$$\frac{G_1}{r_2} = \frac{(dp_s/dr)_{FS} - (dp_s/dr)_{BL}}{1/2\ \rho\ V_{Rel}^2\ \cos\theta}$$

Figure 19. Comparison of Diffuser Loading Parameter G_1/r_2 for Original, Contour No. 2, and Contour No. 3 at 100 Percent Speed.

The contour intermediate between numbers 2 and 3, noted above, has been designated number 5 and is compared to the original contour in Figure 20. This passage shape reduces to a minimum width of 0.30 inch about midway between the rotor blade trailing edge radius of 4.3 inches and the rotor exit radius of 6.5 inches. Calculated values of the effective pressure coefficient using Cos θ in the denominator are presented in Figures 21 and 22 for 60 and 100 percent speed. The values calculated for both subsonic and supersonic rotor blade exit flow remain below the nominal limiting value of 3.0 at 30, 60, and 80 percent speed. At 100 percent speed, the nominal limiting value is exceeded over the first 0.2 inch of radius outboard of the rotor blade trailing edge. The limiting value is closely approached at a radius of 5.6 inches for supersonic exit flow.

Values of effective pressure coefficient using $\text{Cos}^2\ \theta$ in the denominator have been calculated for Contour Number 5. These results have been presented in Figures 23 and 24 for 60 and 100 percent speed. For speeds up to 80 percent, the values calculated do not exceed the nominal limiting value of this parameter of 6.4. At 100 percent speed, the limiting value is exceeded in the region 0.15 inch outboard of the rotor blade trailing edge. This is the only zone where the values approach or exceed the nominal limiting value of the effective pressure coefficient. Contour Number 5 is therefore believed to be generally satisfactory.

PREDICTED COMPRESSOR OPERATION

Analysis of the aerodynamic characteristics of the ROC has produced the compressor operating maps included herein. Calculations were made for inlet guide vane settings of -29.5, 0, and 40 degrees. The -29.5-degree inlet guide vane setting is estimated to produce the design inlet angle of -18.4 degrees entering the rotor blades. Inlet swirl of 31.1 degrees is calculated to be produced by the 40-degree inlet guide vane setting. The first 3 figures (Figures 25, 26, and 27) show rotor total pressure ratio versus mass flow at various percent speeds for the 3 inlet guide vane settings. The vertical portion of each curve represents choked flow.

Figures 28, 29, and 30 show rotor exit static pressure ratio versus mass flow for the 3 inlet swirl angles. The methods used in calculating these compressor maps are presented in Appendix I.

The last 3 figures (Figures 31, 32, and 33) show compressor rotor efficiency versus mass flow. Losses were included in the analysis in the form of total pressure loss coefficients estimated for the inlet system and the rotor blades with a friction coefficient obtained from standard data assumed for the walls of the vaneless rotating diffuser. The computer program has not yet been extended to include the stator and exit system losses.

These calculations require that the friction coefficient applied to the rotating vaneless diffuser be estimated. The value used in these computations was 0.03 and is probably excessively conservative, since large reductions of total pressure in the vaneless diffuser are calculated. Little or no total pressure loss in this zone has been measured in low speed ROC tests, and the measured total pressure ratio at 65 percent speed (see section on High Speed Compressor) was greater than that predicted at 70 percent using a friction coefficient of 0.03. Comparison of these calculations with test results will provide useful correlations for future analyses.

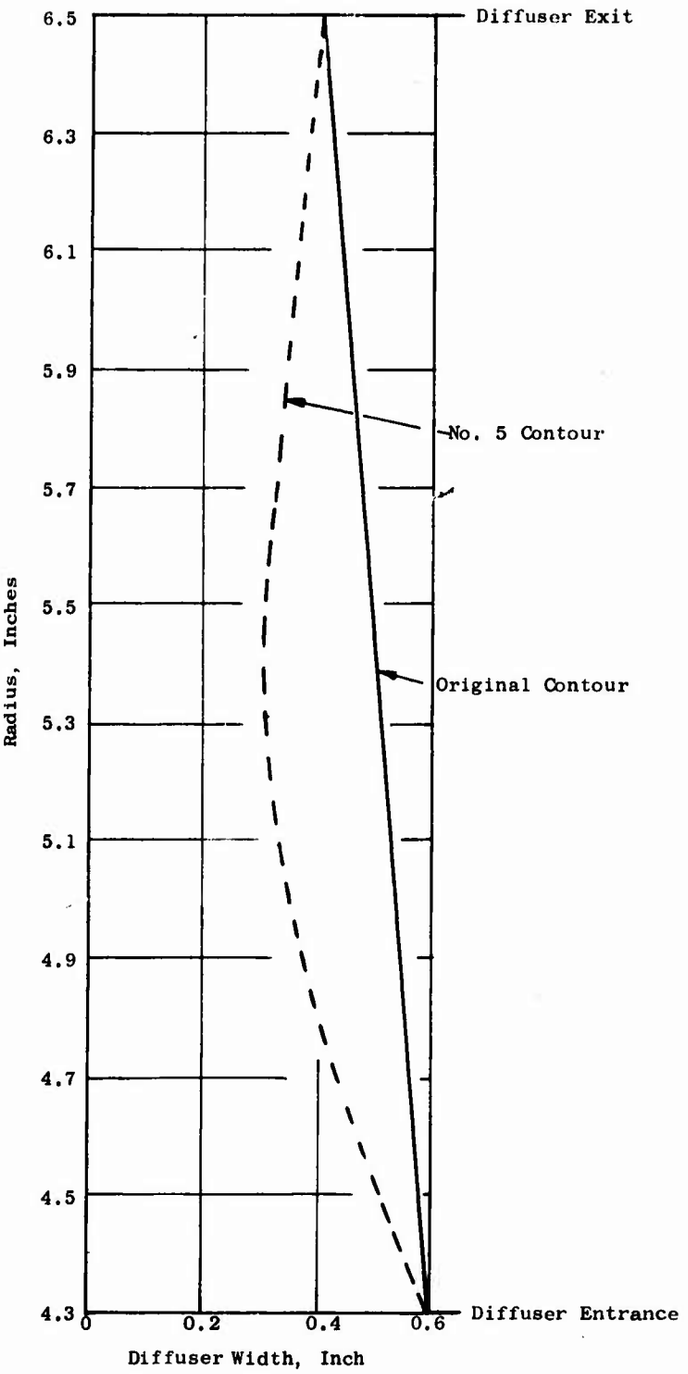

Figure 20. Comparison of Original and Contour No. 5 of Rotating Vaneless Diffuser Passage.

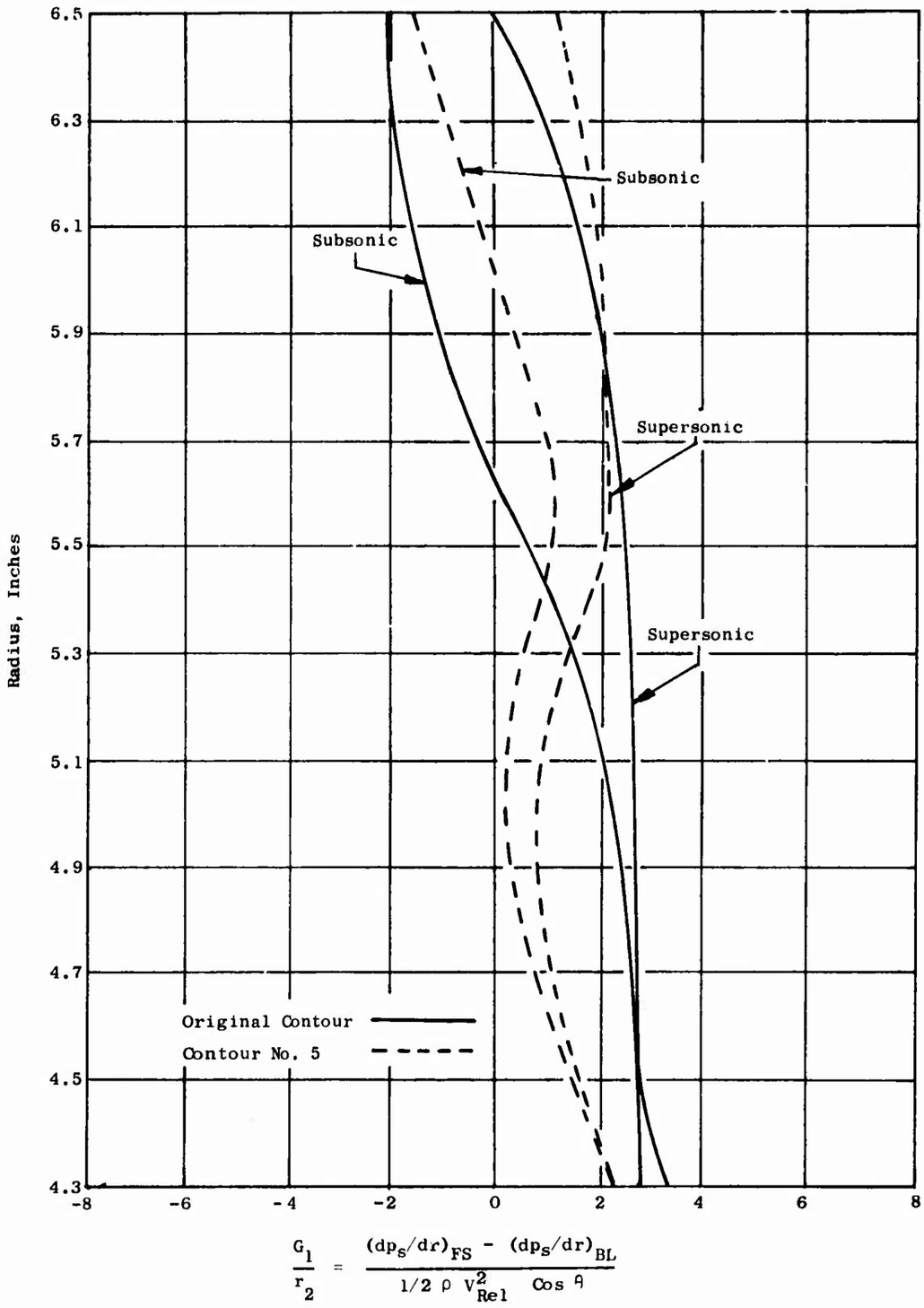

Figure 21. Comparison of Diffuser Loading Parameter G_1/r_2 for Original Contour and Contour No. 5 at 60 Percent Speed.

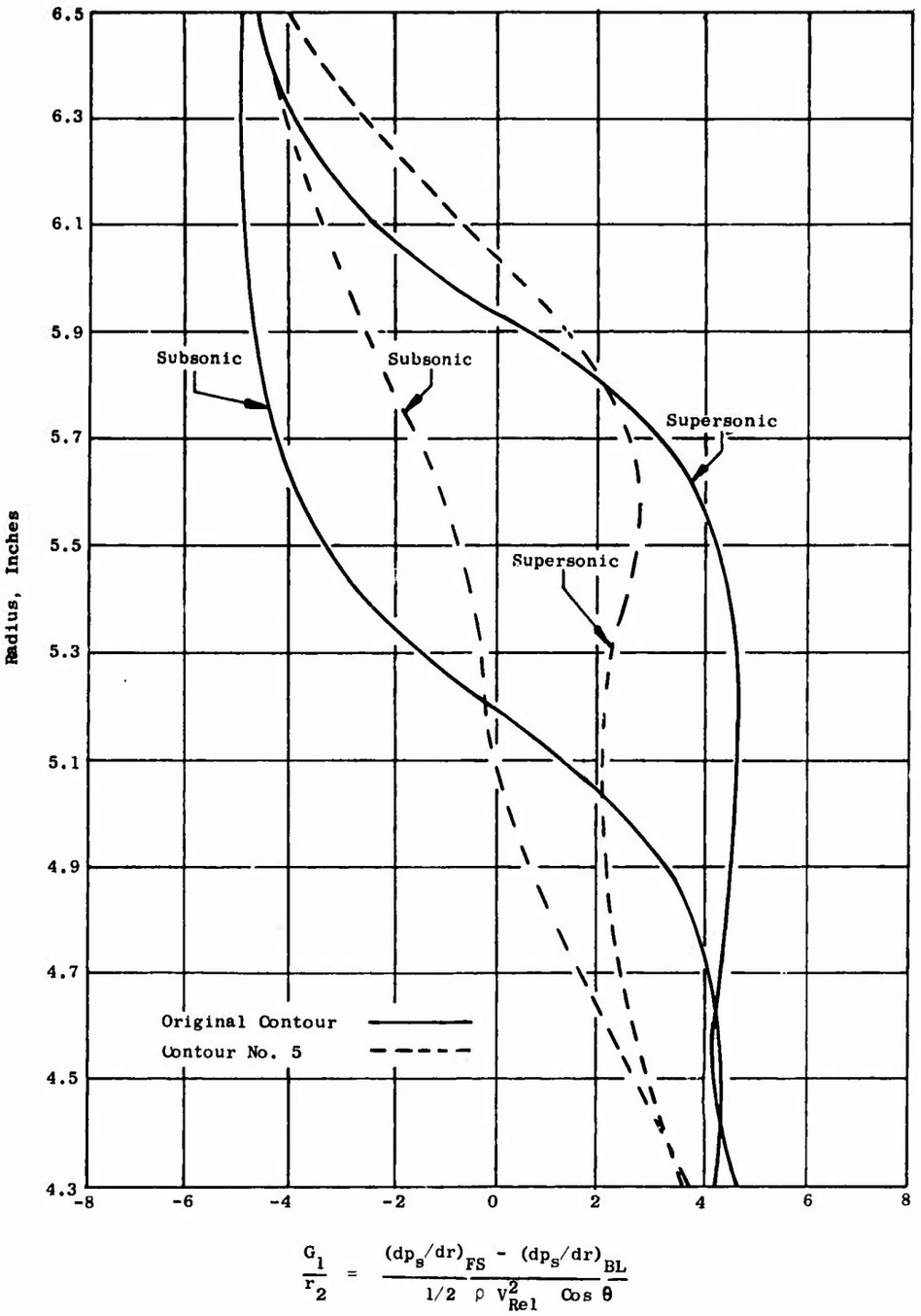

Figure 22. Comparison of Diffuser Loading Parameter G_1/r_2 for Original Contour and Contour No. 5 at 100 Percent Speed.

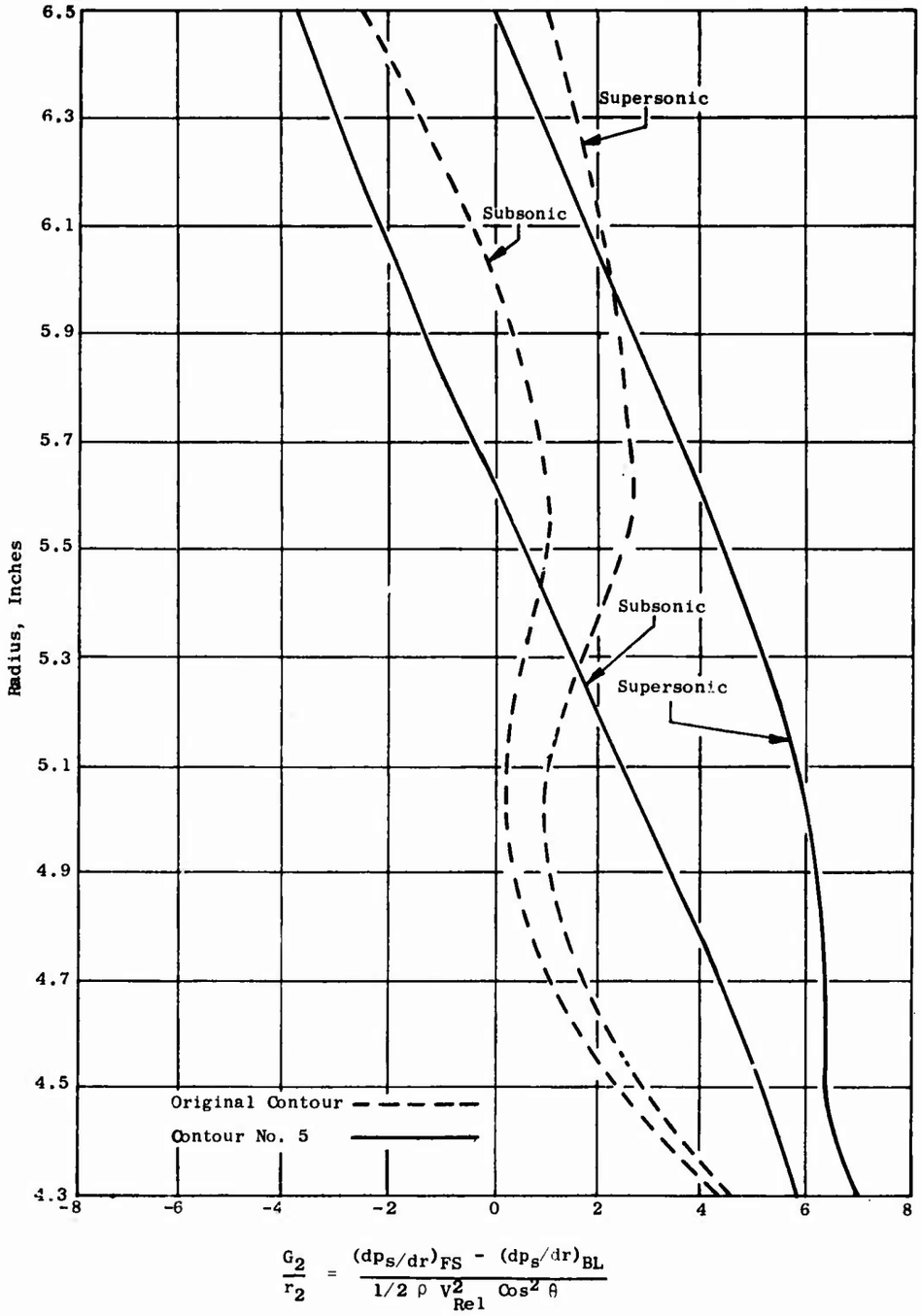

Figure 23. Comparison of Diffuser Loading Parameter G_2/r_2 for Original Contour and Contour No. 5 at 60 Percent Speed.

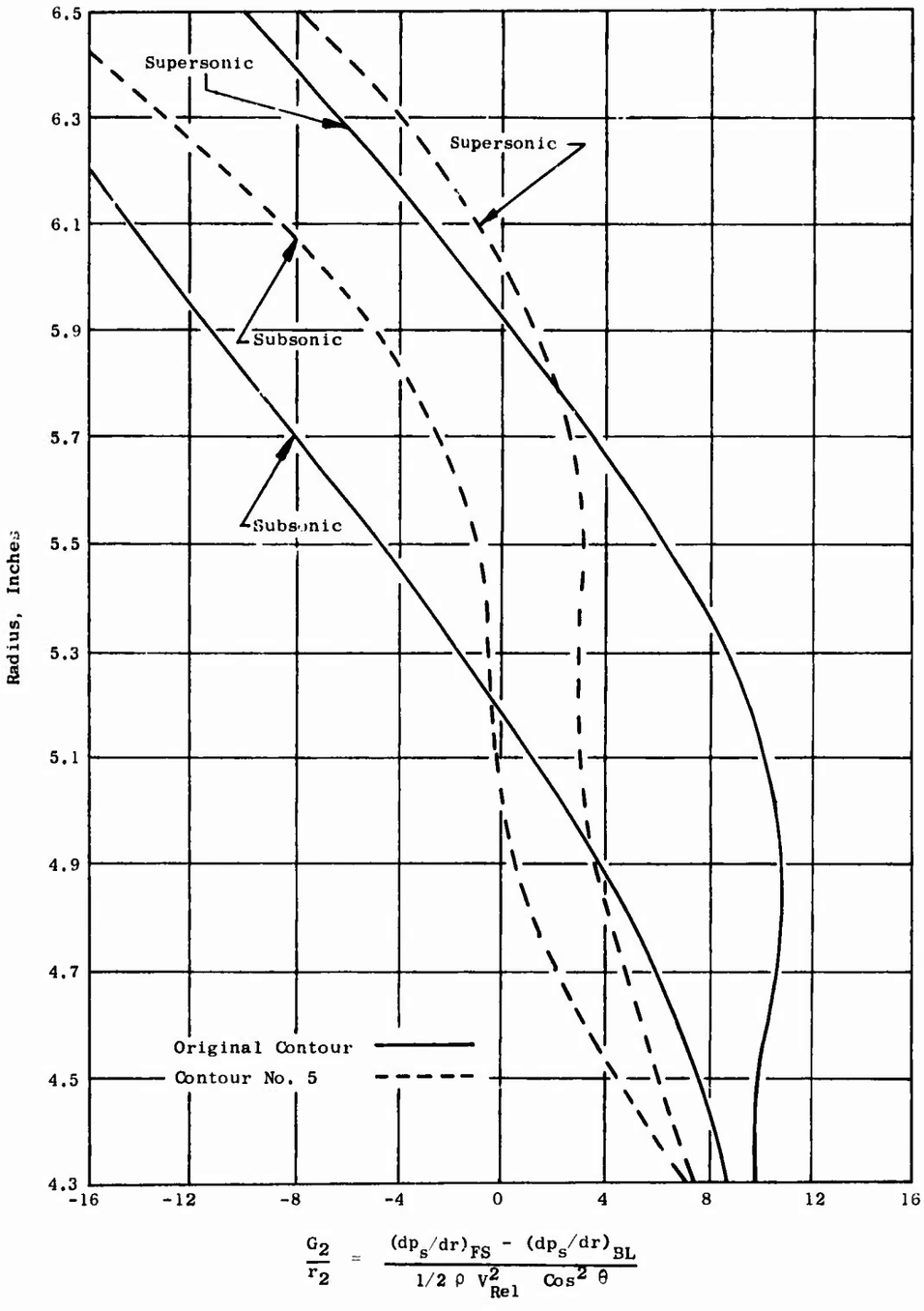

Figure 24. Comparison of Diffuser Loading Parameter G_2/r_2 for Original Contour and Contour No. 5 at 100 Percent Speed.

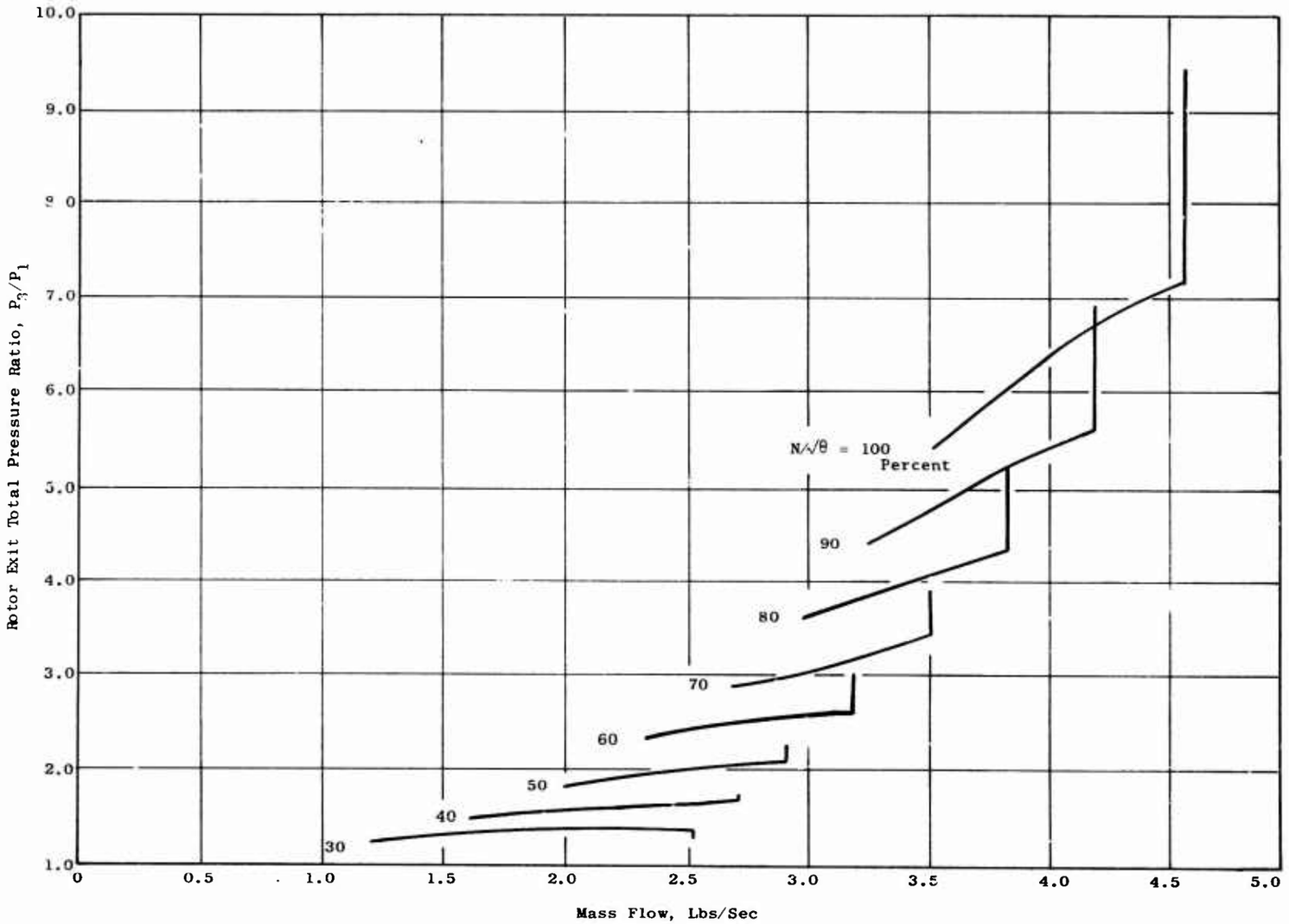

Figure 25. Predicted Rotor Total Pressure Ratio Versus Airflow With -18.4 Degrees Counter-Preswirl Entering the Rotor Blades.

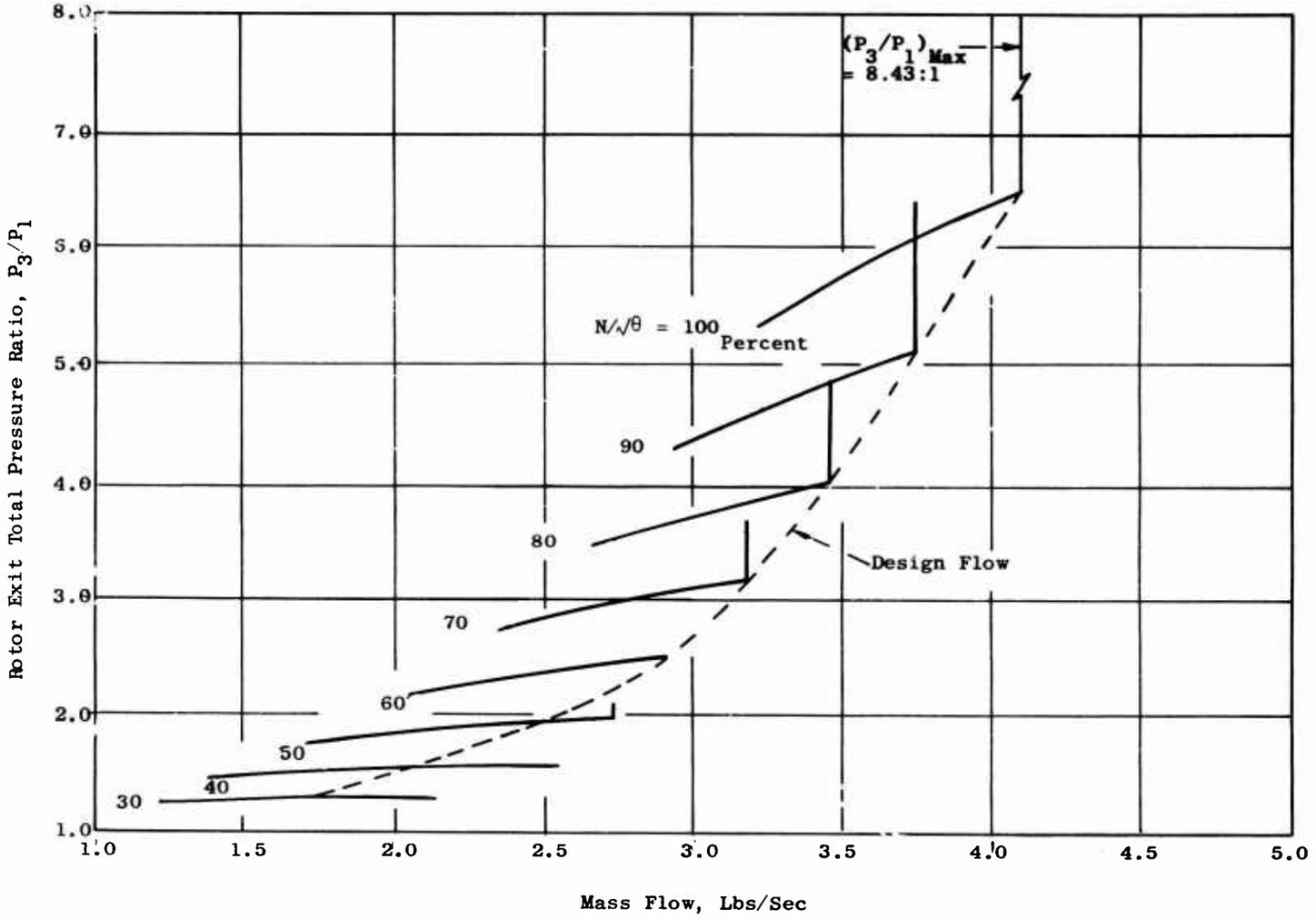

Figure 26. Predicted Rotor Total Pressure Ratio Versus Airflow With 0 Degrees Swirl Entering the Rotor Blades.

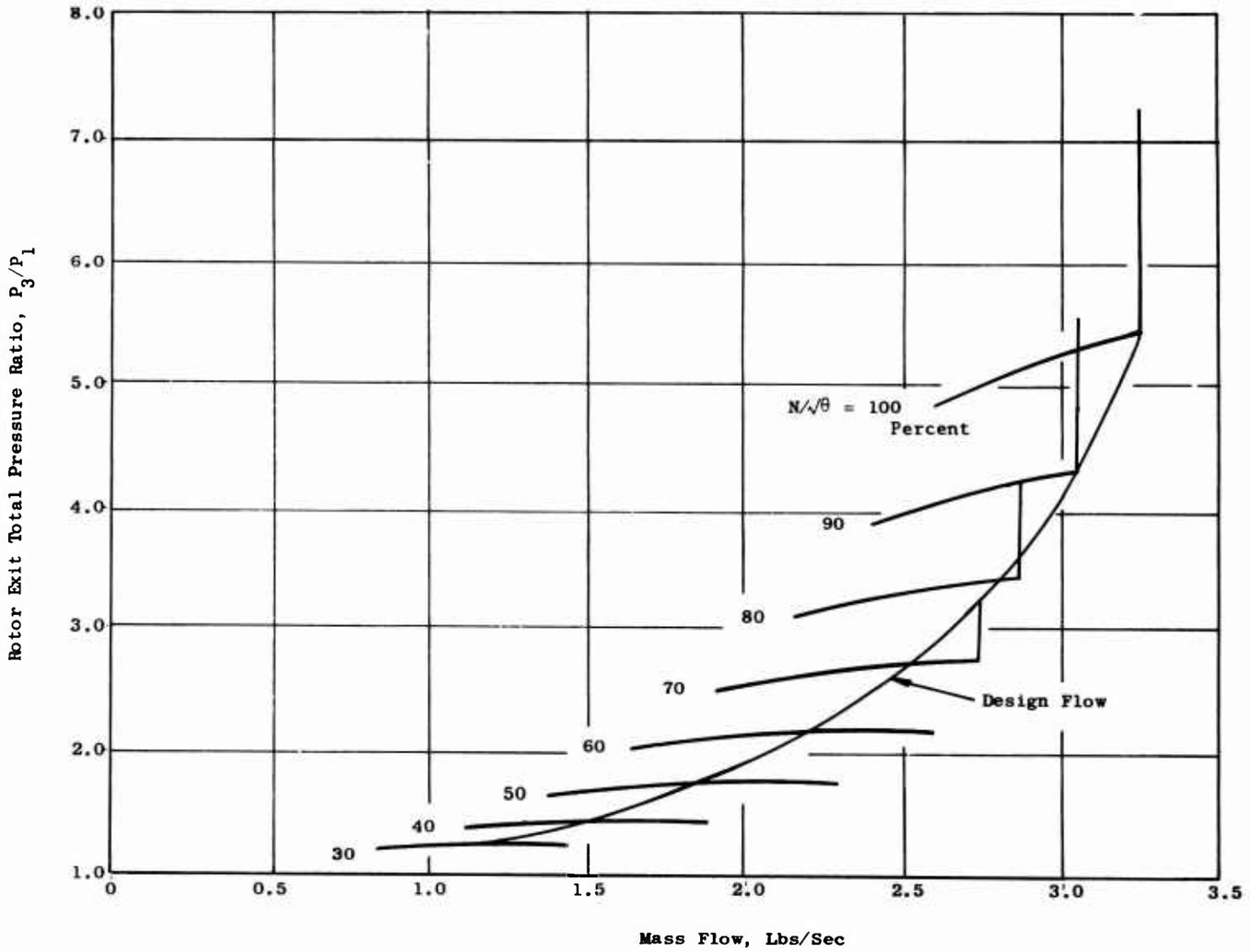

Figure 27. Predicted Rotor Total Pressure Ratio Versus Airflow for Swirl Angle of 31.1 Degrees Entering Rotor Blades.

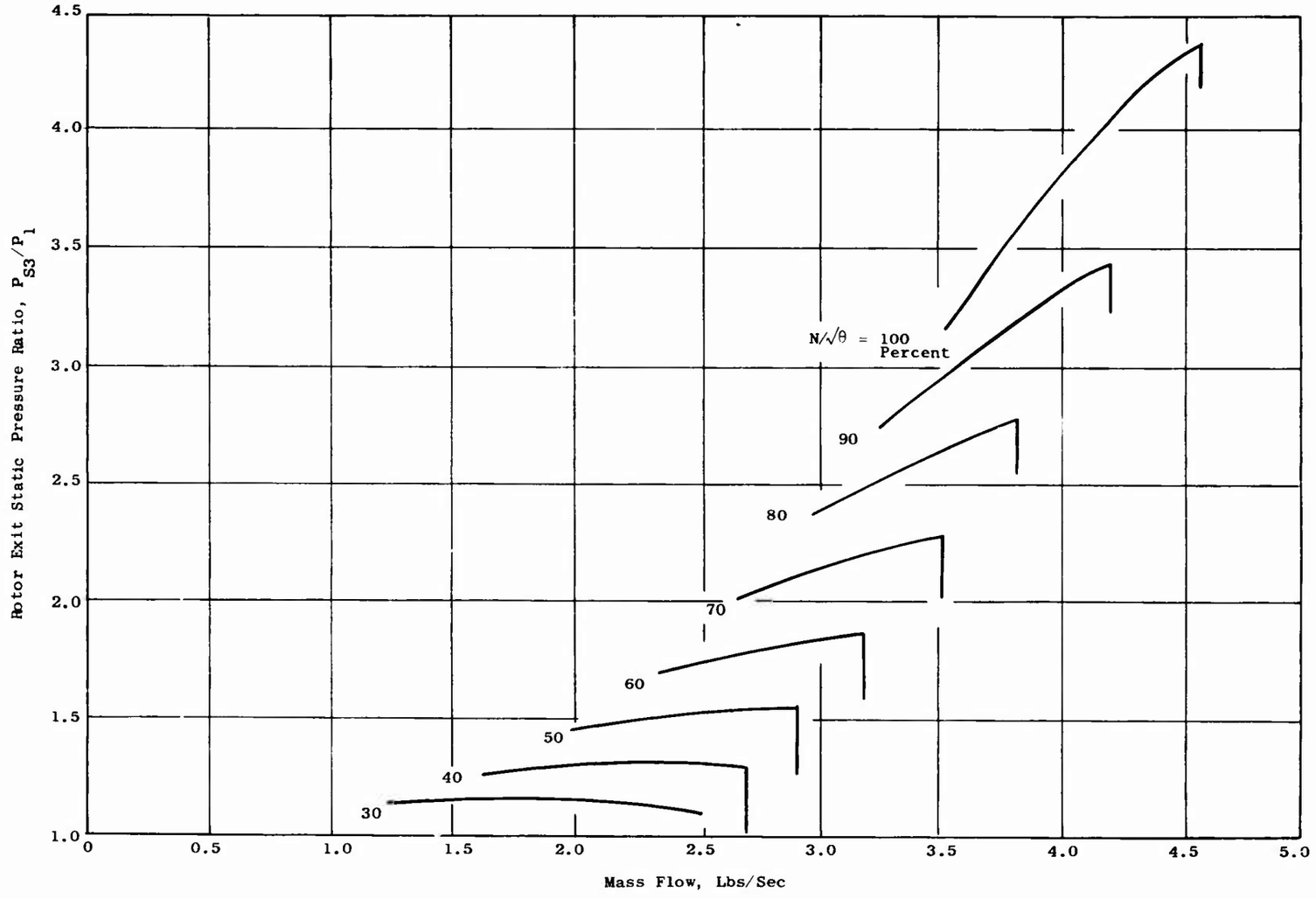

Figure 28. Predicted Rotor Exit Static Pressure Ratio Versus Airflow for -18.4 Degrees Counter-Swirl Entering Rotor Blades.

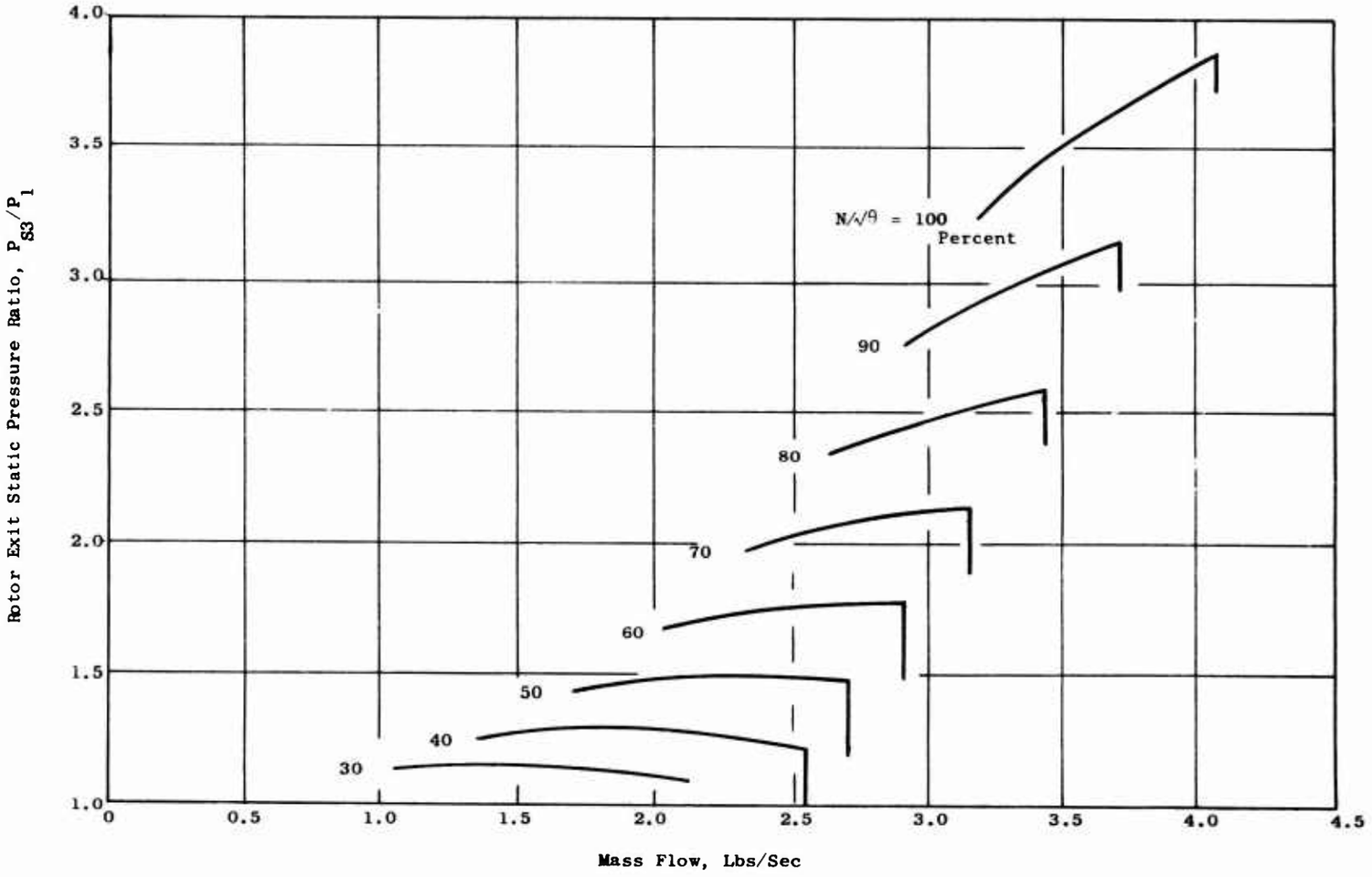

Figure 29. Predicted Rotor Exit Static Pressure Ratio Versus Airflow for 0 Degrees Swirl Entering Rotor Blades.

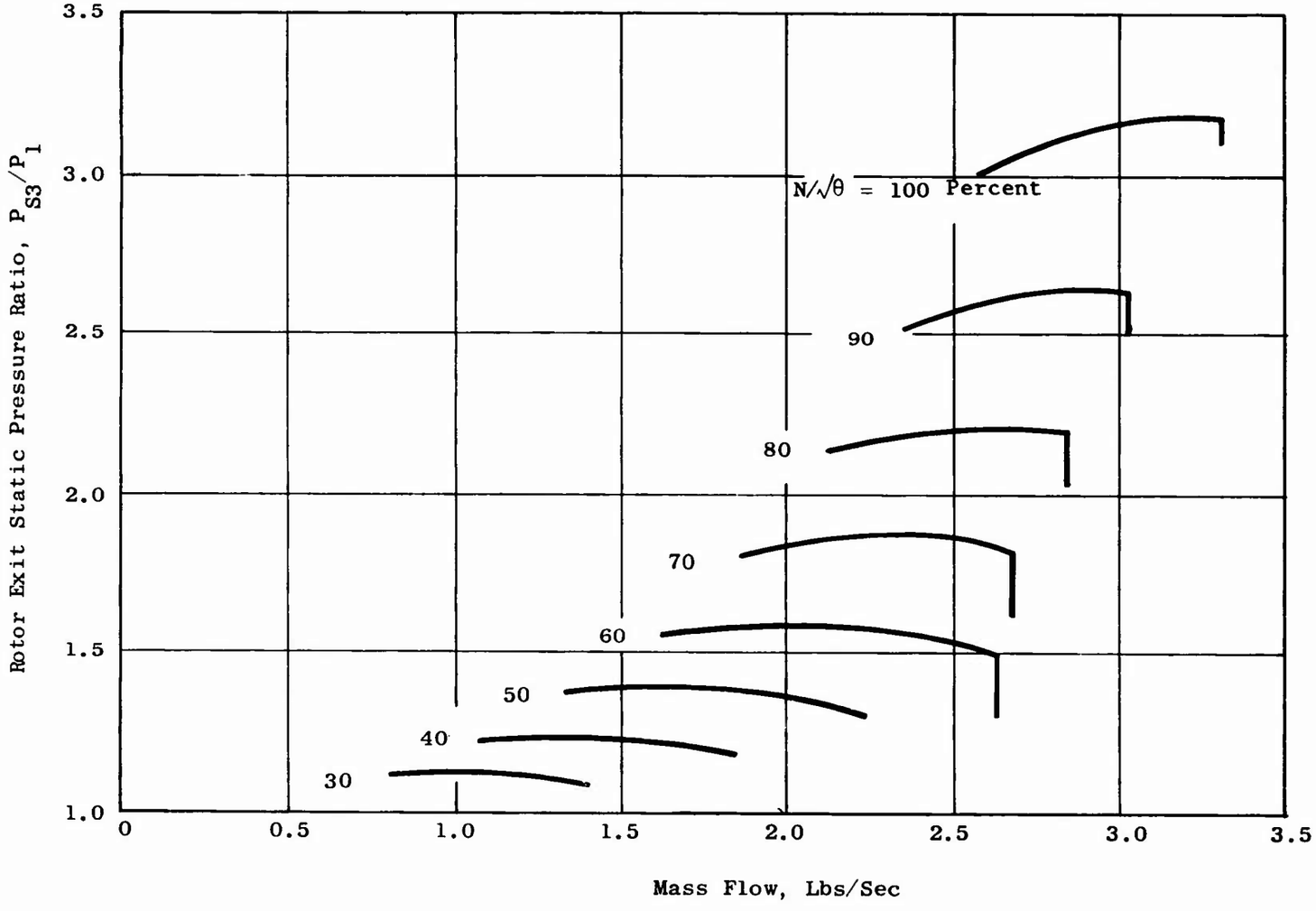

Figure 30. Predicted Rotor Static Pressure Ratio Versus Airflow With 31.1 Degrees Preswirl Entering Rotor Blades.

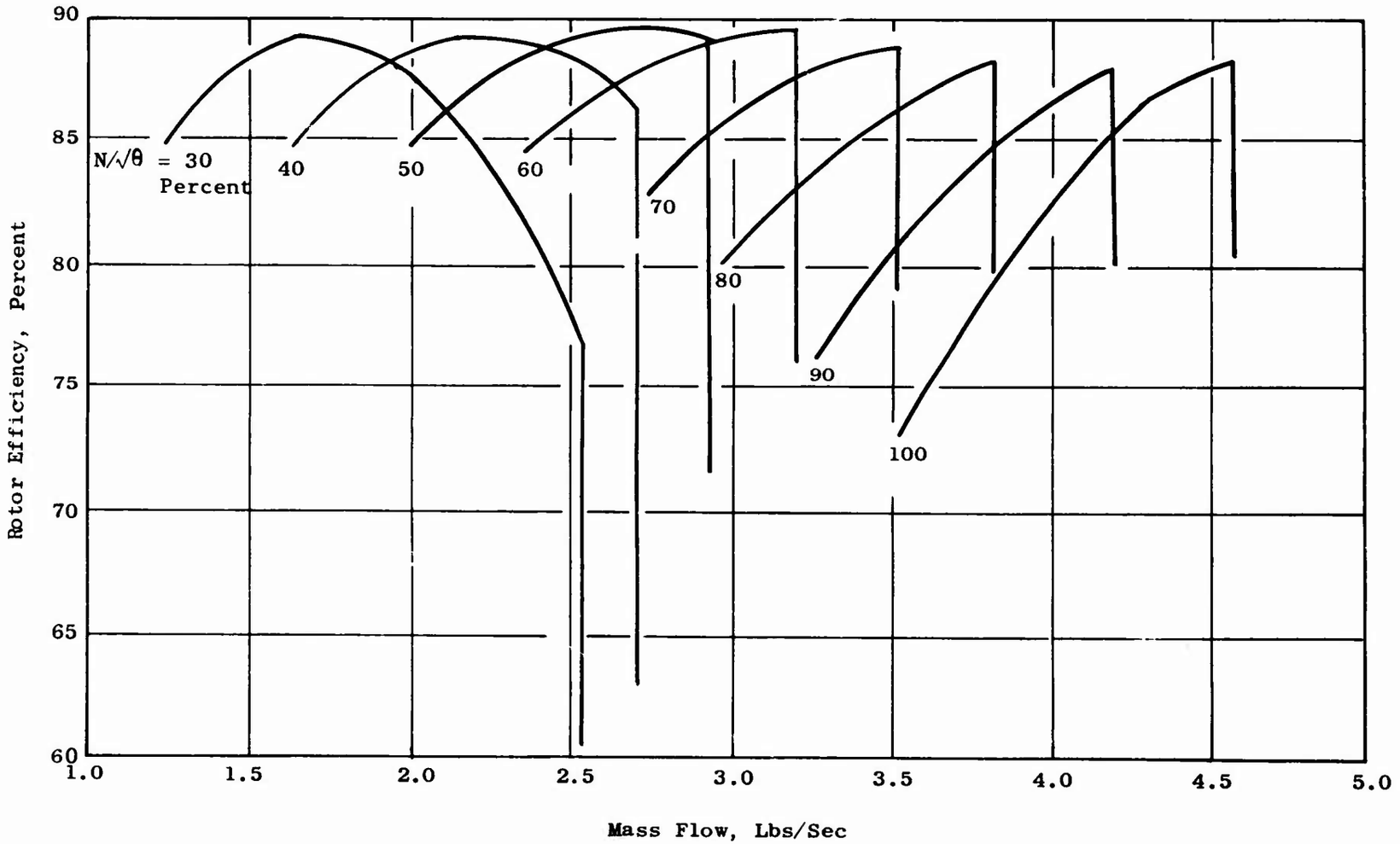

Figure 31. Estimated Rotor Efficiency Versus Airflow for -18.4 Degrees Counter-Preswirl Entering Rotor Blades.

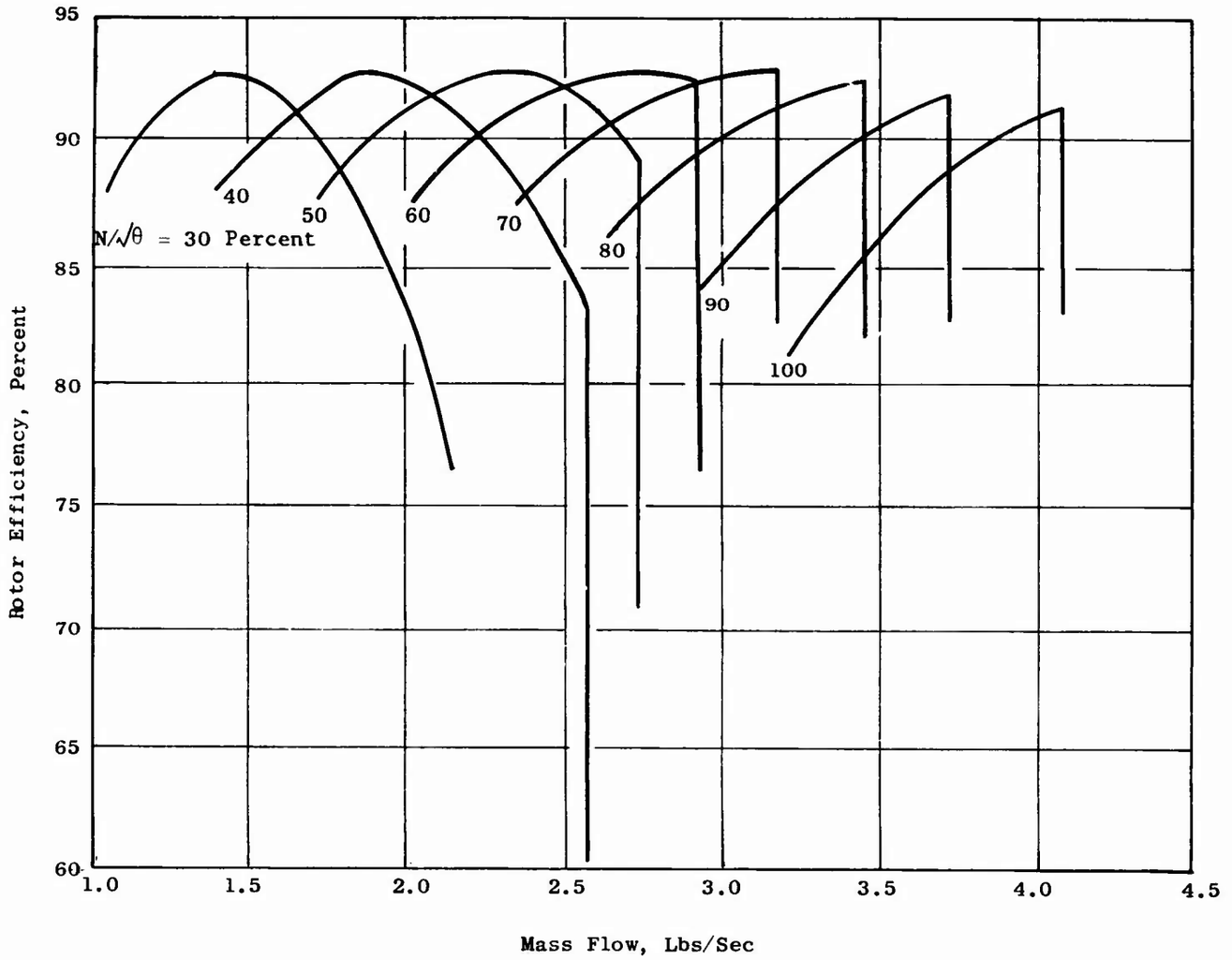

Figure 32. Estimated Rotor Efficiency Versus Airflow for 0 Degrees Swirl Entering Rotor Blades.

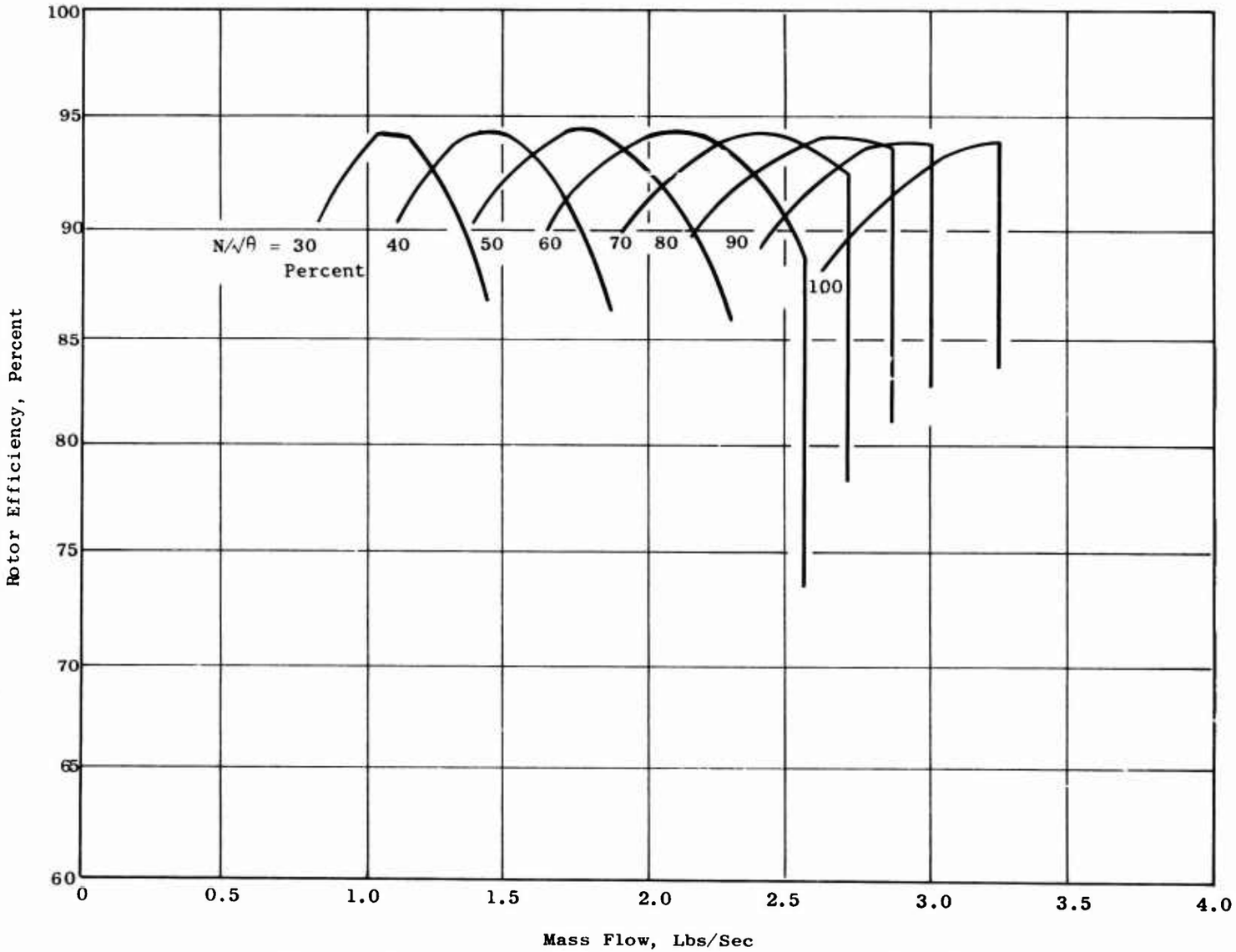

Figure 33. Estimated Rotor Efficiency Versus Airflow for 31.1 Degrees Preswirl Entering Rotor Blades.

MECHANICAL INVESTIGATIONS

STRESS ANALYSIS

All major ROC rotor components (disc, shroud, and blades) and the supersonic stators were analyzed for stresses and deflections.

Disc

The disc was analyzed through the use of the GE wheel and shell computer programs. Effects of wheel speed, thermal growth, blade load, and shaft attachment forces were taken into account. Simplification of the actual disc geometry into a computer model was straightforward, since the disc is essentially symmetric with the centroid of each segment lying on the disc radial centerline.

The disc section at the blade bolt circle was simulated in 2 separate cases:

1) A circumferential notch was substituted for the bolt holes to better estimate stresses.

2) A solid section of reduced material modulus was substituted for the bolt holes to better estimate disc radial growth.

Blade load on the disc was obtained by assuming that the blade mass on the disc side half of the blade acts on the disc. The remaining blade mass on the shroud side of the blade was placed on the shroud.

The stress and deflection distributions in the disc are shown in Figures 34 and 35. Average tangential stress for the main disc cross section was calculated from the above stress distribution to be 97,430 psi. All stresses were within design limits.

Shroud

Stress analysis of the shroud was made much the same as the disc analysis. The main exception was the more difficult computer modeling of the complex shroud geometry. Two separate models were set up. The shroud was broken down into (1) shell elements with radial centerlines and (2) shell elements with centerlines on the shroud mid-thickness line. Results from these 2 types of analysis were very similar, giving confidence in the results obtained. The stress and deflection distributions in the shroud are shown in Figures 36 and 37. Average tangential stress in the shroud cross section was calculated from the above stress distribution to be 81,650 psi on the blade side and 66,380 psi on the seal side. All stresses were within design limits.

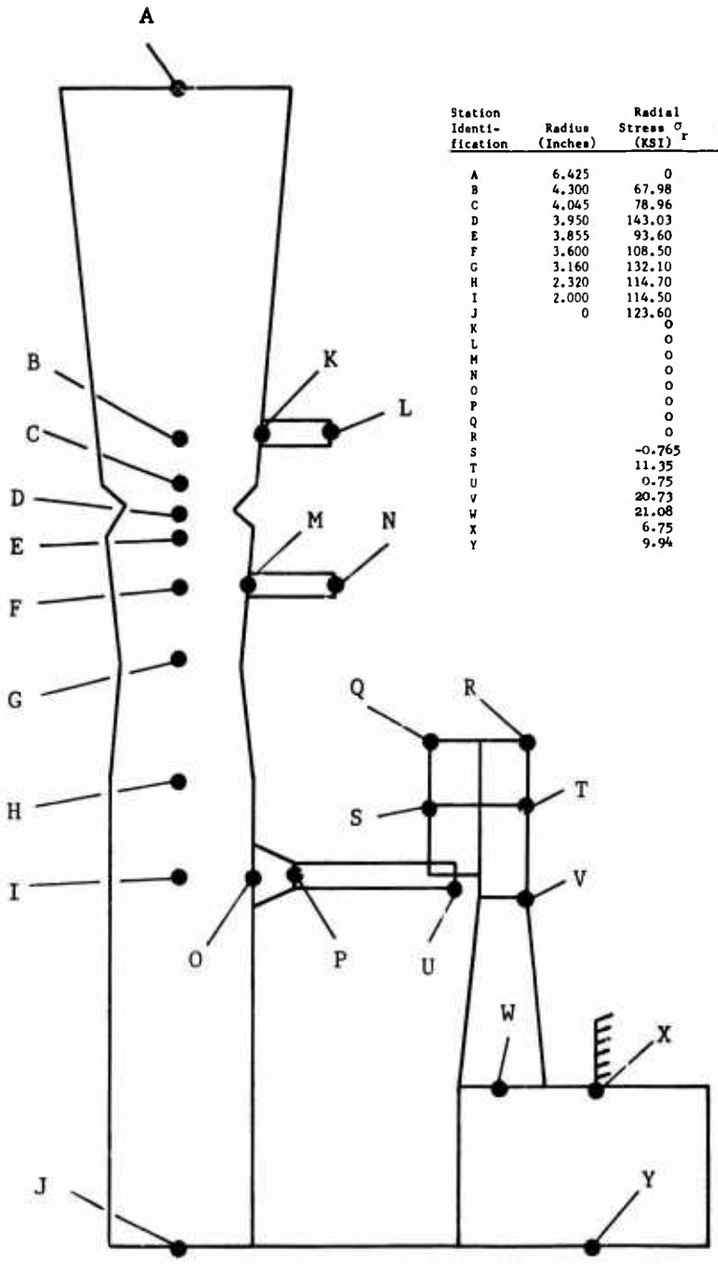

Station Identification	Radius (Inches)	Radial Stress σ_r (KSI)	Hoop Stress σ_θ (KSI)	Effective Stress σ_{Eff} (KSI)
A	6.425	0	30.82	31.12
B	4.300	67.98	87.68	86.34
C	4.045	78.96	94.84	93.47
D	3.950	143.03	117.40	139.40
E	3.855	93.60	101.40	100.20
F	3.600	108.50	108.70	111.90
G	3.160	132.10	119.60	131.00
H	2.320	114.70	117.90	118.10
I	2.000	114.50	118.20	126.40
J	0	123.60	123.60	133.80
K		0	65.17	85.14
L		0	77.89	77.89
M		0	71.95	71.99
N		0	71.21	71.21
O		0	73.48	82.61
P		0	67.09	80.70
Q		0	13.08	15.84
R		0	11.39	17.39
S		-0.765	15.38	19.13
T		11.35	16.60	30.65
U		0.75	19.88	23.87
V		20.73	20.09	38.30
W		21.08	19.06	26.87
X		6.75	8.10	22.38
Y		9.94	9.94	24.22

Figure 34. Stress Distribution on ROC Disc at 100 Percent Speed.

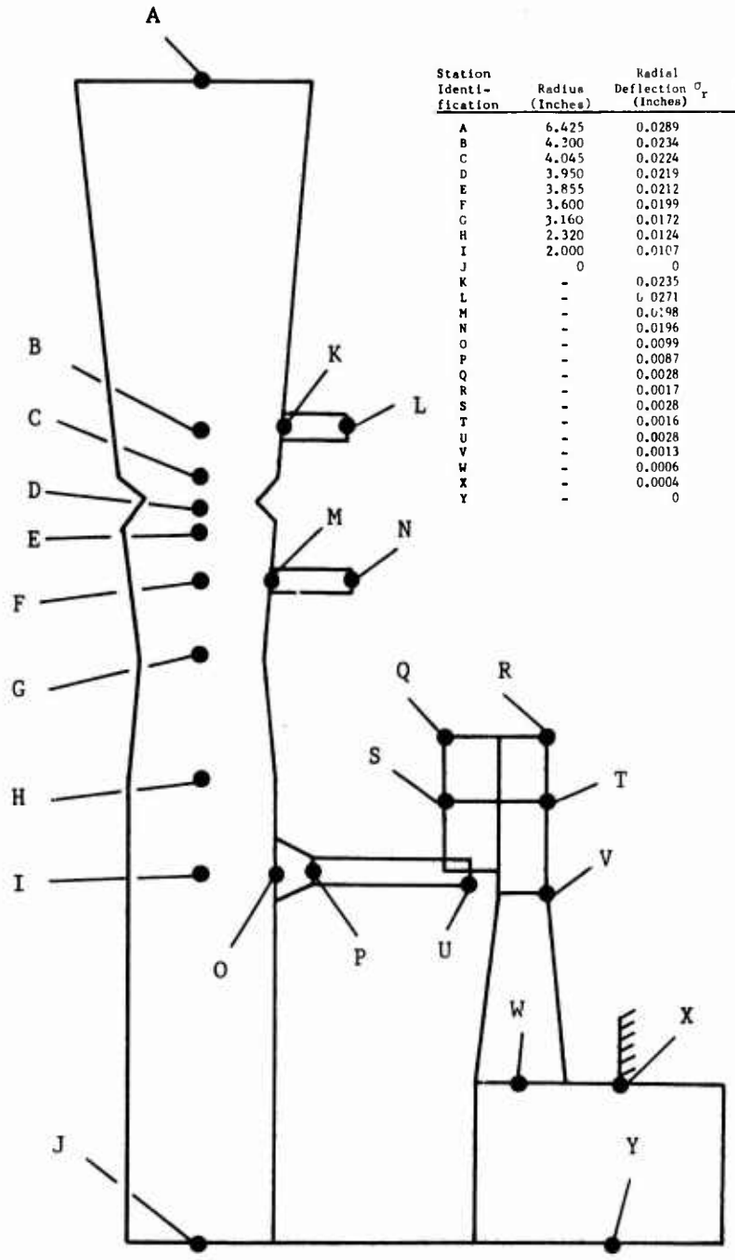

Station Identification	Radius (Inches)	Radial Deflection σ_r (Inches)	Hoop Deflection σ_θ (Inches)	Effective Deflection σ_{Eff} (Inches)
A	6.425	0.0289	0.0035	0.012
B	4.300	0.0234	0.0039	0.015
C	4.045	0.0224	0.0040	0.009
D	3.950	0.0219	0.0040	0.003
E	3.855	0.0212	0.0040	-0.003
F	3.600	0.0199	0.0040	-0.014
G	3.160	0.0172	0.0037	-0.041
H	2.320	0.0124	0.0027	-0.098
I	2.000	0.0107	0.0021	-0.120
J	0	0	0	0
K	-	0.0235	0.0039	0.015
L	-	0.0271	0.0037	0.467
M	-	0.0098	0.0040	-0.014
N	-	0.0196	0.0035	-0.014
O	-	0.0099	0.0021	-0.120
P	-	0.0087	0.0018	-0.368
Q	-	0.0028	0.0047	-0.253
R	-	0.0017	0.0047	-0.254
S	-	0.0028	0.0030	-0.268
T	-	0.0016	0.0030	-0.268
U	-	0.0028	0.0012	-0.285
V	-	0.0013	0.0013	-0.400
W	-	0.0006	0.0002	-0.023
X	-	0.0004	0.0002	-0.023
Y	-	0	0	0

Figure 35. Deflection Distribution on ROC Disc at 100 Percent Speed.

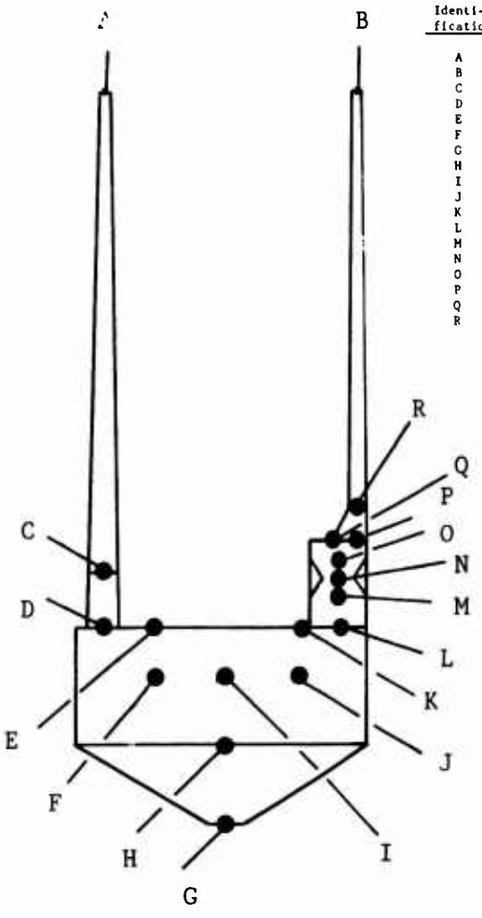

Station Identification	Radial Stress σ_r (KSI)	Hoop Stress σ_θ (KSI)	Effective Stress σ_{Eff} (KSI)
A	0	26.1	26.3
B	0	36.0	36.5
C	37.9	81.0	71.1
D	40.2	88.0	77.2
E	8.9	80.9	84.9
F	8.4	90.8	97.1
G	0	137.7	139.4
H	5.0	112.9	126.4
I	9.0	97.9	107.5
J	9.7	105.2	107.3
K	11.0	94.3	97.2
L	24.6	103.1	99.3
M	24.5	97.8	95.0
N	23.5	41.9	48.6
O	10.5	86.3	87.2
P	16.5	87.5	86.3
Q	10.1	83.1	84.4
R	32.2	90.0	81.0

Figure 36. Stress Distribution on ROC Shroud at 100 Percent Speed.

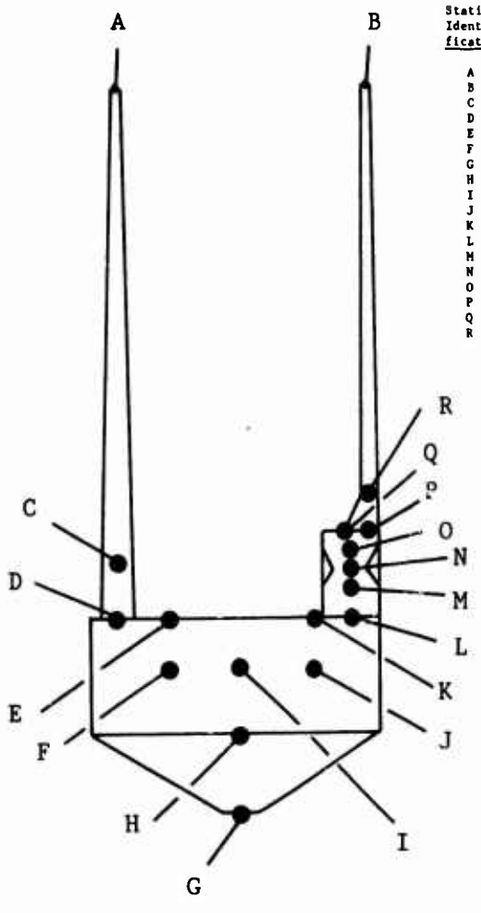

Station Identification	Radial Deflection σ_r (Inches)	Hoop Deflection σ_θ (Inches)	Effective Deflection σ_{Eff} (Inches)
A	0.0268	-0.0060	0.144
B	0.0312	0.0241	0.522
C	0.0216	0.0008	0.179
D	0.0212	0.0016	0.185
E	0.0220	0.0016	0.185
F	0.0221	0.0250	0.228
G	0.0247	0.0055	0.244
H	0.0240	0.0039	0.234
I	0.0236	0.0025	0.228
J	0.0252	0.0025	0.228
K	0.0250	0.0014	0.271
L	0.0260	0.0014	0.271
M	0.0261	0.0006	0.332
N	0.0262	0	0.391
O	0.0262	0.0067	0.448
P	0.0268	-0.0015	0.483
Q	0.0262	-0.0015	0.483
R	0.0274	-0.0030	0.622

Figure 37. Deflection Distribution on ROC Shroud at 100 Percent Speed.

Rotor Blade

The ROC rotor blade is subjected to centrifugal loading, as are all "ordinary" axial compressor blades. In addition, the threaded ROC rotor blades must take all unbalance and transient loads from the shroud which they support. The blade attachment differs greatly from the "usual" dovetail design and requires a new analysis approach.

The unthreaded blades (type P02 of Ti-6Al-4V or type P04 of Ti-6Al-6V-2Sn) were analyzed as pinned-pinned cantilevers under centrifugal loading only. The resultant maximum stresses are shown in Table I where all stresses are within design limits.

The threaded blades (type P01 of Ti-6Al-4V or type P03 of Ti-6AL-6V-2Sn) are stem bolted on the shroud side and stem bolted with platform location on the disc side. The boundary conditions can probably range from pinned-fixed to fixed-fixed depending on the assembly fit-up and amount of stem preload. Since the pinned-fixed condition gives more conservative centrifugal stresses, this condition was assumed for the detailed stress analysis.

Applied tension on the blade stems was set in conjunction with preload tests of Belleville spring washers (see section on Belleville Washer Tests) and blade stress limits. P01 blades were assembled with 15 inch-pounds of stem torque, and P03 blades were to be assembled with 18 inch-pounds of stem torque.

Some disc-to-shroud mismatch was expected due to dimensional tolerances and analysis inaccuracy in sizing both disc and shroud to centrifugally grow the same amount. This mismatch adds bending loads to the threaded blades. A mismatch of 0.005 inch between disc and shroud was assumed.

Allowance for some shroud unbalance was made. The total rotor was to be balanced to 0.7 gram-inch, so any additional unbalance acquired during running was assumed to be 0.3 gram-inch. If the worse case of rotor unbalance acting on the shroud is assumed, the total shroud unbalance would be 1 gram-inch.

Consideration was also made for peak rotor deflection during transient operation at rotor critical speeds. Analysis of the rotor system showed that this peak deflection could be 0.009 inch at the shroud.

Thus, two blade design conditions were analyzed:

1)	Steady-State Loading	a) Centrifugal blade load b) Stem preload c) 1.0-gram-inch shroud unbalance
2)	Maximum Unbalance Loading	a) Steady-state loading above b) 0.009-inch shroud deflection

TABLE I. MAXIMUM BLADE STRESSES

A. P02 and P04 Blades - Steady-State Loading

	80% Speed			100% Speed		
	Stress (KSI)	% of Allow.		Stress (KSI)	% of Allow.	
		P02	P04		P02	P04
Airfoil	15.35	16.3	27.8	24.0	11.4	19.0
Shank	23.80	44.2	30.9	37.2	75.5	51.5

B. P01 and P03 Blades - Maximum Unbalance Loading

	80% Speed				100% Speed			
	Stress (KSI)		% of Allow.		Stress (KSI)		% of Allow.	
	P01	P03	P01	P03	P01	P03	P01	P03
Airfoil	101.45	108.2	107.5	80.3	104.9	110.1	121.0	87.0
Shank	87.40	83.8	92.5	62.1	91.2	94.0	105.5	74.6

	80% Speed		100% Speed	
	Stress (KSI) P01	Stress (KSI) P03	Stress (KSI) P01	Stress (KSI) P03
Allow. Single Amplitude Vibratory Stress on Airfoil	4.0	26.0	0	25.0

The analysis results are shown in Table I. Note that P02 and P04 blade stresses are well below allowable values. P03 is safe up to maximum compressor speeds, since there is an adequate allowance for possible vibratory stress. A check of P01 blade stress shows why it was limited to compressor speeds of 80 percent. The P01 shank stress is 105.5 percent of allowable, indicating relaxation and possible failure of this attachment point. Furthermore, there is no margin for vibratory stress above 80 percent design speed. Although local airfoil stress was calculated to exceed the yield strength of the Ti-6AL-4V alloy, the main bulk of the airfoil will support these areas, and this condition can be tolerated in moderation. Displacement of the rotor is presented in Appendix II.

Supersonic Stator Vane

The primary mechanical design objective of the supersonic stator vane was to insure good aerodynamic geometry by limiting maximum vane deflection to 0.004 inch. Air loading at maximum pressure conditions (see Figure 38) was the design condition assumed. Analysis was made using a GE plate-section computer program. By adjustment in location of the vane support pins, vane deflections were limited to the desired value. The deflection curve for the final vane configuration is shown in Figure 39.

Local bending of the vane support pins was analyzed by hand calculation. The spanwise vane section through the pins was assumed to be a fixed-fixed cantilever beam. Maximum bending stress as well as maximum shear support stress occurs at the pin. Maximum stresses for the pin are:

$$\sigma_{Bend} = 13{,}300 \text{ psi (or 21 percent of allowable)}$$

$$\tau_{Shear} = 786 \text{ psi (or 2 percent of allowable)}$$

Allowable vibratory stress in the pin (taken from 403 stainless steel stress range diagram for 700°F and 10^8 cycles) is 44,000 psi single amplitude. This is more than triple the steady-state stress and appears to be more than satisfactory.

VIBRATION ANALYSIS OF SHROUD

Compromises between aerodynamic requirements and mechanical design limitations resulted in the final design of a shroud with thin, extended tips. Since these tips could be susceptible to vibration, analysis and bench tests to investigate shroud vibration characteristics were made prior to high-speed compressor operation.

Analysis was directed toward calculation of shroud natural frequencies. The shroud has the basic shape of a thin wheel which will have natural frequencies of 2 basic mode shapes (diametral and circumferential). Diametral modes consist of cosine type deflection of the wheel rim with nodes along diameter lines, as seen in Figure 40(a). The particular diametral

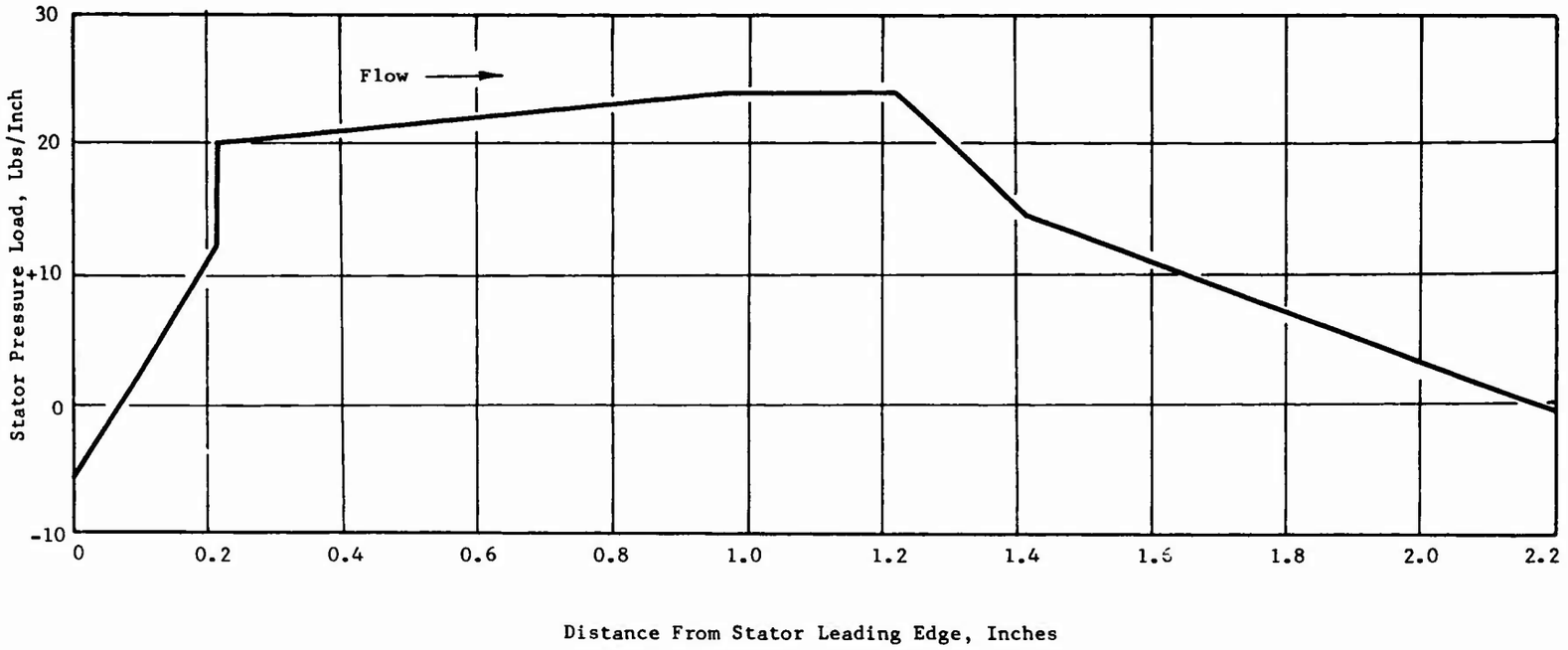

Figure 38. Supersonic Stator Load Distribution.

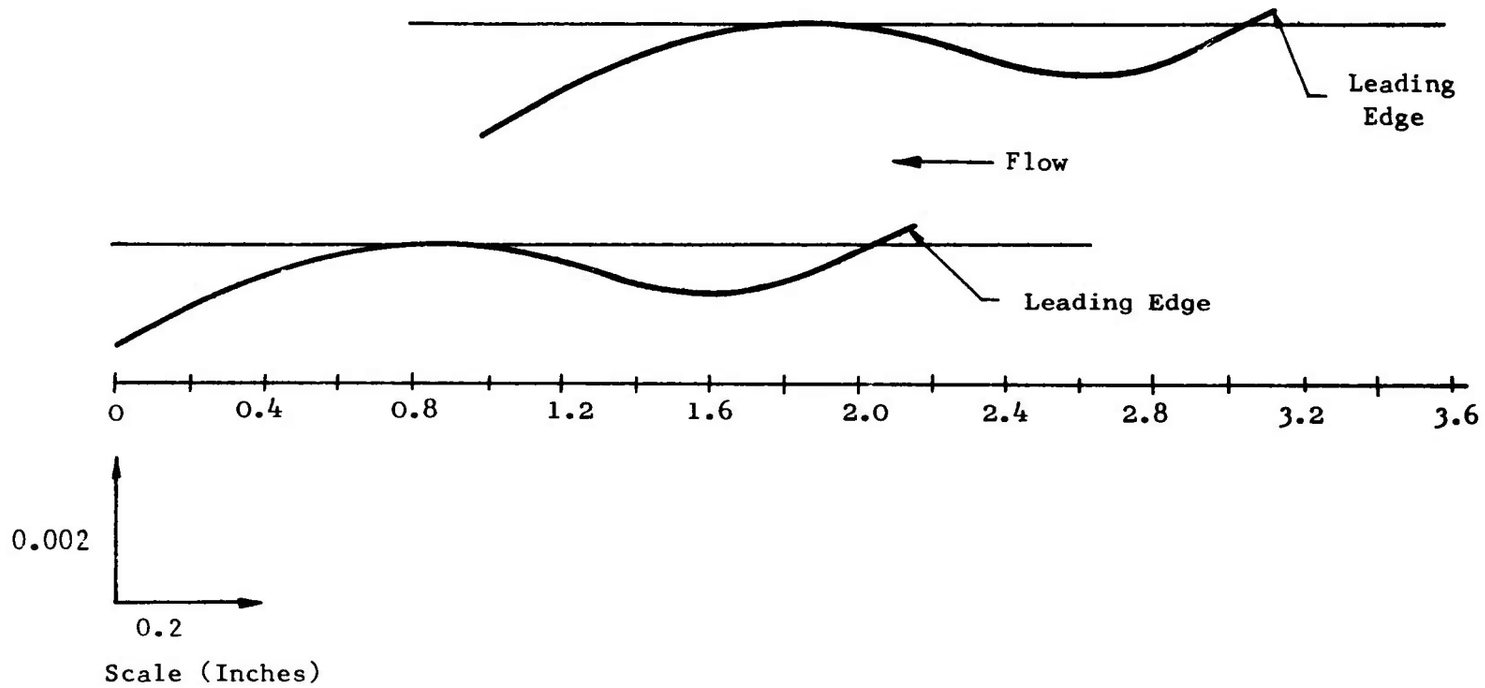

Figure 39. Deflected ROC Supersonic Stator Cascade.

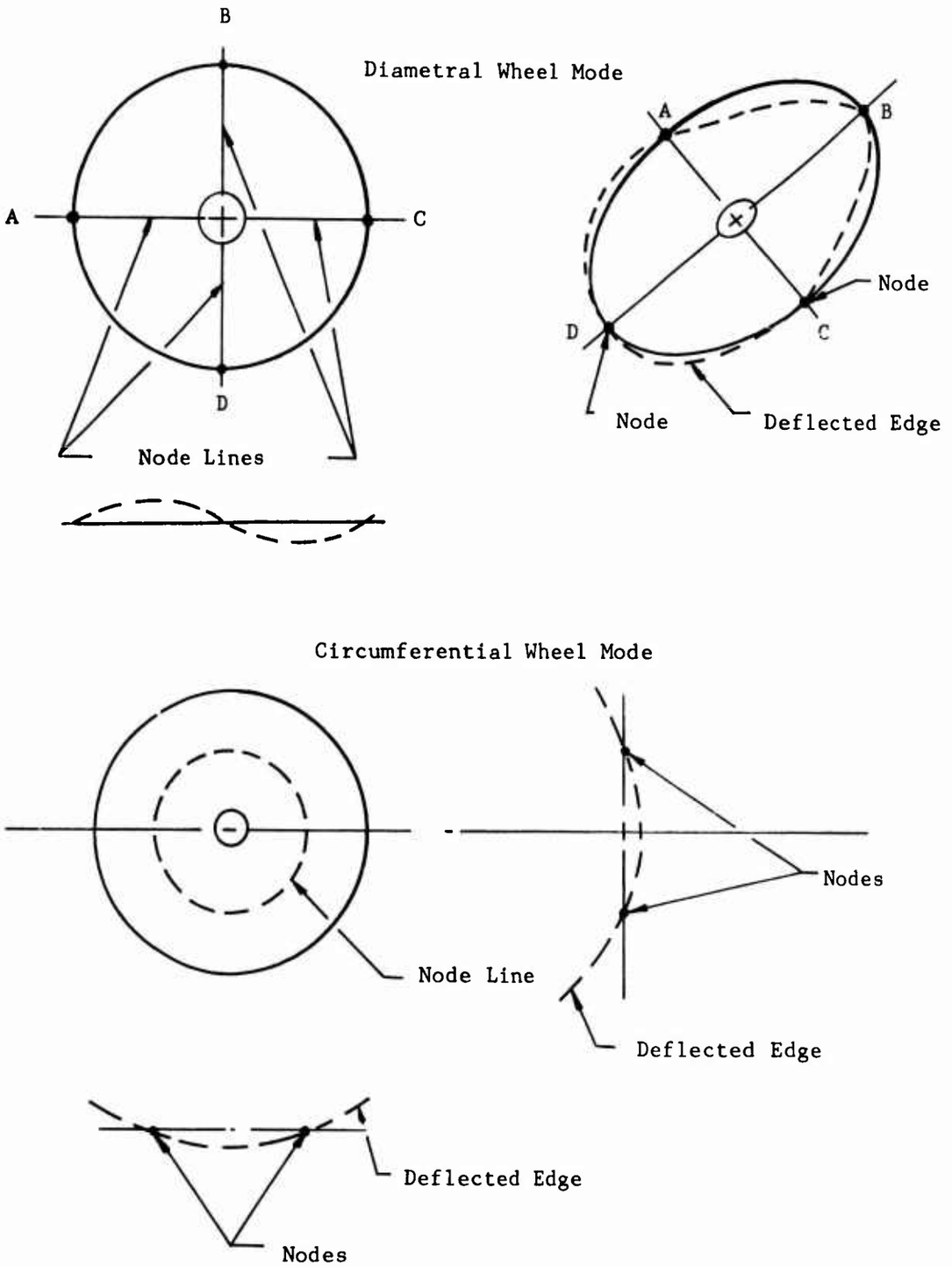

Figure 40. Diametral and Circumferential Vibration Modes of a Thin Disc.

mode of vibration is denoted by the number of full cosine waves developed. For example, the vibration mode shown in Figure 40(a) is a Cos 2θ or 2θ mode since there are 4 node lines or 2 full cosine waves present.

Circumferential, or umbrella, modes consist of symmetric deflection of all wheel elements at the same radius, and nodes are circles at a particular radius, as seen in Figure 40(b). The particular circumferential mode of vibration is denoted by the number of circumferential nodes. As an example, the mode shown in Figure 40(b) is a first mode vibration since it has only 1 node line.

To make a frequency search, the shroud geometry was simplified to model form and an existing GE computer program was modified to accept this shroud model, as shown in Figure 41. The frequency search was made for zero rotational speed and also for various operating speeds. The frequencies at operating speeds were calculated by adding the centrifugal stiffening effect of speed to the frequency for zero speed according to the formula:

$$f = \left[f_s^2 + B\omega^2 \right] \qquad (1)$$

where f = shroud natural frequency at operating speed, cps

f_s = shroud natural frequency at zero rotational speed, cps

ω = compressor rotational speed, radians/second

B = shroud centrifugal stiffening factor

Thus, the shroud frequency for any mode shape will increase as speed increases.

The results of the blade side frequency search up to 1,800 cps are shown in Table II. As will be noted, all shroud modes are found to be diametral. The circumferential modes are more difficult to excite and will be found at higher frequencies well out of the operating range of the ROC.

This analytical approach gives close estimates for zero speed frequencies and the best available calculation for the added effects of rotational speed. However, to obtain an improved understanding of shroud vibration, a bench test of the shroud was made (see section on Shroud Test) to verify the zero speed frequencies. As seen from Table II, the calculated values at zero speed are within 10 percent of the test data.

Combining the best results of test data (the zero speed frequencies) and of the analysis (the B factor stiffening effect) gave the most accurate overall picture of shroud vibration, as shown in Table III.

TABLE II. BLADE SIDE SHROUD VIBRATION - NATURAL FREQUENCIES

	Mode \ RPM	Frequency (CPS) 0	17,000	34,500
Calculated	2θ	750	948	1,391
	3θ	780	987	1,443
	4θ	825	1,047	1,518
Test Data	2θ	700	-	-
	3θ	732	-	-
	4θ	752	-	-

TABLE III. FINAL SHROUD VIBRATION - NATURAL FREQUENCIES

	Mode \ RPM	Frequency (CPS) 0	17,000	34,500
Blade Side	2θ	700	910	1,369
	3θ	732	948	1,420
	4θ	752	987	1,500
Seal Side	2θ	830	1,000	1,390
	3θ	952	1,120	1,520
	4θ	1,040	1,210	1,600

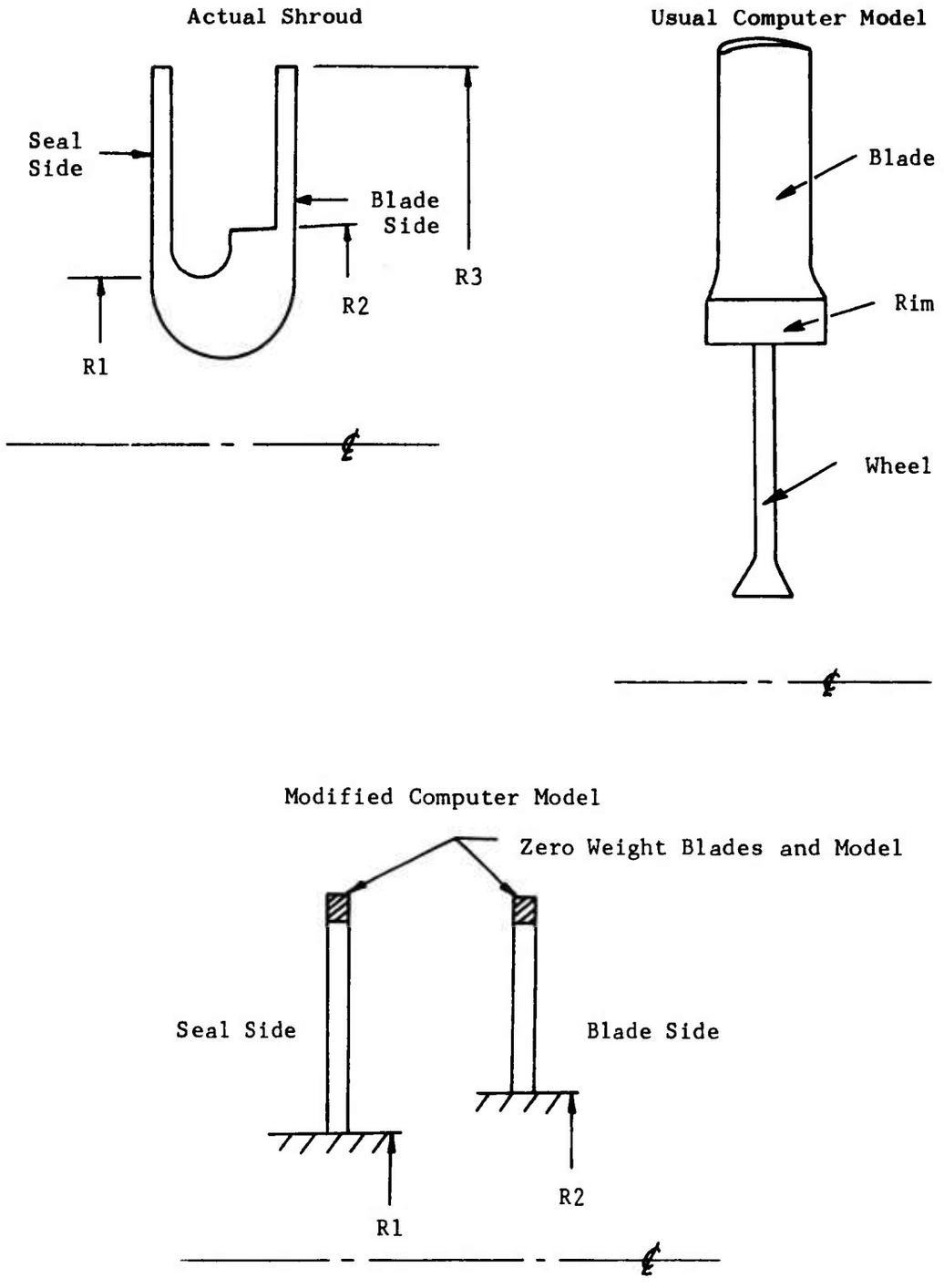

Figure 41. Representation of the Rotating Shroud and the Models Used to Synthesize Rotating Shroud Computer Program.

The tendency of the shroud natural frequencies to be excited can be found from a Campbell plot of frequency versus compressor speed. The theory of the Campbell plot as outlined in References 2 and 3 is as follows. Any of the diametral modes in a rotating wheel pass a stationary point at a certain frequency according to the wheel rpm and the mode frequency. At zero speed, the passing frequency equals the mode frequency. As speed increases, the passing frequency is the difference between the mode frequency and the wheel speed. Thus, when mode frequency equals wheel speed, the wheel mode shape appears stationary to an observer and is susceptible to excitation by any stationary static pressure gradient in the compressor.

The Campbell plot shows these dangerous areas as cross points of a wheel mode line with a node per revolution (or simply, per rev) line. Thus, cross points or critical speed points are noted for 2θ with 2 per rev, 3θ with 3 per rev, etc, in Figures 42 and 43. These plots show that the shroud has been designed to meet the design objective of "no critical speed points between 80 percent and 100 percent design speed".

BENCH TESTS

The ROC components identified as needing empirical investigation were: (1) the rotor blade, (2) the shroud, (3) the supersonic stator vane, and (4) the blade Belleville spring washers. Also tested for calibration and sensitivity were the shroud strain gages and blade strain gages.

Rotor Blade Tests

A preliminary check for possible blade resonant frequencies gave:

Hand Calculation:	$f_{\text{fixed-free}}$	= 1,744 cps
	$f_{\text{fixed-pinned}}$	= 7,650 cps
and Computer Analysis:	no resonance; 0-6,000 cps at search intervals of 30 cps	

The preliminary conclusion from these analyses was that the blade was so stiff that its resonant frequencies were very high. A recommendation was made to bench test the blades, primarily to check local blade-edge vibrations which cannot be easily found by analysis and also to double check the vibration analysis for total blade resonance.

Test objectives were:

1) Identify fundamental resonant frequencies

2) Determine the mode configurations of the fundamental resonant frequencies.

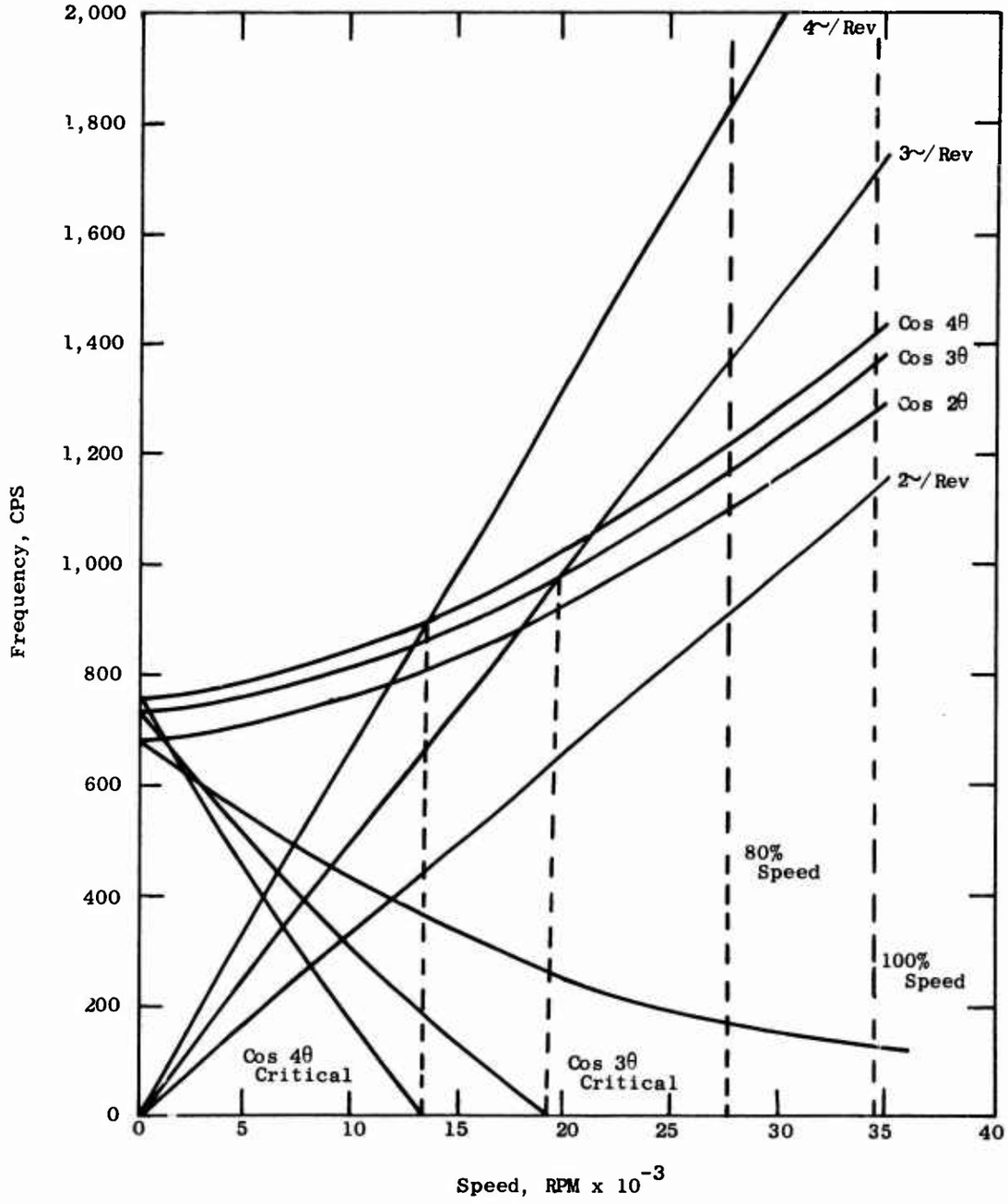

Figure 42. ROC Shroud Campbell Diagram (Blade Side).

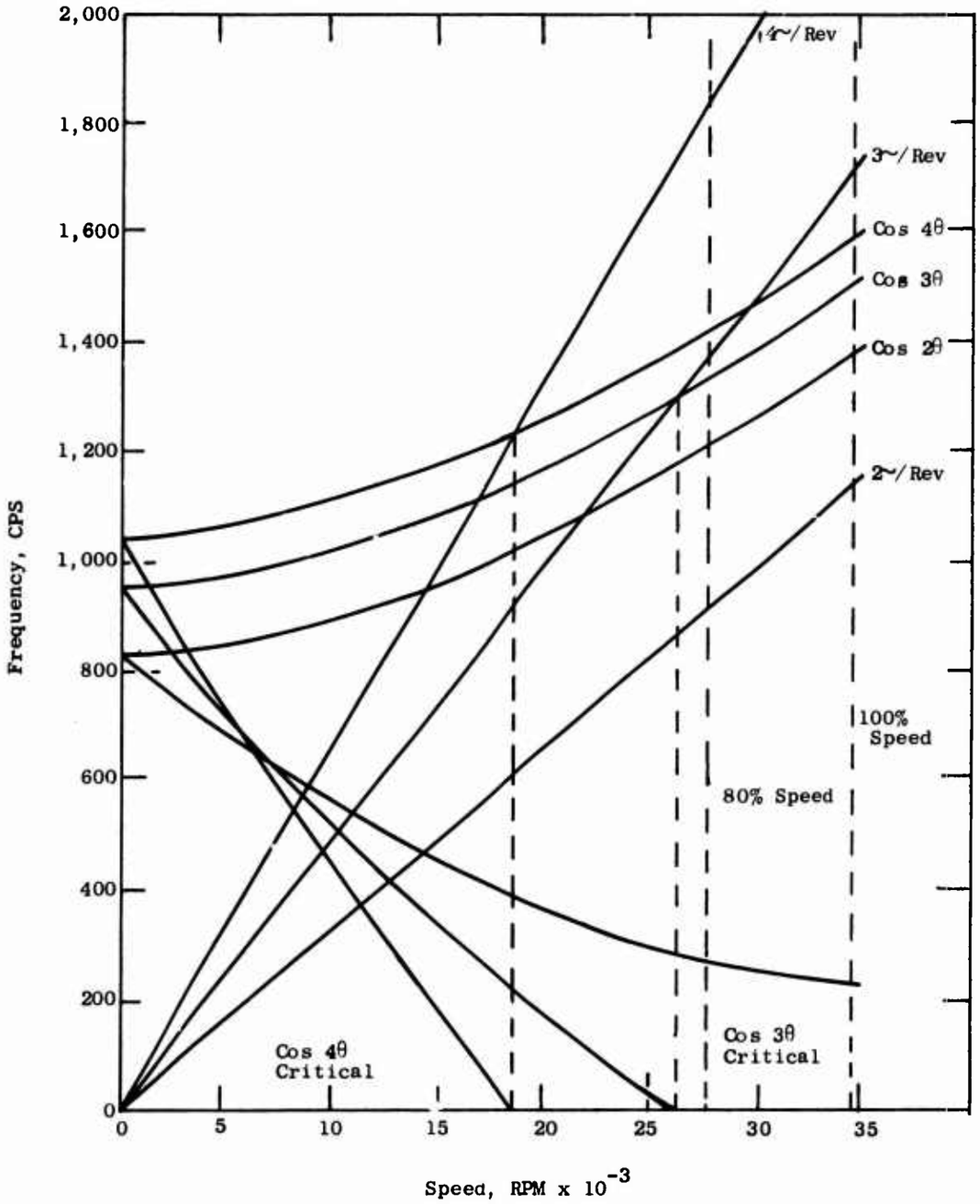

Figure 43. ROC Shroud Campbell Diagram (Seal Side).

3) Investigate stress distributions of the principal modes.

4) Recommend blade strain gage locations and stress limits for ROC testing.

Test Setup

A special fixture was made to hold both threaded (P01) and unthreaded (P02) type blades in a way similar to the actual ROC assembly. Figure 44 shows the blade mounted in the fixture. One P01 and one P02 blade were also instrumented with strain gages once mode shapes (and thus most highly stressed areas) were identified. Figure 45 shows a close-up of an instrumented P02 blade in the fixture and a separate instrumented P01 blade.

Procedure

The detailed testing steps are outlined and the patterns for strain gage locations used on the bench test blades are presented in Appendix III.

Results

All blade resonant frequencies found and the relative stress amplitude measured at each strain gage are shown in Table IV. For each frequency, the most sensitive gage reading is rated as 100 percent; all other gage readings are related to this maximum gage reading in terms of percent.

Conclusions

A complete range of blade resonant frequencies was found; many of these frequencies were local blade edge vibrations. Sizable scatter was noted in determining some resonant points. This was found to be primarily due to variation in the firmness of the blade attachment to the fixture. It was no ed, though, that all resonance frequencies were difficult to excite.

Recommendations

Due to the limited capacity of the slip ring used for pickup of rotor instrumentation signals, the number of blade strain gages installed had to be limited to 12. The gages chosen were those which would pick up the most resonant frequencies possible and those in the most sensitive location for these frequencies. The recommended gage locations for both P01 and P02 blades are presented in Appendix III.

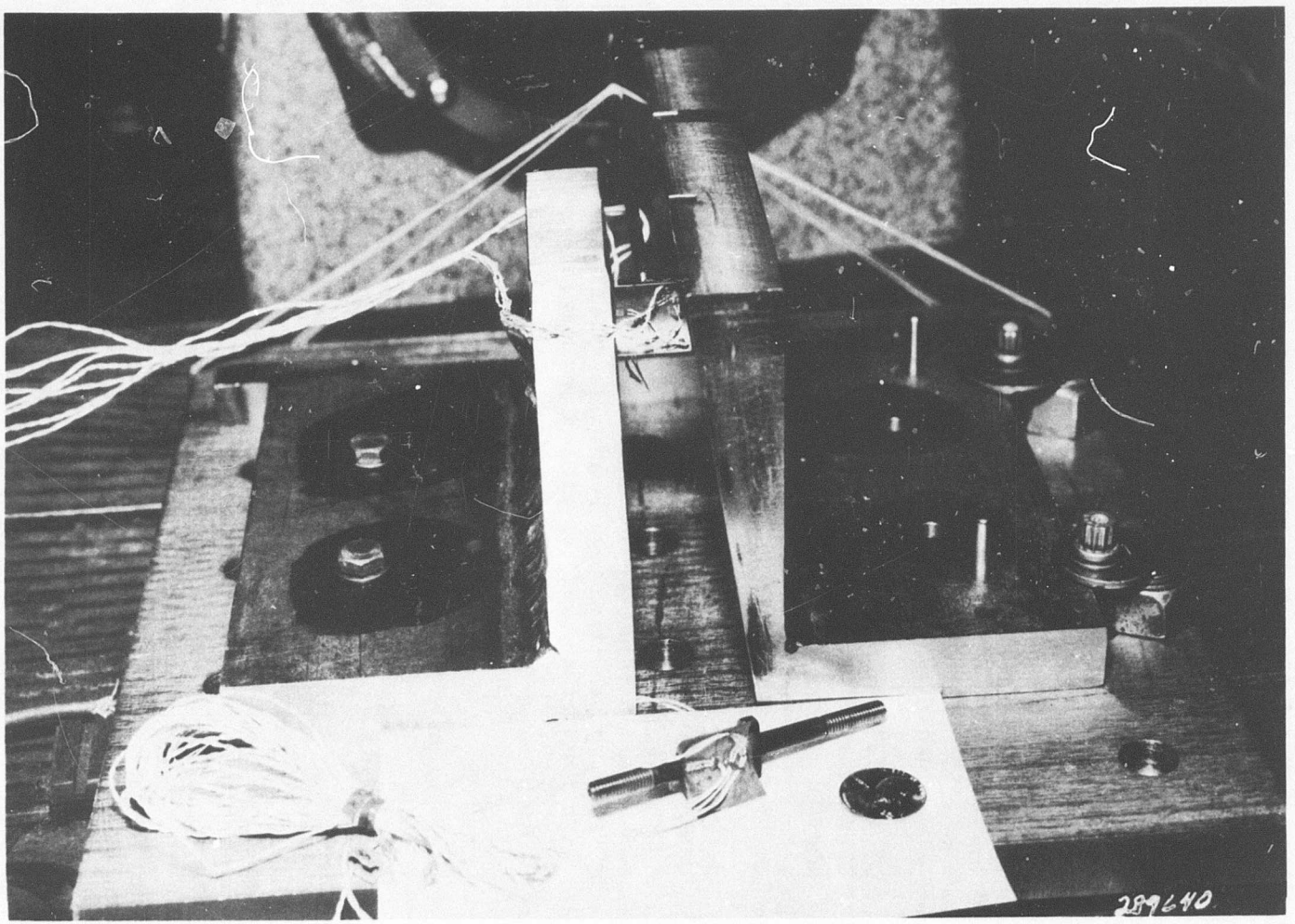

Figure 44. Instrumented Rotor Blade Mounted in Simulated Disc and Shroud for Experimental Vibration Analysis.

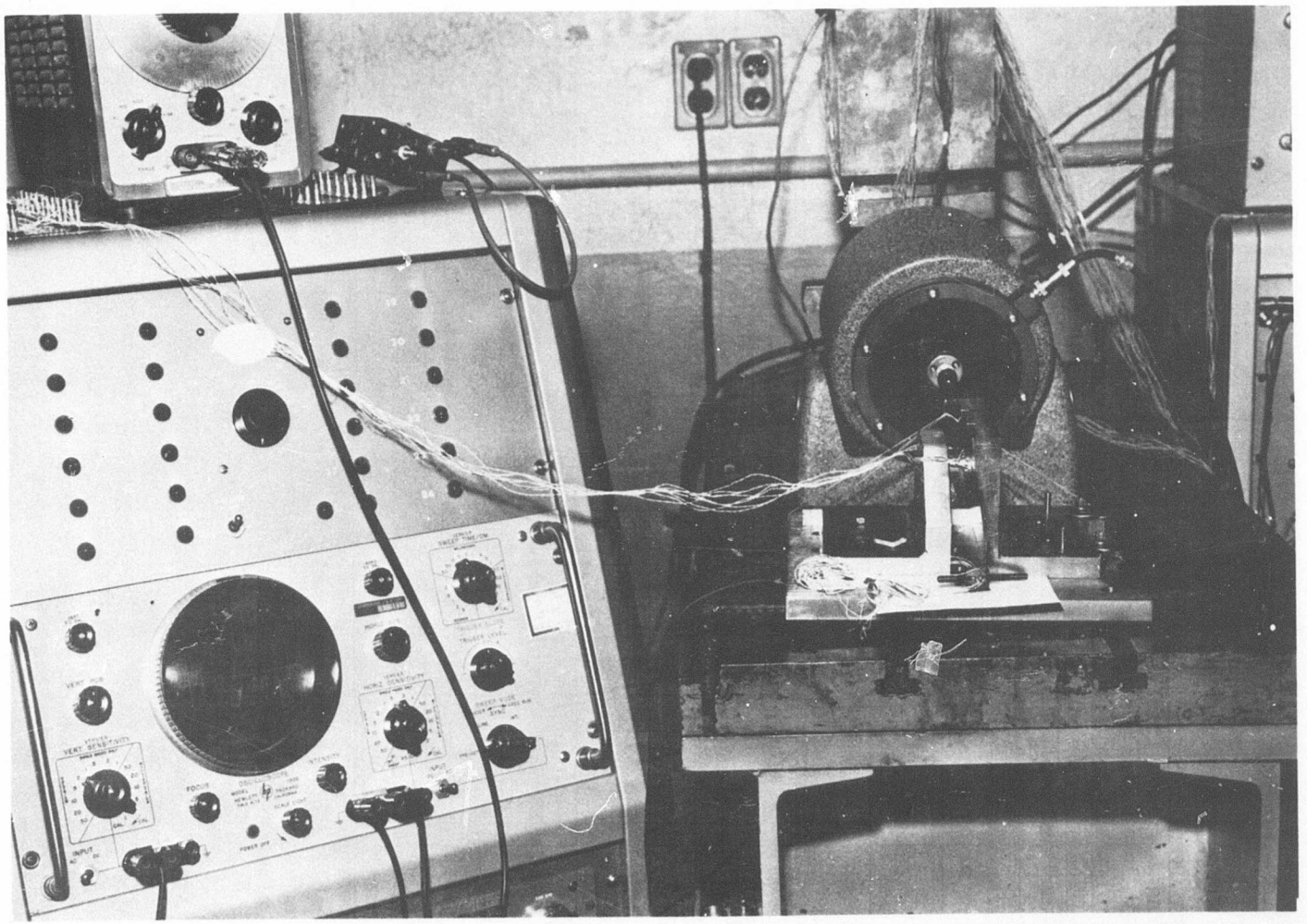

Figure 45. Overall View of Bench Setup for Experimental Analysis of Rotor Blade Vibration.

TABLE IV. STRESS DISTRIBUTION AT RESONANCE ON Ti-6Al-4V ROC BLADES

Frequency (CPS)		Gage Stress (%)					
(Resonance)	(± Range)	a	b	c	d	e	f
Threaded Blades (P01 Type)							
547		4	79	88	13	79	100
723		4	70	68	11	70	100
1,790	40	-	-	100	13-68	-	32-55
2,338	264	6	100	45	14	100	24-100
3,899	91	-	100	30	10-71	100	20-100
4,440	2	-	-	100	13	-	84
4,738	114	-	-	100	29	-	63
5,511	460	-	100	-	24	100	85
9,100	550	18	100	72	30	100	13
11,276	700	33	100	63	20	100	20
Unthreaded Blades (P02 Type)							
657	-	8	100	76	16	100	6
1,197	-	8	100	33	10	100	8
2,067	50	-	100	60	12-40	100	-
2,335	15	-	100	40-77	16-40	100	-
2,905	14	-	42	15-27	0-42	46	-
4,743	119	-	-	100	43	-	-
8,385	167	-	100	35	-	100	-
9,447	184	-	-	100	22	-	-
11,732	168	-	-	56	100	-	-

Shroud Test

Objectives

1) To identify the resonant frequencies of the principal modes (Cos n θ) at zero speed.

2) To establish the stress distribution of Cos 2θ, 3θ, and 4θ modes.

3) To investigate the shroud tip deflections associated with the stresses of the fundamental modes.

4) To set limits on shroud vibration during ROC test runs.

Test Setups

The 2 different bench test setups used are shown schematically in Figures 46 and 47. Setup Number 1 was used to establish the resonant frequencies of the principal modes. The equipment used is shown in Figure 48. Setup Number 2 was used to measure vibratory deflections and stresses. The apparatus and details of this setup are shown in Figures 49, 50, 51, and 52.

Setup Number 1

The shroud mounted on the fixture rests on a rubber pad on the test table. An electromagnet with oscillator and power supply provides the source of excitation. A crystal pickup, in contact with the shroud, detects the shroud response. The electromagnet input signal and the pickup output signal are combined on an oscilloscope in order to establish node lines and phase relationships.

Setup Number 2

The shroud, instrumented with sixteen 350-ohm strain gages located and oriented as shown in Figures 53 and 54 and mounted firmly in the fixture, rests on a rubber pad on the test table. The strain gage leads are connected through a switch box to a readout electronic system consisting mainly of an Ellis amplifier with calibrator and a Tectronic Type 532 oscilloscope.

A telescope and a Bently eddy-current proximity probe (proximeter) for deflection measurements are placed as shown in Figure 52. The Bently probe detector is located in the proximity of the shroud surface; the lead is connected to the Detector Driver. The power for the probe is obtained by a regulated power supply delivering a constant negative 18 volts DC at 25 milliampere (ma). The output voltage of the proximiter is used to drive an oscilloscope calibrated to read deflection in mils.

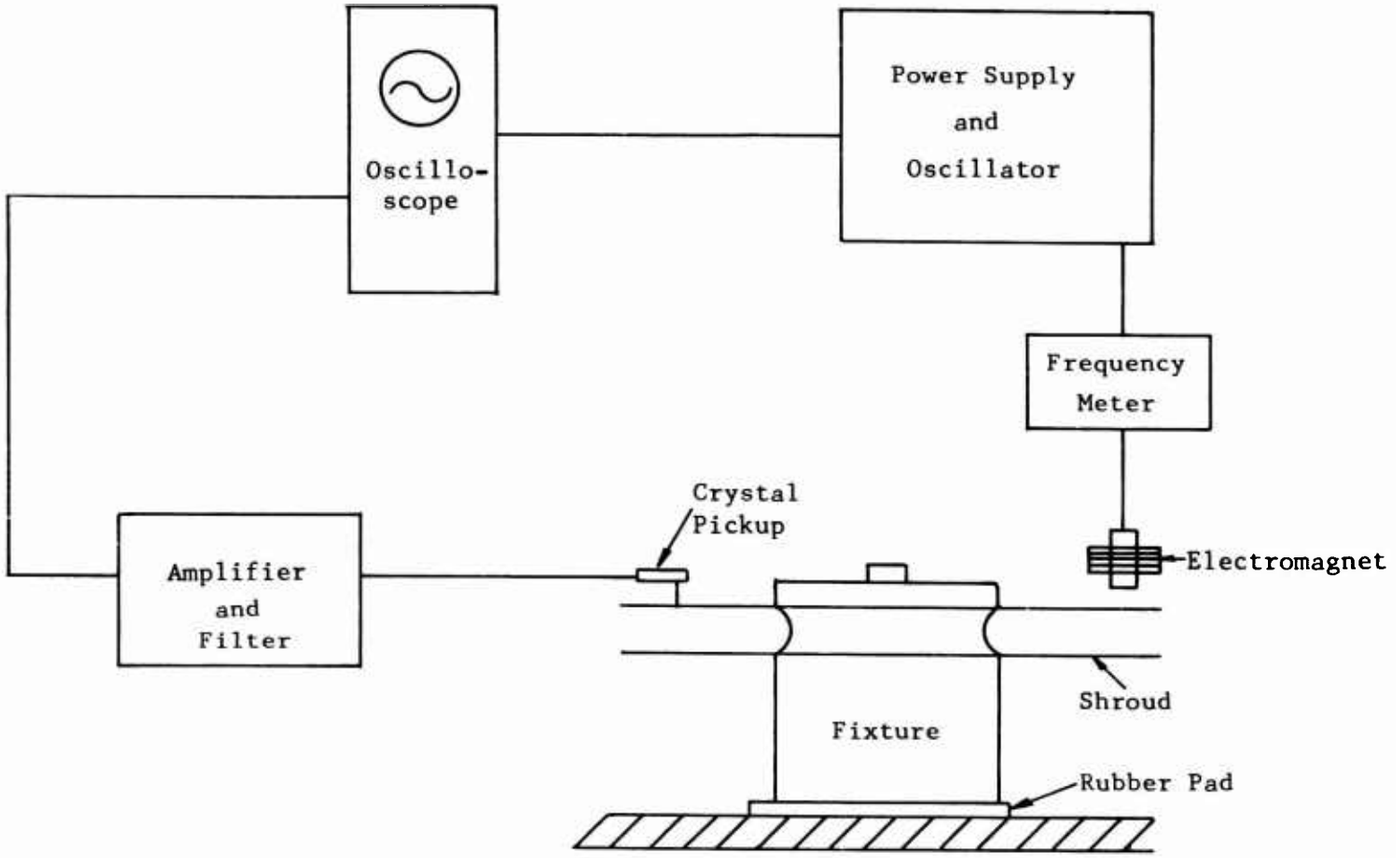

Figure 46. Setup (1) for Frequencies and Modes Investigation.

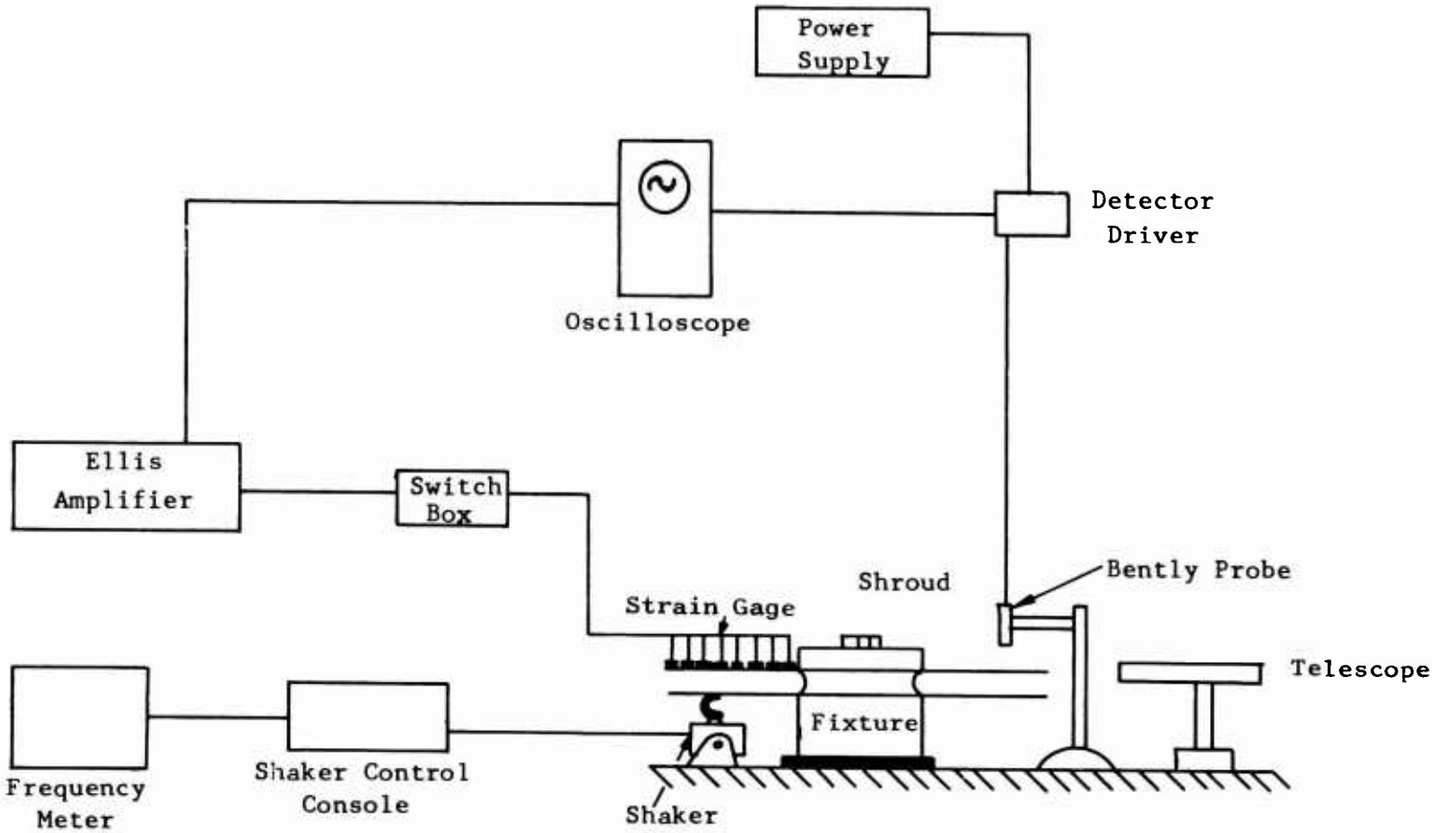

Figure 47. Setup (2) for Vibratory Deflections and Stress Investigation.

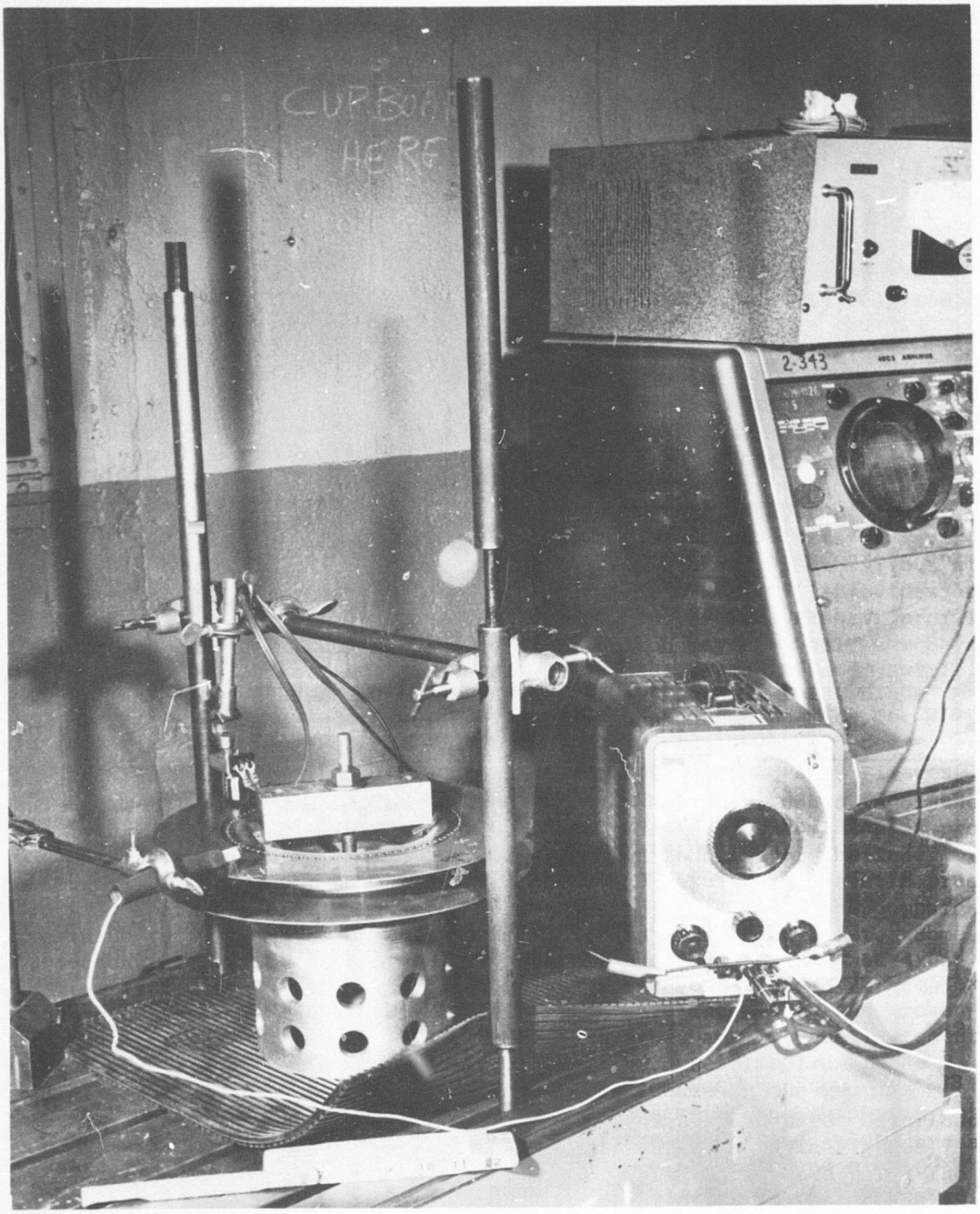

Figure 48. Close-up View of Setup Number 1 Showing Electronic Pickup Used to Detect Rotating Shroud Vibrations.

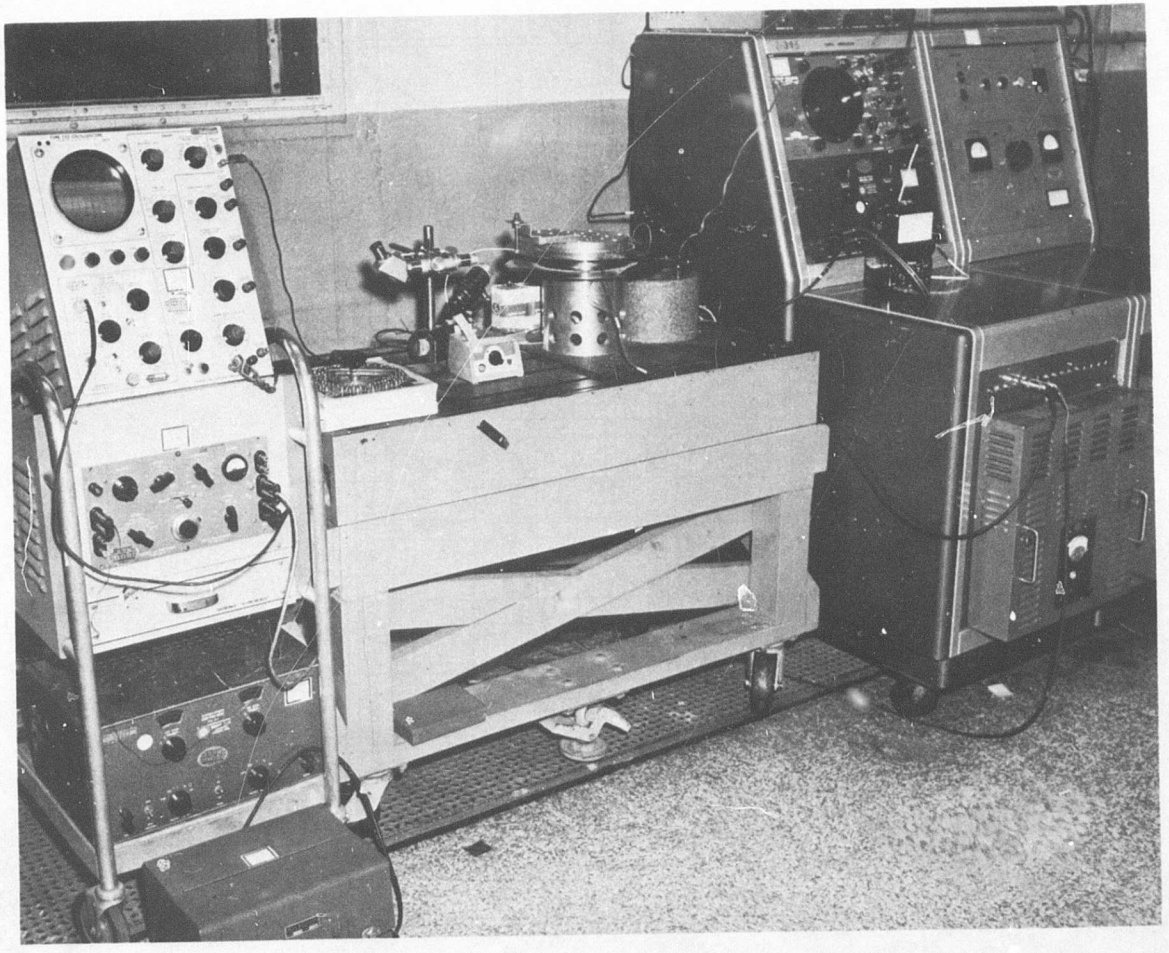

Figure 49. Overall View of Bench Setup for Experimental Analysis of Rotating Vibration Patterns (Setup Number 2).

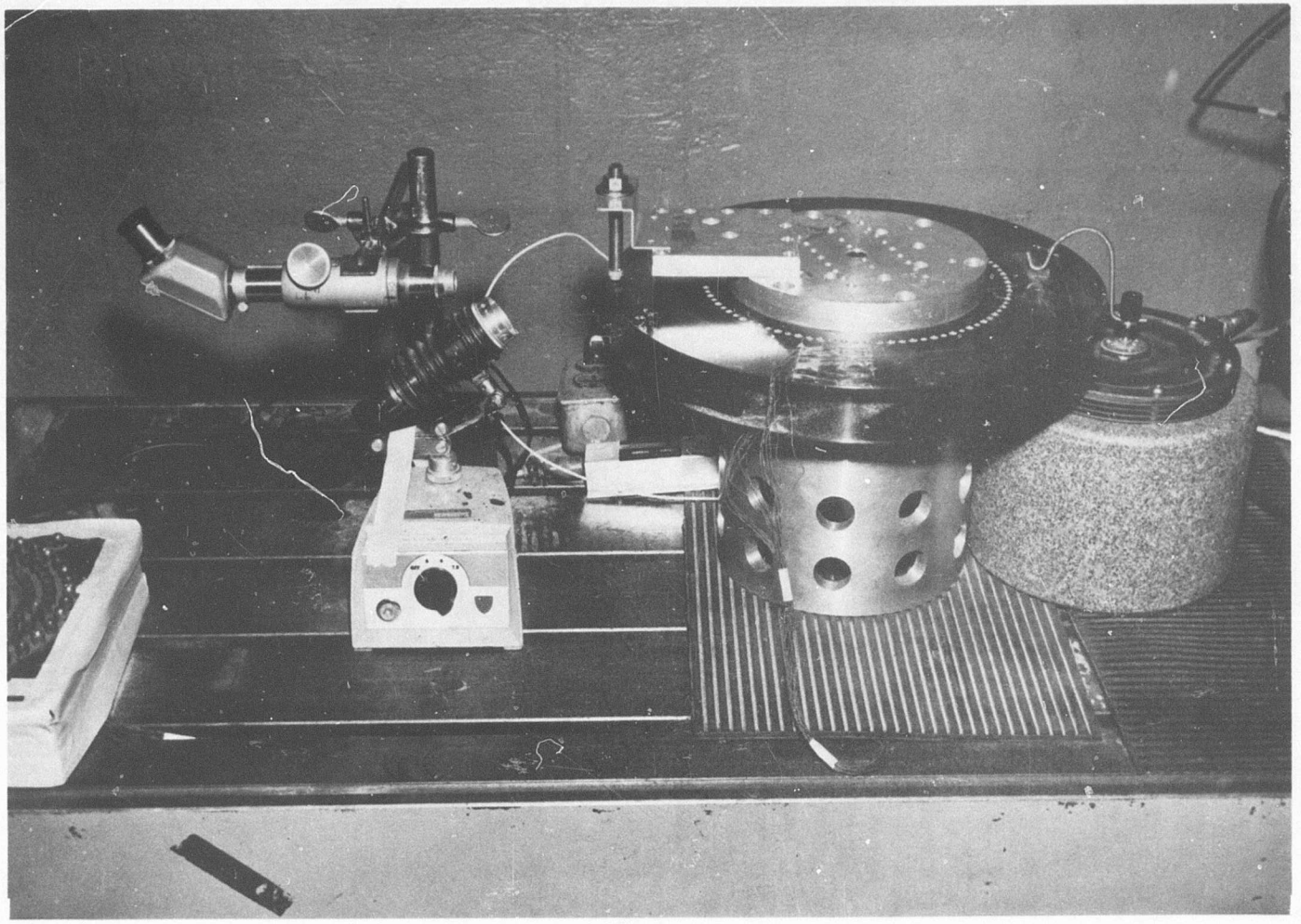

Figure 50. Details of Excitation Mechanism and Deflection Measurement Apparatus.

Figure 51. Close-up View of Rotating Shroud Mounted on the Fixture With the Shaker Used for Setup Number 2.

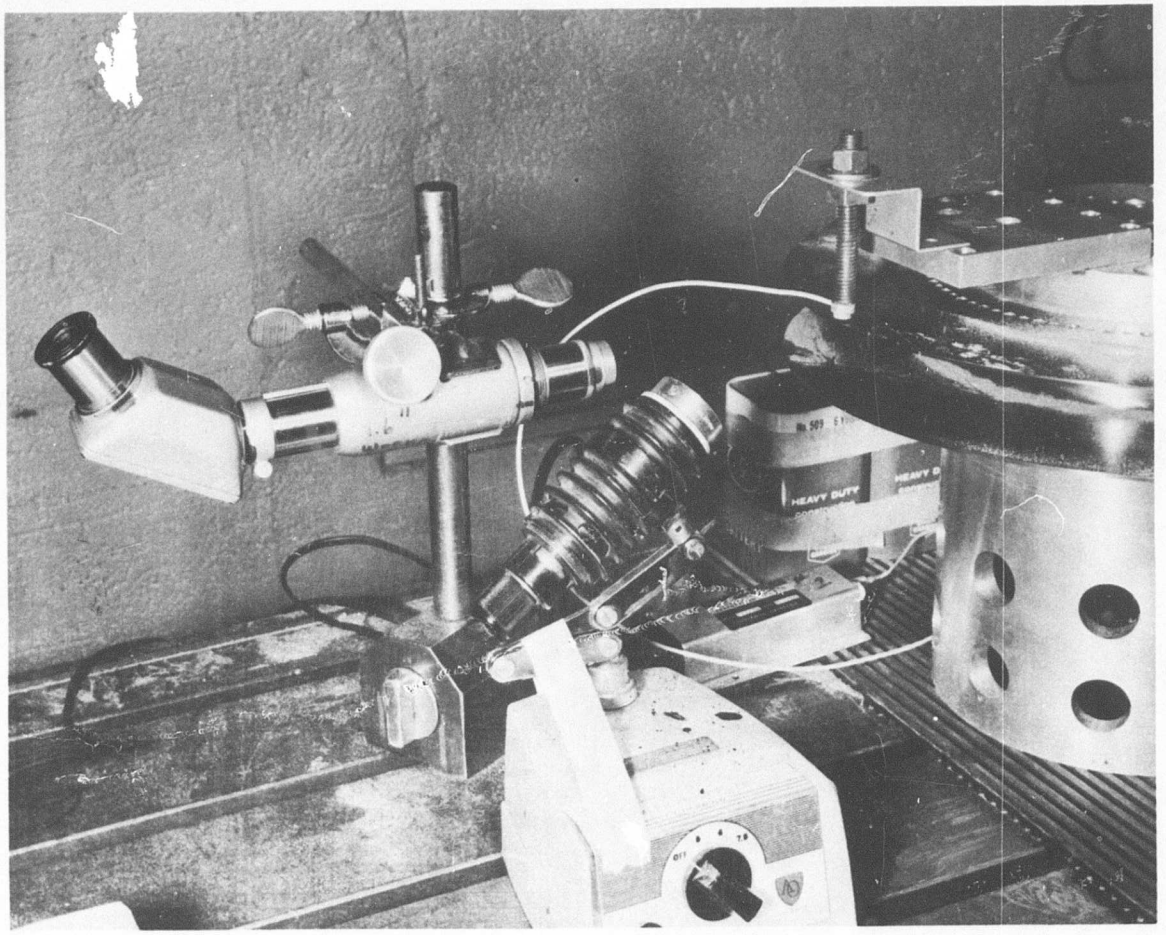

Figure 52. Setup Used to Calibrate the Proximeter Which is Shown Mounted Adjacent to the Rim of the Rotating Shroud.

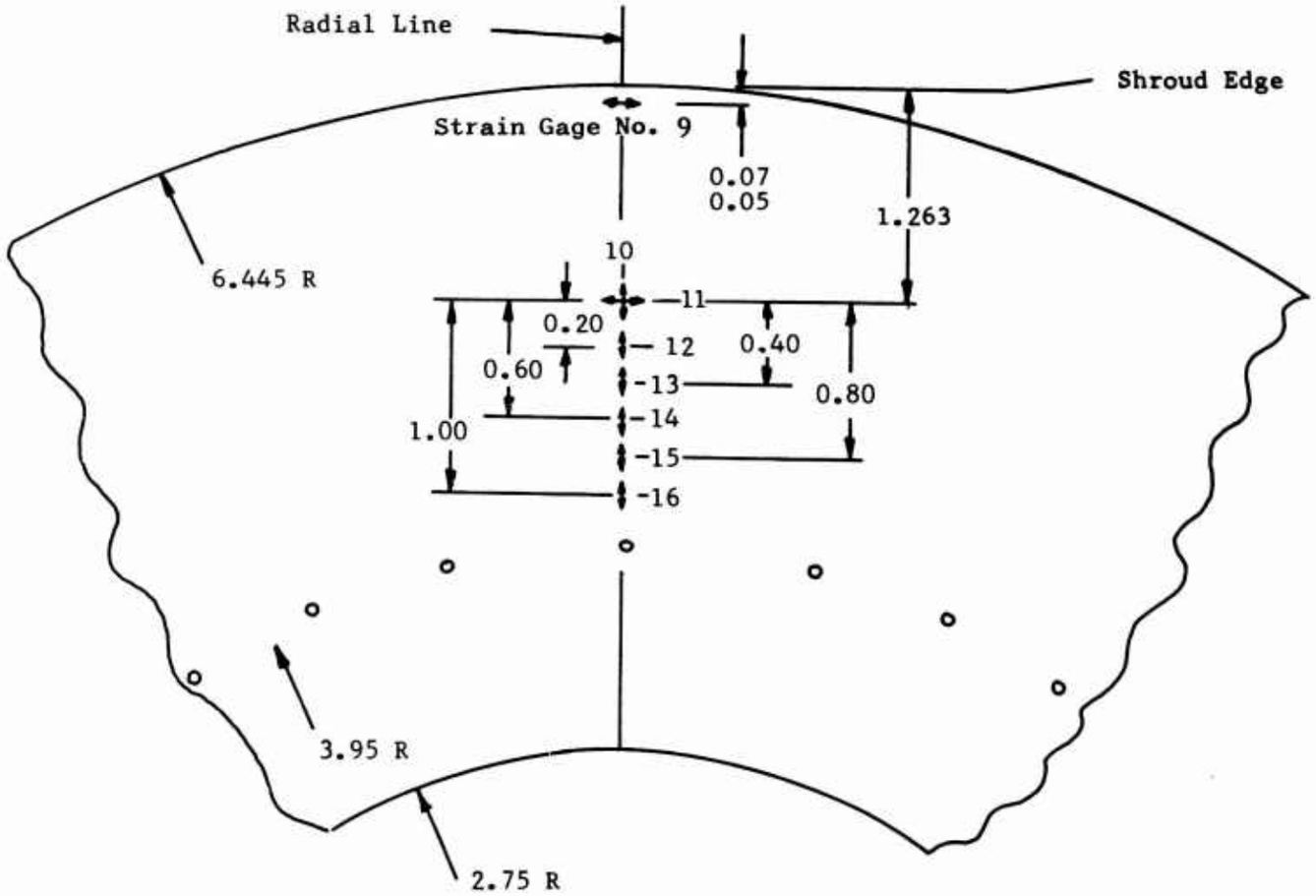

Figure 53. Shroud (Blade Side) Strain Gage Location.

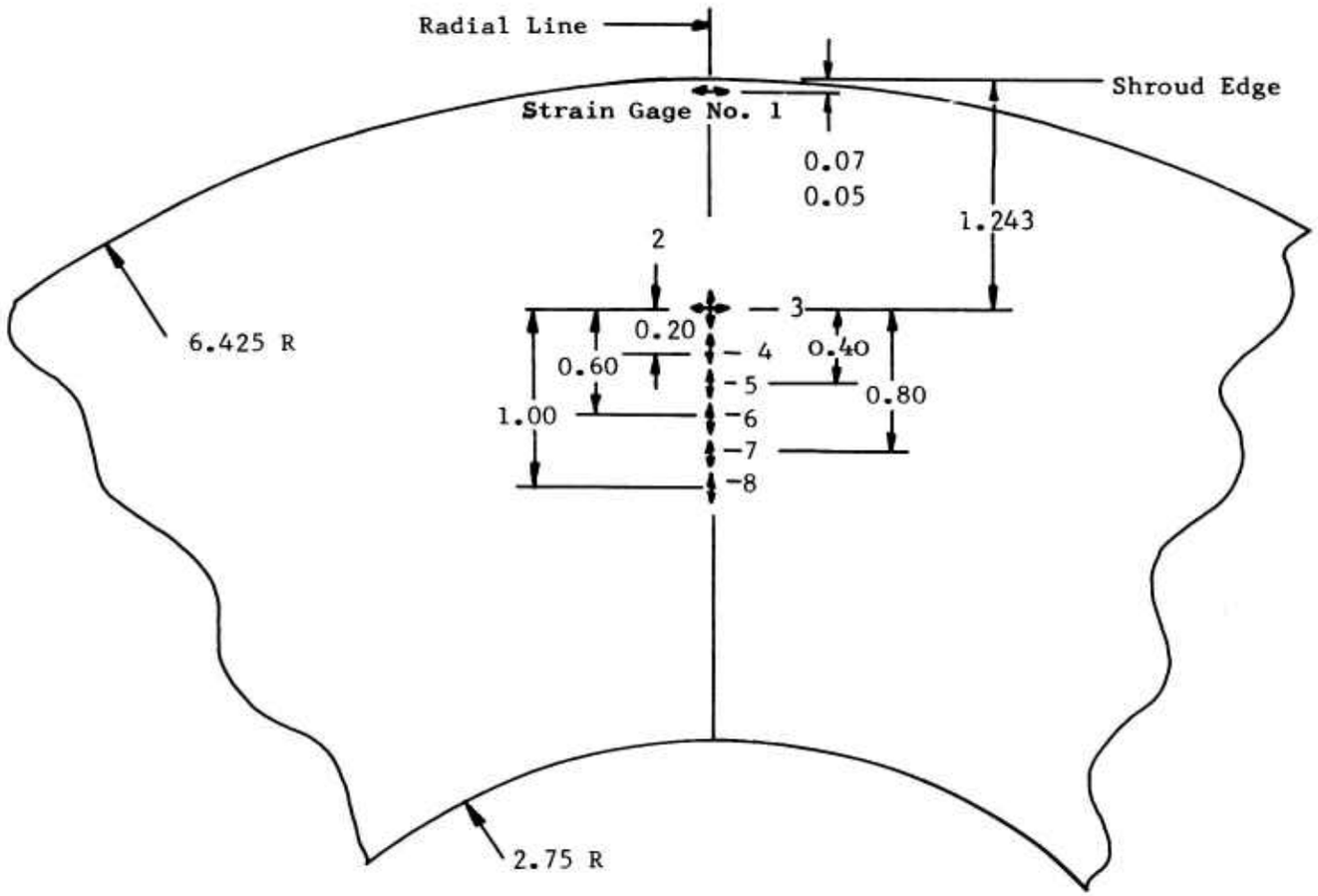

Figure 54. Shroud (Seal Side) Strain Gage Locations.

Excitation of the part is accomplished through a 75-pound electrodynamic shaker with matching power supply and a Berkeley Beckman EPUT meter for frequency reading.

Procedure

The test procedure was as follows:

1) Set up test as described in Setup Number 1.

2) Cement a thin magnetic steel patch (approximately 0.5 x 0.02 inch) on the shroud blade side close to the edge of the disc.

3) With the electromagnet just above the steel patch, perform a frequency scan between 0 and 4,000 cps and record all resonant frequencies.

4) With the crystal pickup and with fine sand, establish nodal patterns.

5) Obtain pictures of sand patterns for several of the principal modes.

6) Repeat steps 2 through 5 on the shroud seal side.

7) Instrument shroud with strain gages as shown in Figures 53 and 54.

8) Make Setup Number 2, mounting the shroud so that the blade side is excited.

9) Obtain Cos 2θ mode frequency.

10) Change the location of excitation until the strain gages are approximately on a radius lying between 2 consecutive radial node lines.

11) Locate telescope and probe to read maximum deflection at the periphery of the shroud.

12) At 2 or more shaker power input levels, record all strain gage readings (both on blade side and seal side) and maximum displacements.

13) Repeat steps 10 through 12 for Cos 3θ and Cos 4θ modes.

14) Mount the shroud so that the seal side is directly subjected to the shaker excitation.

15) Perform steps 9 through 13 for this condition.

16) Procure photographs of the setup and details of the test.

Results

The frequency scans performed with test Setup Number 1 have resulted in the resonant frequencies for both the shroud blade and seal sides given in Table V. The modes associated with these frequencies are also given in this table. Schematic node shapes of the first 3 modes are given in Figure 55. Sand pattern pictures of some of the vibratory modes are shown in Figure 56.

Campbell diagrams have been obtained for Cos 2θ, 3θ, and 4θ modes using the above-zero speed frequencies and other frequency points determined by the following equation:

$$f = \sqrt{f_s^2 + B\omega^2} \qquad (2)$$

where f is the frequency of vibration at the desired speed, f_s is the frequency obtained from the bench test, ω is the rotating speed, and B is the centrifugal stiffening factor which has been determined analytically by computer program analysis. Campbell diagrams so obtained are shown in Figure 43.

Test Setup Number 2 has yielded results which are tabulated in Table VI. Curves of radial stress ratios (gage stresses divided by maximum measured gage stress) versus shroud radius for Cos 2θ, 3θ, and 4θ modes are plotted in Figures 57, 58, and 59 for the blade side and in Figures 60, 61, and 62 for the seal side.

When the shroud blade side was excited at its resonant frequencies, the strain gages on the seal side (gages 1 through 8) showed insignificant response; the same applies for the case when the seal side was excited.

Figures 63, 64, and 65 show how the maximum strain gage stresses on the shroud blade side are related to the respective maximum shroud edge axial displacements at each of the modes analyzed. Figures 66, 67, and 68 show this same relationship for the seal side.

TABLE V. SHROUD VIBRATORY MODES

Vibratory Mode		Resonant Frequency (CPS)	
Cosine	No. of Radial Nodes	Blade Side	Seal Side
2θ	4	700	830
3θ	6	732	952
4θ	8	752	1,040
5θ	10	818	1,196
6θ	12	920	1,414
7θ	14	1,072	1,700
8θ	16	1,266	2,036
9θ	18	1,484	2,422
10θ	20	1,744	2,858
11θ	22	2,044	3,328
12θ	24	2,372	3,834

TABLE VI. SHROUD STRAIN GAGE READINGS

	Blade Side Excited										Seal Side Excited							
	2 Wave			3 Wave				4 Wave			2 Wave		3 Wave			4 Wave		
Frequency (CPS)	682	682	682	696	696	696	696	725	724	725	915	912	947	947	947	1040	1040	1040
Displacement (Mils)	2.23	1.9	3.23	1.25	1.0	0.75	0.25	1.0	0.5	3.0	0.25	0.5	0.5	0.625	0.75	-	0.25	0.5
Strain Gage No.																		
1	46	-	46	62	52	46	23	34	17	69	29	41	16	19	21	39	46	63
2	46	-	69	77	58	52	29	34	17	69	75	133	83	97	125	28	32	44
3	46	-	46	77	52	46	23	34	23	69	35	52	9	14	16	32	37	46
4	46	-	46	69	52	46	29	34	17	69	81	156	88	107	139	32	37	48
5	46	-	46	77	58	46	29	34	17	69	98	168	97	120	153	37	42	56
6	46	-	46	77	58	46	29	34	23	69	98	191	107	125	162	39	46	60
7	46	-	46	77	58	46	29	34	17	69	110	208	116	134	174	44	51	67
8	46	-	46	77	58	46	29	34	17	69	116	226	130	153	195	51	56	74
9	69	46	116	62	46	35	17	93	58	301	29	46	19	23	32	23	25	35
10	463	486	1,158	270	220	208	81	174	93	579	29	46	30	32	46	19	23	32
11	139	116	278	62	46	46	23	34	23	93	29	46	21	28	37	19	23	32
12	556	556	1,389	309	249	255	87	197	110	695	35	46	32	37	51	21	23	32
13	648	648	1,621	340	289	295	104	220	122	764	29	46	32	32	51	19	23	32
14	718	764	1,829	386	336	324	116	249	139	857	35	46	32	39	56	21	23	32
15	787	926	1,991	432	382	371	127	289	162	973	29	46	35	42	56	21	23	32
16	417	463	1,019	262	214	203	81	162	93	533	35	46	28	37	46	21	23	32

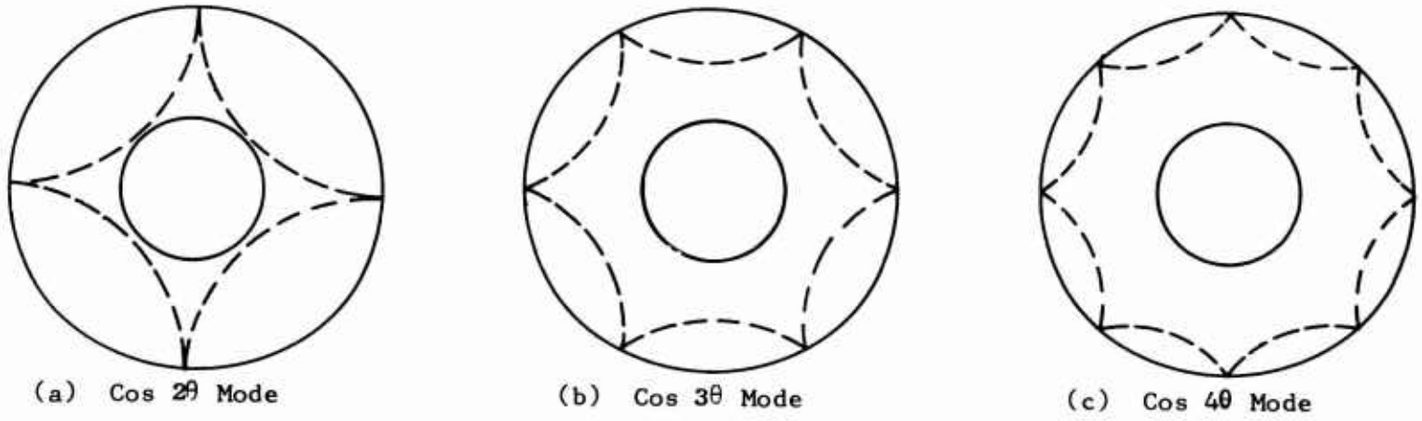

Figure 55. Schematic Shapes of the Principal Shroud Modes.

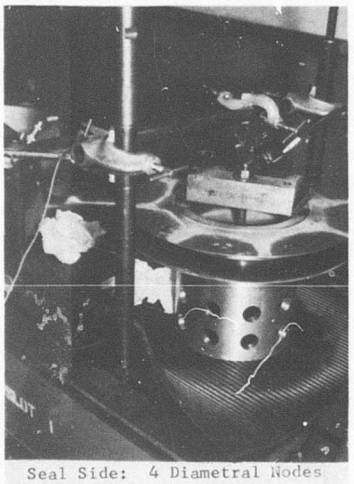

Seal Side: 4 Diametral Nodes
f = 1,040 cps

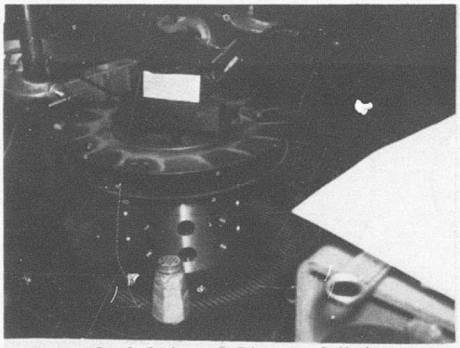

Seal Side: 8 Diametral Nodes
f = 2,036 cps

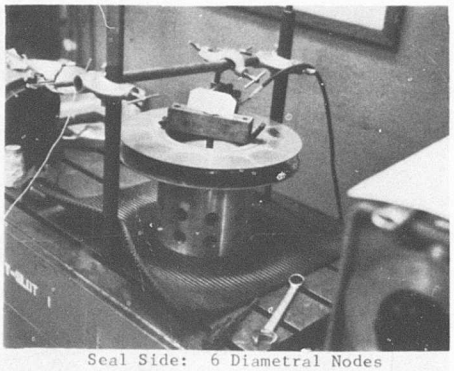

Seal Side: 6 Diametral Nodes
f = 1,414 cps

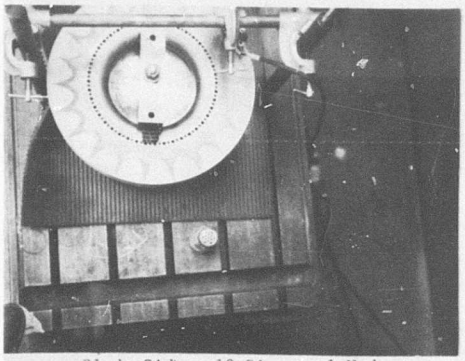

Blade Side: 12 Diametral Nodes
f = 2,372 cps

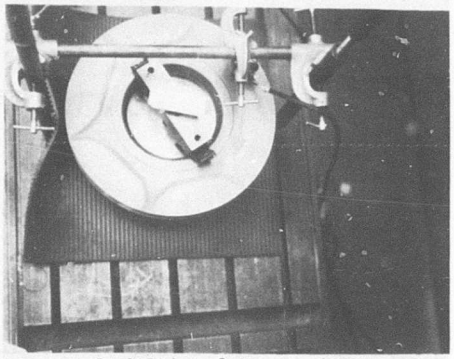

Seal Side: 3 Diametral Nodes
f = 952 cps

Figure 56. Shroud Sand Pattern Pictures.

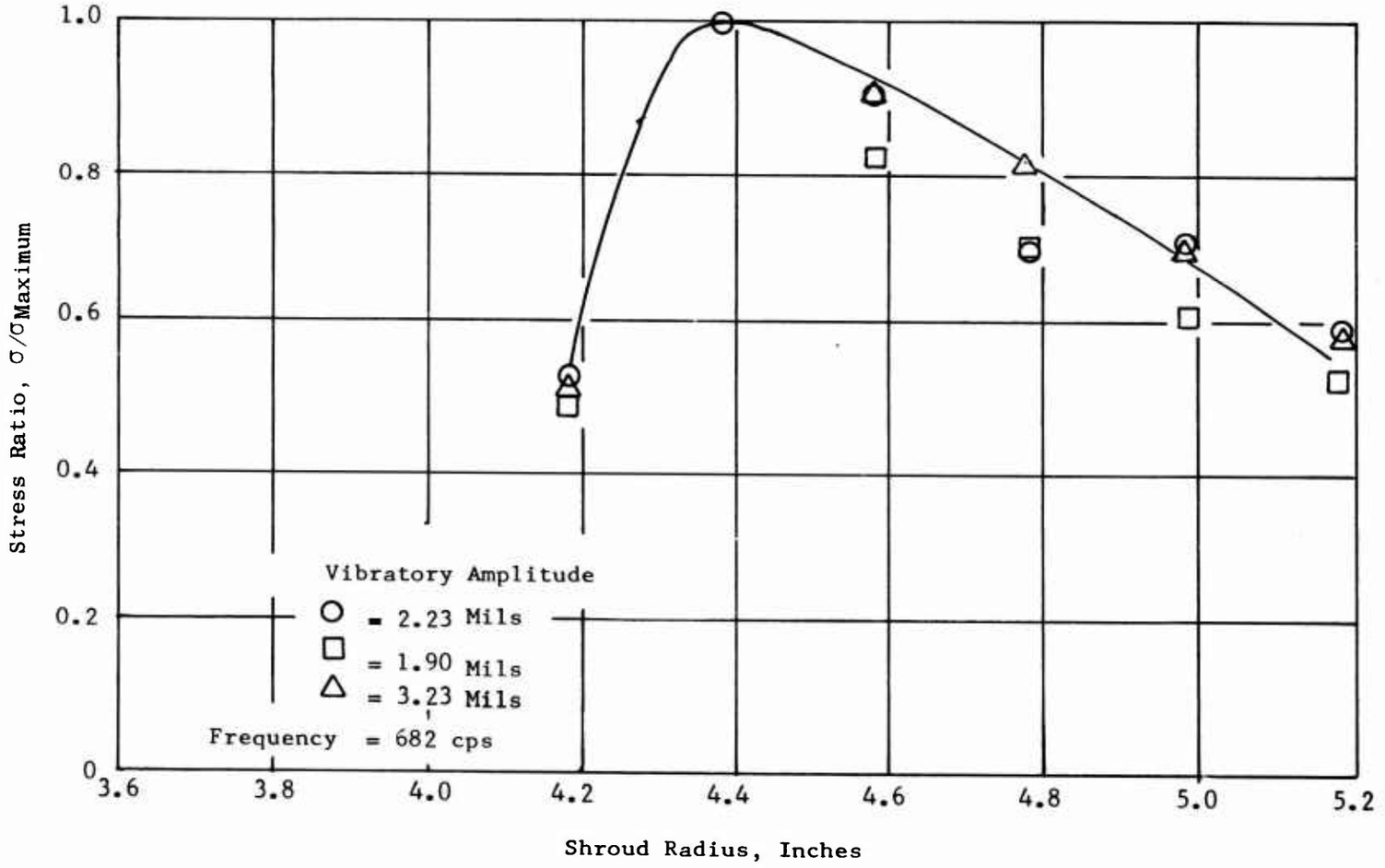

Figure 57. Cos 2θ Mode Shroud Stress Distribution (Blade Side).

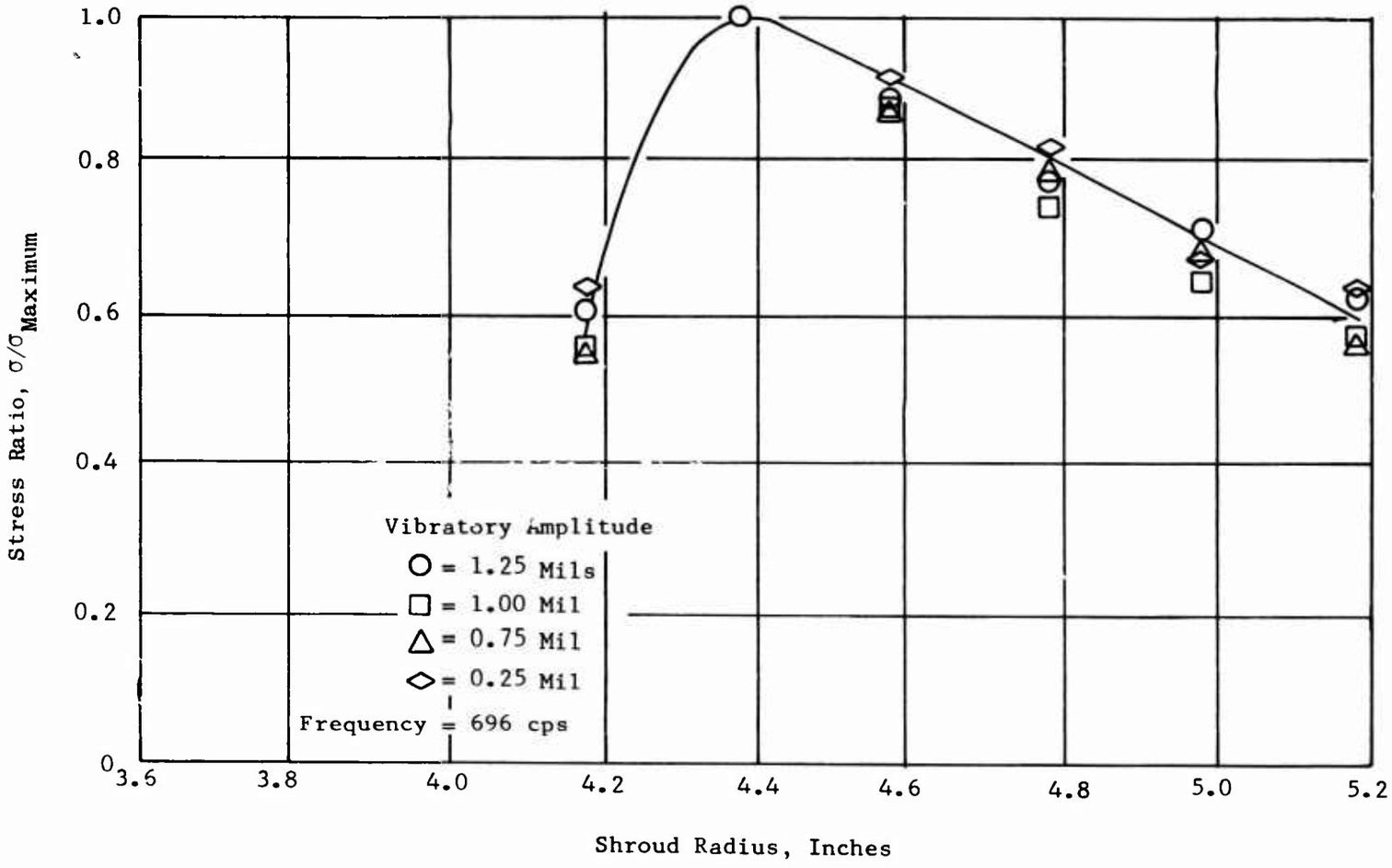

Figure 58. Cos 3θ Radial Stress Distribution in Shroud (Blade Side).

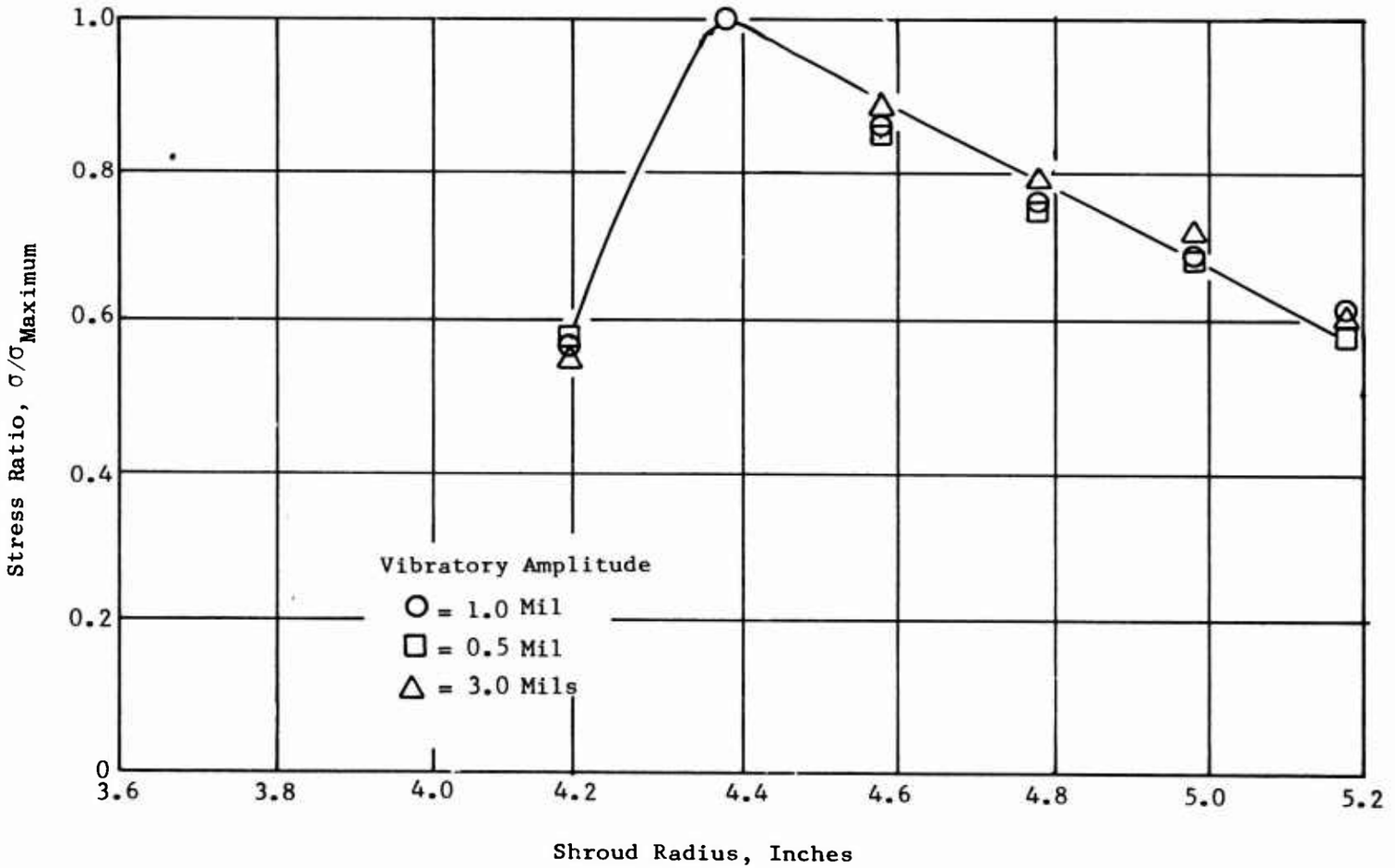

Figure 59. Cos 4θ Radial Stress Distribution in Shroud (Blade Side).

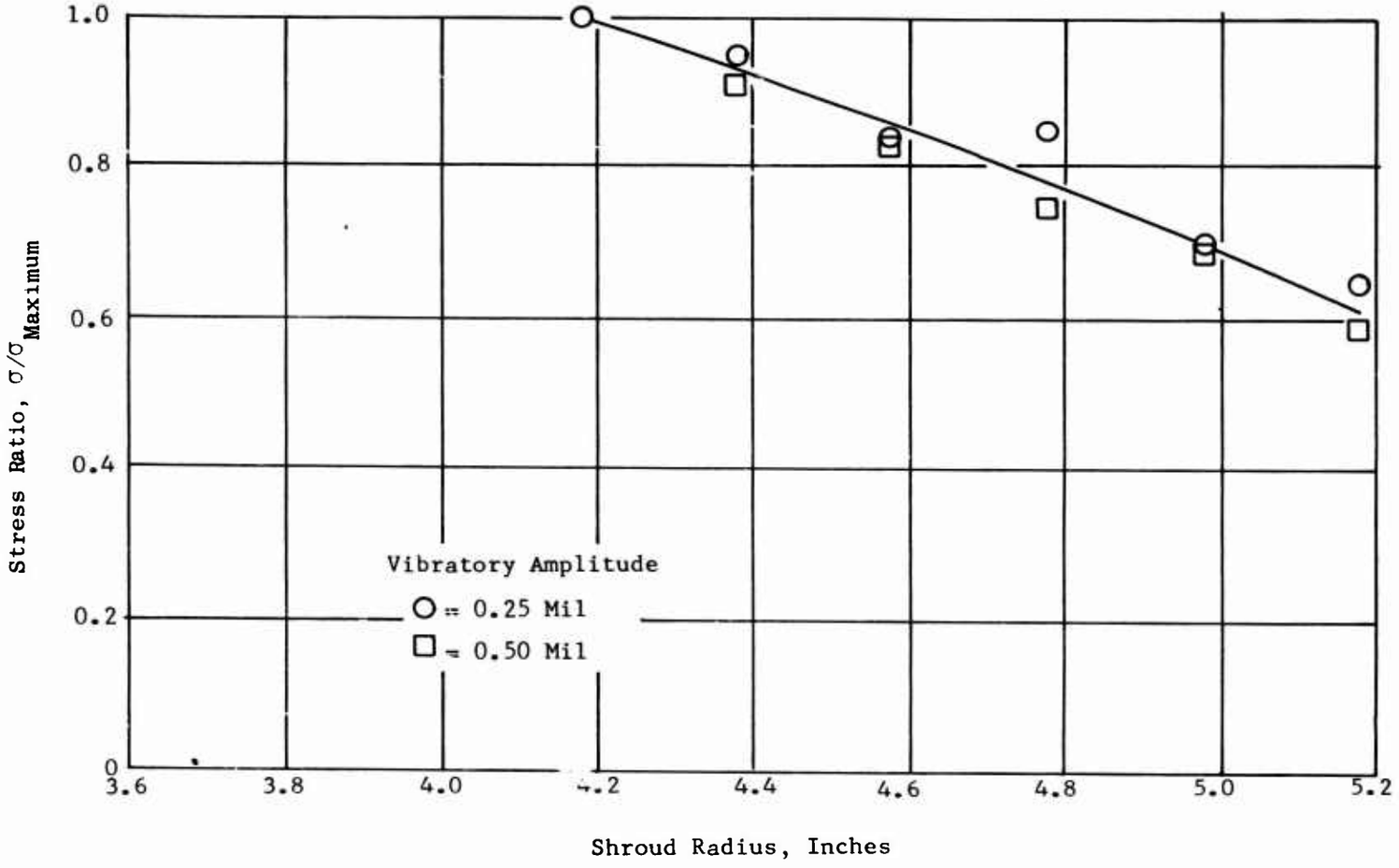

Figure 60. Cos 2θ Radial Stress Distribution in Shroud (Seal Side).

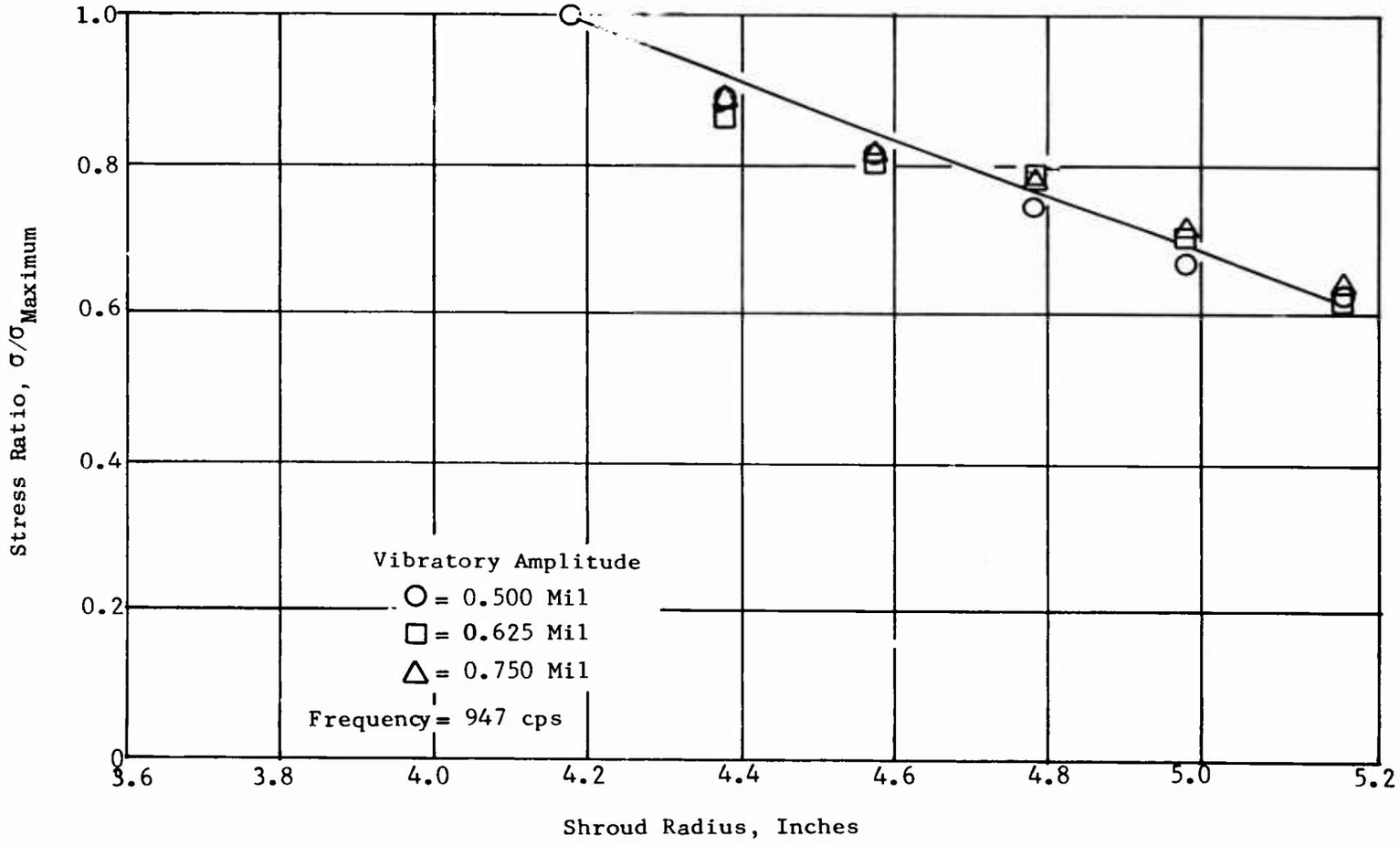

Figure 61. Cos 3θ Radial Stress Distribution in Shroud (Seal Side).

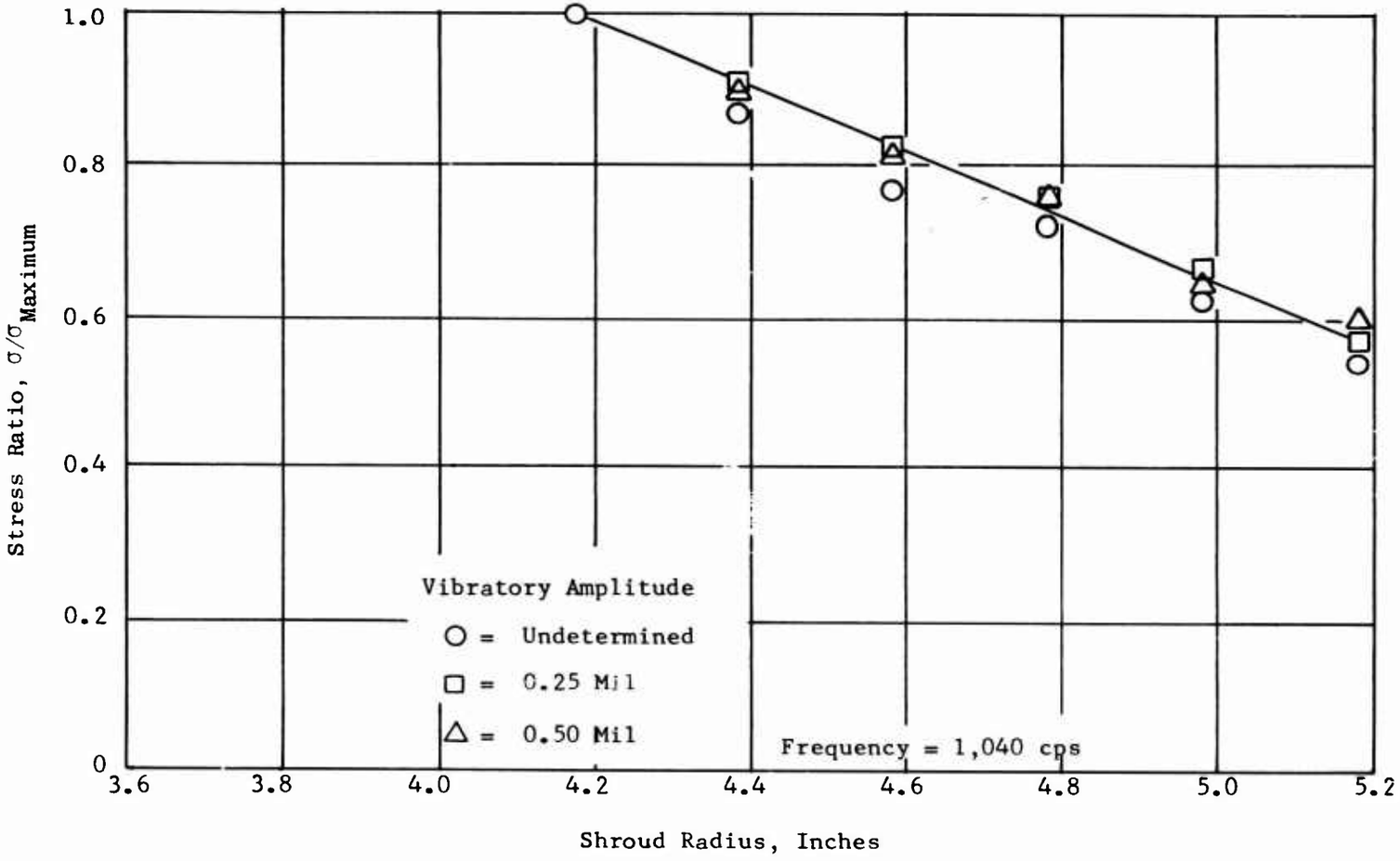

Figure 62. Radial Stress Distribution in Shroud (Seal Side) for Cos 4θ Vibration Mode.

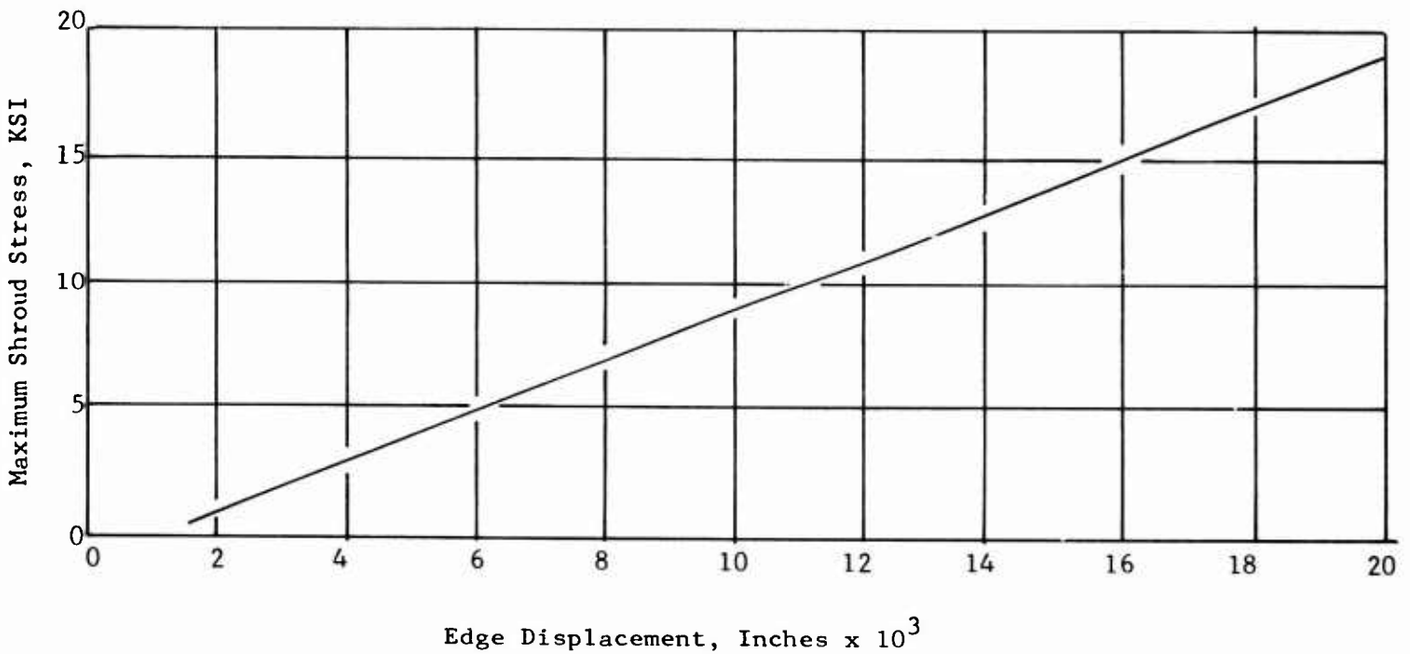

Figure 63. **Blade Side Stress Displacement Curve for Axial Motions of the Shroud Rim for Cos 2θ Vibration Mode.**

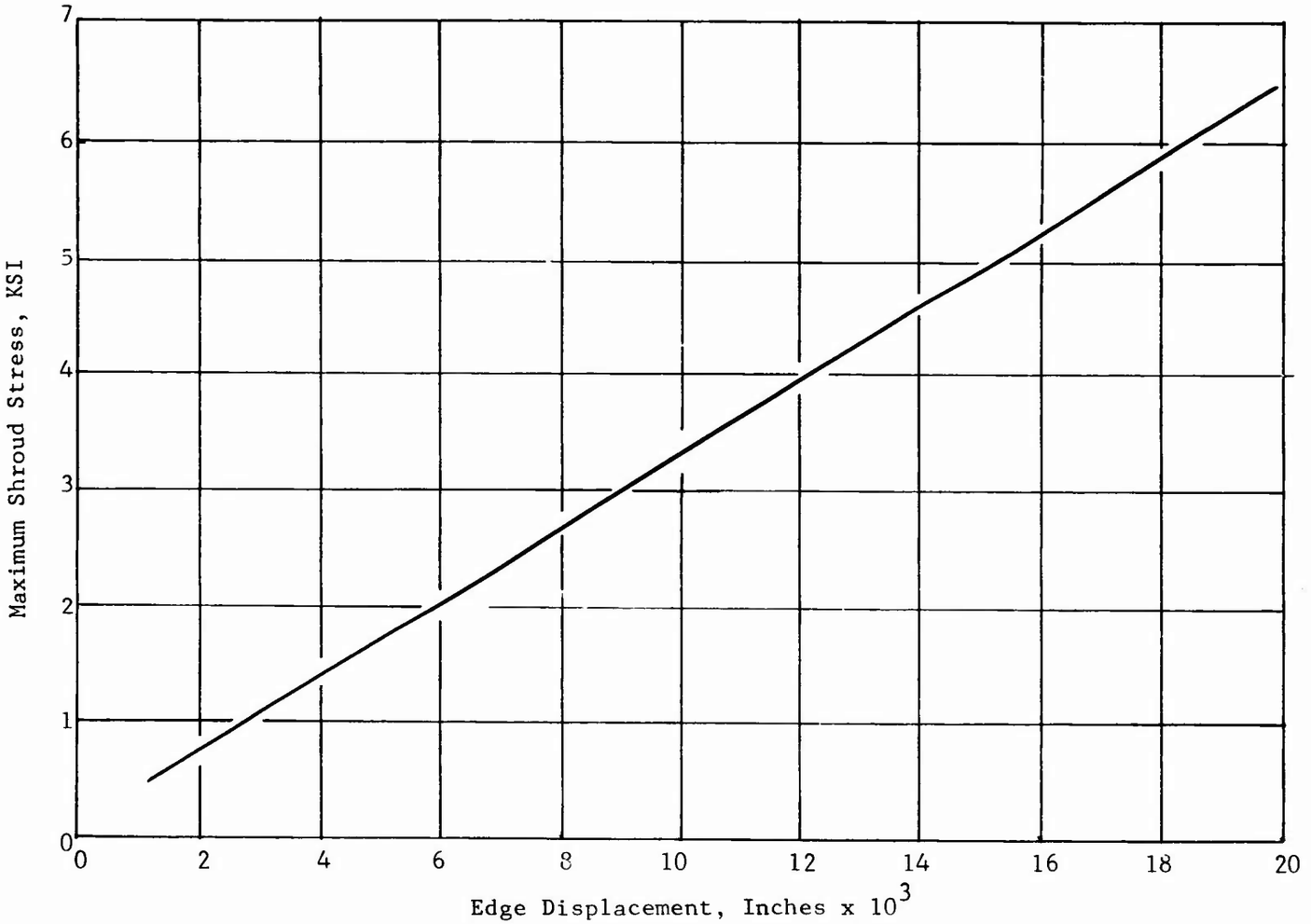

Figure 64. Blade Side Stress Displacement Curve for Axial Motions of the Shroud Rim for Cos 3θ Vibration Mode.

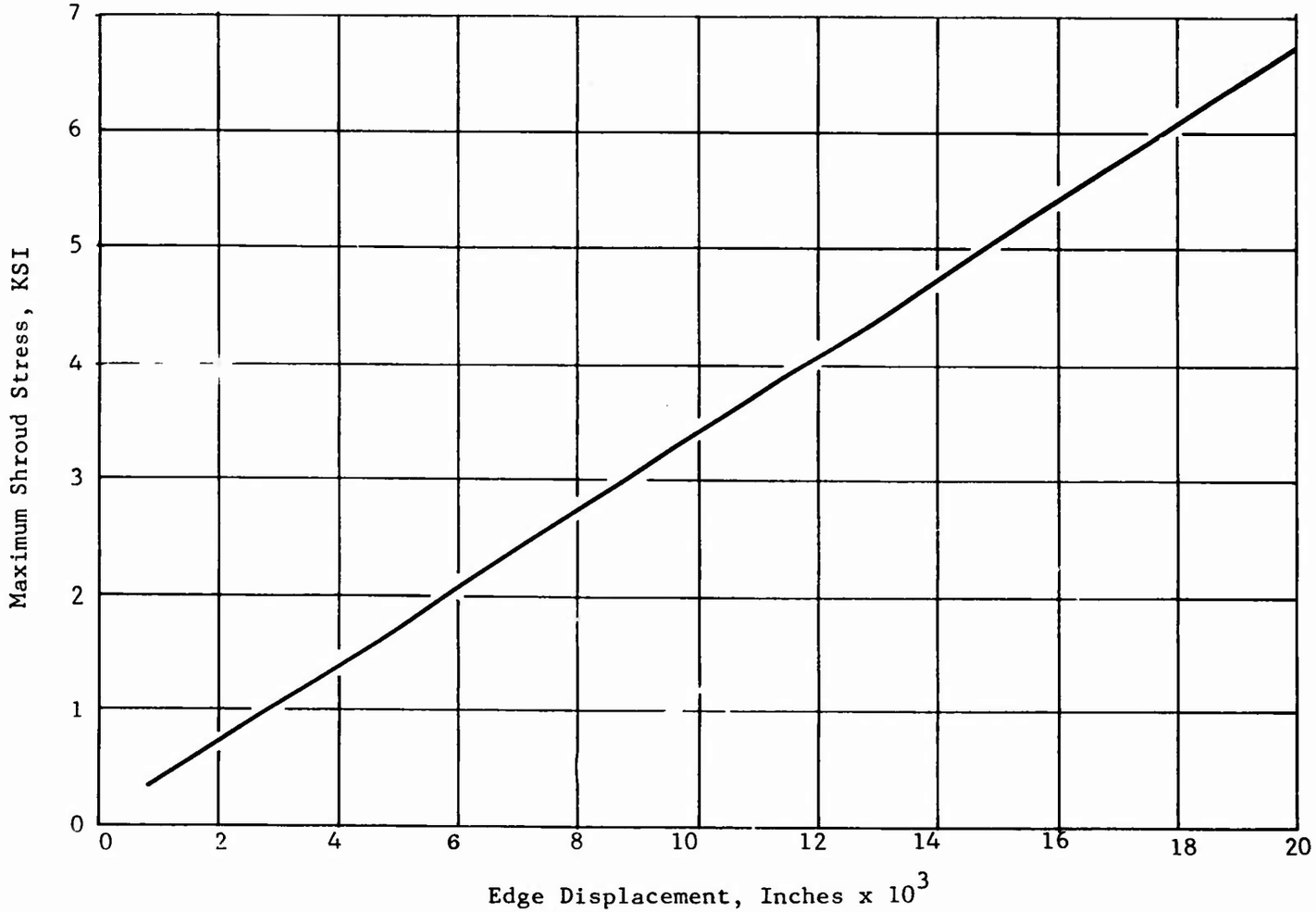

Figure 65. Blade Side Stress Displacement Curve for Axial Motions of the Shroud Rim for Cos 4θ Vibration Mode.

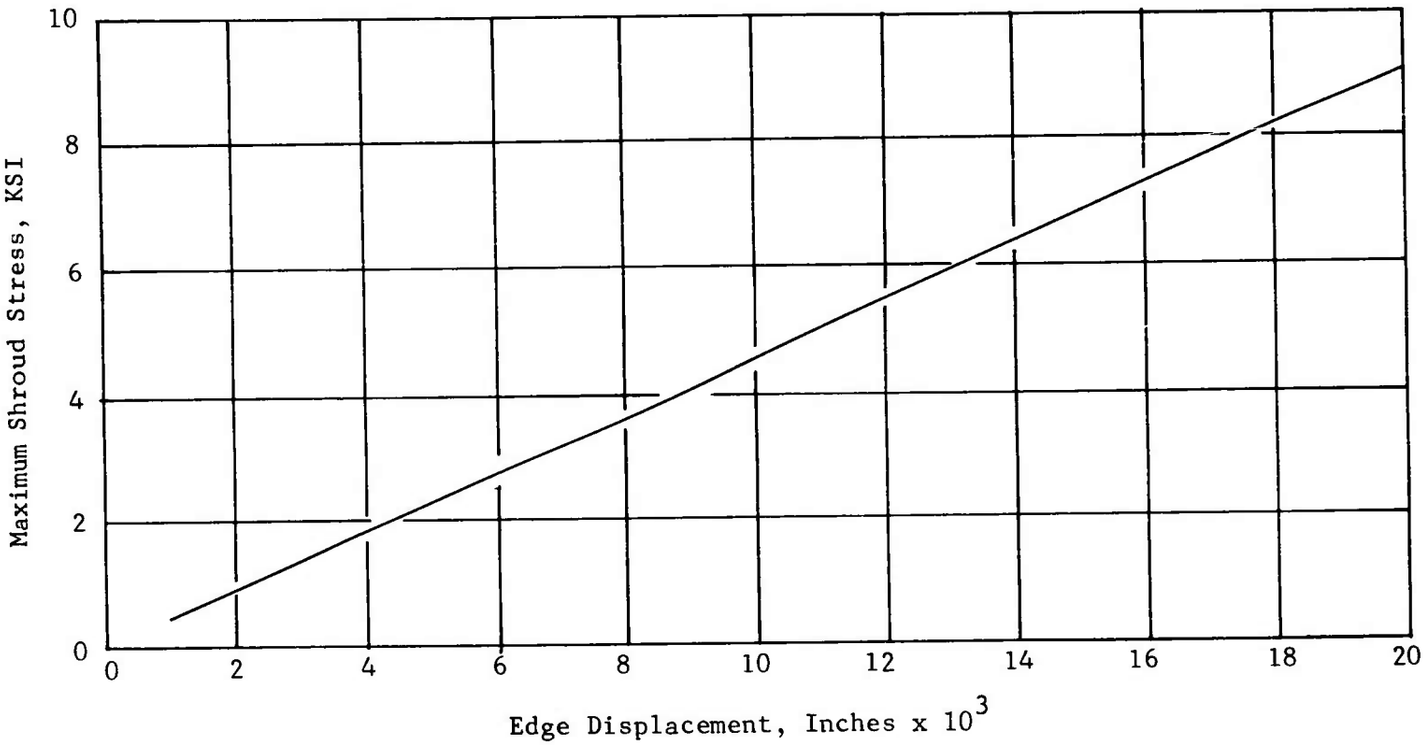

Figure 66. Seal Side Stress Displacement Curve for Axial Motions of the Shroud Rim for Cos 2θ Vibration Mode.

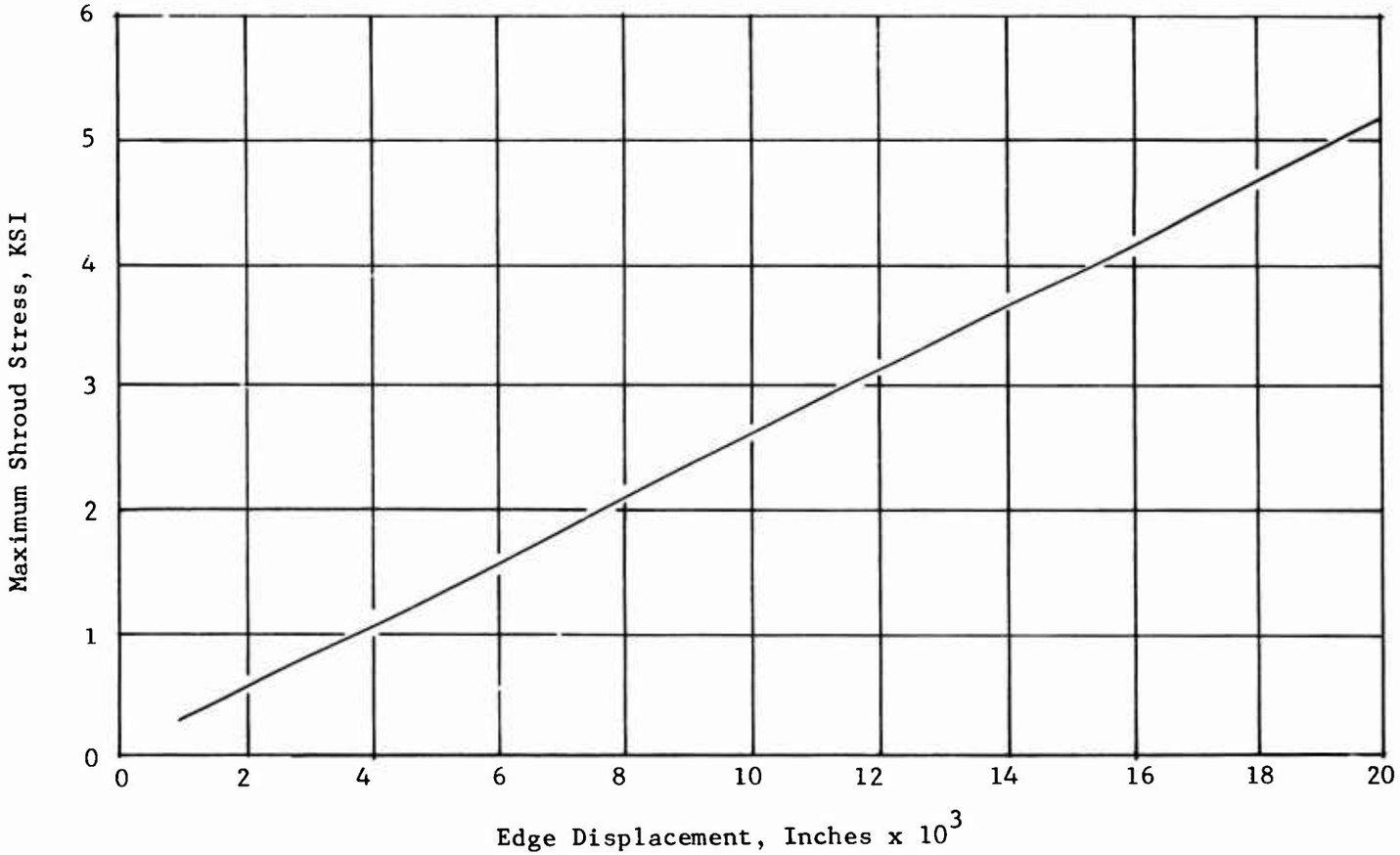

Figure 67. Seal Side Stress Displacement Curve for Axial Motions of the Shroud Rim for Cos 3θ Vibration Mode.

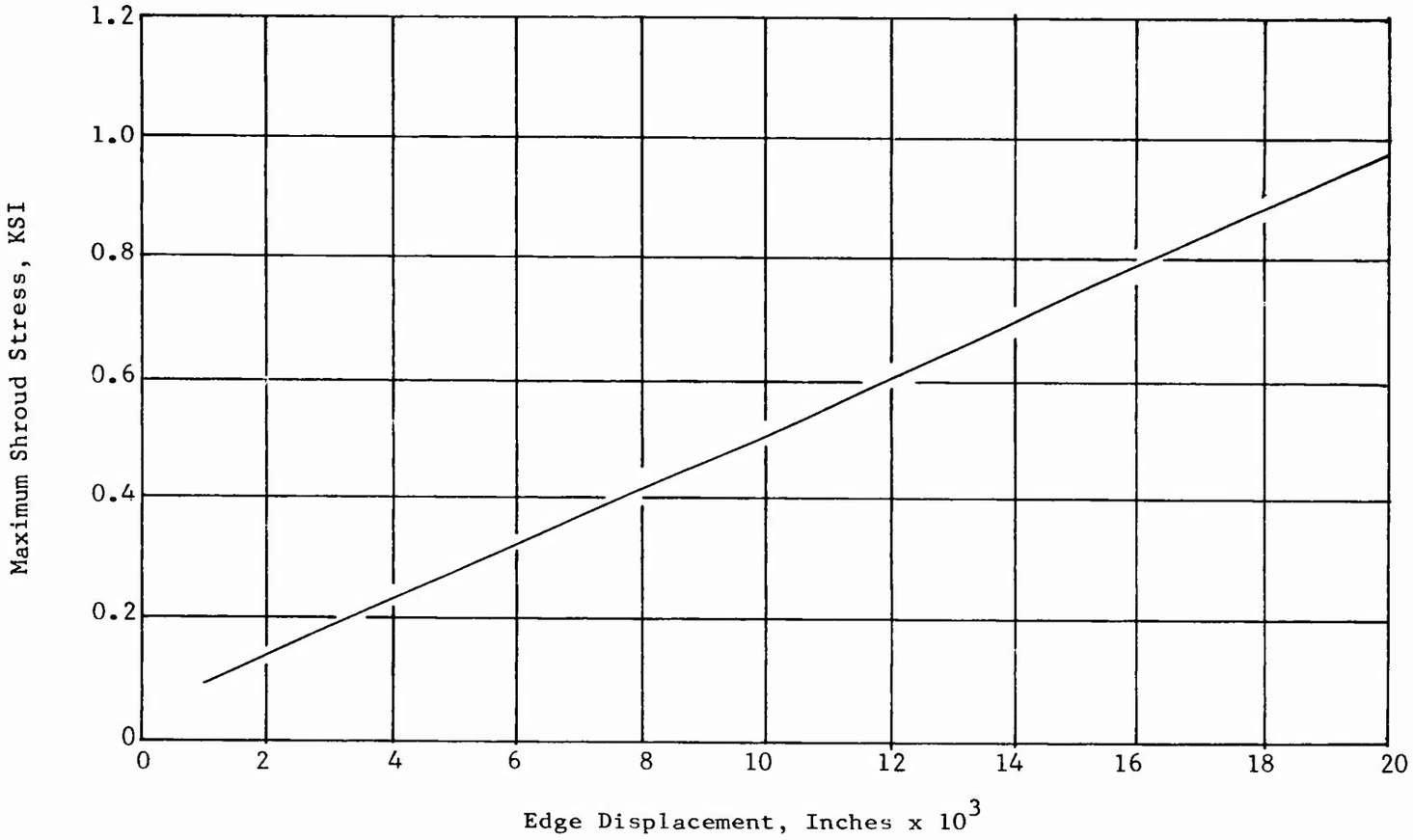

Figure 68. Seal Side Stress Displacement Curve for Axial Motions of the Shroud Rim for Cos 4θ Vibration Mode.

Conclusions and Recommendations

The following conclusions can be made:

1) The shroud blade side and seal side vibrate independently of each other.

2) The resonant frequencies of the blade side are lower than those of the seal side.

3) Assuming that the calculated centrifugal stiffening factor B is sufficiently accurate, the shroud blade and seal sides Cos 2θ mode critical speed occurs above 100 percent speed, that is, above 34,500 rpm.

4) Based on the assumption made in (3), the blade side Cos 3θ and Cos 4θ mode critical speeds occur at 19,500 rpm and 13,500 rpm, respectively.

5) Based on the assumption made in (3), the shroud seal side Cos 3θ and Cos 4θ mode critical speeds occur at 26,100 rpm and 18,600 rpm, respectively.

6) On the blade side, the maximum stress for Cos 2θ, 3θ, and 4θ modes occur between 4.182 inches and 4.382 inches radius, that is, approximately in the region of the fillet of the inner shroud.

7) On the seal side, the maximum stress location is undetermined. However, it is likely that it occurs also in the region of the fillet for the first 3 modes.

Because of the somewhat high level of vibratory activity of the shroud, care should be taken during compressor runs. Cos 3θ mode critical of the shroud seal side can be a problem, since it occurs at almost 80 percent speed.

Some of the higher modes can also be a source of problems because of the ease with which the shroud can be excited.

Further bench testing is advisable, though not absolutely necessary. Depending on the results of the compressor tests, shroud modifications or even a redesign for the Phase III rotor may become necessary.

Bently Nevada "3,000" Series Proximeter Calibration Tests

Objectives

The tests performed on 1 of the displacement probes used for the ROC tests were designed to determine the behavior and the accuracy of this instrument under conditions similar to those present in the high-speed ROC installation.

Test Setup

The test setup is shown schematically in Figure 69. A titanium plate (same material as shroud) was mounted on a small electrodynamic shaker; the probe was held in place by an adjustable fixture with a built-in vernier to determine the steady-state distance between the titanium plate and the proximeter. A heat lamp was used to raise the temperature of the titanium plate above ambient. A power supply was regulated to deliver negative 18 volts DC at 25 ma to the probe through the detector driver portion of the proximeter, shown in Figure 70. The output leads were connected to an oscilloscope and to a digital voltmeter for voltage readings during oscillatory motion of the titanium plate.

The oscillatory amplitude of the plate was measured by an optical telescope.

Procedure

The following procedure was used:

1) Without heat lamp, for several probe-to-part distances, record the proximeter output voltage.

2) Repeat step (1) with heat lamp on.

3) With a probe-to-part gap of 0.090 inch (same gap as in compressor tests) at room temperature, and at a frequency of 100 cps, obtain the AC voltage output for several vibratory amplitudes.

4) Repeat step (3) with heat lamp on.

5) At 4 different vibratory amplitudes, obtain the AC voltage output for several probe-to-part gaps in the range of 0 through 0.090 inch.

6) Record all data and pertinent information.

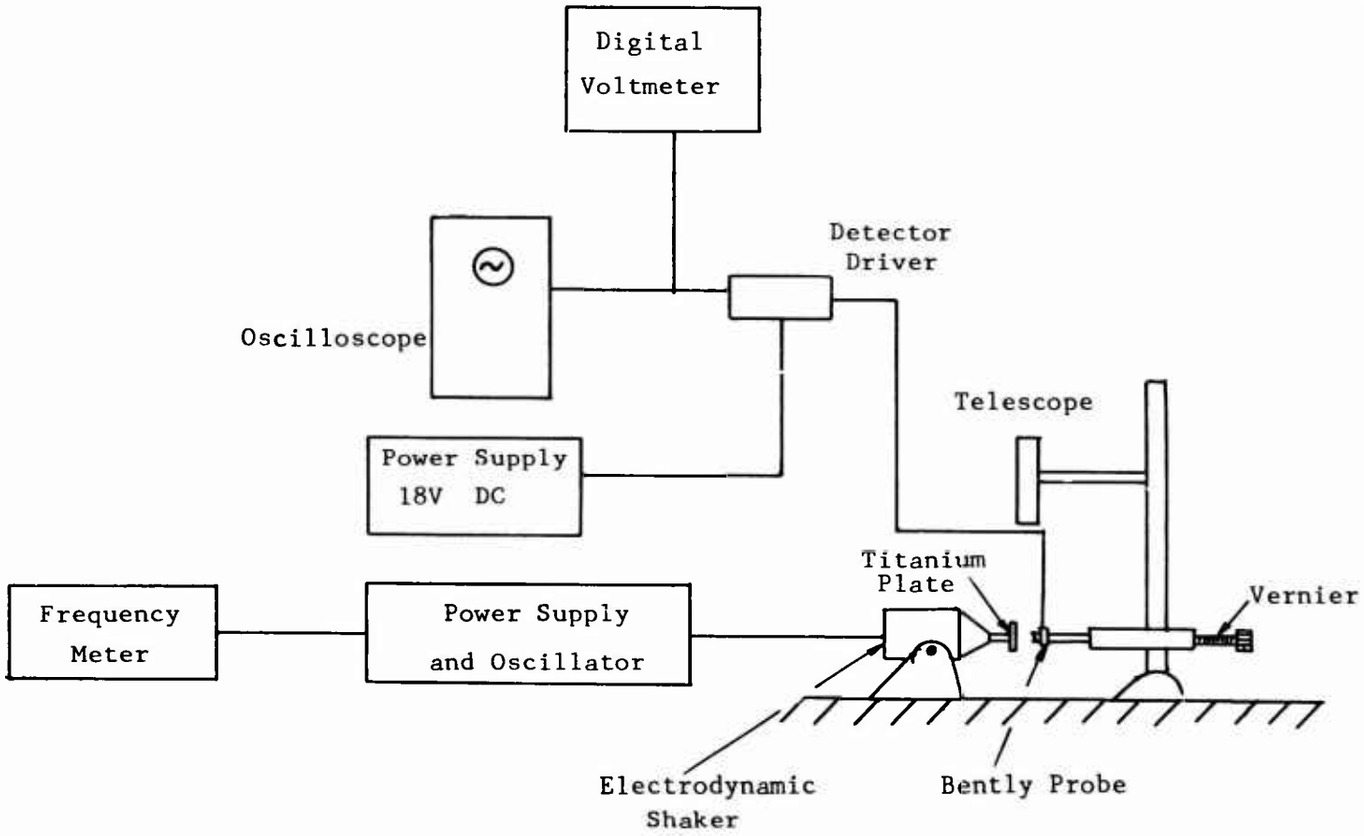

Figure 69. Bently Probe Calibration Test Setup.

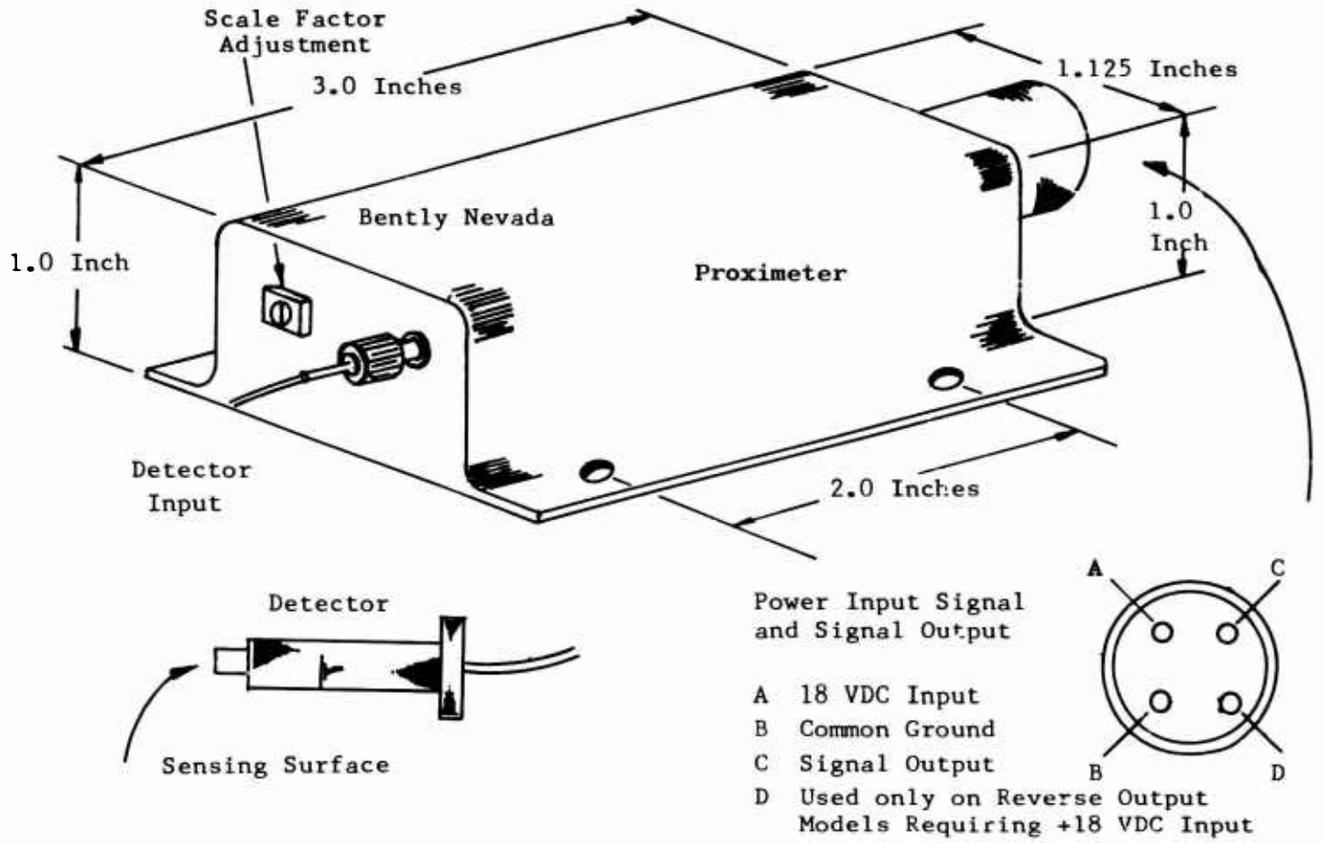

Figure 70. Bently Detector Driver and Probe.

Results

Figure 71 shows the effect of probe-to-part steady-state distance on the DC output voltage. Of the 2 curves plotted in this figure, 1 has been obtained at room temperature, the other with the heat lamp as indicated.

A plot of AC output voltage versus vibratory amplitude is given in Figure 72. The steady-state gap between the probe and the titanium plate was 0.090 inch, and data were obtained both at ambient temperature and above ambient with the heat lamp as indicated in this figure.

To show the temperature effect at various vibratory amplitudes, a curve of the ratio of AC output at temperatures above ambient over AC output at ambient temperature versus vibratory amplitude is given in Figure 73.

A study of the variation of AC output voltage for probe gaps less than 0.090 inch is shown in Figure 74.

In Figure 75, a family of curves has been plotted. Each one represents a specific vibratory amplitude and is a plot of AC output voltage versus probe-to-part steady-state gap.

Conclusions and Recommendations

The results indicate that:

1) At room temperature, a probe-to-part gap of 0.060 inch or greater is recommended; this would minimize errors in measuring vibratory amplitudes, since with gaps greater than 0.060 inch, the DC steady-state voltage changes are minor (Figure 71).

2) At temperatures above ambient, the DC voltage output is more sensitive to the gap, especially at gaps greater than 0.060 inch.

3) At any vibratory amplitude, the AC output voltage is greater with the heat lamp on than at ambient temperature. At amplitudes between 0.005 and 0.025 inch peak-to-peak, the AC output is about 1.7 times greater and reaches a maximum at about 0.010 inch where the output is about 1.96 times greater. At amplitudes of 0.025 inch peak-to-peak and above, the AC output is about 1.7 times greater.

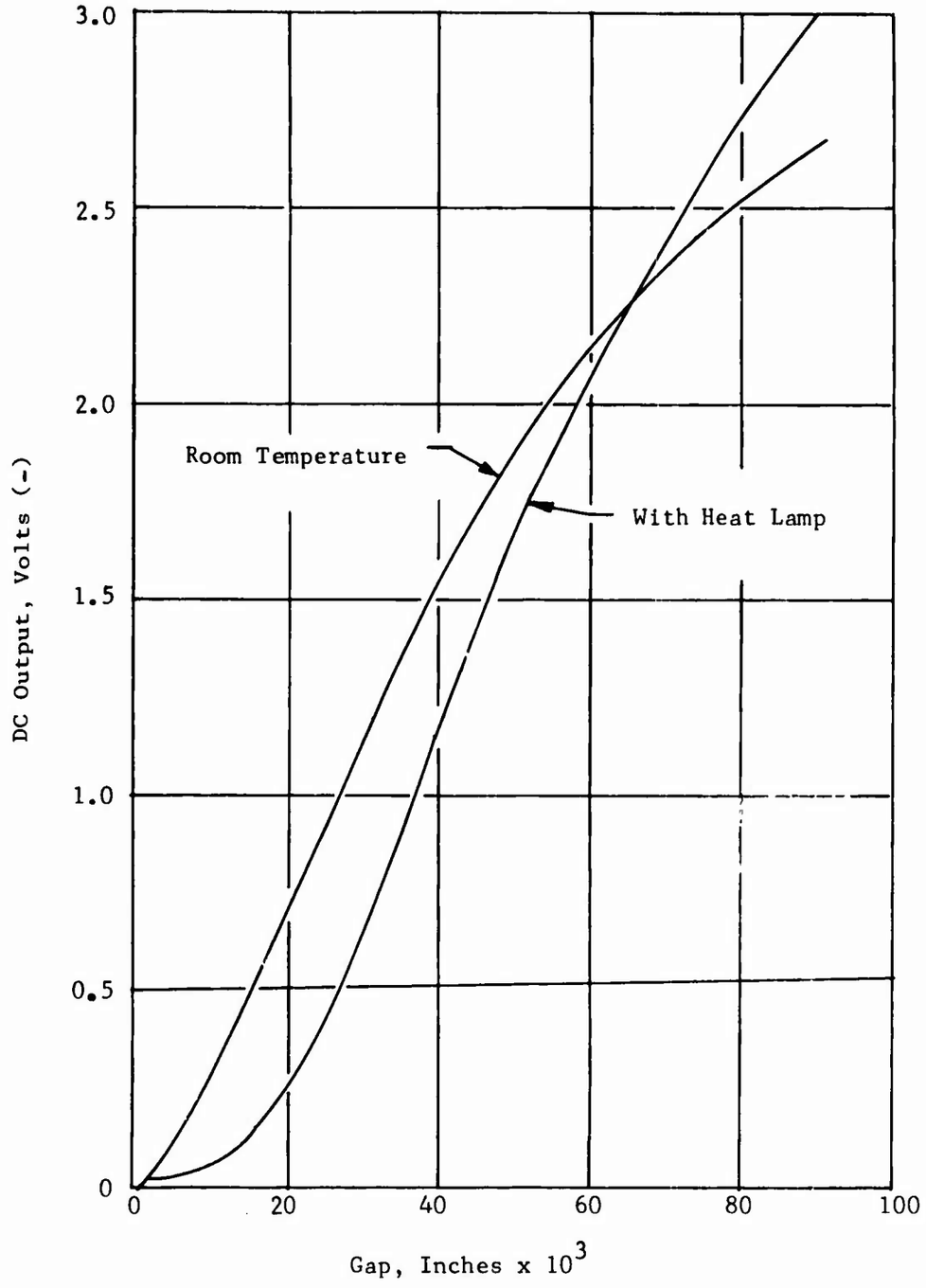

Figure 71. Effect of Probe-to-Part Gap on DC Output Voltage Under Steady-State Conditions With and Without Heating.

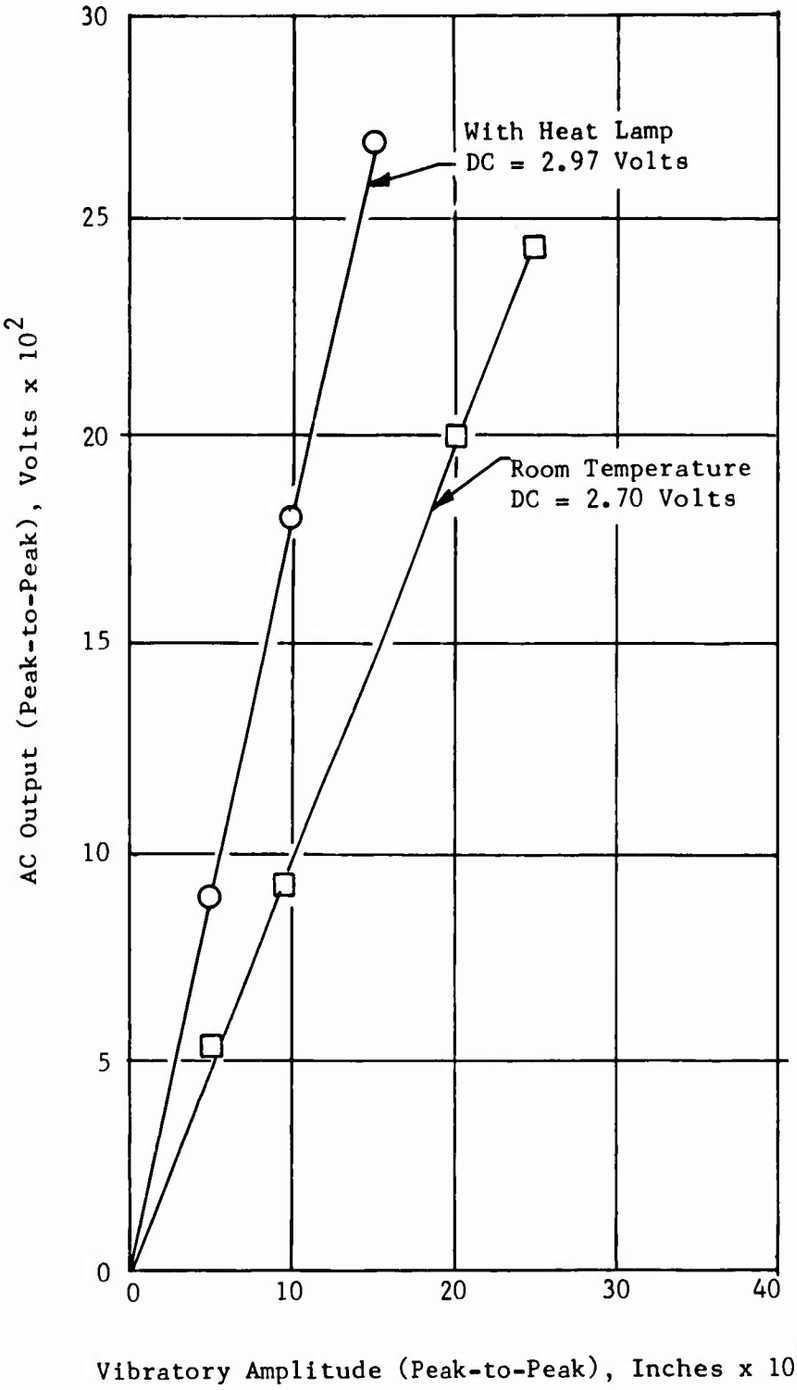

Figure 72. AC Output Voltage - Vibratory Amplitude Relationship of Bently Probe for a Steady-State Gap of 0.090 Inch With and Without Heating.

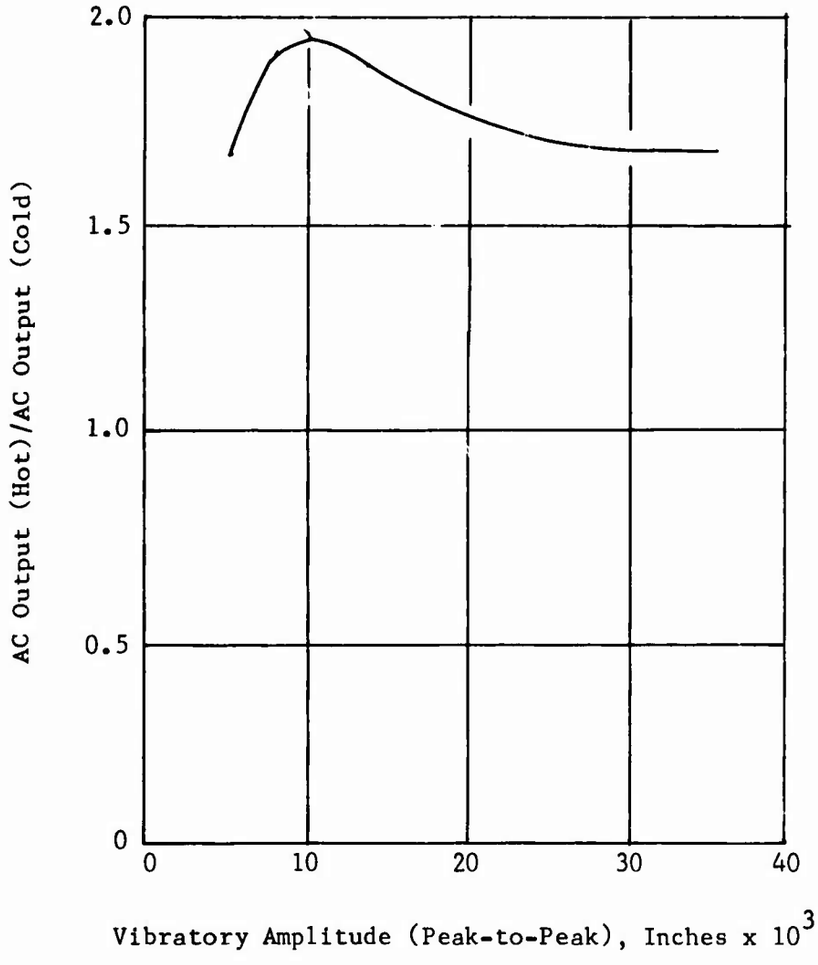

Figure 73. Temperature Effects on Output Voltage Curve for a Steady-State Gap of 0.090 Inch.

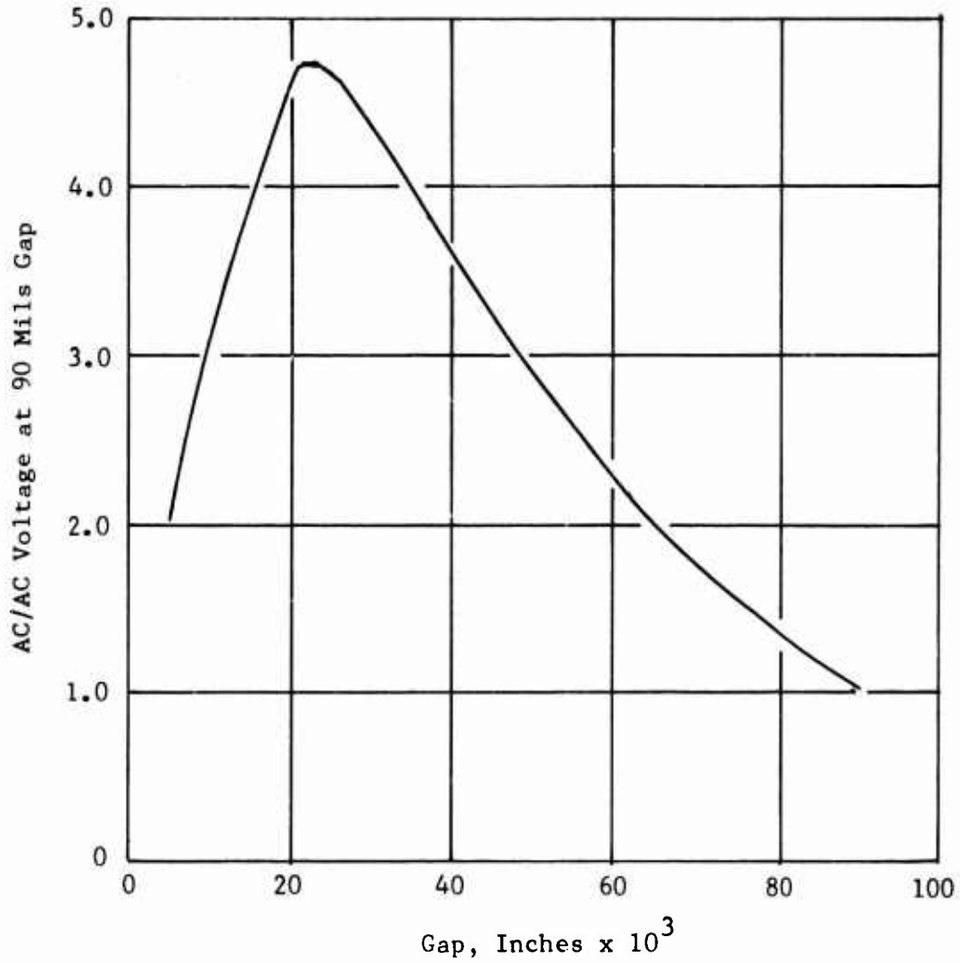

Figure 74. Variation of AC Output Voltage With Gap Width for Bently Probe.

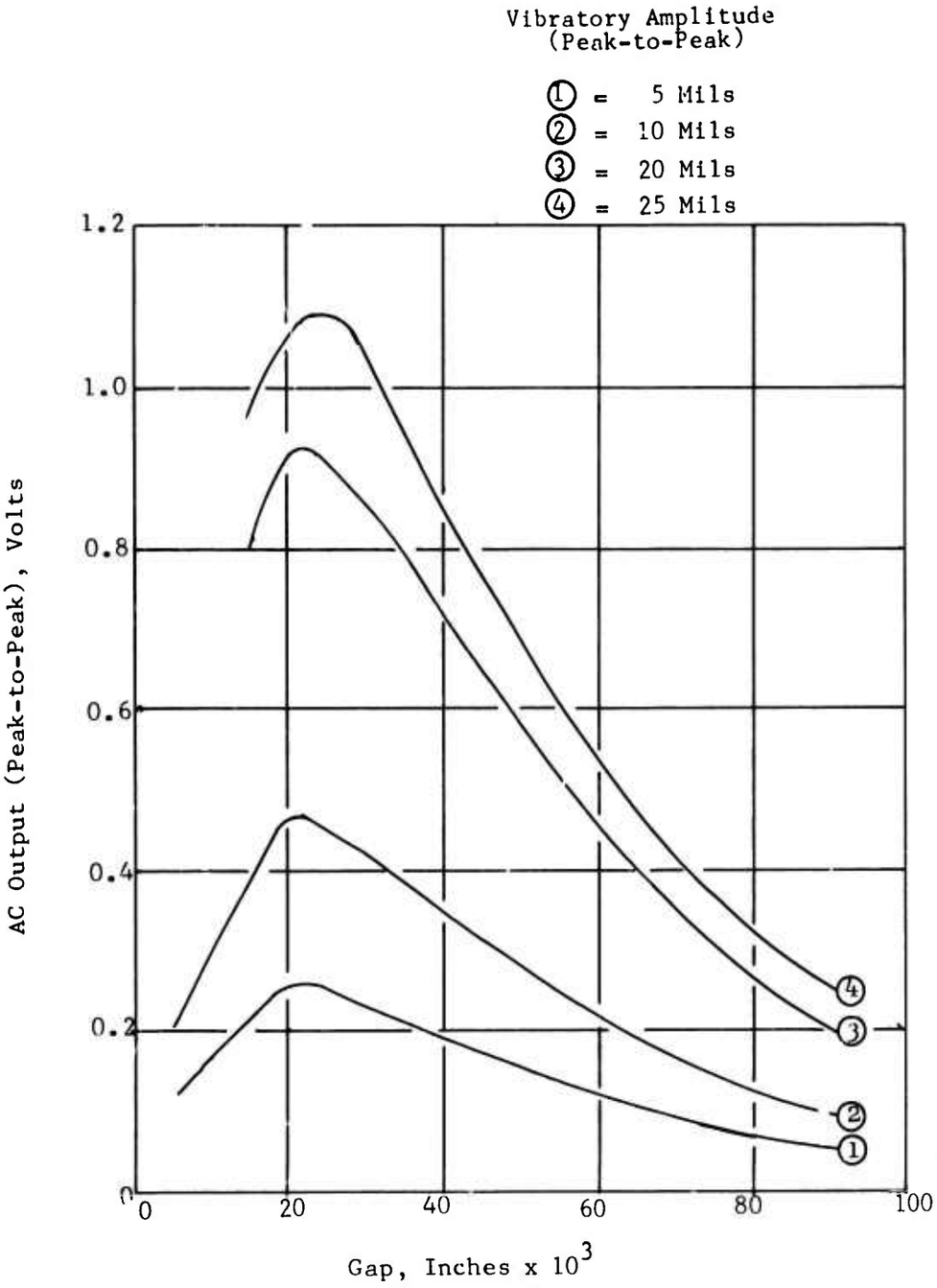

Figure 75. AC Output Voltage Versus Bently Probe Gap for Several Vibratory Amplitudes.

4) The AC voltage output is greater for gaps less than 0.090 inch than for a gap of 0.090 inch. The output also reaches a maximum at about 0.020 inch gap. This is true at all vibratory amplitudes.

Temperature and probe-to-part gap have very definite effects on the response of the proximeter. Unless all parameters involved are extremely well controlled (this is hard to do, especially in a system rotating at high speed), all vibratory displacement measurements are inaccurate and can be a risk when these displacements have to be associated with stress values.

In case of a rotating disc such as the ROC shroud, at any one of the Cos nθ mode critical speeds, the sinusoidal wave form characterizing the vibratory motion becomes stationary in respect to a ground observer; when this occurs, the probe AC output voltage becomes zero and the true maximum displacement cannot be measured. Based on this, the Bently proximeter alone is not sufficient for this type of application.

Supersonic Stator Vane Vibration Tests

Possible pressure field gradients and unknown flow transients that would act on the supersonic stator vanes dictated bench tests of these vanes prior to compressor running.

Objective

1) Establish vane resonant frequencies.

2) Identify the best strain gage location for monitoring behavior of stator vanes during ROC operation.

Test Setup

To closely approximate the pin supports of the supersonic stator vanes in the compressor assembly, the test vane was fixtured between 2 blocks at the 4 vane support pins as shown in Figure 76. Fifteen strain gages (Type EA-06-062AK-120) were mounted on both the concave and convex vane surfaces in the patterns shown in Figure 77. The fixtured stator was then placed in front of an air siren capable of producing excitation frequencies in excess of 10,000 cps.

Procedure

The siren was activated and excited the stator through a range of frequencies. A crystal pickup was used to monitor stator surface deflection and help identify natural frequency mode shapes. Relative strain measurements were taken from all strain gages at each natural frequency.

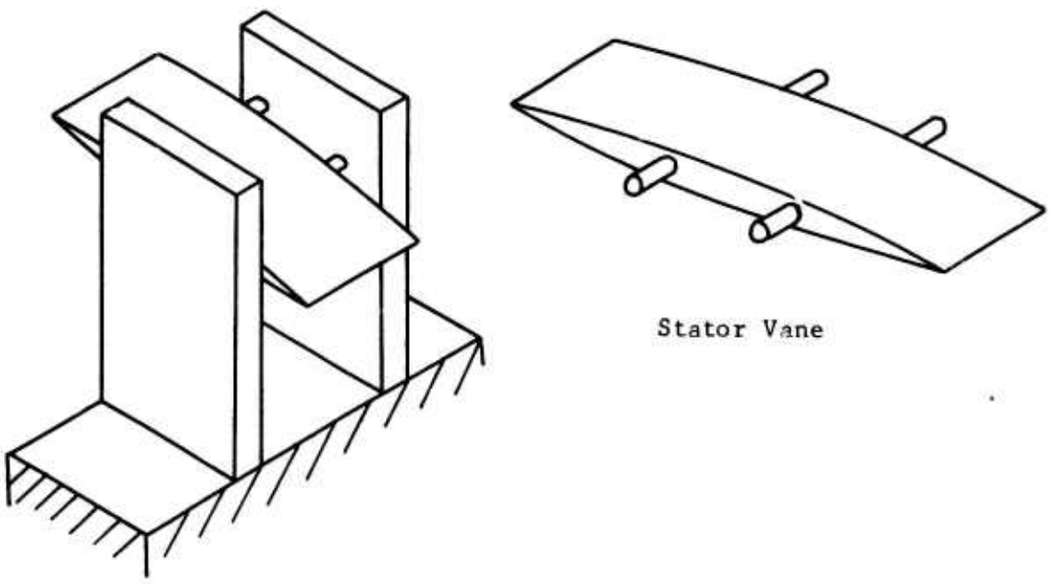

Figure 76. Vibration Test Setup for Supersonic Stator Vane.

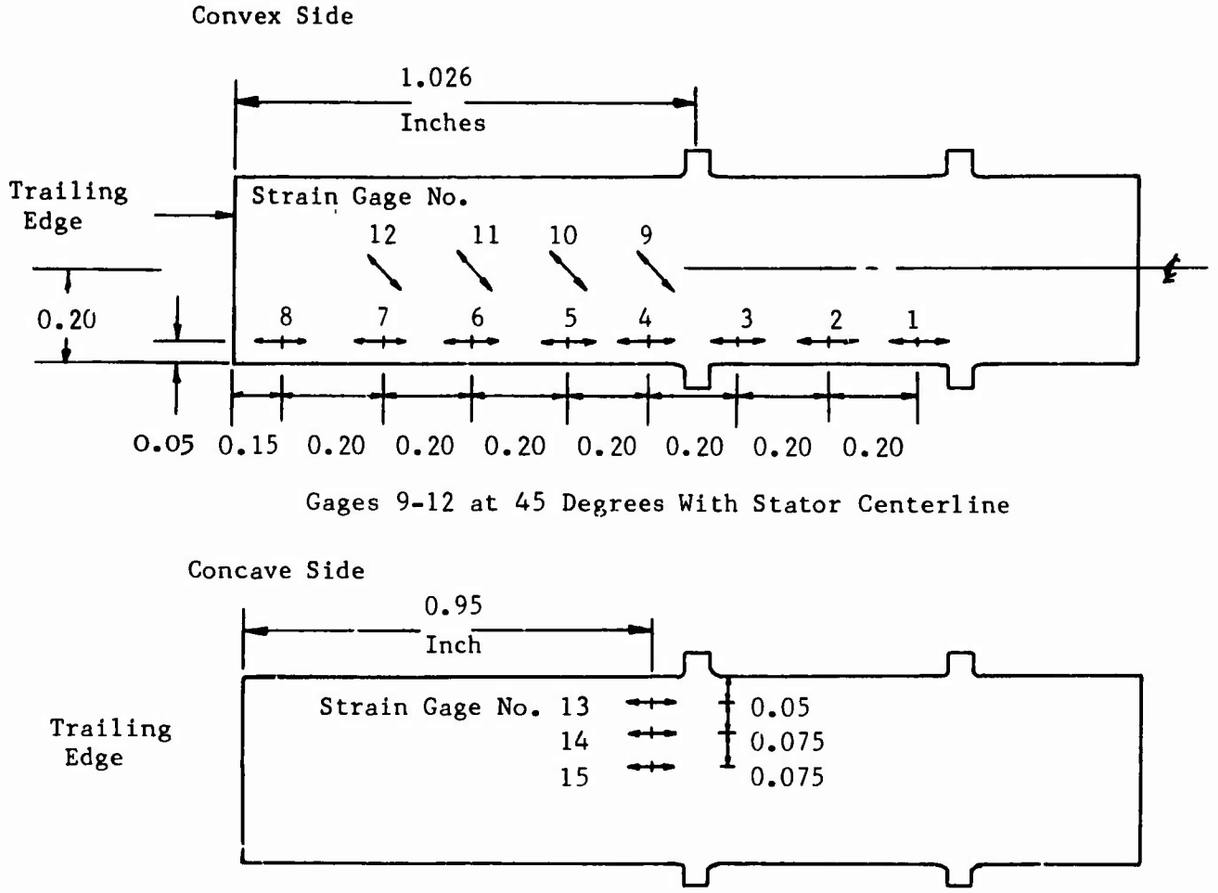

Figure 77. Supersonic Stator Strain Gage Locations.

Results

The relative strains at various stator locations for all resonant frequencies found are listed in Table VII. Mode shapes for the primary frequencies are shown in Figure 78. The fundamental mode was found to be a bending mode at a frequency between 1,800 and 1,900 cps.

Conclusions and Recommendations

Analysis of test results showed that limits must be placed on vane alternating stress to prevent possible vane failure during compressor operation. Stress distribution in the supersonic stator showed that a gage should be placed on the convex side 0.46 inch from the trailing edge, 0.15 inch from the side, and oriented in the leading-trailing edge direction. This gage would be very sensitive to stresses due to bending (most severe mode) yet would monitor torsional modes.

The recommended stator limit stress at this gage is 9,800 psi single amplitude alternating stress in the 1,800-1,900 cps mode at 80 percent compressor speed. This limit is dictated by the vane rear pin bending stress and corresponds to a maximum vane alternating stress of 14,500 psi single amplitude.

Belleville (Conical Spring Washers) Washer Tests

To insure firm attachment of the shroud to the main rotor and to avoid unbalance sensitivity, a constant shroud attachment force (or bolted blade force) was required. Usually, control of initial bolt preload is sufficient to obtain constant force. In the case of the ROC, however, the highly loaded disc and shroud are subject to thinning in the area of blade attachment. This thinning is due to Poisson's effect from high radial and circumferential stress and effectively relaxes the initial preload or stretch in the bolted blades.

Belleville washers (conical) appeared to be the best method to keep a reasonably constant preload on the blade, yet they required small space and added very little additional load to the rotor. Tests were needed, however, to verify this concept and to investigate the load parameters involved.

Objectives

Evaluate the following:

1) Nut torque versus bolt tension versus Belleville washer deflection.

TABLE VII. SUPERSONIC STATOR VANE STRAIN DISTRIBUTION

Strain Gage No.	Relative Strain						
	Freq 1785 (CPS)	Freq 6674 (CPS)	Freq 8465 (CPS)	Freq 9120 (CPS)	Freq 11128 (CPS)	Freq 6307 (CPS)	Freq 6087 (CPS)
1	-53	-33	-55	-57	+34	+65	-26
2	-64	-26	-10	-6	+23	+45	-21
3	-67	-28	+49	+60	+26	+7	+25
4	-100	-42	+76	+96	+100	?3	+35
5	-87	+20	+9	+27	+61	-37	-28
6	-80	+70	-56	-44	+37	-79	-71
7	-63	+100	-100	-100	+29	-100	-100
8	-22	+47	-47	-56	+32	-46	-53
9	-71	-23	+49	+55	?10	-5	-35
10	-68	+16	+14	+12	+19	-29	-27
11	-63	+58	-35	-45	+43	-65	-63
12	-47	+78	-65	-82	+68	-79	-81
13	+96	+35	-69	-78	+75	+4	Out
14	+89	+25	-60	-68	+32	+8	Out
15	+87	+22	-58	-62	+10	+7	-25

Strain Gage No.	Relative Strain						
	Freq 1905 (CPS)	Freq 6798 (CPS)	Freq 8837 (CPS)	Freq 9026 (CPS)	Freq 9225 (CPS)	Freq (CPS)	Freq (CPS)
1	39	-49	+62	(No sensible readings)			
2	51	-35	+20				
3	64	-13	-50				
4	100	-7	-85				
5	95	+30	-18				
6	91	+77	+49				
7	71	+100	+100				
8	25	+53	+50				
9	61	+3	-58				
10	75	+25	-22				
11	71	+61	+29				
12	55	+79	+63				
13	10	Open	Open				
14	96	+9	+76				
15	99	+10	+65				

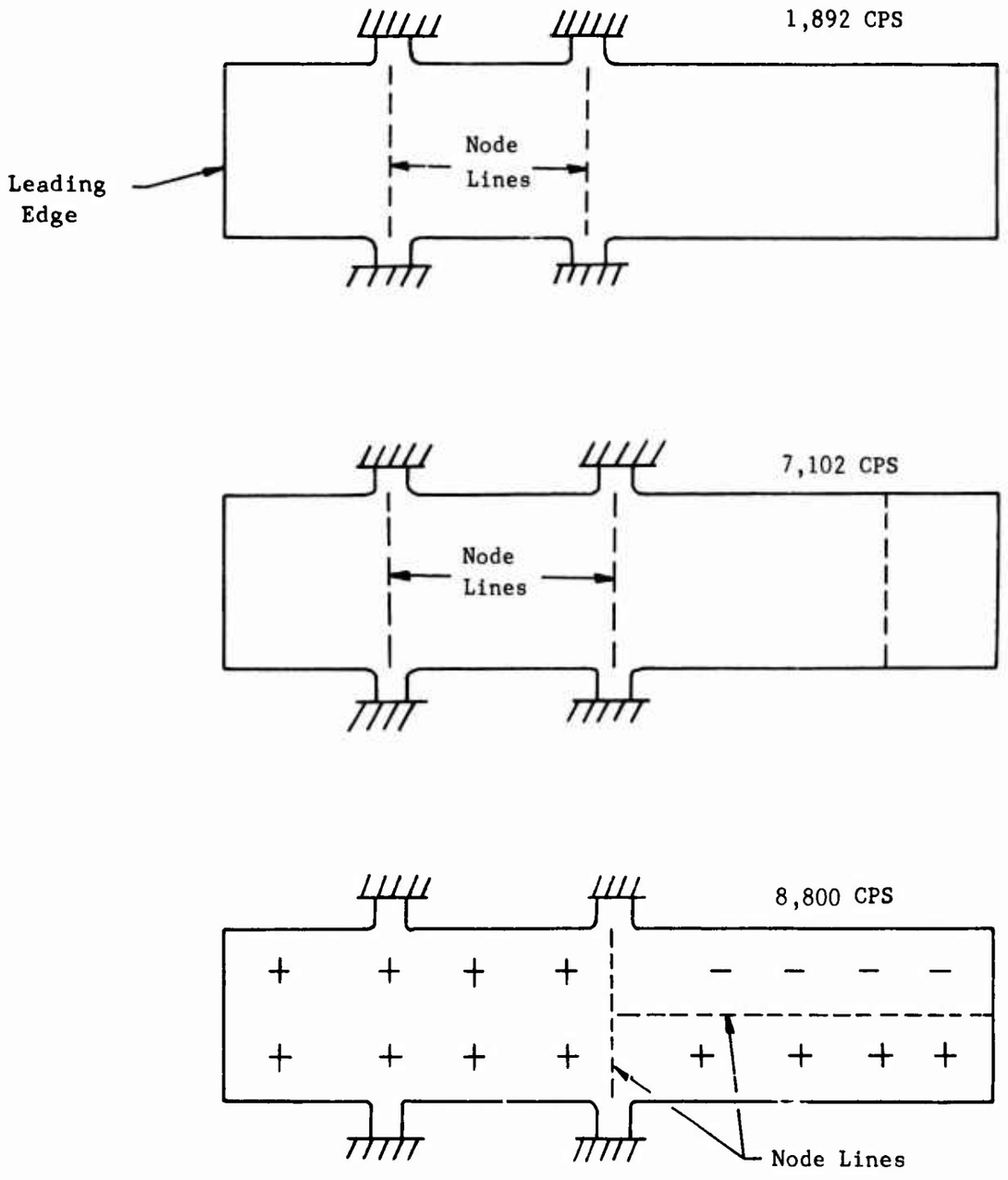

Figure 78. ROC Supersonic Stator Vane Mode Shapes.

2) Torque change versus load and deflection with reuse of nut.

3) Failure load of nut-washer assembly.

Test Setup and Procedure

The setup and procedure are detailed in Appendix IV.

Results

Test results are shown in Figure 81.

Conclusions and Recommendations

The Belleville washers do provide the desired "constant" load over a wide range of deflections, as shown by the essentially flat middle area of the load-deflection curves in Figure 79. Figure 80 can be used to determine assembly torque on blade nuts for the desired bolt tension. Maximum bolt tension will be restricted to a value well below the limit value of 3,025 pounds (required 75 to 85 inch-pounds torque) found.

Operating Precautions

An investigation conducted to identify potential problems of high-speed operation of the ROC and to implement proper procedures is presented in Appendix V.

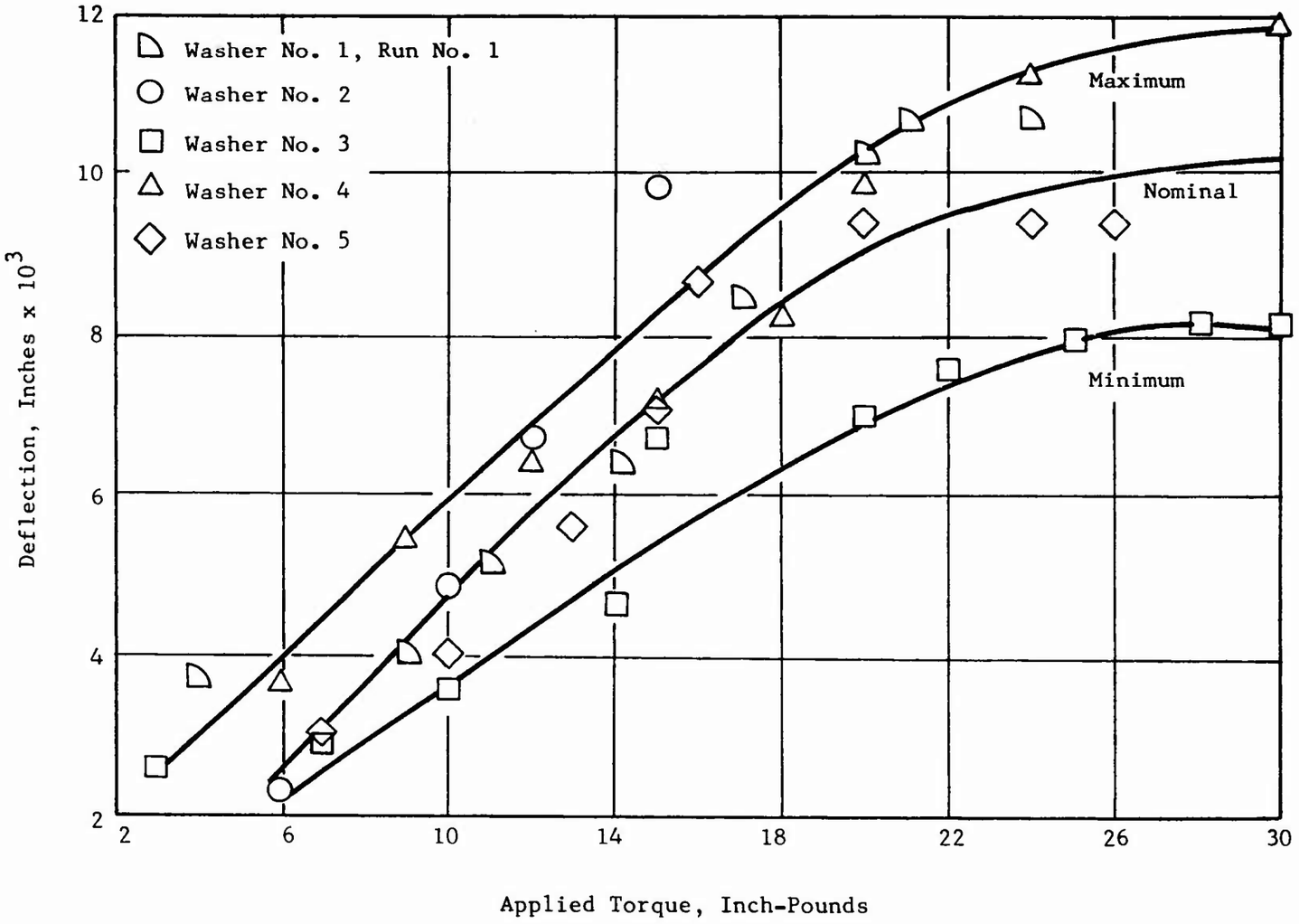

Figure 79. Variation of Deflection With Applied Torque From Belleville Washer Load Tests.

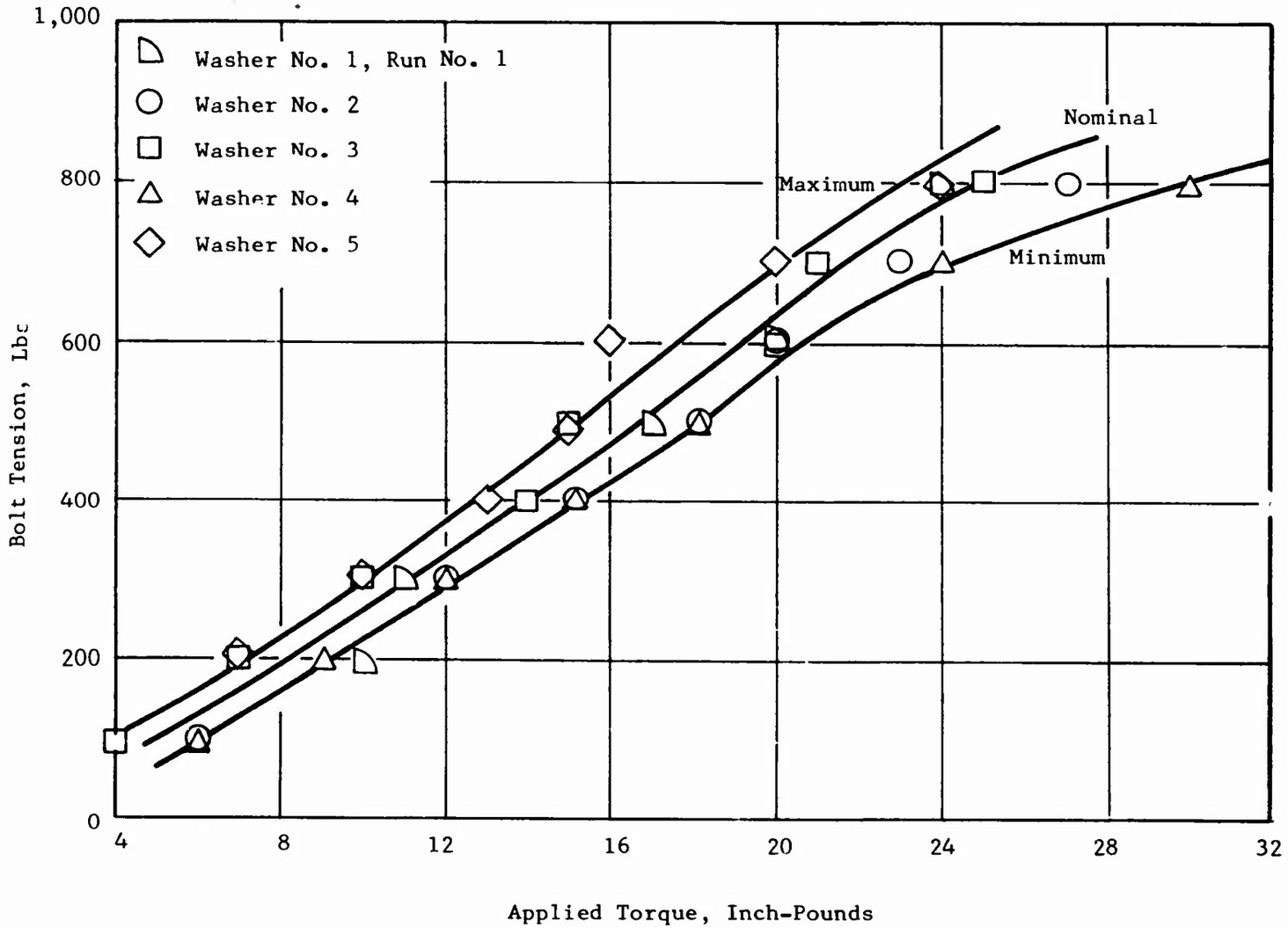

Figure 80. Variation of Bolt Tension With Applied Torque From Belleville Washer Load Tests.

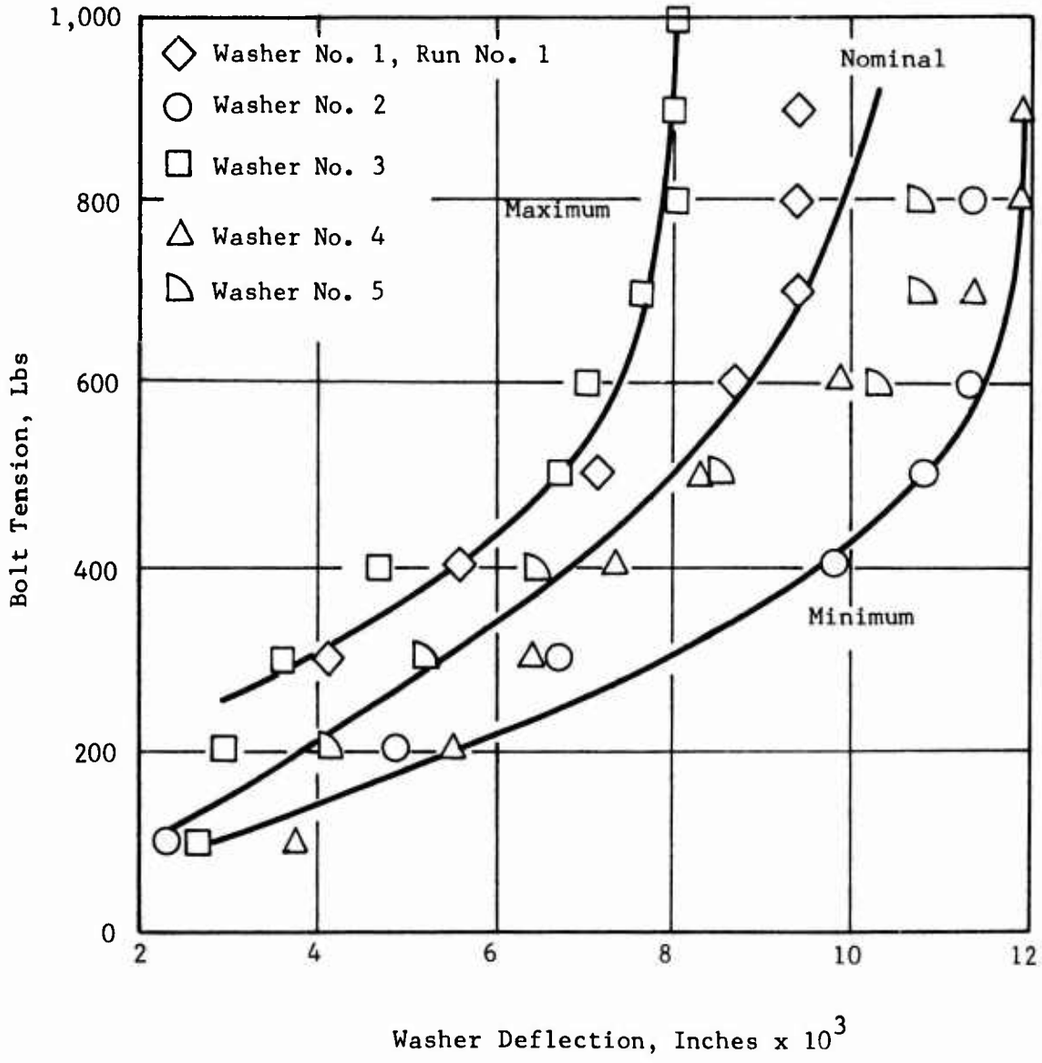

Figure 81. Variation of Bolt Tension With Washer Deflection From Belleville Washer Load Tests.

LOW-SPEED COMPRESSOR INVESTIGATIONS

LOW-SPEED ROTATING VANELESS DIFFUSER RESEARCH

Introduction

Test data obtained from the high-speed compressor indicate that the present design encountered difficulties at corrected speeds of 60 percent and higher. Since this trouble is encountered with increasing speed in a high Reynolds number region, it can be safely assumed that the deterioration in performance is due to compressibility effects. In general, the gross effects of compressibility on compressor performance can be traced to 1 or more of the following 4 effects:

1) Mismatching between compressor components.

2) Choking.

3) Shocking.

4) Changing diffusion parameter values.

Any of these 4 effects can be a cause of performance deterioration.

In the present context, mismatching is intended to signify the off-design operation of successive blade rows and does not apply to the rotor-only configuration.

Choking is significant insofar as the rotor blades are concerned. Under most operating conditions it is the mechanism through which supersonic blade exit velocities are achieved. At most off-design points, the choking phenomena cause the rotor blades to operate off zero incidence (2 or 3 degrees positive) and hence may be a source of trouble.

Shocks, an ever-present problem in supersonic compressor design, are, of course, a possible problem area in the present machine. In the absence of the stator system, any problems due to shocks will be confined to the rotor blade inlet, to the rotor blade passage, and to the rotating vaneless diffuser due to rotor blade trailing edge shocks propagating outward and scroll splitter lip shocks propagating inward.

The changes in diffusion parameter values due to compressibility phenomena are not usually a problem in conventional supersonic compressor design. This is due to the fact that the changes are anticipated, and suitable design restrictions are employed. At the time the high speed compressor was designed, the "effective static pressure rise coefficient C_{Peff}" described in the Phase I report (Reference 1) was believed to be an adequate indication of rotating vaneless diffuser loading. The value

of this parameter was calculated at the high-speed compressor design condition and found to be less than the value found in the low-speed compressor testing. However, if in place of C_{Peff}, the rotating diffuser dimensionless pressure gradient is taken as a loading parameter, then recent analysis (see section on Analytical Investigations) indicates that compressibility has a very significant effect on the diffusion levels encountered in the high-speed ROC rotating vaneless diffuser.

In addition to changes in diffusion level in the radial vaneless diffuser, it has been anticipated that compressibility will also affect the diffusion levels in the inlet system. This was a source of concern during the inlet design, but the only solution to the problem appeared to be to install a circular inlet vane. Although desirable aerodynamically, this did not appear feasible from a mechanical point of view.

The purpose of the low-speed testing to be described below is to attempt to determine whether the increased gradient values encountered in the high speed ROC due to compressibility are sufficient to cause a breakdown in the performance of the rotating vaneless diffuser.

Discussion

The purpose of the rotating vaneless diffuser is to recover maximum static pressure from the high velocity inlet fluid as efficiently as possible. Hence, the 2 most important performance parameters are the static pressure rise coefficient, C_p, and the loss coefficient, $\overline{\omega}$. Analysis of the equations governing the flow in the diffuser indicates that these 2 parameters are in general dependent on the diffuser geometry, Reynolds number, Mach number, flow coefficient, and relative flow angle, as well as on inlet and exit boundary conditions (inlet boundary layer thickness, turbulence level, exit throttle system, etc). For the remainder of this discussion, the following definitions will be used for the above parameters.

1) Geometry (straight-walled diffusers)
   a) Γ = net wall slope
   b) AR_d = diffuser aspect ratio (h_2/b_2)
   c) R = diffuser radius ratio (r_3/r_2)
2) N_R = Reynolds number, proportional to $r_2 U_r$
3) M_r = inlet radial Mach number
4) β_2 = relative flow angle

Hence, $C_P = F(M_2, \phi_2, \beta_2, N_R, \text{etc})$

The "etc" term representing the inlet and exit boundary conditions we shall ignore for the present. From this point on, β_2 (air angle) will be considered defined by β_2* (metal angle) and will be considered a geometric parameter.

Essentially, 2 distinct goals can be identified in the diffuser research program. The first is to determine the value of some diffuser loading parameter such as C_p or to determine the radial extent over which a given level of pressure gradient can be sustained (before separation) for a given set of values for the dimensionless coefficients. This determination can be extended over the range of dimensionless parameter values which can be achieved in the low-speed machine. This problem is straightforward and is only difficult insofar as measuring the dimensionless parameter (including the "etc") is difficult.

The second problem is that of determining a loading parameter in the low-speed regime on the low-speed compressor which can be extended to the high-speed regime on the high-speed compressor. The problem is by no means direct, and must be approached on the basis of experience with other similar type flow machines. Consideration of the flow correlations used with the conventional two-dimensional diffuser suggests that it may be possible to examine the extent to which given pressure gradients can be sustained in the low-speed machine as explained herein. At the present time, this is the main intention behind the proposed testing.

In order to indicate the degree of extrapolation, the correspondence between the low- and high-speed compressor dimensionless parameters is given below:

		High Speed *	Low Speed **
1)	Geometry		
	a) Γ, degrees	5.2	0
	b) AR_d	7.17	8.27
	c) R	1.511	1.451
	d) β_2*, degrees	60	60
2)	N_R	2.25×10^6***	0.67×10^6
3)	M_r	0.78	0.1
4)	ϕ	0.62	0.692

* Based on 100 percent speed, 0 degrees inlet guide vane
** Based on N = 1,800 rpm and $\phi_1 = 1.0$
*** Based on static temperature and pressure

It should be noted that the diffuser flow can be divided into 2 regimes. The first extends from the diffuser inlet to the radial position at which the 2 wall boundary layers meet. The second regime extends from this point to the exit. In the first regime, the geometric parameter AR_d should be of minor importance while the "etc" should be fairly significant. Diffuser separation will probably occur in regime 1 for highly loaded diffusers and in regime 2 for more lightly loaded diffusers. In the description of the test rig, note that 1 of the diffuser walls in the low-speed machine will be held stationary. This will limit the validity of the results to regime 1 only. It is implicitly assumed that the effects which occur in regime 2 will not affect the validity of the results in regime 1. Data on normal two-dimensional diffusers suggest that this assumption is not entirely valid.

General Analysis

Most of the analysis presented herein on the rotating vaneless diffuser has been concerned with diffuser loading on the basis of 2 nondimensional pressure gradient parameters, G_1 and G_2. These parameters are different from the ones described in the section on Analytical Investigations only insofar as they have been nondimensionalized to r_2, the diffuser inlet radius.

$$G_1 = \frac{r_2 \left[\left(\frac{\partial p}{\partial r}\right)_{FS} - \left(\frac{\partial p}{\partial r}\right)_{BL} \right]}{\frac{1}{2} \rho W^2 \cos \beta} \tag{3}$$

$$G_2 = \frac{r_2 \left[\left(\frac{\partial p}{\partial r}\right)_{FS} - \left(\frac{\partial p}{\partial r}\right)_{BL} \right]}{\frac{1}{2} \rho W^2 \cos^2 \beta} \tag{4}$$

where $\left(\frac{\partial p}{\partial r}\right)_{FS}$ = free stream pressure gradient

$\left(\frac{\partial p}{\partial r}\right)_{BL}$ = boundary layer pressure gradient $\left(\rho \frac{U^2}{r}\right)$

r_2 = inlet radius to diffuser

ρ = static density

W = relative velocity

β = relative flow angle

The behavior of the loading parameters has been investigated at both the diffuser inlet and at stations radially outward from the inlet. The behavior at the inlet can generally be expressed in closed form and illustrates clearly the dependence of the initial value of the gradient on the diffuser geometric parameters. In general, the behavior within the diffuser cannot be expressed in closed form, but is easily handled by a computer. This method of solution does not provide as much insight into the behavior of the gradients, but it does provide the necessary information about their behavior within the diffuser. The free stream density is assumed to exist in the boundary layer, and local values of density, relative velocity, and relative flow angle are used to calculate the loading parameter for any radial location.

The expressions giving G_1 at the inlet of the rotating diffuser can be conveniently considered as the sum of an incompressible term (G_{1inc}) and a term which accounts for compressibility effects (G_{1c}) as follows:

$$G_1 = G_{1inc} + G_{1c} \tag{5}$$

where $$G_{1inc} = 2 \sin(\beta_2^*) [\tan (\beta_2^*) + 2/\phi_2] + 2 \cos (\beta_2^*) [1 + AR \tan (\Gamma)] \tag{6}$$

and $$G_{1c} = 2 \cos (\beta_2^*) \left[\frac{M_r^2}{1-M_r^2} \right] \left[1 - \frac{AR \tan (\Gamma)}{1 + (\tan(\beta_2^*) + \frac{1}{\phi_2})^2} \right]$$

$$\left[\tan (\beta_2^*) + \frac{1}{\phi_2} \right] \tag{7}$$

For a given geometry diffuser (β_2, AR, and Γ fixed), the gradient depends on the throttling effects, expressed by the flow coefficient, ϕ and the compressibility effects, expressed by M_r. The gradient increases with decreasing ϕ, as is clearly indicated in Figure 82. The gradient is seen to increase with increasing radial Mach number and, in fact, becomes very large as the radial Mach number approaches unity (this behavior is typical of that predicted by one-dimensional compressible flow analysis as the critical Mach number is approached). In the Analytical Investigations section, it is stated that the value of the diffuser loading parameter at 100 percent speed in the high-speed compressor increased over the value at lower speeds for both the subsonic and supersonic blade exit conditions. A study of equations 6 and 7 indicates that the cause of increase is different for each case. For the subsonic exit, rotor blade choking along with the subsonic exit results in a small value of ϕ_2 and hence a large value of G_{1inc}. The compressor appears heavily throttled to the diffuser. The compressible

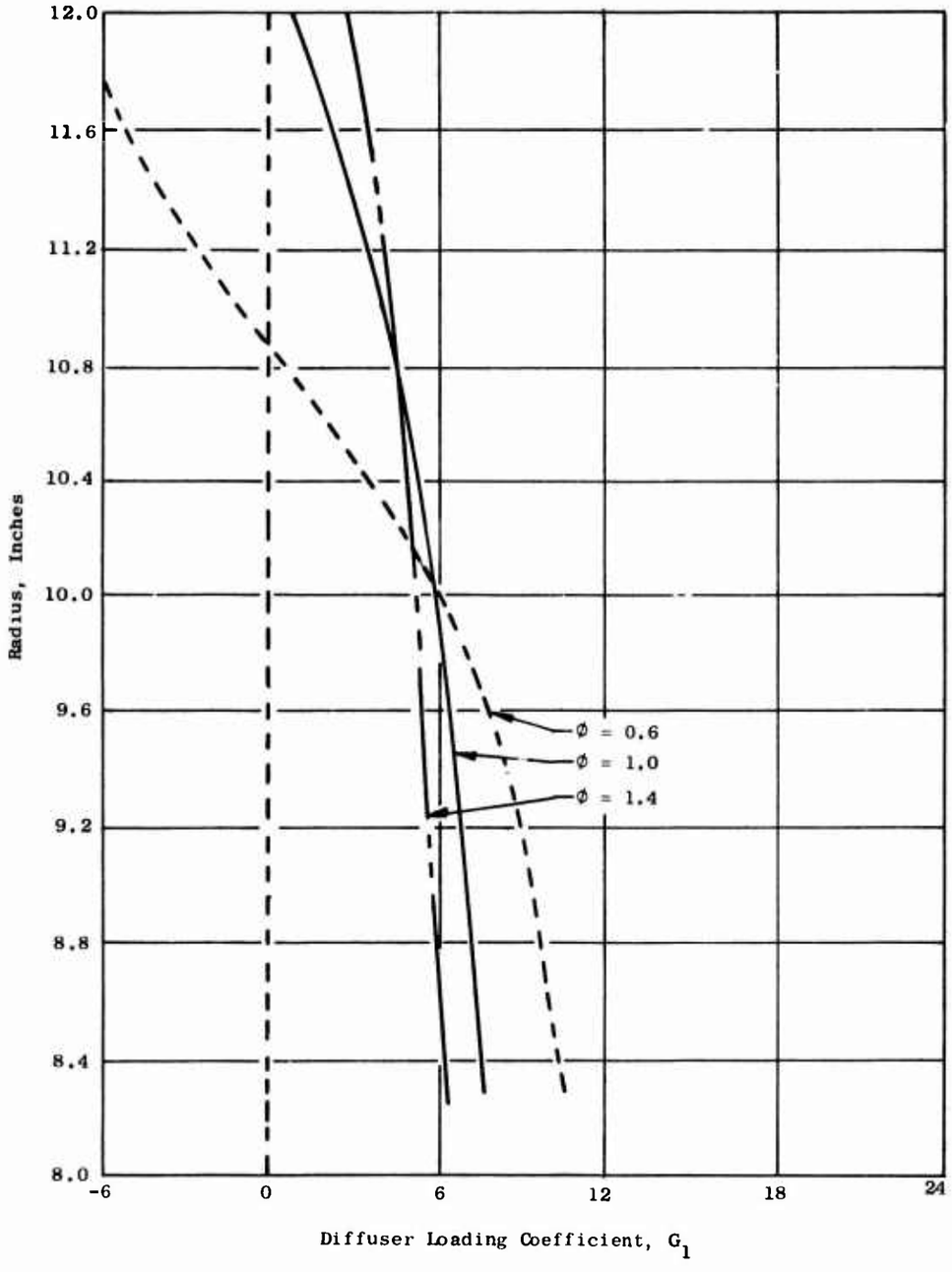

Figure 82. Variation in the Aerodynamic Loading Coefficient G_1 With Radius for Various Flow Coefficients.

correction is small. For the supersonic exit, the opposite is true; the supersonic exit results in a large value of ϕ, the compressor appears unthrottled, and hence G_{1inc} is not excessive. However, the large radial Mach number (0.78) causes the compressible correction term to play a dominant role.

In the case of the low-speed machine, the compressibility term may be neglected, and since $\Gamma = 0$ (zero side wall slope), $R_2 = 8.37$, $\beta_2 = 60$ degrees, the expression for G_1 becomes

$$G_1 = 4.0 + 3.464/\phi_2 \qquad (8)$$

It can be seen, as predicted by incompressible compressor theory, that the parameter is independent of speed. Examination of this equation indicates that in order to achieve gradients of sufficient magnitude to simulate the high-speed compressor (approximately 18), an unacceptably low value of ϕ_2 is required (poor rotor blade performance and diffuser inlet flow can be expected at values of ϕ_2 below 0.45). A possible means of achieving higher gradients without resorting to a lower ϕ_2 is to apply suction to the diffuser walls to increase the rate of diffusion of the radial velocity component. If this is done then the inlet gradient equation becomes

$$G_1 = 4.0 + \frac{3.464}{\phi_2} \left(1 + 0.066 \frac{K_f \sqrt{\Delta P}}{N}\right) \qquad (9)$$

where K_f = suction screen flow restriction coefficient

ΔP = suction screen ΔP in inches of H_2O

N = compressor speed as a fraction of 1,800 rpm

It is seen now that for a given value of screen flow parameter ($K_f = 2.0$ has been determined to be a reasonable value), the initial gradient depends on flow coefficient, compressor speed, and suction ΔP. As previously stated, the reduction in ϕ_2 is limited by rotor blade performance (as well as high speed to low speed similarity considerations); similarly, the reduction in N is limited by diffuser Reynolds number considerations, and the increases in ΔP are limited by the facility suction capability. Using a value of $K_f = 2$, $\Delta P = 16$, $\phi_2 = 0.45$, and $N = 0.556$, the initial value of G_1 can be raised to approximately 18.5. It is not intended that conditions as extreme as these be employed during testing.

The effects of each of the terms ϕ, ΔP, and N on the initial (and downstream) values of G_1 can be seen in Figures 83, 84, and 85 respectively. The value of flow coefficient used in these figures is

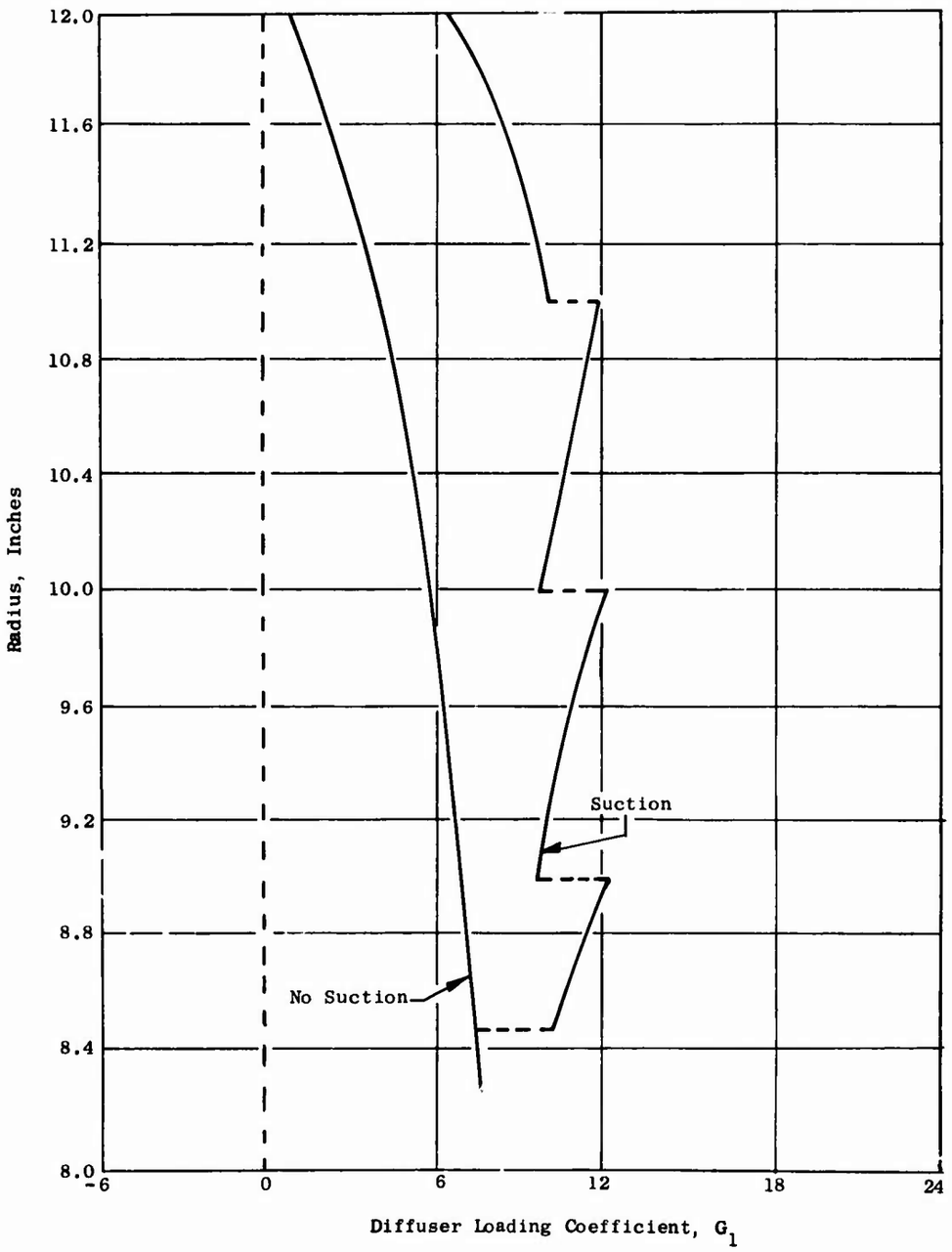

Figure 83. Effect of Suction on the Aerodynamic Loading Coefficient G_1 in the Low-Speed Vaneless Diffuser for ϕ = 1.0.

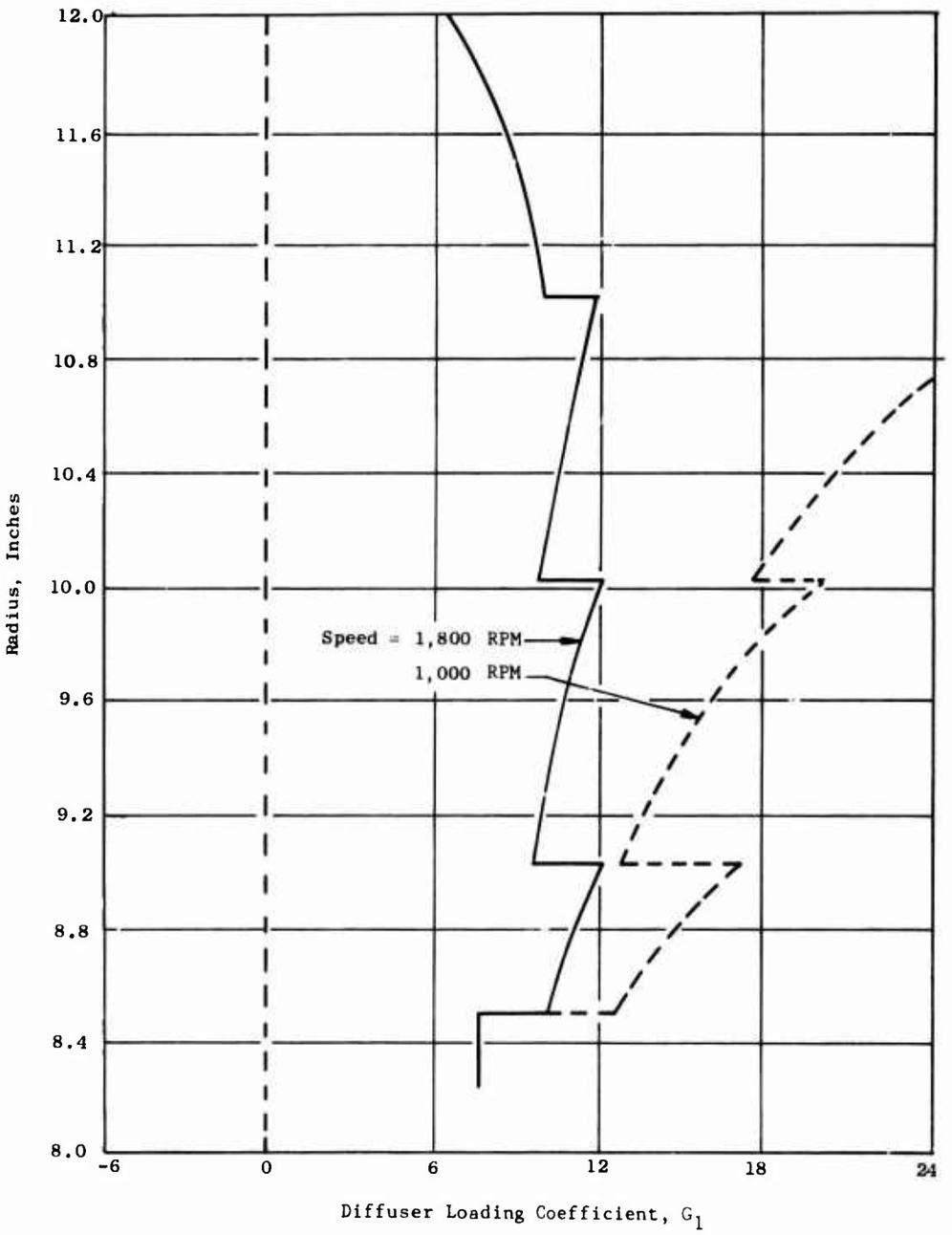

Figure 84. Effect of Rotational Speed on the Aerodynamic Loading Parameter G_1 With Suction for $\phi = 1.0$.

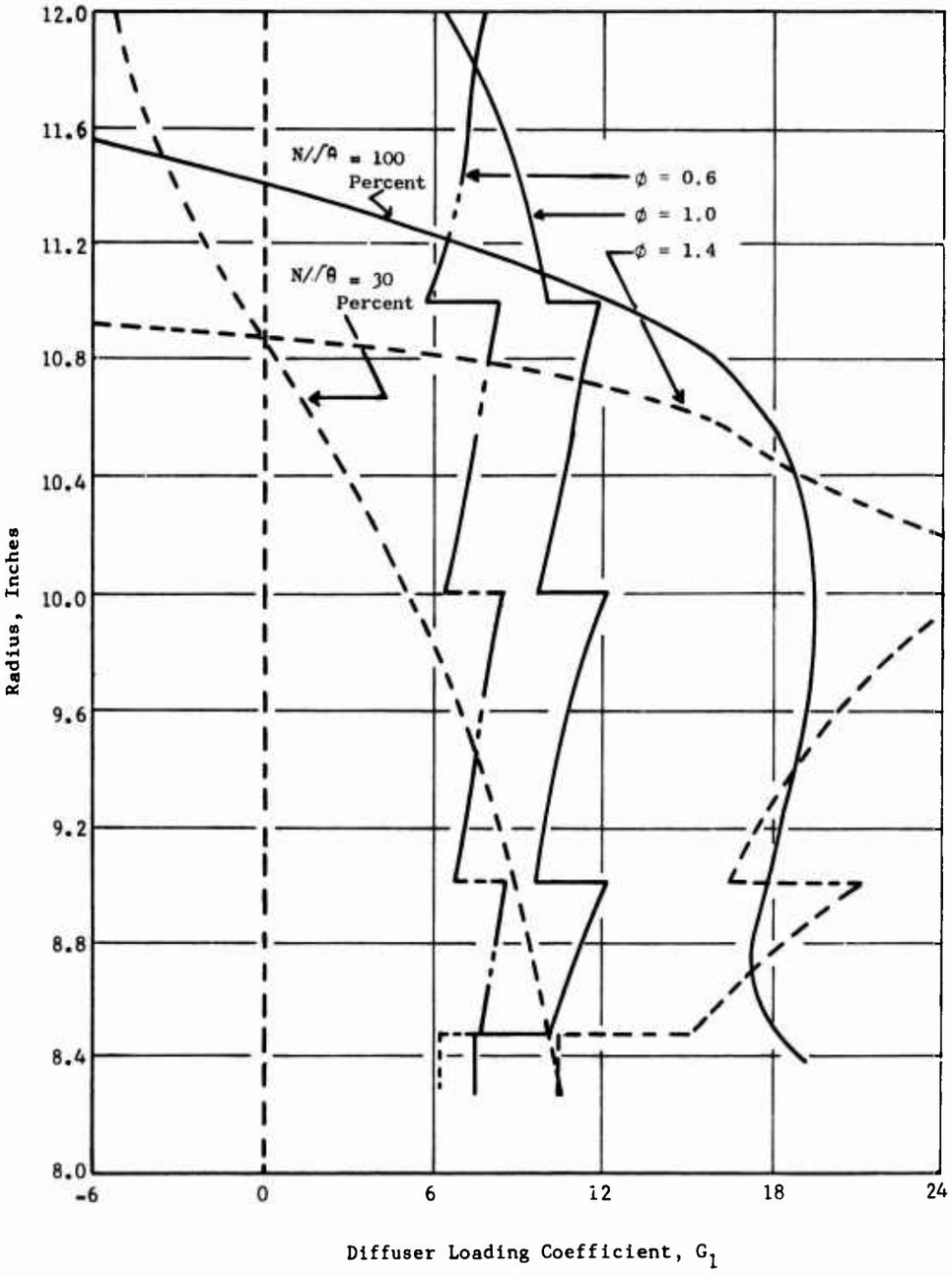

Figure 85. Comparison of the Aerodynamic Loading Parameter G_1 for the Low-Speed ROC at 3 Flow Coefficients in the High-Speed ROC.

ϕ_1, which is the inlet flow coefficient, and not ϕ_2, which was used in the preceding equations. For the low-speed compressor, the relation between ϕ_1 and ϕ_2 is given by $\phi_2 = 0.734\ \phi_1$.

Test Rig

One problem which occurs in trying to investigate in detail the behavior of a rotating vaneless diffuser is that of obtaining aerodynamic measurements. For the low-speed compressor installation, this could be done most easily by holding 1 wall stationary. This restricts the validity of the measurements to those portions of the rotating diffuser in which the effects of wall interaction are small, i.e., the inlet portions of the diffuser. In this zone of the diffuser, the largest gradients are imposed.

Precaution must be taken to prevent the stationary surface (which ordinarily is aerodynamically weaker than the rotating surface) from separating and grossly affecting the flow pattern in the diffuser. This can be done by applying suction to the stationary wall. Besides controlling the stationary wall boundary layer, this suction flow can be used to control the pressure gradient distribution in the diffuser and hence to allow a greater range of diffuser loading (see previous discussion).

The low speed test rig consists of the original low-speed rotor with 1 wall rotating and 1 wall stationary. The stationary wall is perforated and backed up by 4 independent suction chambers. The pressure in these 4 chambers is controlled by 4 circumferential valves which determine the pressure drop between the 4 chambers and the plenum. The plenum can be held at a reduced pressure of approximately 18 inches of water below atmospheric.

Eighteen static pressure taps have been placed radially on the stationary wall (12 on 1 radial line and 6 on a radial line 180 degrees away). Four different radial locations are available for manual probing with a cobra probe (indicating yaw angle and total pressure). The mass flow was determined as in previous low-speed compressor tests using 4 bell-mouth static taps. The plenum and 4 chamber pressures as well as the lower sump pressure were monitored, as were a number of miscellaneous static taps downstream of the rotor. Barometer and cell temperatures were also recorded. The assembly drawing of the modified low-speed test vehicle and the suction chamber details are presented in Figures 86 and 87.

Analysis of Test Rig

A computer program was written to obtain an indication of what the gross operating characteristics of the system described above would be. This program once again uses a one-dimensional diffuser flow analysis,

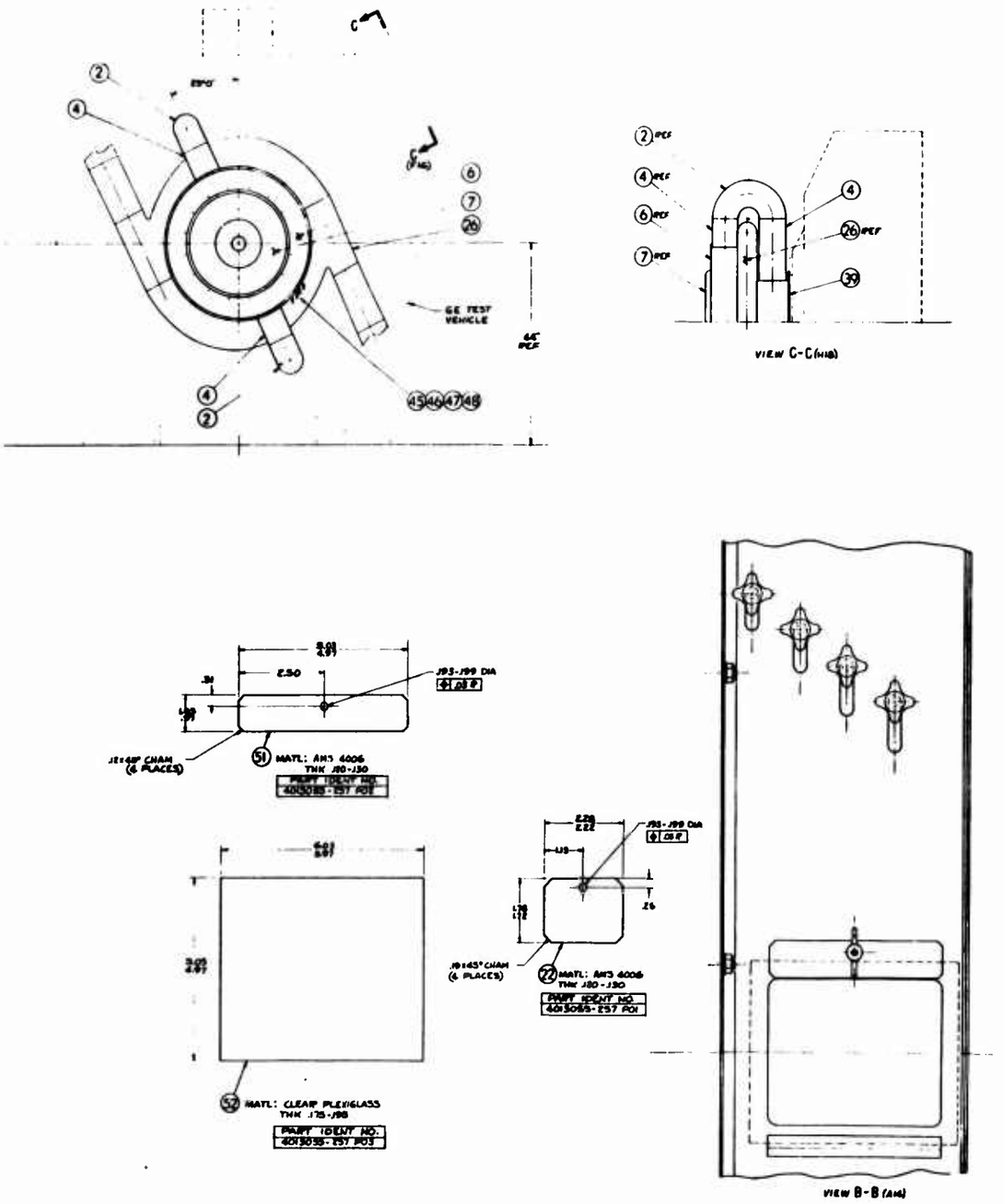

Figure 86. Low-Speed ROC as Modified for the Porous Wall Diffuser Tests.

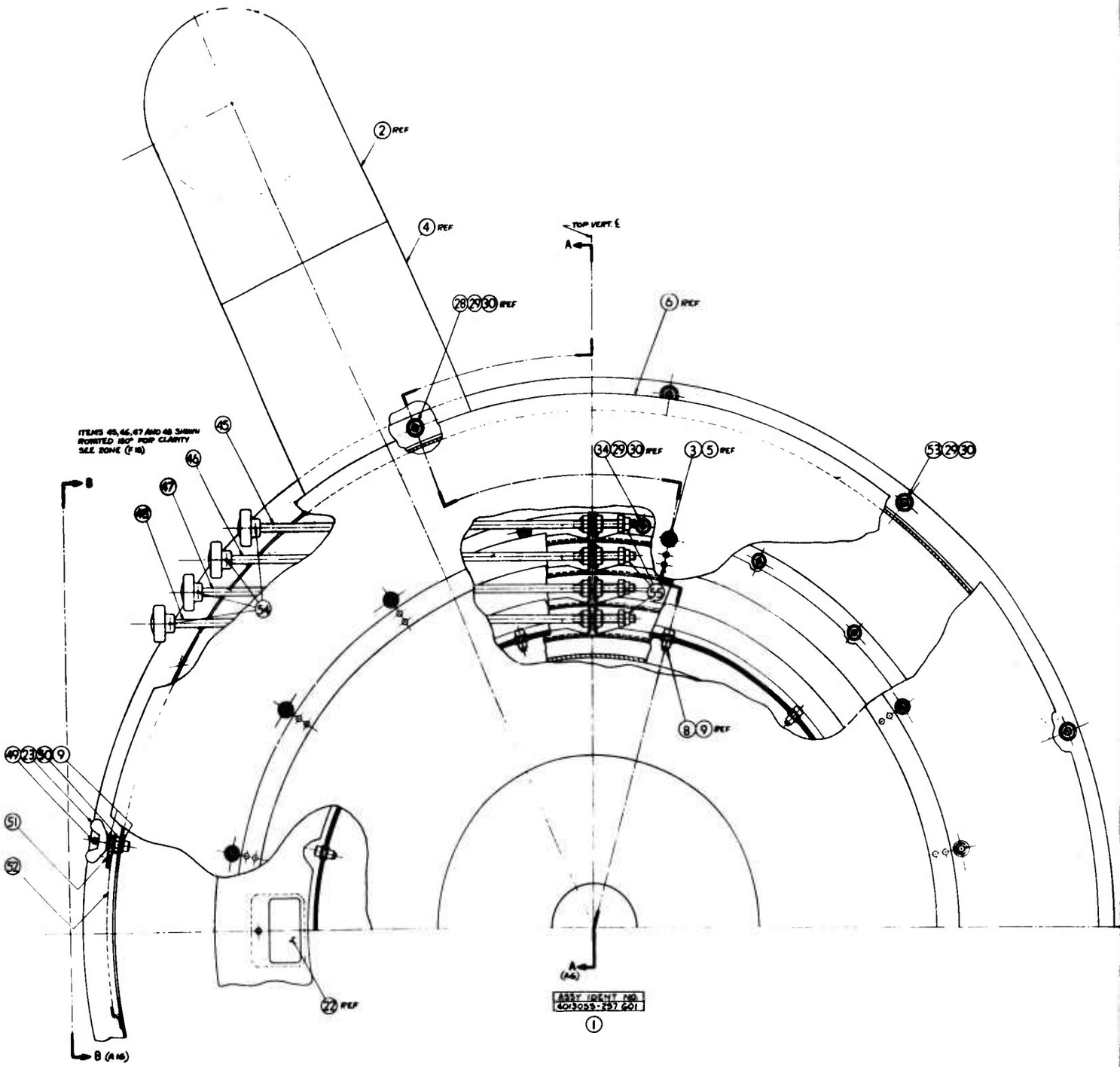

Figure 86. (Continued)

A

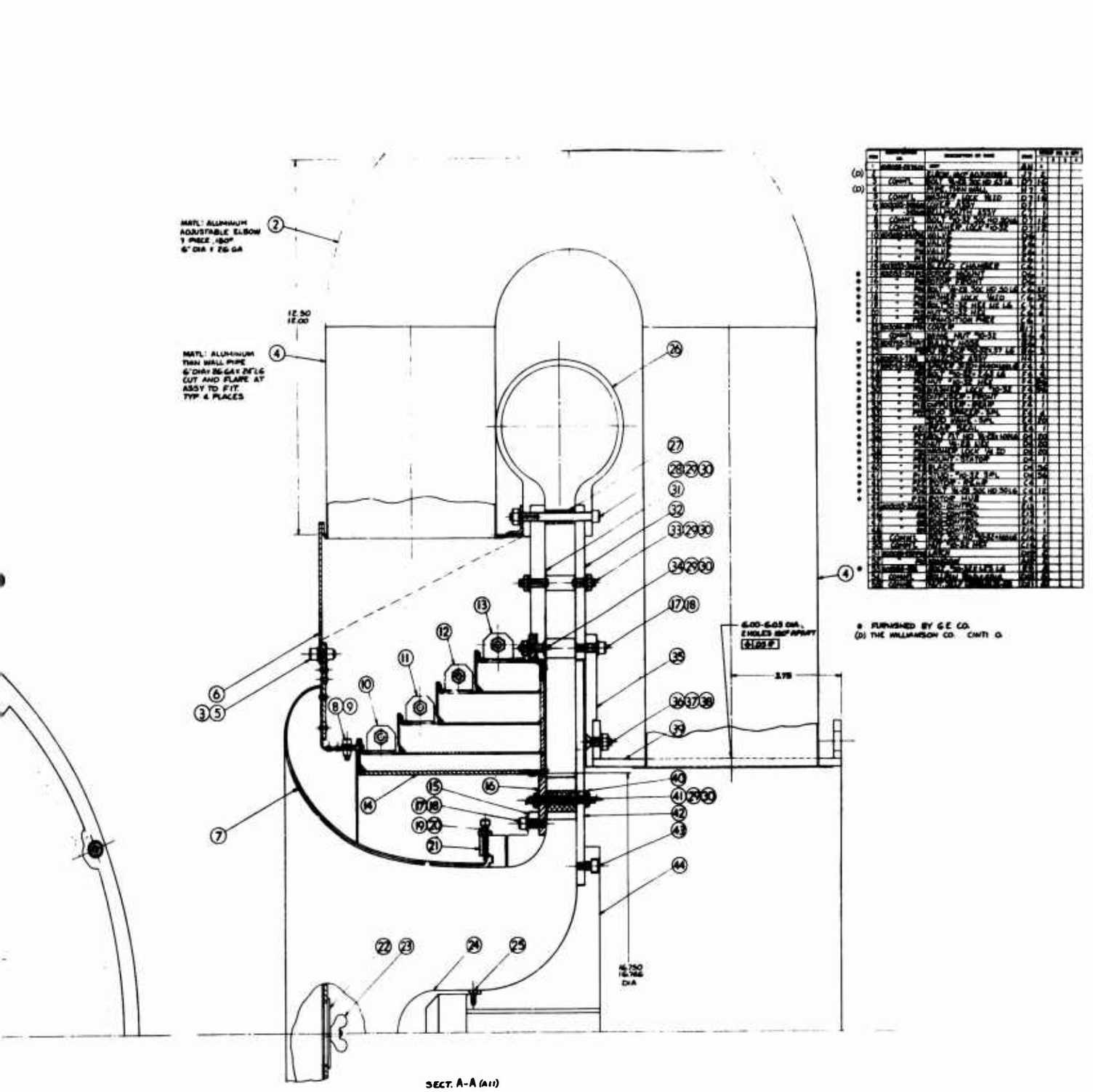
MATL: ALUMINUM
ADJUSTABLE ELBOW
1 PIECE MOP
6" DIA x 26 GA
MATL: ALUMINUM
THIN WALL PIPE
6" DIA x 26 GA x 28" LG
CUT AND FLARE AT
ASSY TO FIT
TYP 4 PLACES
12.50
12.00
6.00-6.03 DIA.
6 HOLES 60° APART
2.75
* FURNISHED BY G E CO.
(D) THE WILLIAMSON CO. CINTI O.
SECT. A-A (A11)

B

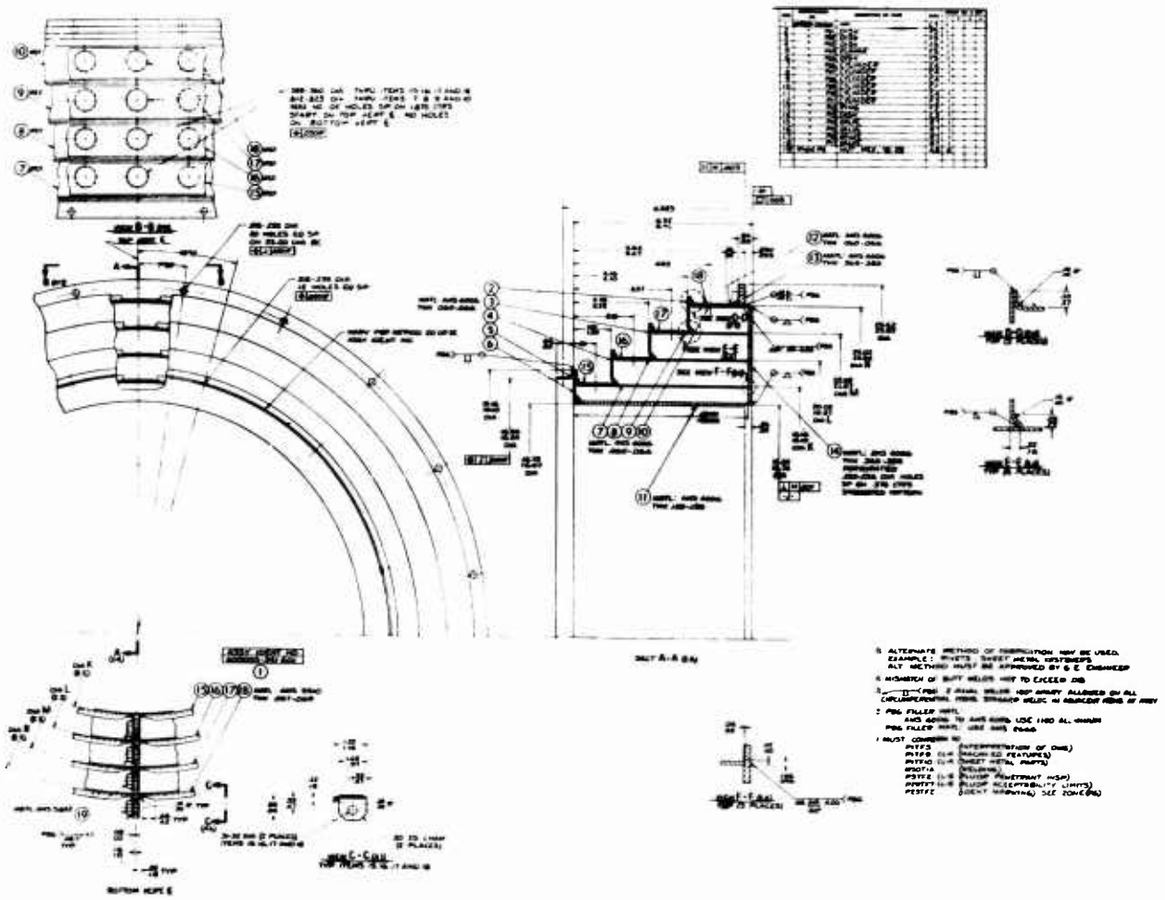

Figure 87. Details of the Suction Chamber Used to Control the Flow Through the Porous Wall.

and in addition, an incompressible analysis of the diffuser to chamber flow, chamber to plenum flow, and plenum to vacuum flow. Each of the flows is assumed to be described by an equation of the form

$$w_x = K_{fx} \frac{\sqrt{\Delta P}}{\rho} \qquad (10)$$

where ΔP = pressure drop

ρ = fluid static density

K_{fx} = appropriate value, screen or pipe coefficient

w_x = appropriate mass flow

The flow diagram used is shown below.

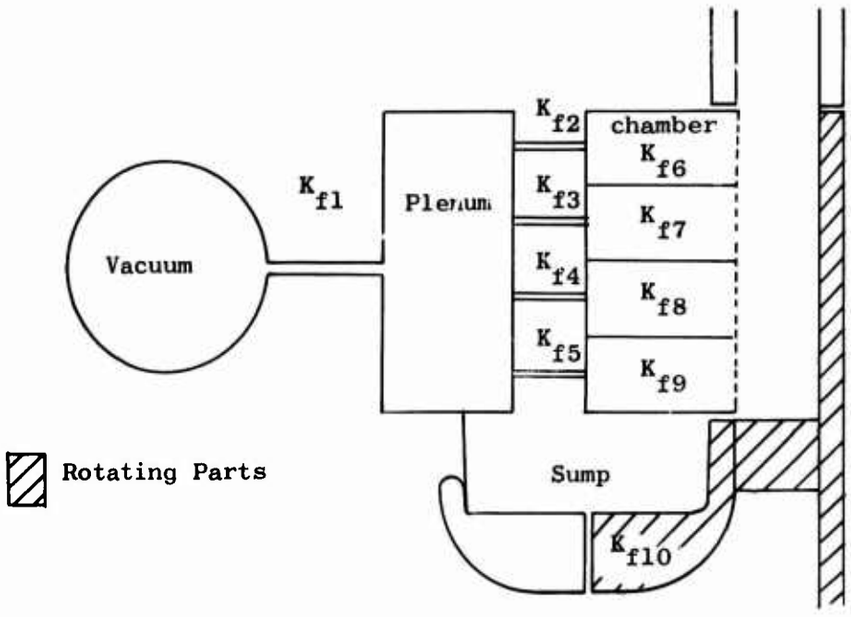

The value of K_{f1} was obtained from the calculated loss coefficient of the pipe system connecting the compressor suction plenum to the vacuum source. The values of K_{f2} to K_{f5} depend on the circumferential valve settings and are input to the program. The values of K_{f6} to K_{f9} are all equal and have been calculated on the basis of the geometry of the proposed perforated mylar screen. The results of the analysis described above on a system with a constant vacuum of 20 inches of water below atmospheric are given in Figures 82 through 85.

Two-Dimensional Flow Conditions

In order to determine the pressure gradient distribution on the rotating wall of the low-speed compressor diffuser, a finite difference numerical solution for the stream function in the diffuser passage was performed. The distribution of the stationary suction velocity with radius used in obtaining this solution was taken from the previously performed one-dimensional analysis. The predicted ideal streamline configuration for $\phi = 0.6$ and $\phi = 1.0$ at a speed of 1,800 rpm is shown in Figure 88. These 2 cases correspond to the one-dimensional case presented in Figure 85.

The static pressure distribution as a function of radius plot for the $\phi = 0.6$ case and the $\phi = 1.0$ case is shown in Figures 89 and 90. It can be seen that the only meaningful difference in the static pressure level across the diffuser is found at the rotor blade exit where the stationary wall suction velocities are high. This figure also indicates that the values of the gradient obtained from measurements on the stationary wall should be entirely satisfactory, and that the nonuniformity of the gradient at the stationary wall should not adversely affect the measurements.

The distribution of gradient with radius for the 2 cases described above is shown in Figures 91 and 92. As was hoped, the gradient distribution, though ragged near the stationary wall, appears quite smooth at the rotating wall. The predicted rotating wall gradients are shown along with those predicted for the high-speed compressor in Figure 93.

Using the same computer program, a simulation of the effect of a separation bubble on the main stream flow was performed. The bubble shape and associated streamline distribution are shown in Figure 94. The static pressure distribution for the diffuser with and without such a flow separation is shown in Figure 95. It can be seen that the change in static pressure on the stationary wall due to a bubble on the rotating wall is quite gradual. Variations in the static pressure distribution of the type shown should be helpful in determining the extent and location of any separations occurring during the low-speed investigations.

VERIFICATION OF DIFFUSER ANALYSIS USING LOW-SPEED COMPRESSOR

Preliminary Tests

The low-speed ROC has been modified as shown in Figures 86 and 87 to incorporate a bleed chamber. One wall of the rotating vaneless diffuser

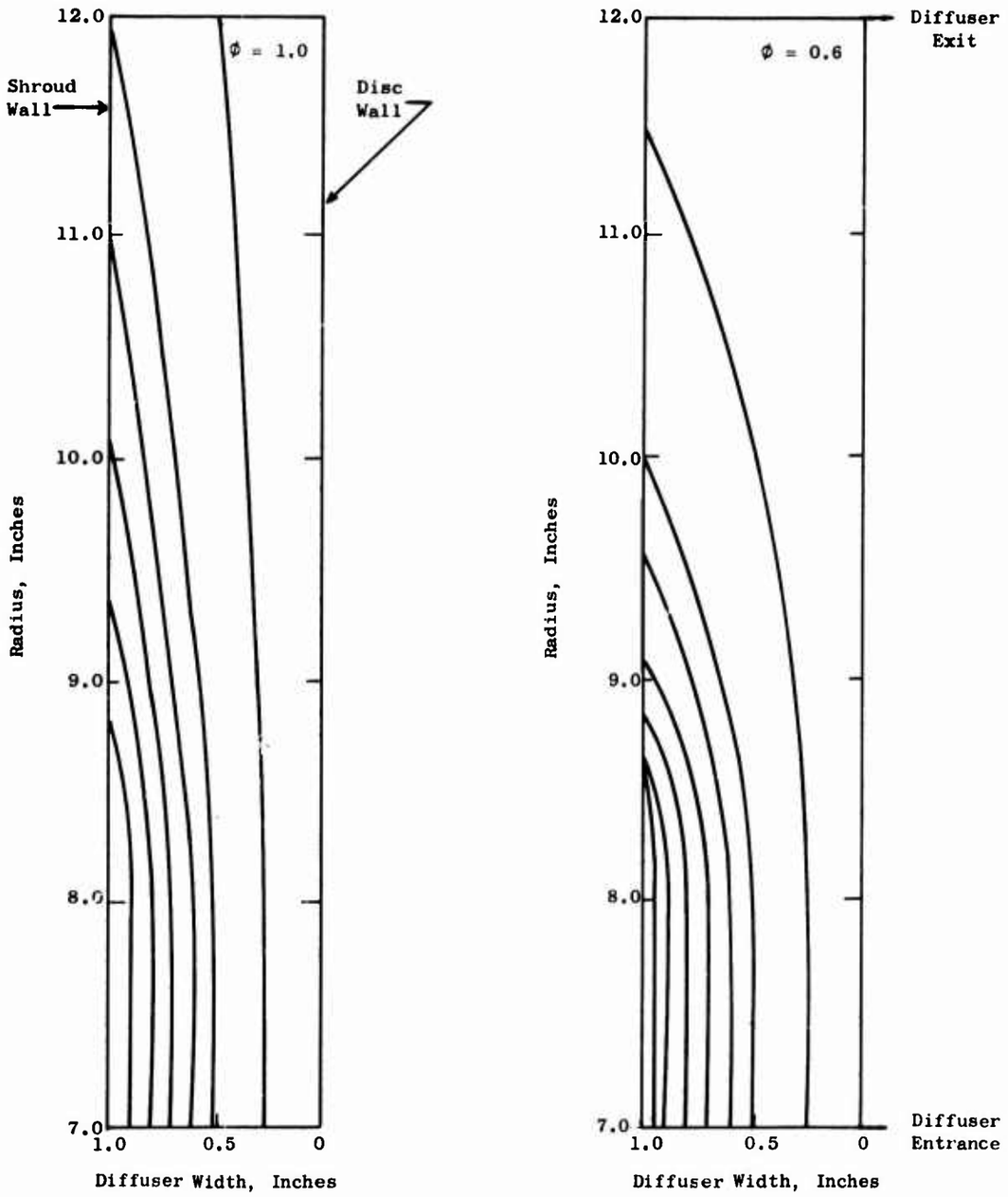

Figure 88. Calculated Streamline Patterns in Rotating Vaneless Diffuser of Low-Speed ROC for 2 Values of Flow Coefficient With Maximum Suction.

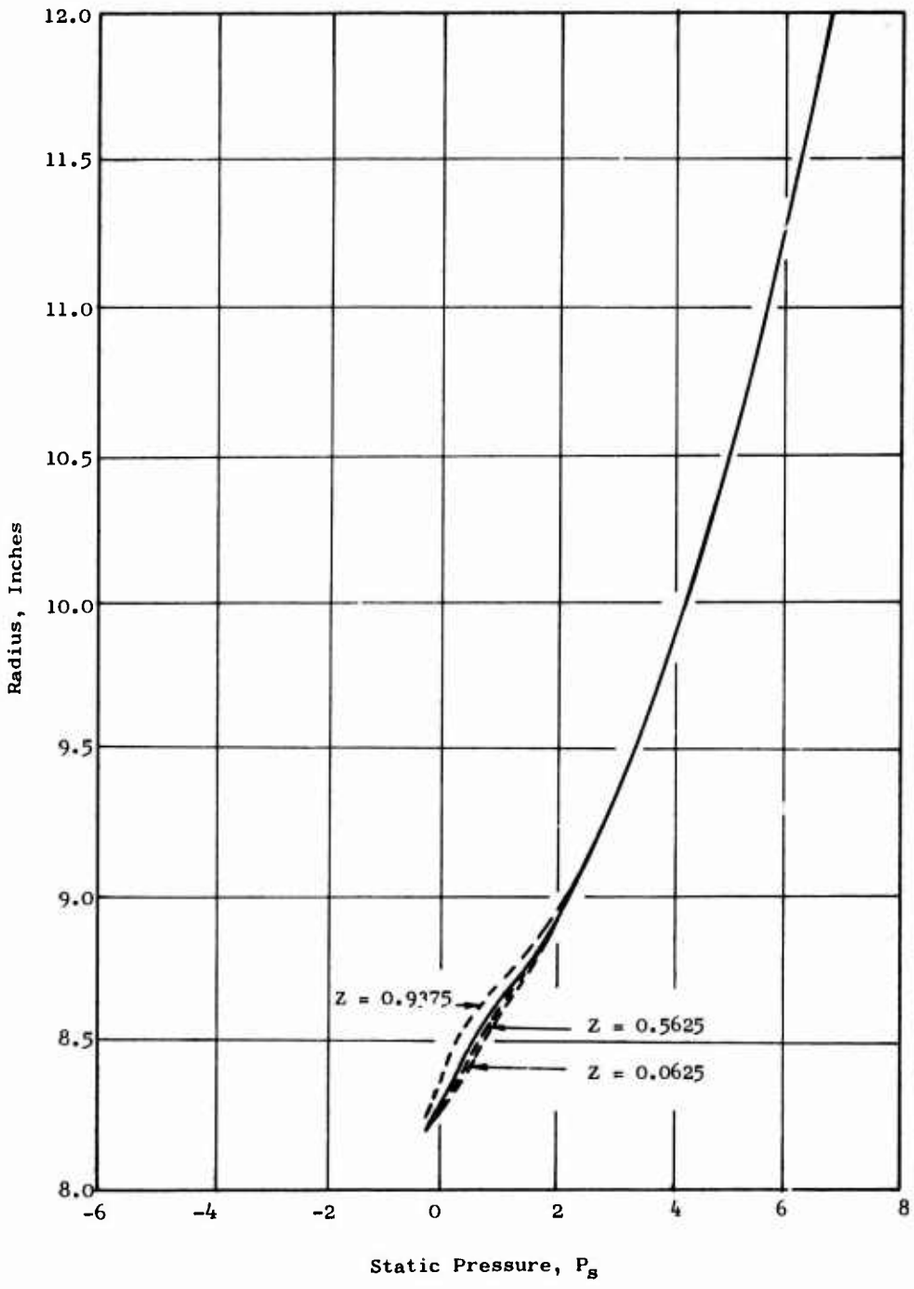

Figure 89. Static Pressure Distribution in the Rotating Vaneless Diffuser of the Low-Speed ROC for Flow Coefficient 0.6 and Several Suction Quantities.

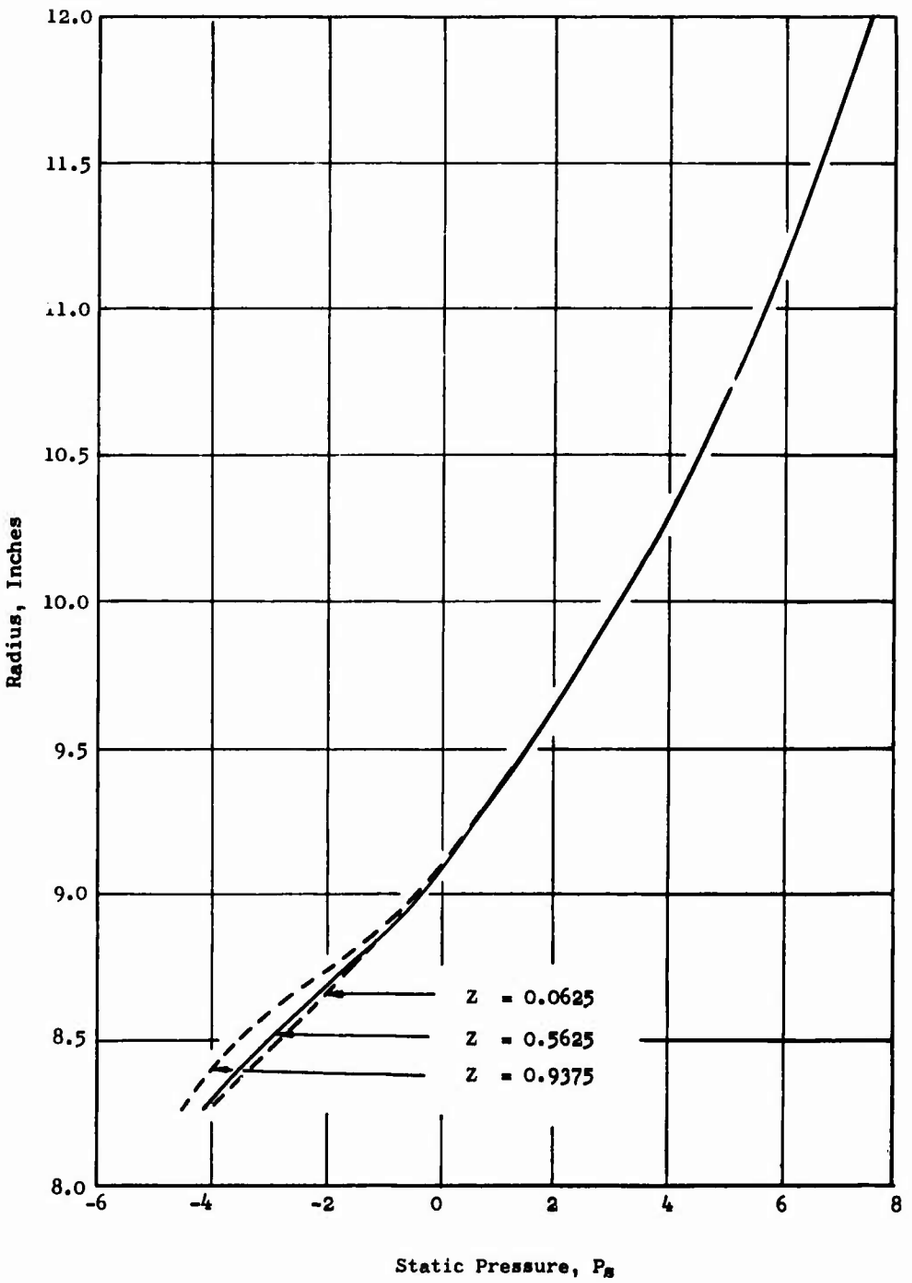

Figure 90. Static Pressure Distribution in the Rotating Vaneless Diffuser of the Low-Speed ROC for Flow Coefficient 1.0 and Several Suction Quantities.

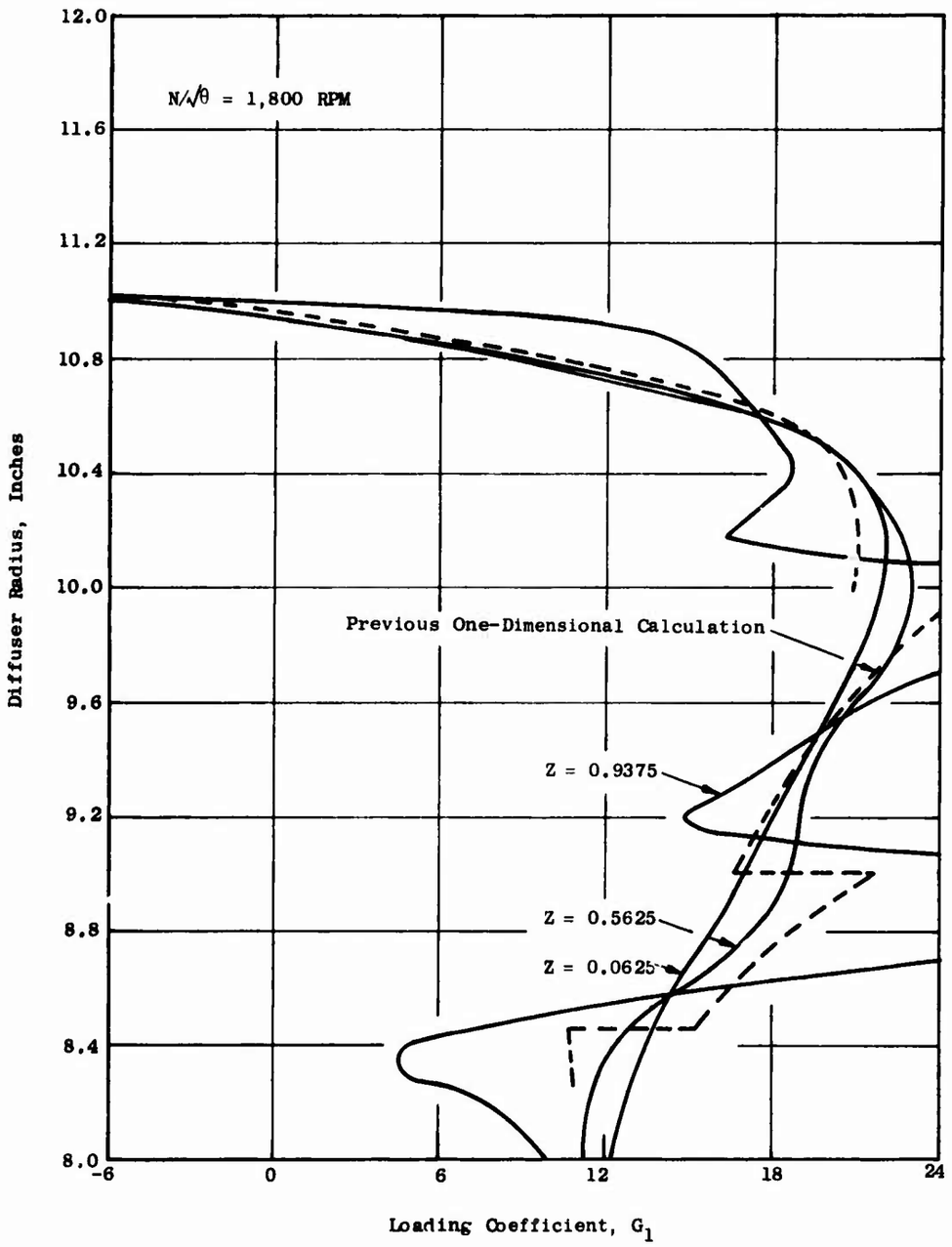

Figure 91. Values of the Aerodynamic Loading Coefficient G_1 on the Rotating Disc Wall of the Vaneless Diffuser for Various Values of Suction Quantity Z, $\phi = 0.6$.

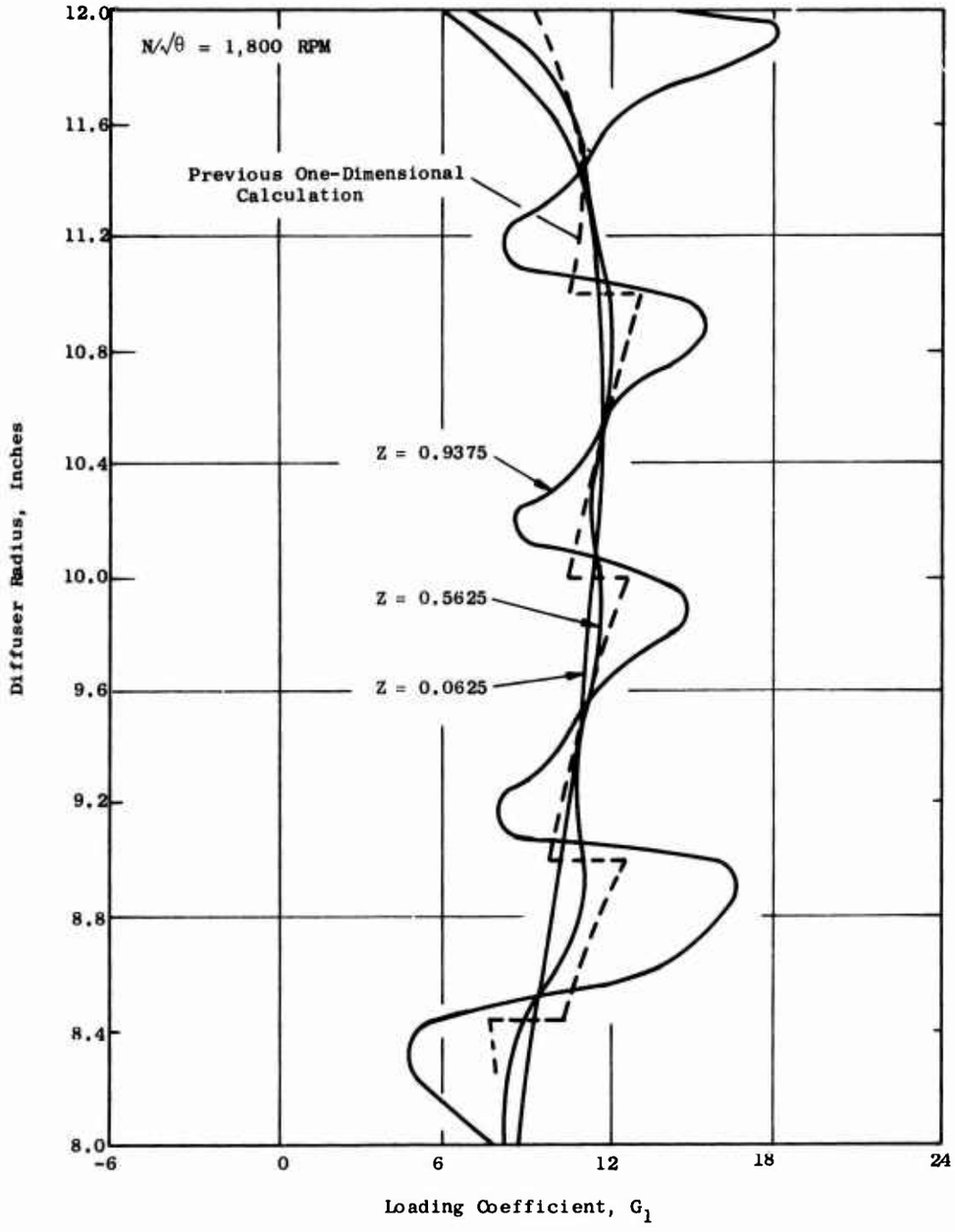

Figure 92. Values of the Aerodynamic Loading Coefficient G_1 on the Rotating Disc Wall of the Vaneless Diffuser for Various Values of Suction Quantity Z, ϕ = 1.0.

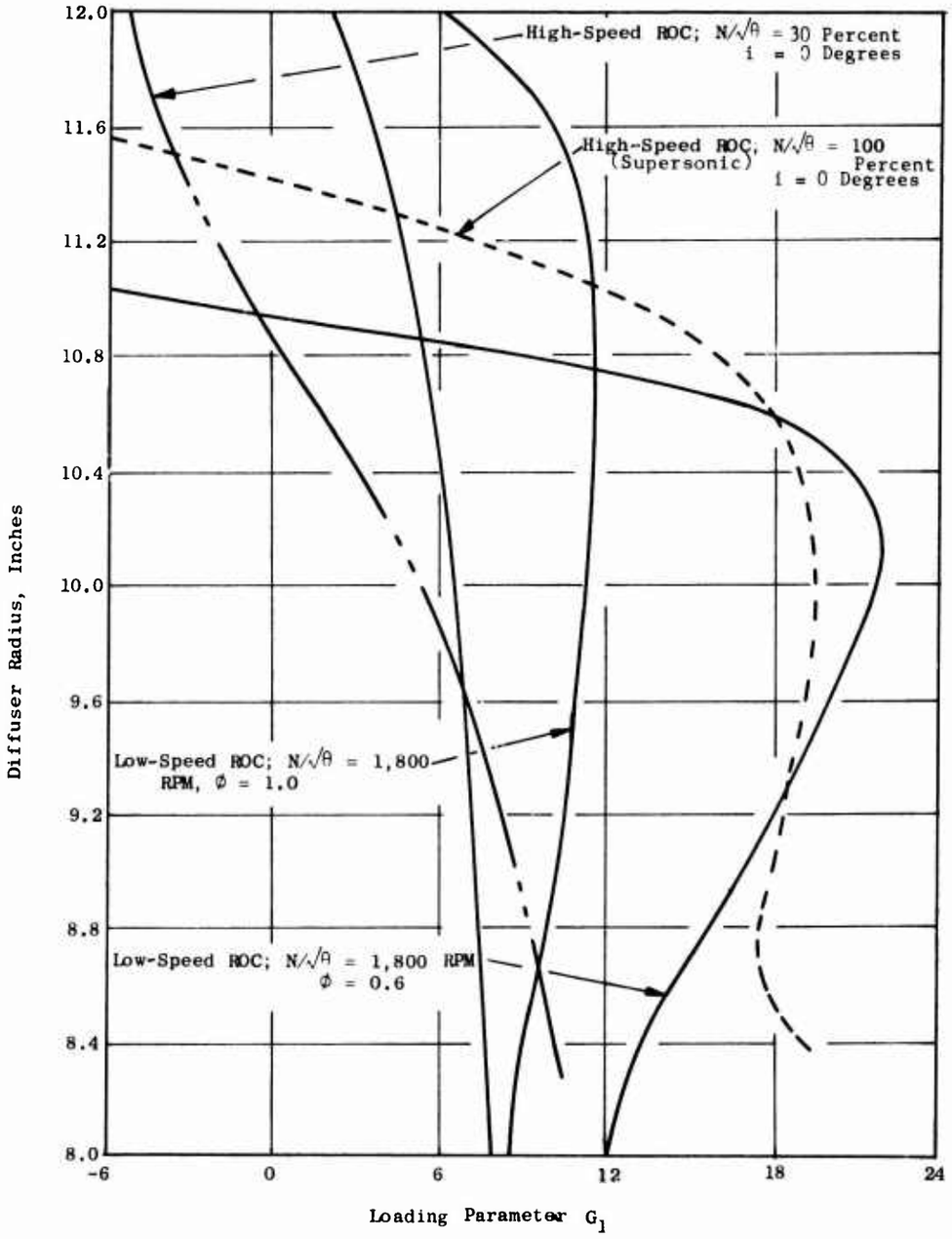

Figure 93. Comparison of the Aerodynamic Loading Coefficient G_1 in the Low-Speed ROC with the High-Speed ROC at 30 and 100 Percent Speed.

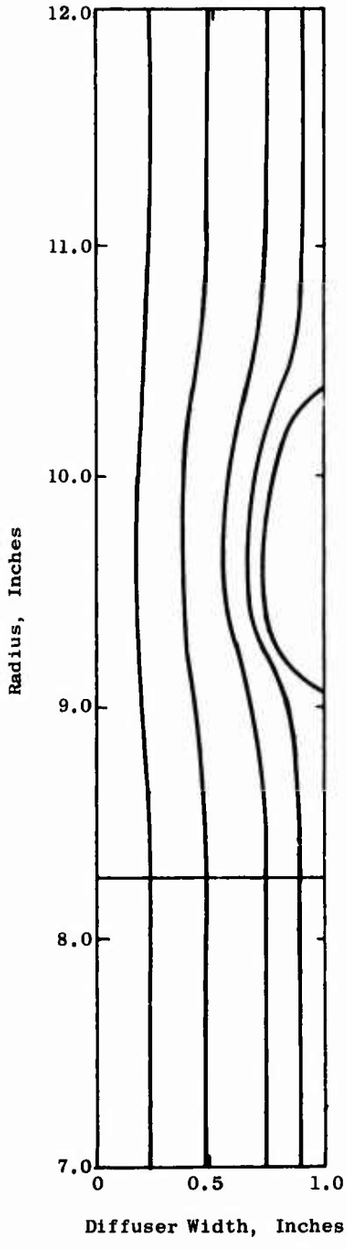

Figure 94. Meridional Streamlines in a Rotating Vaneless Diffuser in the Presence of an Assumed Separation Bubble.

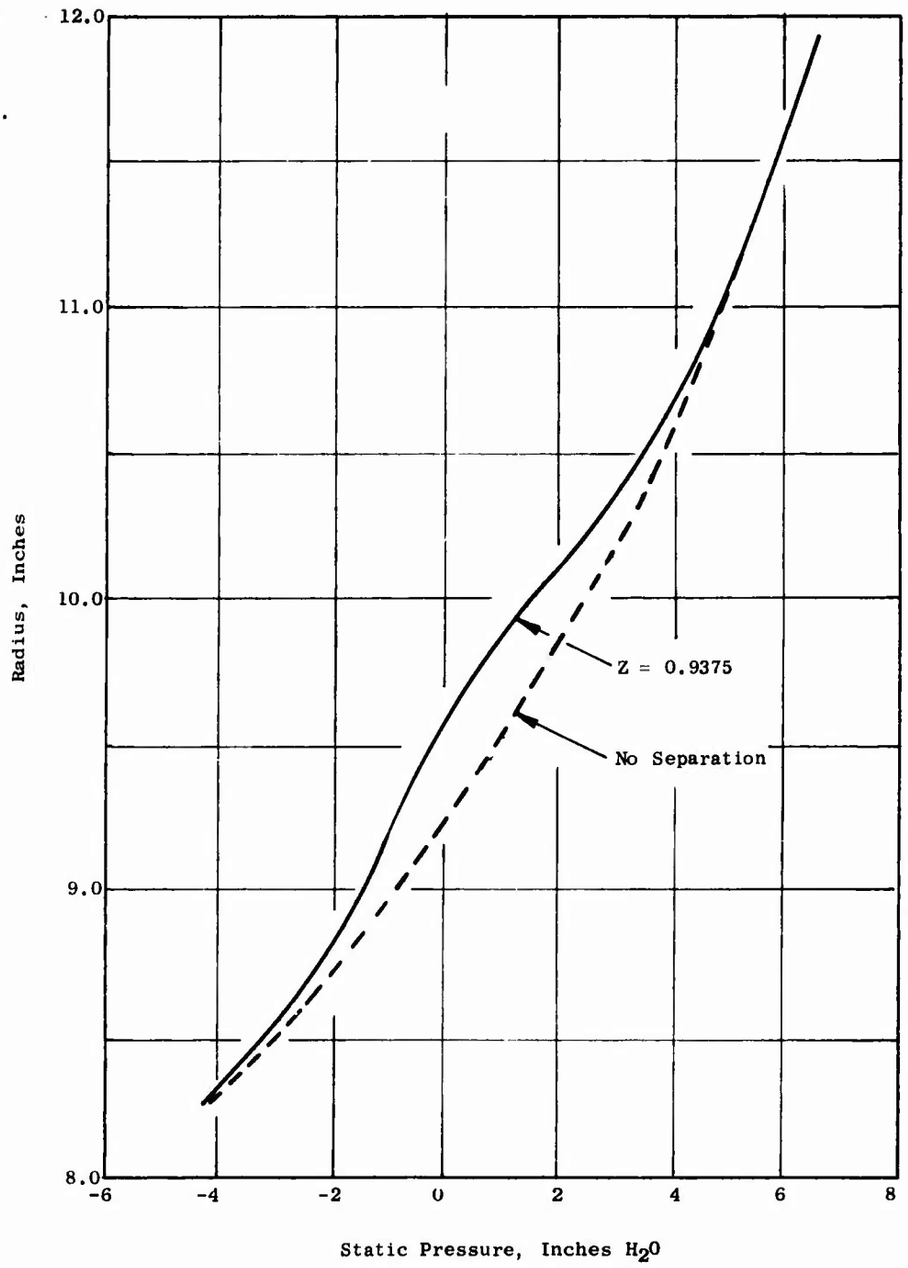

Figure 95. Comparison of the Static Pressure Distribution in the Rotating Vaneless Diffuser With and Without a Separation Bubble.

has been removed (Figure 96) and replaced by a porous stationary wall (Figures 97 and 98). The porous wall is divided into 4 rings so that different vacuum pressures can be applied to each ring. The primary purpose of this arrangement is to impress a severe radial pressure gradient on the remaining rotating vaneless diffuser wall. Instrumentation is provided at 8 radial stations close to the rotor (Figures 99 and 100) to detect the presence of low energy or stalled regions.

A rather extensive amount of low-speed testing has been accomplished. Briefly, it has been determined that the most severe radial pressure gradients impressed on the rotor have not caused flow on the rotating disc wall to separate. These gradients are expressed by the parameter G_1 which has been described in the previous discussion. A value of G_1 of about 15 was believed to be the limit which could be sustained. Reduction of the test data and the estimated values obtained from equation (9) and shown in Figure 101 indicate that values of the parameter $G_1 = 20$ have been impressed on the flow without causing separation of the rotating wall. This result was quite surprising and in one sense disappointing because of the inability to determine the limiting value of this parameter with the equipment as set up. During tests of the most severe pressure gradients, the flow on the porous shroud wall was found to separate and reverse direction while the rotating wall still appeared to have a healthy boundary layer (Figure 102). From a more important viewpoint, the results were very encouraging because the evidence is that vaneless diffusers having rotating walls are an even more powerful diffusing device than was expected.

Since the flow on the rotating wall could not be stalled, a search was instituted to determine the source of high losses in the low-and high-speed ROC. The remote-controlled actuator was placed in a position to permit traverses of the flow at the station closest to the rotor blades. The sensing elements of the probe were about 0.25 inch from the rotor blade trailing edges. A series of traverses was taken at this station holding the flow coefficient at about 1.0 while increasing the bleed from 0 to about 15 inches H_2O bleed suction. With no bleed or with the minimum value of bleed for which there was no flow into or out of bleed chamber number 3, a very large deficit in total pressure occurred over the third of the passage adjacent to the porous wall. As Figures 103 and 104 indicate, as the bleed flow into the suction chambers was increased, a dramatic improvement in the profile of the flow occurred.

Tests of Modified Low Speed Compressor

The results of the porous wall tests were very encouraging, but not completely understandable since it was difficult to understand how such a significant improvement in rotor blade performance could be achieved by porous wall suction at a station downstream of the rotor blades. For this reason, the compressor was modified so that flow occurred only through the 2 clearance gaps between the rotor and the bellmouth and

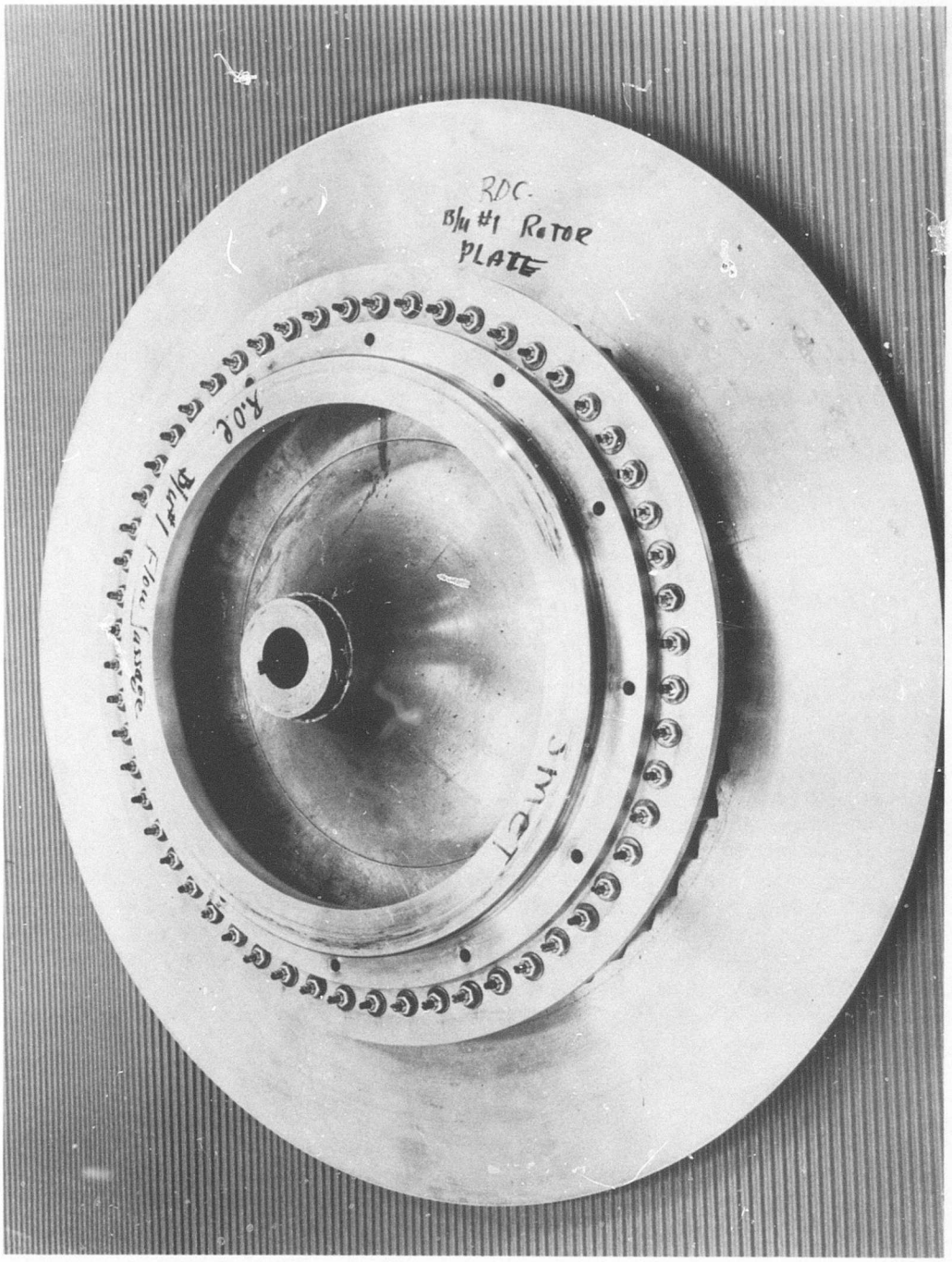

Figure 96. Low-Speed Rotor With 1 Wall of the Rotating Diffuser Removed.

Figure 97. Porous Surface and Bleed Chambers Used With the Low-Speed Rotor.

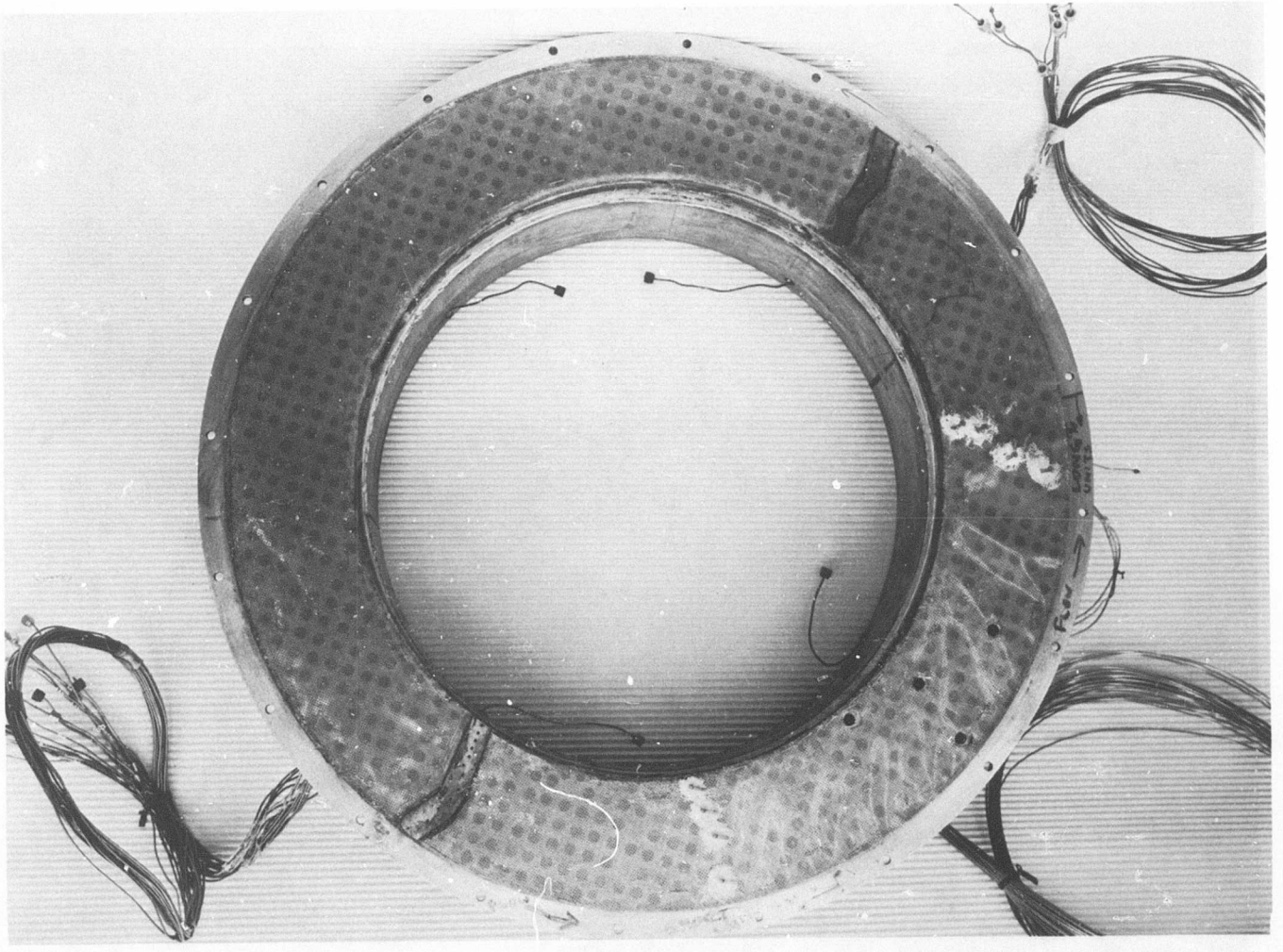

Figure 98. Porous Wall Showing Location of Static Pressure Orifices, Fixed Probe Positions, and Openings for Traversing Probes.

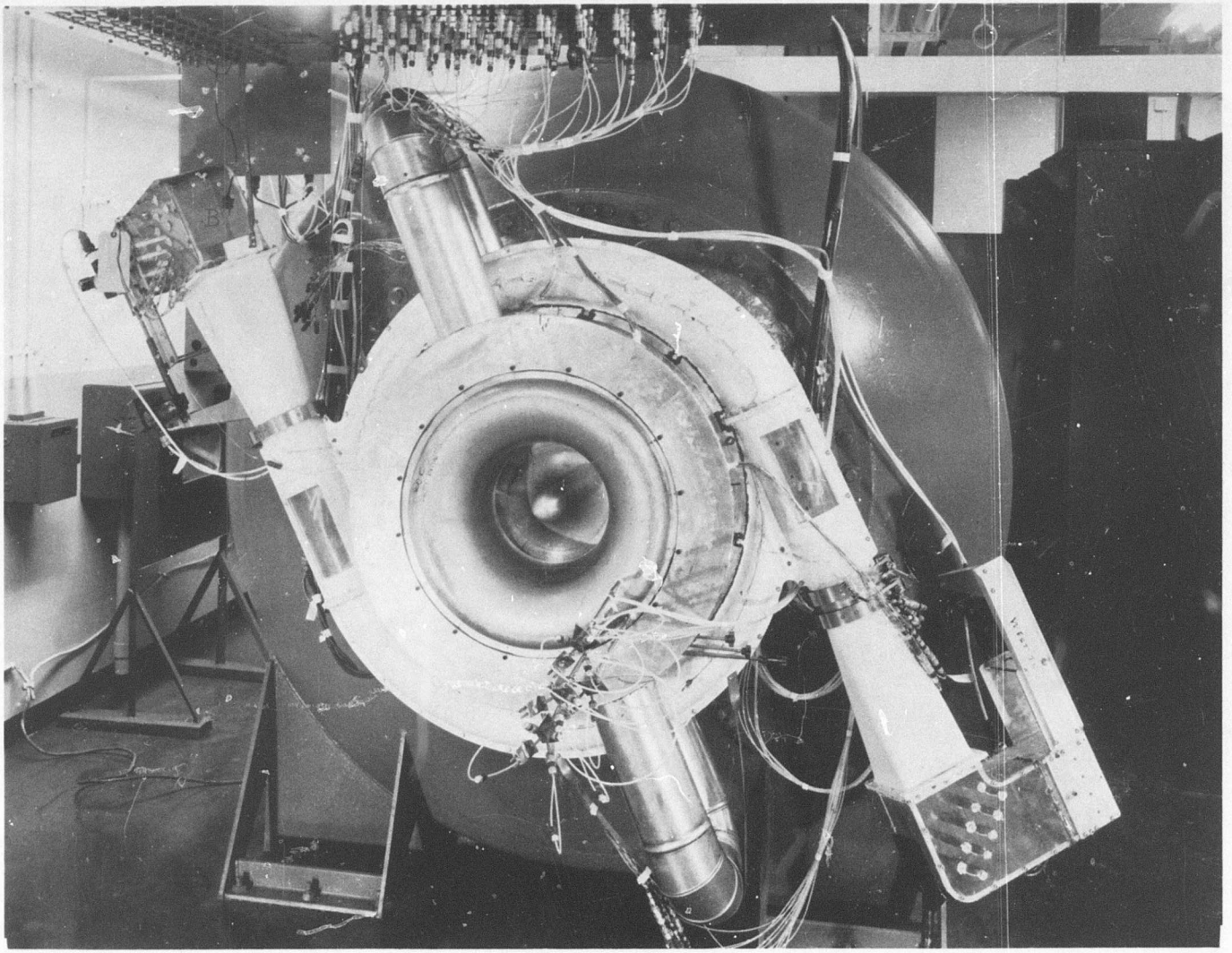

Figure 99. Assembly of Low-Speed ROC Modified With Porous Wall and Bleed System.

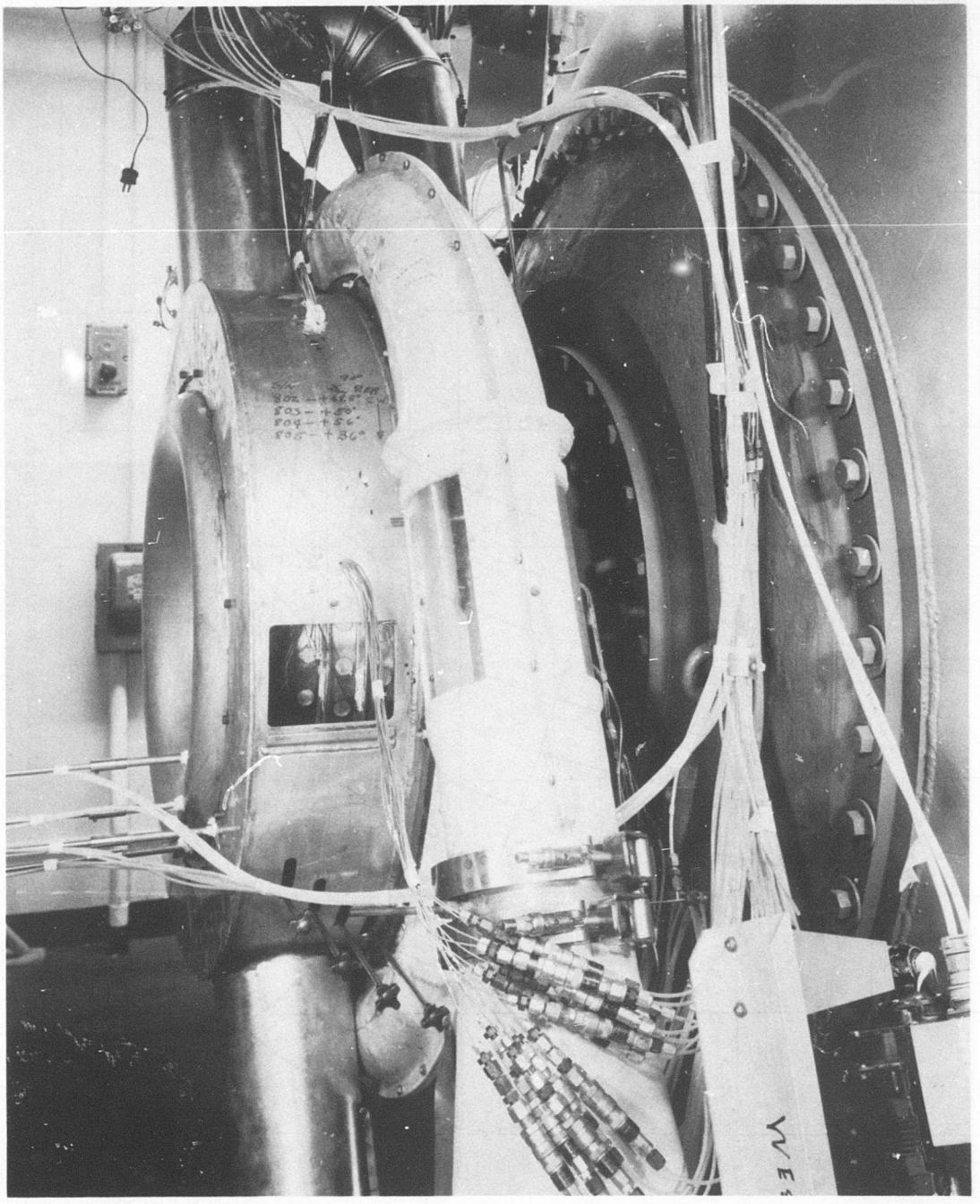

Figure 100. Side View of Modified Low-Speed Compressor.

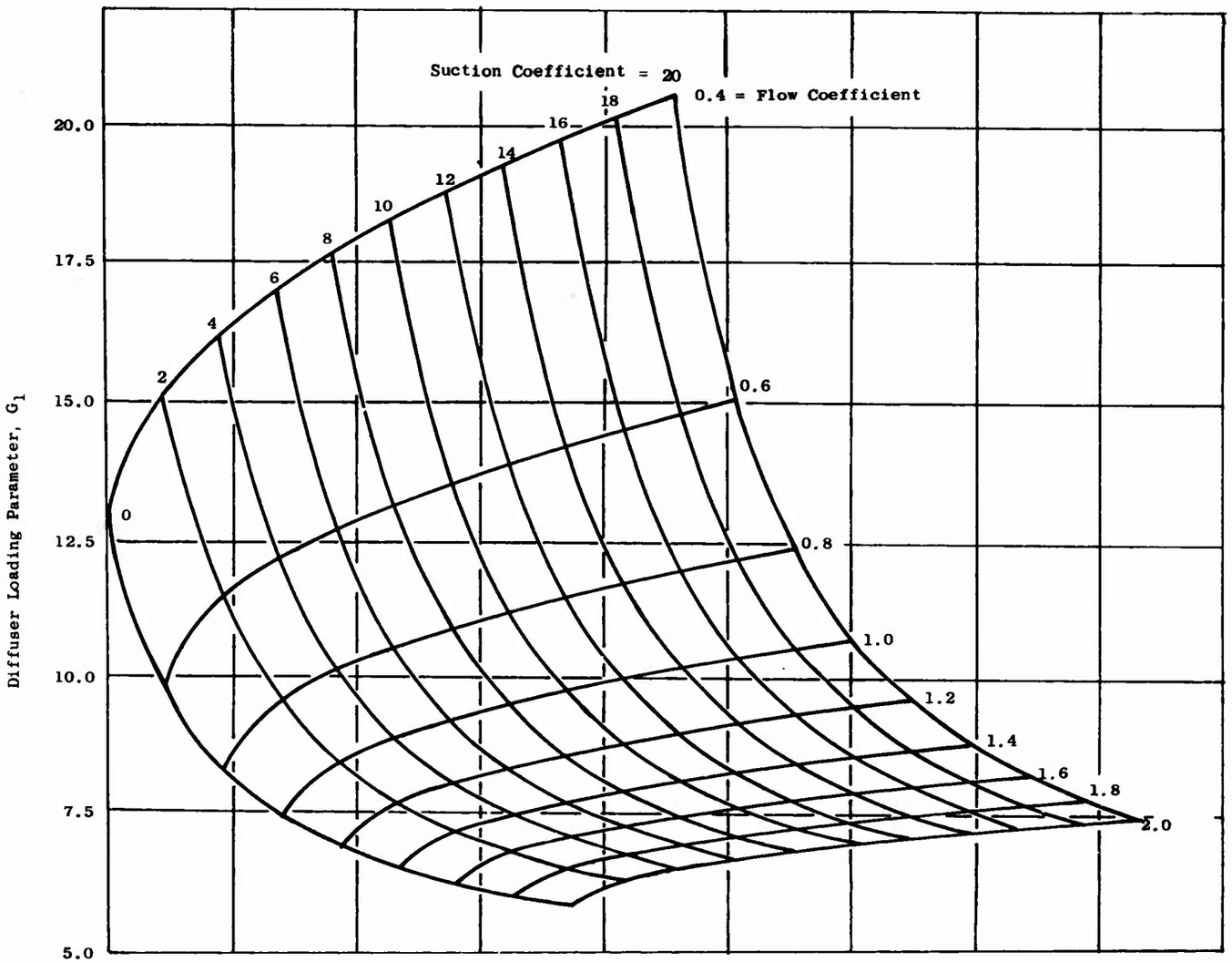

Figure 101. Carpet Plot of Diffuser Loading Parameter G_1 as a Function of Flow Coefficient and Suction Coefficient.

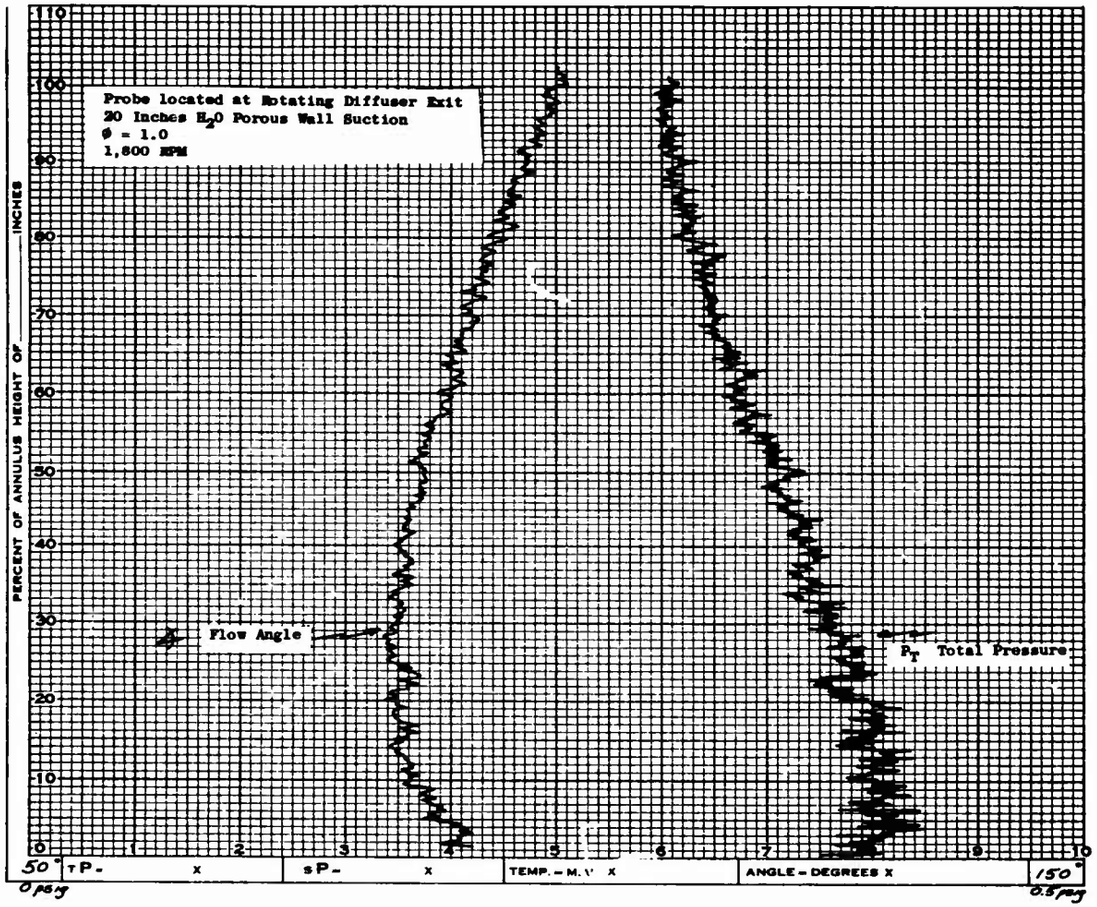

Figure 102. Low-Speed ROC Flow Angle and Total Pressure Distribution for Run Number 3, Reading Number 6.

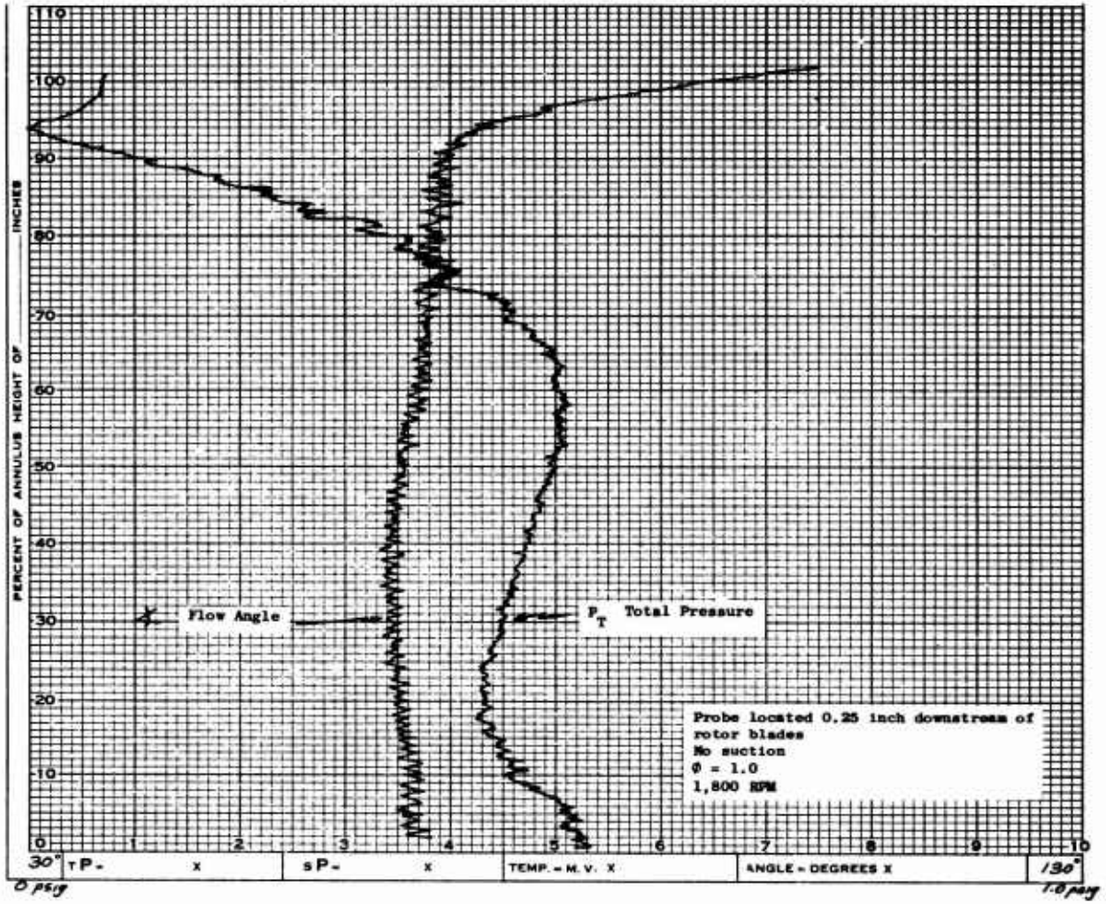

Figure 103. Low-Speed ROC Flow Angle and Total Pressure Distribution for Run Number 7, Reading Number 9.

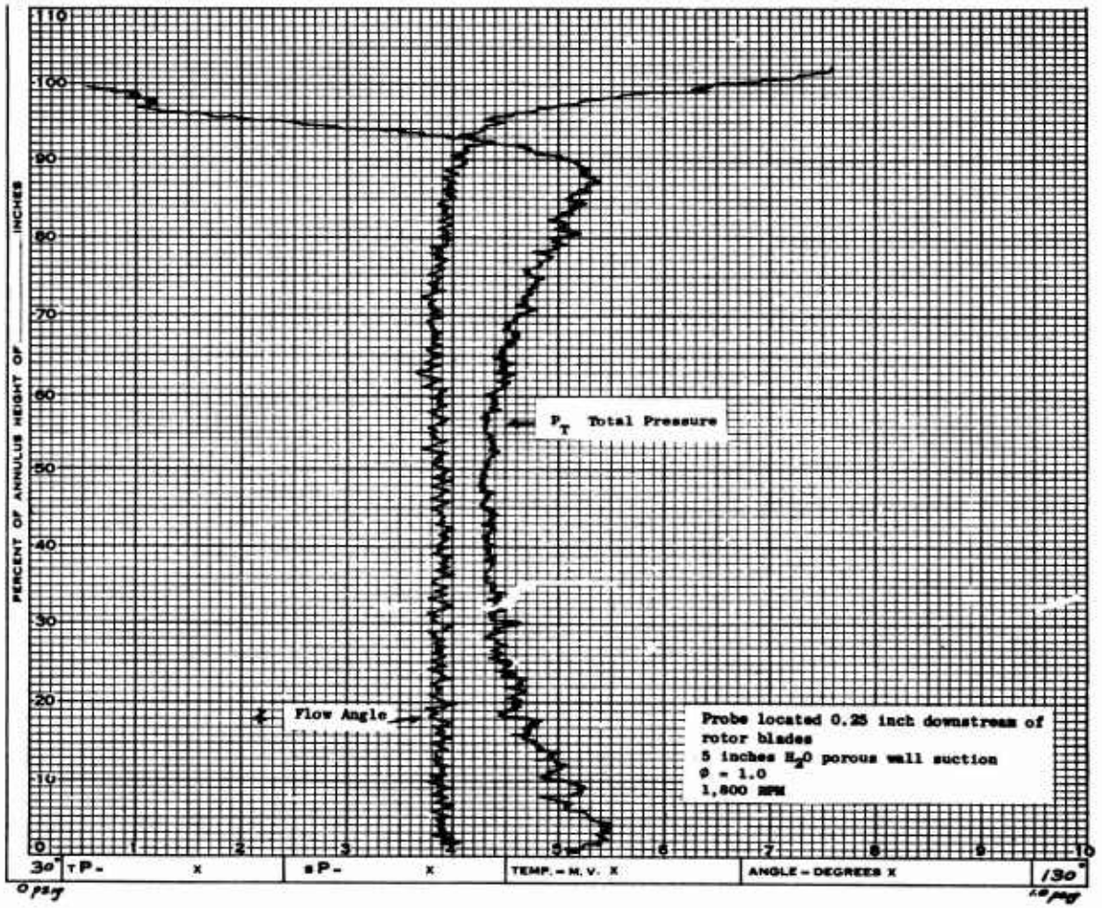

Figure 104. Low-Speed ROC Flow Angle and Total Pressure Distribution for Run Number 7, Reading Number 12.

between the rotor and the bleed chamber. A seal was placed between the rotating curved inlet and the stationary suction chamber (Figure 105) so that boundary layer flow could be drawn independently through the gap between the bellmouth and the rotating shroud and through the gap between the rotor and the suction chamber. The purpose of installing this seal was to determine which of the 2 boundary layer removal devices was most effective in improving the flow in the rotor. Figures 106 and 107 illustrate that at a flow coefficient of 1.0, bleed flow through the 2 clearance gaps was responsible for the remarkable improvement in flow conditions leaving the rotor blades. This finding was verified by a similar series of tests at a flow coefficient of 0.7 (Figures 108 and 109).

Preliminary results indicate that the material used to close off the porous surface of the bleed chamber was not firmly attached during some of the preliminary runs. Apparently, when the low-speed compressor was operated without suction, the loose covering material permitted reverse flow to occur. The compressor was disassembled and the covering material was reattached to the porous wall.

The Teflon seal has not proved to be completely effective, and when flow is drawn through 1 of the clearance gaps a small amount is also drawn through the other due to leakage past the seal.

Typical traverses of total pressure and flow angle taken just downstream of the rotor blades are presented in Figures 110, 111, and 112. These figures are presented in order of increasing flow through the clearance gaps. In Figure 110, the chamber pressures were higher than the static pressures in the flowpath, and reverse flow from the chamber into the compressor was occurring. Under these circumstances, the region of low total pressure extended about 30 percent of the way across the flow passage. In Figure 111, the results of reducing the suction chamber pressure to permit a small amount of flow to be removed from the gap upstream of the rotor blades are shown. The static pressure in the location of the downstream gap was the same in the suction chamber as on the flow passage wall. Therefore, air was neither withdrawn from the compressor nor permitted to leak into the compressor. Under these conditions, the region of low total pressure extended about 22 percent of the diffuser width. The distribution of the flow angle was about the same as that shown in Figure 110, but the level increased by about 1 degree.

Further decrease in the suction chamber pressure so that the flow was drawn through both clearance gaps produced the results shown in Figure 112. The region of low total pressure was limited to a zone which extended only about 7 percent of the diffuser width. The flow angle was maintained at values less than 75 degrees to within 3 percent of the inlet (shroud) wall. Over the remainder of the passage, the flow angle distribution was similar to that of the previous figures, but the

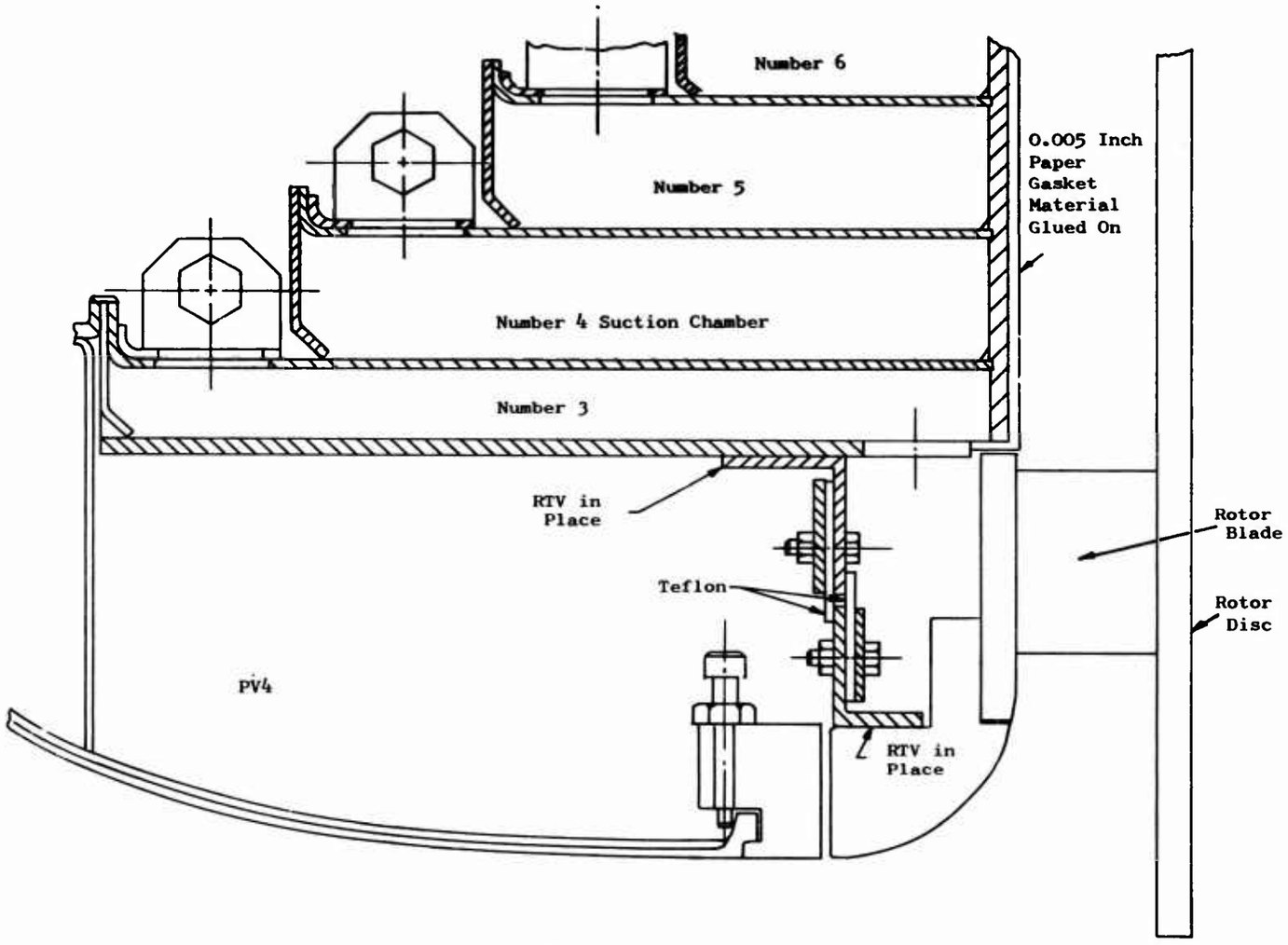

Figure 105. Details of Teflon Seals Installed in Low-Speed Compressor Between Rotor and Blade Chambers.

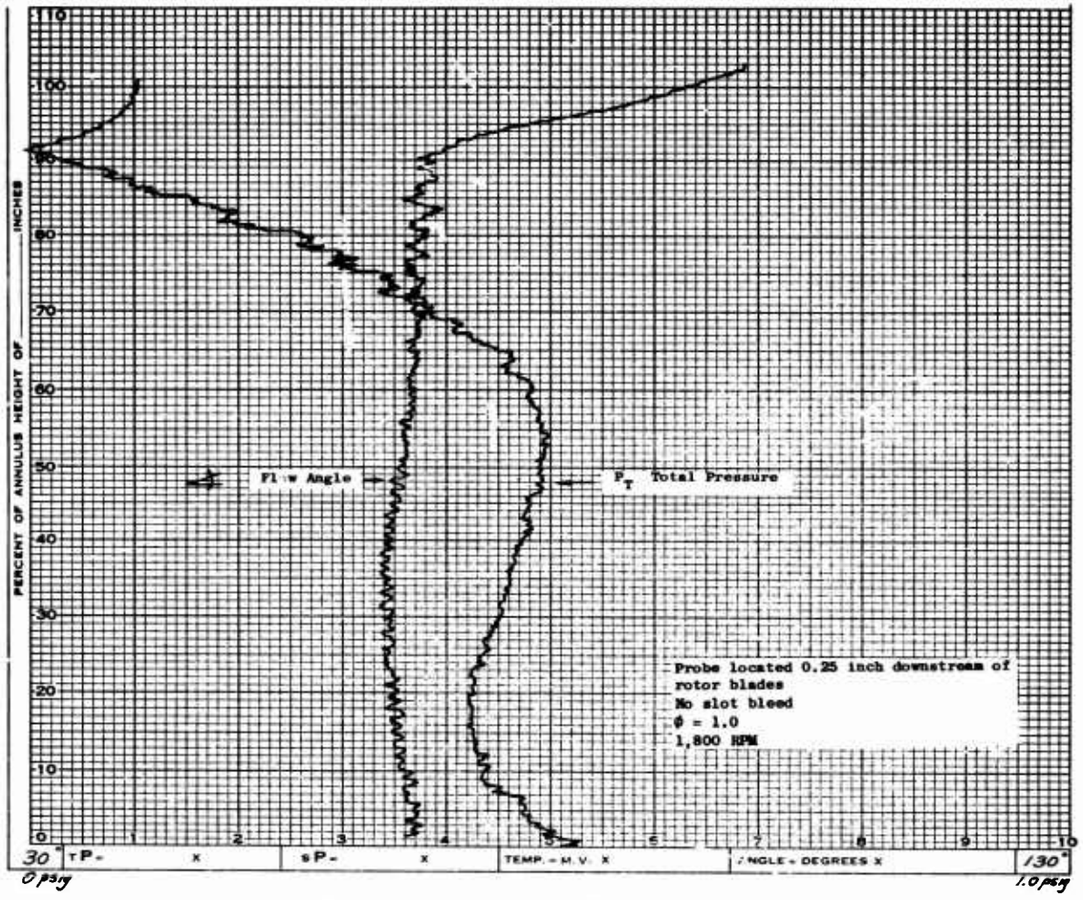

Figure 106. Low-Speed ROC Flow Angle and Total Pressure Distribution for Run Number 8, Reading Number 1.

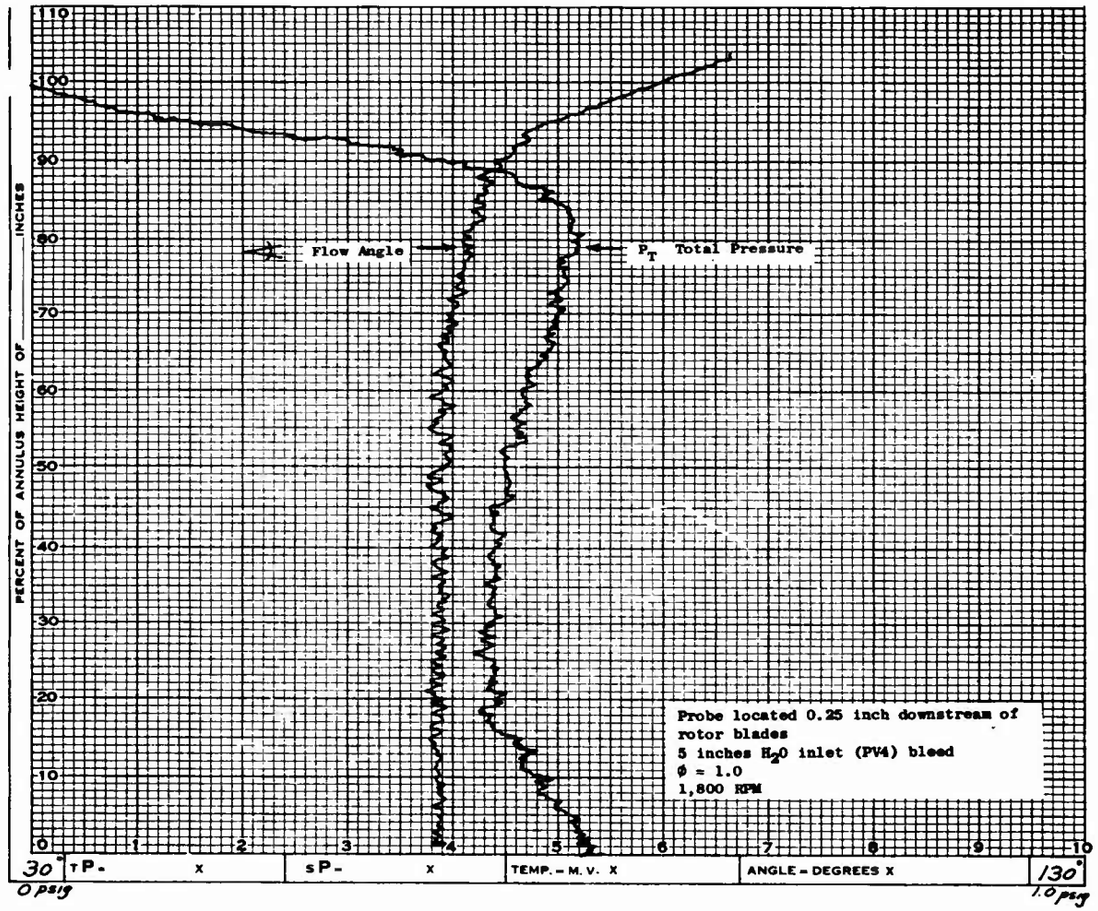

Figure 107. Low-Speed ROC Flow Angle and Total Pressure Distribution for Run Number 8, Reading Number 4.

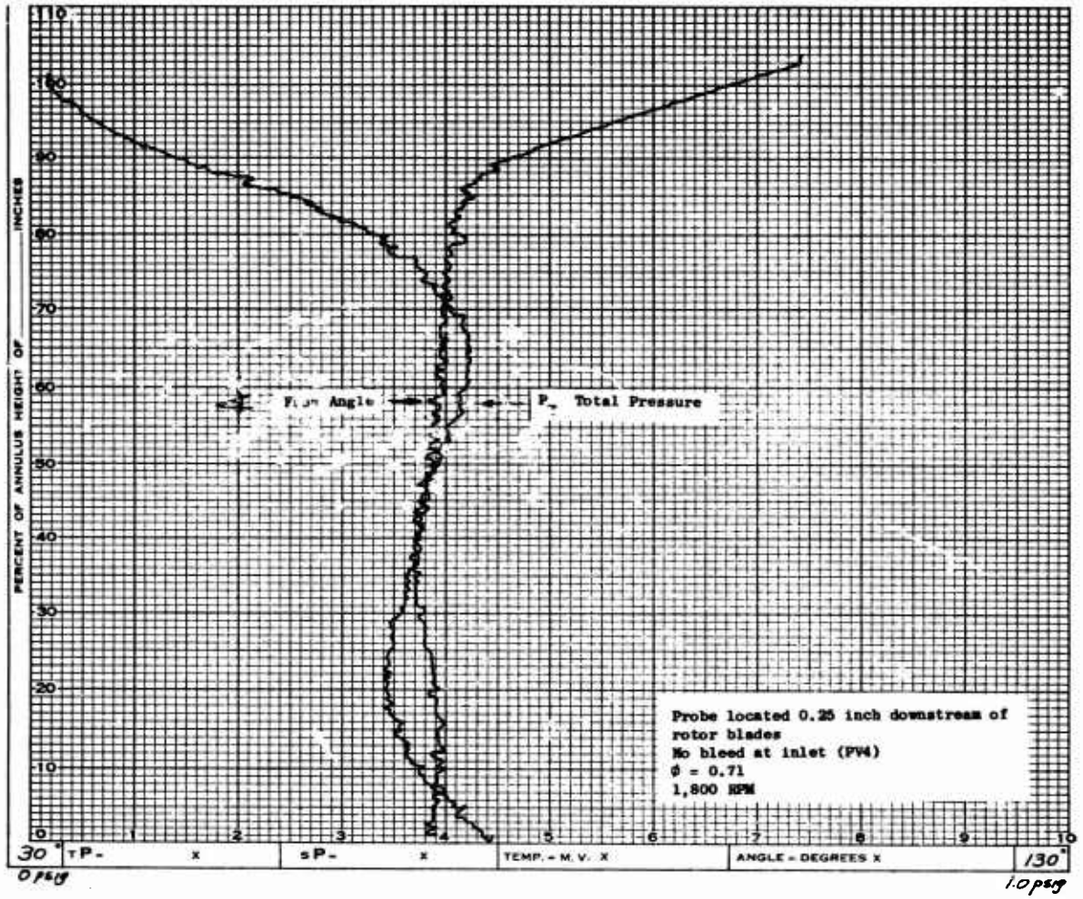

Figure 108. Low-Speed ROC Flow Angle and Total Pressure Distribution for Run Number 9, Reading Number 1.

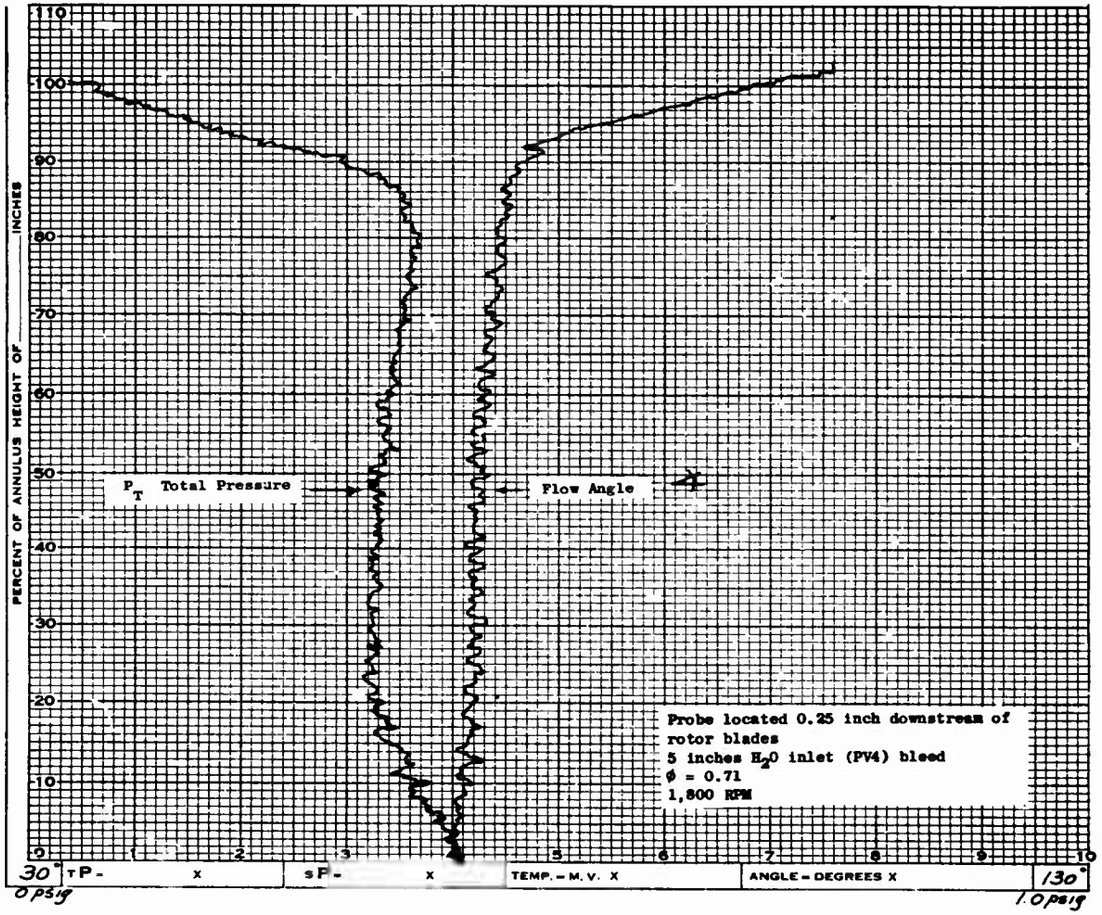

Figure 109. Low-Speed ROC Flow Angle and Total Pressure Distribution for Run Number 9, Reading Number 5.

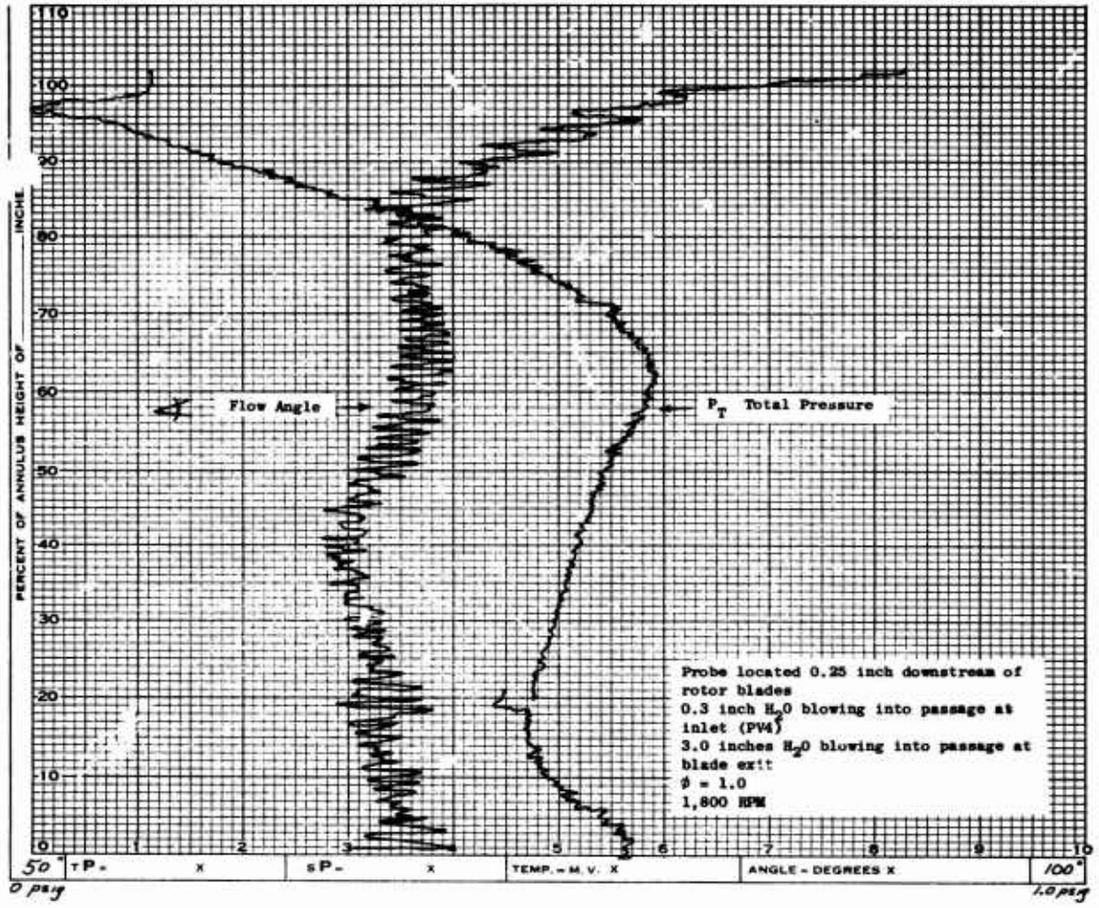

Figure 110. Low-Speed ROC Flow Angle and Total Pressure Distribution for Run Number 20, Reading Number 1.

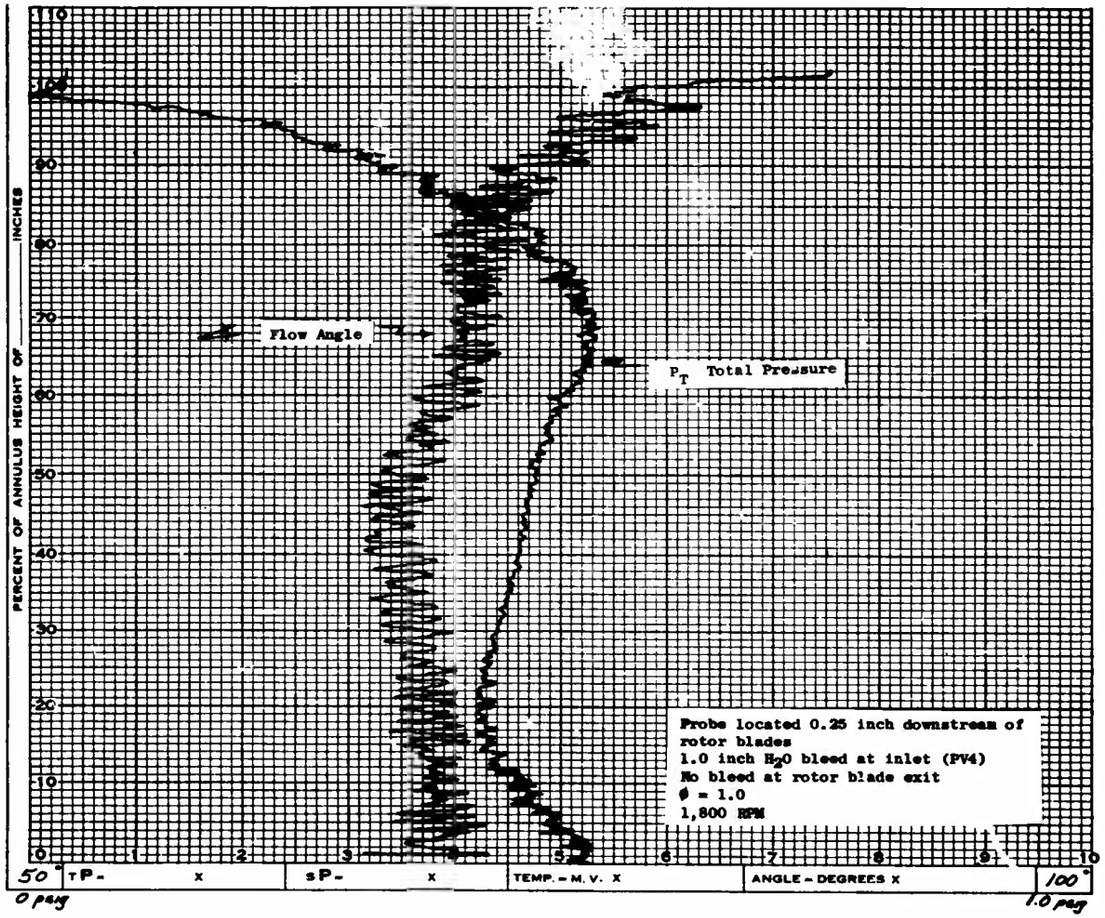

Figure 111. Low-Speed ROC Flow Angle and Total Pressure Distribution for Run Number 20, Reading Number 2.

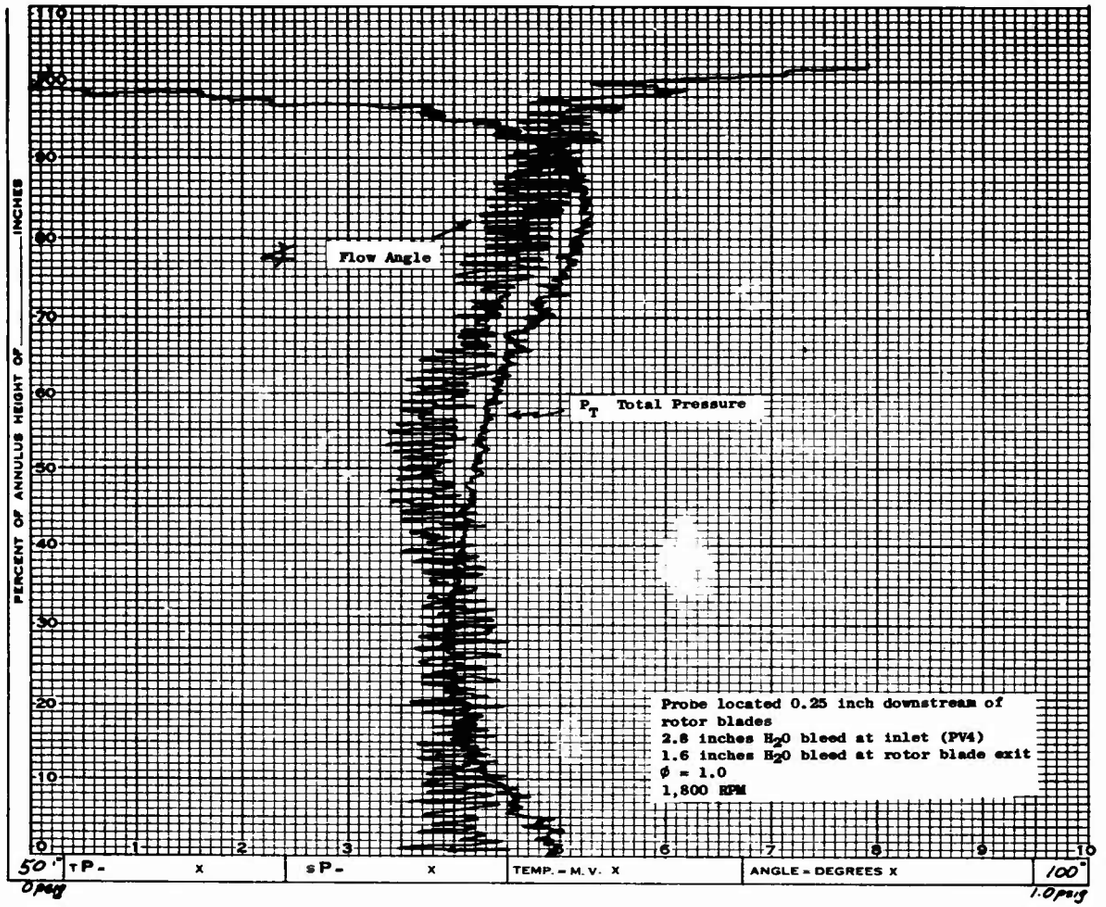

Figure 112. Low-Speed ROC Flow Angle and Total Pressure Distribution for Run Number 20, Reading Number 3.

centerline value was increased to 68.5 degrees. If conditions as good as those shown in Figure 112 can be established at the entrance to the rotating diffuser, very good rotating diffuser performance should be achieved.

Reduced Test Results

The low-speed ROC test data presented during the previous paragraphs in the form of total pressure and flow angle traverses have been analyzed in greater detail and are presented in Figures 113 through 120. Figure 113 presents a typical velocity vector diagram. In Figure 114, the absolute velocity is presented across the width of the passage from the rotating disc wall on the left to the stationary shroud wall on the right. For negative slot suction, there was inflow through the clearance gap between the rotor and the suction chamber downstream of the rotor blades. For the other 3 test conditions shown, flow was being withdrawn through both the clearance gaps upstream and downstream of the rotor blades. The major differences which are seen in these figures are believed to be due to whether flow is being added to the main stream or withdrawn from it. These calculated results confirm in detail what the previously presented traverses of flow angle and total pressure illustrated. With the relatively small amount of bleed flow occurring with 2.8 inches of H_2O, the flow leaving the rotor blades was quite uniform in relative velocity across the diffuser width (Figure 115).

In Figure 116, the effect of increasing the bleed flow can be seen to increase the relative tangential velocity in the region of flow between 20 percent and 5 percent of the shroud wall. In this case, the flow appears to be much stronger and better able to undergo the strong diffusion which occurs in the vaneless diffuser following. The main change observable in the radial velocity (Figure 117) is the difference between the single case with inflow and the 3 conditions with outflow through the clearance gaps. The uniformity of the exit flow was clearly superior when the largest amount of bleed flow was used.

Rather strong variations in the angle of the flow leaving the rotor blades were calculated and are presented in Figure 118. The relative exit flow angle varied from a value of about 50 degrees from radial to about 45 degrees in the center of the passage with a rapid increase to around 53 degrees at a station about 25 percent of the diffuser width of the shroud wall. The reason for these large variations is not clear, particularly for the case of maximum suction which shows the greatest variation of the main stream.

An estimate of the spanwise variation of rotor efficiency is presented in Figure 119. The major effect of increasing the bleed flow was to significantly improve the efficiency in the passage near the inlet shroud wall. In the center of the passage and near the rotating wall,

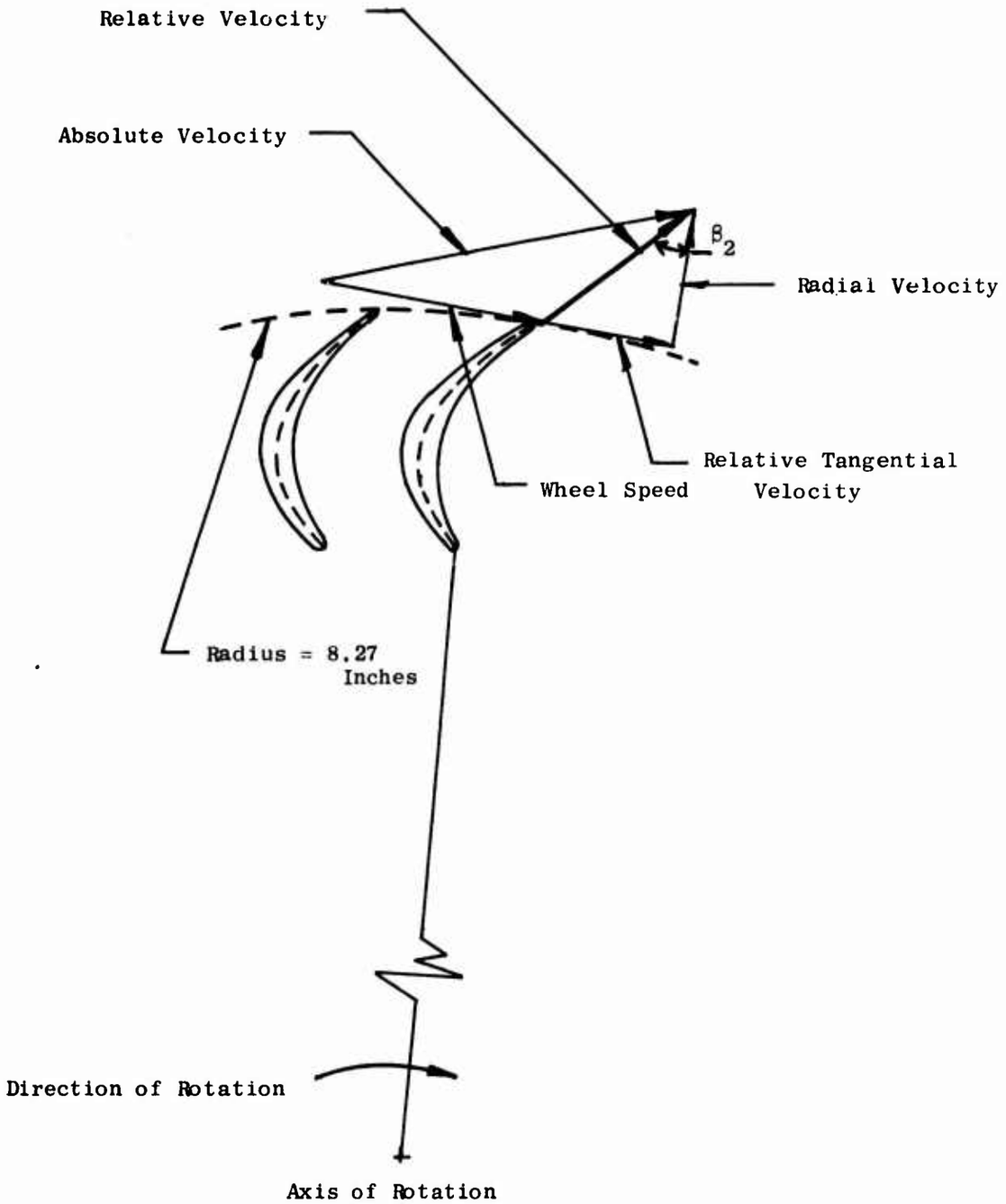

Figure 113. Velocity Diagram for Low-Speed ROC.

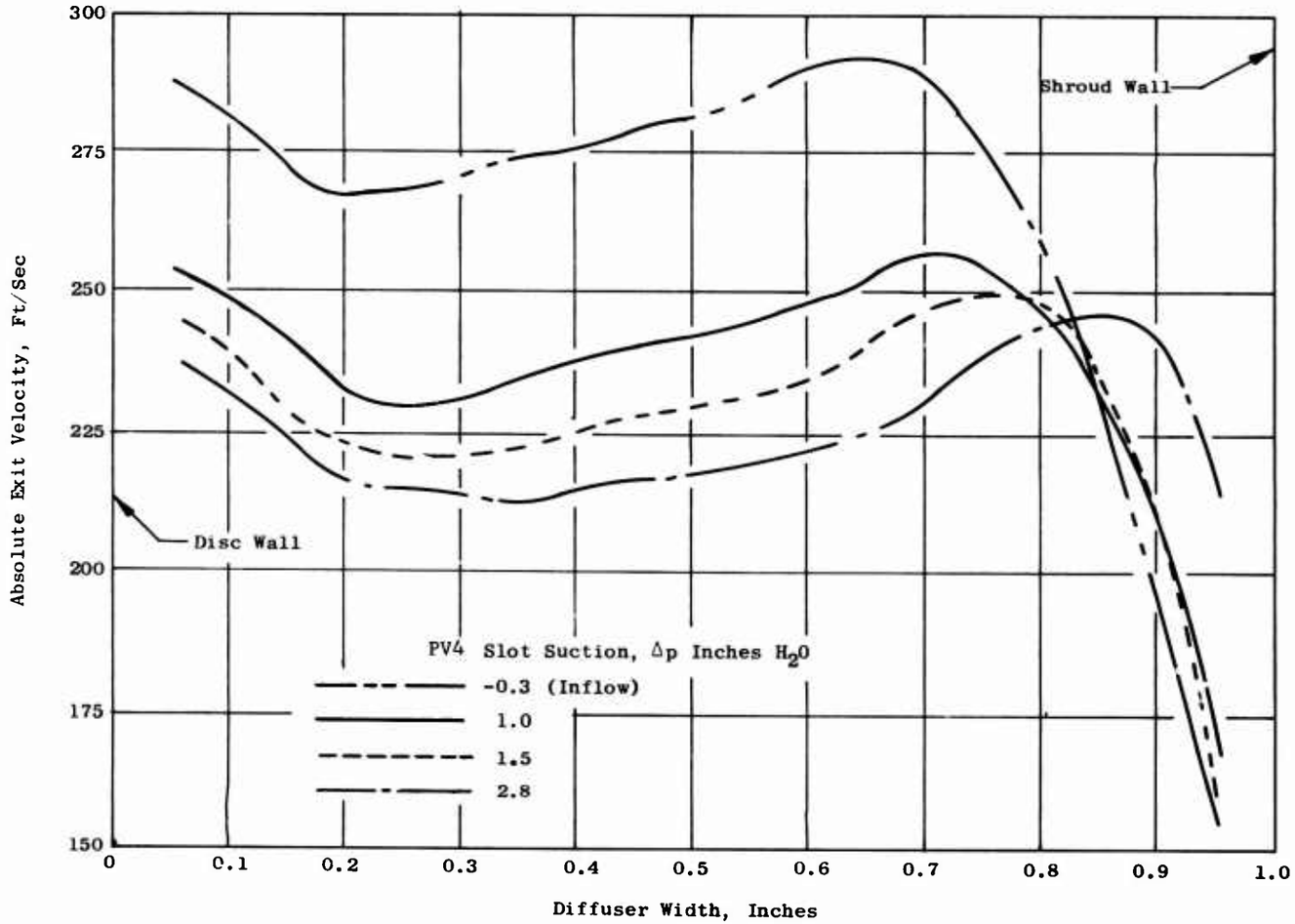

Figure 114. Distribution of Absolute Velocity at Rotor Blade Trailing Edge for Various Suction Quantities for the Low-Speed ROC.

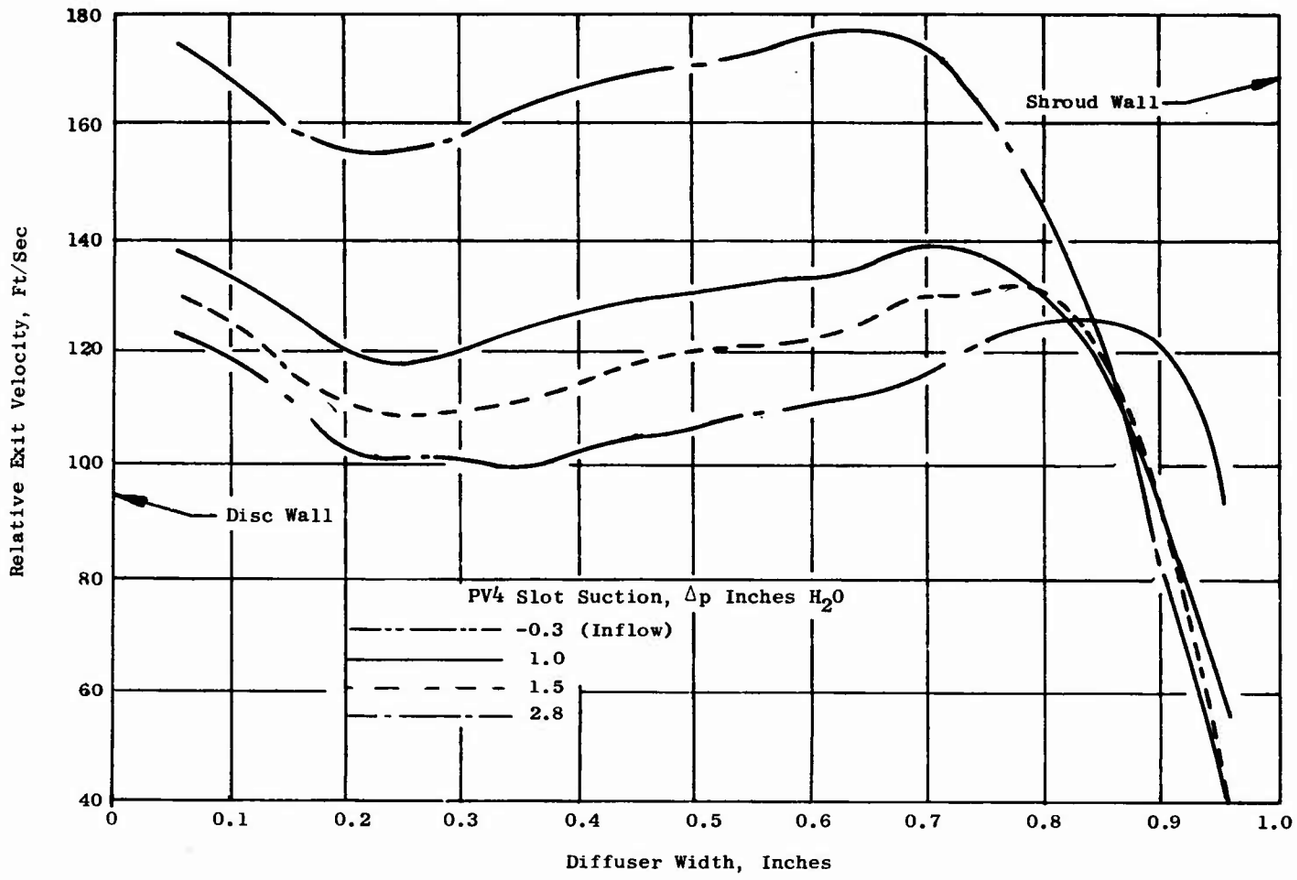

Figure 115. Distribution of Relative Velocity of Rotor Blade Trailing Edge for Various Suction Quantities for the Low-Speed ROC.

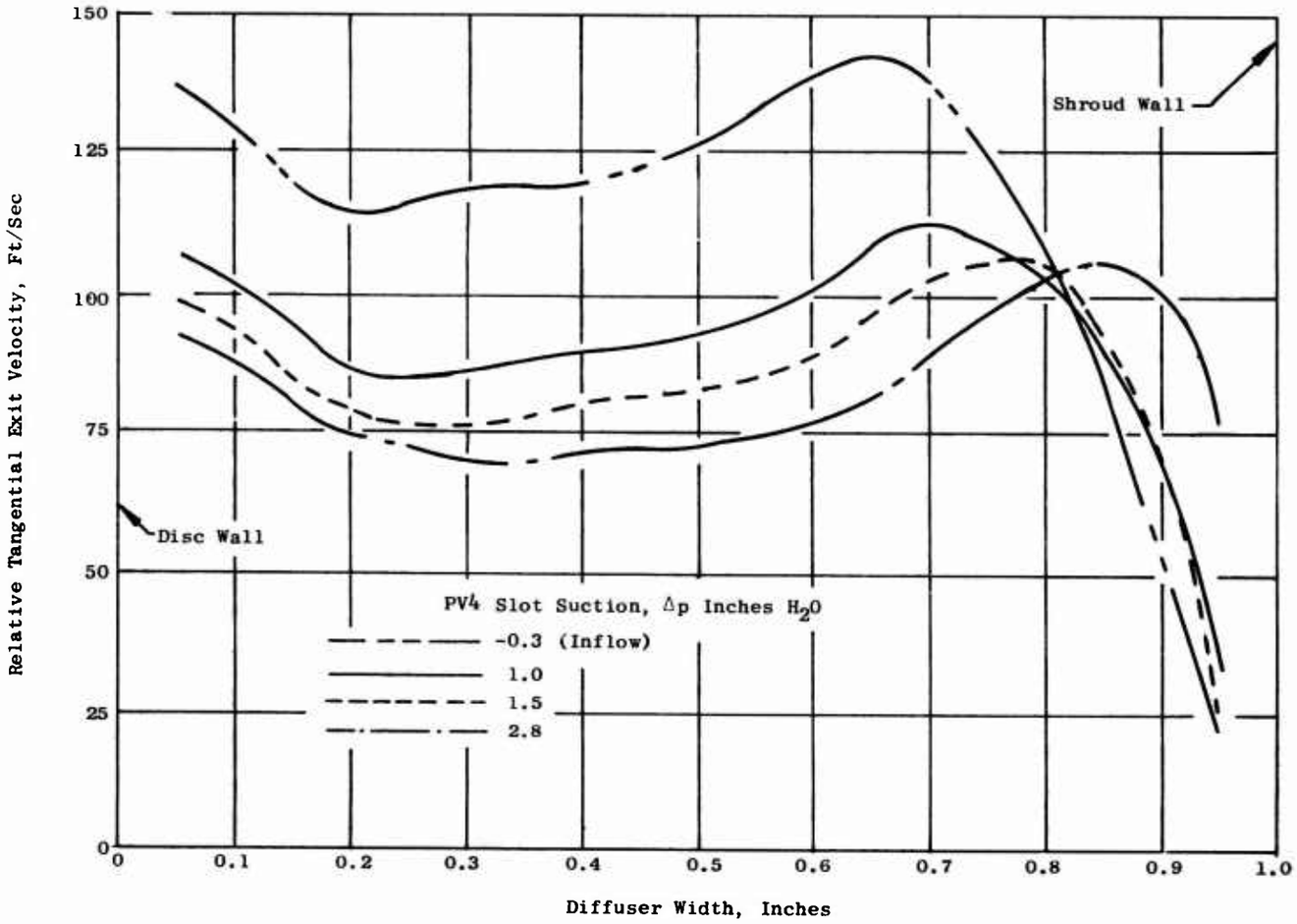

Figure 116. Distribution of Relative Tangential Velocity of Rotor Blade Trailing Edge for Various Suction Quantities for the Low-Speed ROC.

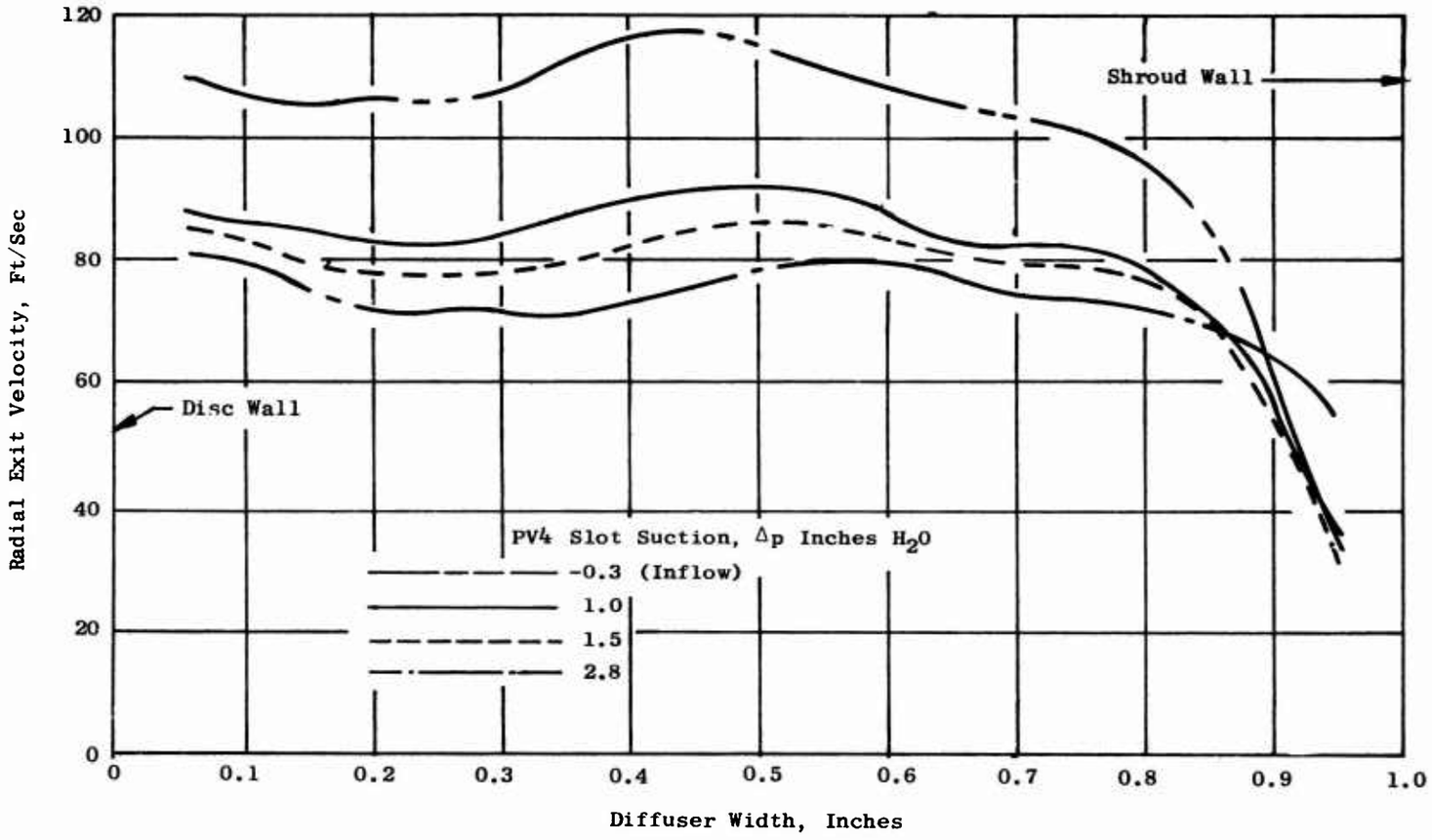

Figure 117. Distribution of Radial Velocity for Rotor Blade Trailing Edge for Various Suction Quantities for the Low-Speed ROC.

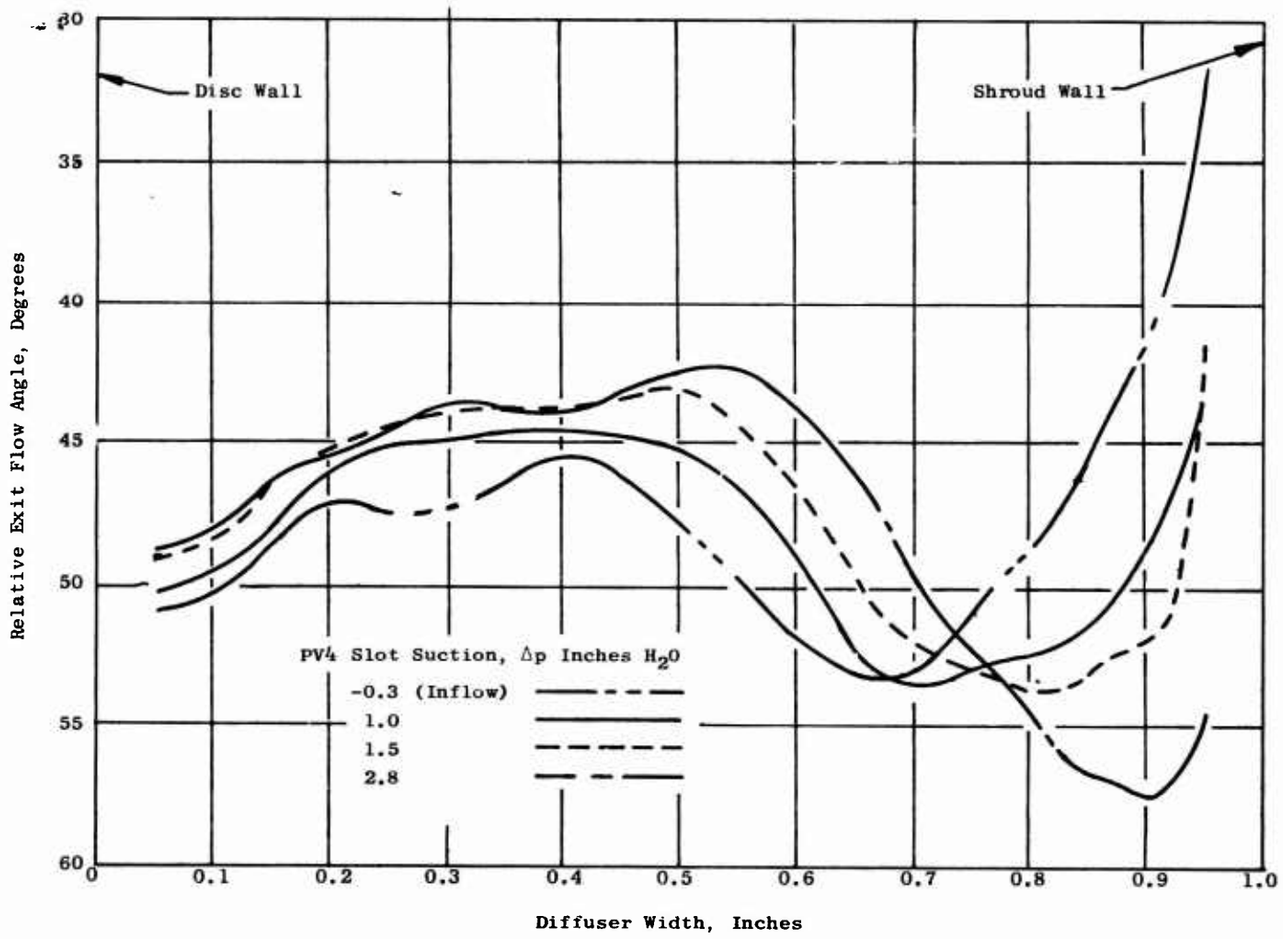

Figure 118. Distribution of Relative Exit Flow Angle at Rotor Blade Trailing Edge for Various Suction Quantities for the Low-Speed ROC.

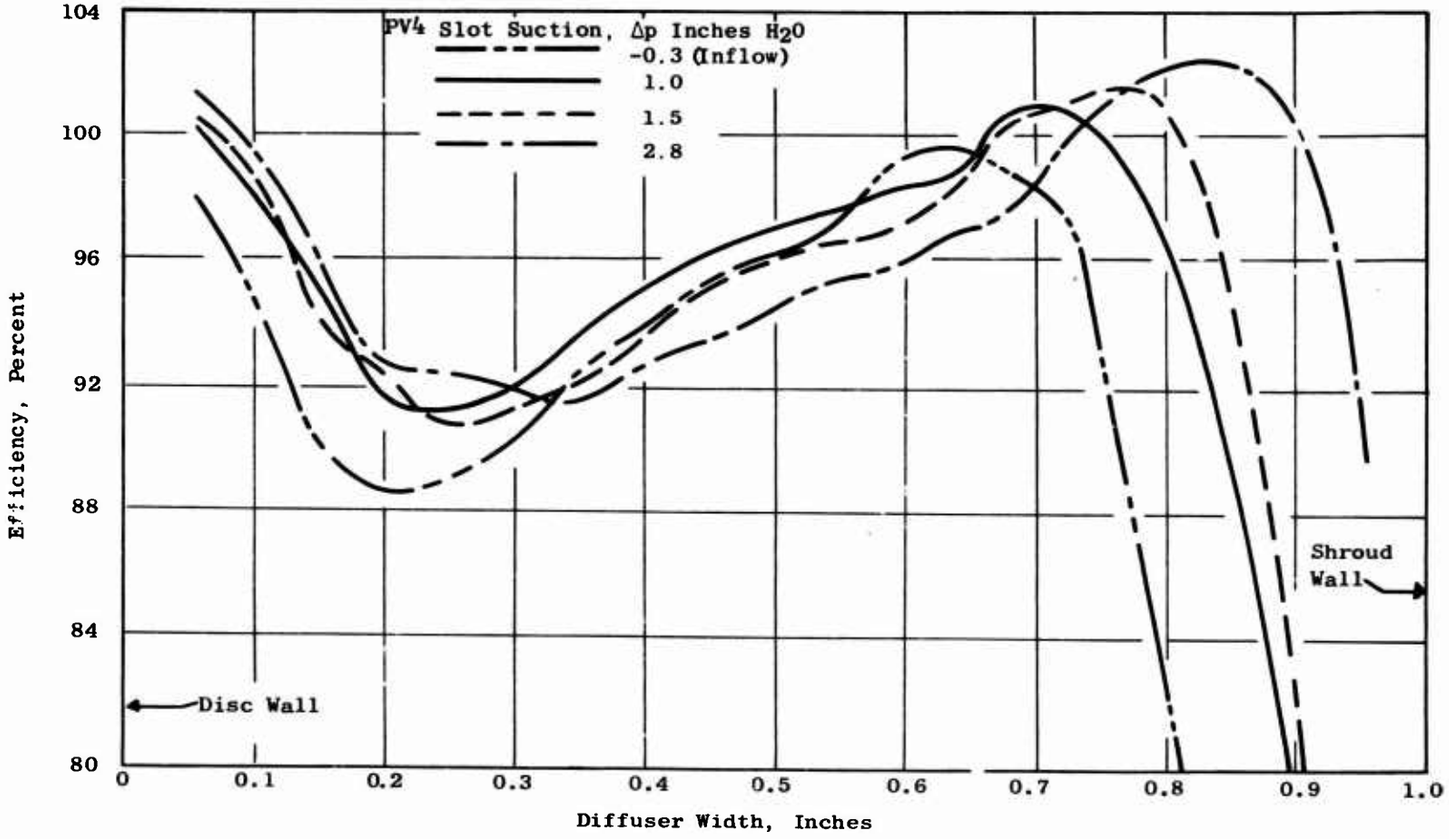

Figure 119. Distribution of Efficiency at Rotor Blade Trailing Edge for Various Suction Quantities for Low-Speed ROC.

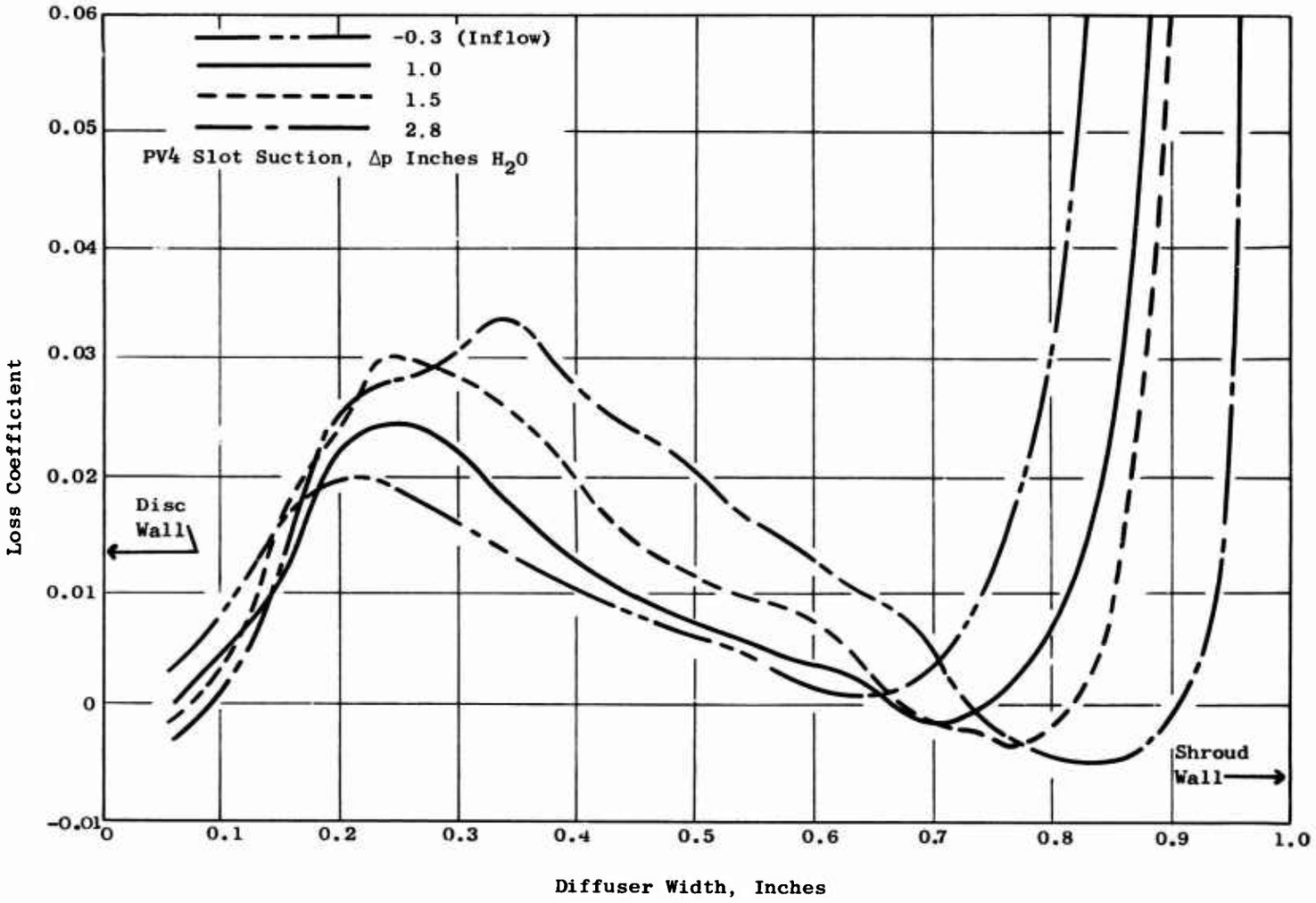

Figure 120. Distribution of Loss Coefficient at Rotor Blade Trailing Edge for Various Suction Quantities for Low-Speed ROC.

the efficiency was much less affected by the amount of bleed flow. The spanwise variation in efficiency shows a minimum at about 25 percent of the passage from the rotor disc and suggests that strong secondary flow was taking place. The flow behavior on the shroud side was quite different and appeared to be dominated by poor flow entering the rotor blades. As the amount of flow being removed was increased, the efficiency near the inlet wall increased rapidly without giving indication of strong secondary flow. Although values of efficiency over 100 percent appear, the observed trends are believed to be correct even though the quantitative values are clearly in question.

Values of rotor blade loss coefficient have been estimated and are presented in Figure 120. It is not surprising that the loss coefficients are generally inversely related to the efficiencies presented in Figure 119. Although the loss levels are in question, the trends are believed to be significant. In the center of the passage, the loss coefficients increase as the suction quantity is increased. One explanation for this is that the static pressure rise coefficient increases from a relatively strong negative value for negative suction to a relatively strong positive value for the maximum suction value shown. Little difference in loss coefficient is seen near the rotating disc, but major variations occur near the inlet side of the flowpath.

Circular Inlet Vane

The use of inlet slot suction is an effective means of improving low-speed ROC rotor performance; but in a high-speed compressor, other approaches may be more practical. Turning vanes have been used frequently in the inlets of centrifugal compressors. Circular inlet vanes have been designed and fabricated for use with both the low-speed and high-speed ROC. A sketch of the turning vane used in the low-speed compressor is shown in Figure 121, and a photograph of the fiber glass part is shown in Figure 122.

The calculated velocity distributions over the contours of the low-speed compressor inlet are presented in Figures 123, 124, and 125. In these figures, the velocity distributions in terms of an upstream reference velocity are presented for the inlet with and without the turning vane. These three-dimensional potential flow calculations of the compressor inlet with the circular vane installed indicated that a constant velocity about 10 percent greater than rotor inlet velocity should occur over the convex surface of the rotating shroud from the bellmouth exit to the rotor blade leading edge. A considerable improvement over the initial configuration was predicted because of a velocity increase of about 25 percent computed in the absence of the flow splitter. The flow is calculated to accelerate continuously over the convex surface of the splitter to a peak value 11 percent greater than rotor inlet velocity, so no aerodynamic problem is anticipated.

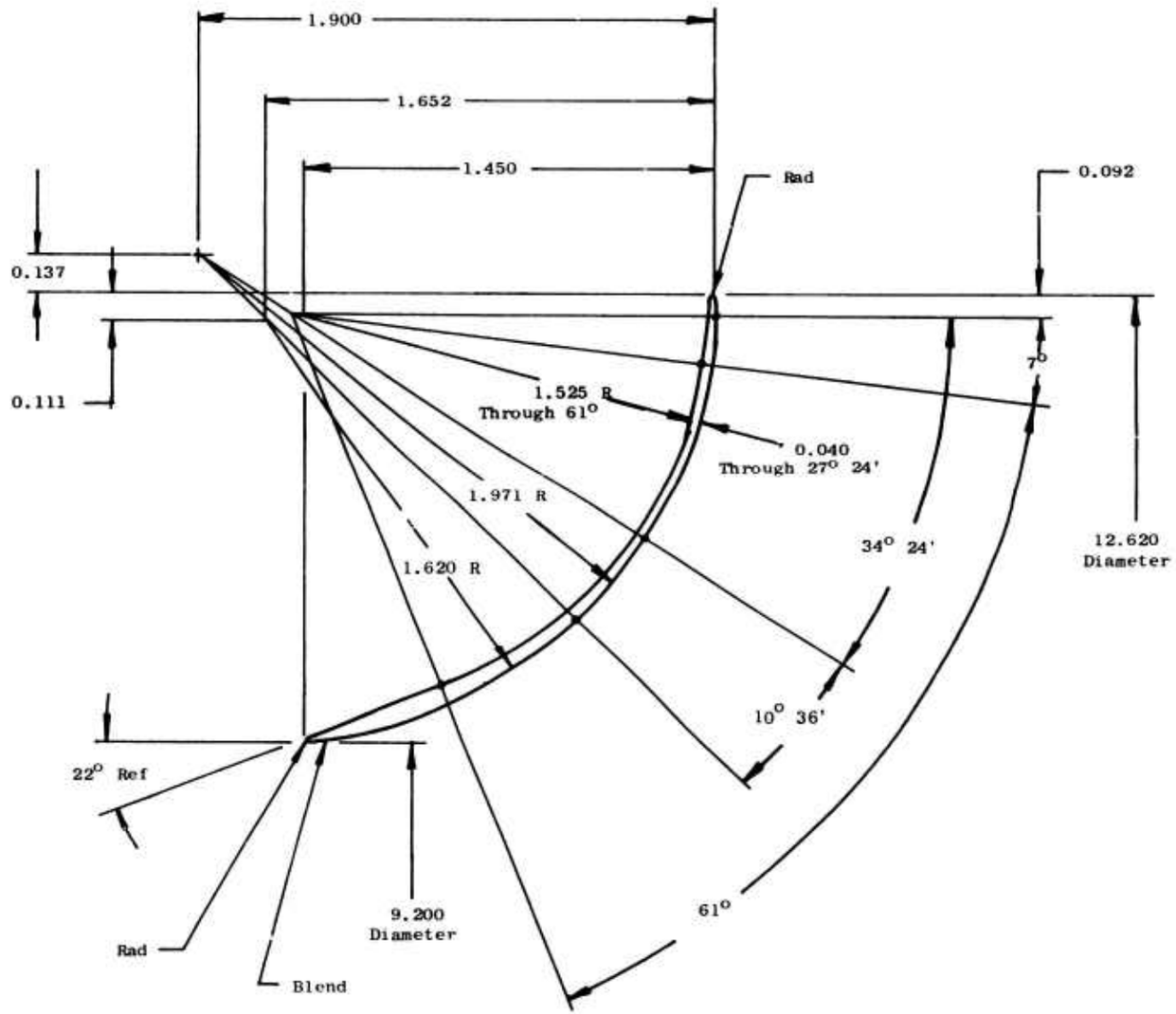

Figure 121. Circular Inlet Vane Used in Low-Speed ROC.

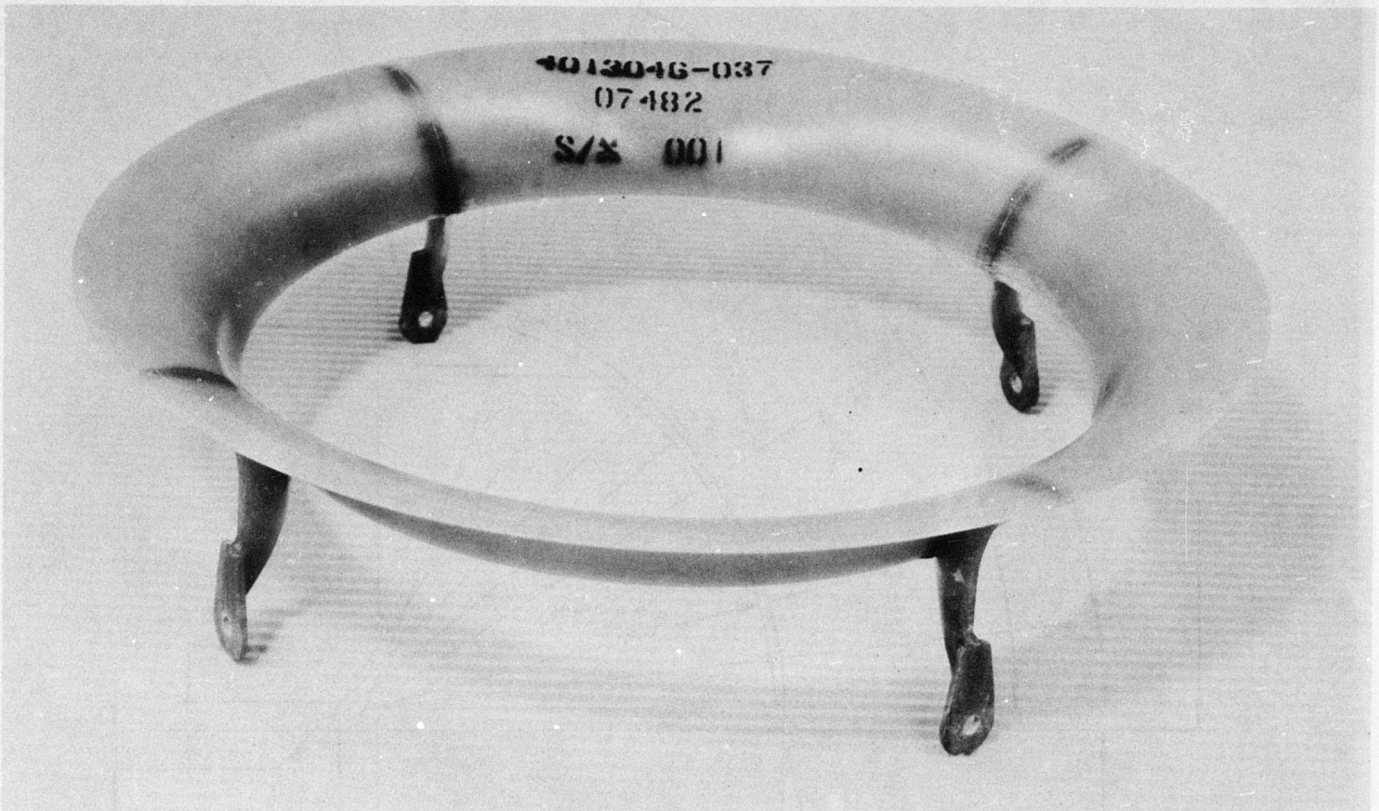

Figure 122. Fiber Glass Circular Vane Used in Inlet of Low-Speed Compressor.

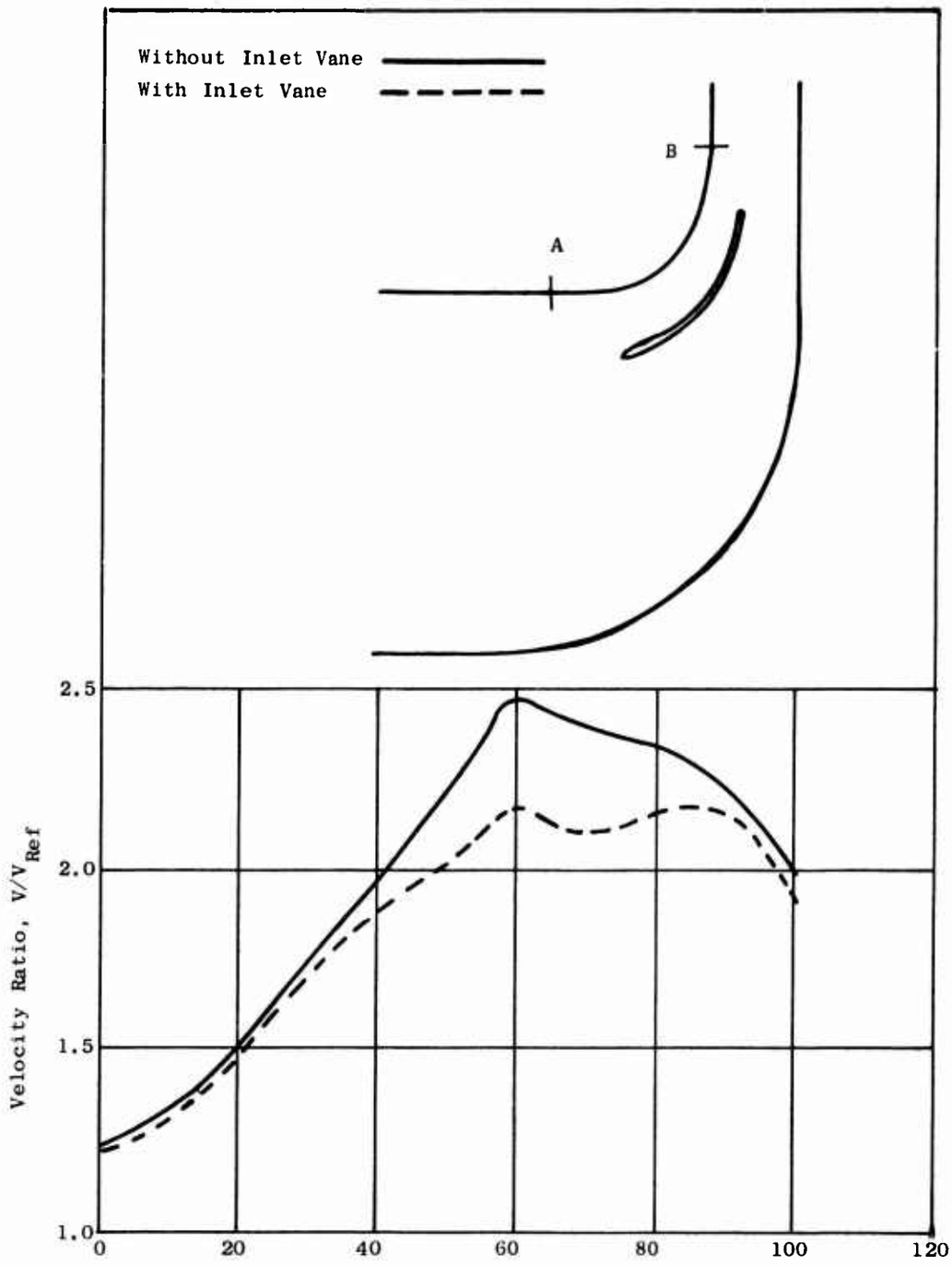

Figure 123. Distribution of Velocity Ratio Over the Outer Surface A-B of the Low-Speed ROC Inlet.

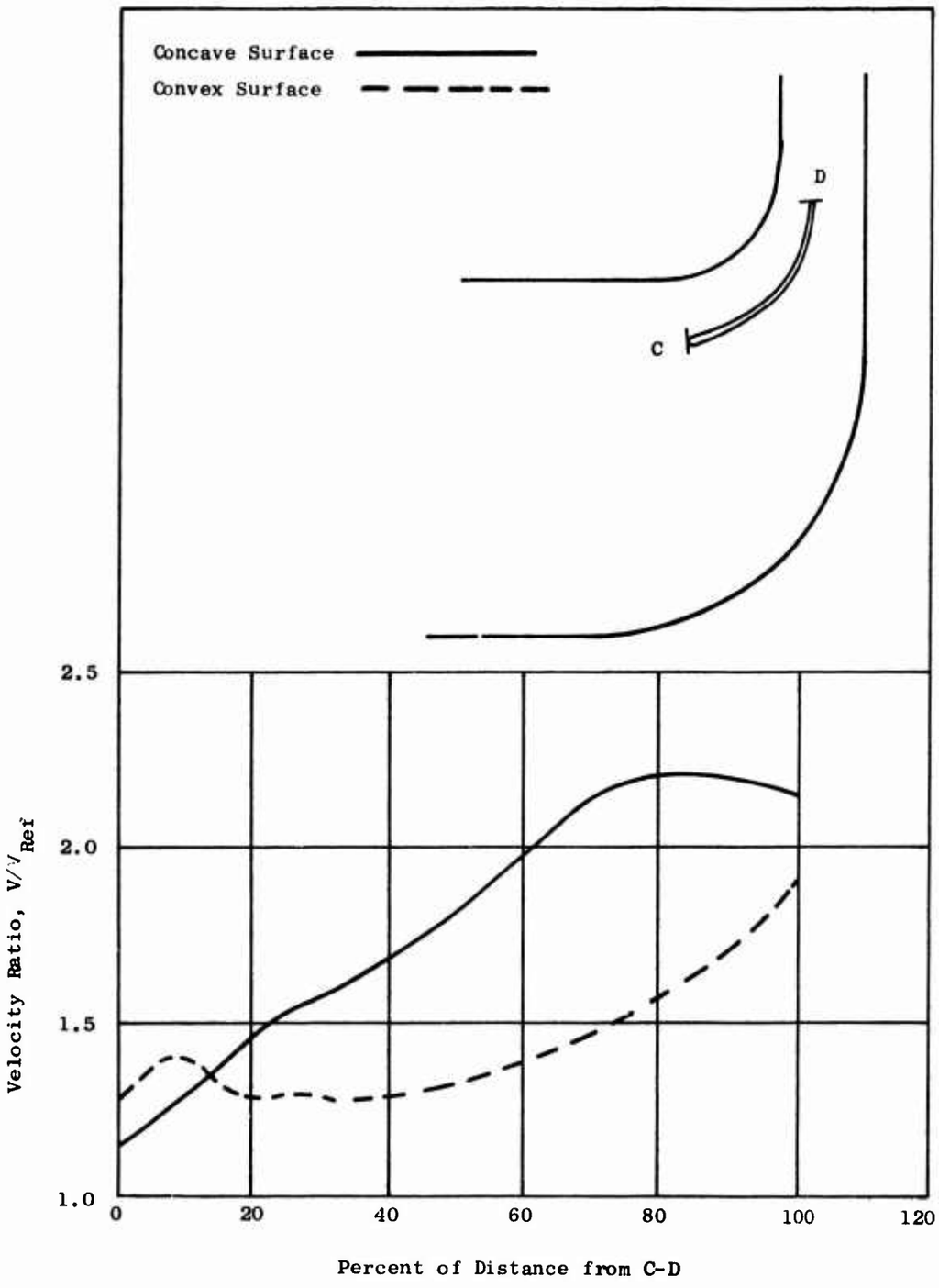

Figure 124. Distribution of Velocity Ratio Over Splitter Surfaces C-D Mounted in Low-Speed ROC Inlet.

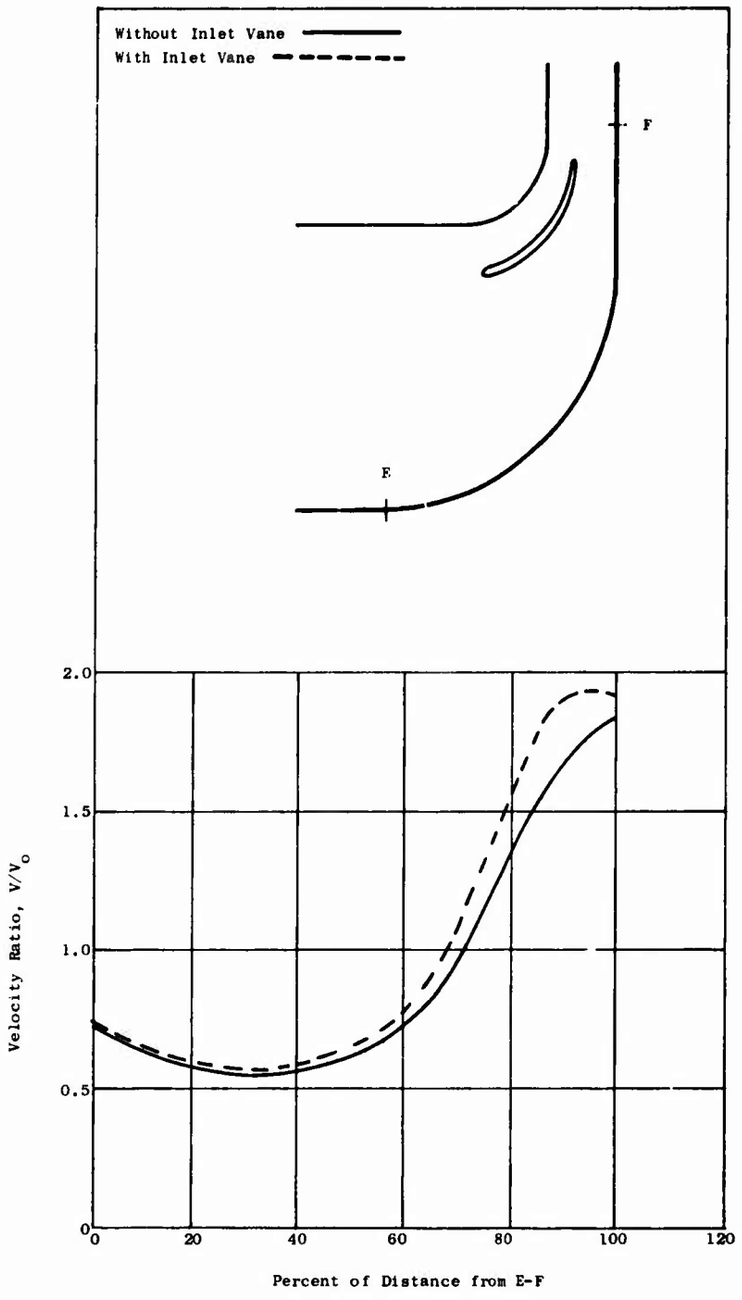

Figure 125. Distribution of Velocity Ratio Over Inner Surface of Low-Speed ROC Inlet.

Tests With and Without Circular Inlet Vane

Directly comparable test runs have been made in the low-speed compressor in the presence of and in the absence of the circular inlet vane. The most striking observation was that the wake of the circular vane could not be found in the total pressure or angle traverse data nor in the velocities which are calculated using the traverse data (Figures 126 through 132). This result confirms the presence of strong pressure gradients in the rotor flow which produce strong secondary cross-passage motions of low energy flow. The low energy flow from the circular vane wake must gravitate or centrifuge toward the low pressure zone or sink formed by the convex curvature of the shroud inlet and the convex side of the rotor blades. This flow then appears downstream of the rotor blades as part of the shroud wall boundary layer.

The presence of the circular vane appeared to improve the performance of the rotor. Although the improvement was greatest (percentage-wise) near the shroud, higher total pressures, velocities, and efficiencies were observed or calculated all across the span.

Tests With Varying Radial Pressure Gradients

The tape which had been covering the porous surface during the tests of varying slot suction was removed to permit airflow to pass into bleed chamber numbers 3, 4, 5, and 6. The purpose of the final series of low-speed runs was to impress very strong radial static pressure gradients on the aft or disc wall of the rotating diffuser. Although this was the intention during the first series of runs, the original porous surface fabrication was not very good. Furthermore, a number of operating problems were discovered and solved during the course of the earlier runs. Data were taken at constant 1,800 rpm with varying suction quantities. Three radial locations of the traversible survey probe were used: station 3.5 at 8.68 inches radius (Figures 133 through 135), station 4.5 at 9.36 inches radius (Figures 136 through 138), and station 5.5 at 10.25 inches radius (Figures 139 through 141). The net result of these tests is that although more severe radial pressure gradients were impressed on the rotating wall (denoted exit wall on figures) of the vaneless diffuser (G_2 = 28) than are calculated to exist in the Phase III rotor at 100 percent speed (G_2 = 20; see Figure 85), the rotating wall showed no tendency toward separation. The total pressure remained high at the wall and the flow angle did not deviate from midstream values. An indication of decreasing total pressure near the rotating wall can be seen in Figure 138 in the 0 to 7 percent span region, but little or no flow angle change was observed and the rotating wall flow is believed to be strong under these severe conditions.

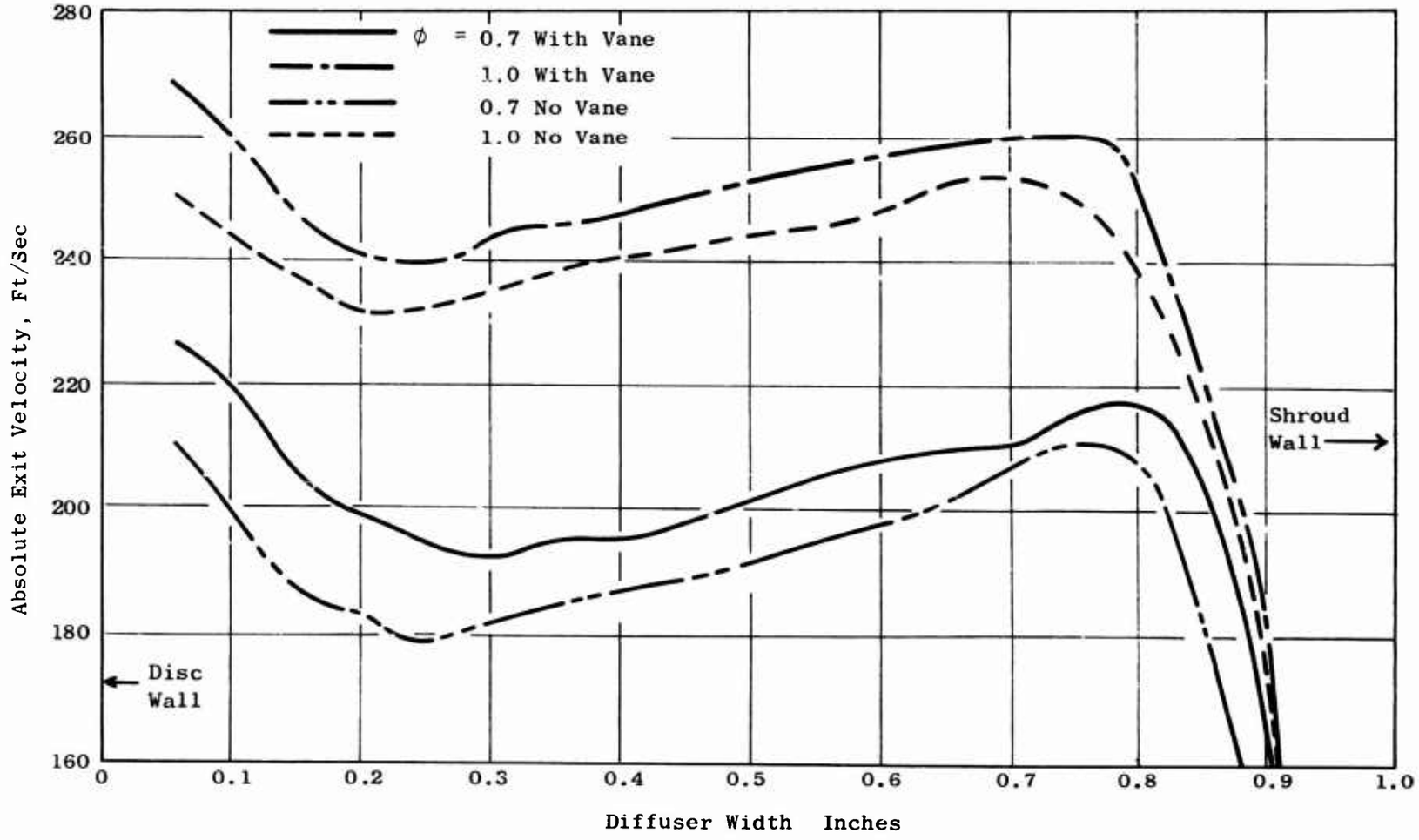

Figure 126. Distribution of Absolute Exit Velocity at Rotor Blade Trailing Edge for Various Suction Quantities for Low-Speed ROC.

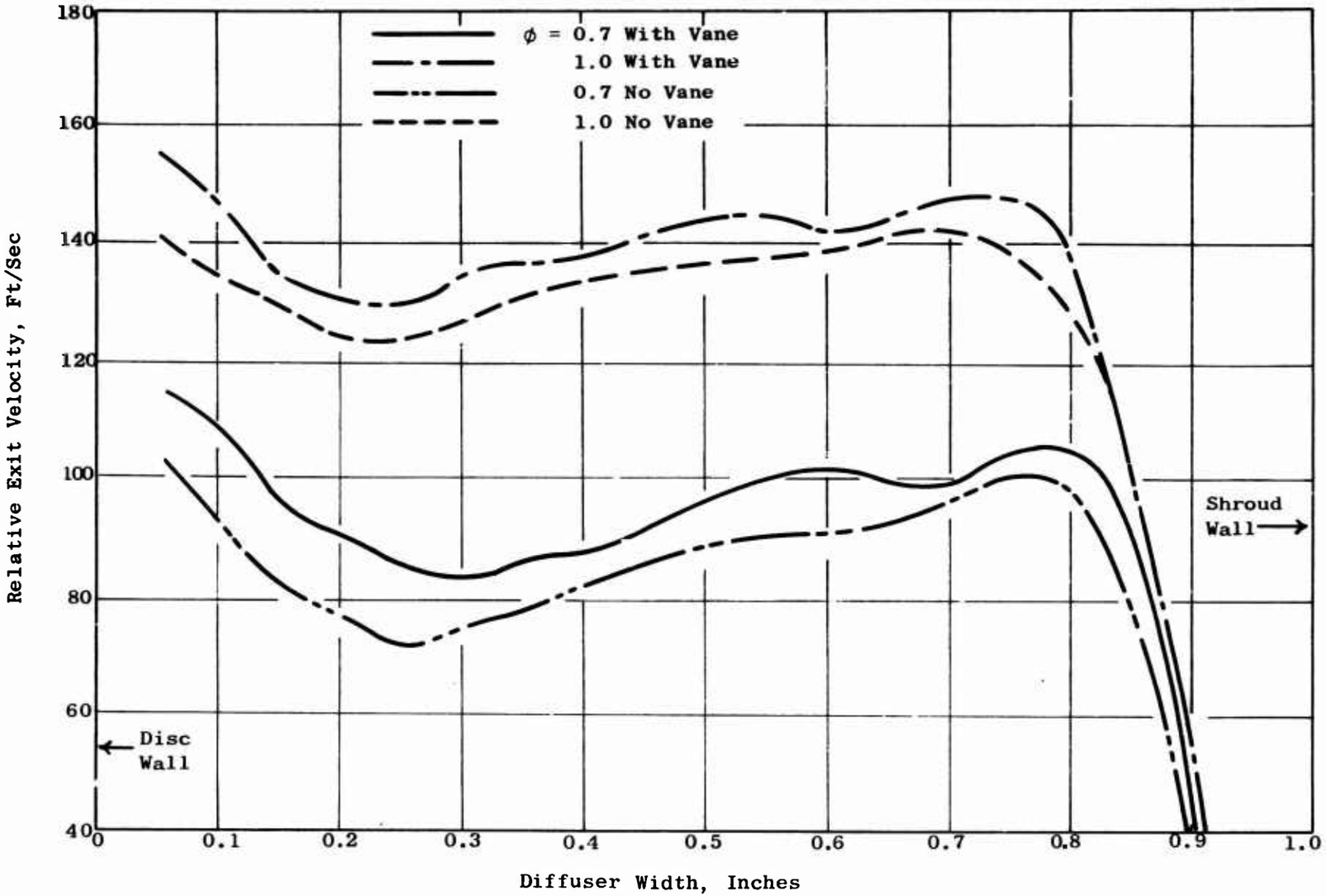

Figure 127. Distribution of Relative Exit Velocity at Rotor Blade Trailing Edge for Various Suction Quantities for Low-Speed ROC.

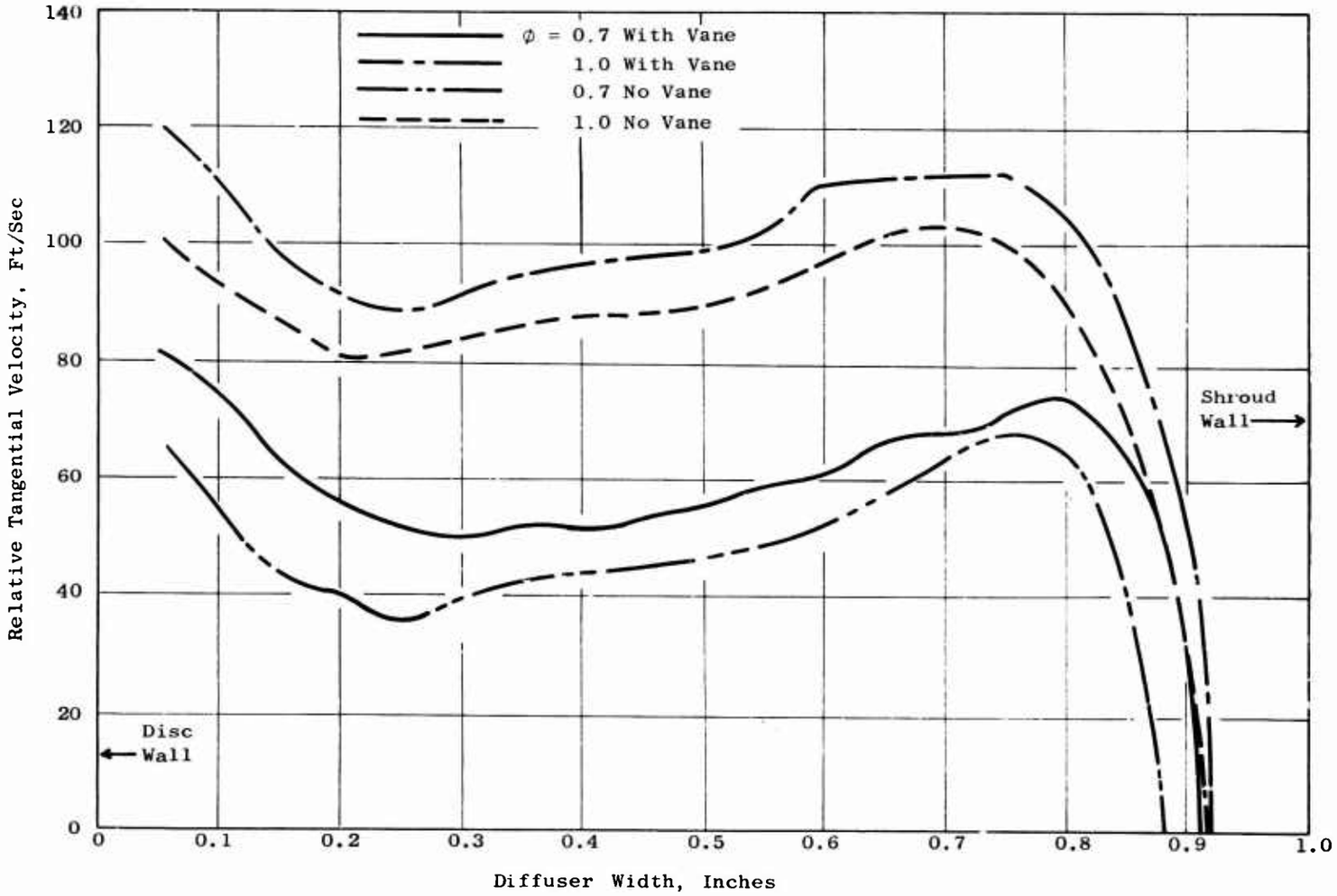

Figure 128. Distribution of Relative Tangential Velocity at Rotor Blade Trailing Edge for Various Suction Quantities for Low-Speed ROC.

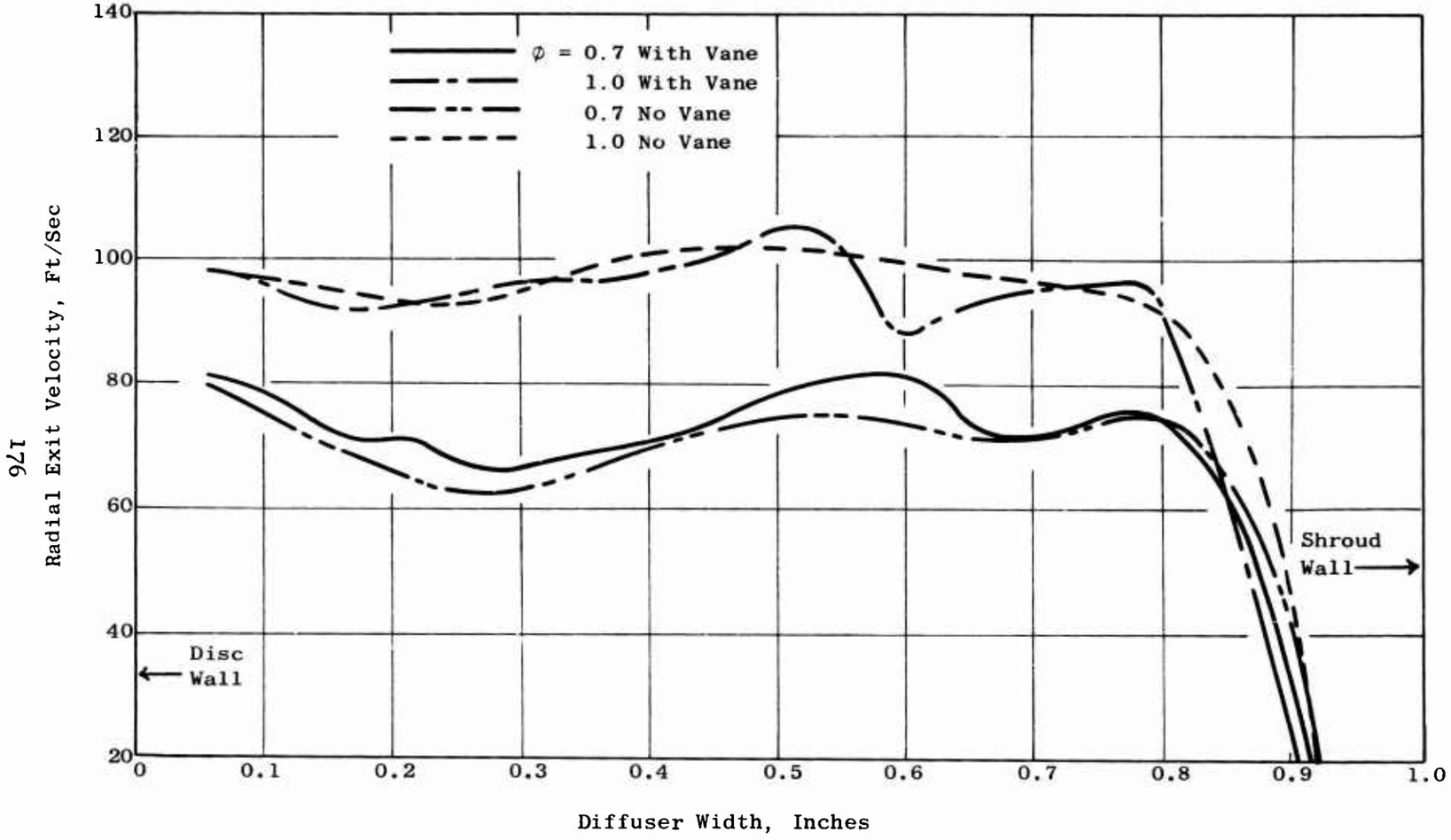

Figure 129. Distribution of Radial Exit Velocity at Rotor Blade Trailing Edge for Various Suction Quantities for Low-Speed ROC.

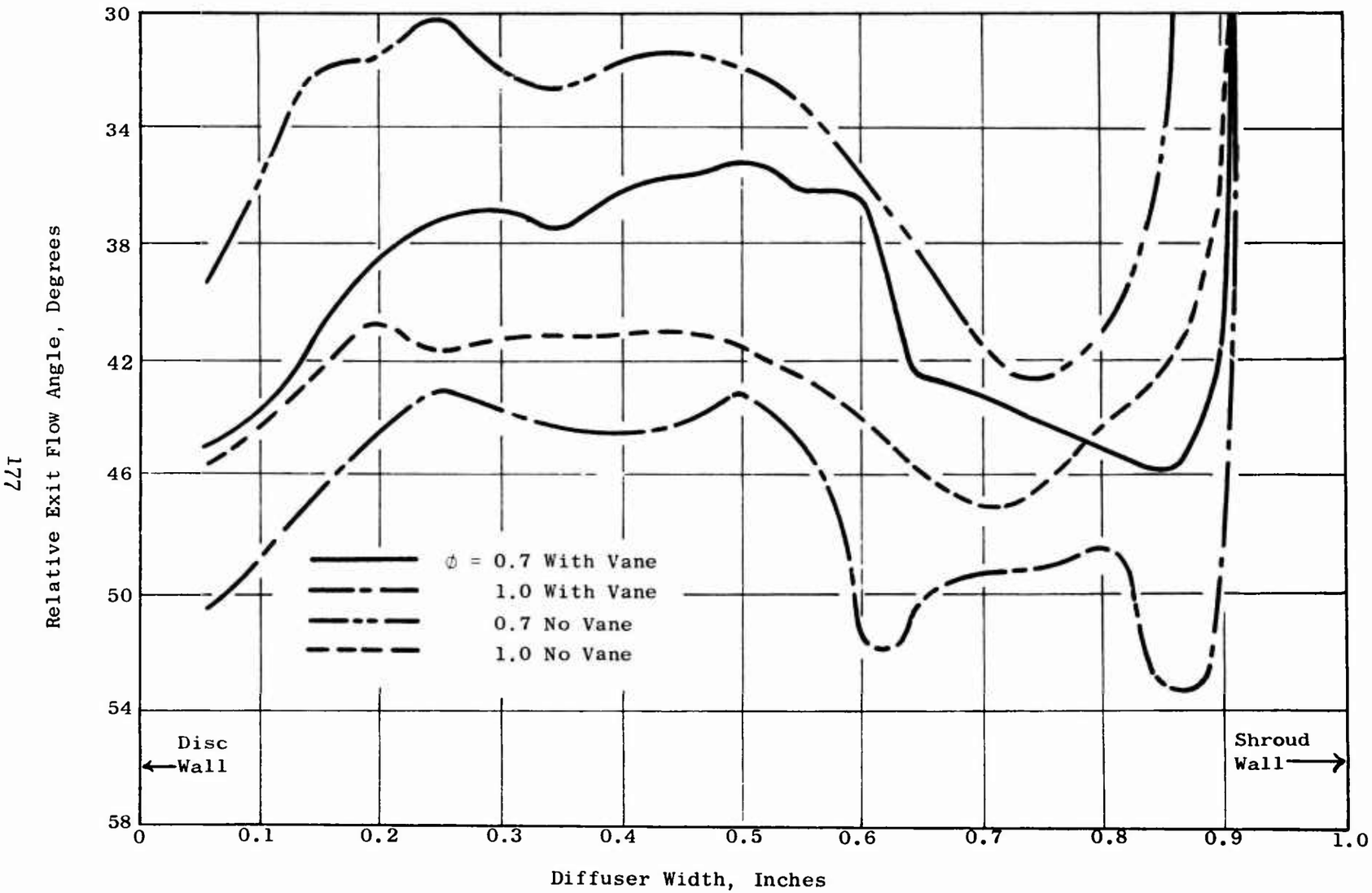

Figure 130. Distribution of Relative Exit Flow Angle at Rotor Blade Trailing Edge for Various Suction Quantities for Low-Speed ROC.

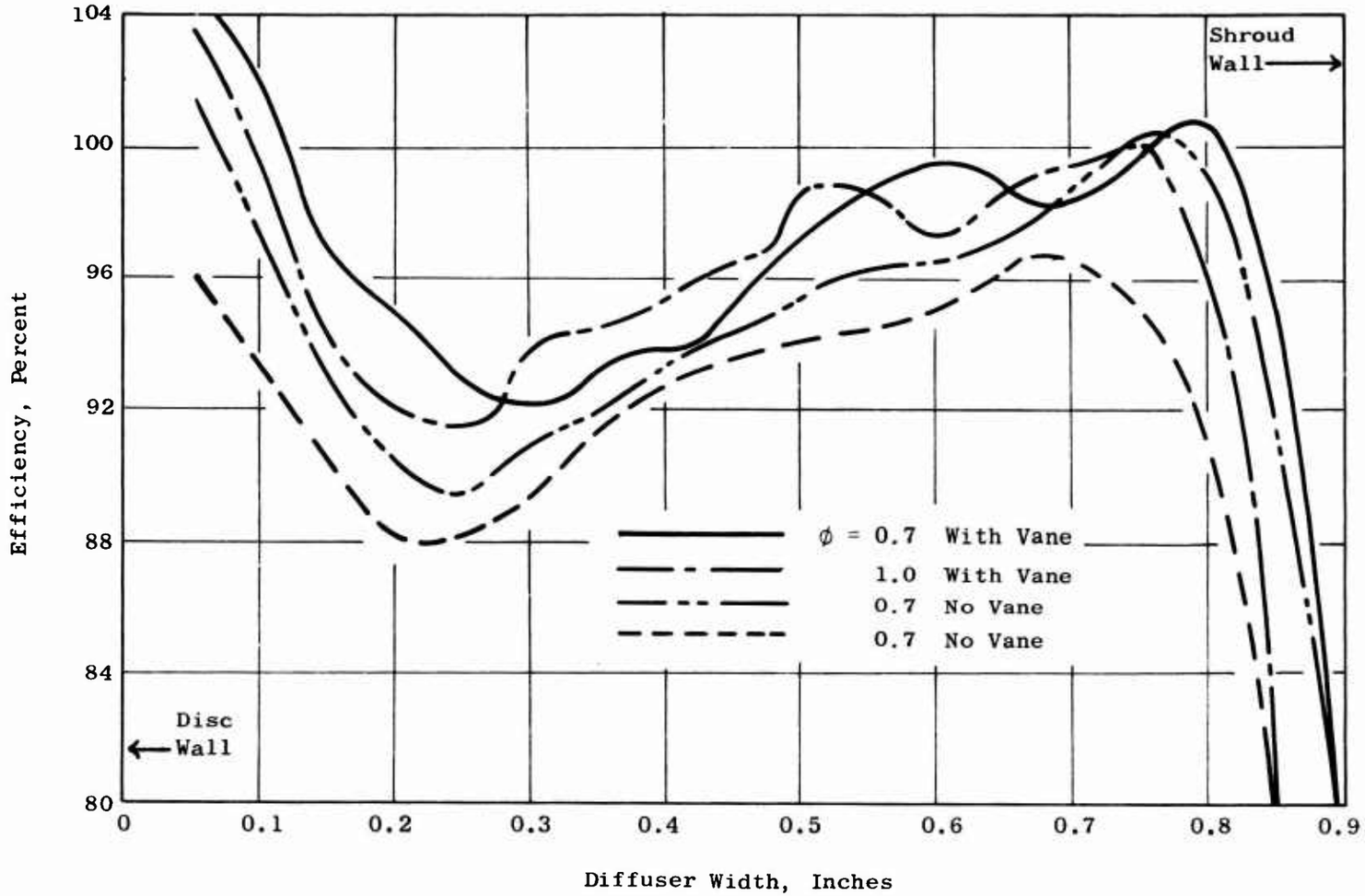

Figure 131. Distribution of Efficiency at Rotor Blade Trailing Edge for Various Suction Quantities for Low-Speed ROC.

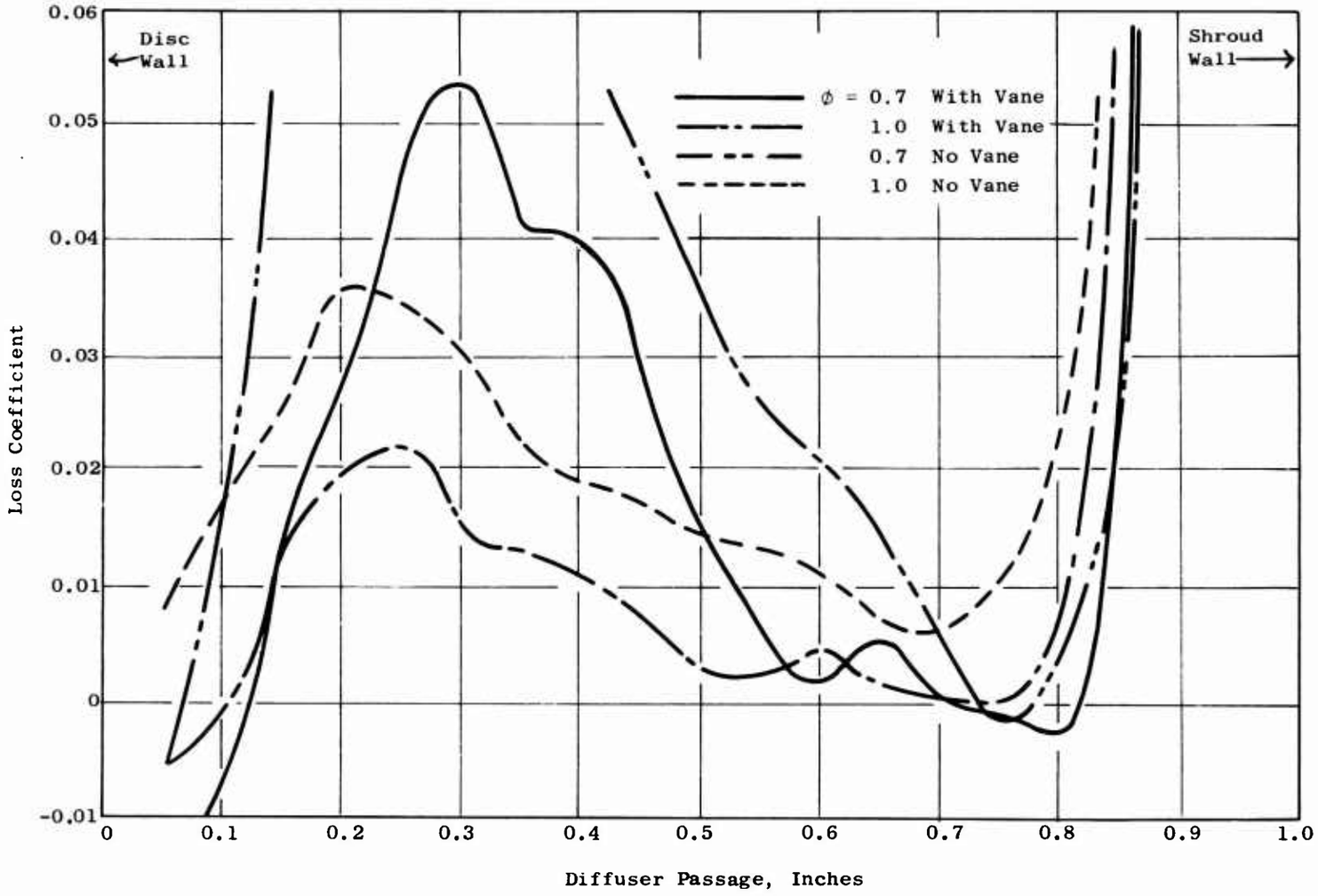

Figure 132. Distribution of Loss Coefficient at Rotor Blade Trailing Edge for Various Suction Quantities for Low-Speed ROC.

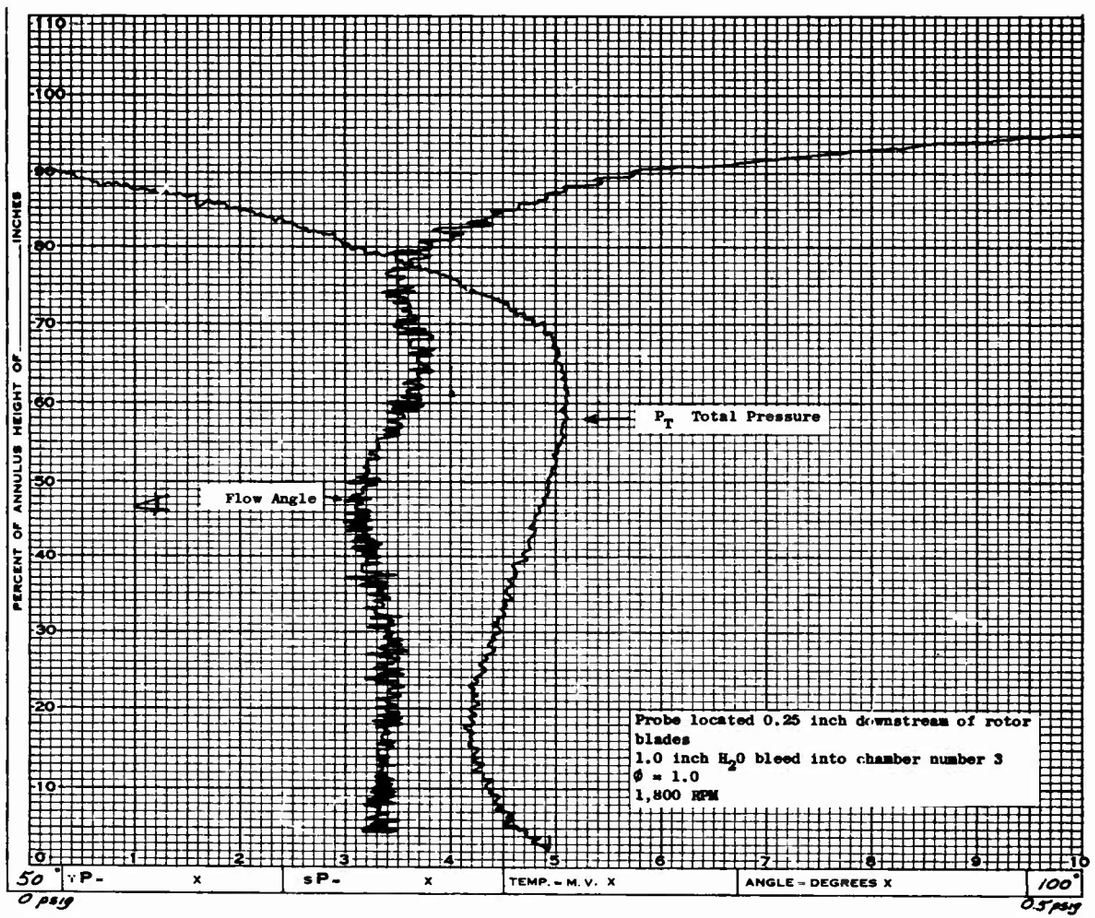

Figure 133. Low-Speed ROC Flow Angle and Total Pressure Distribution for Run Number 27, Reading Number 2, With Inlet Vane.

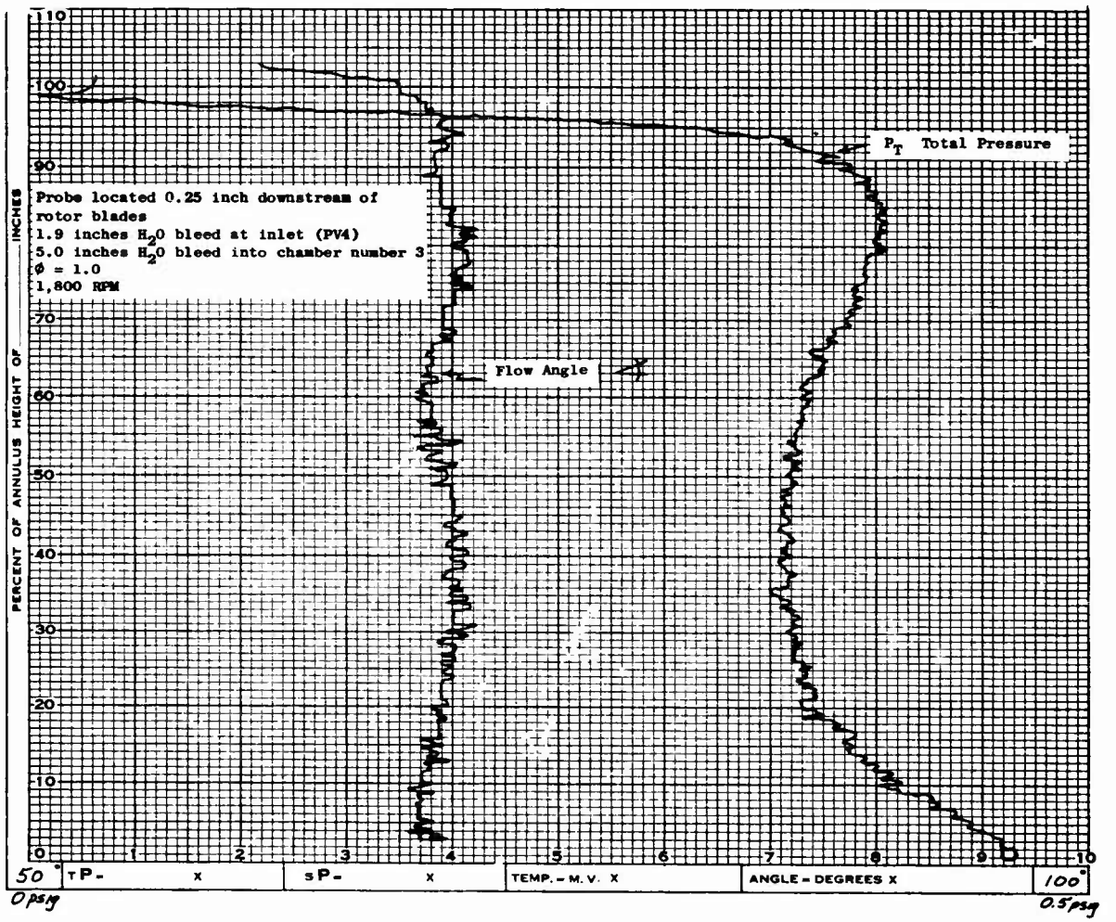

Figure 134. Low-Speed ROC Flow Angle and Total Pressure Distribution for Run Number 27, Reading Number 3, With Inlet Vane.

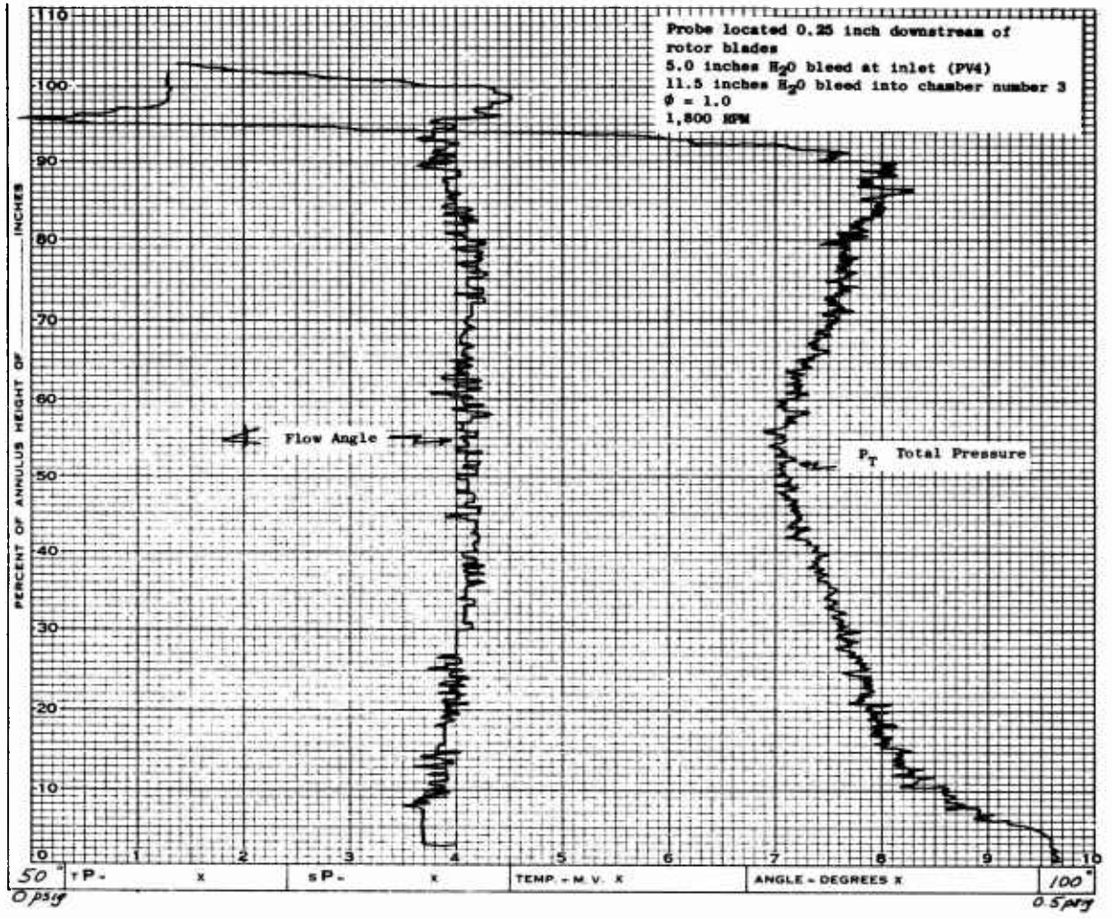

Figure 135. Low-Speed ROC Flow Angle and Total Pressure Distribution for Run Number 27, Reading Number 6, With Inlet Vane.

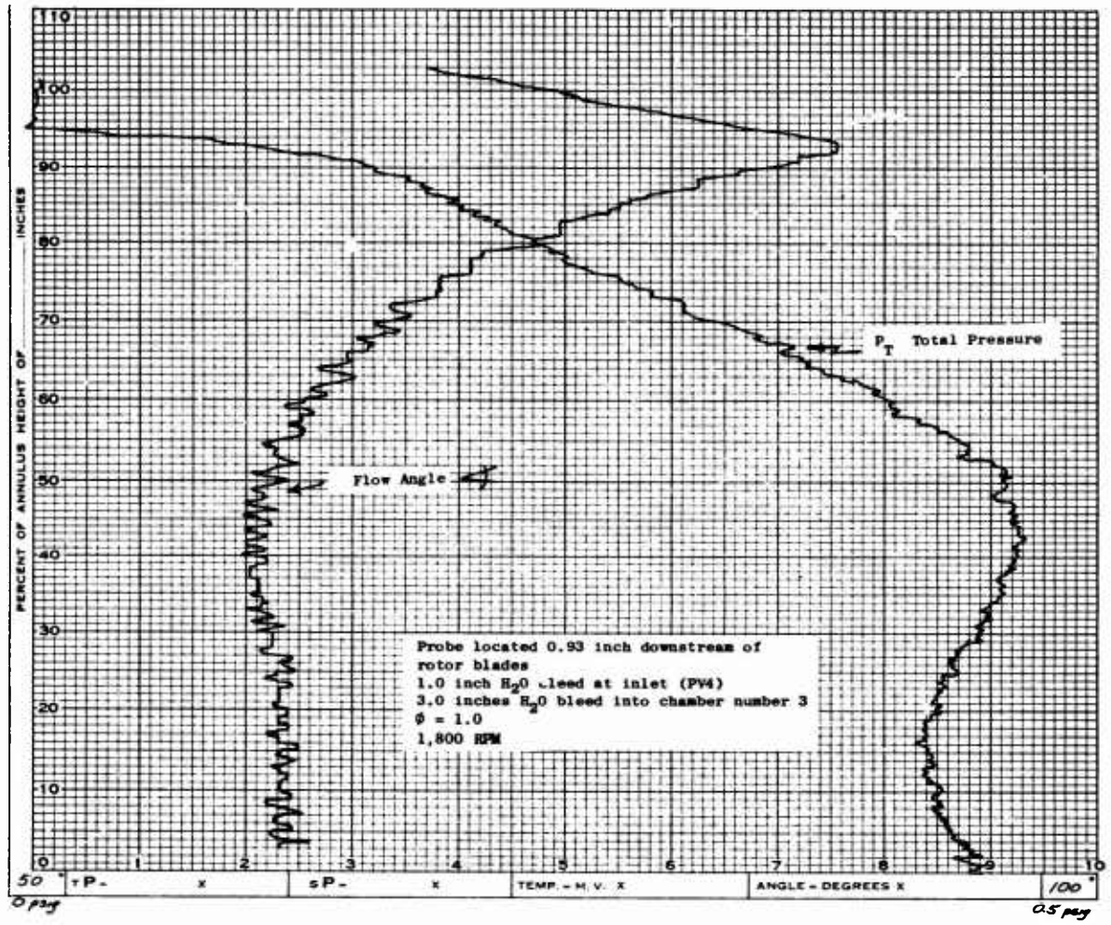

Figure 136. Low-Speed ROC Flow Angle and Total Pressure Distribution for Run Number 32, Reading Number 3, With Inlet Vane.

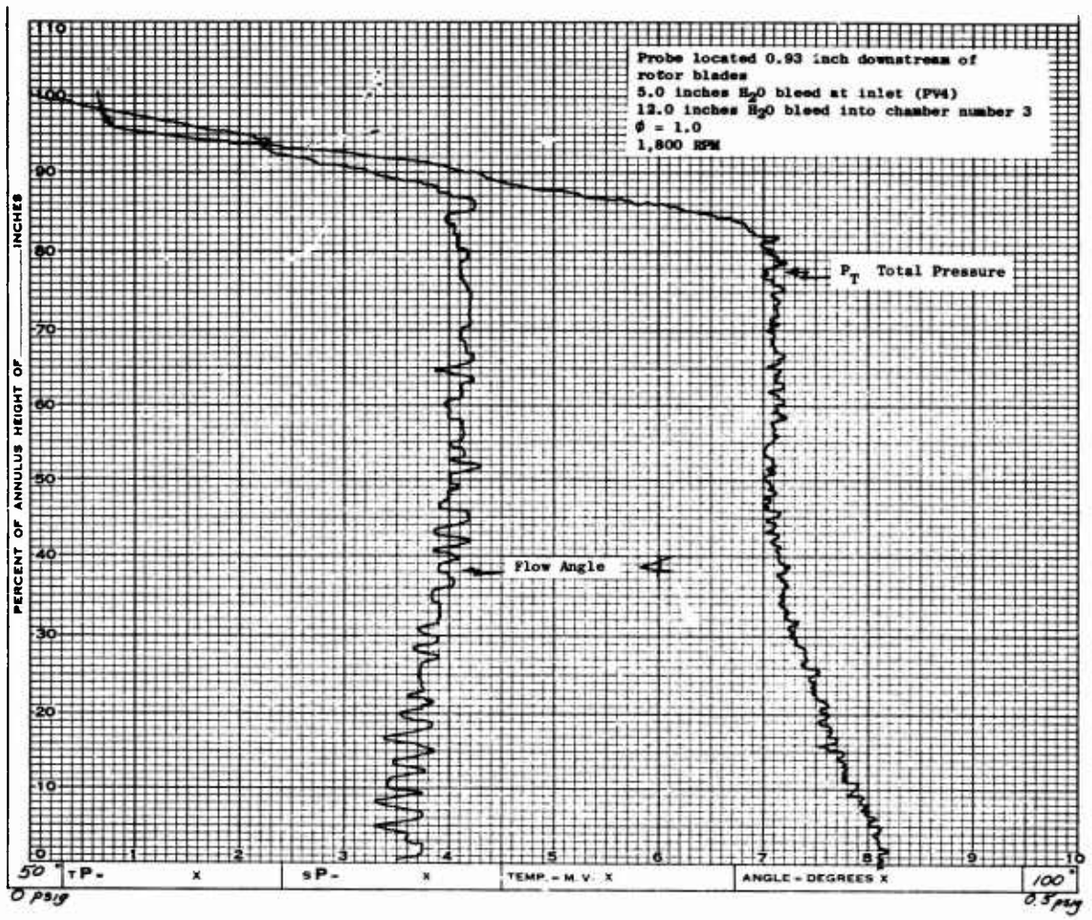

Figure 137. Low-Speed ROC Flow Angle and Total Pressure Distribution for Run Number 32, Reading Number 7, With Inlet Vane.

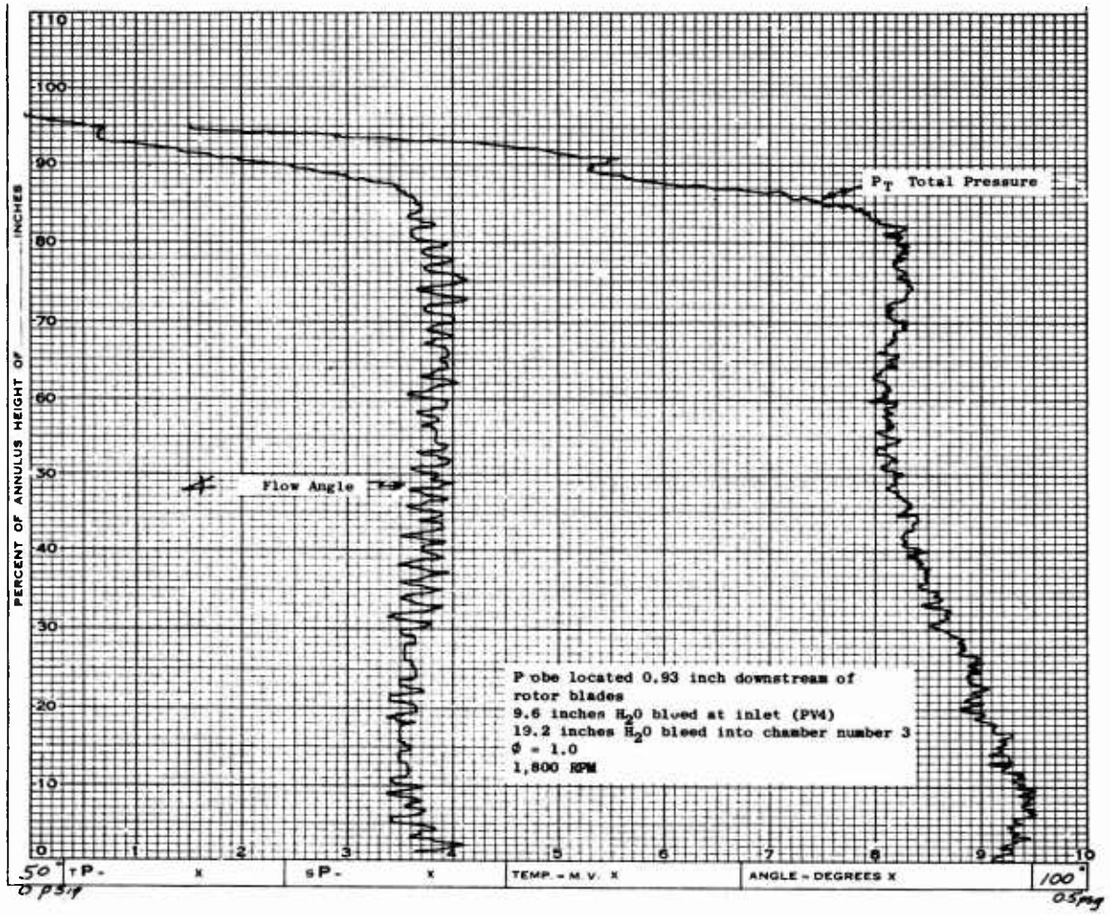

Figure 138. Low-Speed ROC Flow Angle and Total Pressure Distribution for Run Number 32, Reading Number 8, With Inlet Vane.

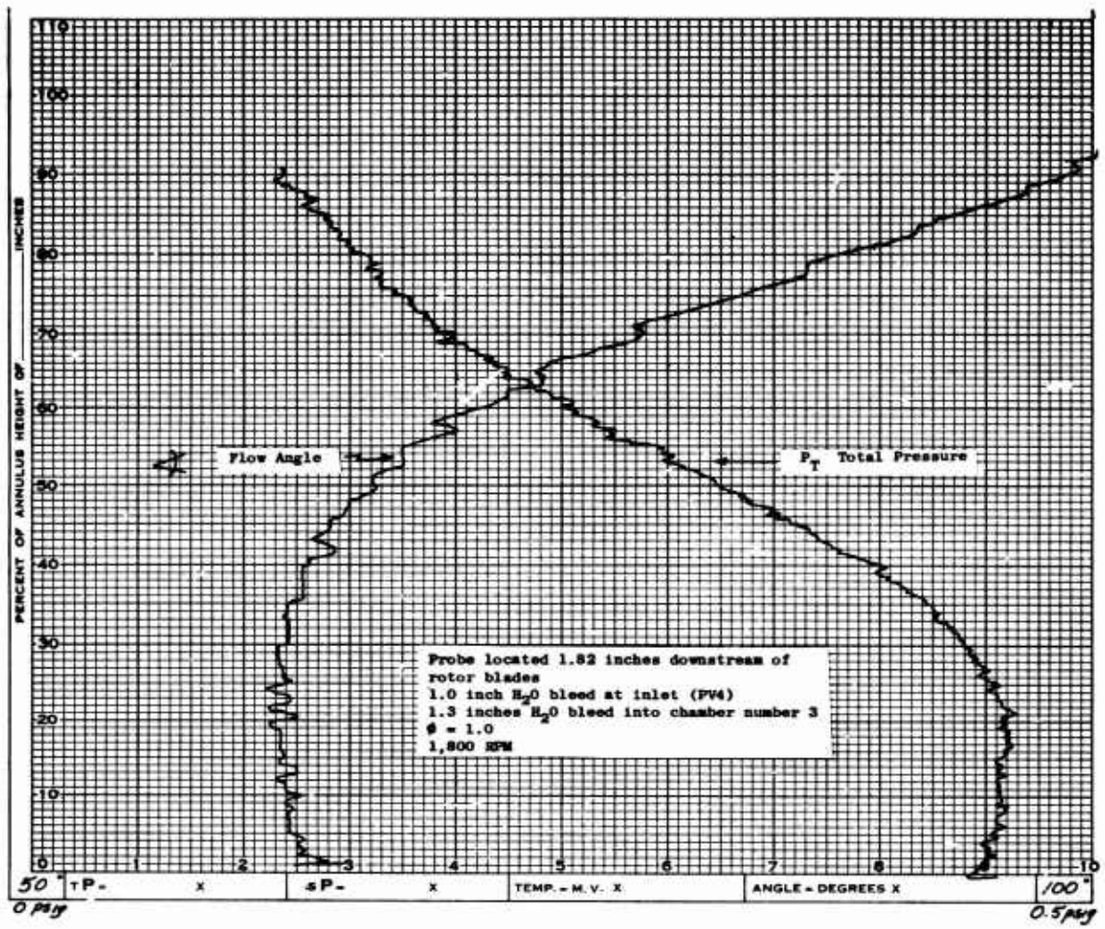

Figure 139. Low-Speed ROC Flow Angle and Total Pressure Distribution for Run Number 31, Reading Number 2, With Inlet Vane.

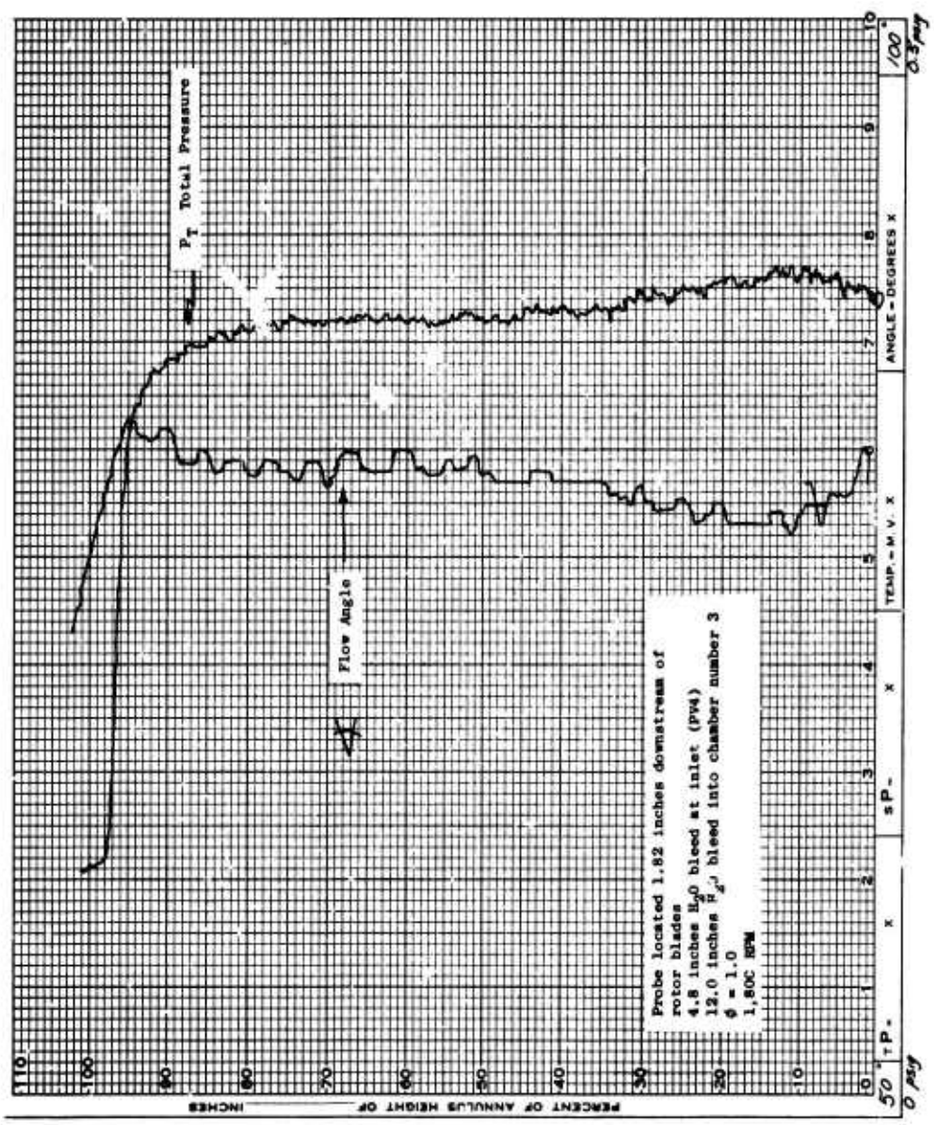

Figure 140. Low-Speed ROC Flow Angle and Total Pressure Distribution for Run Number 31, Reading Number 6, With Inlet Vane.

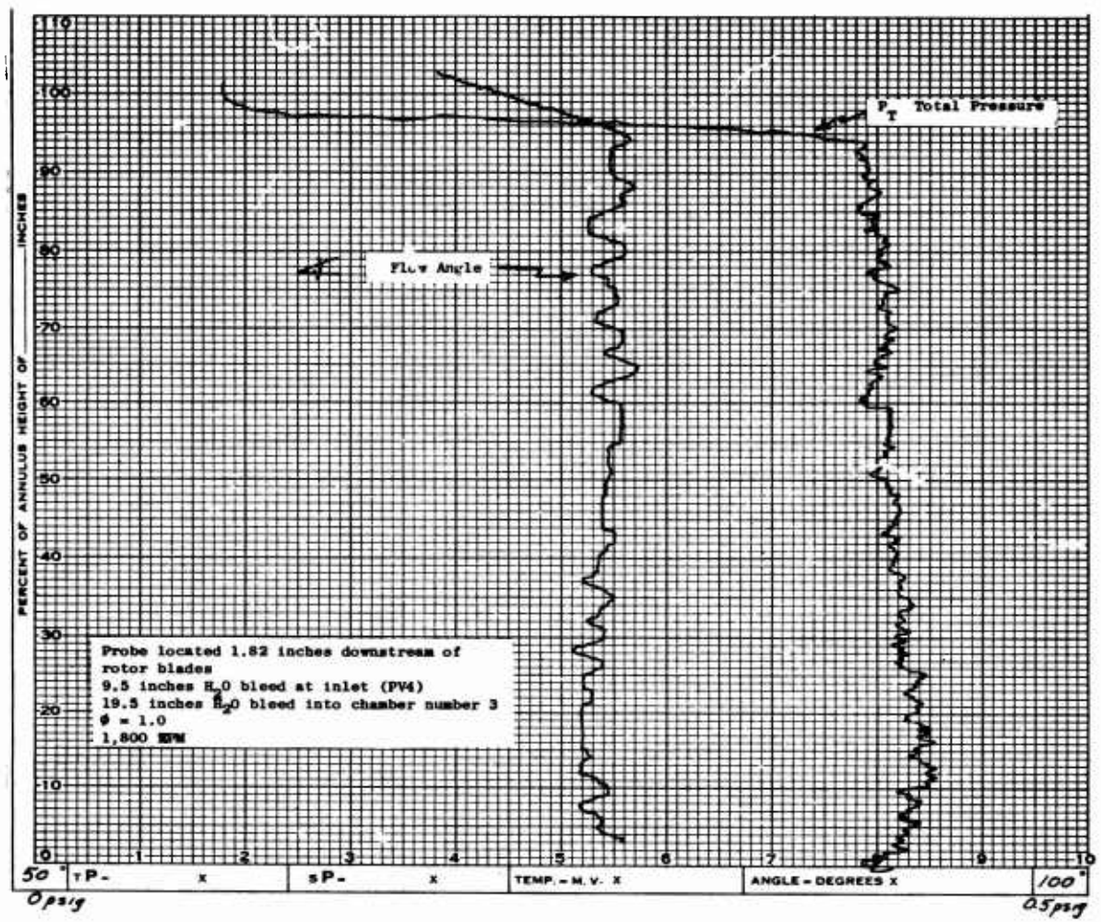

Figure 141. Low-Speed ROC Flow Angle and Total Pressure Distribution for Run Number 31, Reading Number 7, With Inlet Vane.

EXPERIMENTAL INVESTIGATION OF THE HIGH-SPEED COMPRESSOR

GENERAL DISCUSSION

The overall assembly of the high-speed ROC was presented as Figure 215 in the Phase I report of this investigation (Reference 1). The first buildups of the compressor were made as was shown in Reference 1, with the exception of the subsonic and supersonic stator vanes which were omitted during the first tests to permit direct measurement of the rotor performance.

Test Vehicle

Figure 142 shows the stand which carries the high-speed compressor. The frame (Figure 143) supports the high-speed gearbox illustrated on Figure 144. The main bearing housing for the high-speed shaft is presented in Figure 145. The aft outer stator casing is attached to this bearing housing. Another view of the main bearing housing including the 2 seal plates is shown in Figure 146. These 2 seal plates are used to control the clearance between the high-speed rotor and the stationary casings. The flange containing external gear teeth used to rotate a spacer between the 2 sets of bearings in the main bearing housing is shown in Figure 147. Miscellaneous other small parts are also shown in this figure, including the bullet nose and fairing which are part of the stationary centerbody of the test vehicle. The high-speed shaft and bearings are shown assembled in Figure 148. A stator vane actuator and the mount for the drive screw of the actuator are illustrated in Figure 149. Two views of the inlet guide vane assembly are shown in Figures 150 and 151. These figures are views looking upstream from the rotor and downstream at the inlet guide vane assembly. As can be seen in the downstream view, the clearance between the variable portion of the inlet guide vanes and the inner casing is larger than is satisfactory for these purposes. The inner contour of each vane was extended approximately 0.020 inch to reduce these gaps to an acceptable value before assembly of the compressor. An external view of the upstream compressor casing is shown in Figure 152, and an internal view is shown in Figure 153. The removable splitter lips can be seen in the latter figure. Also shown is 1 of the dowel pins which are used to locate the compressor casings with respect to each other. The transition section which conducts the flow from the exit scroll of the compressor casings to the measuring station, the sections used for measurement purposes, and the 90-degree elbows are shown in Figure 154.

Rotor

A step-by-step balancing procedure was conducted as the rotor was assembled. First the rotor shaft alone was balanced. Then the shaft

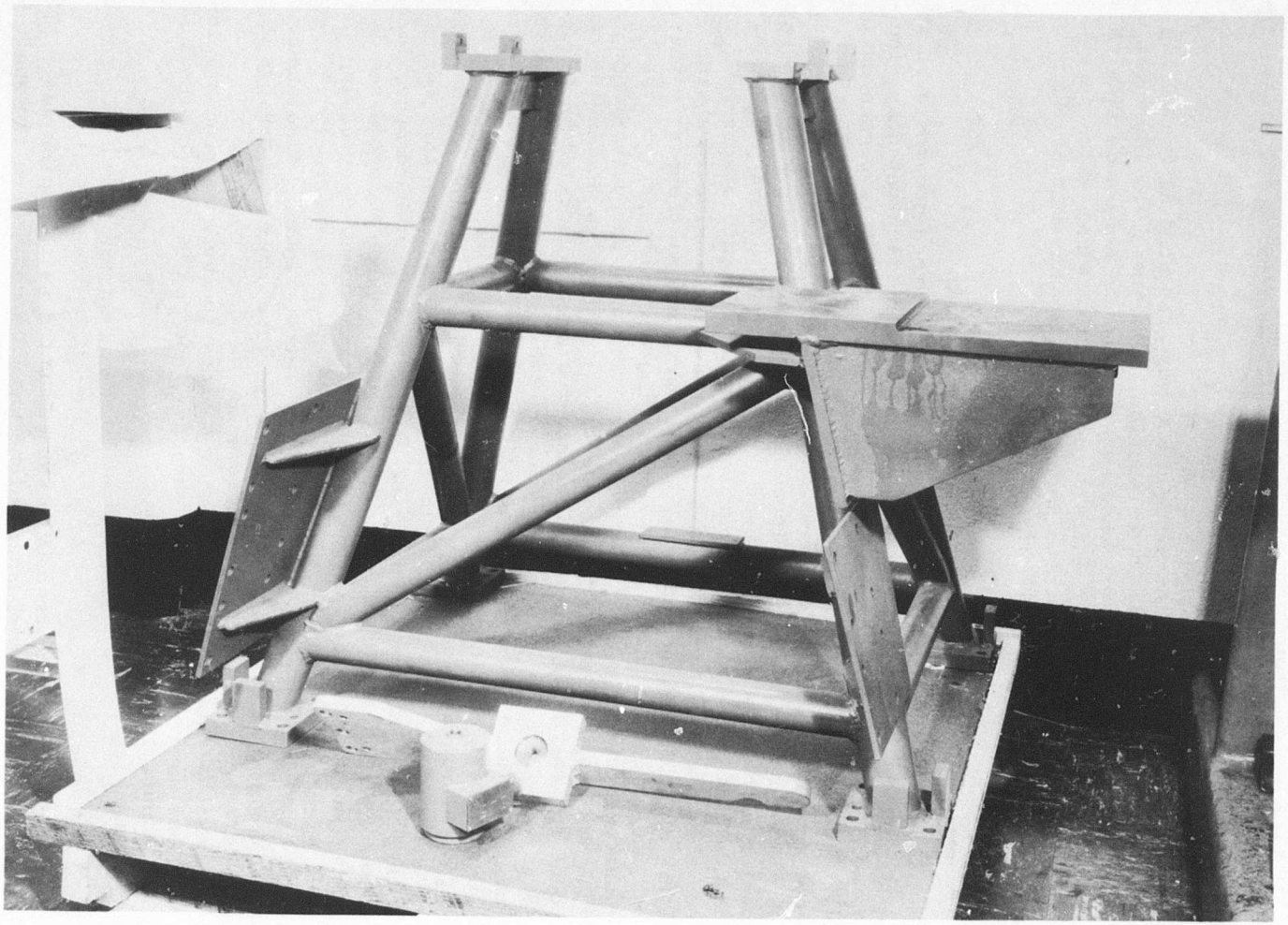

Figure 142. Main Frame for Supporting High-Speed Test Vehicle.

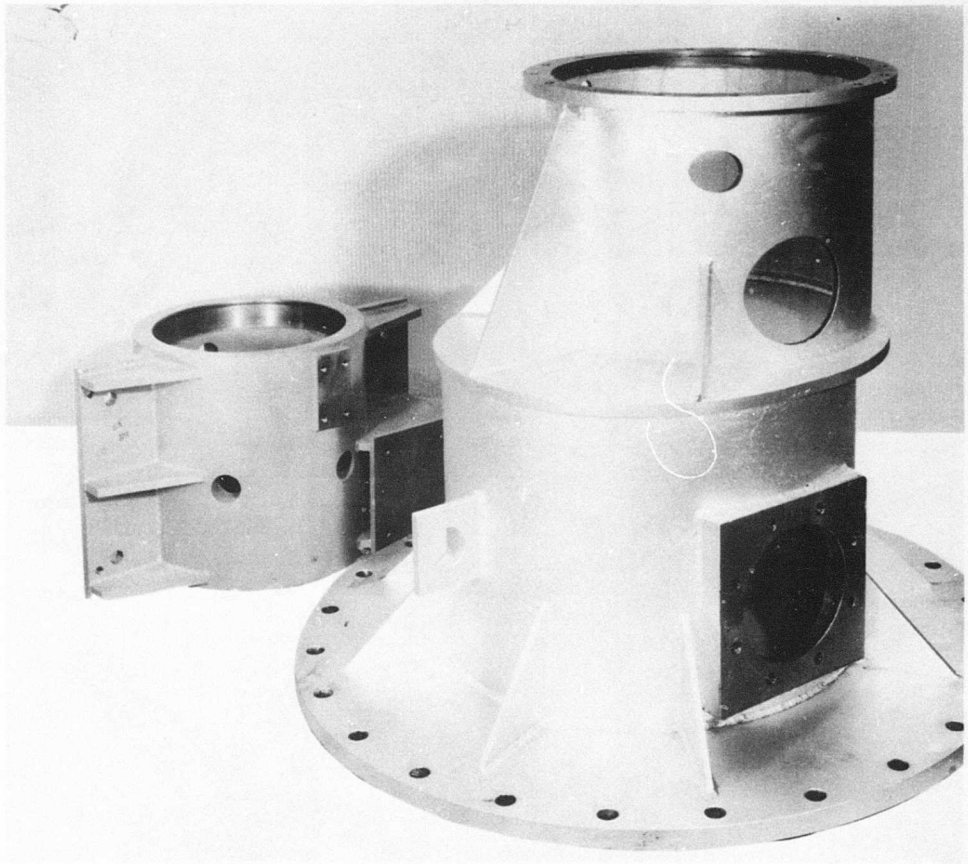

Figure 143. Casing for Mounting High-Speed Gear and Test Vehicle.

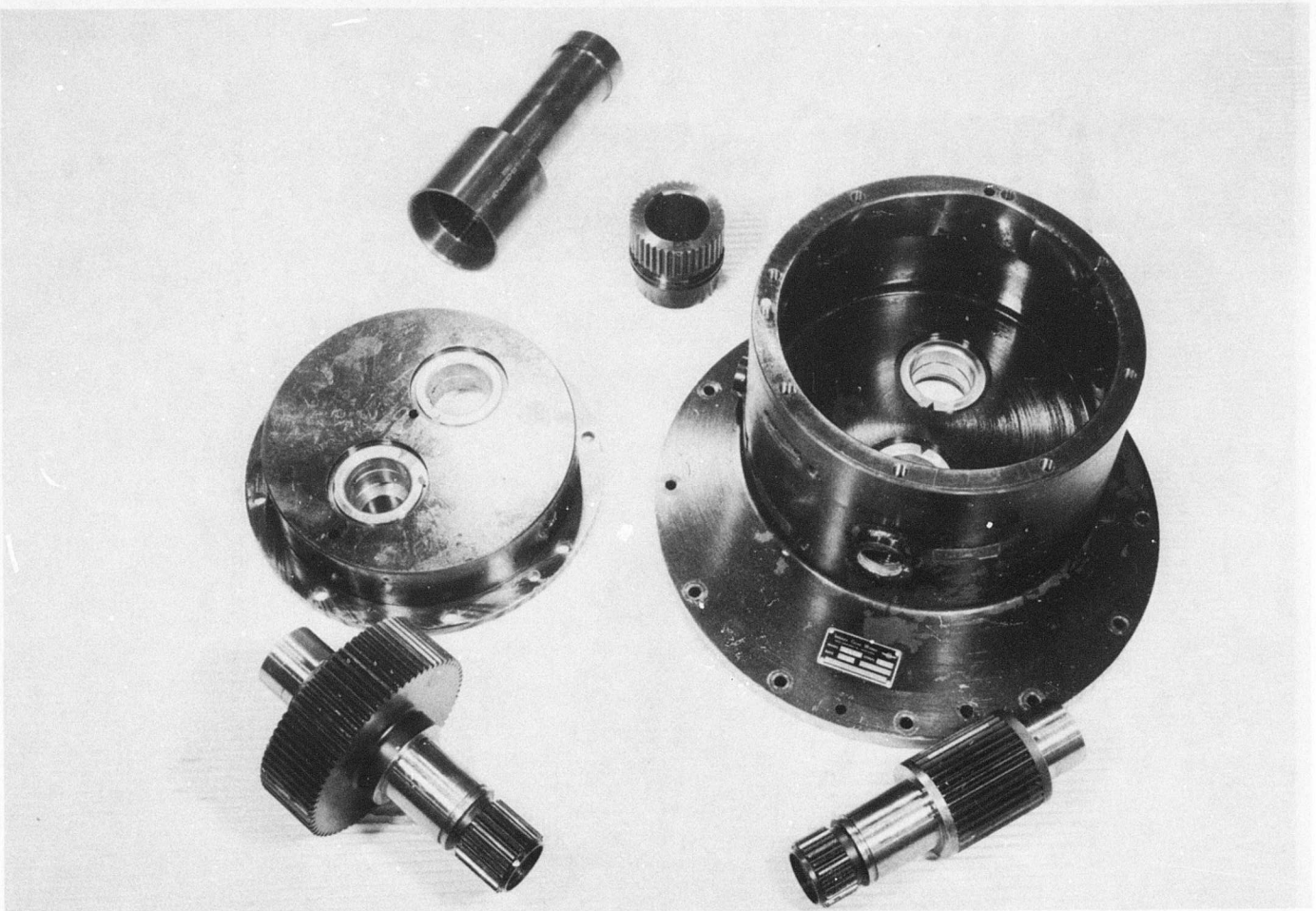

Figure 144. High-Speed Gearbox and Gears.

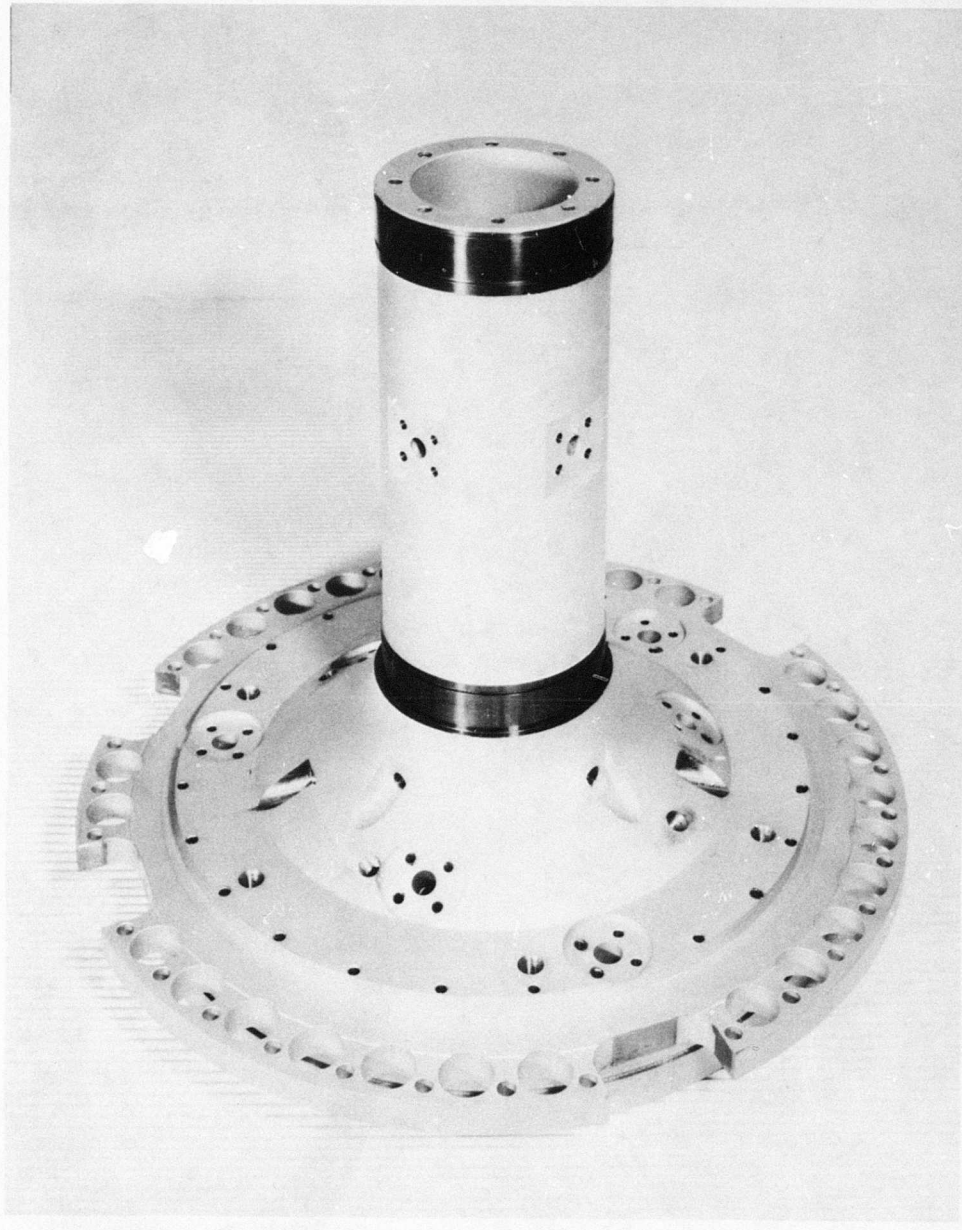

Figure 145. Housing for Supporting High-Speed Main Bearing Shaft.

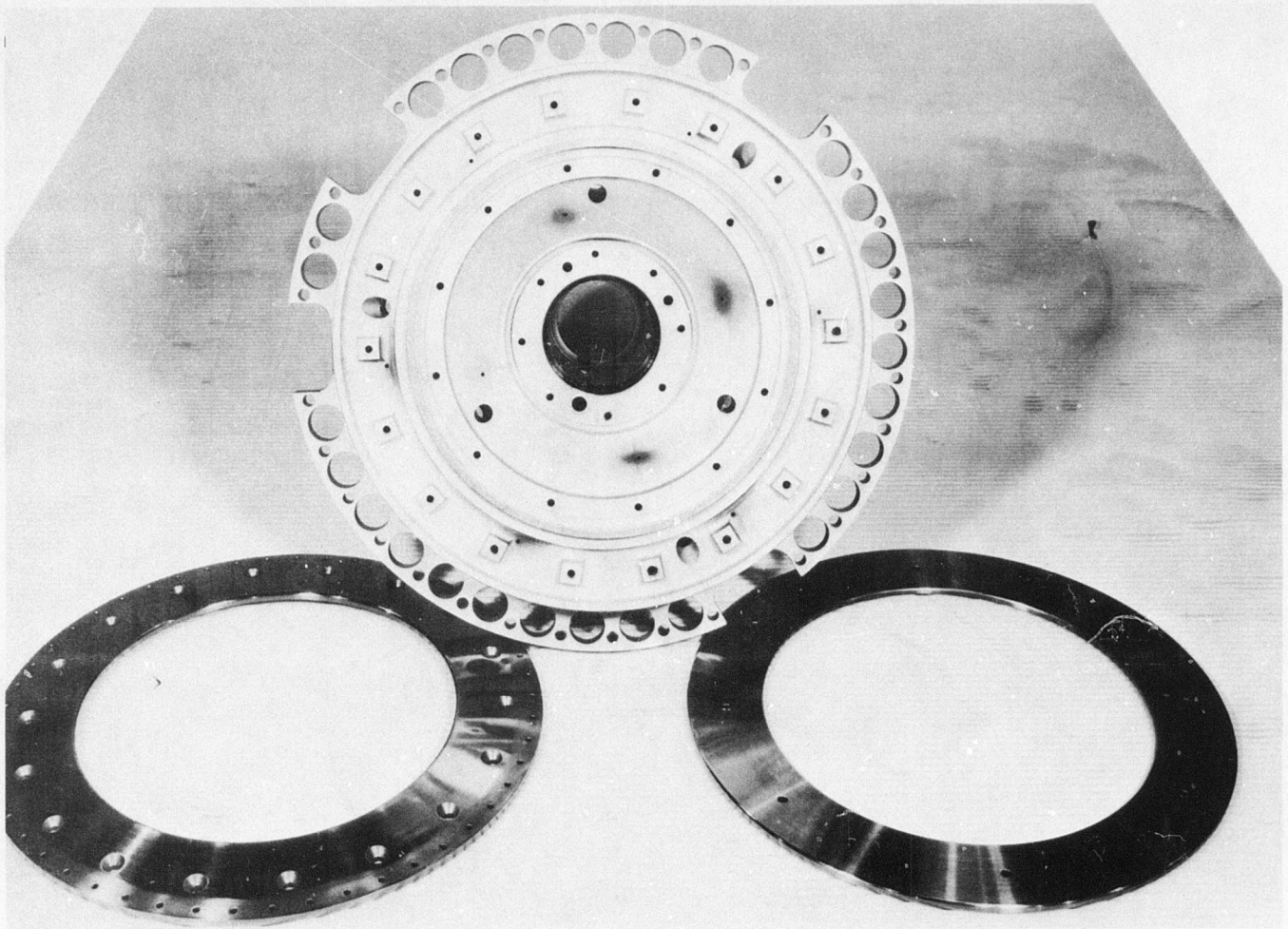

Figure 146. Front View of Bearing Housings Including Seal Plates.

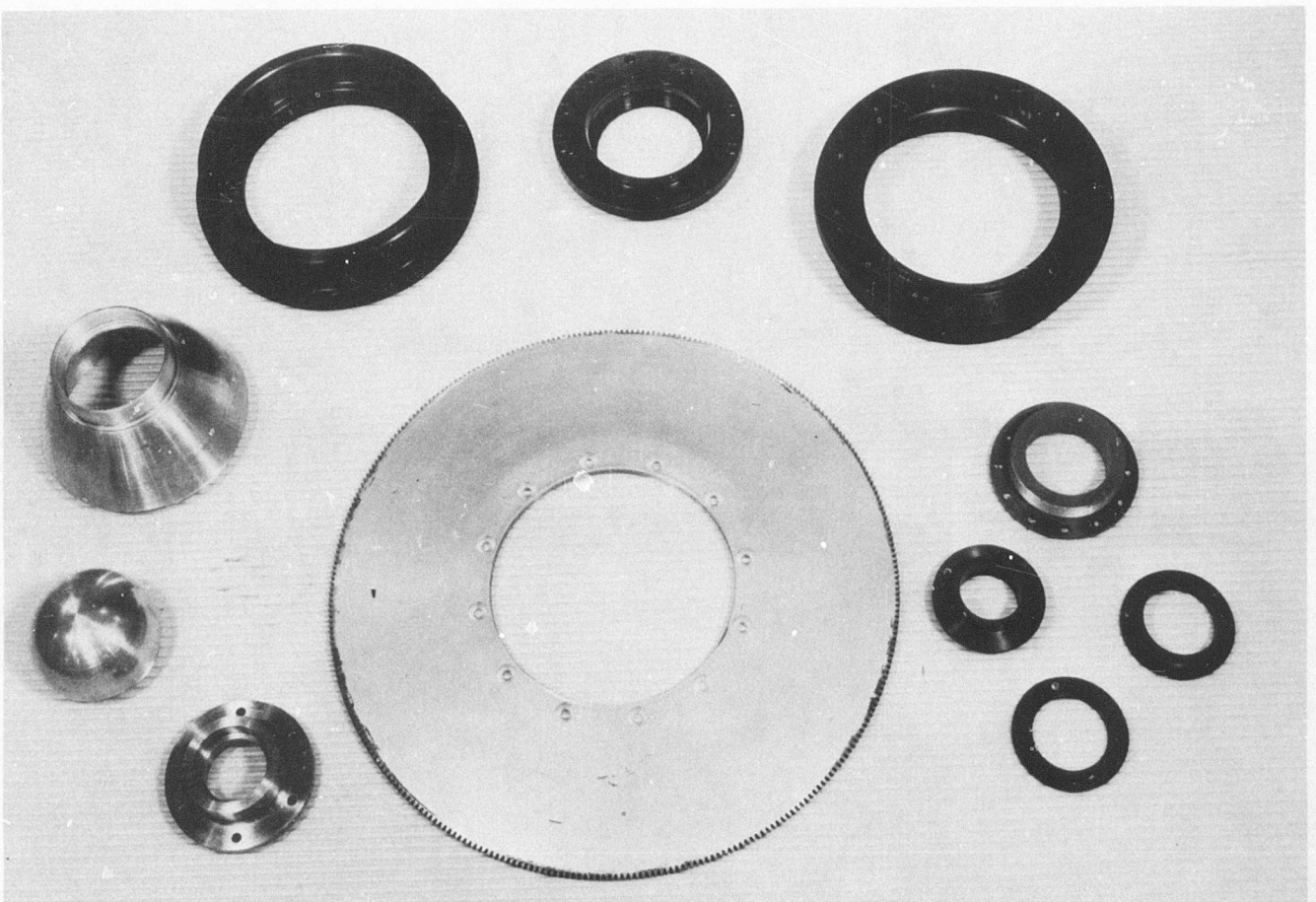

Figure 147. Miscellaneous Seals and Spacers Used With the High-Speed ROC.

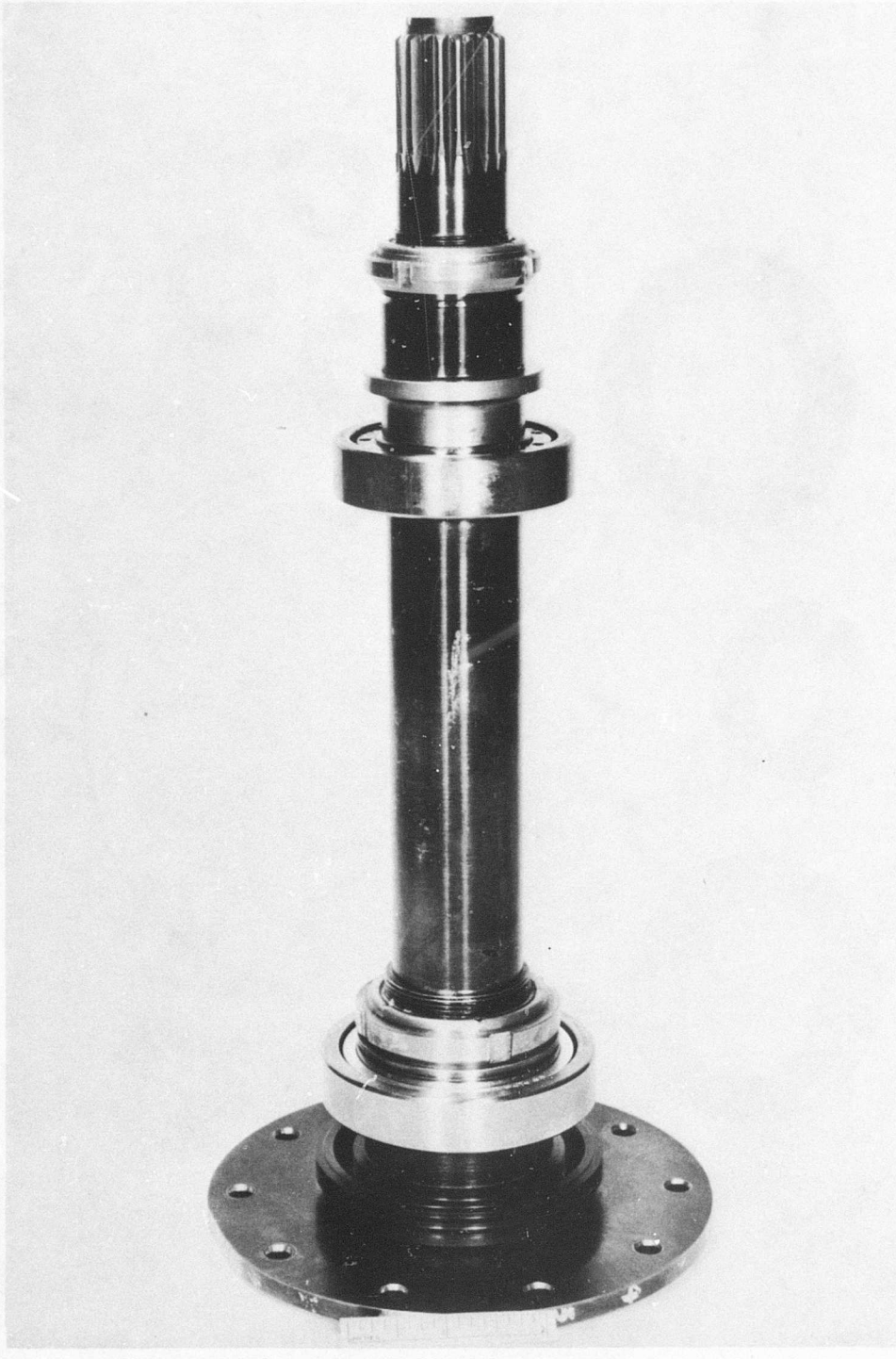

Figure 148. Assembly of Rotor Shaft and Bearings for High-Speed ROC.

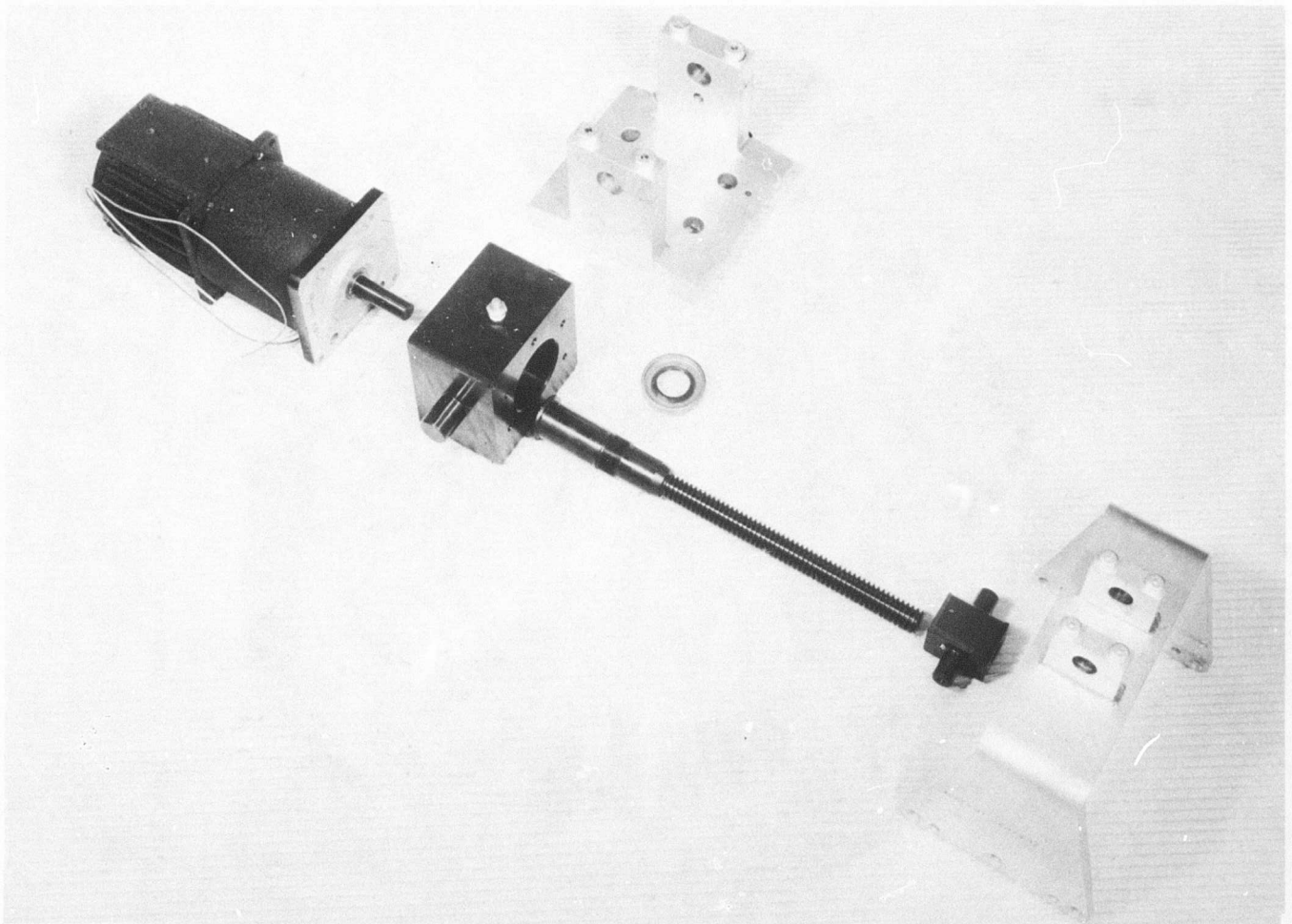

Figure 149. Motor, Reduction Gear, Pivotal Mounting, Drive Screw and Bracket for Actuating Supersonic Stator Blades.

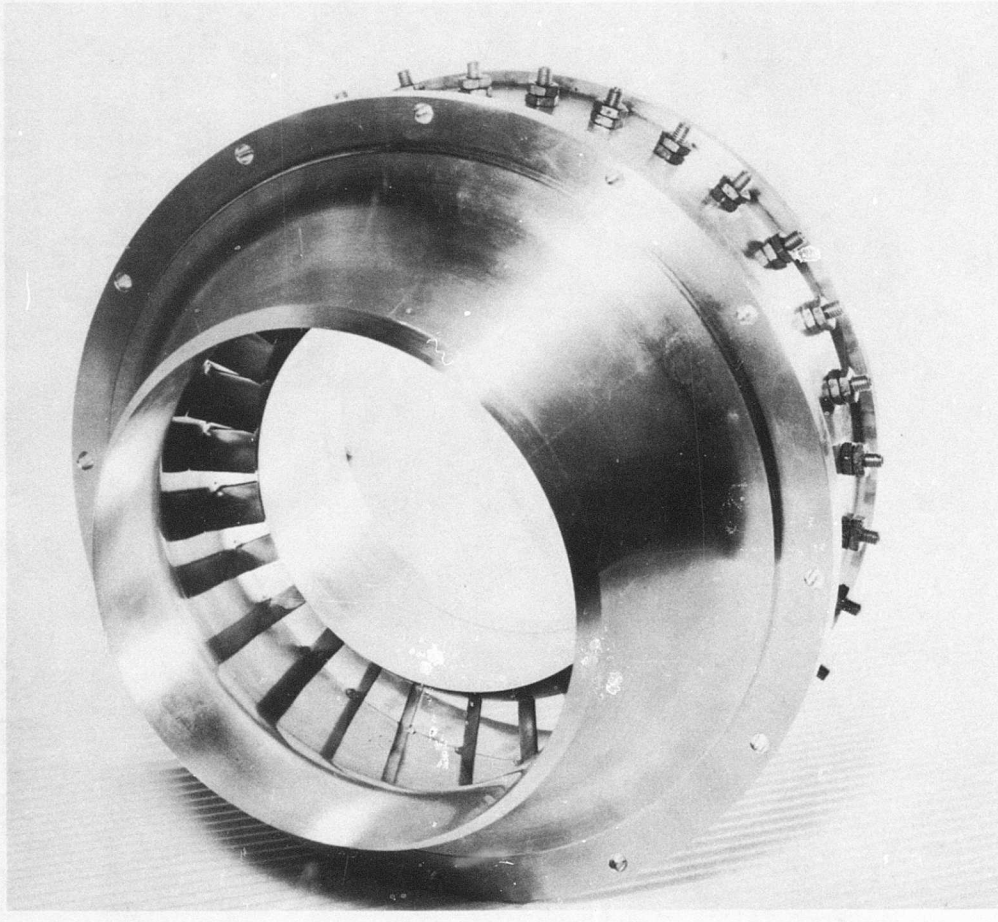

Figure 150. Downstream View of Inlet Guide Vane Assembly.

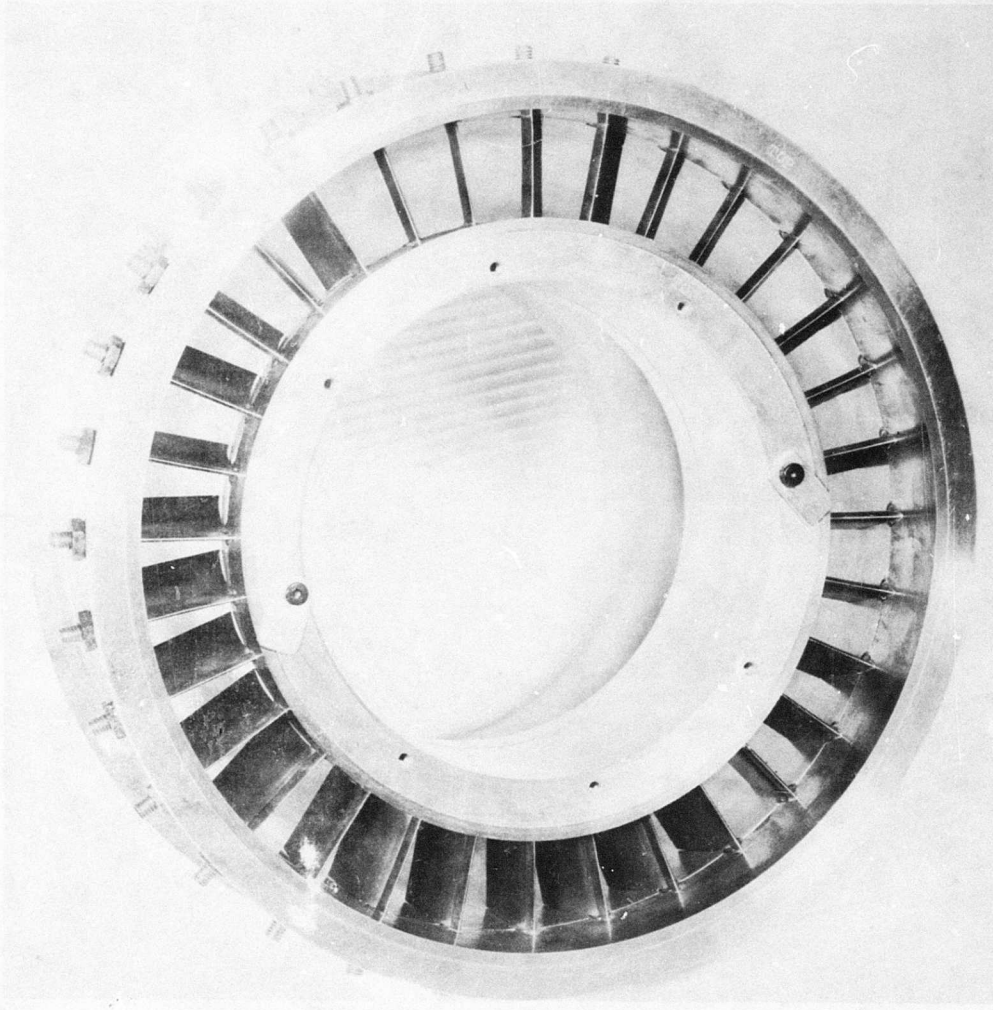

Figure 151. Upstrea View of Inlet Guide Vane Assembly.

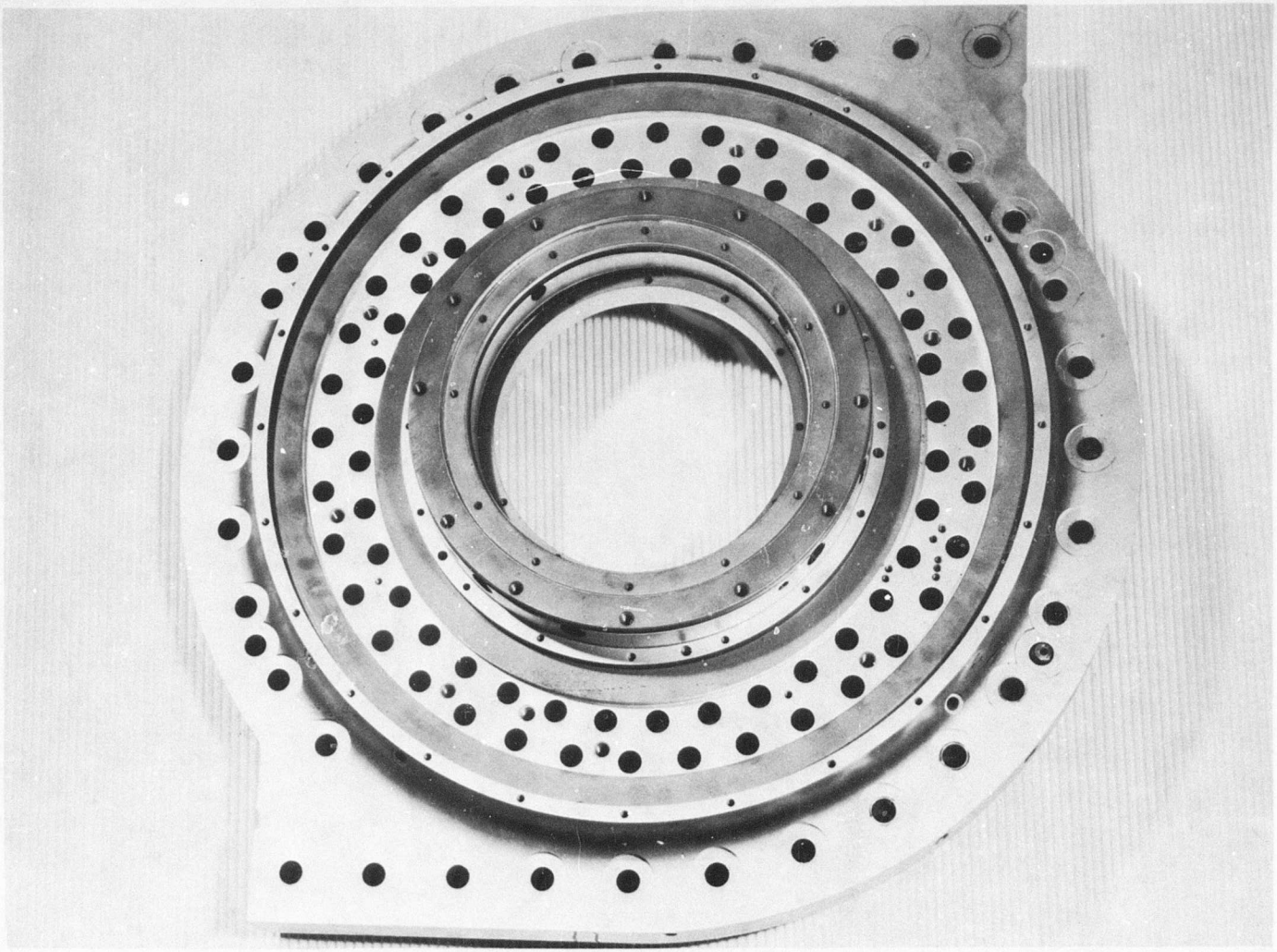

Figure 152. External View of Forward Compressor Stator Casing.

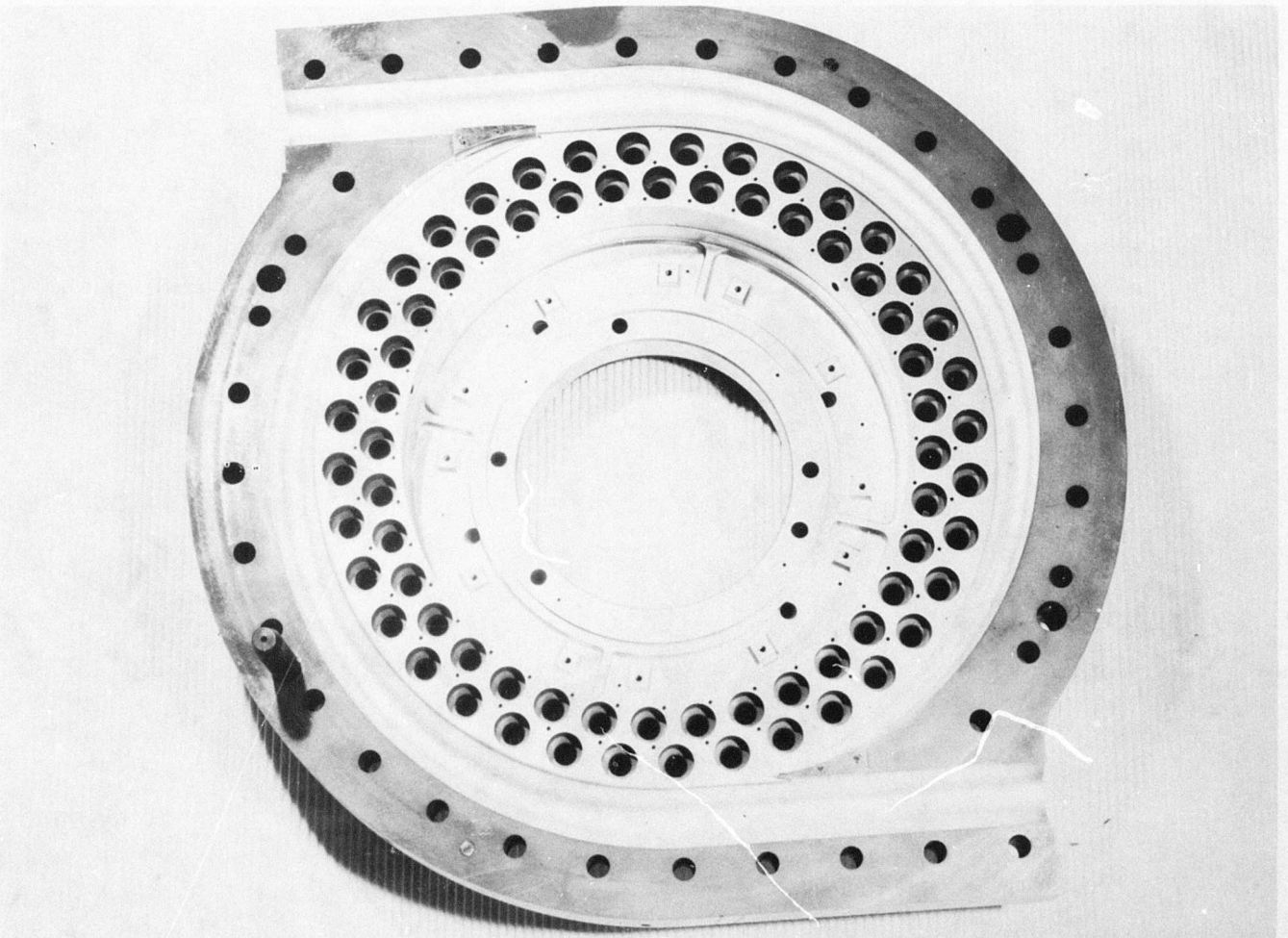

Figure 153. Internal View of Forward Compressor Stator Casing.

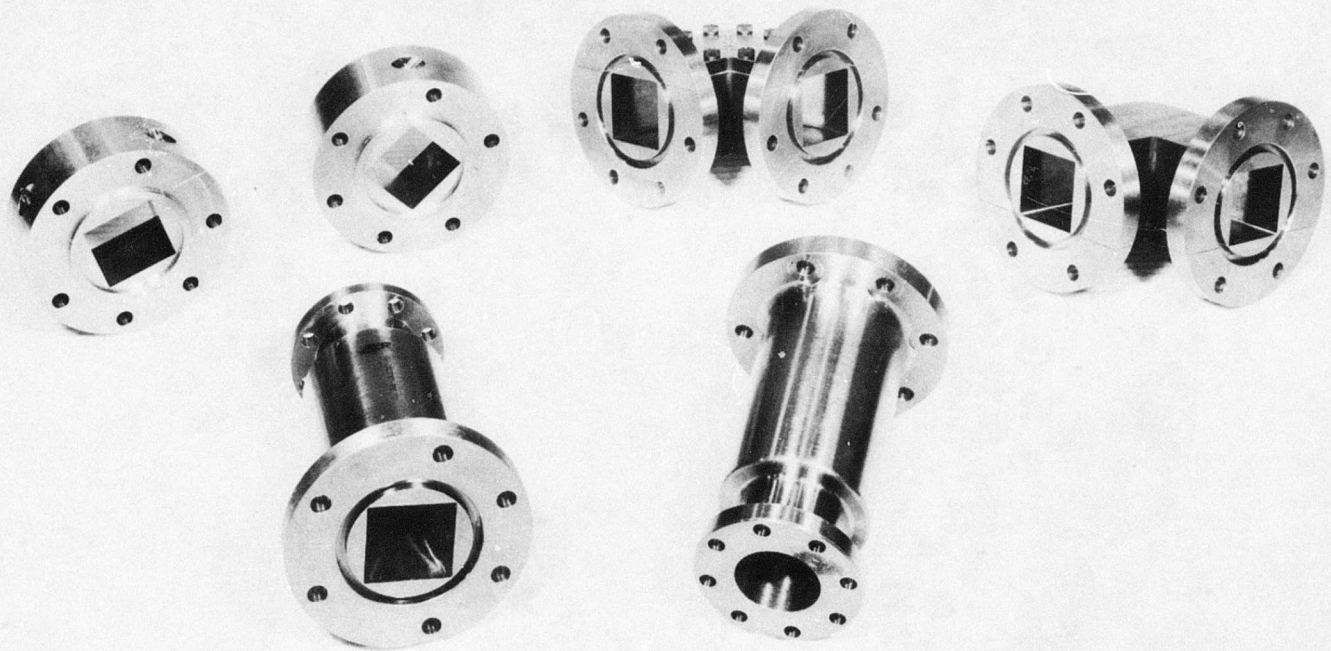

Figure 154. Compressor Exit Ducts and Elbows.

and the disc were assembled and balanced. The rotating centerbody was then attached to the disc and this group (Figure 155) was balanced. A very satisfactory matching of the rotor blades and the disc was obtained with minimum rework (Figures 156 and 157). The nature of the flame-sprayed surface necessary for attachment of strain gage leads can be seen in these figures. The partial assembly of all rotor blades and the disc shown in Figure 158 indicate the very high solidity of the rotor blades.

The fact that it was possible to install the rotating shroud (Figure 159) on all of the 44 long-shank and 44 short-pin rotor blades without rework is an indication of the very accurate blade-to-blade spacing which was achieved. Photographs of the assembled rotor are shown in Figures 160, 161, and 162.

Installation of the Test Vehicle in the Cell

Assembly of the gearbox housing, the high-speed bearing housing, and the compressor rotor is shown in Figure 163. A photograph of the high speed compressor after installation of the compressor stator casings and instrumentation is shown in Figure 164.

ROC INSTRUMENTATION

Introduction

The purpose of the ROC instrumentation is to provide sufficient information to:

1) Evaluate the compressor performance.

2) Aid in locating and diagnosing mechanical and aerodynamic deficiencies.

3) Insure that the compressor is operated within prescribed safe limits.

The fulfillment of the instrumentation function, in general, entails both a data collection operation and a data reduction operation. The data collection operation ordinarily consists of 5 steps:

1) Definition of parameter to be monitored and the region of interest.

2) Definition of a suitable "signature" which may be monitored if it is not possible to monitor the parameter directly, either because of its nature or its location.

3) Measurement of the signature (or the parameter directly) in terms of a transmittable signal.

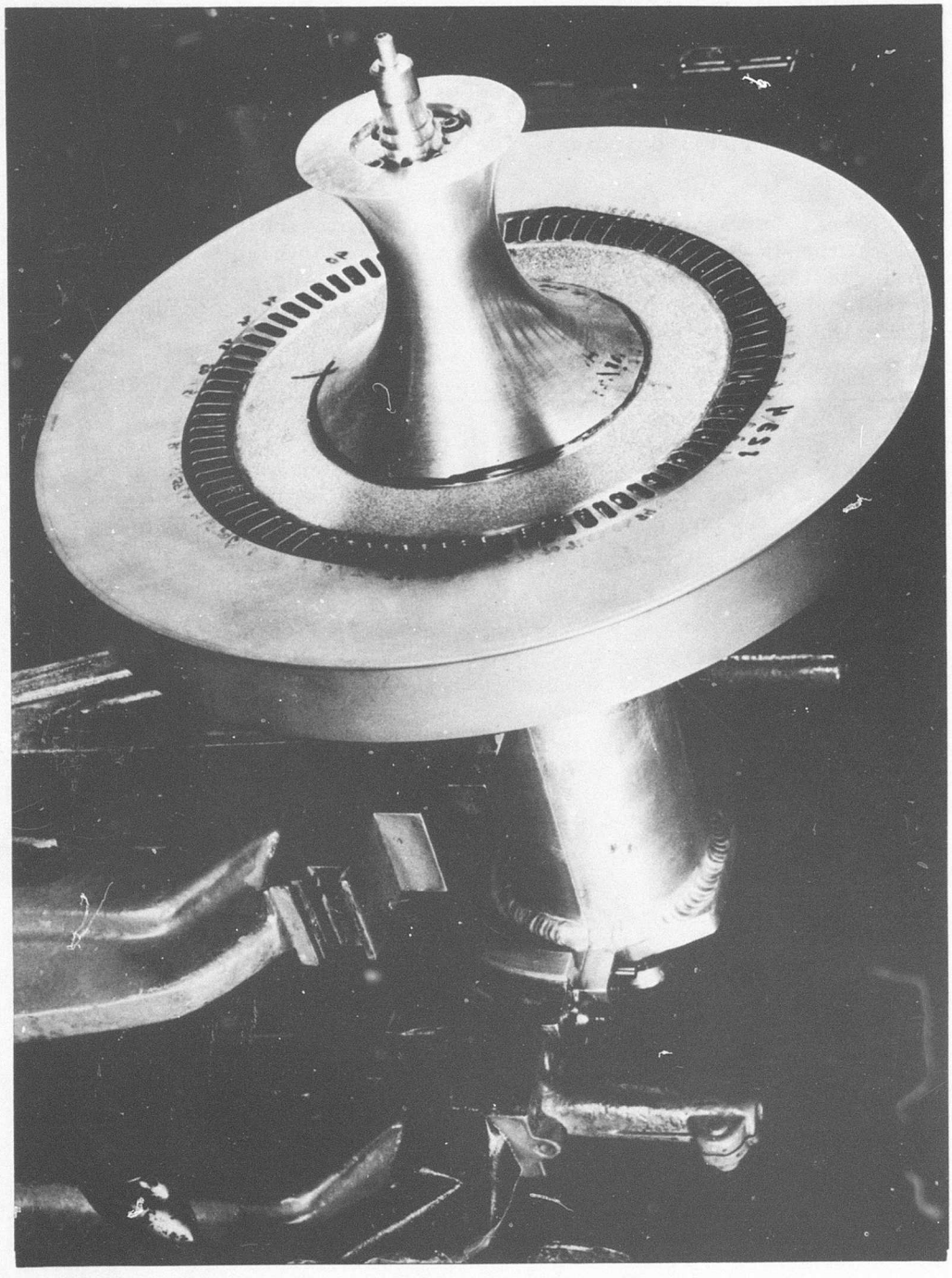

Figure 155. Assembly of Rotor Disc and Rotating Centerbody Mounted on the Balancing Machine.

Figure 156. Trial Assembly of Alternate Long Shank and Short Pin Rotor Blades in Rotor Disc.

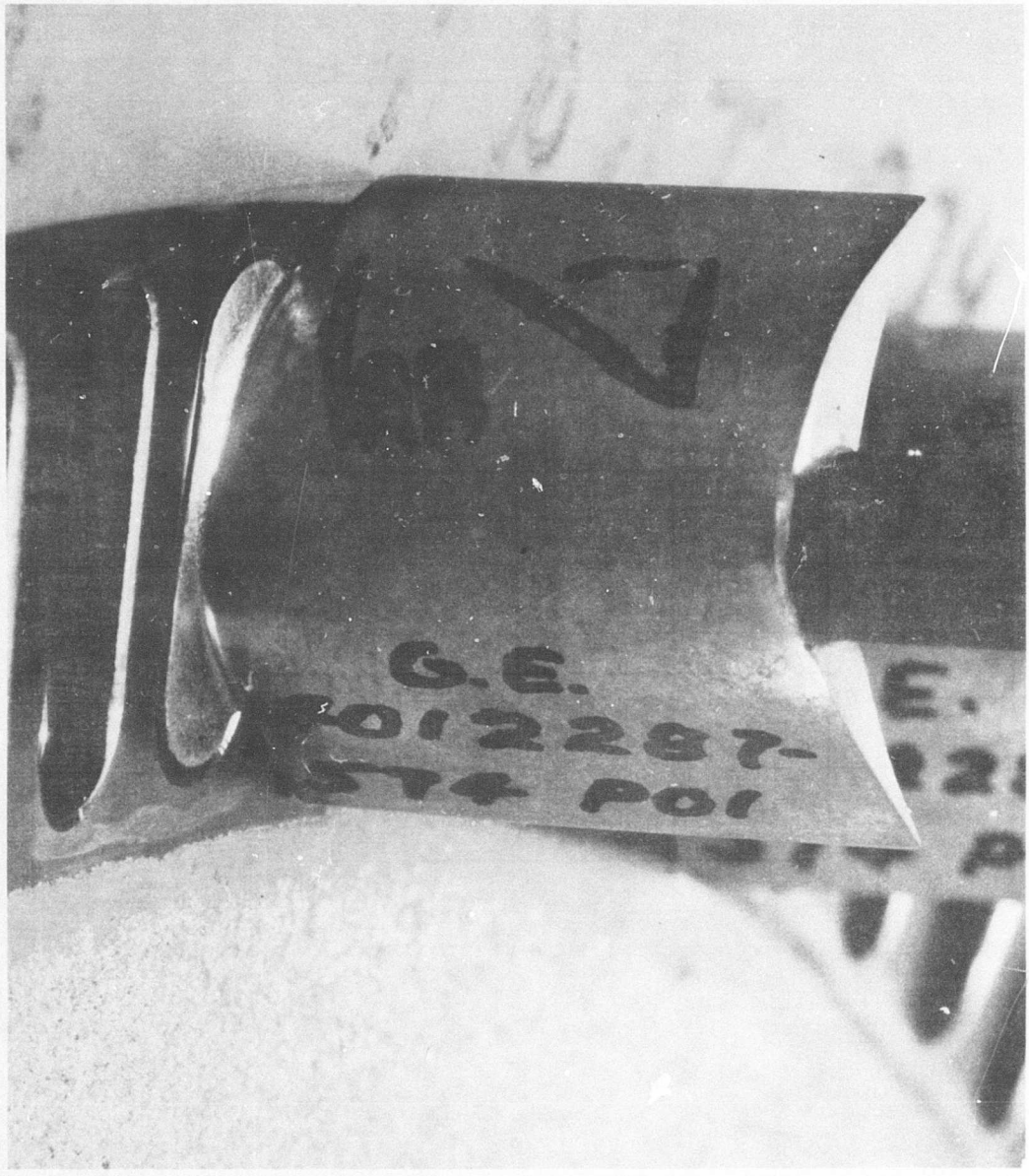

Figure 157. Close-up of Long Shank Rotor Blade Seated in Rotor Disc.

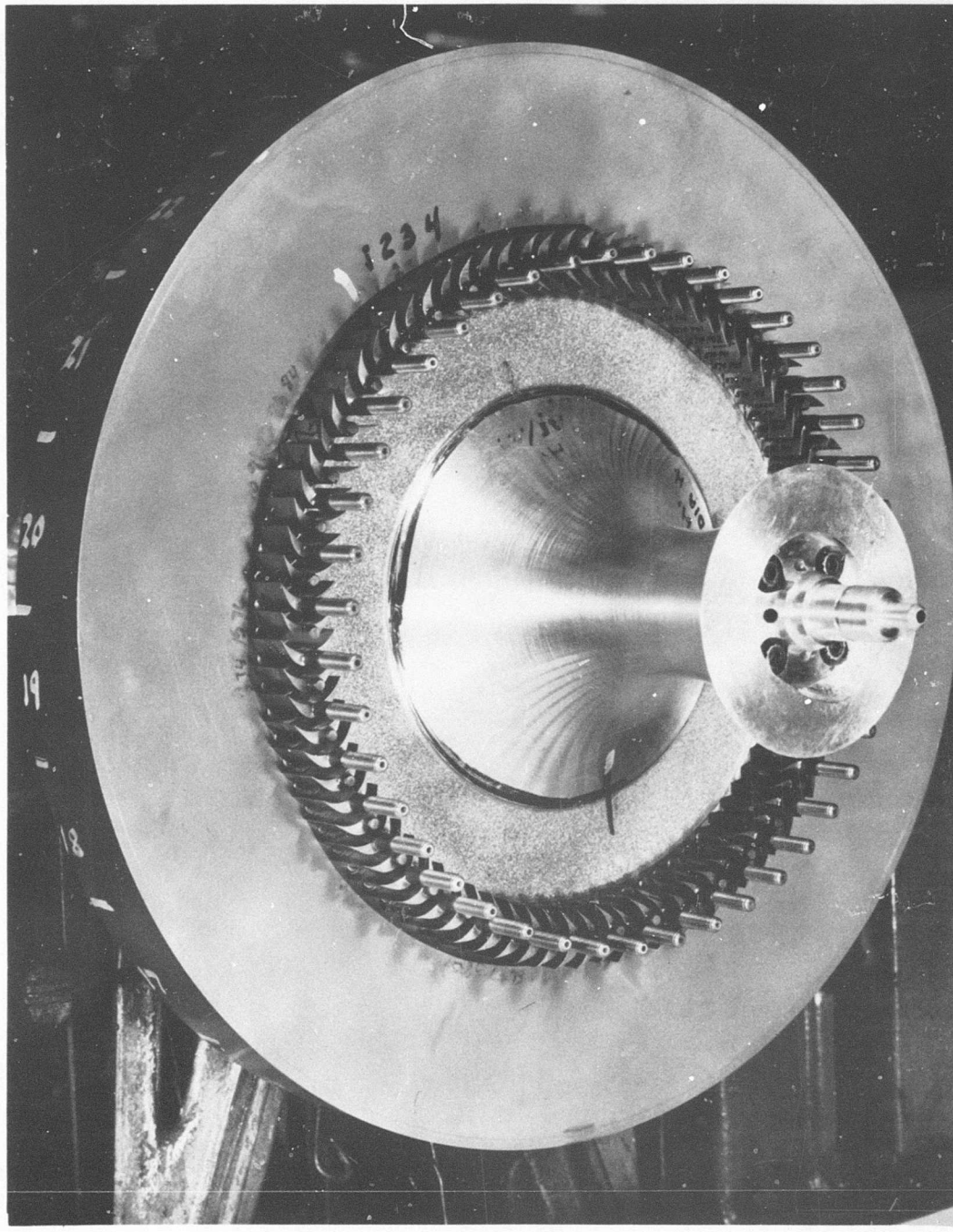

Figure 158. Preliminary Assembly of Rotor Disc Blades and Centerbody.

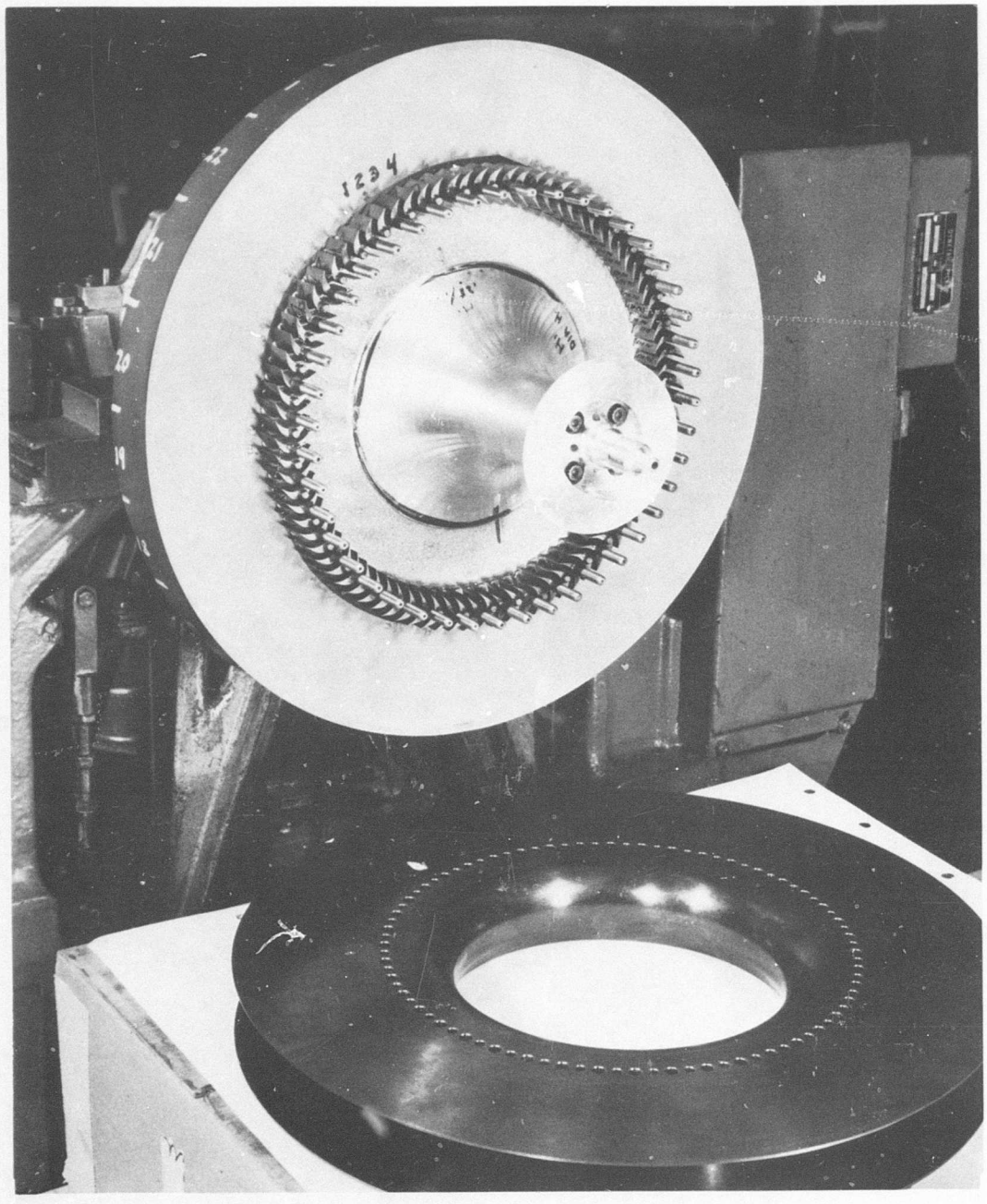

Figure 159. High-Speed ROC Rotor Prior to Assembly of Rotating Shroud.

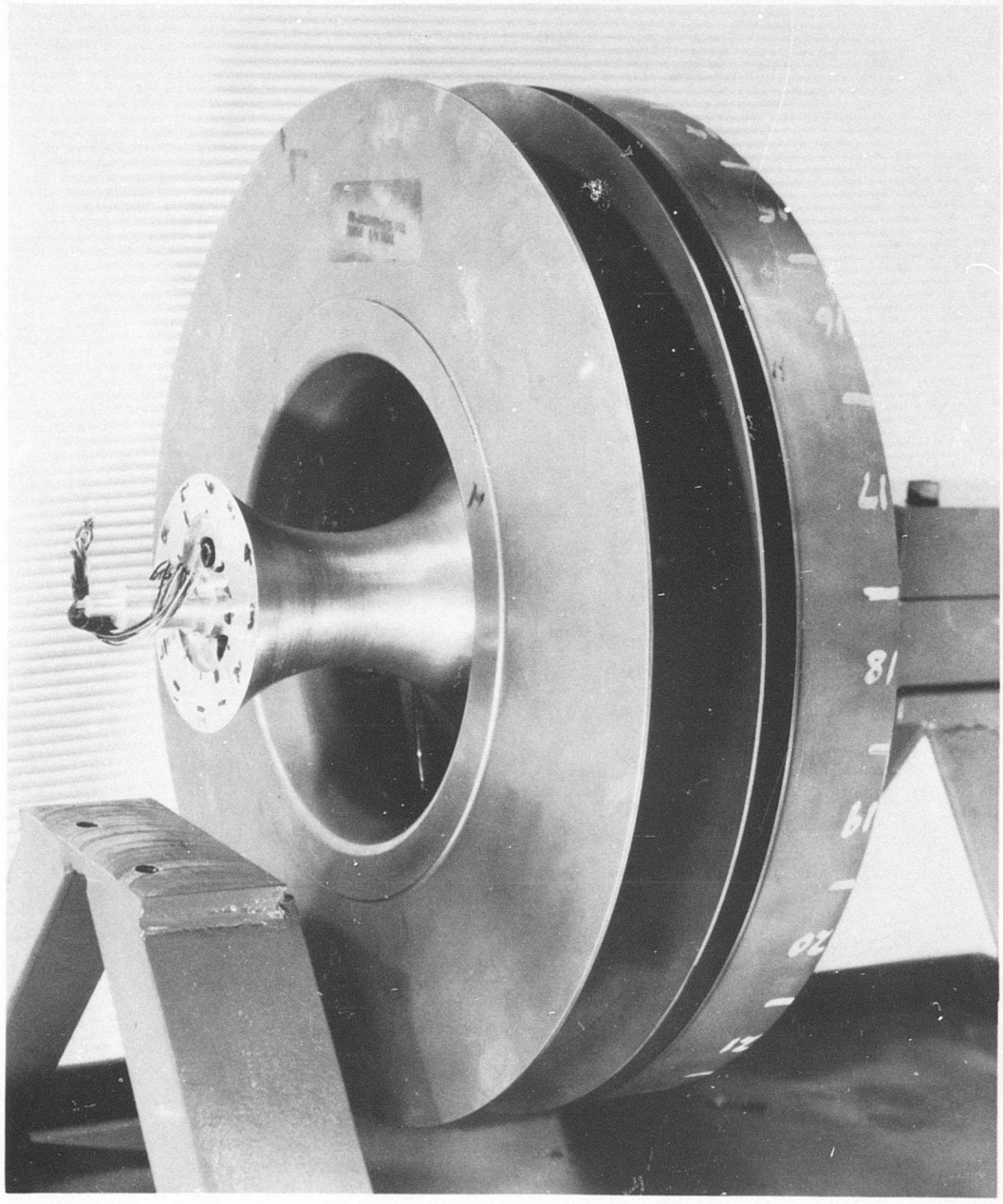

Figure 160. Inlet Side of Assembled Rotor.

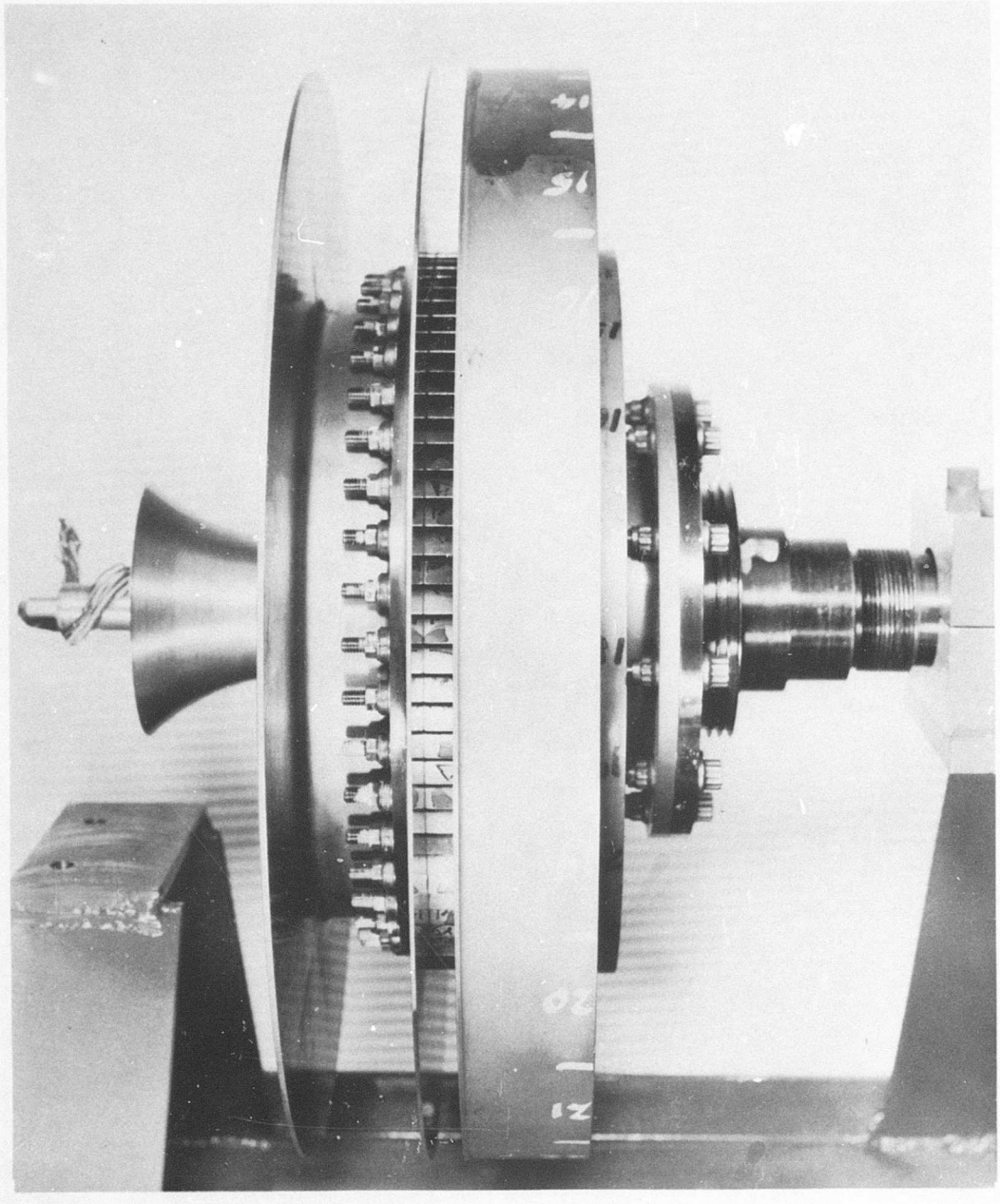

Figure 161. Exit of Assembled Rotor.

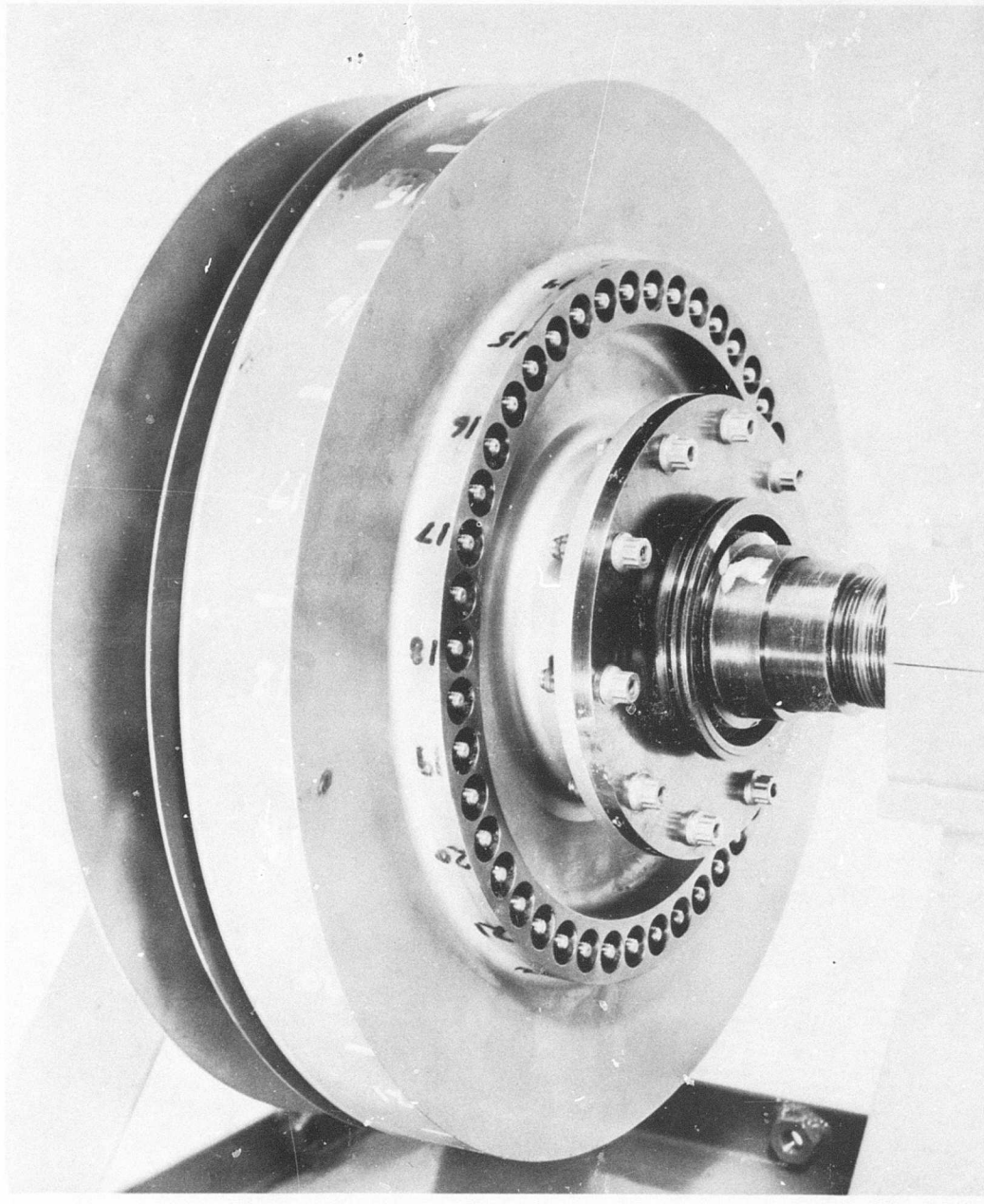

Figure 162. View of Assembled Rotor and Shaft.

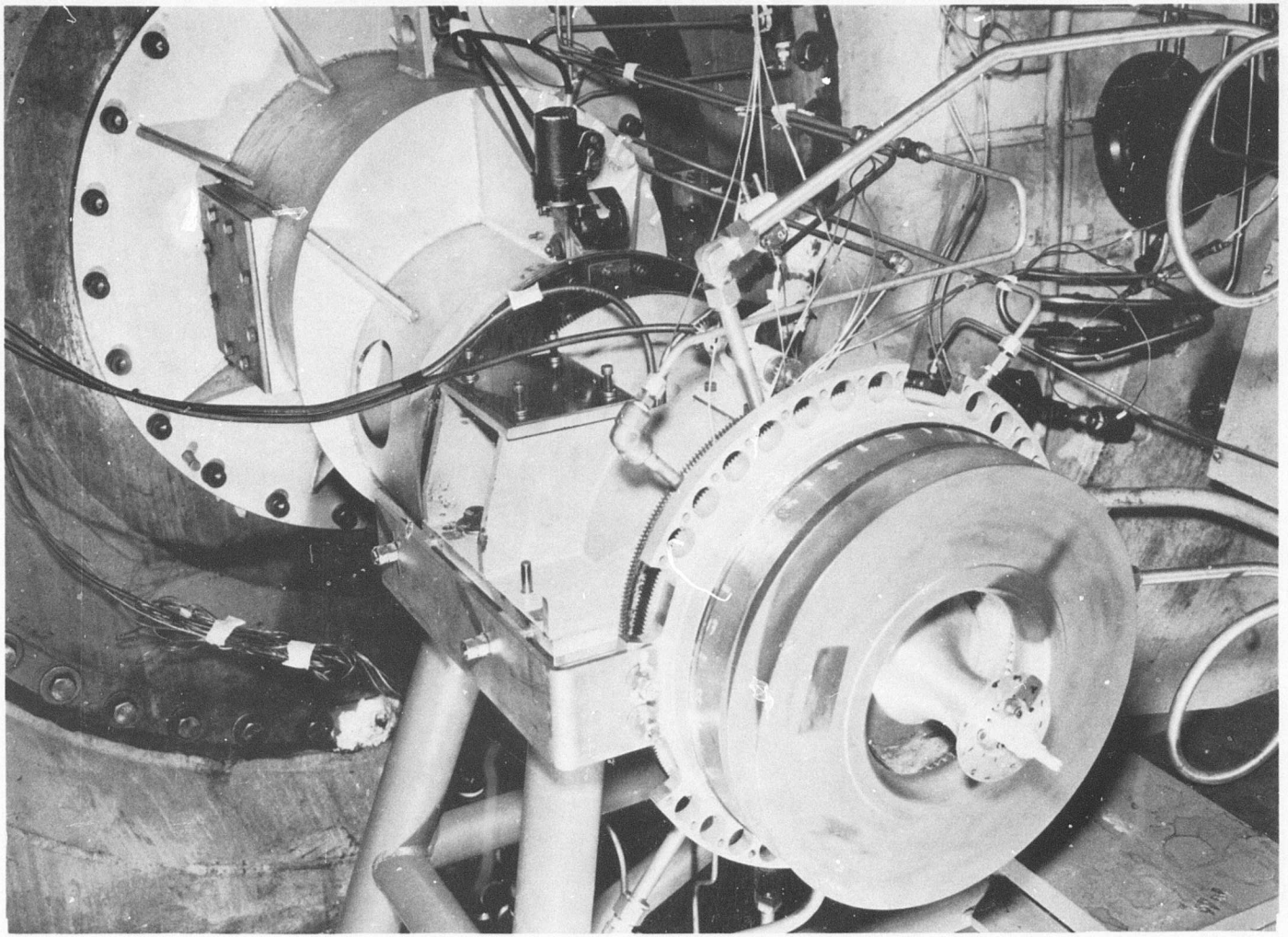

Figure 163. High-Speed Test Vehicle Installed in Cell.

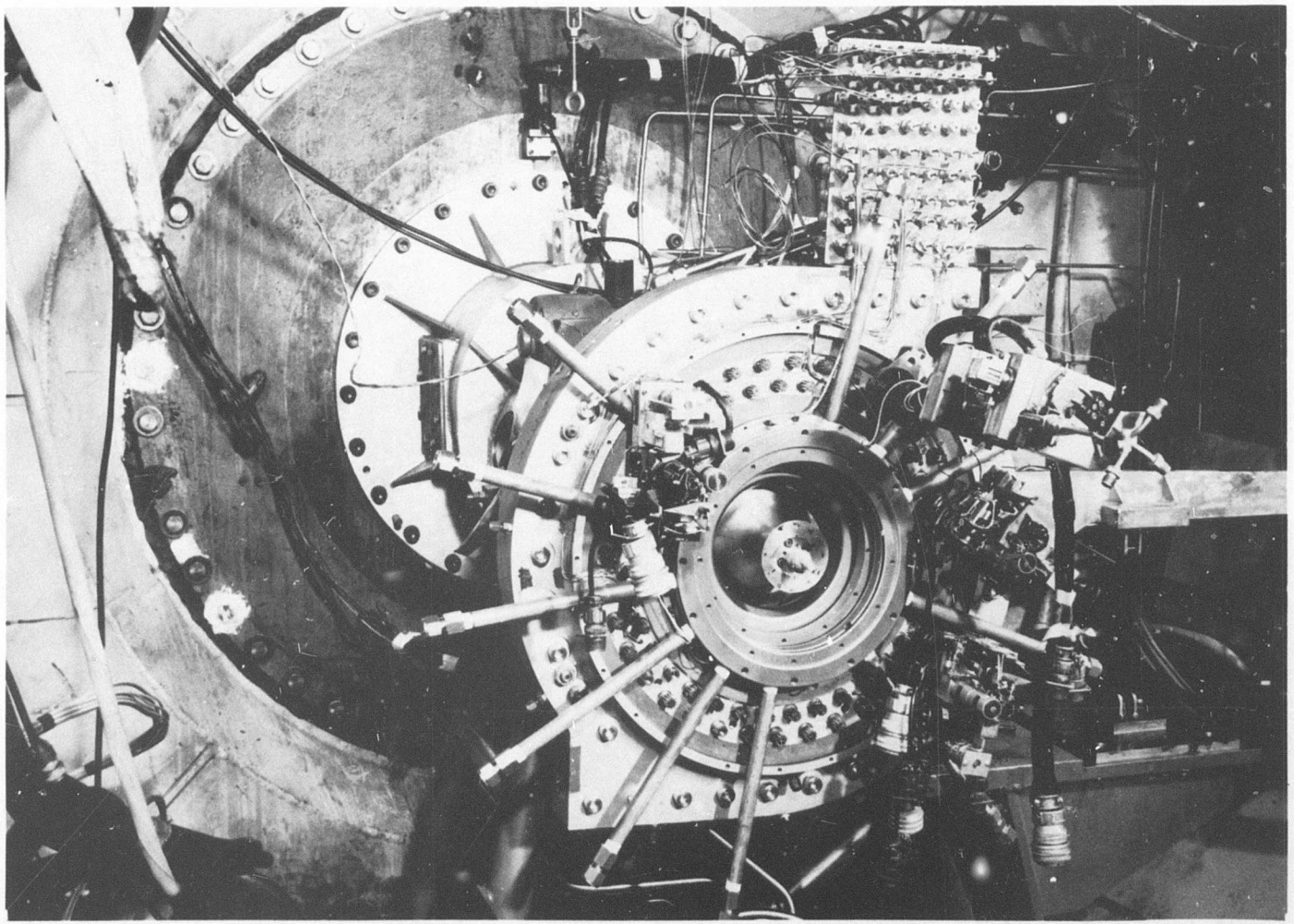

Figure 164. Stator Casing Showing Location of Traverse Instrumentation Installed in Test Cell.

4) Transmission of the signal to the display station.

5) Display of the signal by means of a suitable readout device.

The data reduction operation entails:

1) Compensating for bias introduced by the transmission system or the display system (relating value on readout device to transducer signal).

2) Relating the transducer signal to the value indicated (requires transducer characteristic curves).

3) Relating the value of the signature to the value of the parameter in the region of interest (in most cases an attempt is made to determine the value that the parameter would have had if the instrumentation were not in place).

4) Comparing the value of the parameter measured with other parameters to evaluate the significant system variables (efficiency, thermal distribution, stress levels).

Data Collection Rotating Diffuser and Supersonic Stator Exit

On the basis of the final hardware designs, the original fixed position instrumentation at the rotating diffuser exit and at the supersonic stator exit was replaced by traversable instrumentation.

The diffuser exit survey used a combination total pressure and yaw angle probe (3 tubes) supported from supersonic stator spindles. The sensor was placed at the rotating diffuser exit. The total temperature measurement used a 5-element axial rake of unshielded thermocouples located at the supersonic stator centerline. The static pressures were measured just outside the rotating diffuser exit by means of 8 circumferentially placed static pressure taps in the stator casing.

The supersonic stator exit will employ both the yaw and temperature probes described above using the subsonic stator spindles (this can be done, since the stator casing holes for the supersonic and subsonic spindles are identical). In addition, a 9-element total pressure rake (radial orientation) will be used to evaluate the supersonic stator wake. This element will be traversable in the axial direction. Static pressure will be obtained using 8 circumferentially spaced taps in the stator casing.

Data Reduction: Calculation of Compressor Adiabatic Efficiency

Introduction

Two efficiency parameters will be used to monitor the ROC performance during test. The first, the aerodynamic efficiency, does not include the losses due to windage, bearing friction, etc; the second, the mechanical efficiency, includes these effects. The former is used for the ROC target performance. The equation for these 2 efficiencies is given below:

$$\eta_A = \frac{H_{2i} - H_1}{H_2 - H_1} \tag{11}$$

$$\eta_M = \frac{H_{2i} - H_1}{\left(\frac{2\pi NT}{60Jw}\right)} \tag{12}$$

where H_1 = specific total enthalpy at inlet (Btu/lb)

H_2 = specific total enthalpy at exit of station under observation

H_{2i} = isentropic specific total enthalpy from inlet to station under observation based on measured pressure ratio

w = compressor mass flow (lb/sec)

T = shaft torque (ft-lb)

N = shaft rotation speed (rpm)

J = conversion factor (778 ft-lb/Btu)

The terms $(H_{2i} - H_1)$ and $(H_2 - H_1)$ may be determined from Reference 4, or if perfect gas with constant properties is assumed, from the expressions

$$T_{2i} - T_1 = T_1 \left[\left(\frac{P_{t2}}{P_{t1}}\right)^{\frac{\gamma-1}{\gamma}} - 1 \right] \tag{13}$$

$$H_{2i} - H_1 = C_{p_1} (T_{2i} - T_1) \tag{14}$$

$$H_2 - H_1 = C_{p_2} (T_{2i} - T_1) \tag{15}$$

In this case, the aerodynamic and mechanical efficiencies become

$$\eta_A = \frac{C_{p_1} T_1 \left[\left(\frac{P_{t2}}{P_{t1}} \right)^{\frac{\gamma-1}{\gamma}} - 1 \right]}{C_{p_2} (T_2 - T_1)} \tag{16}$$

$$\eta_M = \frac{T_1 C_{p_1} \left[\left(\frac{P_{t2}}{P_{t1}} \right)^{\frac{\gamma-1}{\gamma}} - 1 \right]}{\frac{2\pi NT}{60Jw}} \tag{17}$$

An investigation was made to determine the sensitivity of both efficiencies to the accuracy of measurement of the parameters involved in equations 16 and 17. For this investigation, the following "exact" values of the parameters were chosen as being representative of what could be expected in test:

$T_1 = 520^{\circ}R$

$T_2 = 1159^{\circ}R$

$P_{t1} = 1$ atm

$P_{t2} = 12.7$ atm

$w = 4.91$ lb/sec

$N = 34{,}500$ rpm

$T = 186$ lb-ft

$$\eta_A = 84.8$$

$$\eta_M = 83.0$$

$$C_{p_1} = 0.2438$$

$$C_{p_2} = 0.2451$$

$$\gamma = 1.3928$$

These C_p need not be the same if average properties are assumed, since their respective temperature ranges $(T_{2i} - T_1)$ and $(T_2 - T_1)$ differ.

The results are shown in Tables VIII and IX.

Effect of Non-Constant Fluid Properties

As can be seen from Tables VIII and IX, the efficiency calculations are very strongly affected by the choice of fluid properties. In general, it will be most convenient to consider the ratio of specific heats, γ, to be a function of inlet total temperature, compressor pressure ratio, and inlet air relative humidity. The constant-pressure specific heat can most conveniently be considered a function of inlet temperature, exit temperature (actual or isentropic), and inlet air relative humidity.

The proper values of γ (average) and C_p (average) for use in equations 16 and 17 were derived using Reference 4 as a calculation, and as yet do not include the effects of humidity. From these curves, it was determined that γ (average) and C_p (average) could satisfactorily be represented by the analytical expressions given below:

$$\gamma = 1.14116 + 0.008\ P - (0.0022 + 0.00027\ P)\ \frac{T_1}{100} \qquad (18)$$

$$C_p = 0.2395 + 0.0094\ \left(\left(\frac{T_2}{1000}\right) - 0.4\right)^2 + 0.006\ \left(\left(\frac{T_1}{1000}\right) - 0.5\right) \qquad (19)$$

Effects of Static and Dynamic Profiles on Total Pressure

A second possible source of significant error in the efficiency calculations can occur because of errors in the evaluation of the exit total pressure. The accurate evaluation of this parameter at the rotor exit is complicated by the fact that it is associated with a

TABLE VIII. SENSITIVITY CHECK ON AERODYNAMIC EFFICIENCY CALCULATION

$$\eta_A = \frac{C_{p1}\, T_{t1}\left[\left(\frac{P_{t2}}{P_{t1}}\right)^{\frac{\gamma-1}{\gamma}} - 1\right]}{C_{p2}\left(T_{t2} - T_{t1}\right)}$$

$$\eta_A = \frac{(0.2438)\ (520)\left[\left(\frac{12.7}{1}\right)^{\frac{1.3928-1}{1.3928}} - 1\right]}{(0.2451)\ (1159 - 520)}\ (100)$$

$$\eta_A = 84.8 \text{ Percent}$$

Parameter	Exact Value	Assumed or Measured Value	Change in Parameter	Change in Parameter (Percent)	Change in Efficiency (Percent)
T_{t1}, ^{o}R	520	521.04	+1.04	0.2	+0.309
T_{t2}, ^{o}R	1159	1156.1	+2.9	-0.25	+0.385
P_{t1}, inch Hg	29.921	29.891	-0.03	-0.1	+0.047
P_{t2}, atm	12.7	12.827	0.127	1.0	+0.470
γ	1.3928	1.4	0.0072	0.5	+1.570
C_{p1}	0.2438	0.24	0.0038	1.5	+1.28
C_{p2}	0.2451	0.24	0.0051	2.1	-1.78

TABLE IX. SENSITIVITY CHECK ON MECHANICAL EFFICIENCY CALCULATION

$$\eta_M = w\, C_{pl}\, \frac{T_{t1}\left[\left(\frac{P_{t2}}{P_{t1}}\right)^{\frac{\gamma-1}{\gamma}} - 1\right]}{\left(\frac{2\pi}{60J}\right)\tau N} \quad (100)$$

$$\eta_M = \frac{(4.91)\ (0.2438)\ (520)\left[\left(\frac{12.7}{1}\right)^{\frac{1.3928-1}{1.3928}} - 1\right]}{\left(\frac{2 \times 3.14}{60 \times 778.2}\right)\ (186)\ \ (34{,}500)} \quad (100)$$

η_M = 83.0 Percent

Parameter	Exact Value	Assumed or Measured Value	Change in Parameter	Change in Parameter (Percent)	Change in Efficiency (Percent)
T_{t1}, ^{o}R	520	521.04	+1.04	0.2	+0.166
P_{t1}, inch Hg	29.921	29.891	-0.03	-0.1	+0.046
P_{t2}, atm	12.7	12.827	0.127	1.0	+0.460
τ, lb-ft	186	185.1	-0.9	-0.5	+0.440
N, rpm	34,500	34,465	-35	-0.1	+0.083
γ	1.3928	1.4	0.0072	0.5	+1.54
C_{pl}	0.2438	0.24	0.0038	1.5	+1.25
w, lb/sec	4.91	4.935	0.025	0.5	+0.420

time unsteady circumferential total pressure profile. An axial total pressure profile due to the rotating diffuser wall boundary layer will also exist. The unsteadiness of the total profile is due to the fact that the total pressure probe is stationary with respect to moving rotor blade wakes. Since a total pressure probe with sufficient dynamic response to permit measurement of the unsteady profile is not available, this source of error in the total pressure measurement cannot be monitored. If one extrapolates from the results of the low-speed wake diffusion tests, there is a good chance that the blade wakes in the high-speed machine will be strongly attenuated at the rotating diffuser exit. In any case, the total probe will read a time averaged pressure rather than a mass averaged pressure; hence, the calculated efficiency will be conservative.

Since continuous total pressure traverses in the axial direction will be possible, a mass averaged total pressure based on the time averaged profile is possible. In any case, if an area averaged total pressure is used in place of mass averaged pressure, the efficiency calculation will again be conservative. Whether a mass averaged or an area averaged pressure in the efficiency calculation is used will depend on the calculation method employed.

Study of Available Computation Techniques

Four methods for calculating compressor efficiency are available at the present time:

1) Slide rule (during testing - intermittent).

2) Analog computer (during testing - continuous).

3) Data net (digital - during testing - intermittent).

4) High speed digital (off test - batch).

Each calculation method differs in its ability to account for the effects described previously:

1) Steady fluid property profiles (area averaged versus mass averaged).

2) Unsteady fluid property profiles (time averaged versus mass averaged).

3) Non-constant fluid properties.

A rough summary of the apparent abilities of each technique is shown in Table X. The methods used for data analysis are presented in Appendix VI.

TABLE X. REVIEW OF COMPUTATIONAL CAPABILITIES

	Time	Type	Static Profile	Dynamic Profile	Fluid Properties
1. Slide Rule	D	I	A	T	G
2. Analog	D	C	A	T	F
3. Data Net	D	I	M	T	AA
4. High Speed Digital	O	B	M	M	G

Legend

A = Area average
B = Batch
C = Continuous
D = During test
F = Fixed
G = Gas tables or graph
I = Intermittent
M = Mass average
O = Off time
T = Time average
AA = Analytic approximation

Test Vehicle Rotor Components

The axial motions of the outer edge of the rotating shroud were measured using 2 Bently Nevada proximeter sensors. These devices were used to measure running clearances. They have adequate frequency response to detect all expected vibrational modes of the shroud edge. Calculations of the shroud stresses due to sinusoidal waves indicate that wave amplitudes of ± 0.010 inch will generate stresses of ± 7,500 pounds per square inch (psi). The resolution of the proximeter is stated to be approximately ± 0.001 inch, so that the presence of edge waves can be observed at low stresses in the material.

Station and Instrumentation Definitions

The general philosophy of ROC instrumentation has been discussed in the introduction on page 203. This discussion defined the parameters which will be evaluated to determine the ROC performance. The stations at which the measurements will be made are listed in Table XI and are shown diagrammatically in Figure 165, and the various parts of the compressor test vehicle are identified in Figure 166. A listing of the quantities measured at the above stations is given in Table XII. The first column of Table XII indicates the symbol which shall be used to designate the quantity. The second column indicates the number of probes or measurement heads which were used to collect the data. The 4 columns which follow indicate the particular buildup during which each specific measurement was required, and the last column briefly describes the quantity measured.

Instrumentation Sensors and Actuators

Sketches illustrating the probes used for making total pressure and angle surveys and total temperature measurements of the ROC rotor exit are presented in Figures 167 and 168. Supersonic flow occurs at this station, so high air loads are exerted on the instruments. The shanks pass through and are supported by spindles on each side of the flow passage. This arrangement is much stronger than single support and provides constant blockage or throttling at all immersion depths of the sensor.

The probes are mounted in L. C. Smith actuators. These actuators (Figure 169) permit variable immersion and rotation and provide indication of immersion depth and angular position of the instrument.

The Lebow slip ring assembly used to transfer electrical signals from rotor strain gages and thermocouples to stationary contacts was tested at the vendor's plant. A brief description of these tests and the very satisfactory results are presented in Appendix VII.

TABLE XI. ROC STATION DEFINITION

Station	Location
0	Tank condition or compressor inlet
0.05	Inlet screen inlet
0.1	Inlet screen exit
0.25	Inlet guide vane inlet
0.50	Inlet guide vane exit
0.75	Inlet duct
1.0	Rotor blade inlet
2.0	Rotor blade exit
3.0	Rotor exit (Rotating Diffuser)
4.0	Supersonic stator inlet
4.5	Supersonic stator passage
5.0	Supersonic stator exit
5.25	Subsonic stator inlet
5.50	Subsonic stator passage
6.0	Subsonic stator exit
7.0	Scroll inlet
7.25	Scroll centerline
7.50	Scroll outside diameter
7.75	Splitter lip
8.0	Diffuser
9.0	Elbow

Reference Figure 165

TABLE XII. ROC RESEARCH INSTRUMENTATION - PHASE II

Location and Identification	Number	Buildup A	Buildup B-C	Buildup D-E	Buildup F	Description
Pressures						
ΔPV-1	2	X	X	X	X	Venturi ΔP
UP_tV-1	2	X	X	X	X	Venturi upstream total
OP_s-1	6	X	X	X	X	Tank static pressure
0.25 P_t	4	X	X	X	X	Inlet guide vane inlet totals
0.25 P_s	8	X	X	X	X	Inlet guide vane inlet statics
*0.50 P_t	1				X	Inlet guide vane exit total pressure and angle
0.50 P_s	8				X	Inlet guide vane exit statics
0.75 P_s	2	X	X	X	X	Inlet duct static pressure
3.0 P_s	18	X	X	X	X	Rotor exit static pressure
*3.0 P_t	1	X				Rotor exit total pressure and yaw
4.0 P_s	6		X			Supersonic stator inlet
4.5 P_s	2	X	X	X	X	Supersonic stator passage static
*5.0 P_t	1	X	X			Supersonic stator exit total and yaw
*5.0 P_tR	1		X			Supersonic stator exit total rake
5.0 P_s	8	X	X	X	X	Supersonic stator exit statics
5.5 P_s	3		X	X	X	Subsonic stator passage static
*5.5 P_t	1	X	X			Subsonic stator spindle cobra
*6.0 P_t	1			X	X	Subsonic stator exit total rake

* Traversable instrumentation

X Required instrumentation

TABLE XII - Continued

Location and Identification	Number	Buildup A	Buildup B-C	Buildup D-E	Buildup F	Description
7.0 P_s	6	X	X	X	X	Scroll inlet statics
7.25 P_s	8			X	X	Scroll centerline statics
*7.25 P_t	1			X		Scroll centerline total and yaw traverse
7.5 P_s	2			X		Scroll outside diameter statics
7.75 P_s	7			X		Splitter lip statics
8.0 P_s	16			X	X	Diffuser wall statics
*8.0 P_t	15			X		Diffuser totals
9.0 P_s	8			X	X	Elbow statics
*9.0 P_t	15				X	Elbow exit totals
Additional Pressure Instrumentation						
UCV-ΔP	2	X	X	X	X	Upstream coolant flow orifice ΔP
UCV-P_t	1	X	X	X	X	Upstream coolant flow orifice total
DCV-ΔP	2	X	X	X	X	Downstream coolant flow orifice ΔP
DCV-P_t	1	X	X	X	X	Downstream coolant flow orifice total
DRPS-1	4	X	X	X	X	Disc rear static pressure (Radius - 425)
DRPS-2	4	X	X	X	X	Disc rear static pressure (Radius - 5.733)
UTV-T_t	3	X	X	X	X	Venturi upstream total
OT_t	2	X	X	X	X	Tank air temperature
0.05 T_t	4	X	X	X	X	Screen inlet total
3.0 T_t	1	X				Rotor exit total rake
5.0 T_t	1		X			Supersonic stator exit rake
*8.0 T_t	1	X	X	X		Diffuser exit totals rake
*9.0 T_t	1			X	X	Elbow exit totals rake

TABLE XII - Continued

Location and Identification	Number	Buildup A	Buildup B-C	Buildup D-E	Buildup F	Description
Additional Temperature Instrumentation						
UCV-T_t	2	X	X	X	X	Upstream coolant orifice total
DCV-T_t	2	X	X	X	X	Downstream coolant orifice total
DTT-1	2	X	X	X	X	Disc top thermocouple
DRT-1	2	X	X	X	X	Disc rear thermocouple
RTE-1	2	X				Rotor trailing edge thermocouple

Reference Figure 165

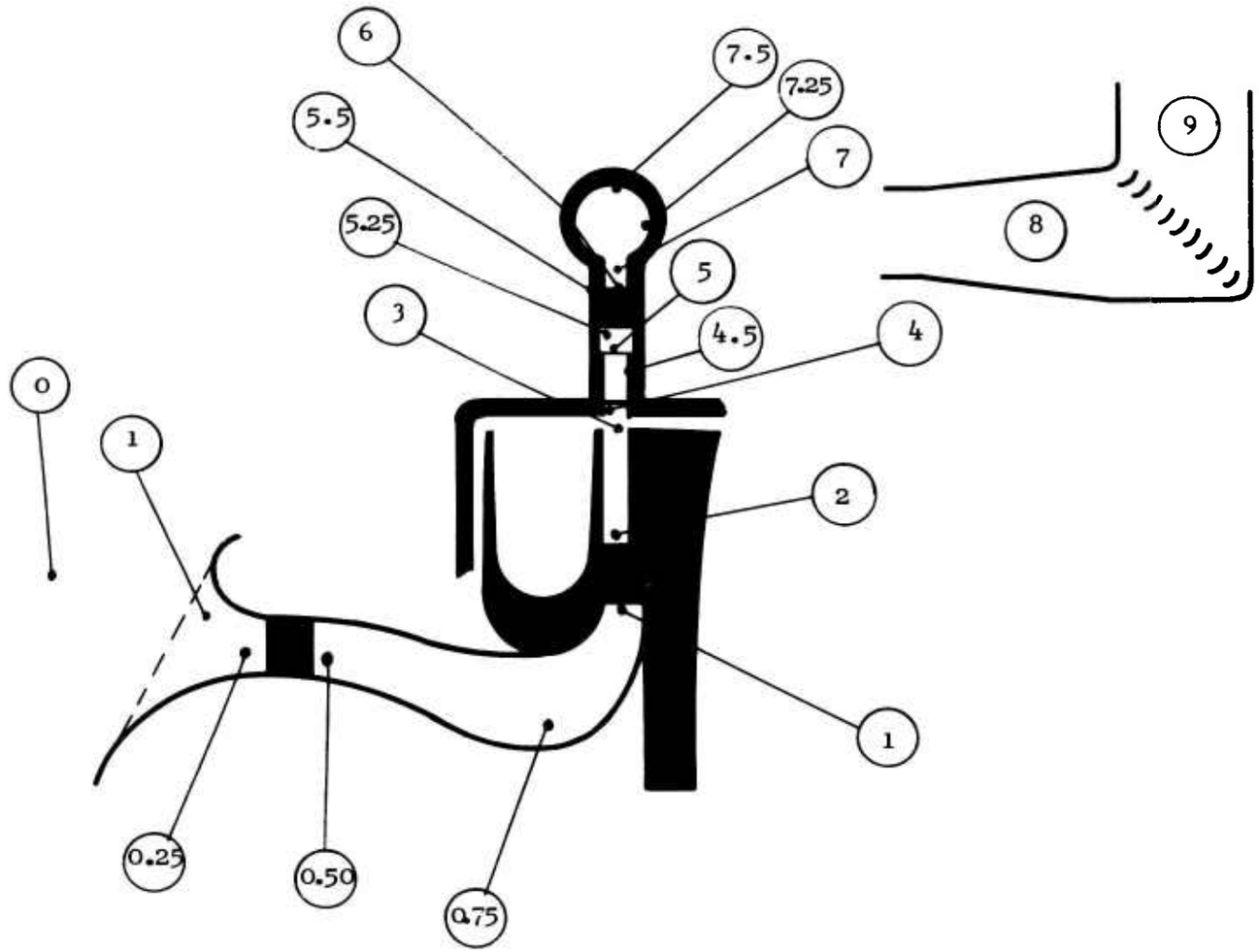

Figure 165. Sketch of High-Speed ROC Illustrating Location of Instrumentation Stations.

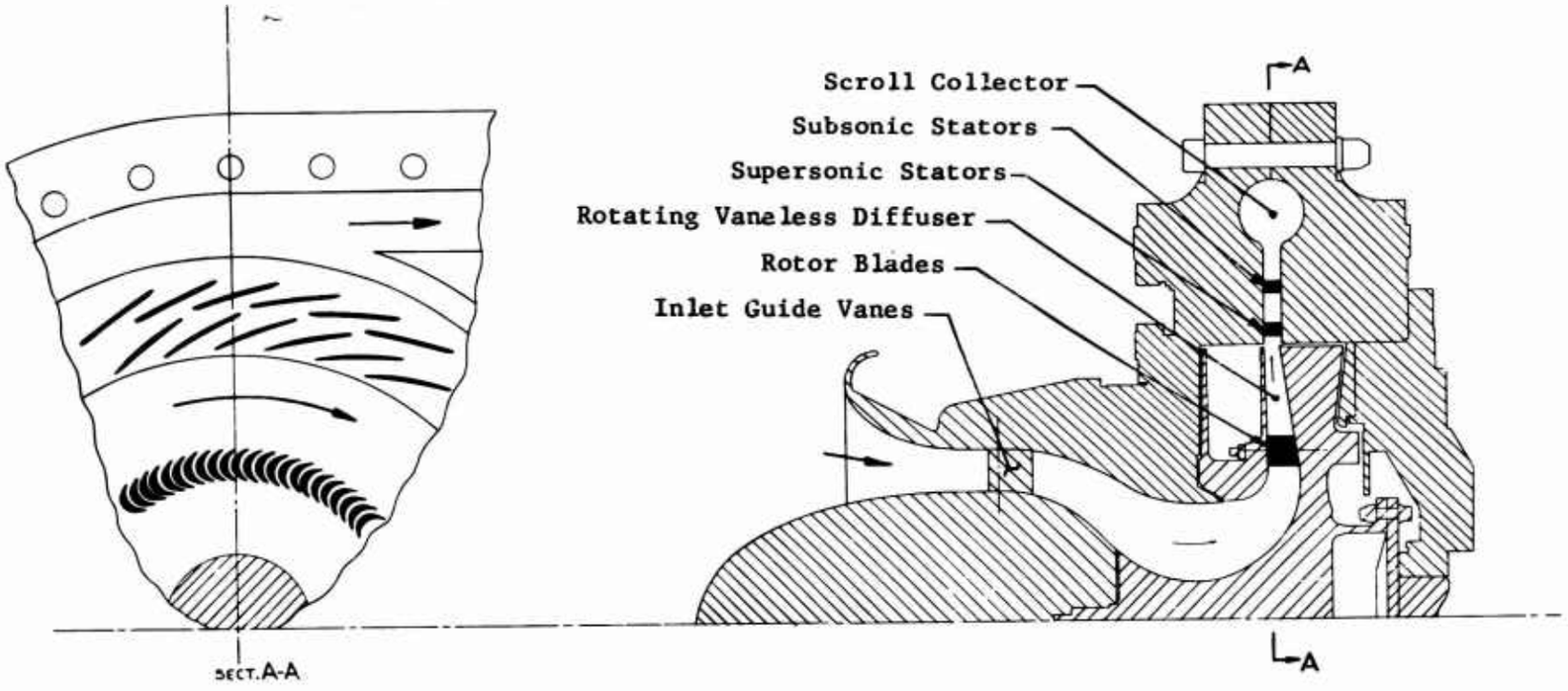

Figure 166. High-Speed ROC and Nomenclature of Various Parts.

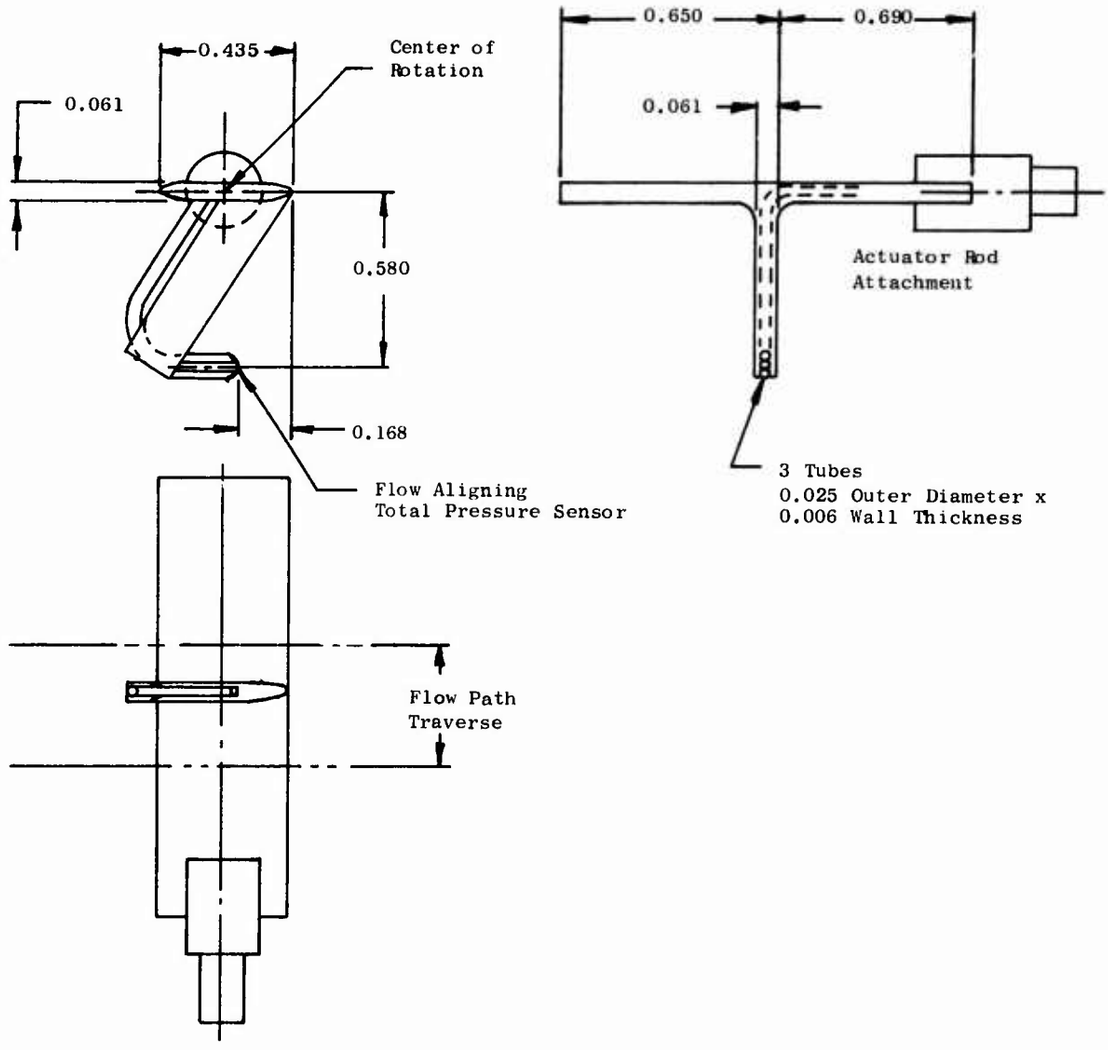

Figure 167. Details of Yaw and Total Pressure Probe Used in High-Speed ROC.

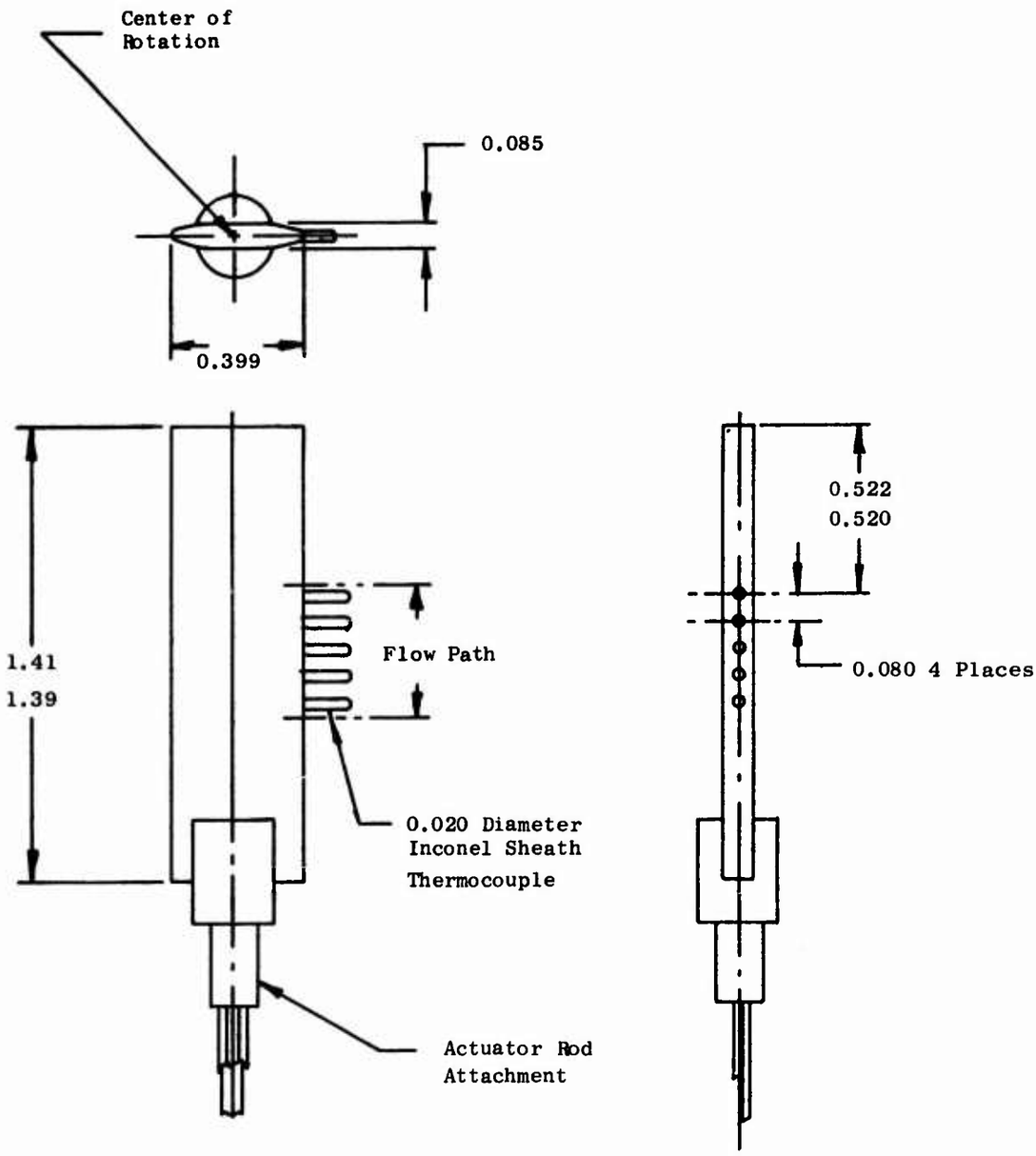

Figure 168. Details of 5-Element Temperature Rake Used in High-Speed ROC.

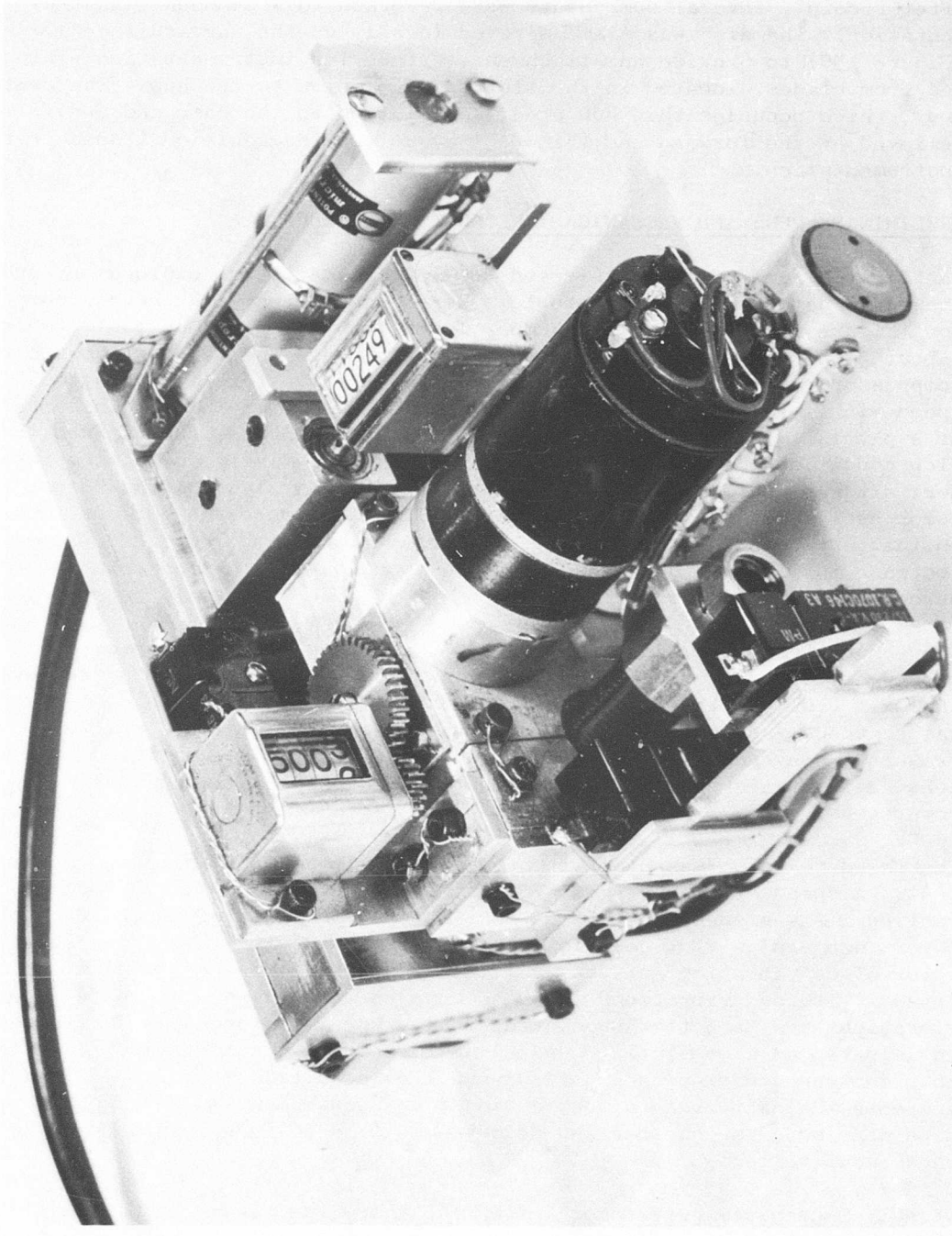

Figure 169. Probe Actuator - Typical of Those Used in High-Speed ROC Investigation.

After receipt, several components were reworked to accommodate instrumentation. The disc was flame sprayed locally on the forward face (Figure 155) to provide an attachment surface for instrumentation wiring led from blades, located in the slotted area, down to the hub. The centerbody, which occupies this hub area, was slotted on the base end and relieved at the forward end (Figure 158) to provide additional space for instrumentation.

PRELIMINARY RUNS AND MECHANICAL CHECKOUT OF BUILDUP A

The first 3 runs of the high-speed ROC were primarily of exploratory and shakedown nature as various problems were encountered with the new compressor (Figure 170). During Run Number 1, Buildup A, speeds up to 10,400 rpm (about 33 percent of design speed) were obtained. The airflow through the compressor was much lower than the calculated value for this rotational speed with inlet guide vanes set for zero degrees of turning. In spite of a partial mismatch between rotor and exit flow areas, the off-design flow conditions caused no significant vibration activity in the compressor. It was decided to employ an auxiliary exhaust system, the "booster compressor", having a pressure ratio of 1.4, to reduce the back pressure on the test compressor and permit higher airflows to be obtained. Some increase in flow was obtained by this method, but the design value of 30 percent speed could not be obtained.

The second test was made on May 5, 1966. Inlet guide vanes were reset closed at + 40 degrees to reduce airflow at a given rpm and thus relieve the exit flow problem. A maximum speed of 17,330 rpm (~50 percent speed) was reached. Again, no blade vibratory stresses above 1,000 psi were measured. Several points of low shroud vibration were identified, but were easily traversed during acceleration and deceleration of the compressor.

The third test run was made with the same configuration as in the previous test. A speed of 24,250 rpm (~70 percent speed) was reached. Rotor cooling air was used above 50 percent speed. In spite of the fact that lower than design flow coefficients were obtained with increasing speed, rotor blade vibration activity remained very low. However, medium intensity shroud vibrations were encountered near 70 percent speed. These vibrations are directly associated with aerodynamic forces and have been anticipated as a possibility under "disturbed flow" conditions. Rather than continue testing under off-design flow conditions, it was decided to increase the exit area to meet design flow requirements. This would permit more meaningful mechanical and aerodynamic data to be obtained from the subsequent tests.

Overall mechanical performance after the third run can be summarized as follows. The bearing and drive system performed smoothly with no observed critical speeds. Rotor balance and alignment were excellent and the rotor

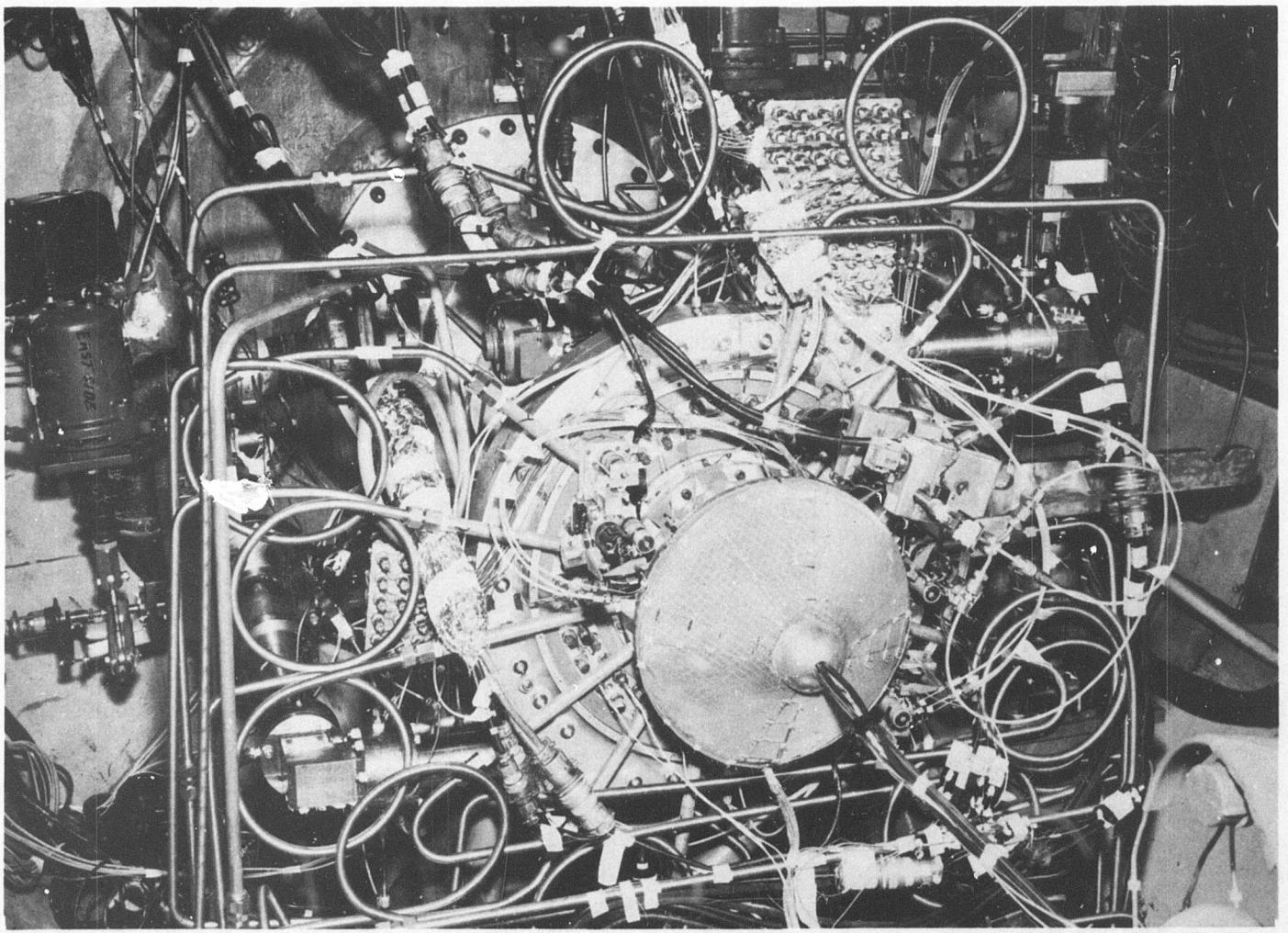

Figure 170. Assembly of High-Speed ROC Prior to Tests of Buildup A.

blades were noticeably resistant to vibration. Shroud vibration was observed, but appeared to be in very close agreement with predicted characteristics.

The compressor was operated for approximately 9 hours during these series of runs. Various difficulties were encountered with the analogue computer which had been programmed to compute and plot compressor air weight flow, pressure ratio, and efficiency during any particular run. The electronic device used to convert digital readout to engineering units was not functioning during this run. This prevented use of the program prepared for use with the locally placed console of a time-sharing computer system to average values and calculate performance quantities. Slide rule and desk calculator operations were employed to reduce manually observed data so that airflow and pressure ratio could be known.

Aerodynamic Results

The reason for the low airflow experienced during these early runs is that the ROC, like any high-pressure-ratio compressor, is designed with the exit system compatible for the high-speed, high-pressure-ratio case. In high-speed, high-pressure-ratio operation, the density ratio that is produced through the compressor is large and the exit area through the scroll arms is correspondingly small. As indicated in Appendix VIII, the Mach number leaving the exit arms of the compressor for design conditions was calculated to be 0.14. The exit area was set as large as possible within the expected static pressure rise limitations of the supersonic stators, the subsonic stators, and the scroll. At the same time, other operating conditions were investigated as shown in this appendix. It was found that the condition of zero inlet guide vanes and 60 percent speed with supersonic exit conditions from the rotor was not critical as far as choking in the exit arms is concerned.

It should be noted that several conditions are different from the ideal situation calculated and recorded in Appendix VIII. The first and most obvious difference is the absence of the supersonic and the subsonic stator blades. For the first buildup, these stator blades were omitted to permit placement of instrumentation close to the rotor exit in order to make accurate measurements of the rotor exit flow. In the absence of these stator blades, the exit system is much less efficient, and, in fact, the experimental evidence is that all of the dynamic pressure leaving the rotor is lost in the exit system between the rotor exit and the exit arms from the scroll. The low total pressure available to drive the flow through the exit arms restricts the flow through the compressor. Furthermore, the effect of the exit restriction on the airflow produces a relatively high static pressure downstream of the compressor rotor. Only the subsonic regime of flow leaving the rotor could be established. The total pressure ratio produced by this compressor is significantly higher with supersonic exit flow than with subsonic exit flow from the rotor. In the original buildup configuration, the

compressor was in a situation where it would produce more total pressure ratio and pump more flow if the static pressure downstream of the rotor could be reduced. Due to the restriction on the exit flow, the back pressure could not be reduced, and therefore, the total pressure produced was relatively low, although very close to the value calculated for subsonic flow leaving the rotor.

Using the data obtained during the first run, the weight flow which the compressor could be expected to pass under the restrictions of the exit area existing was estimated. From these calculations, it was concluded that design incidence angle into the rotor blades could be obtained at 33 percent speed if the inlet guide vanes were closed 40 degrees from the axial direction. For these test conditions, a weight flow of 1.22 pounds per second (pps) at a total pressure ratio of 1.28 was predicted. The inlet system was removed and the inlet guide vanes were set on the bench to a 40-degree-closed position. During Run Number 2, test readings were taken at approximately 16, 24, and 33 percent design speed using the booster compressor. As shown in Figure 171, the test points fell very close to the predicted line. At 33 percent speed, the maximum flow obtained was 1.23 pps with a total pressure ratio of 1.29. The rotor efficiency at this 40-degree-closed inlet guide vane setting was 89.6 percent, not including the total pressure drop across the inlet screen. When the rotor efficiency was corrected for the inlet screen total pressure drop, the rotor efficiency was calculated to be slightly above 90 percent. Since the rotor efficiency number includes the losses of the 40-degree-closed inlet guide vane system, the rotor blades, and the rotating diffuser, the value calculated is very encouraging.

Even more encouraging are the results of the total pressure and flow direction traverse which were taken at the rotor exit. These are shown in Figure 172. For this low-speed operating point, the calculated value expected on the angle traverse was about 75 degrees from radial. This number consists of the calculated angle of approximately 73 degrees plus 2 degrees calibration factor at the local Mach number of about 0.40. As shown in Figure 172, the average value observed was about 78 degrees. Only a small variation in flow angle is seen over 90 percent of the diffuser width. The total pressure traverse, also seen in Figure 172, is remarkably constant over 90 percent of the diffuser width. Sensitivity of the total pressure transducer was approximately 0.1 psi, so the constancy of the reading should be a true value. The uniformity of the exit flow in direction and total pressure is encouragement that the rotor was working as designed and that the inlet guide vane system was working satisfactorily at these conditions of 40 degrees inlet guide vane closure and 33 percent design speed.

At 33 percent speed, several weight flows were set by closing the compressor exit throttles. Airflows corresponding to angles and incidence of 3, 6, and 9 degrees were established without difficulty, and test points were

taken at these airflows. These points are indicated in Figure 171. A rough value of the rotor efficiency uncorrected for the inlet screen loss was 85 percent at the +9-degree incidence condition.

Test speeds of 40 and 50 percent were also set during this second run. In order to maintain low temperature gradients in the rotor disc and rotating shroud, cooling air was introduced into the chambers upstream and downstream of the rotor at these higher speeds. Due to the use of large seal clearances to prevent rubs during this run, a relatively large amount of cooling airflow, approximately 15 percent, was permitted to bleed into the compressor at 40 degrees and 50 percent speed. The points obtained are shown on Figure 171. It was not possible to obtain high enough airflow to accomplish design incidence relative to the rotor blades. The lowest incidence that could be obtained was +7.5 degrees at both 40 and 50 percent speed. It is likely that these values are close to stall of the compressor rotor blades. Nevertheless, total pressure ratios close to the calculated values were obtained for these test points. During 1 of the accelerations, a steady-state condition was attempted at 14,800 rpm. After several seconds of operation at this speed, the proximeters indicated that vibration of the outer rim of the rotating shroud was occurring, and the compressor was decelerated at this time to 40 percent speed (13,800 rpm). This critical speed of 14,800 rpm was traversed satisfactorily in accelerating to 50 percent speed.

A third run of the high-speed ROC was conducted. The test plan was to obtain data at 60, 70, and 80 percent speed. A satisfactory operating point at 60 percent speed was obtained, as shown in Figure 173. The weight flow pumped by the compressor was 1.8 pounds compared to the zero incidence value of 2.2 pounds at this speed. The total pressure ratio observed was about 2.15 as compared to the predicted value of about 2.04 at this rotor incidence angle (about +9 degrees) at 60 percent speed. The compressor was then accelerated to 24,200 rpm, which corresponded to 70 percent speed. The point was established with no indication of compressor vibration. After 90 seconds of steady-state operation at this speed, a change of the cooling airflow was made. This change caused a rapid buildup in shroud vibrations to an unacceptable value, and the compressor was decelerated rapidly.

Following inspection of the test vehicle and using the records available at that time, the compressor was reaccelerated to 65 percent speed and a test point was taken at that condition. The total pressure ratio observed was 2.6 at 65 percent speed, which is slightly greater than the value of 2.5 which was calculated for 70 percent speed. The airflow of about 1.94 pps corresponded to an incidence angle of about 9 degrees with respect to the rotor blades. The high pressure ratio obtained at this point indicates clearly that the compressor was not stalled. This was verified by the low blade vibration signal indicated by the strain gages. The observed value corresponded to maximum vibrational stresses of approximately $\pm$800 psi, a very low level for the materials used. Following the

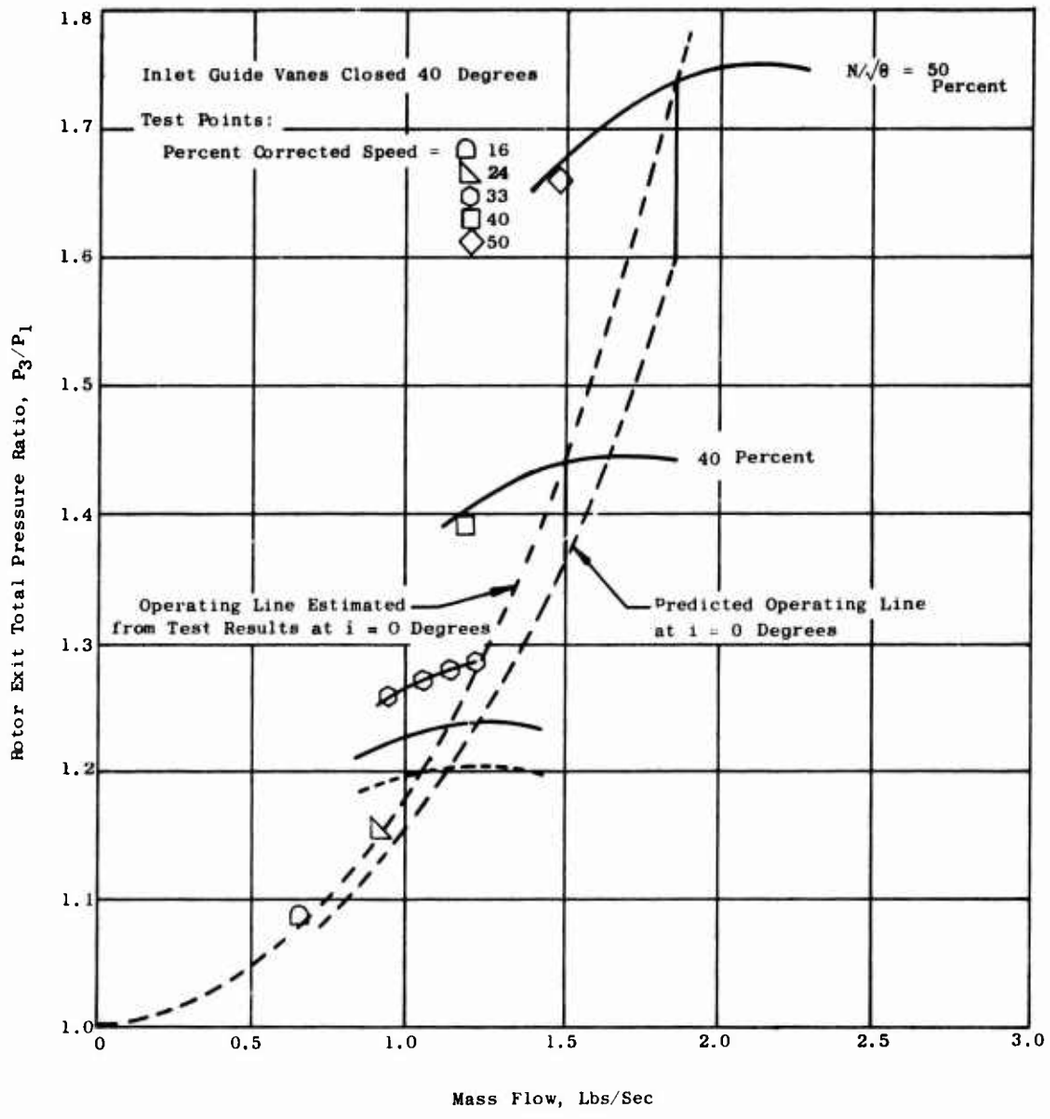

Figure 171. Comparison of Test Results With Predicted Performance for Run Number 2, Buildup A.

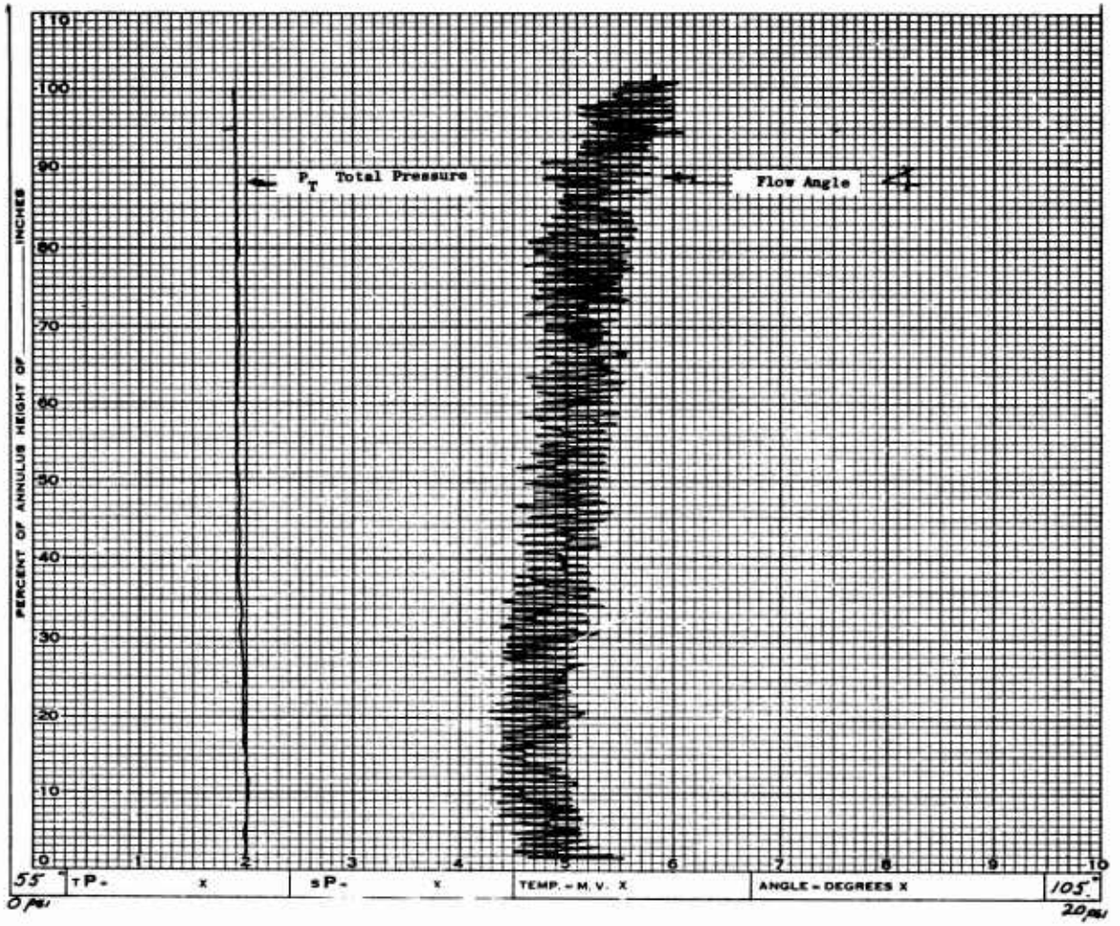

Figure 172. Traverses of Flow Angle and Total Pressure for Run Number 2, Reading Number 18, at Rotor Exit (Station 3) at 33 Percent Speed.

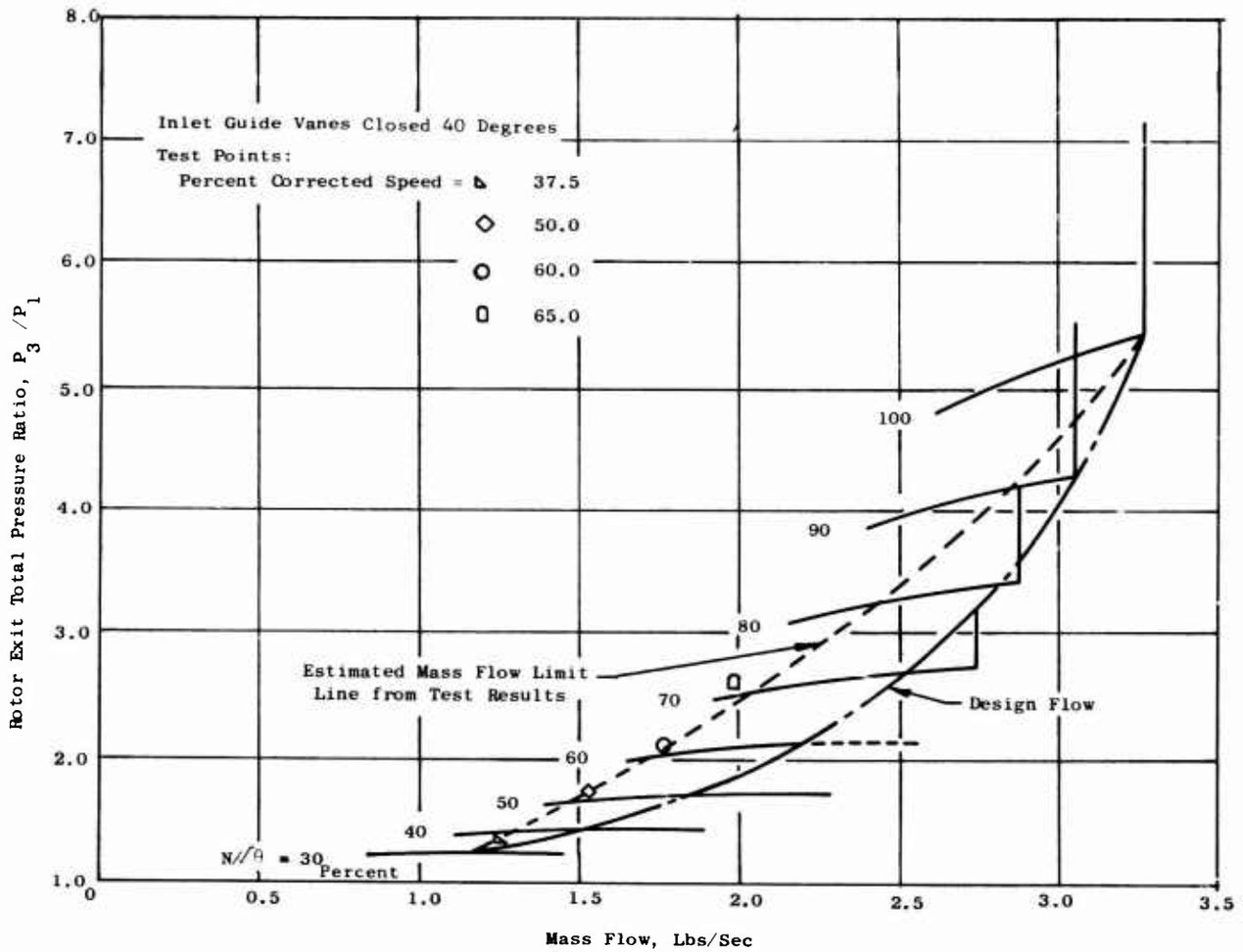

Figure 173. Comparison of Operating Line Obtained During Run Number 3 of Buildup A With Predicted Performance.

test reading at 65 percent speed, a slow acceleration of the compressor was made to 68 percent speed. At this point the proximeters indicated the buildup of vibration of the rotating shroud rim. After 15 to 20 seconds of operation at this condition to obtain strain gage data records on magnetic tape, the compressor was shut down and the run completed.

Reviews of the aerodynamic and mechanical information obtained during these test runs of the high-speed ROC were held with appropriate General Electric personnel. In their opinion, the additional mechanical performance information which would be obtained by operation of the ROC to 80 percent speed did not justify the risk involved, considering that useful aerodynamic performance information would not be obtained during such operation. The decision was made not to operate the compressor until the flow restriction had been removed from the compressor exit system.

Inspection of Compressor

A post-test visual inspection was made of the compressor after Run Number 3 of Buildup A with the following observations.

All rotor connections were tight, but several blades were nicked on their leading edge (see Figures 174 and 175), apparently by foreign particles passing through the compressor. Possible sources of such particles were: flame spray or nichrome pieces from the disc; nichrome pieces from casing instrumentation; dirt from the slip ring cavity, rotor cooling lines, or tank floor. Since 10 micron filters are used on the cooling lines and inlet velocity although the previously cleaned tank was only 0.34 feet per second maximum, these areas appeared ruled out as sources of the damage particles. Close inspection of the disc instrumentation nichrome appeared in equally good condition. It was discovered, however, that grease from the rotor damper bearing had been drawn into the inlet and foreign particles may have followed the same route into the compressor. To prevent this occurrence, the slip ring cavity was blanked off from tank pressure, presenting a no-flow condition past the bearing. All nicked leading edges were smoothed out and judged reliable for further testing in view of the very low blade vibratory stresses encountered.

Also noted in the rotor visual inspection was a damaged slip ring flexible connector, apparently bent during compressor disassembly. Replacement of this part and reconnection of the rotor instrumentation leads were required and were accomplished without difficulty.

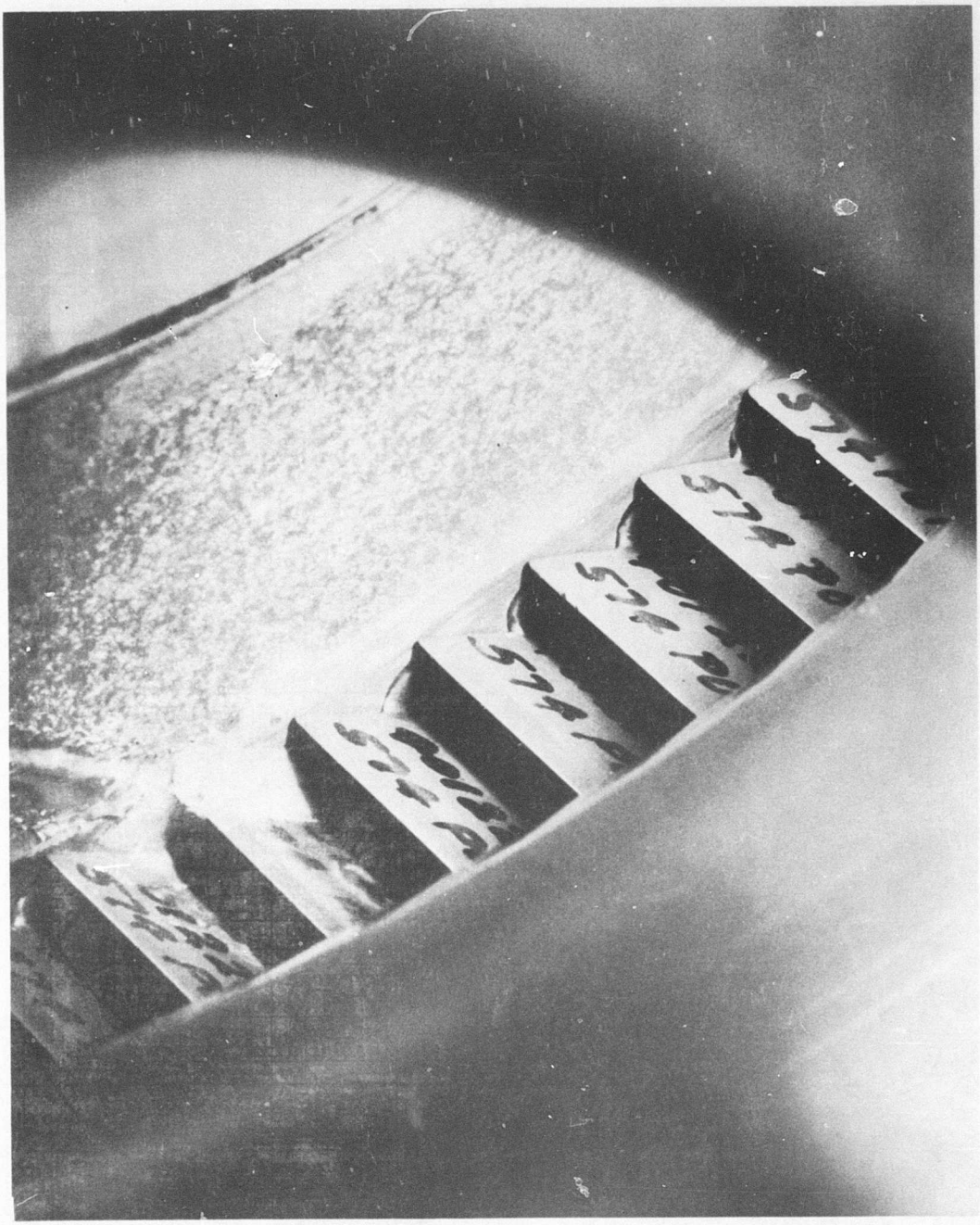

Figure 174. Rotor Blade Leading Edges Showing FOD Encountered During Tests of Buildup A - Sector 1.

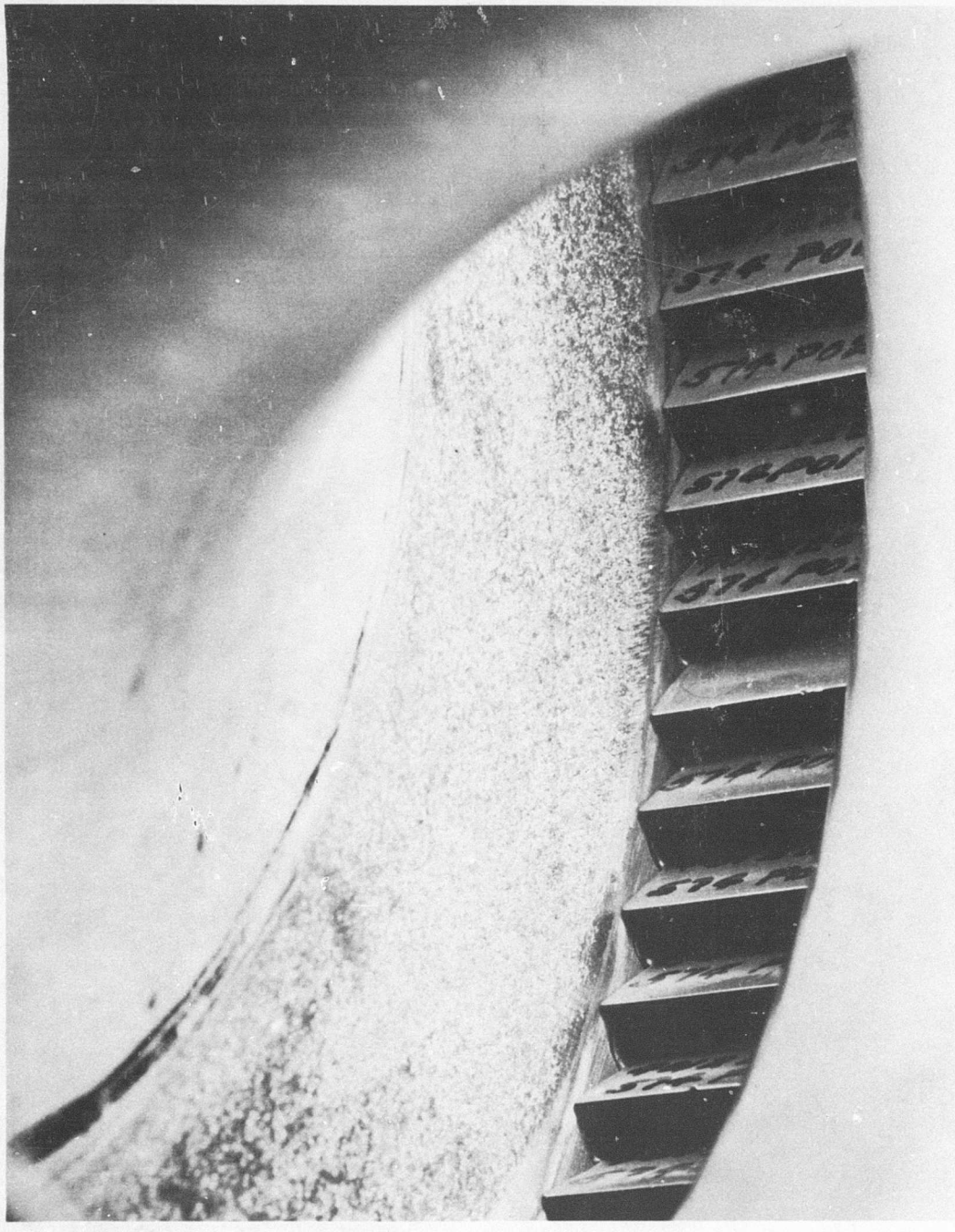

Figure 175. Rotor Blade Leading Edges Showing FOD Encountered During Tests of Buildup A - Sector 2.

TESTS OF SECOND COMPRESSOR CONFIGURATION (BUILDUP B)

The air exit system was modified and the rotor blade leading edges were reworked (Figure 176) prior to testing Buildup B. The method selected for permitting higher flow through the rotor consisted of removing approximately half of the subsonic stator spindles (these spindles control the subsonic stator angular position when the subsonic stators are installed) and installing air removal tubes in place of the spindles. The exit flow area was thereby increased by about 7.0 square inches to a total exit area of about 10.5 square inches. The two 1.50-inch-diameter scroll exits have a total area of 3.5 square inches. Tripling the exit area was expected to provide more than adequate area to permit design airflow at 50 percent speed and above.

Thirty sets of air bleed tubes were procured. Due to interference with the lines bringing cooling air to the compressor rotor and due to the interference with instrument probe actuators, only 27 of the bleed tubes could be used for Buildup B. Modifications to the exit system consisted of adding 4 manifolds, each constructed of 3-inch-diameter pipe. The manifolds were located to minimize the length of run of the small lines from the air bleed tubes in the stator casing to a manifold. Two of the manifolds were located on the east side of the compressor, 1 being upstream and 1 being downstream of the compressor. The 2 manifolds on the east side were joined to discharge through a manually operated 3-inch valve to the return system. A similar arrangement was made on the west side of the compressor. The bleed tubes, the manifolds, and the 3-inch valves added to the exit of the compressor are referred to as system B while the original is referred to as system A. An analysis of the exit system flow losses based on ASME and NASA data was conducted. The analysis indicated that the compressor should be operated with the hand valves open in system B at compressor speeds up to 60 percent. For operation at speeds above 60 percent, closing the 3-inch valves in system B may be done in order to obtain all of the desired test points by remote, accurate control through the throttles in system A. In other words, at high speed, the exit area provided by system B may be so large that complete closing of the throttles in system A may not be adequate to reduce the compressor airflow to the desired quantities.

Aerodynamic Results

At about 33 percent speed, using the Buildup B configuration with the inlet guide vane set for no turning and with 27 "relief tubes" installed, quite satisfactory performance was obtained (Figures 177, 178, and 179). The variation of rotor total pressure ratio was very close to the predicted value for subsonic operation. The use of the enlarged exit area due to the relief tubes permitted attainment of weight flow about 30 percent greater than the design value for zero incidence. The static pressure rise obtained across the rotor during Run Number 4 agreed with

Figure 176. Reworked Rotor Blade Leading Edges in Sector 1.

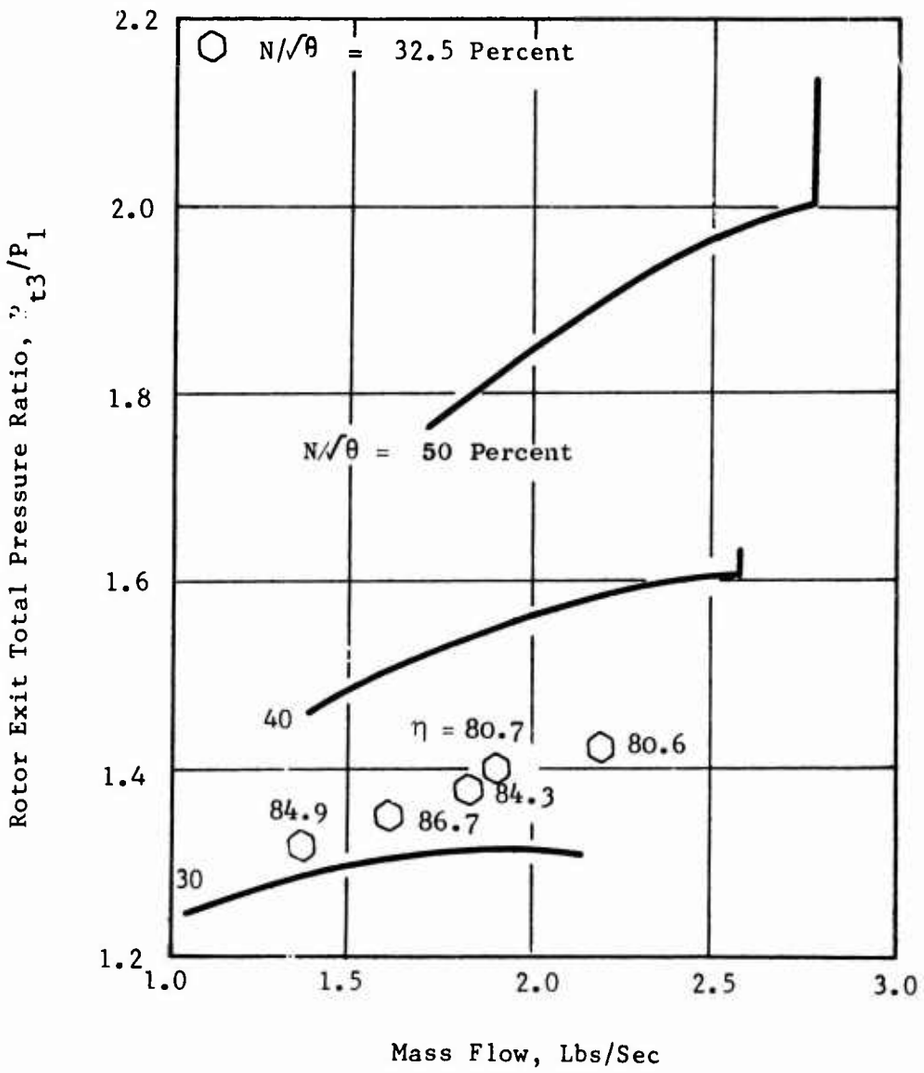

Figure 177. Total Pressure Ratio Versus Mass Flow for Run Number 4 (Buildup B).

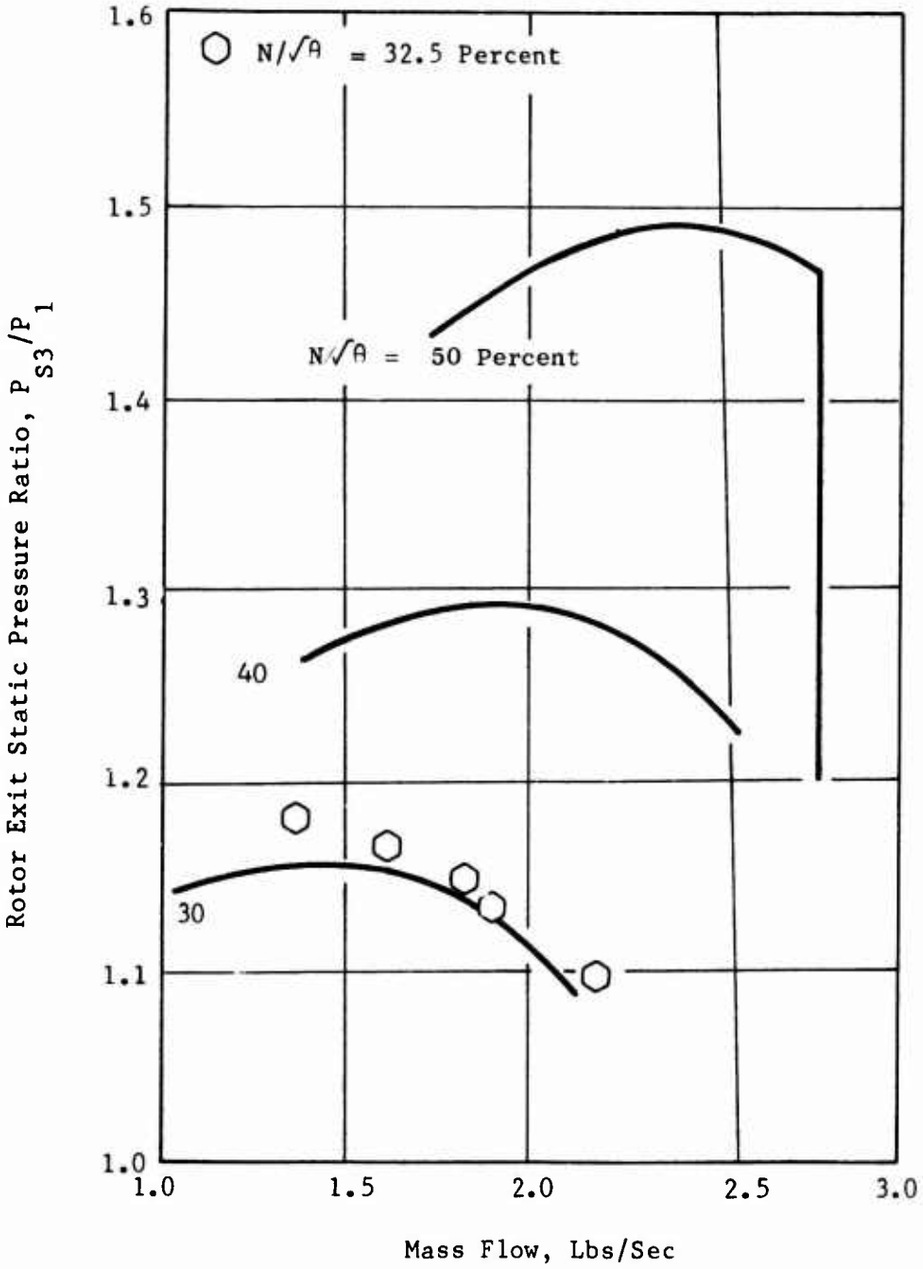

Figure 178. Static Pressure Ratio Versus Mass Flow for Run Number 4 (Buildup B).

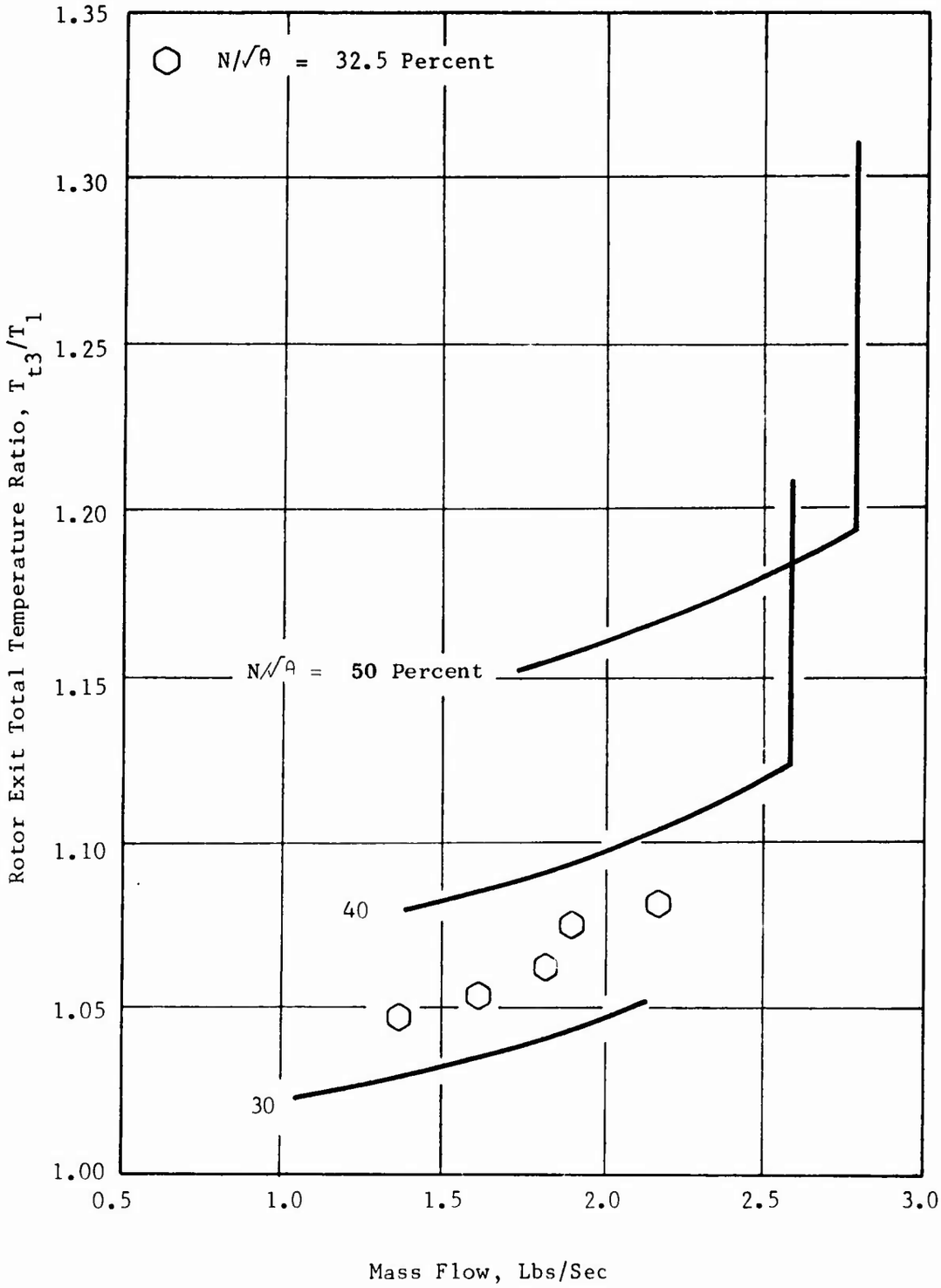

Figure 179. Total Temperature Ratio Versus Mass Flow for Run Number 4 (Buildup B).

the calculated value at a weight flow of 1.36 pps, but decreased as the weight flow was increased to a flow of 2.35 pps. For all weight flows, the rotor exit total temperature was higher than the predicted values. This result is consistent with the observation of lower static pressures, and therefore higher rotor blade exit velocities and higher work.

Run Number 5 was the first attempt to obtain high-speed test data with this new compressor. For various reasons, but primarily due to unfamiliarity with the mechanical and aerodynamic performance of the compressor, no data points were taken at total or static pressure ratios approaching predicted values. The total temperature ratios, however, agreed quite well with the values predicted for supersonic rotor operation at 64, 74, and 77 percent of design speed (Figures 180, 181, and 182).

During the last run of Buildup B (Run Number 6), encouraging results were obtained at 60 percent speed. An airflow of 2.91 pps, which is very close to the predicted choke flow value, was obtained with a pressure ratio of 2.60 and a rotor efficiency of 84.4 percent. The rotor static pressure ratio at this condition was 1.41, which corresponds reasonably well with the predicted value for the supersonic exit flow condition. The measured rotor exit temperature was 723 degrees Rankine as compared to a predicted value of about 737 degrees Rankine. The rotor exit flow angle of about 74.5 degrees observed was about 3 degrees farther from radial than was predicted for the observed conditions of static pressure.

At the higher speeds, the performance was less satisfactory. For example, at 67.3 percent speed the peak efficiency observed was 76.1 percent. This maximum efficiency value was obtained in the subsonic flow regime. Similarly, at the higher speeds, the static pressure ratios measured were significantly less than those predicted for either subsonic or supersonic operation (Figures 183 and 184). In general, work input as observed in the form of total temperature rise (Figure 185) corresponded quite closely to the predicted values for supersonic flow exiting from the rotor blades. Rotor exit flow angles were generally in the range predicted as shown in Figure 186.

During the course of this run, very strong circumferential static pressure variations were observed at the rotor exit. These variations were as great as 20 inches of mercury, and almost as great as the static pressure rise being produced by the rotor. It was believed that these pressure variations were seriously affecting the rotor performance. The use of stator blades in the exit system should effectively isolate the rotor from these strong pressure variations believed to originate in the scroll collector. It was decided to install the supersonic stators for the next buildup.

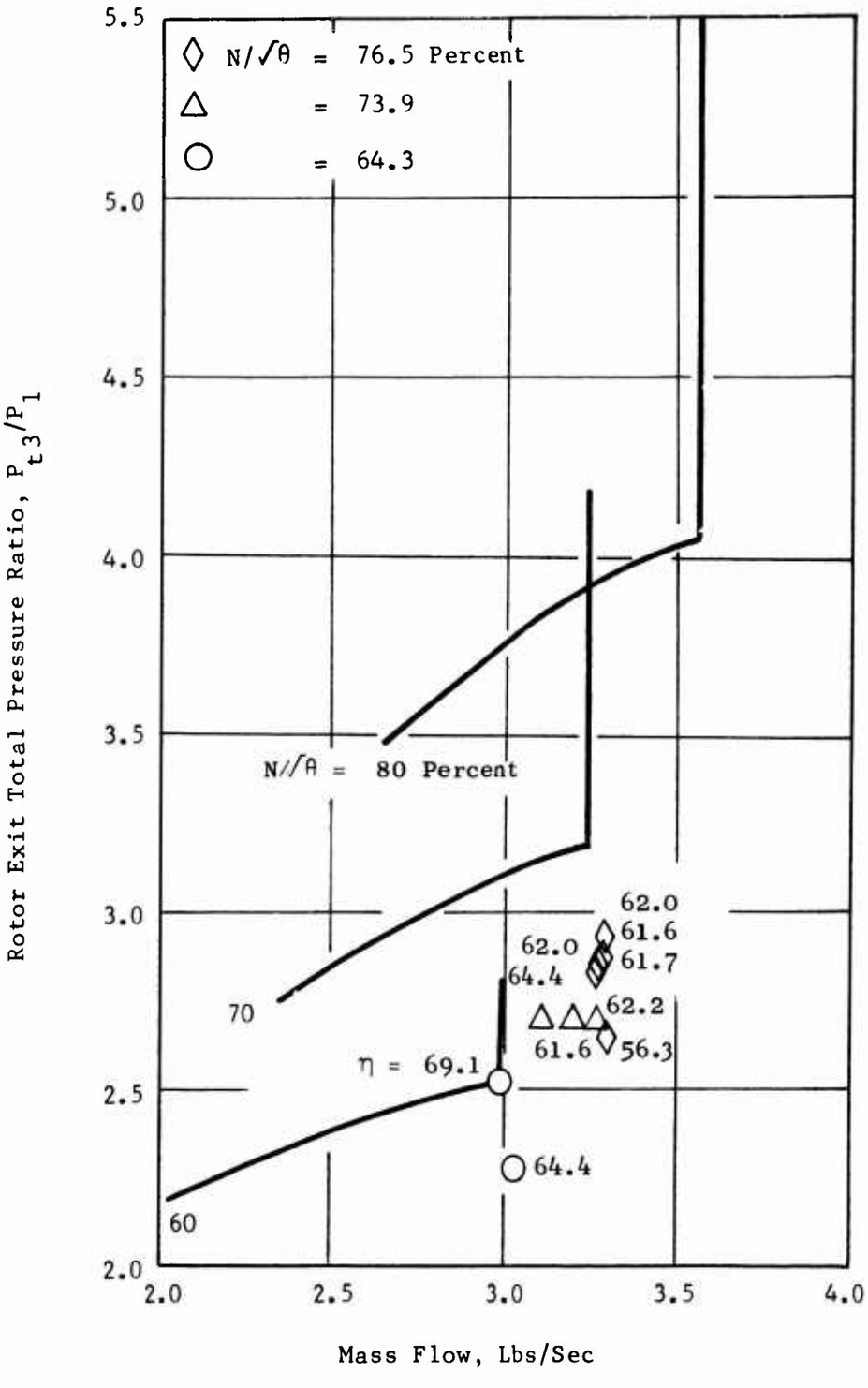

Figure 180. Total Pressure Ratio Versus Mass Flow for Run Number 5 (Buildup B).

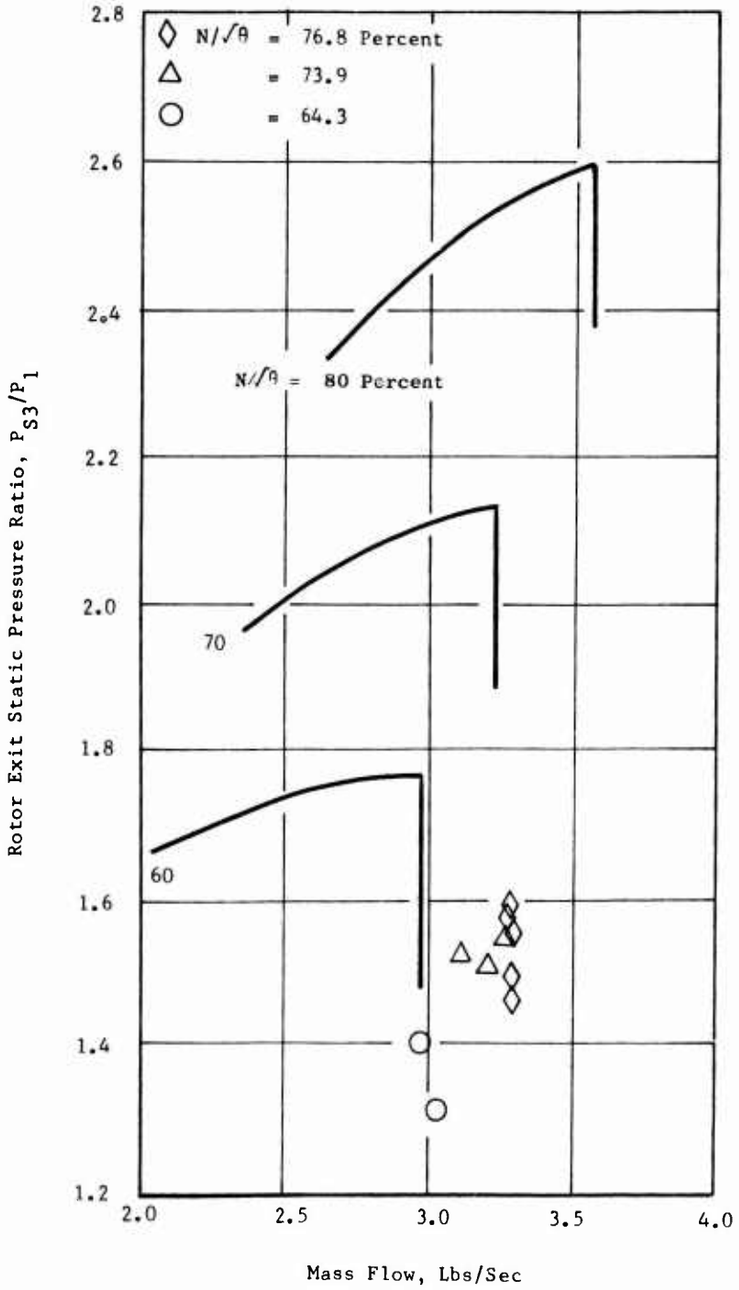

Figure 181. Static Pressure Ratio Versus Mass Flow for Run Number 5 (Buildup B).

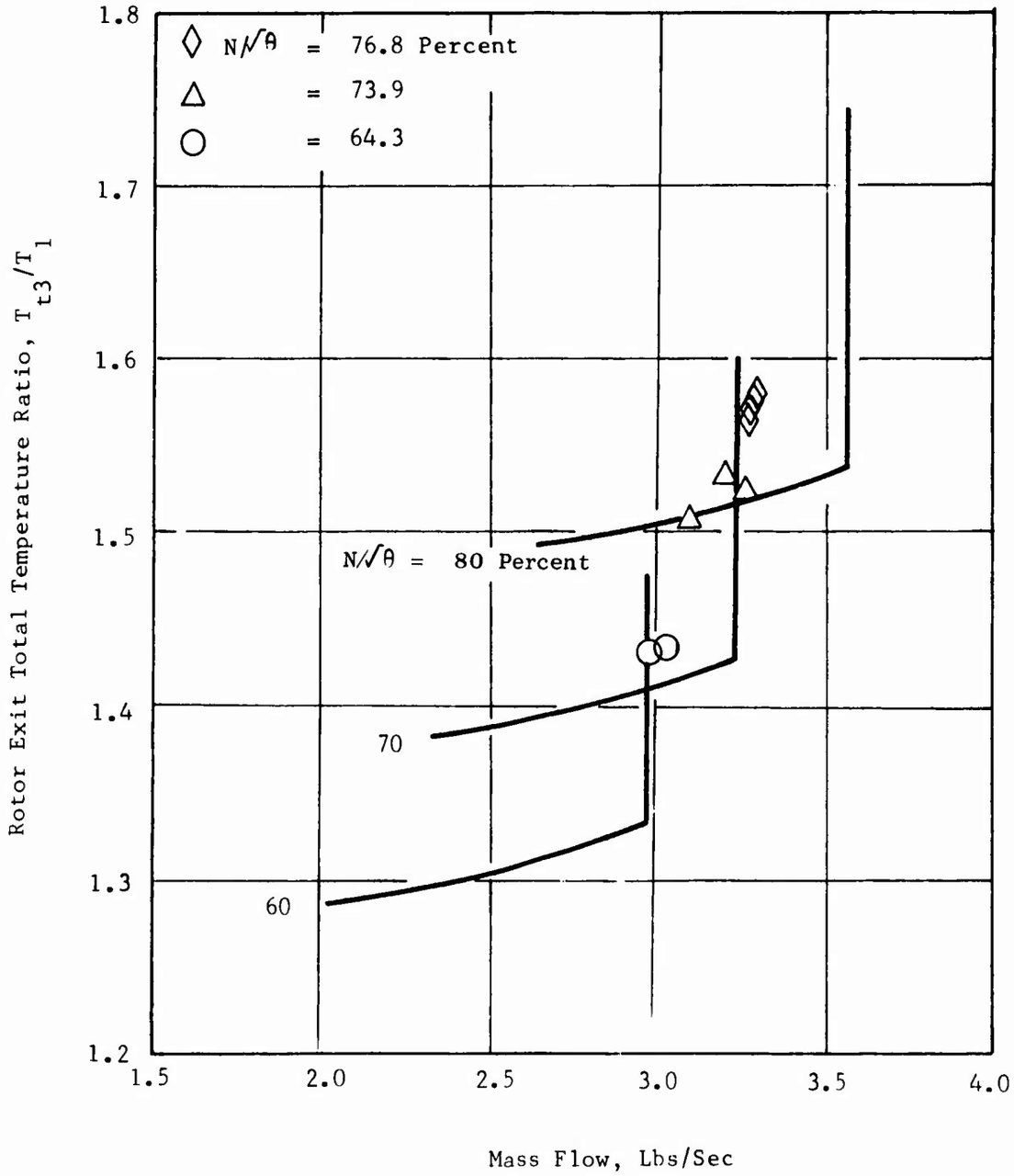

Figure 182. Total Temperature Ratio Versus Mass Flow for Run Number 5 (Buildup B).

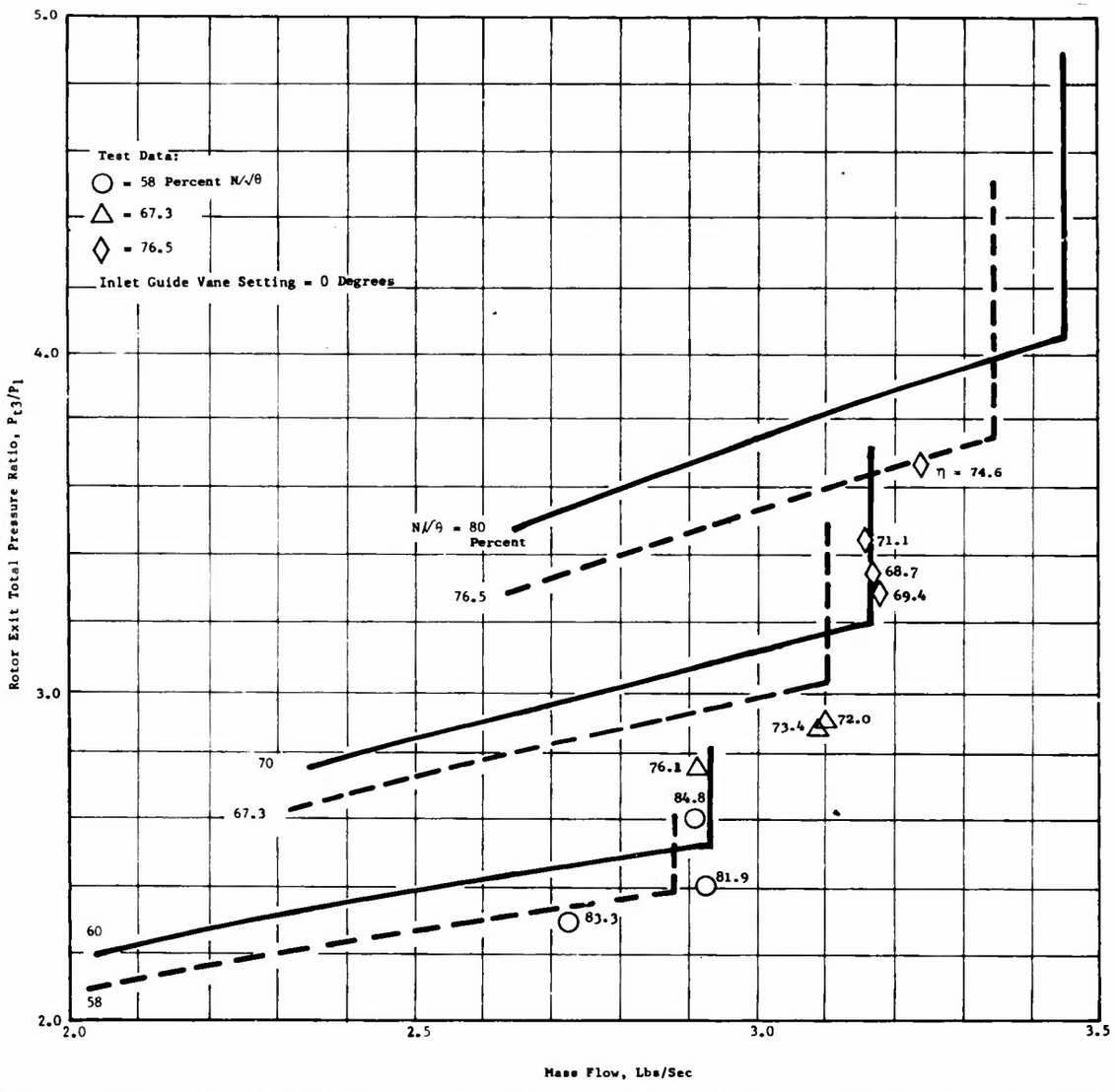

Figure 183. Total Pressure Ratio Versus Mass Flow for Run Number 6 (Buildup B) Without Stators.

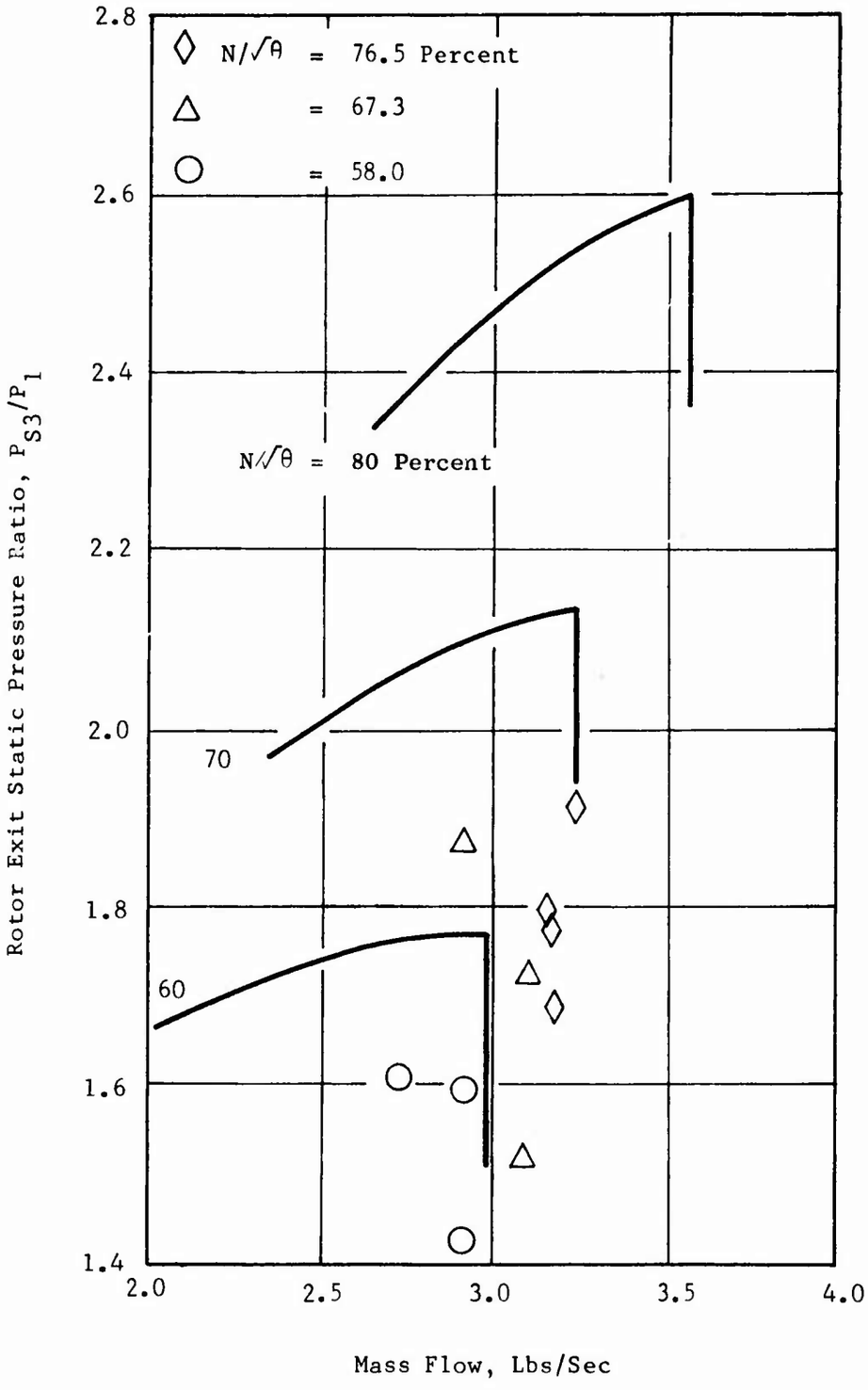

Figure 184. Static Pressure Ratio Versus Mass Flow for Run Number 6 (Buildup B).

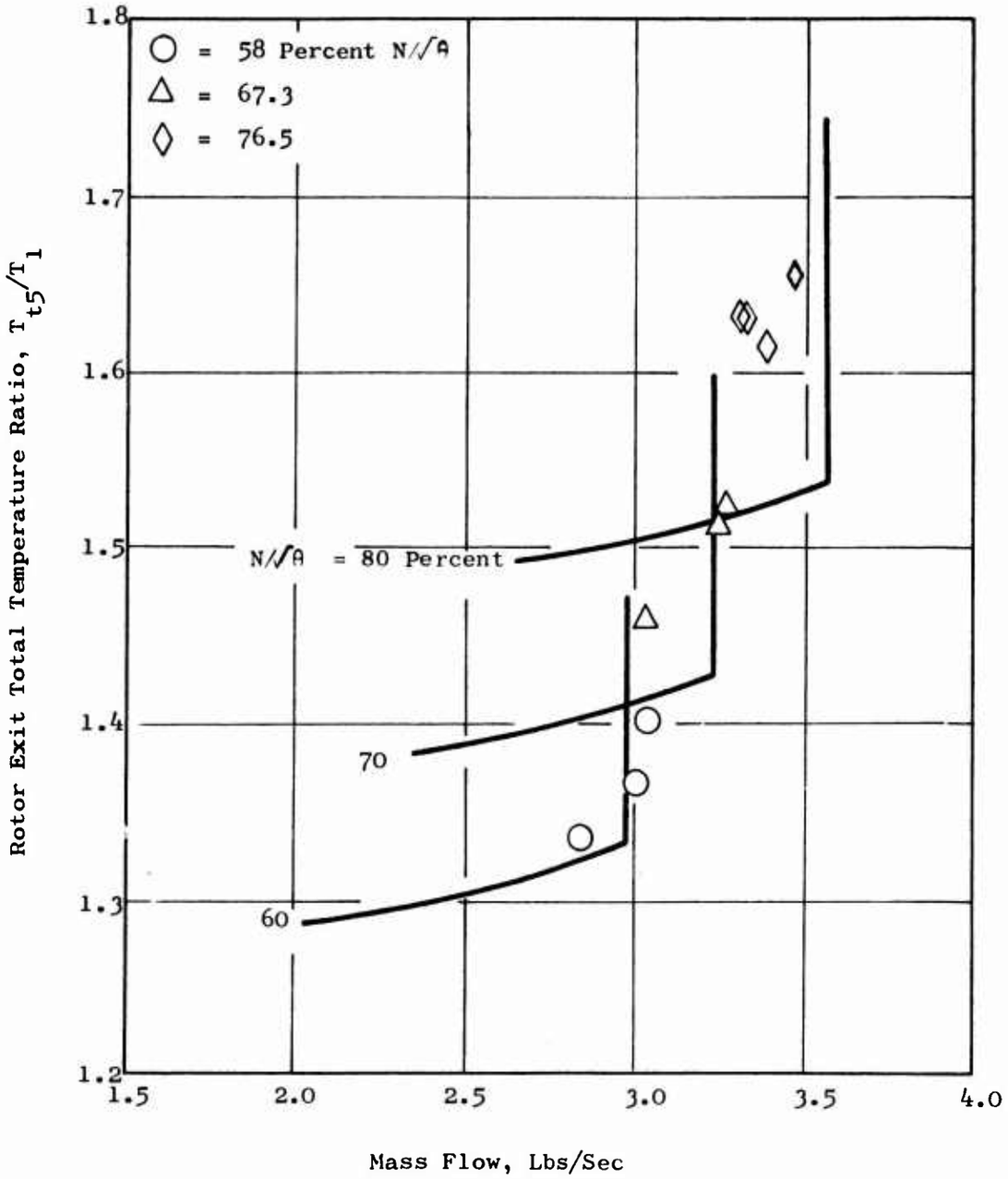

Figure 185. Total Temperature Ratio Versus Mass Flow for Run Number 6 (Buildup B).

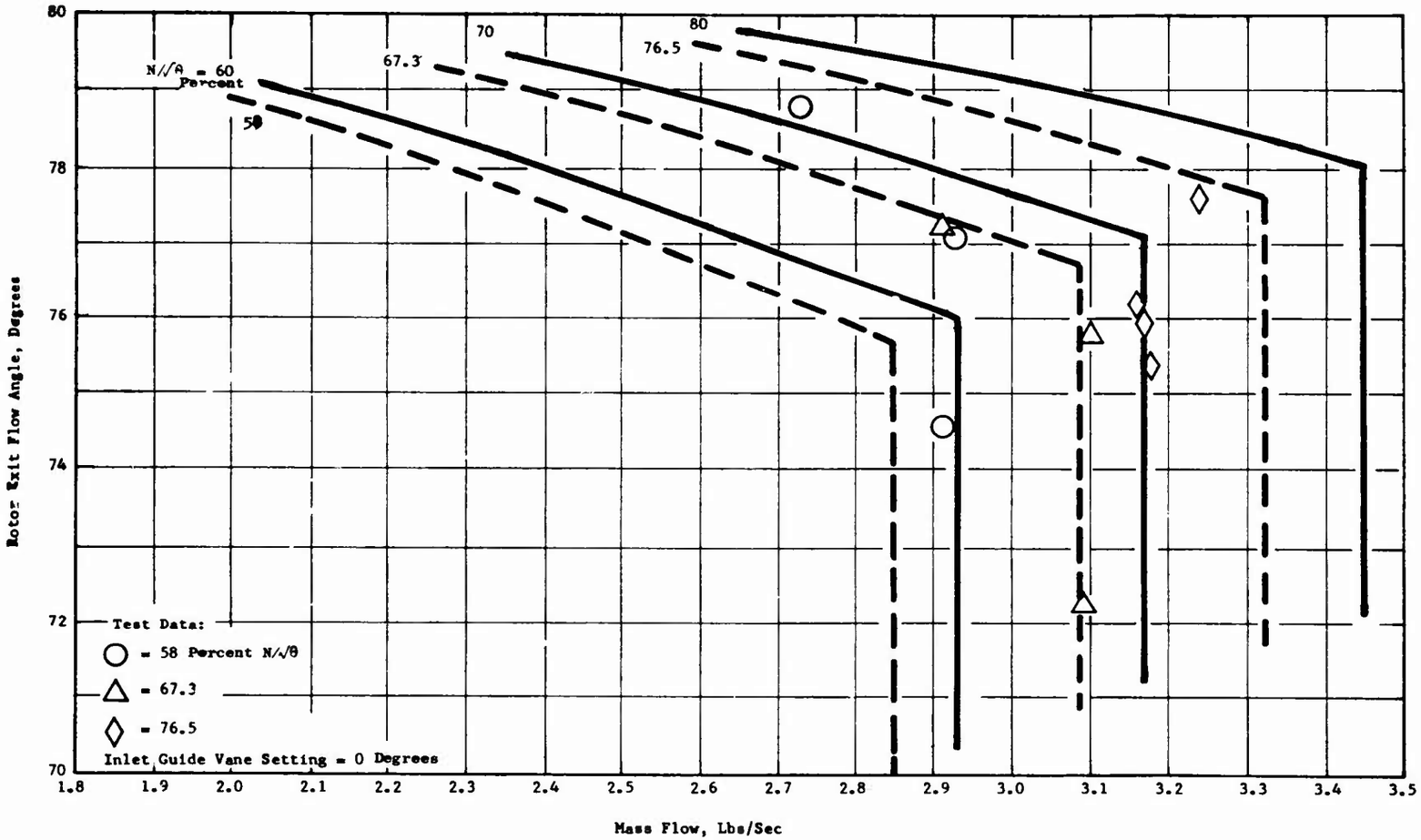

Figure 186. Rotor Exit Flow Angle Versus Mass Flow for Run Number 6 (Buildup B) Without Stators.

TESTS OF BUILDUP C

Compressor Configuration

This configuration included the use of a J85 bellmouth and a conical fairing to extend the inlet upstream. This was done to improve the compressor inlet temperature distribution. The supersonic stators and their actuator were installed. The stator angle could be varied from 71 to 86 degrees from radial. The test plan called for running at 60, 70, and 80 percent speed, but testing was discontinued without achieving 80 percent speed due to several facility problems (camera and automatic temperature and overspeed tripout failures) and inoperable stators (probably due to overheating). Improved provision for cooling air was made prior to the next test of Buildup C.

The preliminary assembly of the supersonic stators which were installed for Buildup C is shown in Figure 187. The position of the instrumentation which is shown in detail in the next series of photographs can be observed. The ports of the auxiliary air removal or "B" exit system which replace a spindle for the subsonic stators can be seen. A close-up of the supersonic stators which include 1 of the 2 stators equipped with a strain gage is shown in Figure 188. A close-up of the total pressure rake which is used to traverse the stator wakes is shown in Figure 189. The angle setting of the rake is determined by the cobra probe shown in Figure 190. The total temperature rake is shown in Figure 191.

Predicted Performance

New compressor operating maps (Figures 192 and 193) were drawn in preparation for the first test of Buildup C, Run Number 7. Dashed curves are given for the actual corrected speeds which were planned for that series of tests. Figure 192 shows rotor total pressure ratio versus mass flow. Solid curves included on this graph are preliminary data from test Run Number 7. Figure 193 shows rotor exit static pressure ratio versus mass flow, and solid curves are from this test run.

Aerodynamic Results Obtained at 58 Percent Speed

The test results of Buildup B obtained at 20,800 rpm or 58.6 percent speed indicated a close approach to the calculated values of airflow and total pressure ratio. The work input by the rotor as indicated by the total temperature rise (Figure 194) was also very near the calculated value for a friction coefficient of 0.03 in the rotating wall diffuser. The static pressures at rotor exit were generally less than the calculated value, and the rotor efficiency was low (84.8 percent). The results obtained using Buildup C showed improved static pressure at rotor exit (station 3.0), but the stator losses caused the stage efficiencies measured to decrease.

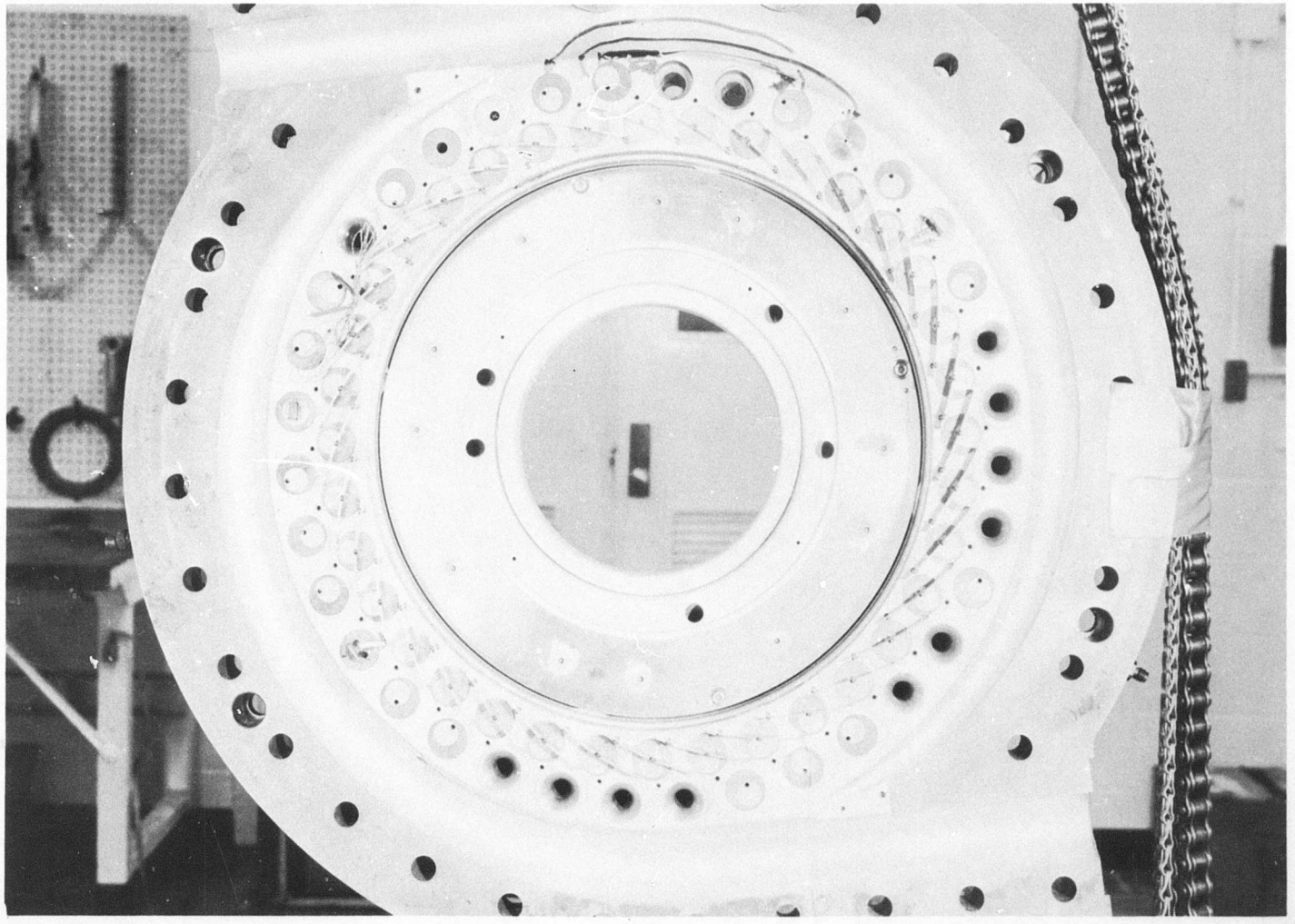

Figure 187. Preliminary Assembly of Supersonic Stator Vanes in Forward Compressor Stator Casing.

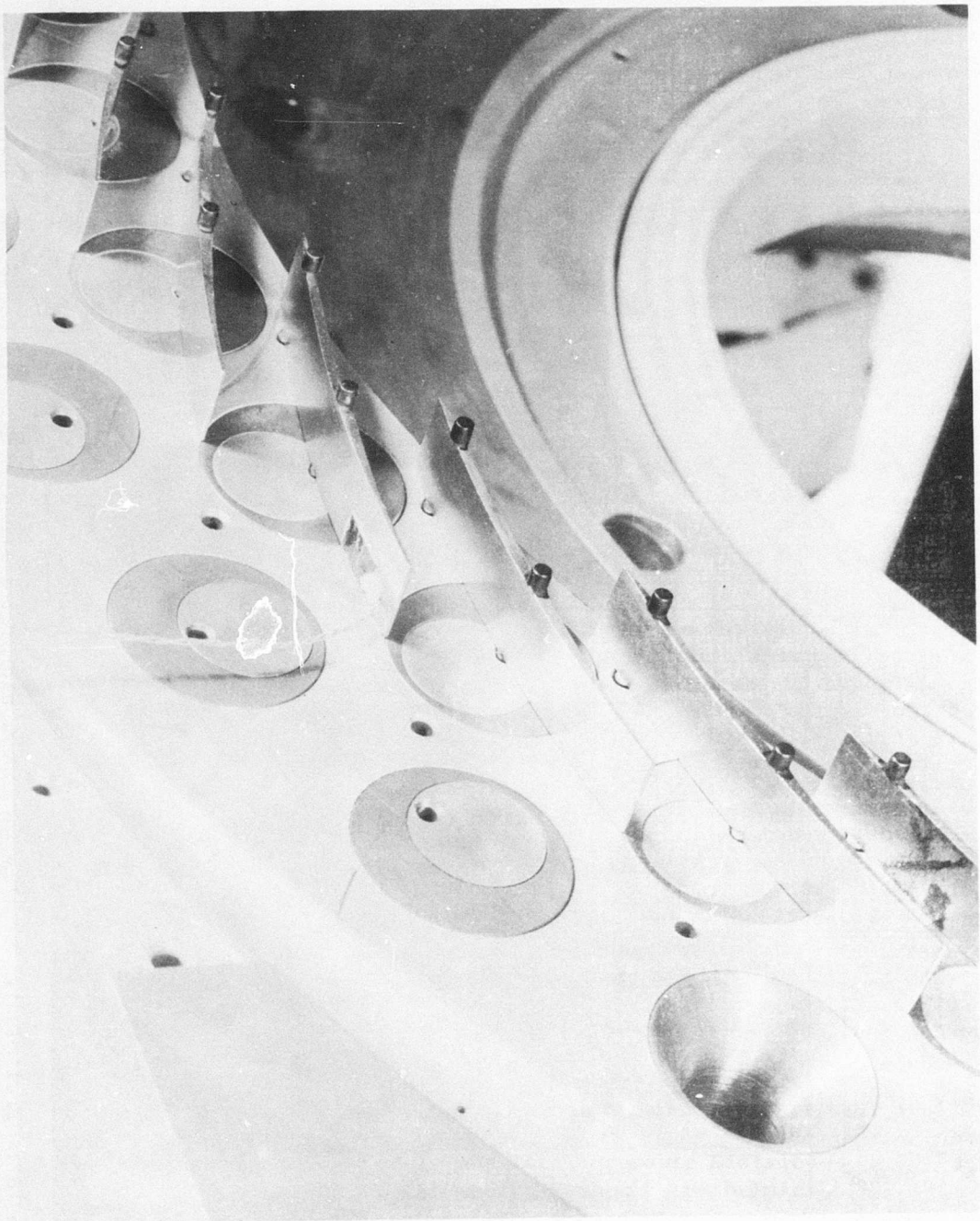

Figure 188. Supersonic Stator Vanes Including 1 of the 2 Vanes Having Strain Gages.

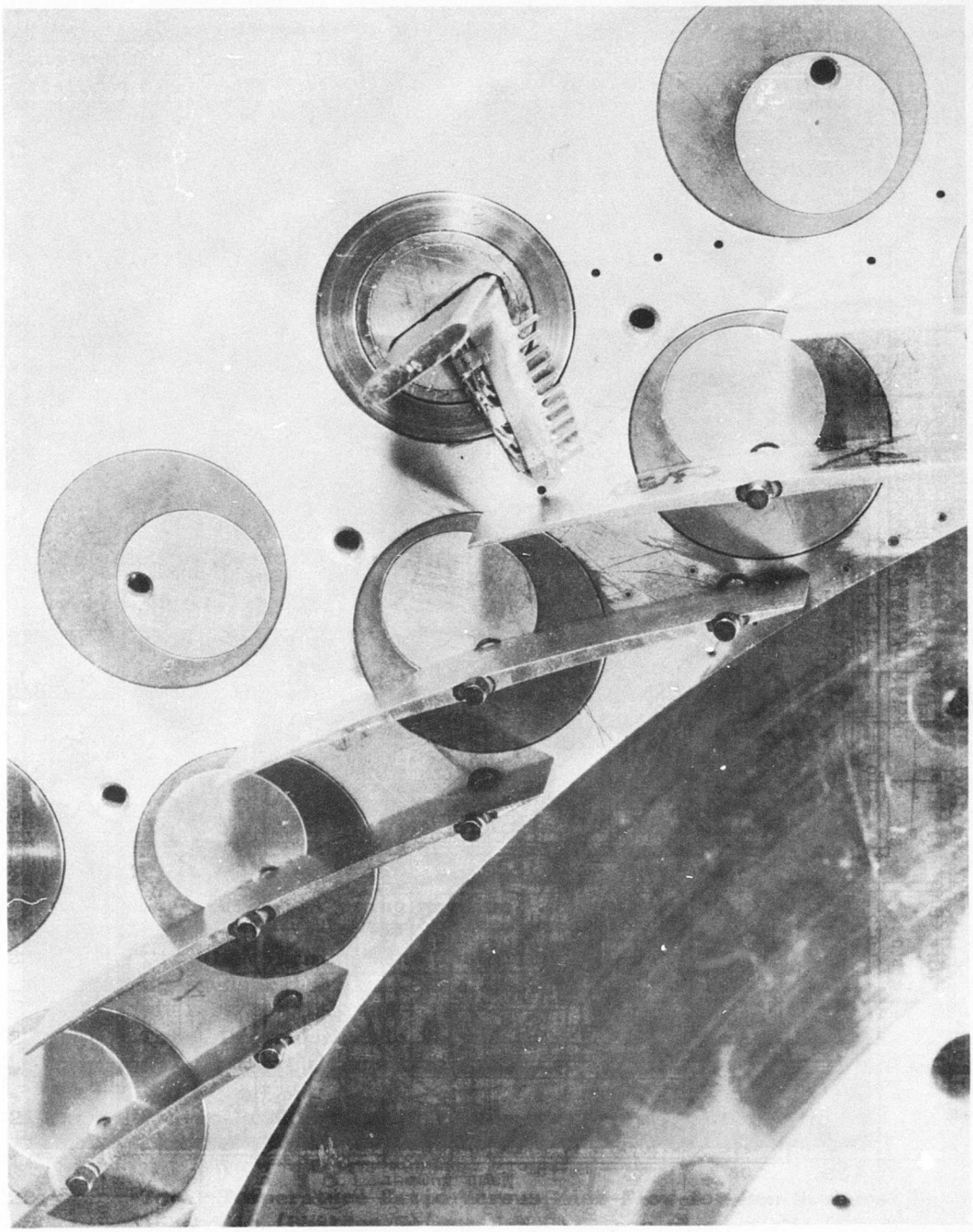

Figure 189. Total Pressure Rake and Static Pressure Orifice Locations Adjacent to Supersonic Stators.

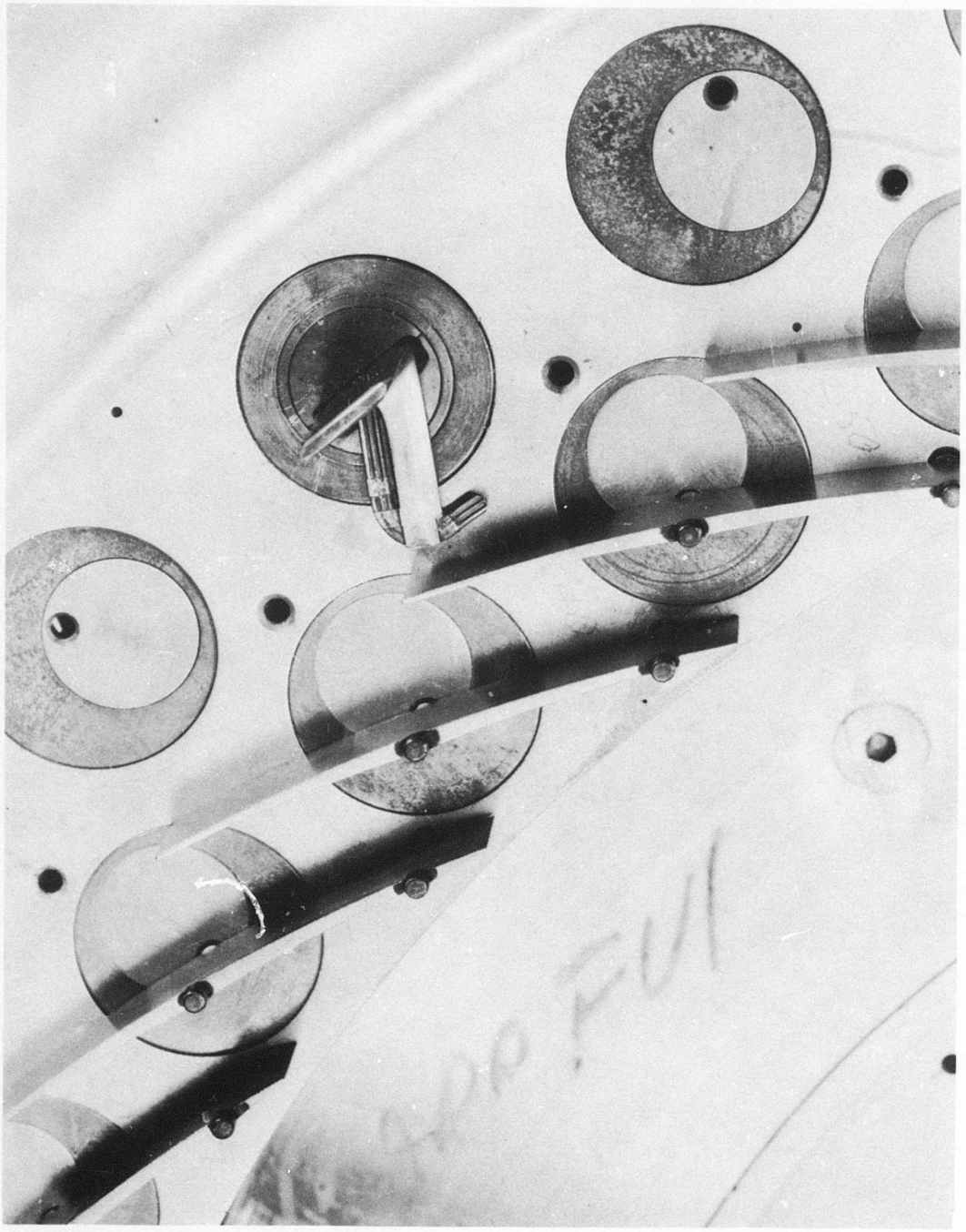

Figure 190. Cobra Probe Containing Total Pressure and Yaw Tubes Located Downstream of the Supersonic Stator Vanes.

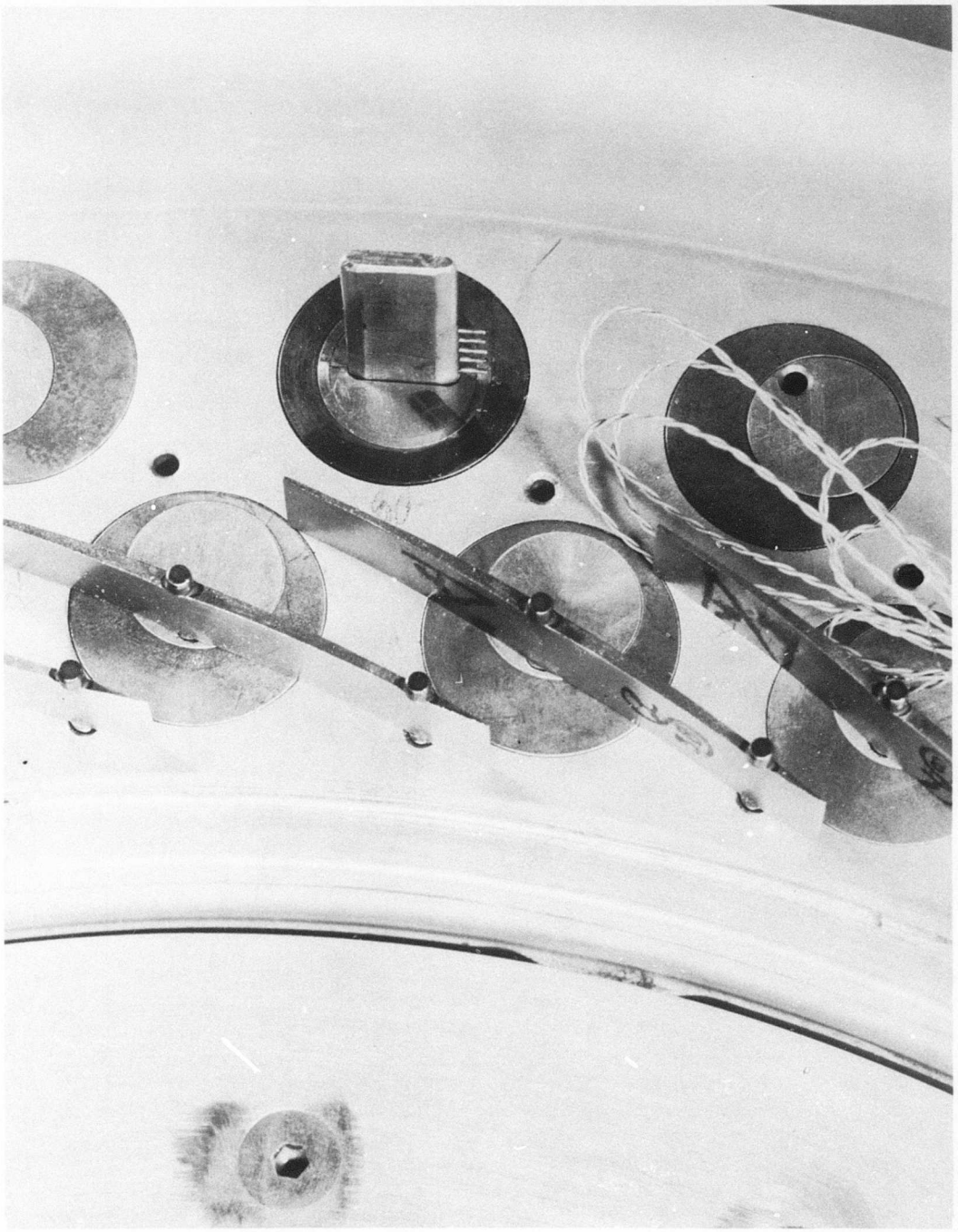

Figure 191. Total Temperature Rake Located in Subsonic Stator Spindle.

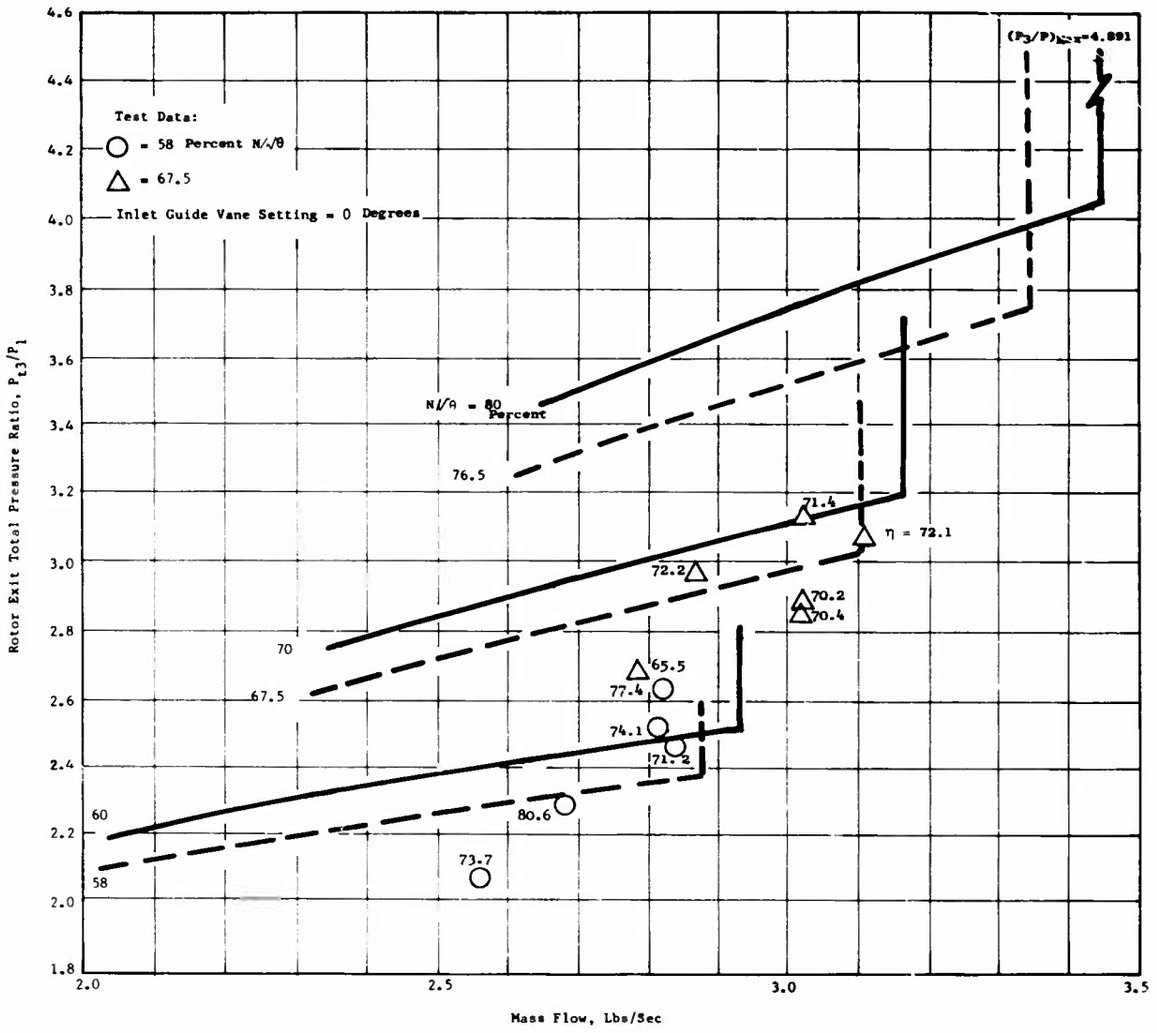

Figure 192. Total Pressure Ratio Versus Mass Flow for Run Number 7 (Buildup C) With Supersonic Stators.

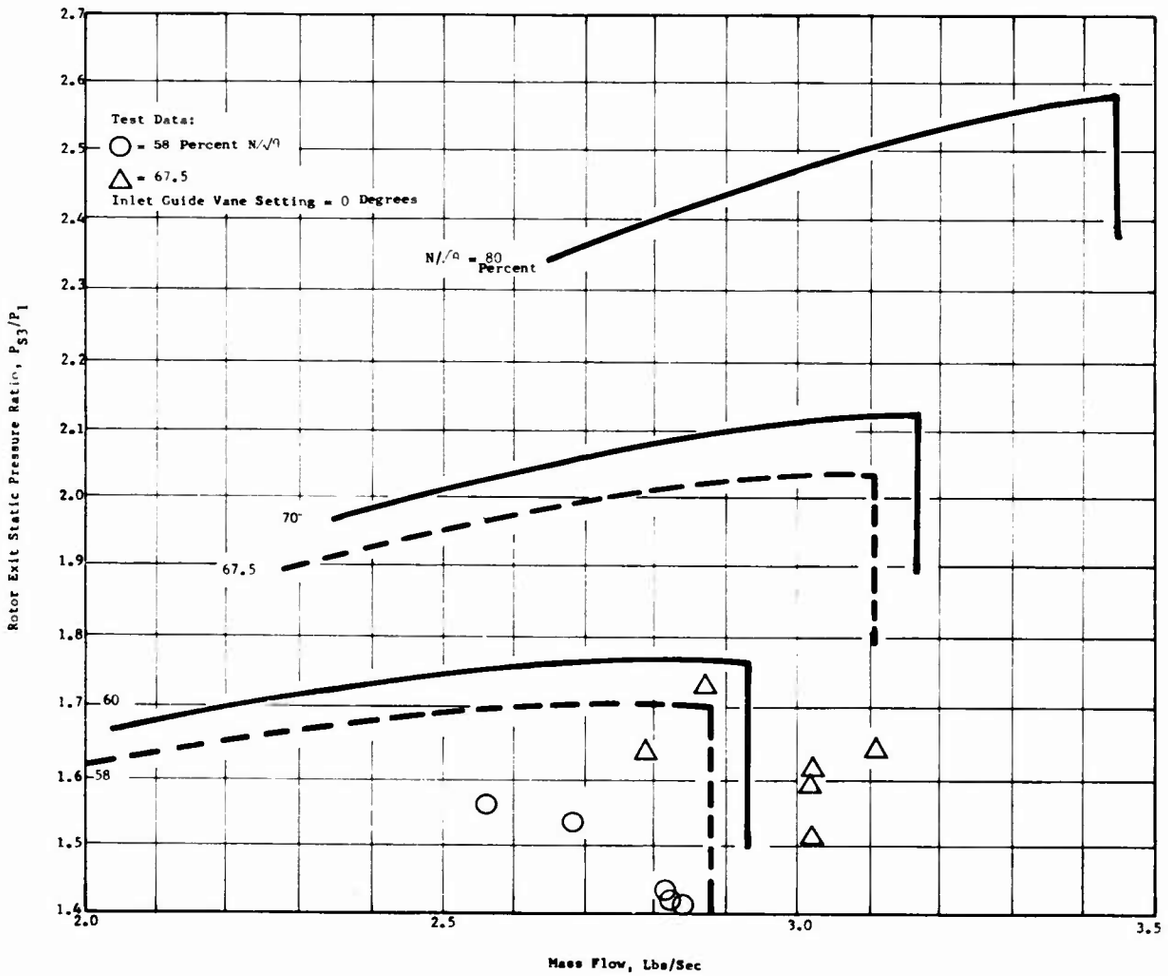

Figure 193. Static Pressure Ratio Versus Mass Flow for Run Number 7 (Buildup C) With Supersonic Stators.

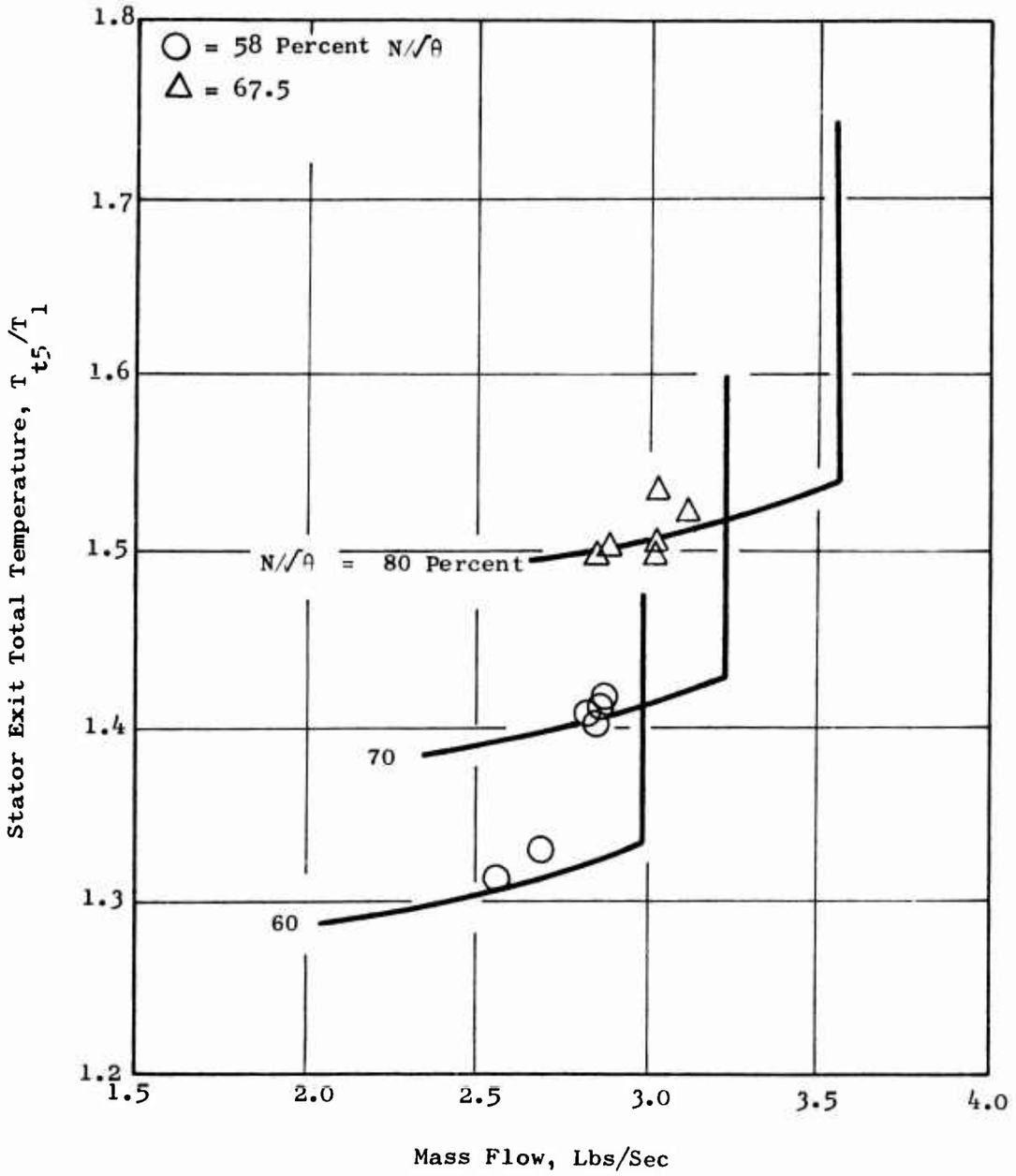

Figure 194. Total Temperature Versus Mass Flow for Run Number 7 (Buildup C) With Supersonic Stators.

During tests of Buildup C during Run Number 7, the supersonic stators were effective in reducing the circumferential static pressure variations at rotor exit. At 20,800 rpm, a variation from maximum to minimum static pressure of about 0.6 psi was observed, compared to about 2.0 psi before installing the stators. The stators were also effective in regard to the total pressure observed at plane 5.0, downstream of the supersonic stators. Optimum settings of the stator angle (75 degrees) and the throttle valves were required to obtain the highest total pressure. The efficiency obtained at maximum total pressure ratio of 2.64 was 77.44 percent (Figure 192) and may be considered as a "stage" value, since the total pressures used were measured downstream of the stators. The airflow was 2.82 pps compared to the predicted value of 2.88 pps at 58 percent speed.

The test procedure used was to set the stators about 1 degree more open than the angle predicted for the beginning of the supersonic flow regime. The acceleration to the desired test speed was made with throttles partially opened from the maximum total pressure condition. On speed, the throttles were closed until a maximum total pressure was obtained. Further throttling produced slightly increased static pressure at plane 3.0 with some decrease in total pressure at plane 5.0. Stator angle variations from 71 degrees to 76 degrees were tested at 20,800 rpm, and 75 degrees yielded maximum total pressure.

Closing the throttle or the stators too much caused a sudden decrease in airflow and total pressure, but did not "stall" the compressor since no blade or rim vibrations were observed. A new steady-state operating point was established with a reduced "stage" efficiency of 73.7 percent with the stators at 76 degrees. An intermediate point was obtained at a pressure ratio of 2.28, W_a of 2.79 pps, and efficiency of 80.6 percent. For these 2 subsonic exit flow points, the static pressure was higher than that obtainable with supersonic rotor exit flow. Probably, further throttling would have produced higher static pressure at rotor exit, but lower total pressure and reduced airflow.

The static pressures at rotor exit were closer to the prediced values for Buildup C tests (Figure 193) than for Buildup B runs at the same speed, 20,800 rpm.

Results Obtained at 67 Percent Speed

At 24,250 rpm, 70 percent uncorrected speed or 67.5 percent corrected speed, the maximum total pressure ratio obtained was 3.13 compared to the Buildup B maximum of 2.9. The maximum static pressure at rotor exit obtainable with supersonic flow leaving the rotor was about 10 psig compared to the predicted value of about 15 pounds per square inch gage (psig). The stage efficiency values were low, 70.2 to 72.2 percent, although they compare well with the rotor efficiencies of from 72.0 to 76.1 percent obtained during Run Number 6 of Buildup B.

The supersonic stators appeared to operate very well. With an inlet Mach number of about 1.0, the exit Mach number was 0.58. The static pressure rise coefficient is calculated to be 0.555, which is slightly greater than the value obtained in transonic cascade tests at this Mach number (see Reference 1). The stator loss coefficients could not be accurately calculated because the stator inlet total pressure could not be measured, but the wakes looked small on the manometers compared to the inlet dynamic pressure (19.7 psi or 40 inches of mercury).

Preliminary Analysis

The problem of low rotor efficiency and low static and total pressure seemed to be centered in the rotating vaneless diffuser. The possibility exists that as the rotor speed was increased, a local diffusion limit was exceeded. This may occur near the rotor blades exit where the maximum value of radial pressure gradient, dp/dr, occurs and the rotor blade wakes exhibit minimum total pressure. A localized, high loss, separated flow region may occur which reattaches to the rotating walls at a larger radius where the radial pressure gradient is less steep. The uniformity of the exit flow and the apparently excellent stator performance indicate that either the high loss process is very steady or is enclosed in a separated torus. This latter type flow has been observed in conventional vaneless diffusers of high swirl angle.

Lower RPM Tests

Buildup C was tested at 30, 40, and 50 percent corrected speed during Run Number 8. The purpose of these low-speed runs was to determine whether the high rotor efficiency which had been obtained in earlier runs (with the inlet guide vanes closed 40 degrees) would be obtained with the present configuration. If high efficiency were obtained at lower rpm, an aerodynamic loading limit could be established.

The results of Run Number 8 of Buildup C are presented in Figure 195. The total pressure ratio measured downstream of the supersonic stators agreed very well with the predicted rotor exit total pressure ratio at 30 percent speed. Peak efficiency was apparently about 83 percent. These results are contradictory in that the total pressure downstream of the stators should be less than that calculated downstream of the rotor (and therefore upstream of the stators), or the efficiency should be higher than the calculated value. The contradiction occurs because the total pressure observed is higher than predicted, while at the same time the temperature rise measured is greater than that predicted.

At 40 percent speed, measured total pressure agreed reasonably well with the predicted rotor exit total pressure ratio. The peak efficiency measured was 80.8 percent, again considerably lower than the predicted value for this rotational speed.

At 50 percent speed, supersonic exit conditions from the rotor blades were clearly established. The observed static pressure agreed well with predicted values (Figure 196), as did the total temperature (Figure 197). During the run, it was found that small changes in the stator blade angle had a significant effect on compressor performance. Maximum pressure ratio and efficiency under supersonic operating conditions were obtained with the stator blade angle set at 75 degrees. The total pressure ratio observed was 2.28 with an efficiency of 77.9 percent. The weight flow agreed very closely with the predicted value of 2.73 pps.

During the course of taking several wake surveys at spanwise stations downstream of the supersonic stators, the flow and the total pressure ratio suddenly changed. A new steady-state point of operation still at 50 percent speed was established at an airflow of 2.48 pps and a total pressure ratio of 1.92 and an efficiency of 78.6 percent. There was no mechanical change, such as rotor blade or shroud vibration, when this significant aerodynamic change occurred. This behavior may be quite useful in future engines, in that when a "stall" of this kind occurs it has little or no effect on the mechanical parts of the compressor. In fact, this behavior is not a stall, but merely a transition from supersonic to subsonic flow at the rotor blade exit.

The results of these low-speed runs indicate that the compressor efficiency is low over the entire speed range from 30 to 80 percent with the inlet guide vanes set in the axial direction (this statement ignores a peak rotor efficiency of 84.8 percent which was obtained at 60 percent speed during Run Number 6 of Buildup B in the absence of the supersonic stators).

As a result of the performance observed during Run Numbers 7 and 8 of Buildup C, and the belief that separation in the vaneless diffuser was the cause of the trouble, it was decided to attempt to relieve the radial pressure gradient in the diffuser as much as reasonably could be done for the next run. This was accomplished by closing the inlet guide vane to 40 degrees from axial direction to increase the rotational speed for a given relative velocity and mass flow into the rotor. At rotor blade exit, then, a similar situation was expected to exist in that for a given exit relative velocity and free stream static pressure rise, the rotational speed of the walls of the vaneless diffuser would be increased. It is the difference between the free stream static pressure rise and that produced in the boundary layer due to the rotation of the diffuser walls that is the effective diffuser loading. This parameter should be reduced by inlet guide vane closure. Unfortunately, the net result of this experiment was a decrease in the performance at all speeds tested (30, 50, 60, and 70 percent). In retrospect, it may be that increased inlet losses resulted from the high tangential velocities incurred by closing the inlet guide vanes 40 degrees. Thus, increased inlet losses may have overshadowed any benefits in rotating diffuser performance due to the reduced aerodynamic loading.

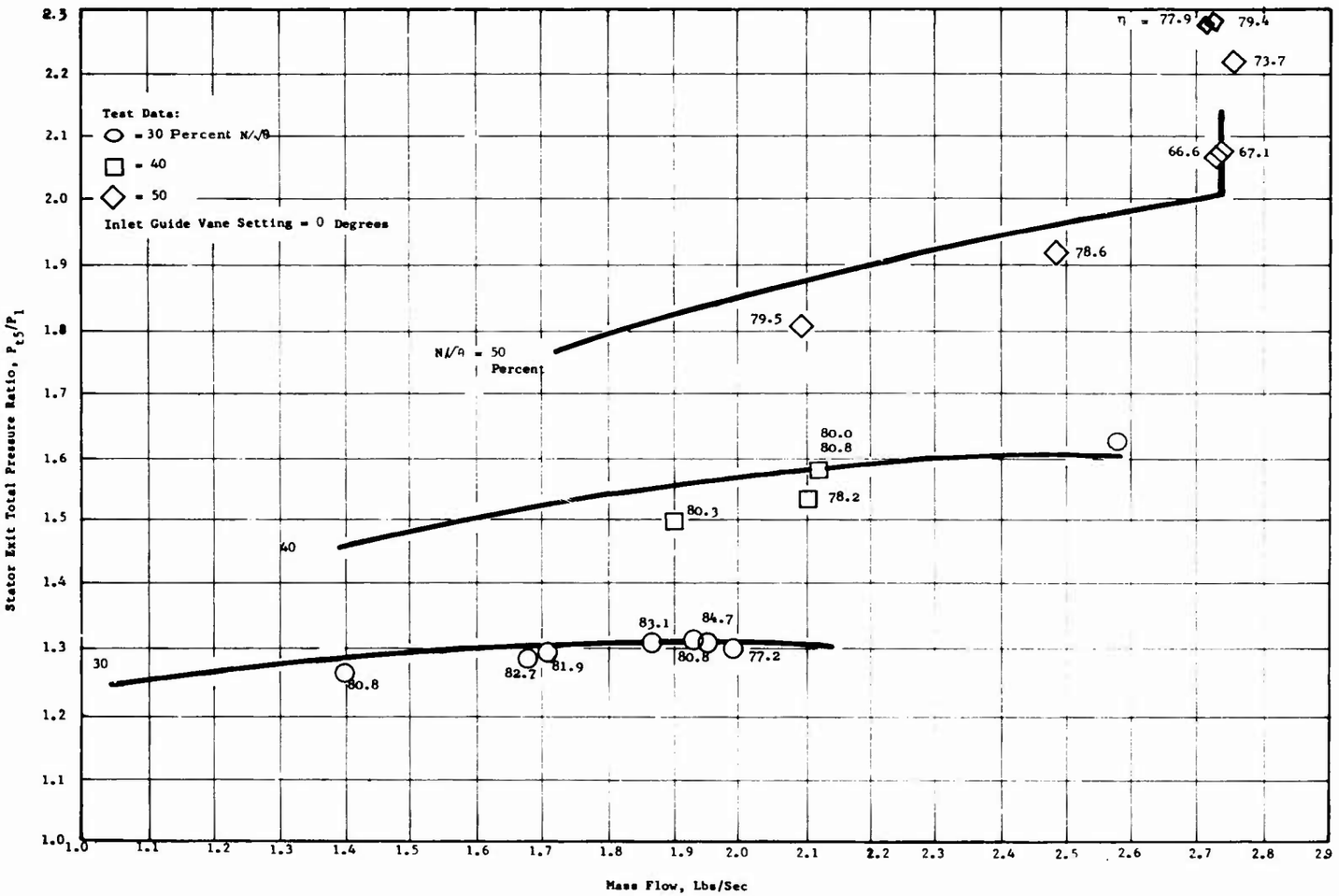

Figure 195. Total Pressure Ratio Versus Mass Flow for Run Number 8 (Buildup C) With Supersonic Stators.

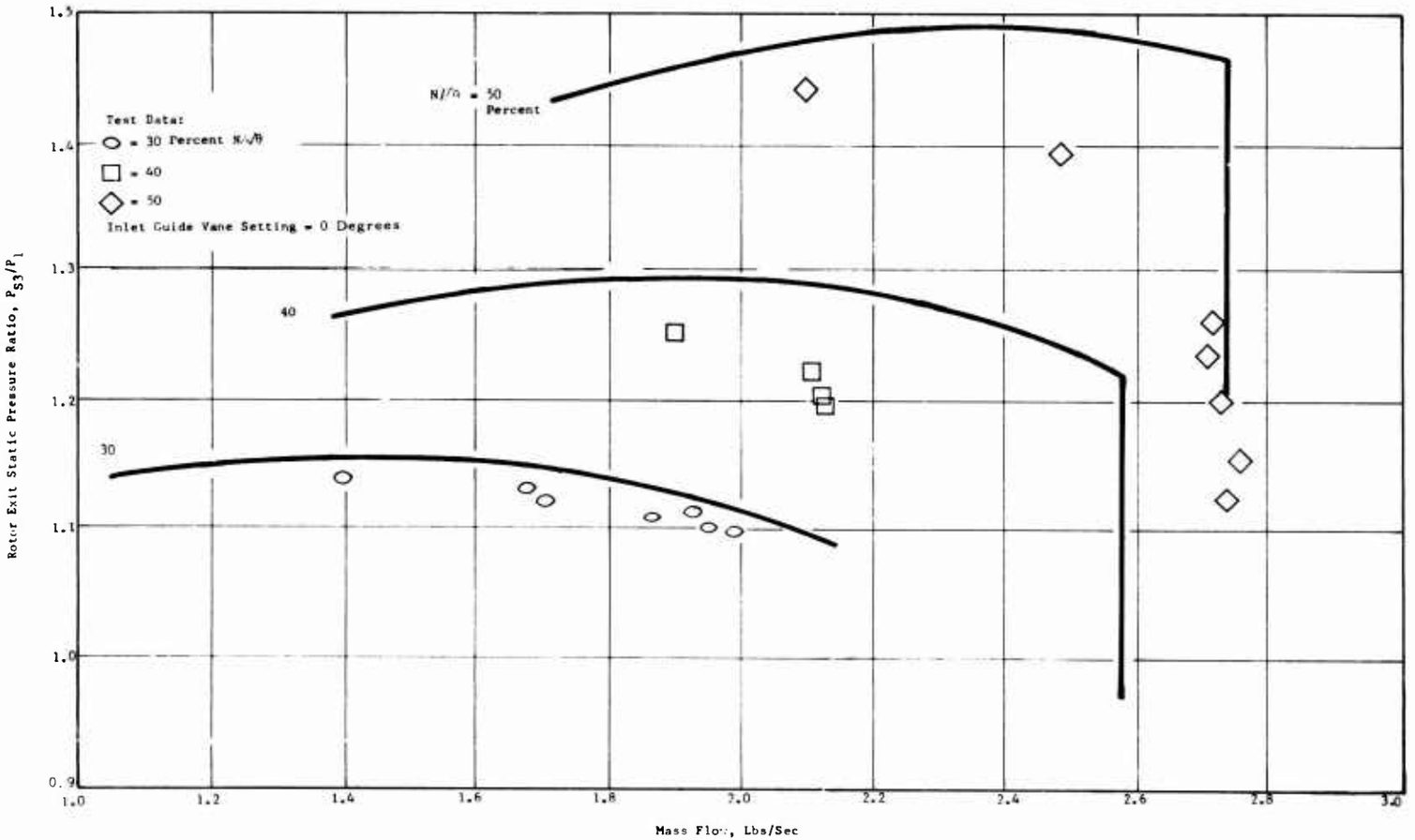

Figure 196. Static Pressure Ratio Versus Mass Flow for Run Number 8 (Buildup C) With Supersonic Stators.

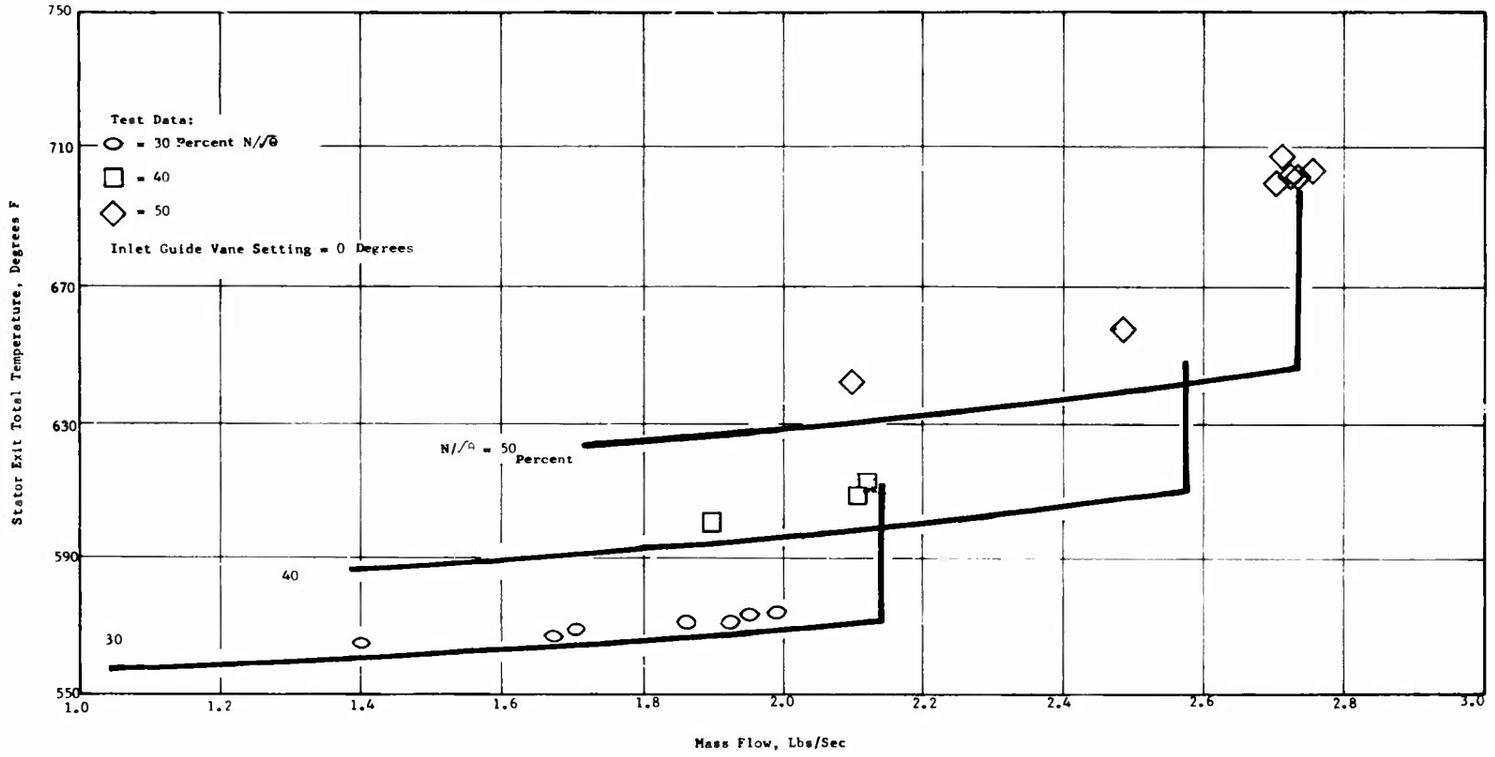

Figure 197. Total Temperature Versus Mass Flow for Run Number 8 (Buildup C) With Supersonic Stators.

This result suggests that there is not a sharp aerodynamic loading limit which is exceeded in this compressor as the speed is increased in the range from 30 to 80 percent speed. Analyses of the radial pressure gradients within the rotating wall vaneless diffuser were begun in an attempt to understand the observed performance of this rotor (see section on Analytical Investigations).

Examination of Disassembled Rotor

The series of runs of the compressor configuration designated Buildup C consisted of tests over the range of speeds from 30 to 70 percent with inlet guide vanes closed 40 degrees axial. The results of these runs were discouraging, in that the performance measured was less throughout the speed range than with the inlet guide vanes set axially. Therefore, the test vehicle was disassembled for aerodynamic and mechanical examination.

Several sources of differences between calculated and measured rotor performance at high speed are possible. The inlet guide vane system, including the flow path up to the rotor, is a potential source of high losses. For this reason, the flow path was examined in detail for evidence that would suggest high inlet losses. The rotor blading may have been a source of high loss, particularly if the inlet system was not providing a uniform flow into the rotor blades. Careful attention was given to the patterns visible on the disassembled rotor blades. The vaneless diffuser portion of the rotor is also believed to be a potential source of significant loss, as is described in detail in the Analytical Investigations section of this report. For this reason, the flow path sides of the rotating shroud and disc have been closely examined.

Flow separation in a region just outward from the rotor blade trailing edges could account for the high total pressure loss and low static pressure which were observed in the rotor performance at high speeds. In Figure 198, there is seen a dust pattern on the rotating shroud which extends about 0.5 to 0.75 inch radially outward from the exit of the rotor blades. This pattern was not observed on the disc, and suggests a region of separation on which fine particles (of Teflon generated by contact of the labyrinth seal with the forward face of the rotating shroud) have been deposited due to reversed, zero, or low flow velocity.

Flow patterns which appeared adjacent to the rotor blades on the rotating shroud are shown in Figure 199. These patterns are distinguished by relatively heavy deposits close to the convex surface of the rotor blades beginning about 60 to 70 percent chord, and by a remarkably clean region which appears to be tangent to the concave surface in the trailing edge region. The regularity of these patterns is remarkable and can perhaps best be seen in Figure 198. A smaller but equally consistent dirt deposit is visible near the convex surface of each rotor blade in the leading edge region (Figure 199). In this figure, a

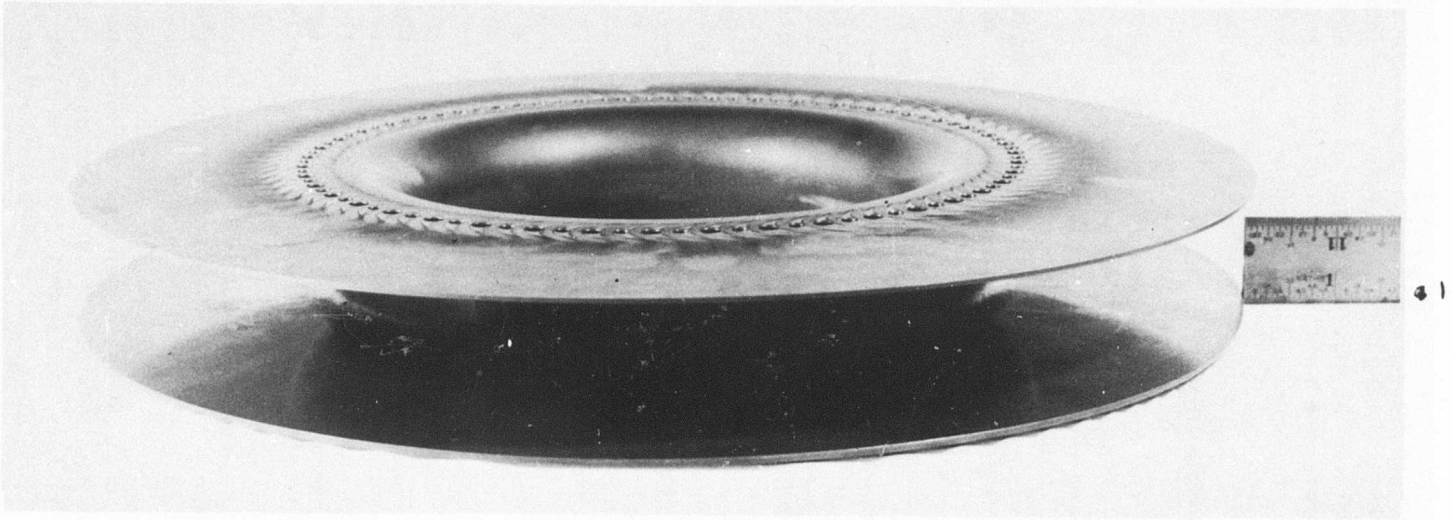

Figure 198. Phase II Rotor Sharp Shroud Showing Dust Patterns Observed After Testing Buildup C.

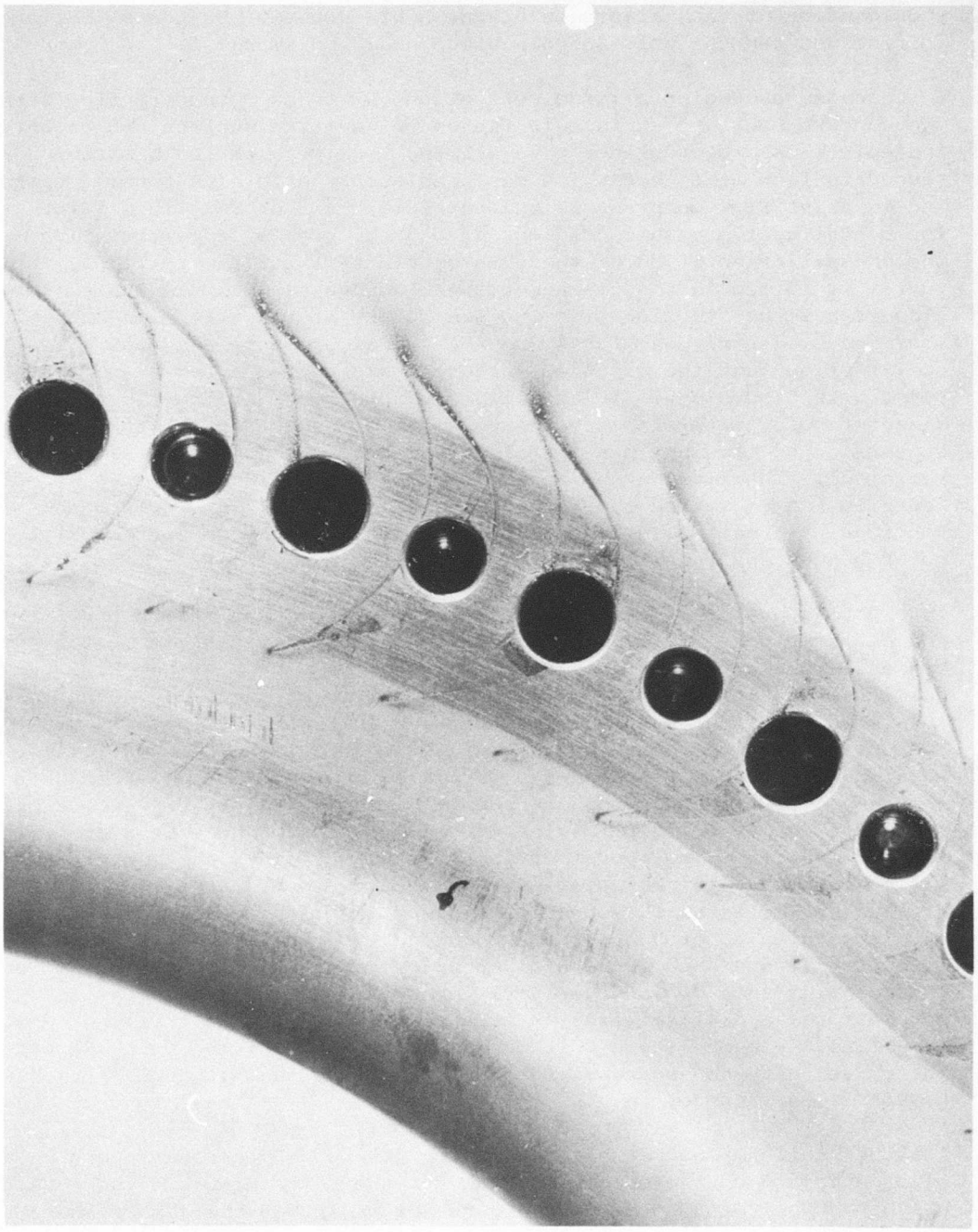

Figure 199. Dust Patterns on Rotor Shroud Adjacent to Rotor Blades.

region of deposit just downstream of each large bolt hole can be seen at the location of each alternate blade. This deposit suggests that the fairing between the bolt and the blade could be improved.

In cascades producing a large deflection, a strong secondary flow from the concave pressure surface to the convex suction surface can be anticipated. These rotor blades have all the requirements for a strong secondary flow like that which has been observed in high turning cascades and in axial flow compressors and turbines. A factor in this rotor is the centrifugal pressure gradient due to the high speed of rotation and the unusual orientation of these rotor blades. It is very likely that a vortex is formed in the passage between blades as with usual high turning blades, but that the location and trajectory of the vortex is significantly modified by centrifugal force and the radial pressure gradient. Partial confirmation that the expected vortex exists near the convex surface can be seen in Figure 199. In this figure, some material from the smaller diameter hole, seen slightly to the right of center in this figure, appears to be flowing in a spiral path close to the convex surface of the blade. The flow in the separated zone, which is assumed to be moving radially inward toward the rotor blades, is probably drawn into the vortices originating in the juncture between the convex surface of the rotor blades and the walls of the rotor.

Interesting patterns of a white powder believed to be Teflon particles and of lampblack-like soot were seen on the concave surface of the rotor blades. The convex surfaces are almost entirely free of deposits. The particles appear much more prominent and of larger size and roughness in these figures than in actuality. As seen in Figure 200, a very consistent narrow band of white particles was deposited adjacent to the rotating shroud. Although a few particles adhered to the leading edge, the general pattern did not start until about the 25 to 30 percent chord position. These white particles did not appear on the disc side of the rotor blades, but the source of the Teflon particles, the labyrinth seal, was in contact with the rotating shroud; therefore, there was no source of such particles on the opposite side of the flow path. This evidence of a separated zone on the concave rotor blade surface suggests poor inlet conditions such as a thick boundary layer entering the blades on the rotating shroud. Another striking feature of the white particle deposits was a distinct line on each rotor blade at the trailing edge. This line, seen in Figure 201, marks the boundary of the white deposit, but is so sharp and so consistent on each blade that it appears to have greater significance.

A rather uniform soot deposit beginning at about 50 percent chord was also deposited on the concave surface of the rotor blades. The nature of this deposit can be seen in Figure 201, although the rather sharp demarkation between the clean zone in the forward half and the deposit in the rear half could not be photographed until later when the blades were removed from the rotor (Figure 202).

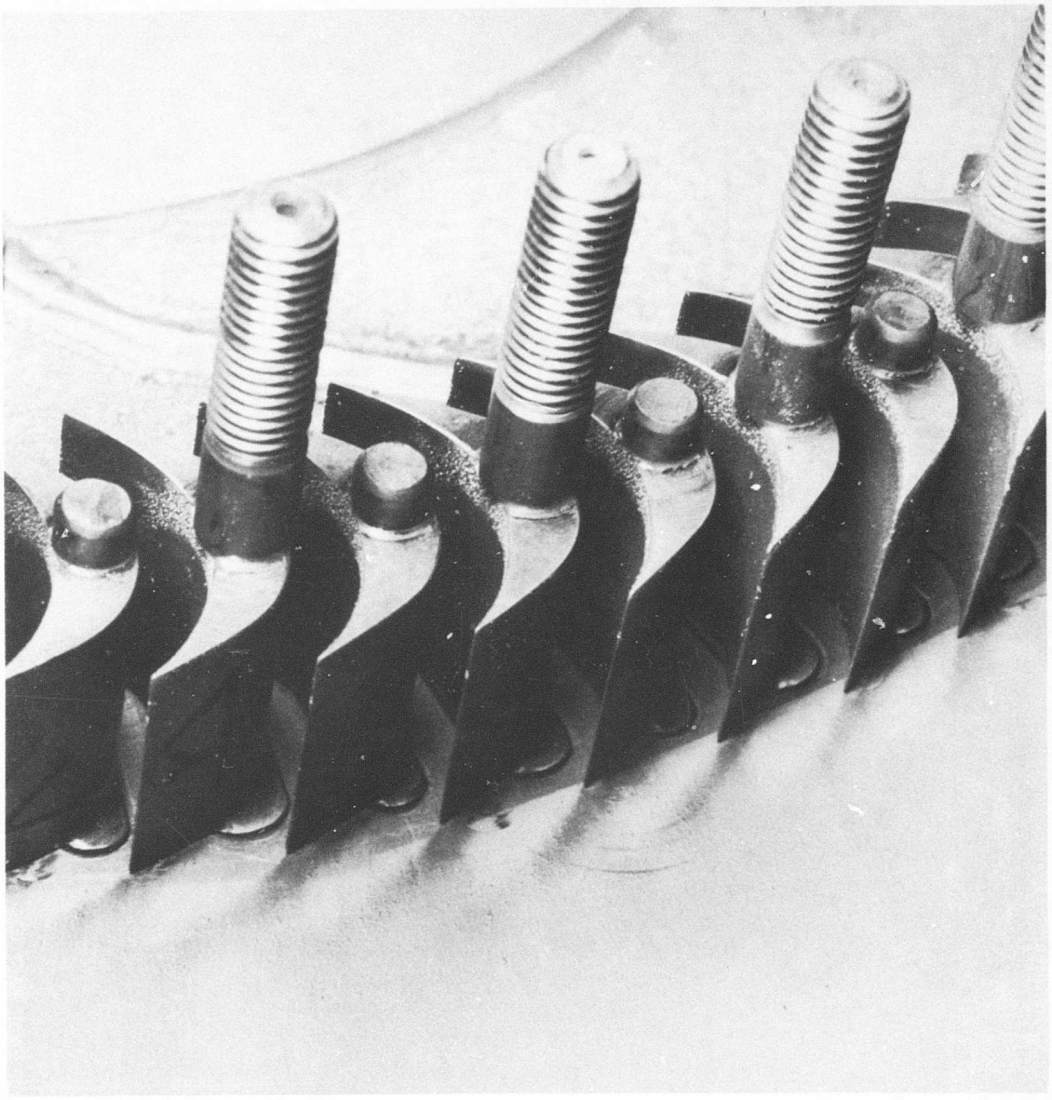

Figure 200. Dust Patterns on Rotor Blades and Disc Following Tests of Buildup C.

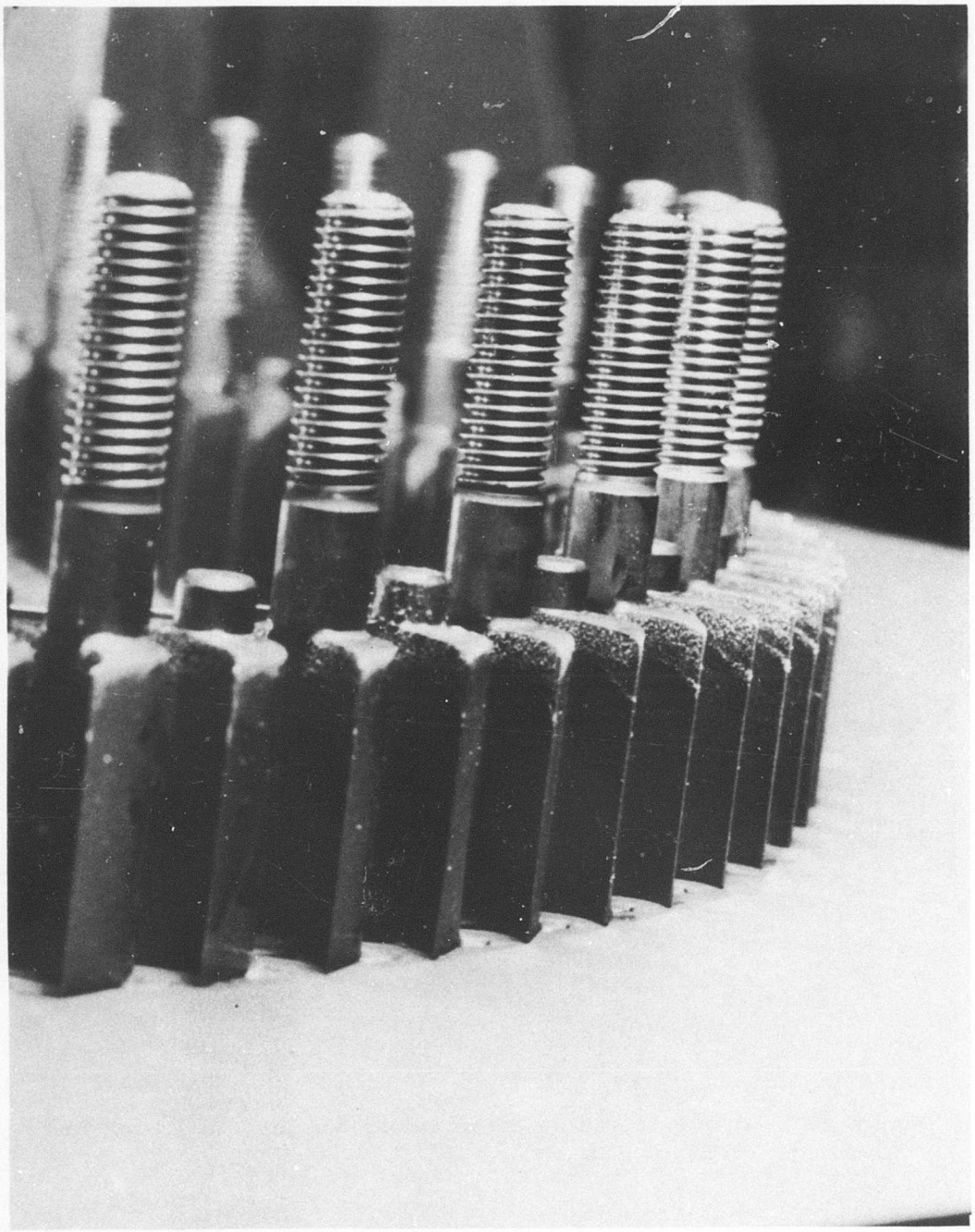

Figure 201. Patterns Left on Rotor Blades - White Particles are Teflon Originating from the Forward Seal.

(a) (b) (c)

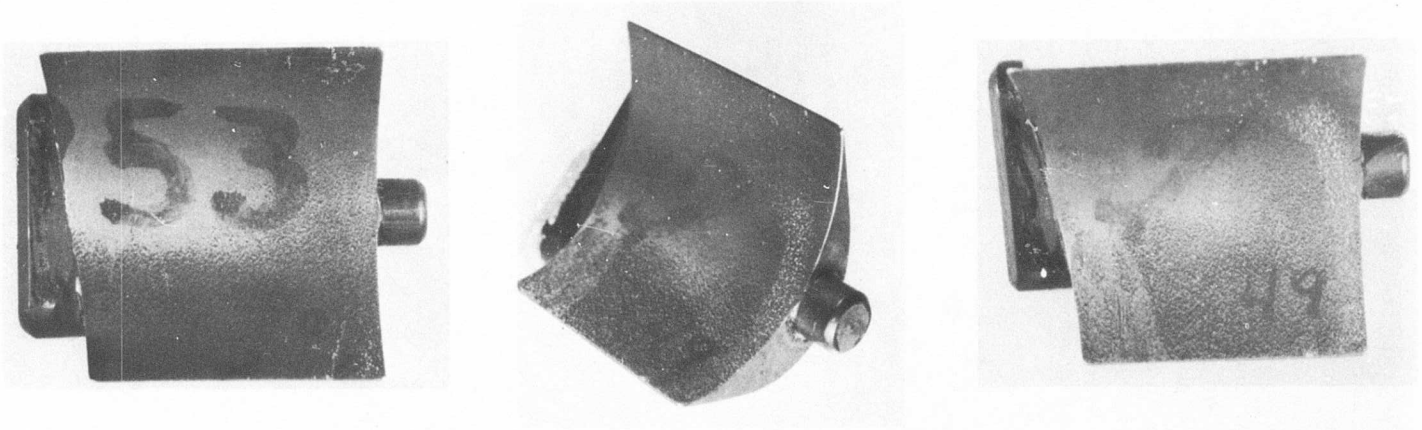

Figure 202. Dust and Teflon Particle Patterns on Convex Surface of Rotor Blades Following Test of Buildup C.

Somewhat less well defined patterns are also observed on the disc side of the flow path. Radial streaks originating near the rotor blades can be seen in Figure 203. As seen in this figure, alternating clean and deposit zones were observed just outward of the rotor blades on the disc. The radial streaks can also be observed in this figure. This evidence suggests that a separated zone was not present on the disc side of the flow path, but that the corner vortex of similar strength appeared on the disc side as on the shroud side. Of course, these patterns indicate only what was happening in the boundary layer, and represent accumulated deposits that occurred over a range of rotation speeds and perhaps at inlet guide vane settings other than 40 degrees closed, which was the last configuration tested before these photographs were made.

TESTS OF BUILDUP D

Compressor Configuration

The high-speed ROC was assembled and checked out for mechanical operation of Buildup D. Buildup D consisted of: (1) the original high-speed rotor, (2) a modified inlet without inlet guide vanes and with only a small central member to carry strain gage and thermocouple leads forward to the slip rings, (3) no stators, (4) a modified scroll collector having about 78 percent greater area at most circumferential locations, and (5) larger exit elbows and ducts upstream of the throttle valves.

The use of either the radial inflow or the axial-flow inlet guide vane system with the low-speed ROC reduced the compressor efficiency by a minimum of 5 percent as compared to the simple bellmouth inlet (Reference 1). A strong possibility existed that the axial-flow inlet guide vane system used in Buildups A, B, and C of the high-speed ROC reduced the high-speed rotor performance a similar amount. The deposits observed on the high-speed rotor blades (Figure 202) support this possibility. The deposit that can be seen in these figures was most extensive near the rotating shroud. This suggests a region of low velocity flow which could be at least partly due to poor inlet flow. A new inlet assembly (Figure 204) was fabricated for use in Buildup D. The purpose of this inlet was to bring the flow up to the rotor at low velocity with a rapid acceleration near the rotor entrance. This inlet was intended to simulate the use of the simple bellmouth in the low-speed ROC tests and, therefore, to improve significantly the high-speed rotor performance.

As noted previously, it was found necessary to increase the flow area of the exit system of the high-speed ROC in order to obtain design flow in this compressor. To accomplish this, the exit system was modified by temporarily installing tubes through the subsonic stator spindle openings. Although this modification was successful in increasing the compressor airflow to the design value and more, the multiple tubes and the secondary exit system greatly complicated assembly and disassembly of the high-speed compressor. Furthermore, this temporary system could not be

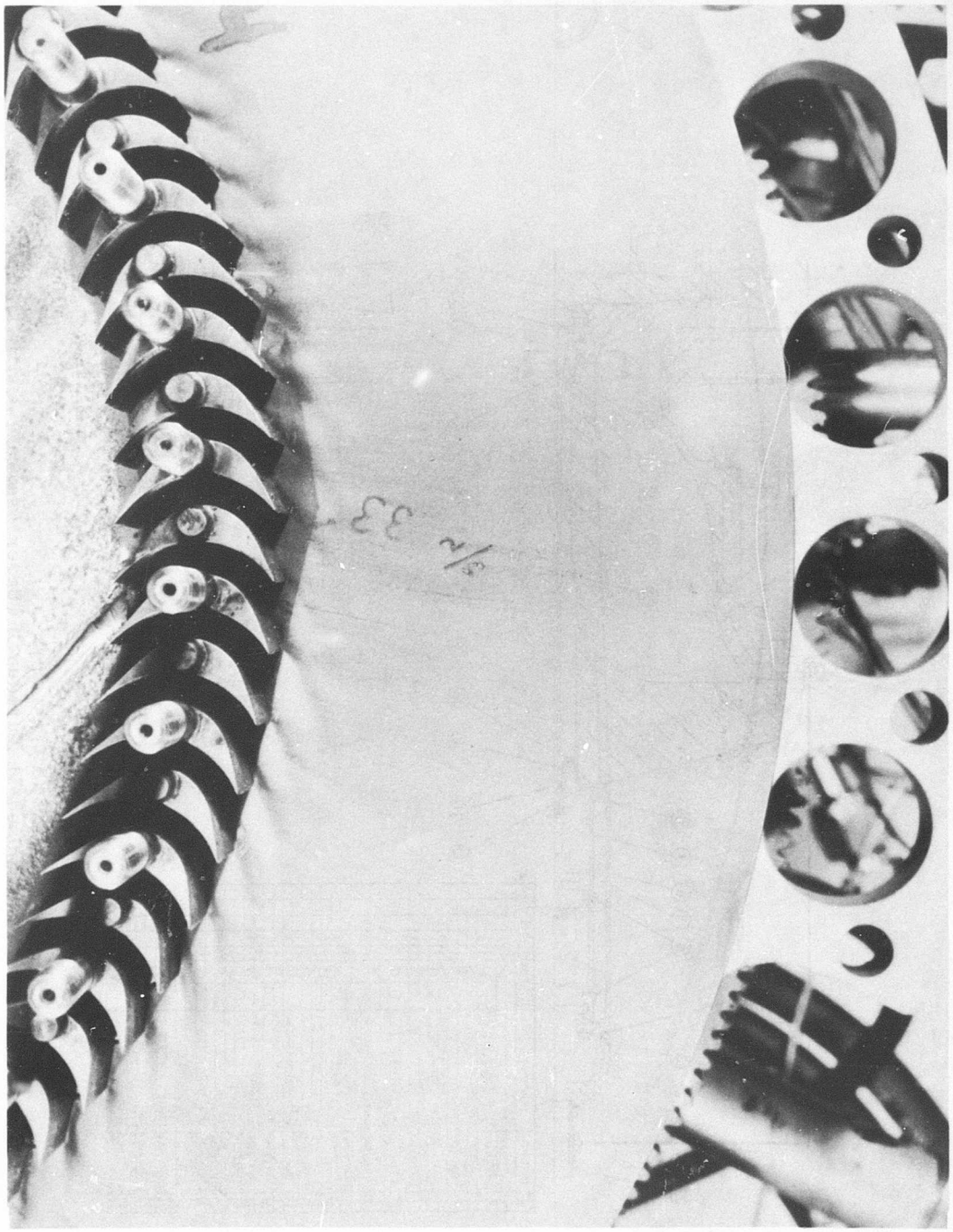

Figure 203. Dust Patterns on Rotor Disc Following Tests During Buildup C.

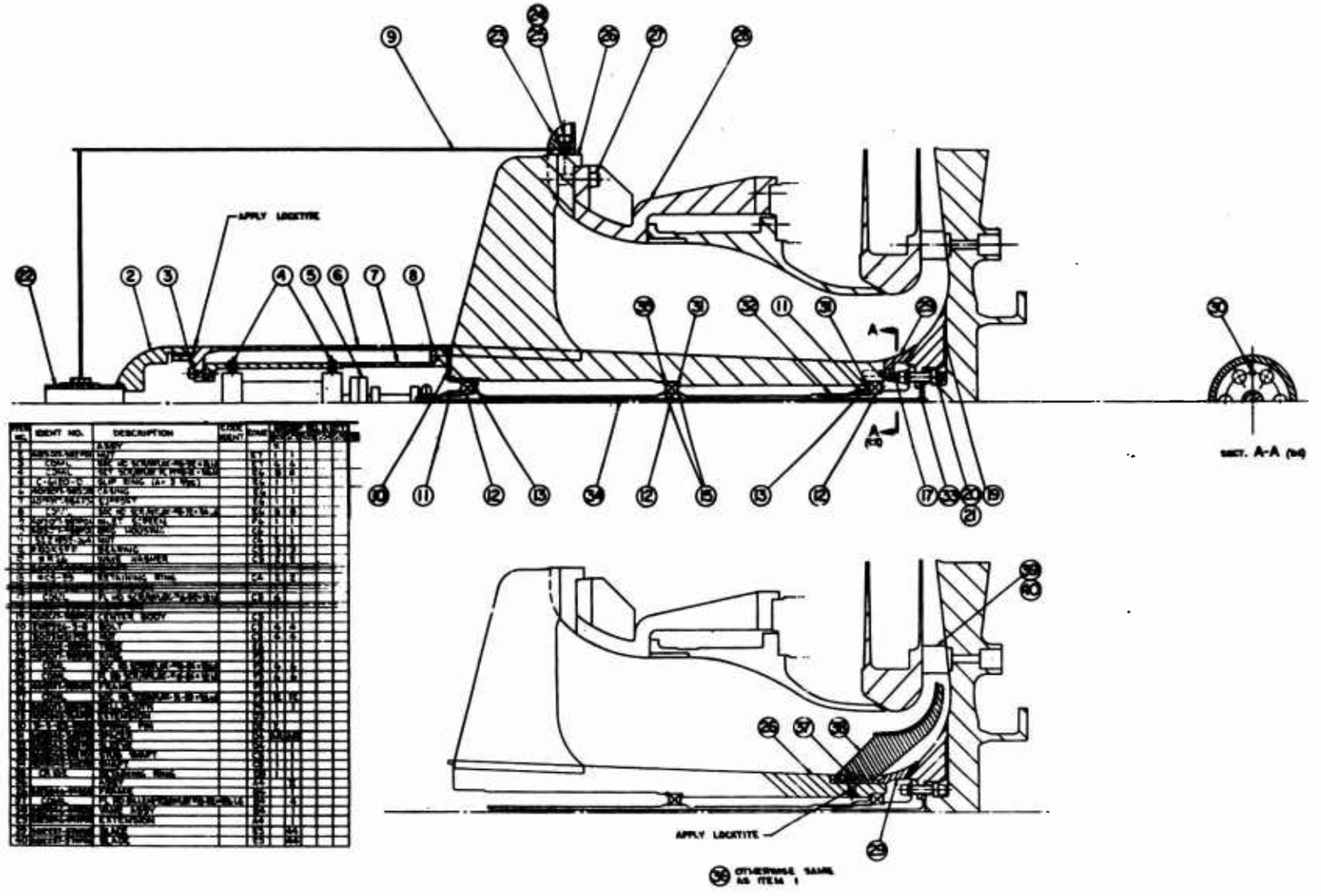

Figure 204. Modified Inlets Used in Buildup D (Upper Drawing) and Buildup F (Lower Drawing).

used with subsonic stators. A more permanent modification of the exit system was designed to be used as the exit system during the remaining buildups. The new exit system consists of enlarging the scroll area by about 78 percent at all circumferential locations. This improvement of the exit system should have alleviated the circumferential static pressure gradients observed in previous tests.

Improved Rotor Instrumentation

When rotor teardown prior to Buildup D was scheduled, improvements in rotor instrumentation (see Appendix IX) were planned for incorporation during the subsequent assembly. Overall instrumentation was simplified by reducing the number of strain gages from 12 to 6 and also by eliminating all diode circuits. This was possible because the rotor blades have shown an impressive absence of vibration. Detailed vibration monitoring was no longer required, but 2 instrumented blades were retained. Strain gages were added to the shroud on both the forward and aft rims. This allows monitoring of the previously unobserved aft or blade-side rim and improves measurement of the forward or seal-side rim. Two thermocouples were retained in the same disc locations as in the previous rotor assembly.

The assembly of the compressor is shown in Figure 205 before the inlet screen was attached and before the canvas screen was put in place. The enlarged exit pipe and elbows can be seen at the compressor exit. In the close-up photograph, stationary total pressure probes just upstream of the rotating shroud can be seen (Figure 206). Two of the strain gage leads on the rotor are also visible. The compressor is shown in Figure 207 after installation of the inlet screen.

Aerodynamic Performance

Test points obtained during Run Number 10 on January 31 and during Run Number 11 on February 3, 1967, are presented in Figures 208, 209, and 210. The performance of the compressor rotor in the presence of the new "open" inlet system was very encouraging in the low-speed range. At 30 and 40 percent speed, peak efficiencies varying between 90 and 92 percent were obtained. This performance represents a significant increase over previous test results at these speeds. The measured total pressure ratio (Figure 208) and static pressure ratio (Figure 209) appear to agree quite closely with predicted values. Leakage into the exit system between the throttle valves and the booster compressor occurred since this part of the system is at less than atmospheric pressure when the booster compressor is operating. Pressure and temperature readings were not affected by the leakage, and corrections have been applied to the airflow values so the general performance can be compared with previous runs (Figure 210).

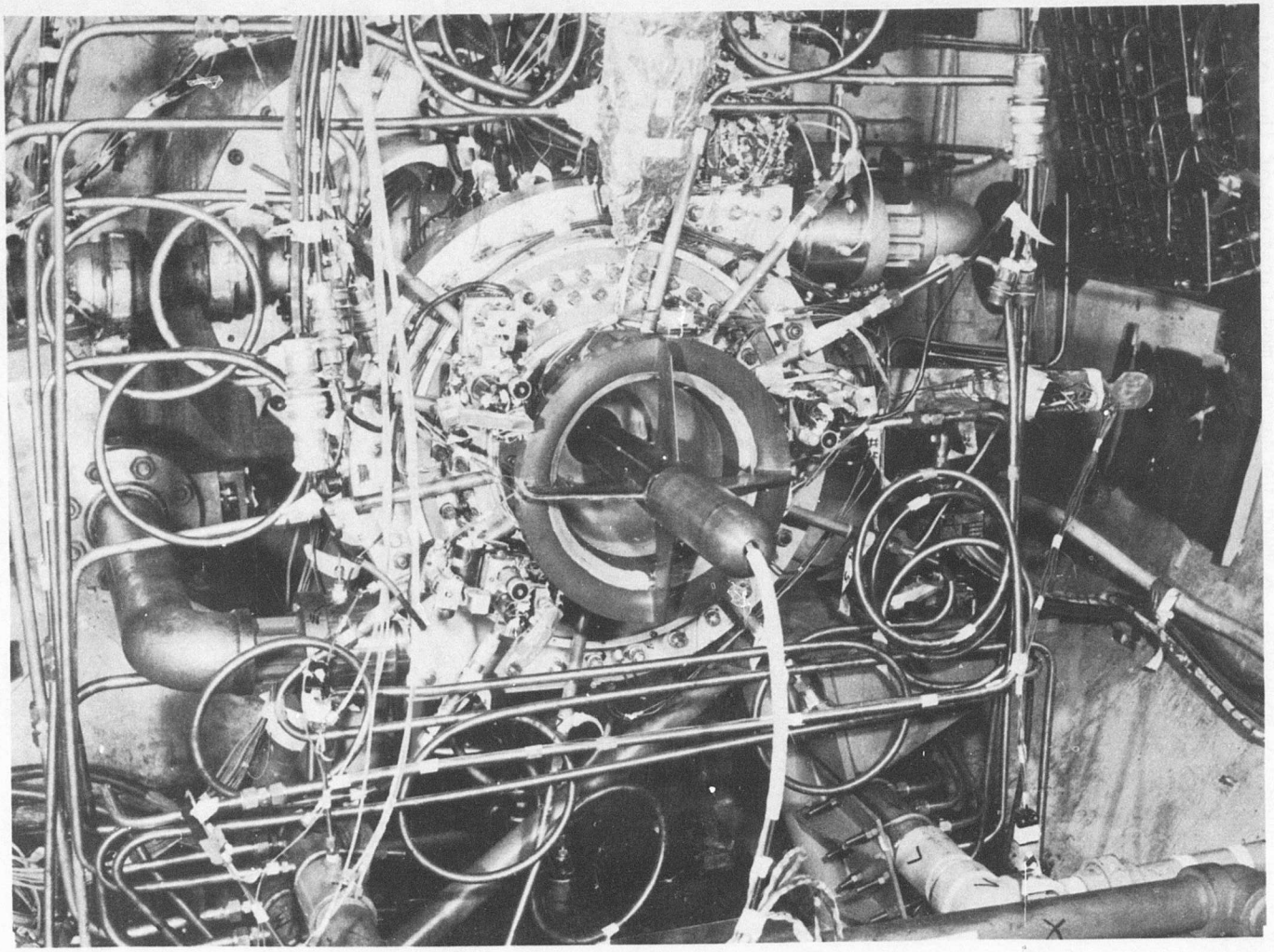

Figure 205. Assembly of High-Speed Compressor Prior to Test of Buildup D.

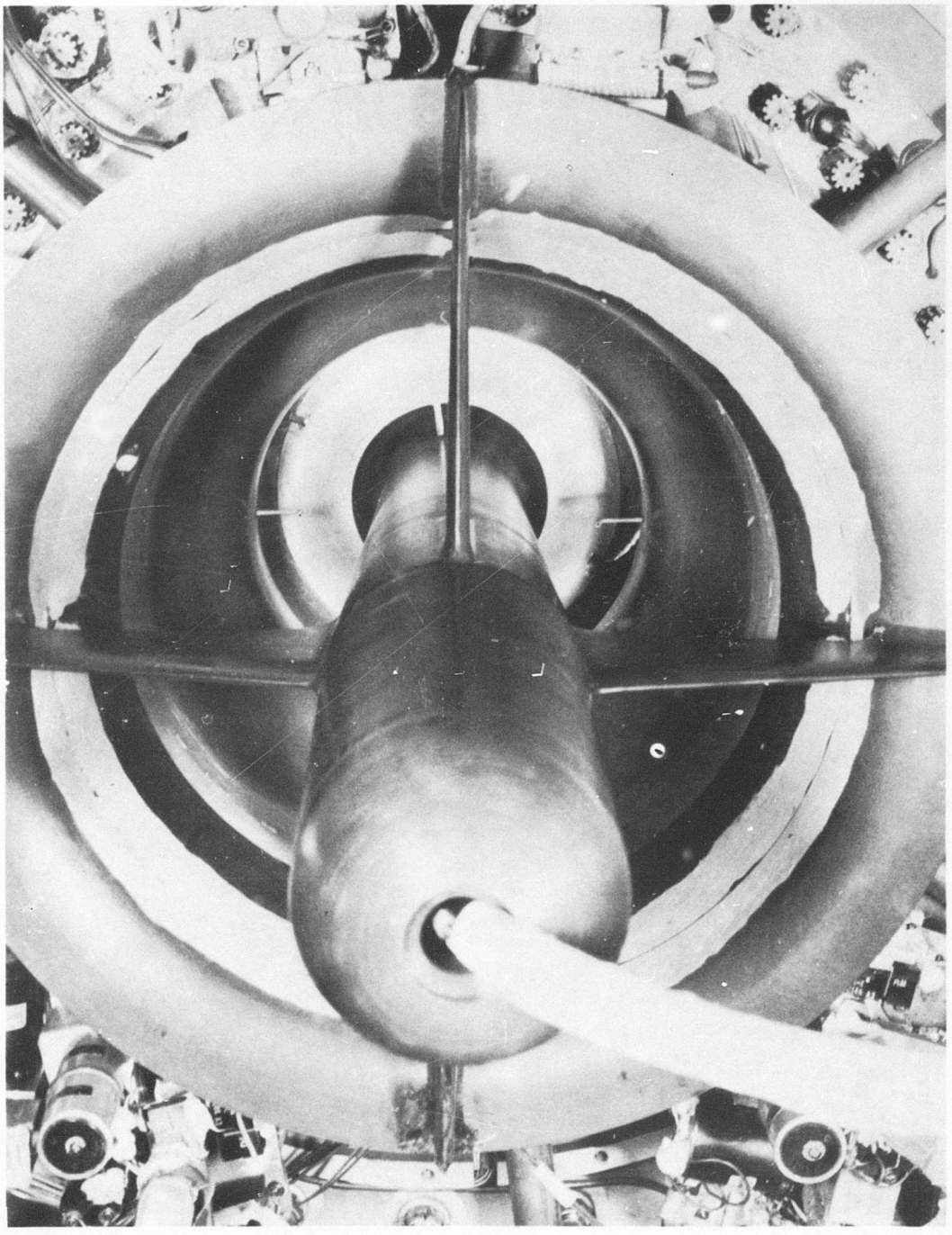

Figure 206. Close-up of Open Inlet Used in Buildup D.

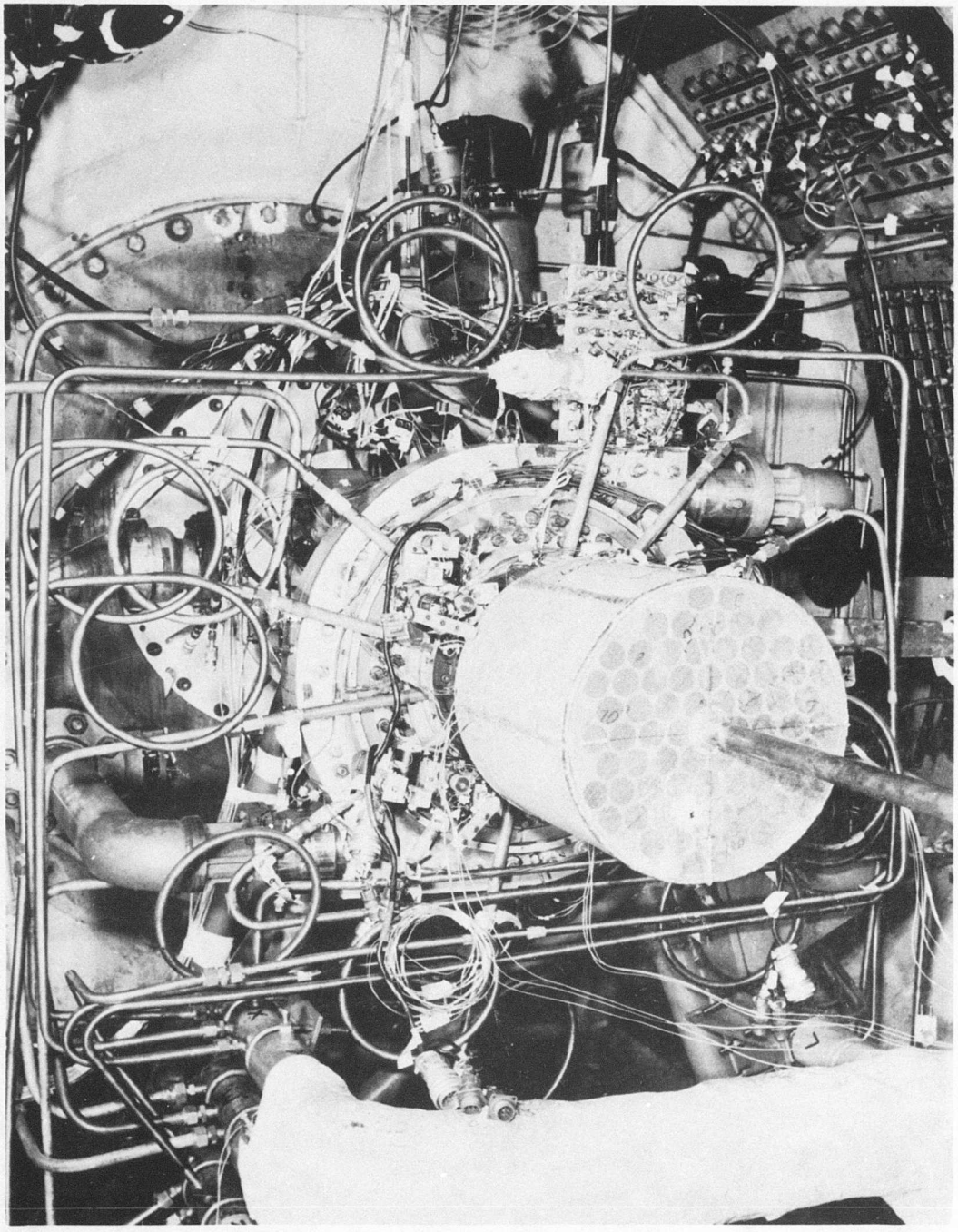

Figure 207. Assembly of Compressor for Test of Buildup D After Installation of Inlet Screen.

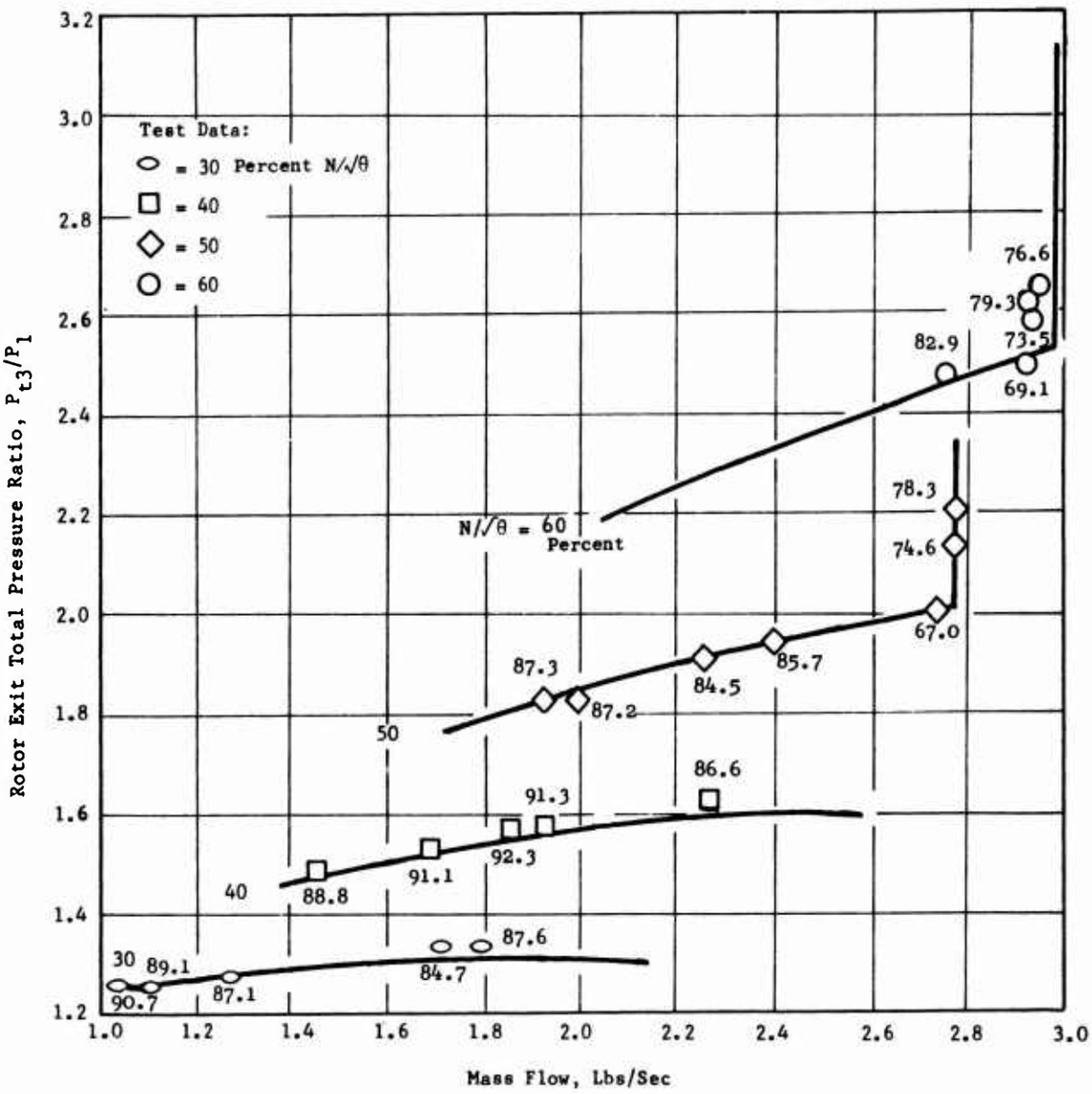

Figure 208. Total Pressure Ratio Versus Mass Flow for Run Numbers 10 and 11 (Buildup D) With Open Inlet.

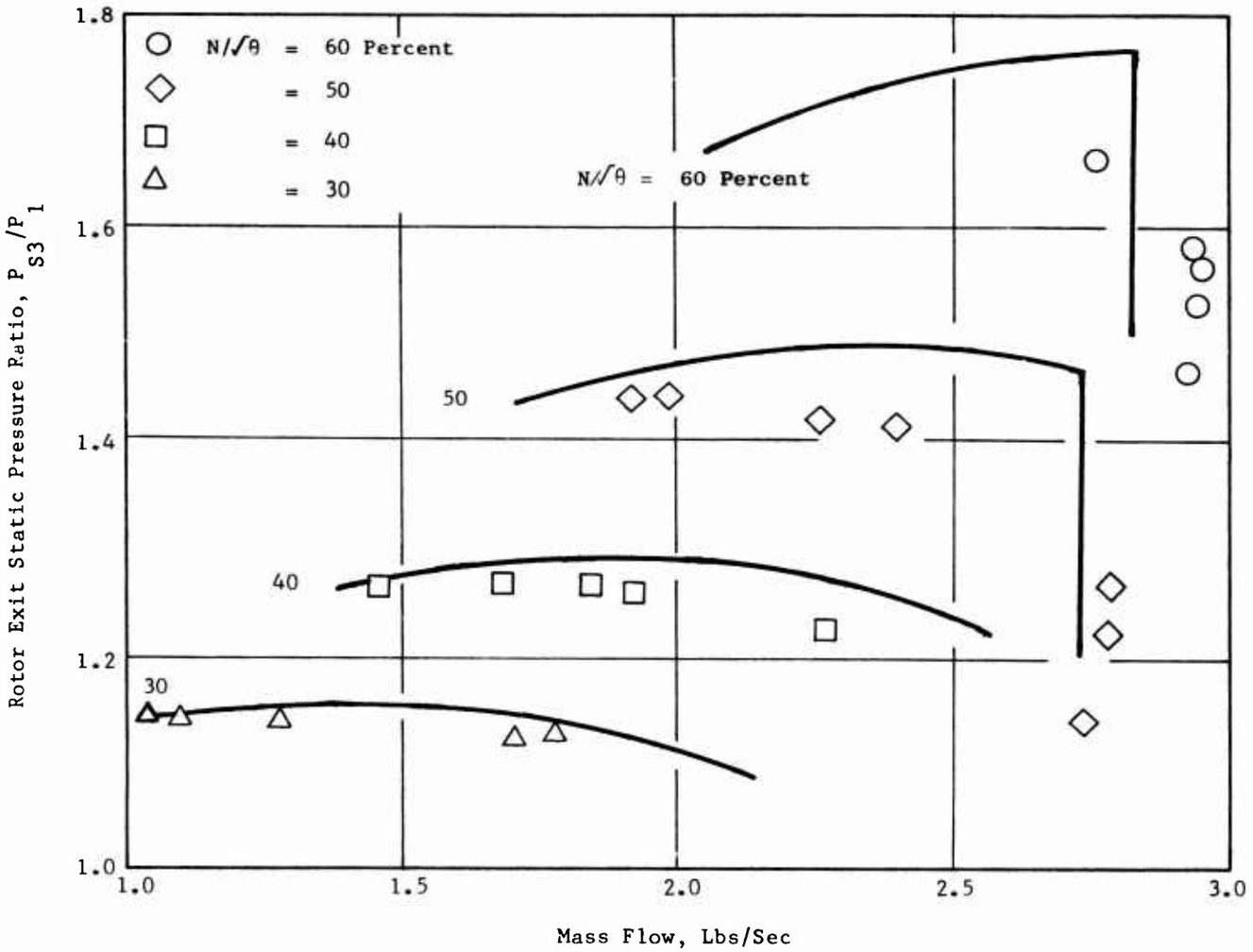

Figure 209. Static Pressure Ratio Versus Mass Flow for Run Numbers 10 and 11 (Buildup D) With Open Inlet.

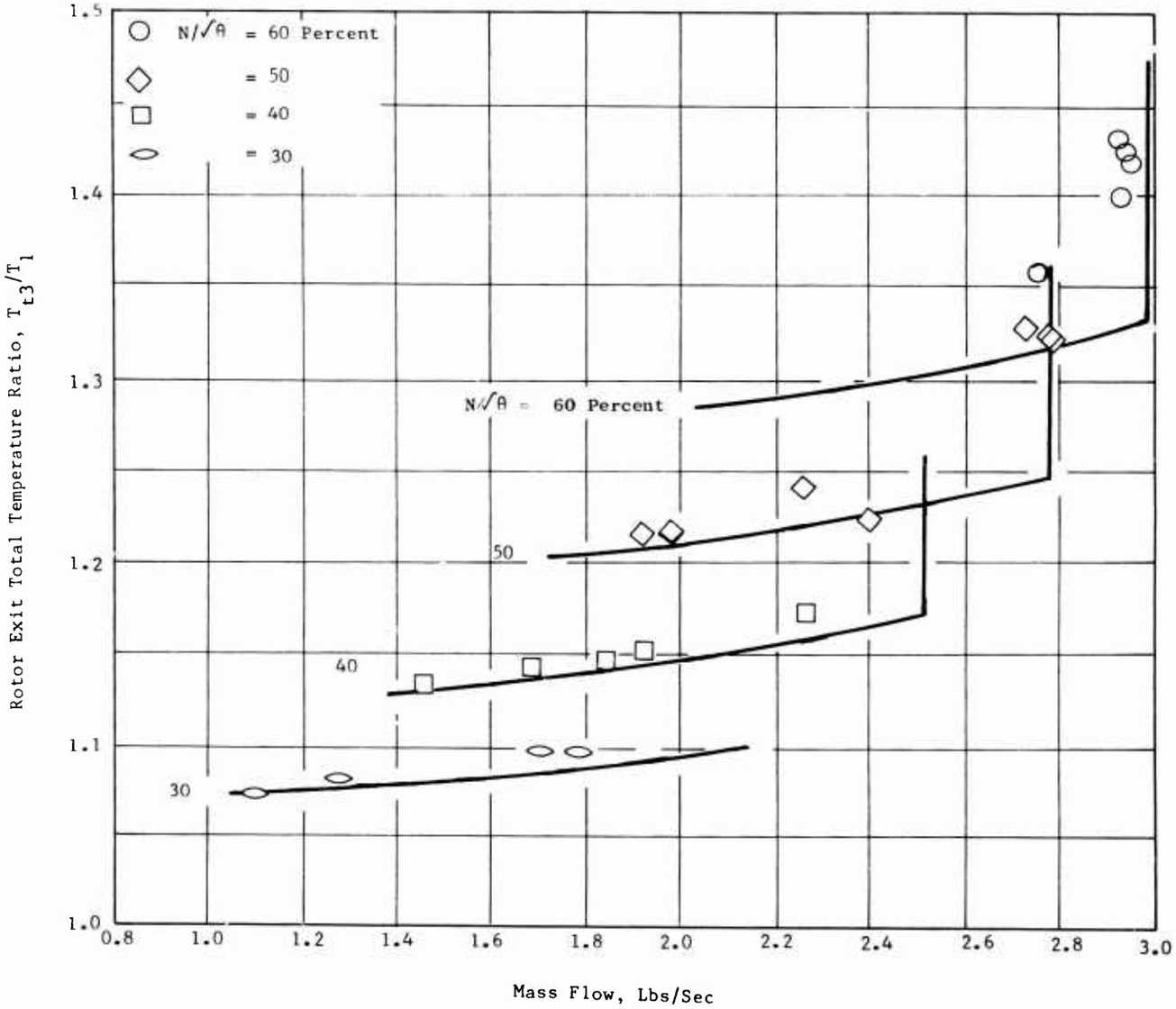

Figure 210. Total Temperature Versus Mass Flow for Run Numbers 10 and 11 (Buildup D) With Open Inlet.

At 50 percent speed, a gain in peak efficiency of about 3 percent was measured in comparison with best previous results. The total pressure ratio of 2.2 averaged out slightly greater than the calculated value of 2.14 which had been predicted. The static pressure ratio was slightly lower than the predicted values at all airflows. The measured maximum static pressure ratio was 1.44 compared to the predicted value of 1.49. From these results it is concluded that the new inlet did permit a significant increase in compressor rotor performance at low and medium rotational speeds.

A few points were also taken at higher speed conditions. At 60 percent speed, an average total pressure ratio of 2.64 was measured as compared to the predicted value of 2.82. At this speed, distribution of total pressure in the axial direction across the rotor exit was not very uniform for the supersonic rotor blade exit condition. Although 4 of the 5 probe positions yielded steady readings of angle and total pressure, the fifth probe location nearest the rotor disc gave indications of unsteady reverse flow. The single data point taken at 65 percent speed illustrates the nonuniformity of rotor exit total pressure during the higher speed runs. The average total pressure of the first 4 tubes was about 42 pounds per square inch absolute (psia) or a total pressure ratio of 2.9. The fifth station near the rotor disc indicated a total pressure of 34.9 psia or a total pressure ratio for that station of only 2.4. It is believed that flow separation within the rotor is occurring at rotational speeds at 60 percent and above. Although the new inlet improved the flow entering the rotor, the flow was still weak on the shroud side under the severe radial static pressure gradient. At high speeds, the flow on the disc apparently separated and did not reattach on that side of the flow path in the rotating diffuser. This flow pattern produced high losses, and the behavior was different from that of previous buildups.

A very severe circumferential static pressure gradient was observed at station 3.0 (rotor exit) during Buildup D runs. For most runs at the higher speeds, circumferential pressure differences of from one-third to one-half atmosphere were recorded. The maximum difference observed was about 20 inches of mercury or two-thirds of an atmosphere. The rotor performance must have been affected by these strong 2/rev pressure fields. Better performance was obtained previously during tests of Buildup C at high speed when supersonic stators were employed. These stators effectively isolated the rotor from the static pressure differences occurring in the stationary vaneless diffuser and scroll collectors.

It was anticipated that the increased area of the modified scroll (to permit pumping rated airflow) used in Buildup D would reduce the magnitude of the circumferential static pressure gradients. Actually, the

observed gradients increased by a factor of about 4. Improved compressor performance, particularly at intermediate speeds from 45 to 65 percent, should be obtained by employing supersonic stators in Buildup E.

TESTS OF BUILDUP E

Compressor Configuration

An extensive series of tests was conducted with the modified inlet, the original rotor, and the supersonic stators which comprise Buildup E. The partial assembly of the supersonic stators having strain gages is shown in Figure 211. This photograph also illustrates the modified exit scroll which has been employed in both Buildup D and E. Figure 212 is a close-up of the supersonic stator which has been equipped with 3 total pressure tubes. The addition of the stator strain gages and total pressure tubes restricted the motion of the stators to about 3 degrees on either side of the 75-degree setting. In previous tests using the supersonic stators, 75 degrees was found to be close to the best setting for most test points. The runs during Buildup E were the first in which strain gage readings of the rotating shroud rims were obtained. Throughout all the running, sensible information was obtained from at least 1 gage on the seal-side rim and 1 gage on the blade-side rim. This was the first opportunity to observe the stresses in the rotating shroud. This information was decisive in preventing operation in the subsonic exit flow regime at 60 percent speed. Mechanical data useful for rotor design at 100 percent speed operation were obtained at 60, 70, and 80 percent speed.

Aerodynamic Performance

At 30 percent speed, the compressor performance was quite close to that predicted, as shown in Figures 213, 214, and 215. Efficiencies of 80 percent were obtained at flows of 1.78 and 2.08 pps. The rather sudden decrease in efficiency at weight flows less than 1.7 pps may be explained by improper incidence entering the supersonic stators (no attempt to change the stator angle was made because of the stator instrumentation). At 40 percent speed, the pressure ratio was slightly less than the predicted values over the weight flow range from 2.0 to 2.2 pps. The efficiencies (maximum 81.9 percent) measured downstream of the stators were much lower than anticipated, since in the previous buildup, rotor efficiencies of 92 percent were observed in this operating range. The fact that these efficiencies are lower than those obtained at either 30 or 50 percent speed remains unexplained.

At 50 percent speed, the total pressure ratio was significantly lower than the predicted values at weight flows lower than 2.4 pps. At near choke weight flow, a close approach to the expected total pressure ratio was obtained. Maximum efficiency of 83.6 percent was obtained at a corrected speed of 52.4 percent. This point, like the point shown at 56.7 percent speed, was obtained during 1 of the many attempts to obtain subsonic operation without shroud rim or vehicle vibration at 60 percent

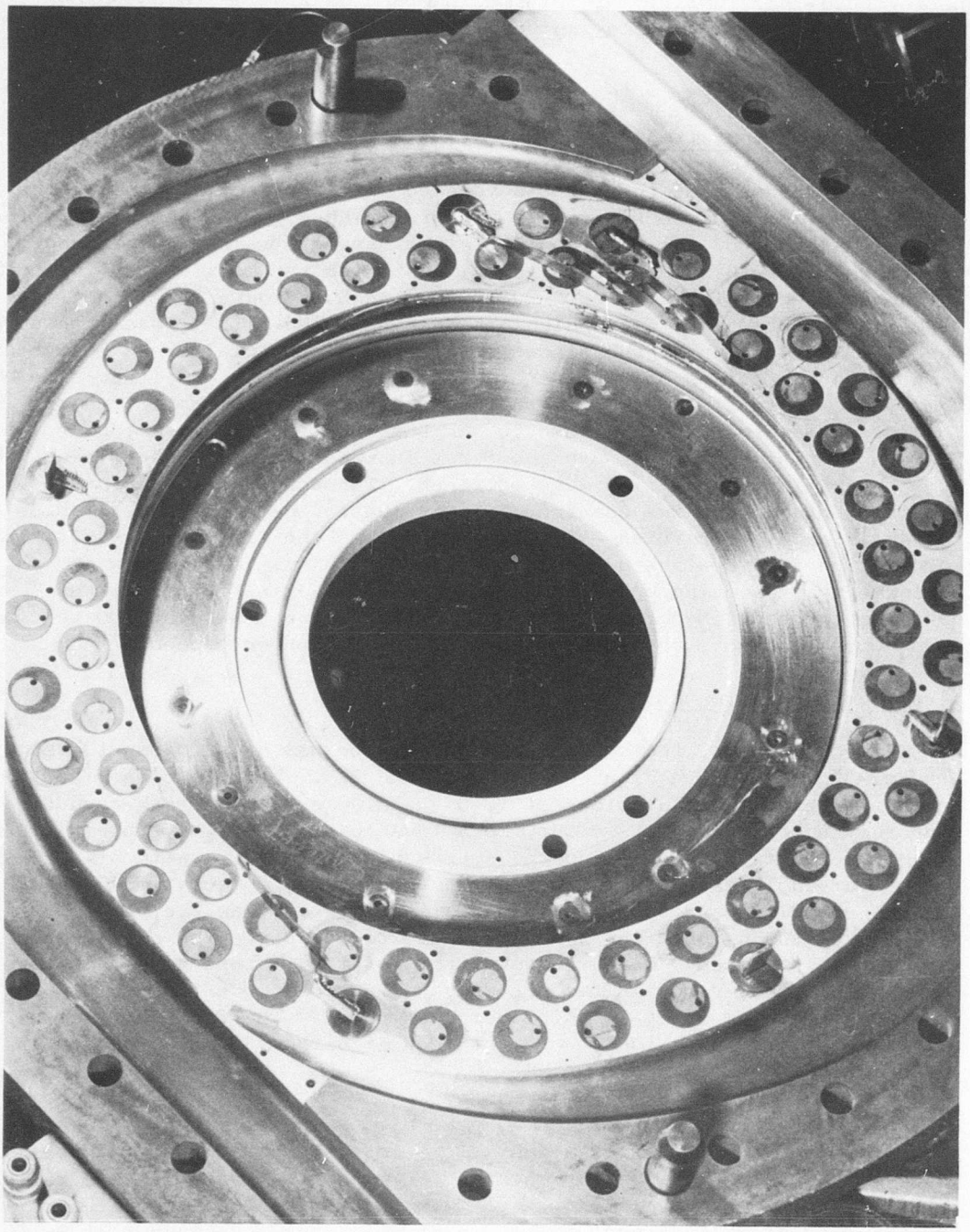

Figure 211. Reworked Scroll Collector in the Upstream Compressor Stator Casing.

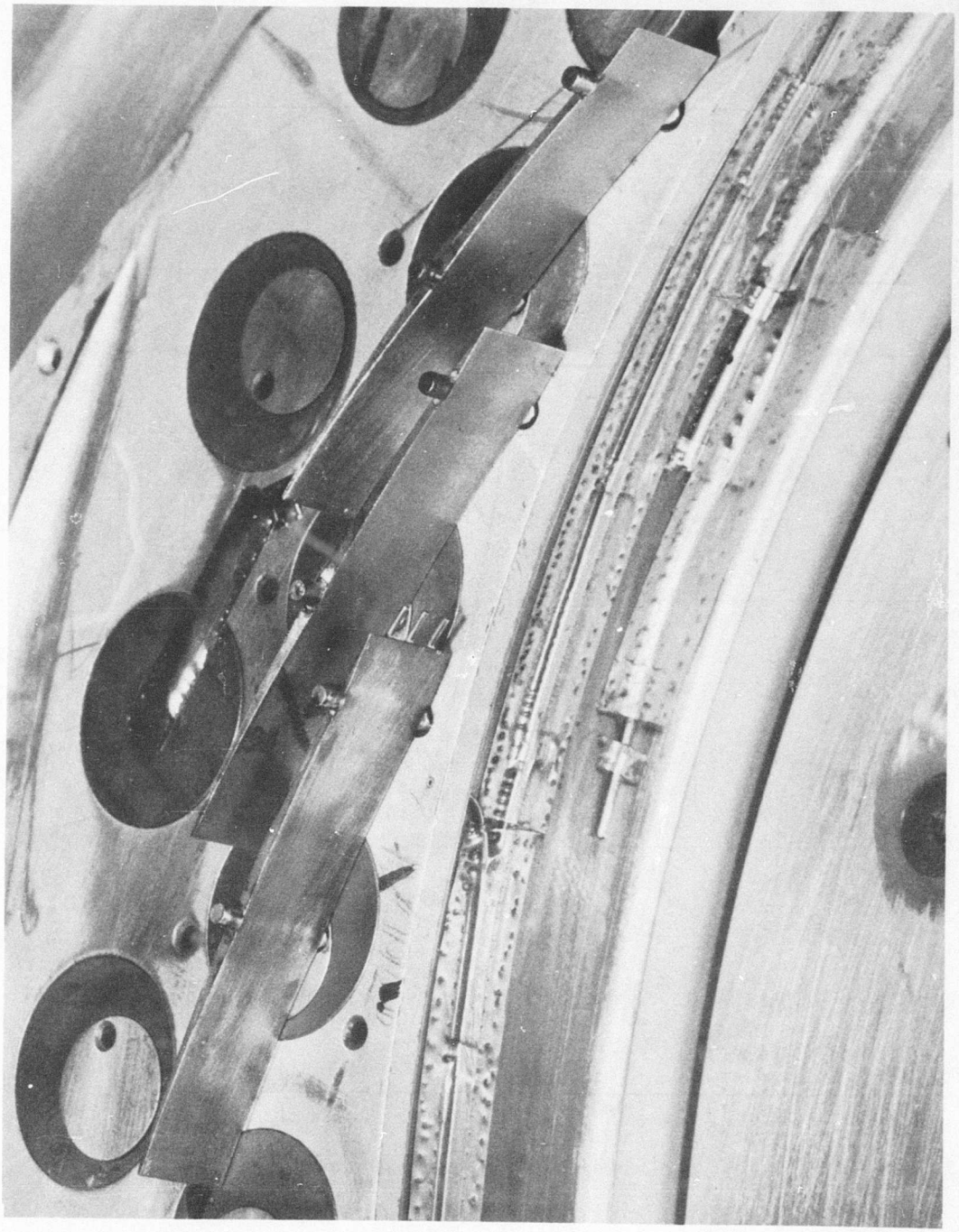

Figure 212. Total Pressure Tubes Installed on Leading Edge of Supersonic Stator Vane.

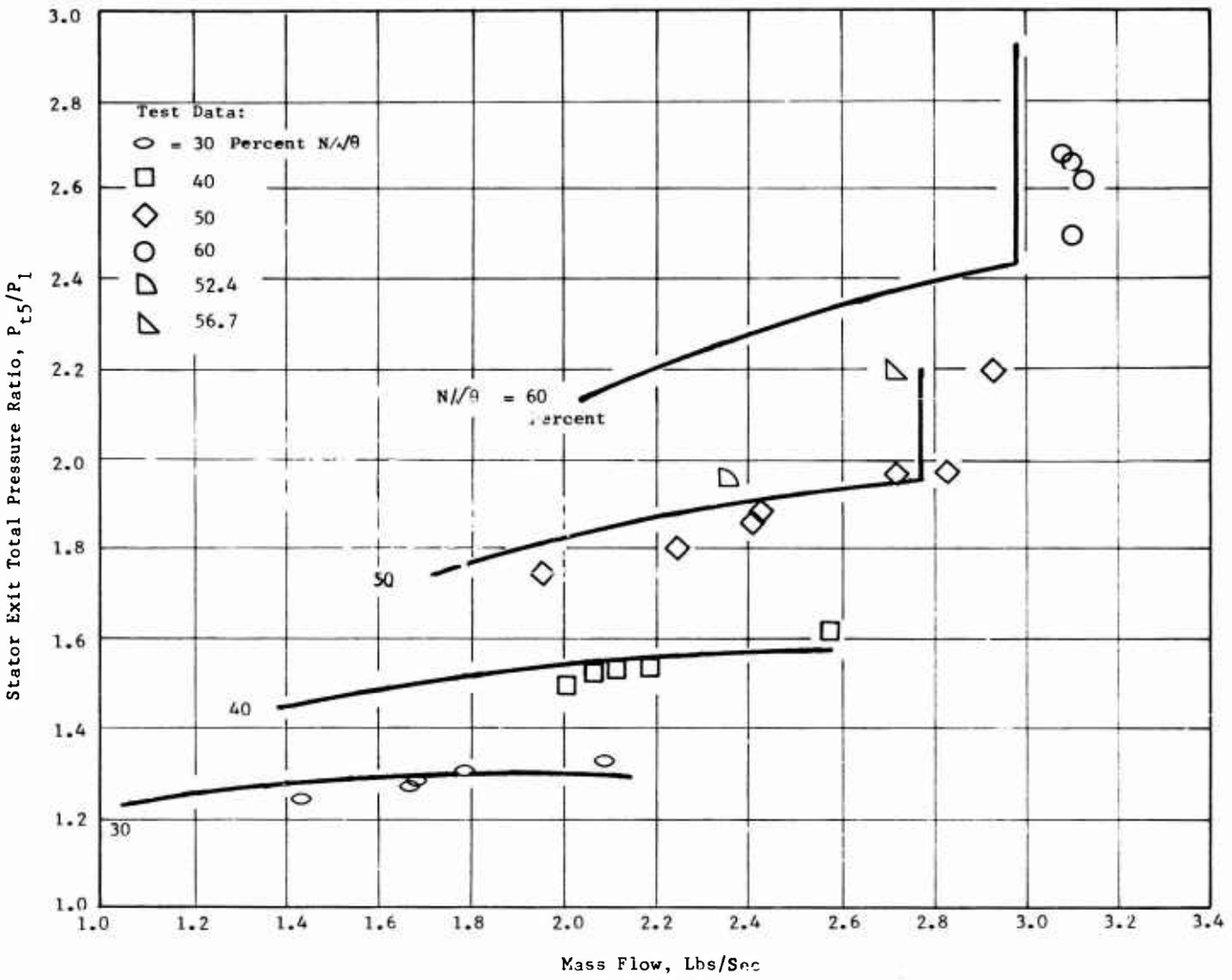

Figure 213. Total Pressure Ratio Versus Mass Flow for Run Numbers 12 and 13 (Buildup E) With Open Inlet.

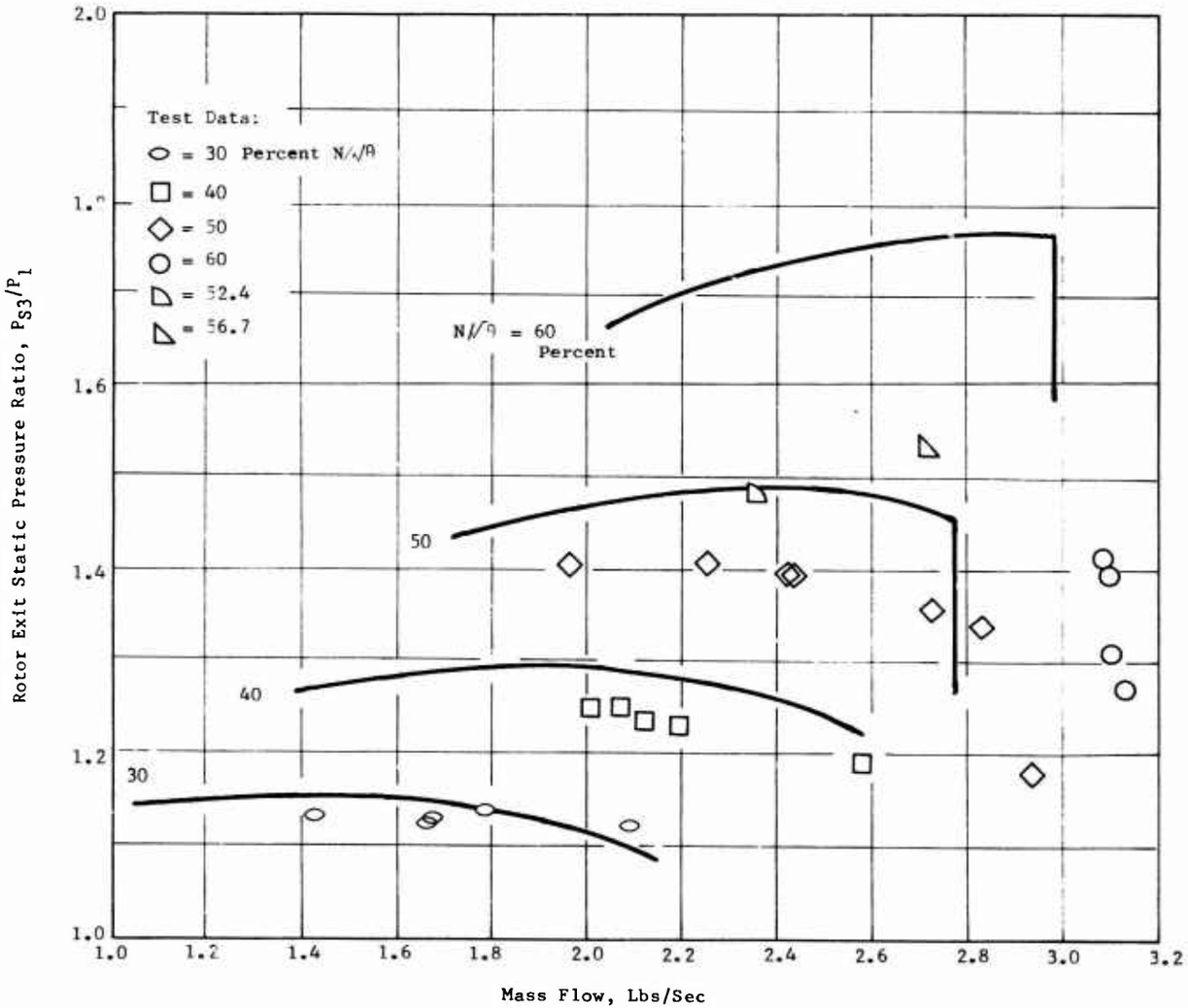

Figure 214. Static Pressure Ratio Versus Mass Flow for Run Numbers 12 and 13 (Buildup E) With Open Inlet.

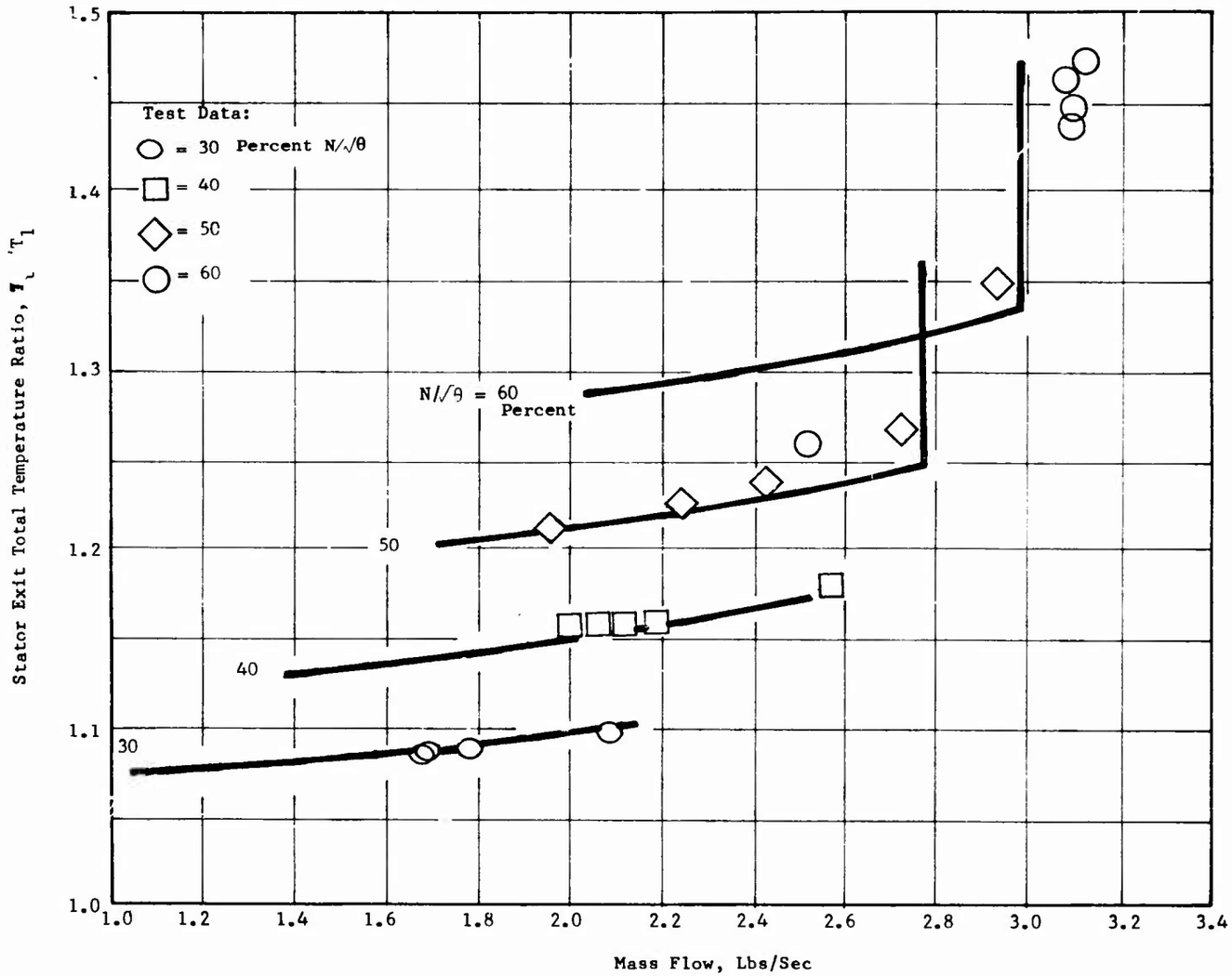

Figure 215. Total Temperature Ratio Versus Mass Flow for Run Numbers 12 and 13 (Buildup E) With Open Inlet.

speed. The best performance at supersonic rotor exit conditions could not be obtained at 50 percent speed due to vibrations of the test vehicle, but a test point at pressure ratio 2.2 with an efficiency of 72.3 percent was observed.

As noted previously, many attempts were made to obtain steady-state flow conditions without excessive vibrations at 60 percent and higher speeds. A satisfactory operating condition was established with supersonic exit flow, but as the compressor was throttled in attempting to obtain maximum supersonic performance, test vehicle vibrations again restricted the back pressure which could be applied and the total pressure which could be obtained. At 70 and 80 percent speed, the observed stresses were so high that operation for a sufficient period to obtain aerodynamic data was not considered to be safe.

Comparison of the total pressure measured downstream of the stators during tests of Buildup E with similar data taken during tests of Buildup C indicates a 5-percent increase in efficiency at both 30 and 50 percent speed. Only a marginal improvement, about 1 percent, appears to have been obtained at 40 percent speed by the use of the modified inlet system in Buildup E.

The results of these tests strongly suggest that a primary problem of the low- and high-speed ROC is concentrated at the sharp turn which occurs at the inlet to the rotor. This possibly has existed since the program was initiated and has been studied using various calculation procedures from the beginning of the contract (see Reference 1). It has now become strongly evident that methods for improving the inlet flow, such as the use of a circular inlet vane, must be employed to realize better overall compressor performance.

Air Injection Into Rotor

On the basis of information obtained during testing of the low-speed ROC and on the evidence of dirt and Teflon powder deposits on the high-speed compressor rotor blades, flow separation probably occurs on the rotating shroud upstream of the rotor blades in both the low- and high-speed rotors. In previous buildups, attempts have been made to improve the flow entering the rotating shroud by removal of boundary layer flow through the slot between the end of the bellmouth and the rotating shroud. The amount of flow which could be removed through this gap was limited by the small size of the tubes through which the flow must be drawn and by the fact that leakage between the rotor and the Teflon labyrinth seal must also be drawn into this same exhaust system. For this reason, the piping was rearranged for the third run of Buildup E so that high pressure air could be injected through the gap between the end of the bellmouth and the rotating shroud. The conditions for energizing the boundary layer entering the rotor are not ideal because the slot makes an angle of about 25 degrees with the flow, rather than being tangent to the lowest point of the rotating

shroud. Nevertheless, because flow injection could be done quickly, it was believed desirable to investigate the possibility of improving rotor performance by this means.

A series of tests was run from 30 to 56 percent speed, the highest which could be obtained without producing serious rotor vibrations. At each speed, air was blown through the slot at a series of slot total pressures or injection velocities. The initial calculations of compressor performance made during the course of the runs indicated a very significant improvement in compressor efficiency as the injection pressure was increased. Corrections to these values have been made on the conservative basis of mass weighting the compressor inlet pressure and temperature. The compressor efficiencies corrected by this method indicate a 2- to 5-percent increase in efficiency at 30 percent speed. At 40 percent speed, an increase of about 3 to 4 percent was calculated. At 48 and 56 percent speed, little or no increase in efficiency is obtained after the correction. These results suggest that although improvement is obtained at low speed, the causes of the losses at high speed have not been affected beneficially by inlet blowing through the gap just upstream of the rotating shroud.

TESTS OF BUILDUP F

Compressor Configuration

Three major changes were employed in the ROC for Buildup F. A circular inlet vane was employed in the inlet to the rotor (Figures 216 and 217) to assist in turning the flow from the axial to the radial direction. The second major difference from previous buildups was the use of new rotor blades having slightly increased chord length with the additional length added to the trailing edge region (Figure 218). These rotor blades are constructed of an improved titanium alloy for use in the Phase III rotor, but became available prior to the assembly of Buildup F. The third major difference was the use of subsonic stators. In previous buildups, the supersonic stators have been employed to isolate the rotor from the strong circumferential static pressure gradients occurring in the scroll collector. The choice of the subsonic stators to fulfill this function was made in order to permit the use of instrumentation close to the rotor exit. Except for the use of the curved inlet vane, the inlet system was the same as in Buildups D and E; that is, the open inlet without inlet guide vanes was employed.

Aerodynamic Performance

The test results obtained during Run Numbers 15 and 16 of Buildup F are by far the most encouraging recorded in this program. Rotor performance up to 70 percent speed indicates that the contract targets may be attained at full speed. Experimental difficulties interfered with obtaining a continuous record of total pressure and flow angle data across the span

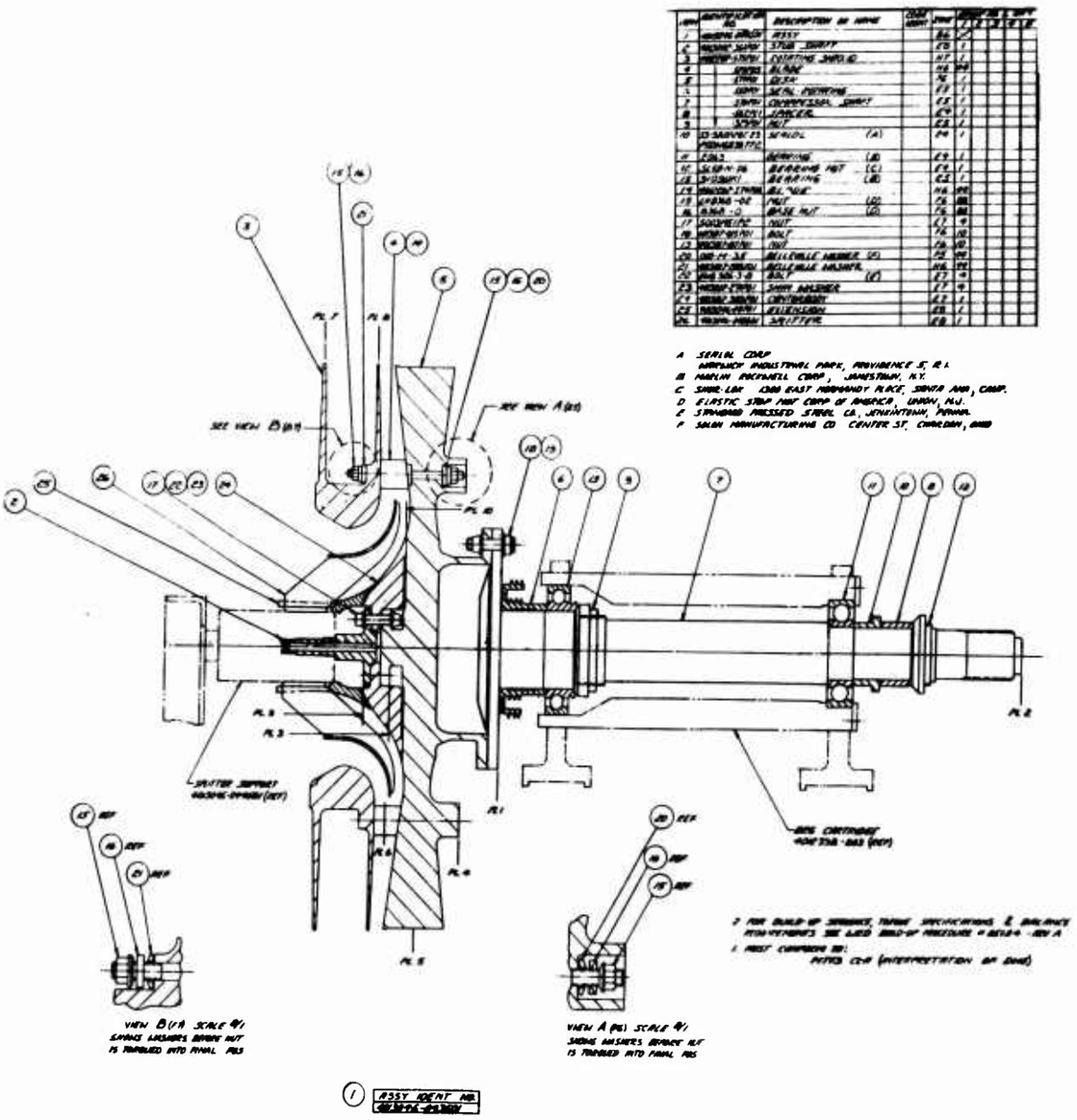

Figure 216. Rotor and Circular Inlet Vane Tested as Buildup F.

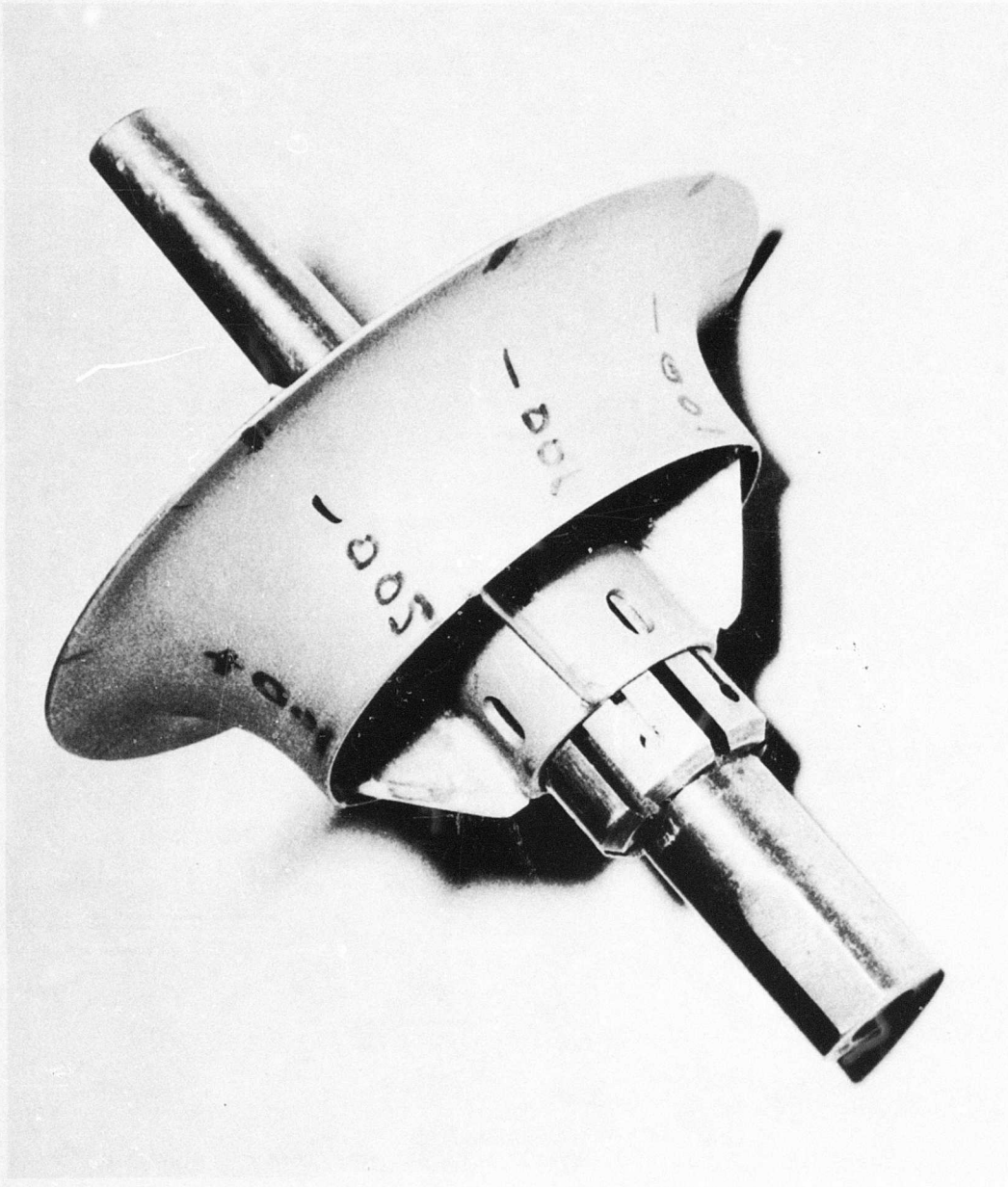

Figure 217. Side View of Circular Vane Used in Buildup F.

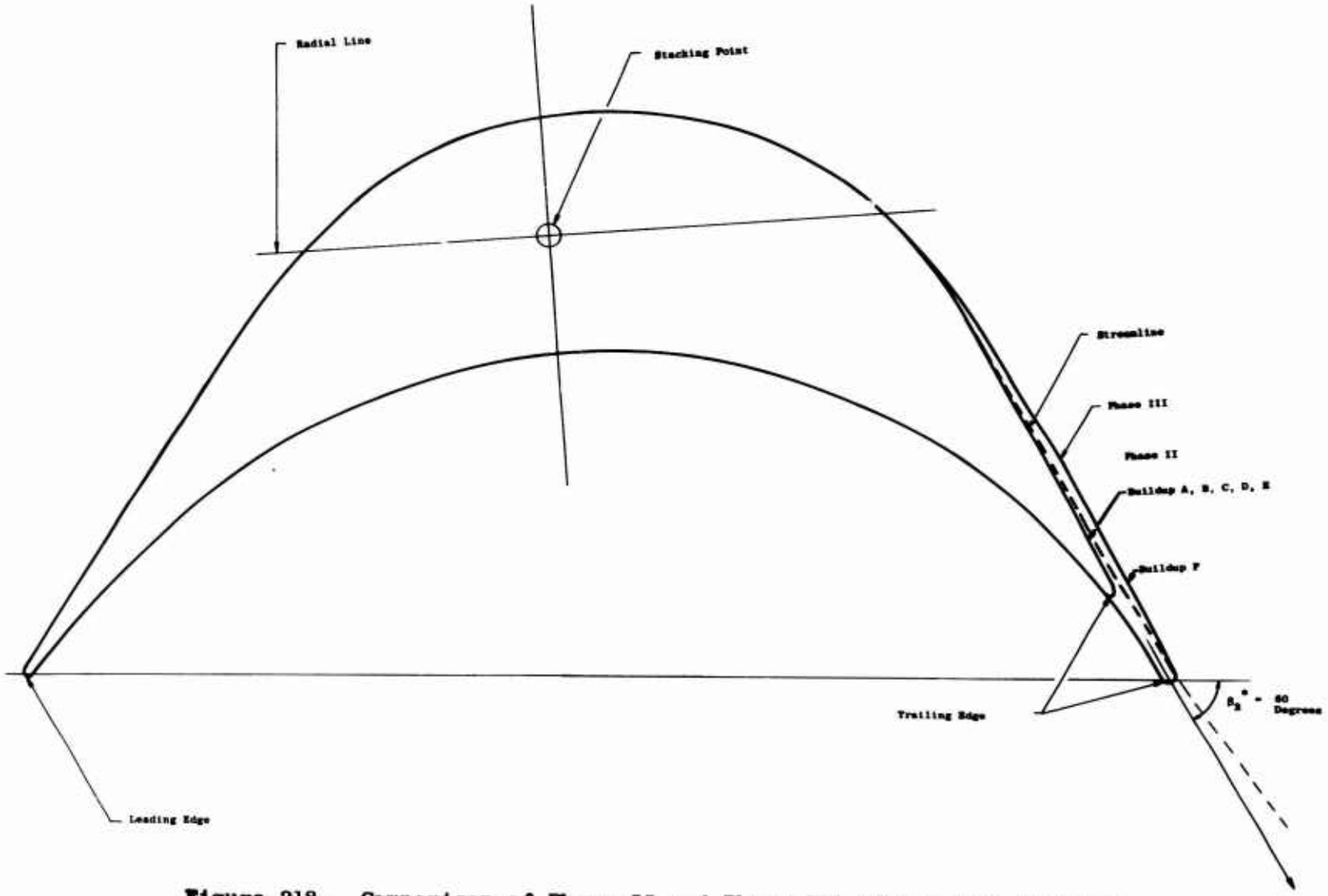

Figure 218. Comparison of Phase II and Phase III Rotor Blade Sections.

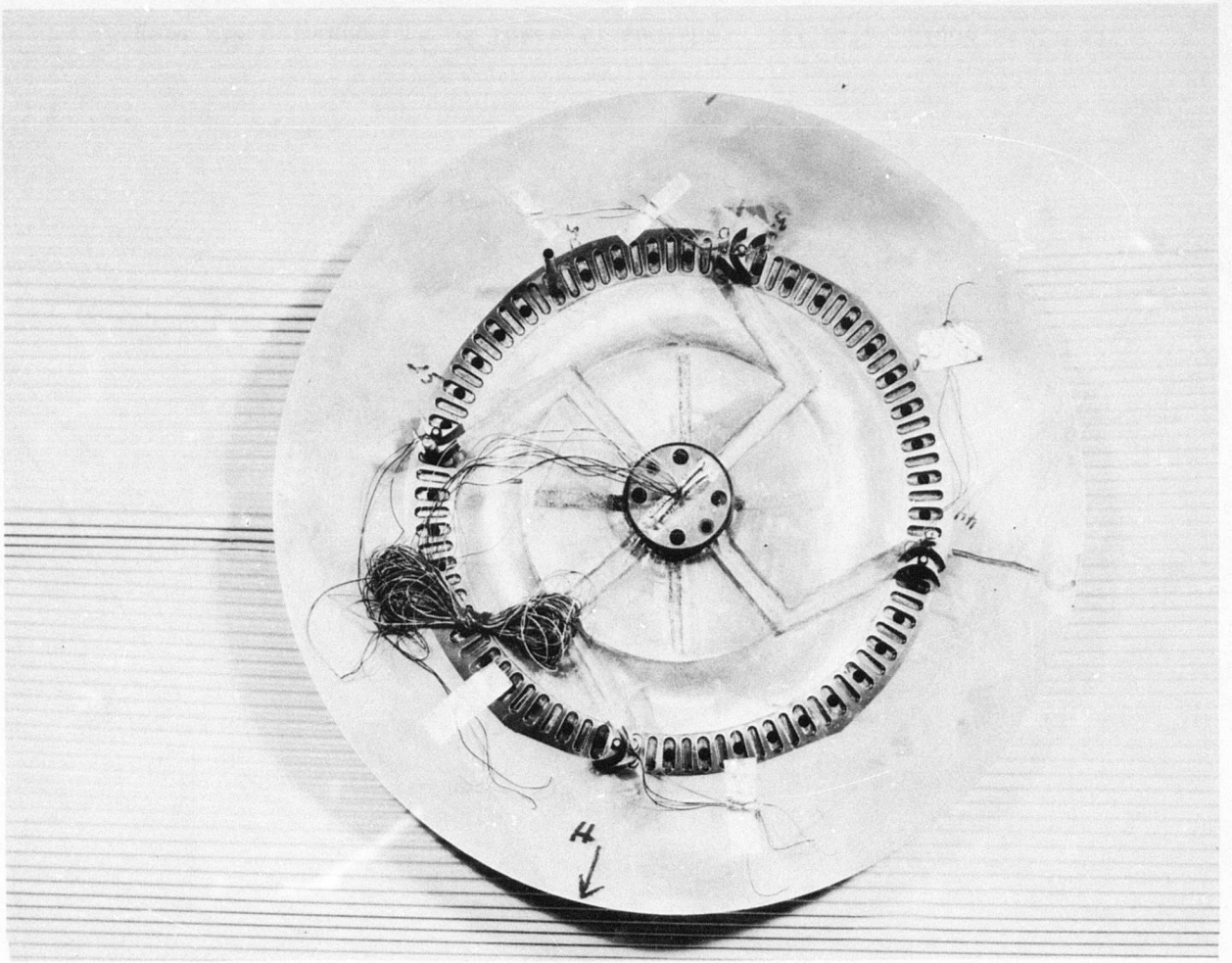

Figure 219. Preliminary Assembly of New (Phase III) Rotor Blades and Strain Gage Leads Prior to Testing Buildup F.

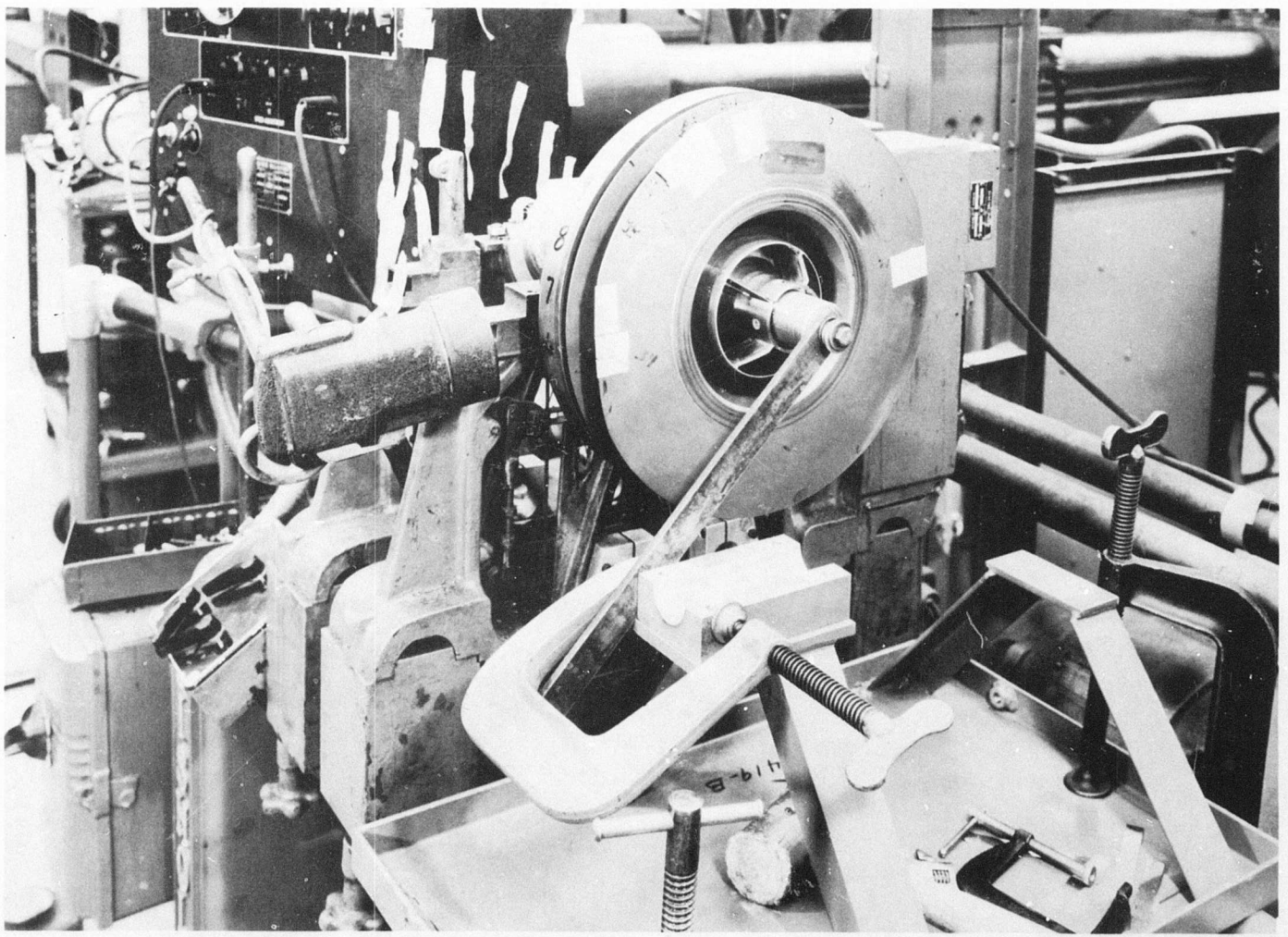

Figure 220. Assembly of Compressor Rotor and Circular Inlet Vane Mounted in Balancing Machine.

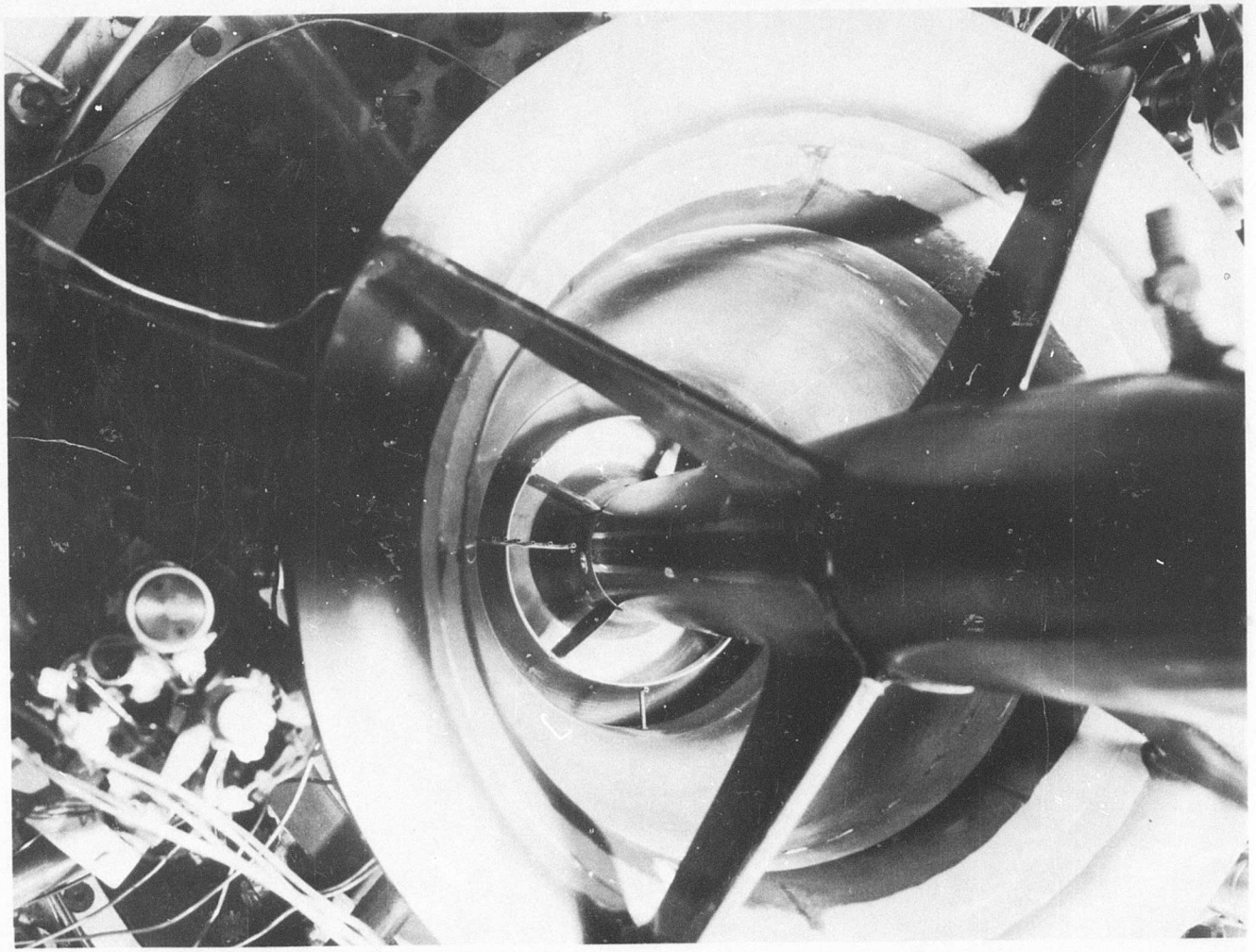

Figure 221. Circular Turning Vane Installed in Inlet of High-Speed Compressor.

of the rotor exit. One of the 2 cobra probes used for flow angle and total pressure measurement was connected improperly, and only crude traces of the traverse results could be obtained. Evidence that a small leak was occurring in the exit system of the compressor was observed because the flow measured by the venturis differed depending on whether the booster compressor was used or not. The maximum leakage is estimated to be 0.2 pps. The leak in the system was in such a location that with the booster operating, a higher flow would be indicated. With the booster not operating, and particularly at higher compressor pressure ratios, a lower flow would be measured by the venturis than was actually passing through the compressor. Since the booster was used only for a very short part of the run at low speed, the results are believed to be consistent with themselves.

All of the temperature ratios and efficiencies quoted in this description of Buildup F test results will be corrected values, whereas all previously reported temperatures and efficiencies have not been corrected. The effect of applying the probe calibration corrections to the temperature readings is to reduce the efficiency at low speed about 5 percent and at high speed about 4.5 percent based on the Mach number at the rotor exit. When the temperatures were measured downstream of the stators, the Mach number would be lower, in general, and therefore the amount of correction would be less.

At 30 percent speed, the ROC was operated over a broad range of flow from 0.74 pps to 1.95 pps (Figures 222 through 224). Only at the very lowest flow was there any indication of flow instability. Fluctuating flow was indicated by a sound measuring probe located just upstream of the inlet bellmouth of the compressor. The peak rotor efficiency observed of 84.7 percent (Figure 225) is about as high as in any previous buildup when the calibration correction is applied. The measured rotor total pressure and total temperature ratios were slightly higher than predicted. The measured static pressure ratios agreed very well with the predicted values of about 1.15 (Figure 224).

Only a few data points were taken at 40 percent speed because of the desire to obtain data at high speeds during these 2 runs. Although the curve which results from the few points taken suggests that the peak efficiency would fall between 2.2 and 2.3 pps (Figure 225), the data taken at other speeds indicate that had the compressor been throttled to the lower flows, perhaps down to as low as 1.8 pps, a higher efficiency than the maximum value observed of 85.7 percent might have been obtained. At both 30 and 40 percent speed, the total pressure ratio at rotor exit was slightly greater than that predicted. This is also true for the total temperature ratio across the rotor (Figure 224). The static pressure ratio at 30 and 40 percent speed was very close to the predicted value for the subsonic regime at rotor exit. In general,

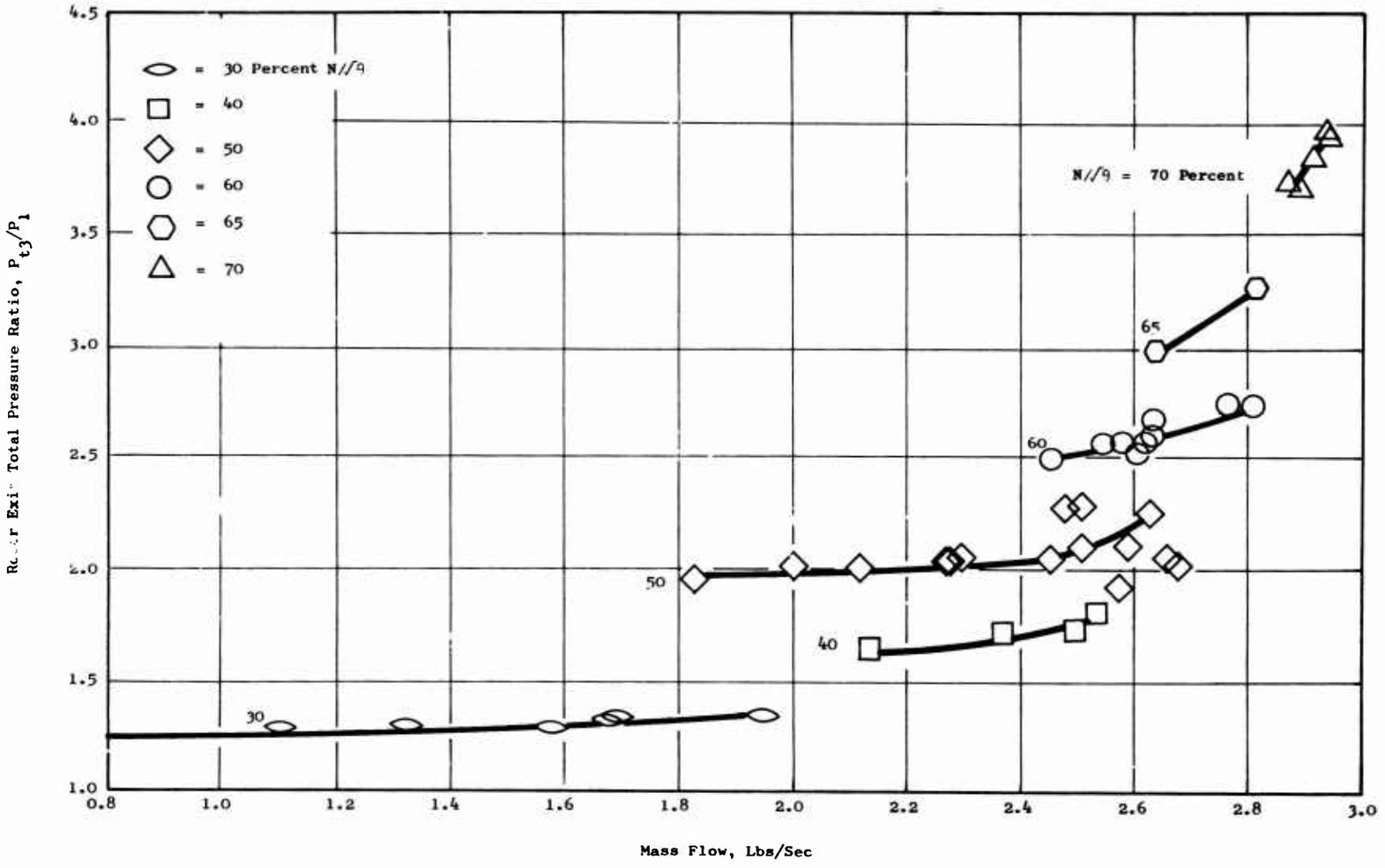

Figure 222. Total Pressure Ratio Versus Mass Flow for Run Numbers 15 and 16 (Buildup F).

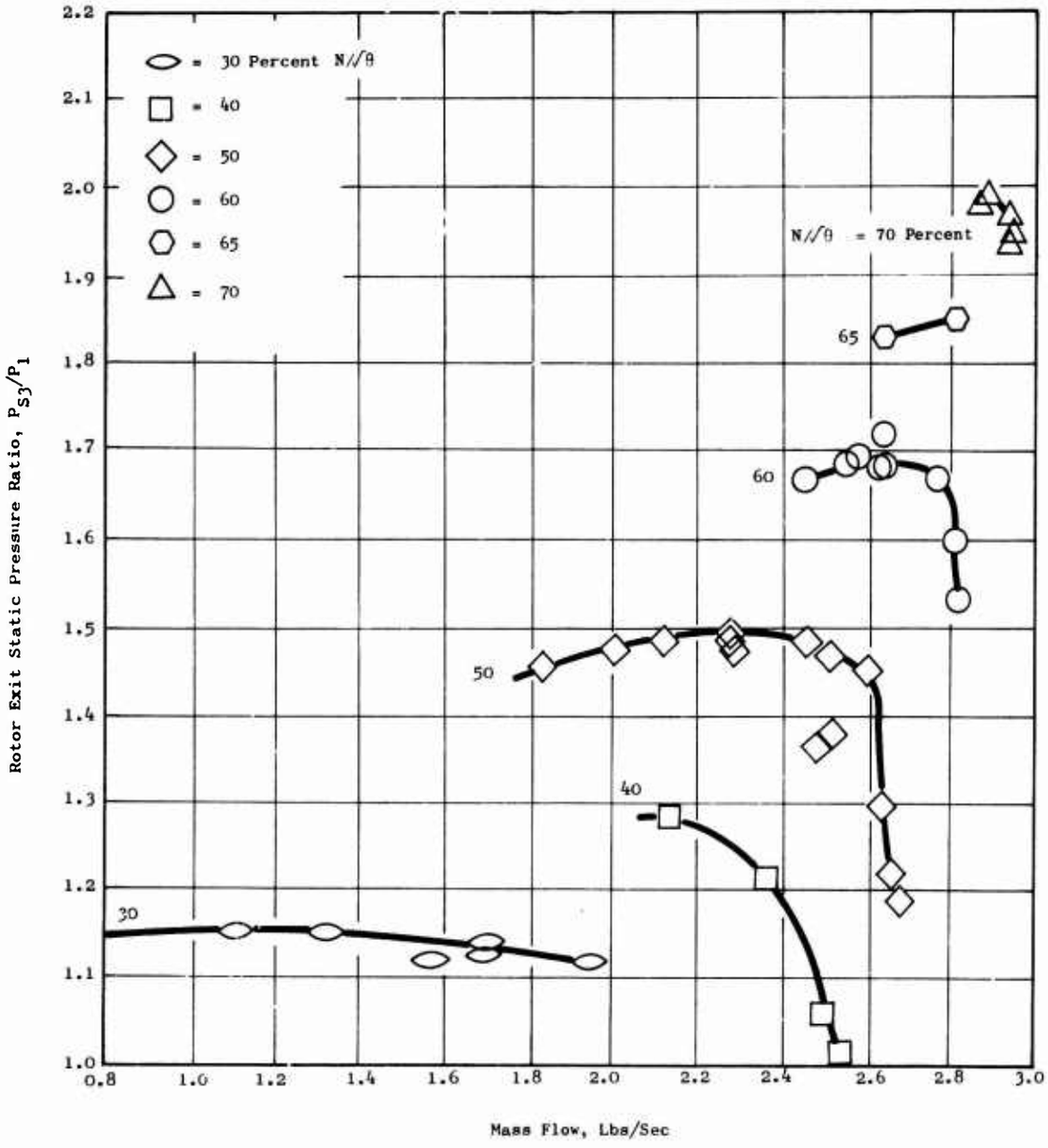

Figure 223. Static Pressure Ratio Versus Mass Flow for Run Numbers 15 and 16 (Buildup F).

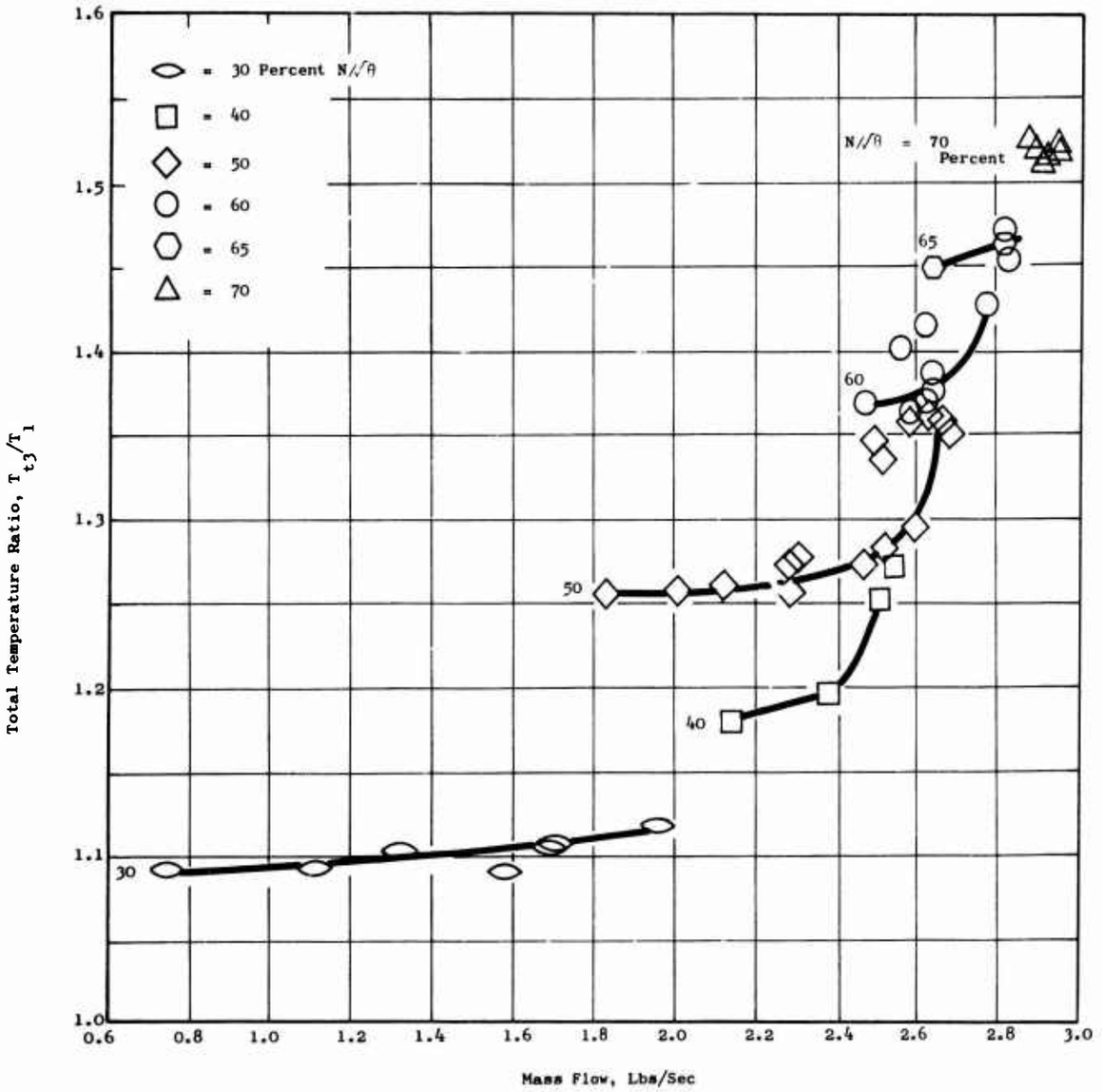

Figure 224. Total Temperature Ratio Versus Mass Flow for Run Numbers 15 and 16 (Buildup F).

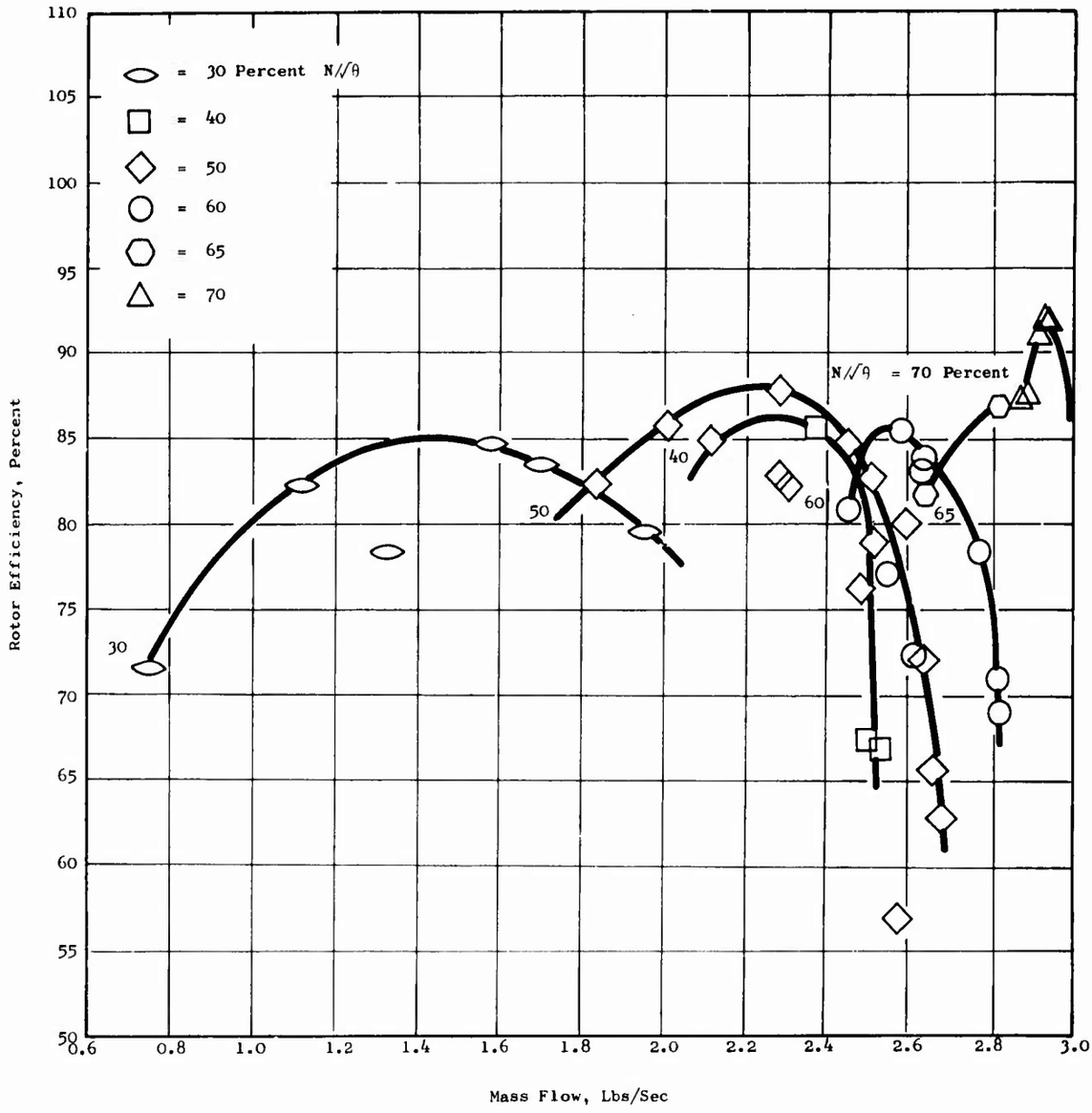

Figure 225. Rotor Efficiency Versus Mass Flow for Run Numbers 15 and 16 (Buildup F).

the rotor performance at 30 and 40 percent speed is, if anything, slightly better than predicted at these speeds in the absence of inlet guide vanes.

About 15 test points were taken at 50 percent speed. Three of these points were taken at the end of the second Run 16 after the stator actuation system had jammed and after the seal had rubbed. The seal rubbing probably opened up an enlarged clearance at the inlet to the rotor. The maximum rotor efficiency at this speed of 87.8 percent (Figure 225) was obtained at an airflow of 2.28 pps and a rotor total pressure ratio of 2.05. A very close approach to a calculated maximum airflow for this rotor of 2.73 pps at 50 percent speed was observed. The small difference from predicted maximum flow of about 0.1 pps could very well be due to the leakage in the compressor exit system upstream of the flow measuring venturis. The compressor was throttled to a minimum flow of 1.83 pps before the sound probe and accelerometers on the test vehicle indicated unsteady flow and vibrations. The maximum rotor static pressure ratio of 1.495 was identical to the predicted value for 50 percent speed with subsonic flow at exit of the rotor blades. The rotor total temperature ratio (Figure 224), like the rotor total pressure ratio (Figure 222), was significantly higher than the predicted values (Figure 226).

As has been the continuing experience with this rotor, difficulty was encountered in establishing safe rotor operation conditions at 60 percent speed, at other than a very narrow range of airflows. Rotating shroud vibrations resulted in stresses in the range of 30,000 psi which were almost continuous at this speed, and extreme care in adjusting the throttle or the stator angle was necessary to insure safe operation. Drive motor tripouts have been encountered due to excessive vibration of the test vehicle when operating at 60 percent speed. Peak efficiency of 85.5 percent was observed at an airflow of 2.57 pps with a rotor total pressure ratio of 2.57. The maximum airflow observed about 2.82 pps was about 0.1 pps less than the calculated maximum, but this difference is believed to be due to the leakage in the exit system. The rotor total pressure ratios were higher than the predicted values, and the rotor total temperature ratios were significantly higher than predicted for 60 percent speed. The maximum observed rotor static pressure ratio of 1.69 corresponds to a calculated value of about 1.77 at the same airflow of 2.6 pps.

One point at 65 percent speed was taken during Run Number 16 while accelerating to 70 percent speed. A corrected rotor efficiency of 86.9 percent and a total pressure ratio of 3.26 and an airflow of 2.82 was measured. No attempt was made to obtain optimum performance at this speed. A relatively long test sequence with a duration of 1 hour and 20 minutes was conducted at 70 percent speed during Run Number 16. The fact that only 6 data points were taken during this time is partially explained by the difficulty in establishing test points without inciting rotor or test vehicle vibrations, but even more so because serious efforts were made to establish the validity of the test data recorded during this run.

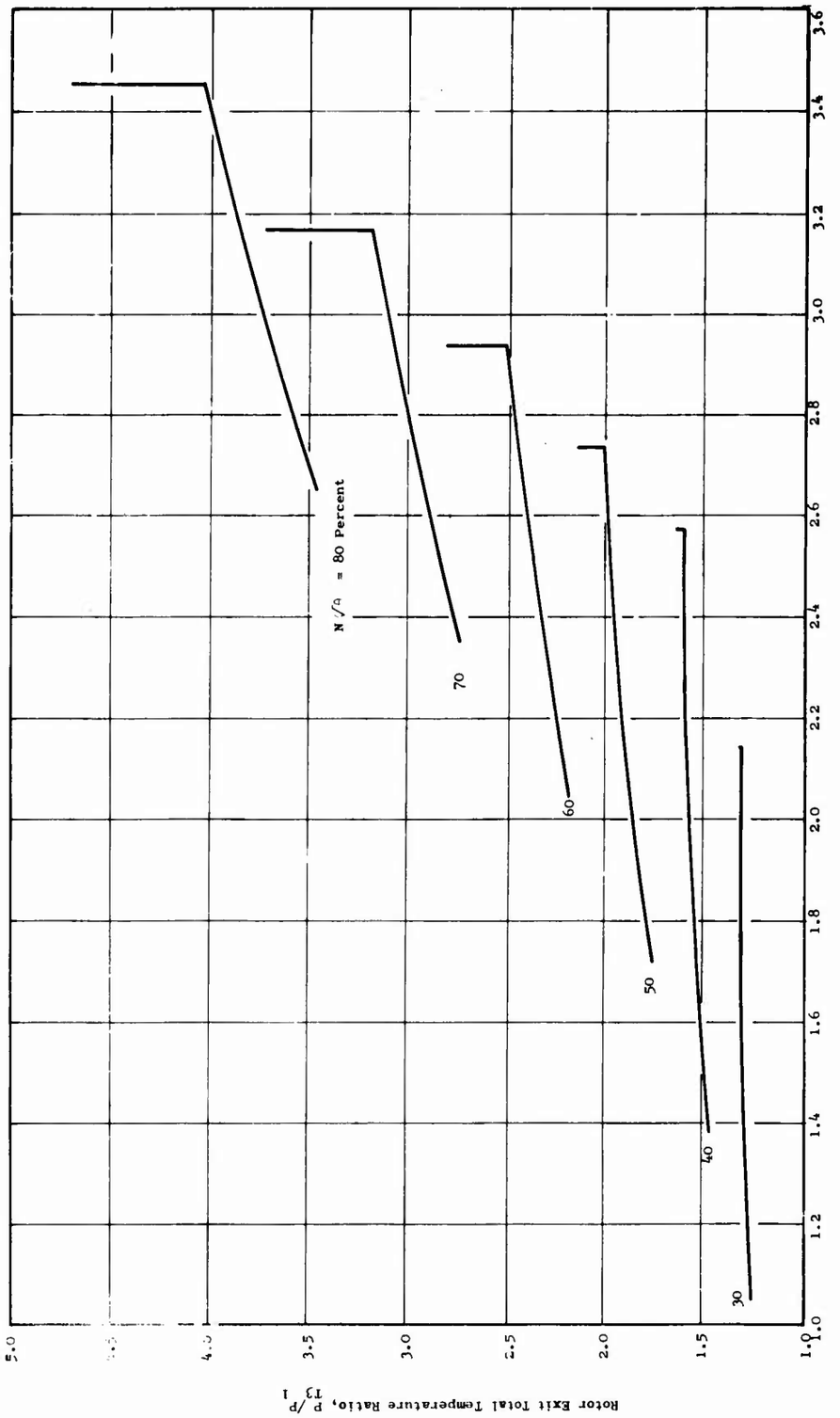

Figure 226. Predicted Total Pressure Ratio Versus Mass Flow for ROC Rotor Without Inlet Guide Vanes.

Calibration of the transducers being used to measure the rotor total and static pressure data was accomplished between Readings 29 and 30. A maximum rotor efficiency of 92.1 percent was observed at an airflow of 2.94 pps and a rotor total pressure ratio of 3.97. The measured rotor static pressure ratio of 1.97 corresponds to a predicted value of about 2.1 for subsonic exit flow from the rotor for this airflow at 70 percent speed. The maximum rotor total temperature ratio of 1.52 is higher than the predicted value for subsonic exit conditions of approximately 1.41 at an airflow of 2.9 pps. The observed maximum total temperature ratio does correspond to the values previously observed during Run Numbers 10 and 11 (Buildup D) with supersonic rotor blade exit flow conditions at 70 percent speed.

Observations

At the higher speeds, the evidence as to whether the flow leaving the rotor blades is subsonic or supersonic is somewhat contradictory. The problem of deducing exactly what flow regime exists is complicated by the fact that at 60 percent and higher speeds, the flow range over which this rotor can be operated without encountering unsafe vibrations is rather limited. It is possible that when attempts are made to impress high back pressures on the rotor, the rotor blade flow separates to some extent, perhaps just to the extent that sonic flow is produced at the rotor blade exit. A flow behavior of this type is considerably more complicated than that considered by the simplified prediction methods used herein. In general, the rotor performance observed during these two runs in Buildup F has been very satisfactory. The upward trend of the maximum efficiency curve with increasing speed (Figure 225) is most encouraging. The rapidly increasing upward slope of the total pressure ratio versus speed curve is also very encouraging and gives indication that target performance may be within reach of this type of compressor rotor.

Appearance of Rotor Blades Following Run Numbers 15 and 16 of Buildup F

Examination of the rotor blades following the first and second run of Buildup F revealed a significantly different deposit pattern than that seen after Buildup C (Figure 202). The Buildup F pattern was characterized by a clean zone on the concave surface extending spanwise from the leading edge to about 25 percent chord rearward near the shroud to about 35 percent chord near the disc. A relatively uniform dirt deposit showing radial streaks covered the majority of the concave surface. Most blades showed a small triangular clean wedge near the disc with the apex at about 75 percent chord, enlarging toward and extending to the trailing edge. The only deposits visible on the convex surface of the blades were narrow triangular zones adjacent to shroud and disc beginning at about 60 and 70 percent chord, respectively, enlarging toward and extending to the trailing edges. Unfortunately, all parts were cleaned before

photographs could be taken. The general impression obtained from visual inspection was that the flow must have been much more uniform and more closely approached two-dimensional conditions than during tests of Buildup C.

Aerodynamic Performance (Run Numbers 17 and 18)

The primary purpose of Run Numbers 17 and 18 using the Buildup F configuration was to operate the compressor at 80 percent speed to determine whether the encouraging performance obtained at 70 percent speed would continue at higher speeds. During Run Number 17, which was conducted on December 28, 1967, test data were taken at 30, 40, 50, 60, 65, 70, and 80 percent speed.

The test point taken at 30 percent speed was intended as a repeat of the maximum efficiency obtained during Run Number 16. As shown in Figure 227, a rotor efficiency of 84.2 percent was obtained at an airflow of 1.59 pps, which corresponds very well to the peak efficiency of 84.7 percent obtained previously. Traverses of total pressure and flow angle were taken near the rotor exit at 2 circumferential stations 70 degrees apart (Figures 229 through 236). Total pressure was very uniform across the rotor exit span, and the flow angle was constant within ± 1 degree over 80 to 90 percent of the span. High frequency response static pressure crystals were employed during these runs. At 30 percent speed, fluctuations of about 0.5 psi were observed at a frequency about 88 times that of the rotor, or 1 per blade. All of these results were very encouraging.

At 40 percent speed, the maximum rotor efficiency obtained during Run Number 17 of 89.1 percent was significantly better than that obtained previously. The improvement in performance was probably due to throttling the compressor to a weight flow of 1.92 pps, lower by about 0.2 pps than set previously during Run Number 16. Total pressure and flow angle traverse results were also very encouraging at 40 percent speed showing uniform conditions to within about 10 percent of the rotating shroud wall. One of the yaw traverses showed uniform flow angle adjacent to the disc, but the other indicated about a 3-degree increase in flow angle as the probe approached the last 10 percent span (0.040 inch) of the disc. Only minor (0.5 to 0.75 psi) static pressure fluctuations at approximately 72/rev rate were observed.

At 50 percent speed, an increase in maximum efficiency from 87.8 to about 89.2 percent was obtained. The total pressure ratio observed was 2.06, about the same as the pressure ratio obtained during Run Number 16 at a similar airflow. Traverses of flow angle indicated variation of from 2 to 3 degrees across the rotor exit span. Total pressure traverse results at both circumferential stations indicated a minimum total pressure at the center of the exit passage with a

maximum at the shroud and disc walls. One total pressure traverse indicated a variation of about 0.5 psi while the other showed a variation of 1.0 psi with average value of about 15 psig. Minor static pressure fluctuations of about 1.0 psi were observed with a frequency of around 60/rev. Photographs of typical oscilloscope traces from the crystal signals are presented in Appendix XI.

In many previous runs, difficulty was observed in attempting to set 60 percent speed because of rim vibrations of the rotating shroud. During Run Number 17, the temperature was sufficiently low so that the actual rpm of the rotor was below the critical speed previously observed. Several test points were taken in attempting to obtain improved rotor performance. Only a slight improvement from the previous high value of 85 to 86 percent was obtained by closing the subsonic stator vane angle from 75.0 to 75.8 degrees. A significant variation was noticed between the traverse results obtained at 1 circumferential station in comparison with the other. One traverse indicated a very nearly uniform total pressure varying only between 24.5 and 26.5 psig with the highest value near the rotating shroud. The flow angle traverse indicated a variation of from a minimum of 75 degrees to a maximum of 77 degrees. Both results indicated that the flow was quite uniform. The other traverse indicated uniform total pressure from the rotating shroud to a point about 75 percent of the span from the shroud. From there to the disc, the total pressure decreased from a maximum value of 25.5 psig to a minimum of about 19 psig near the disc. The associated angle traverse indicated a variation of from 79 degrees at the shroud to a minimum of 72.5 degrees at 70 percent span with an increase to about 82 degrees near the disc. These circumferential differences may actually occur in the flow, since 1 of the traverses is closer to an exit arm of the exhaust system where significant static pressure differences occur. Since the stator performance influences the exit scroll performance, the results observed suggest that increased rotor efficiency probably could be obtained at 60 percent speed by finding an optimum combination of subsonic stator angle and throttle setting.

The fluctuation of the static pressure was not nearly so regular during operation at 60 percent speed; in fact, the first point taken at this speed, Reading Number 52, exhibited only random variations of 1.0 psi with occasional change of 2.0 psi. For the fourth point, Reading Number 56, a 0.1-second trace showing about 34 revolutions showed 3 cycles of a "slow" static pressure variation of about 5 psi. Why the static pressure should vary over a 0.03-second period of 10 to 11 rotor revolutions is not clear.

The test point taken at 65 percent speed yielded an efficiency of 85.4 percent at an airflow of 2.72 pps. This corresponds very well with the 2 previous points taken at 65 percent speed during Run Number 16. Some

vibrational problems were observed at this speed, so extended running was not conducted and no attempt was made to find an optimum subsonic stator vane setting. Random static pressure variations of from 1 to 4 psi were observed.

The vibrational problem that existed at 65 percent speed also appeared at 70 percent and 72 percent speed where 1 point was taken at a pressure ratio of 3.32. Since the compressor conditions are far different from those obtained during Run Number 16 where a pressure ratio of 3.97 was obtained, it is not surprising that a low efficiency (72.4 percent) was obtained at this single test point. One to four pressure pulses per revolution of 5 to 10 psi pressure change appeared, superimposed on a higher frequency 1 psi variation.

For various reasons, but primarily because this was the first extended running at 80 percent speed and also because of the high vibration level which persisted, the testing at 80 percent speed proceeded quite cautiously. The first point was taken with stator vanes set at 77.5 degrees, rotor exit static pressure of 27.95 psia and an airflow of 2.88 pps with an efficiency of about 57 percent, and a total pressure ratio of 3.21. Closing the subsonic stator vane angle to 79.0 degrees from radial and further throttling the compressor to a rotor exit static pressure of 32.37 psia increased the airflow to 2.93 pps, increased the total pressure ratio to 4.035, and increased the efficiency to about 71 percent. Rotor rim vibrations persisted at this condition. Further closure of the stators to 80.0 degrees and minor throttle closure caused a drop in static pressure to 31.81 psia, increased airflow to 2.97 pps, and increased total pressure ratio to 4.29 with 75.3 percent rotor efficiency. Rim vibrations continued at a significant level. High frequency (30 to 40/rev.) pressure changes of small (2 to 4 psi) amplitude were observed with random (1 to 4/rev.) pulses of from 5 to 15 psi pressure change appearing occasionally. A change in the subsonic stator vane angle of 81.5 degrees produced a dramatic improvement in the compressor performance. The shroud rim vibrations dropped to about one-third of their previous value, and increases in total and static pressure occurred. The rotor appeared to be running much more smoothly than at any other test condition above 50 percent speed. Unfortunately, the increased static pressure caused the axial load on the shaft to exceed the preset limit, and a tripout occurred before a complete reading could be obtained. Due to the lateness of the hour, the test was concluded on this encouraging note.

Prior to Run Number 18, an acoustic probe was inserted into the inlet of the ROC. Sound data were recorded at speeds of 30, 40, 50, 60, 65, 72, and 80 percent. Following the sound data tests and with the sound probe still in place, test points were taken at 70 and 80 percent speed (Figures 227 and 228). The first 80 percent speed point was taken with the subsonic stator vanes set at 81.4 degrees from radial. A rotor

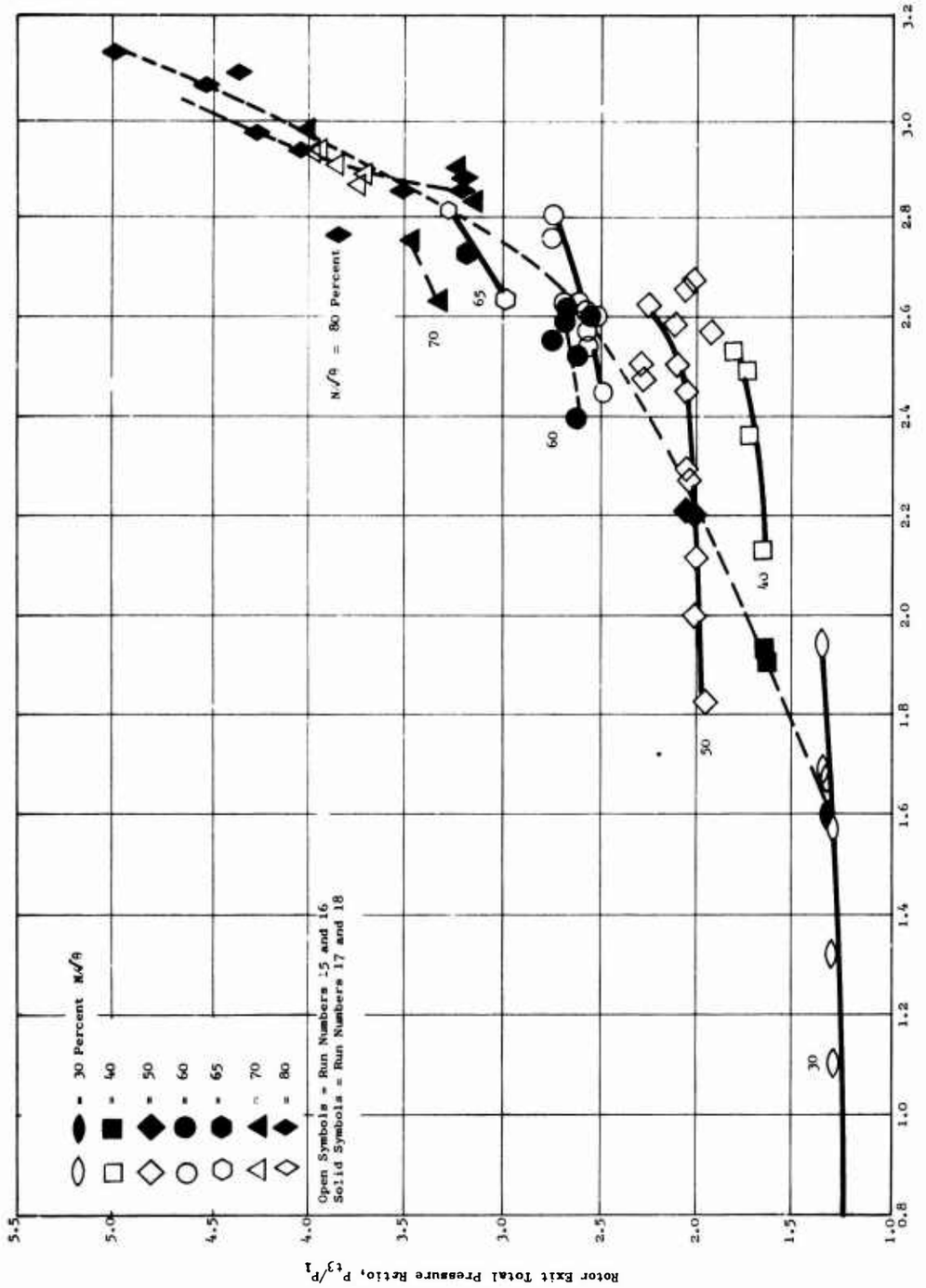

Figure 227. Total Pressure Ratio Versus Mass Flow for Buildup F.

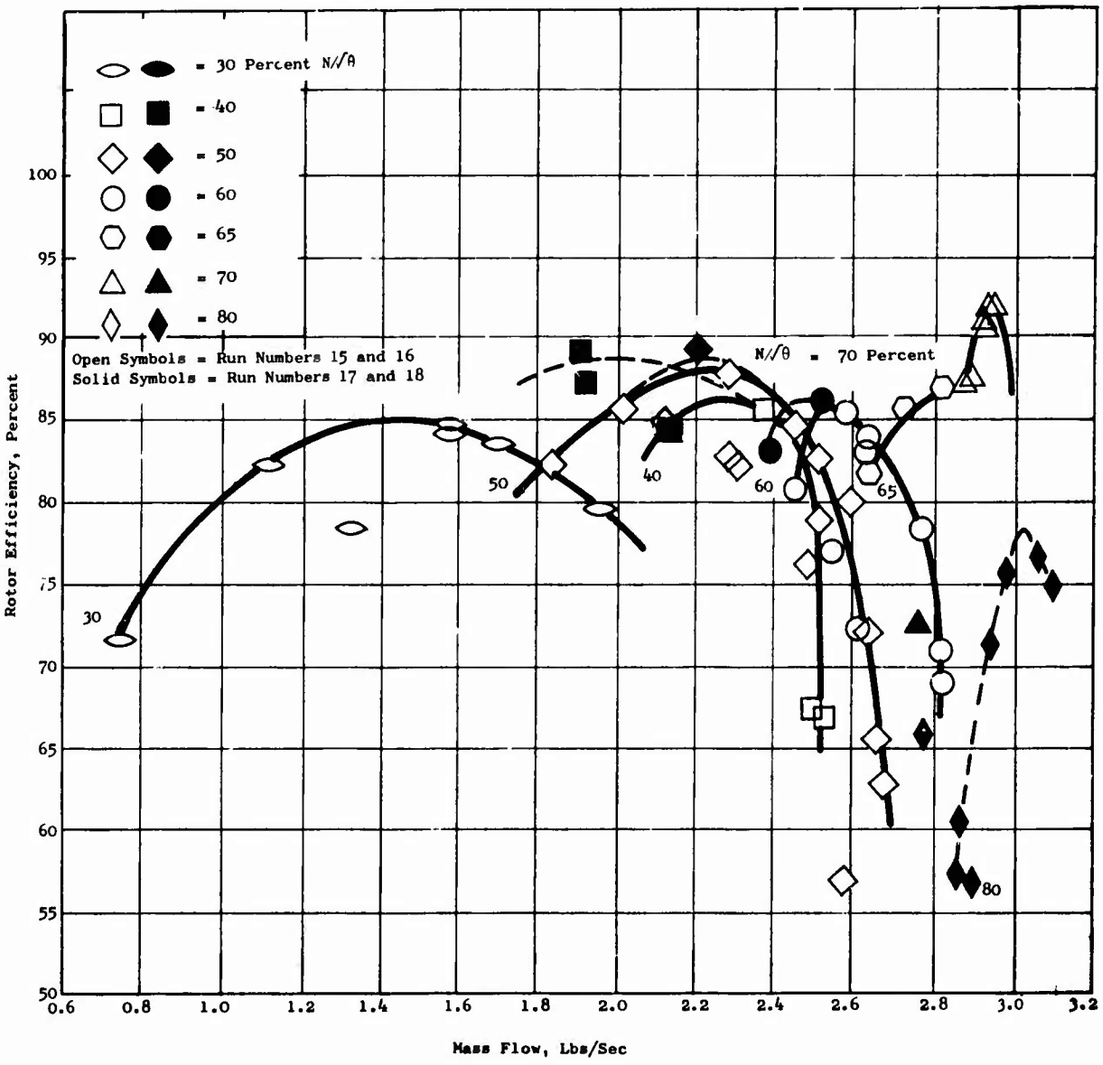

Figure 228. Rotor Efficiency Versus Mass Flow for Buildup F.

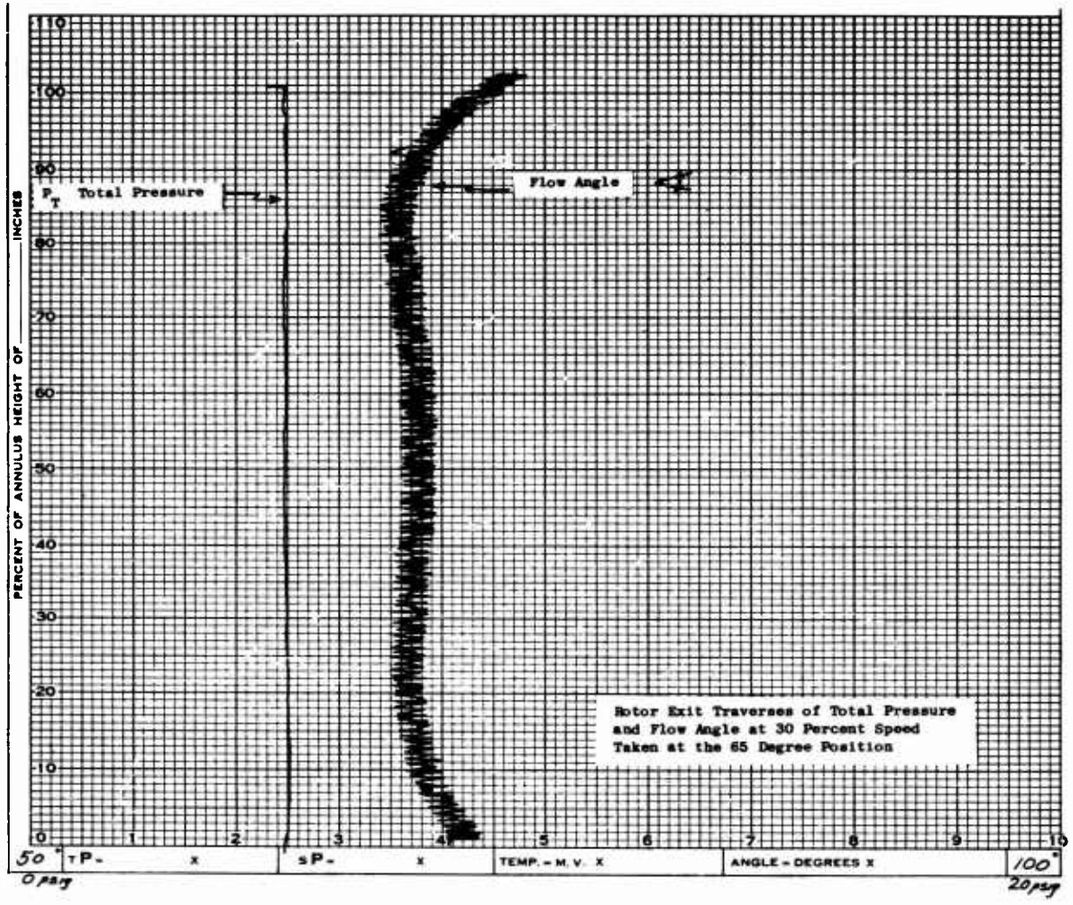

Figure 229. High-Speed ROC Flow Angle and Total Pressure Traverses for Run Number 17, Reading Number 48, With Circular Inlet Vane at 65 Degrees Position.

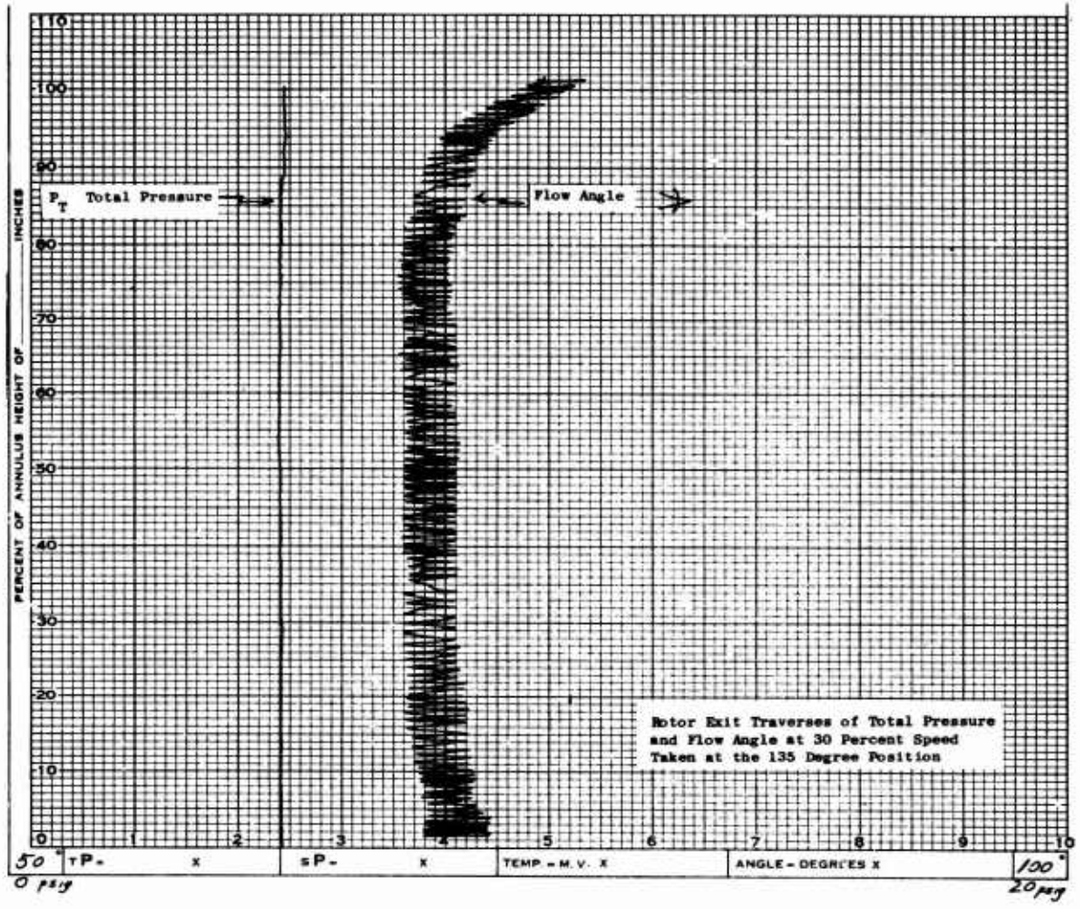

Figure 230. High-Speed ROC Flow Angle and Total Pressure Traverses for Run Number 17, Reading Number 48, With Circular Inlet Vane at 135 Degrees Position.

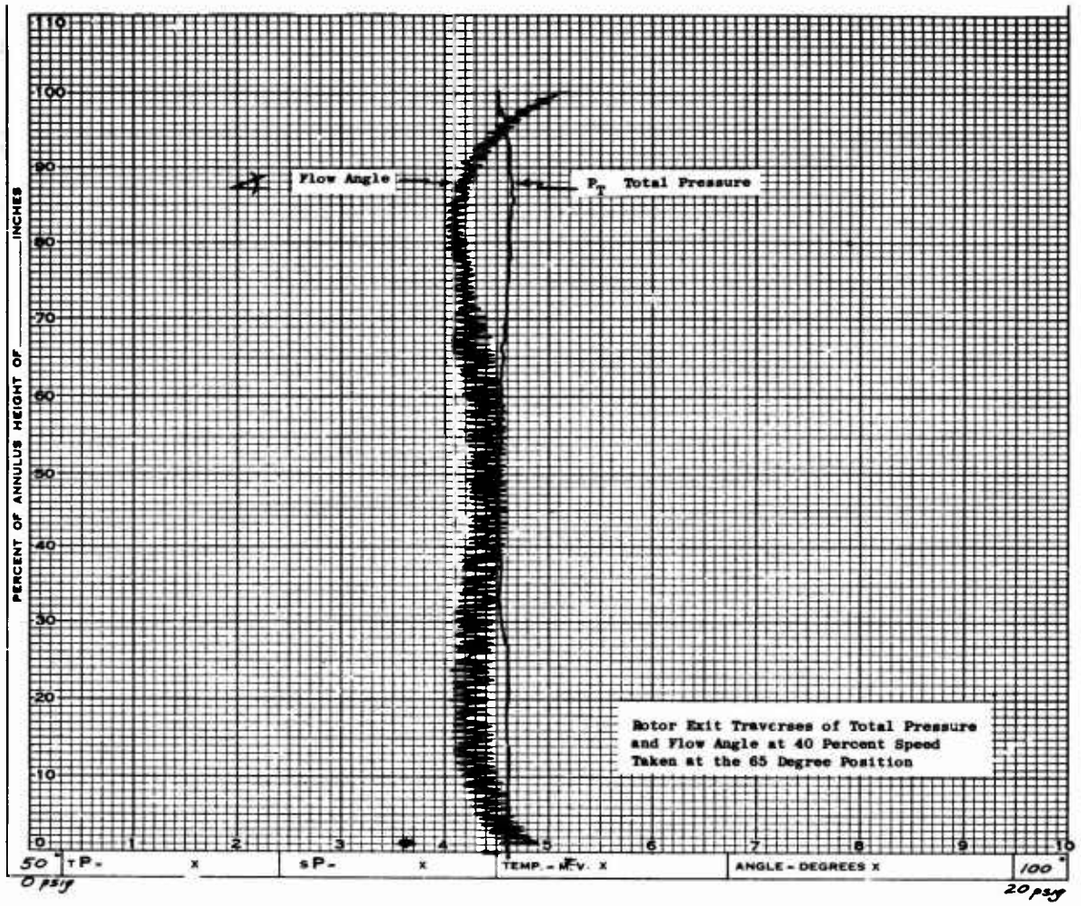

Figure 231. High-Speed ROC Flow Angle and Total Pressure Traverses for Run Number 17, Reading Number 49, With Circular Inlet Vane at 65 Degrees Position.

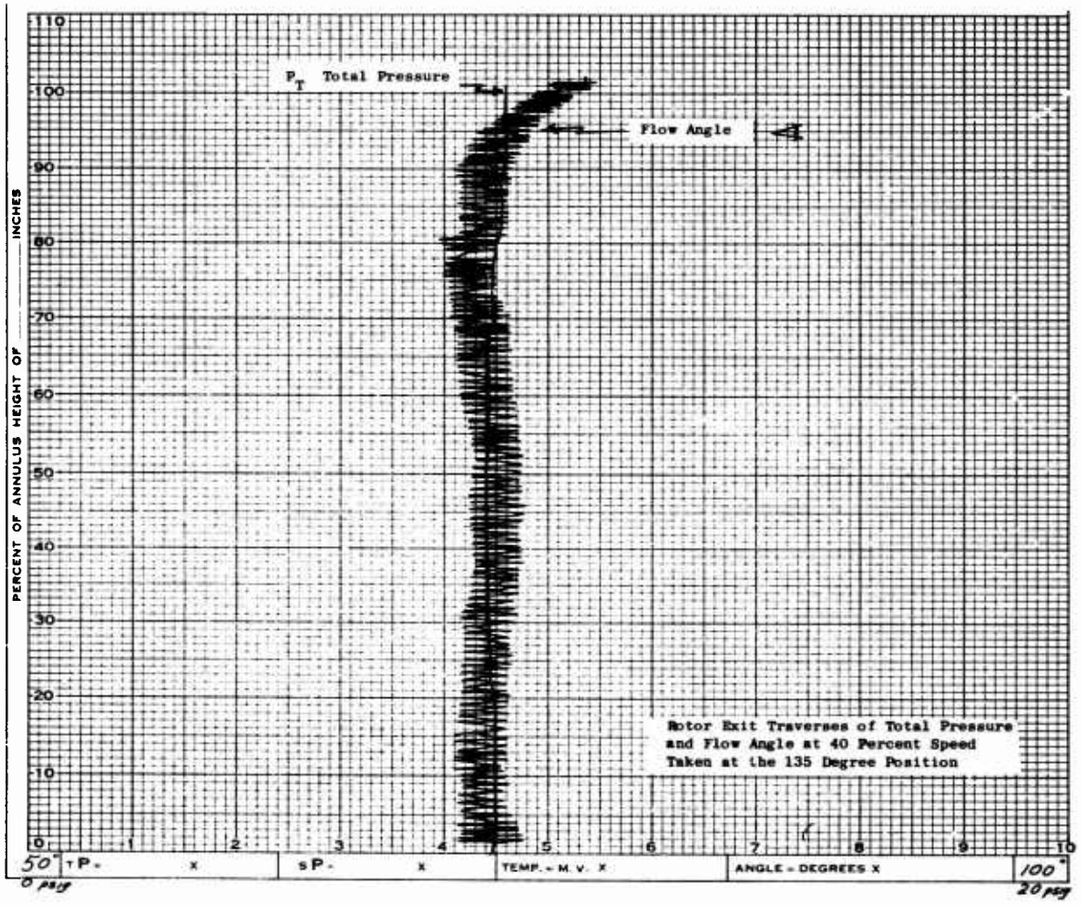

Figure 232. High-Speed ROC Flow Angle and Total Pressure Traverses for Run Number 17, Reading Number 49, With Circular Inlet Vane at 135 Degrees Position.

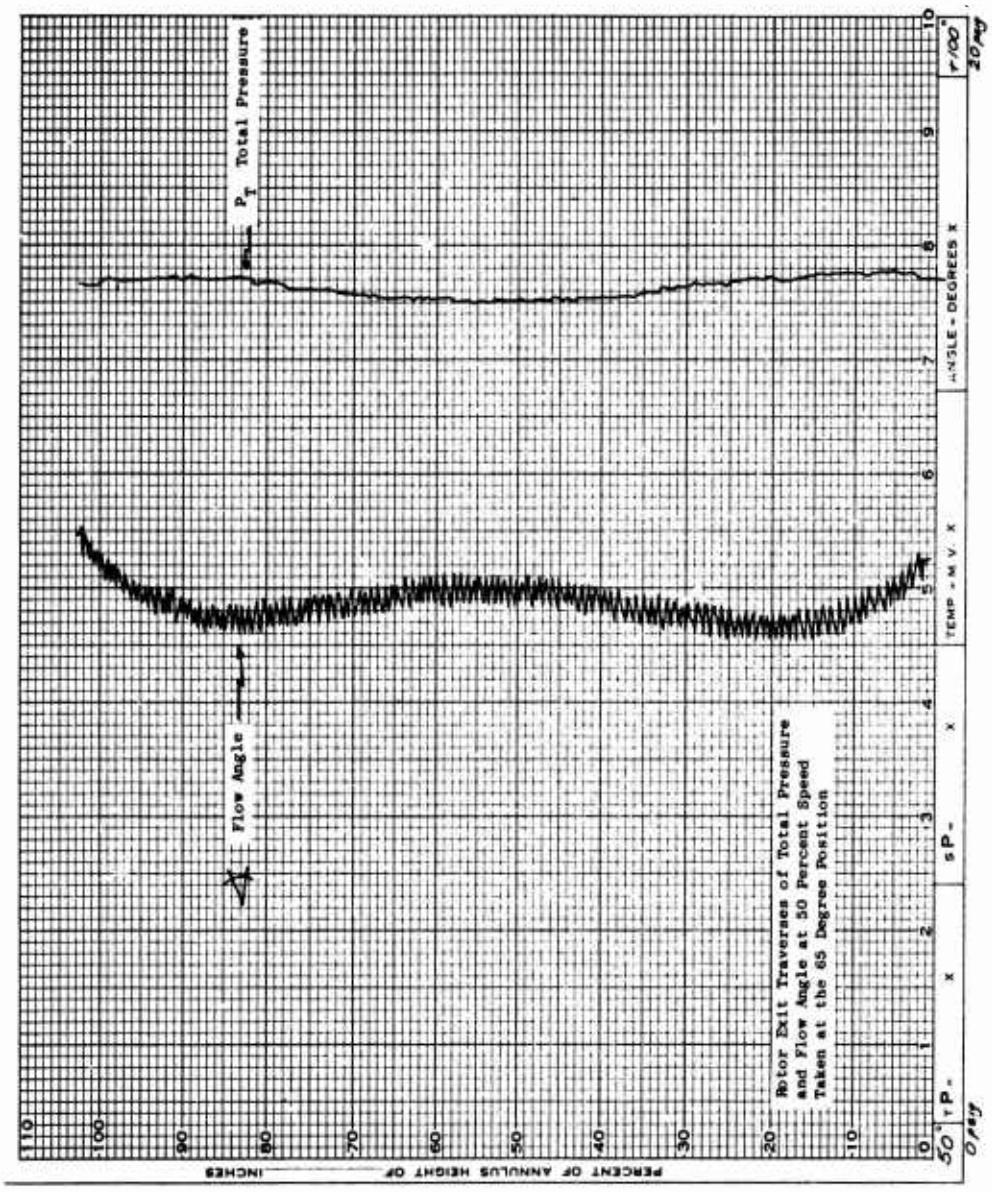

Figure 233. High-Speed ROC Flow Angle and Total Pressure Traverses for Run Number 17, Reading Number 51, With Circular Inlet Vane at 65 Degrees Position.

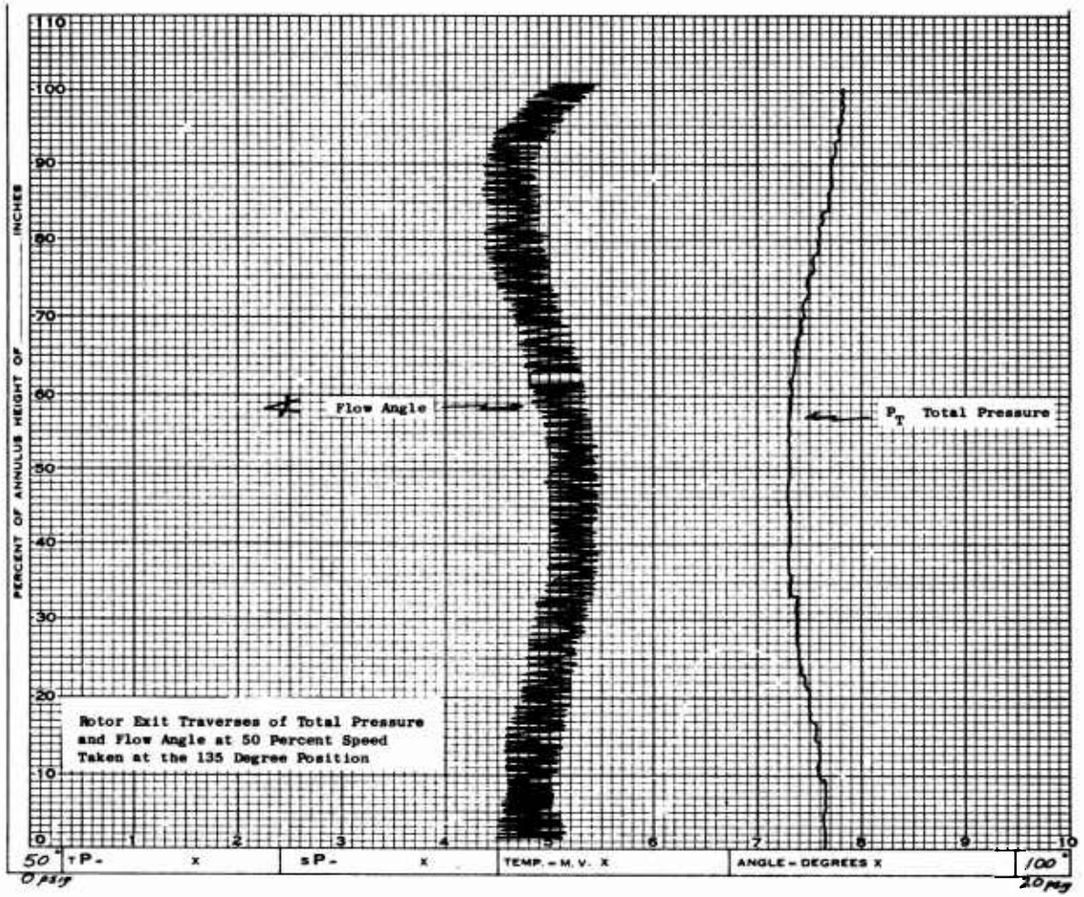

Figure 234. High-Speed ROC Flow Angle and Total Pressure Traverses for Run Number 17, Reading Number 51, With Circular Inlet Vane at 135 Degrees Position.

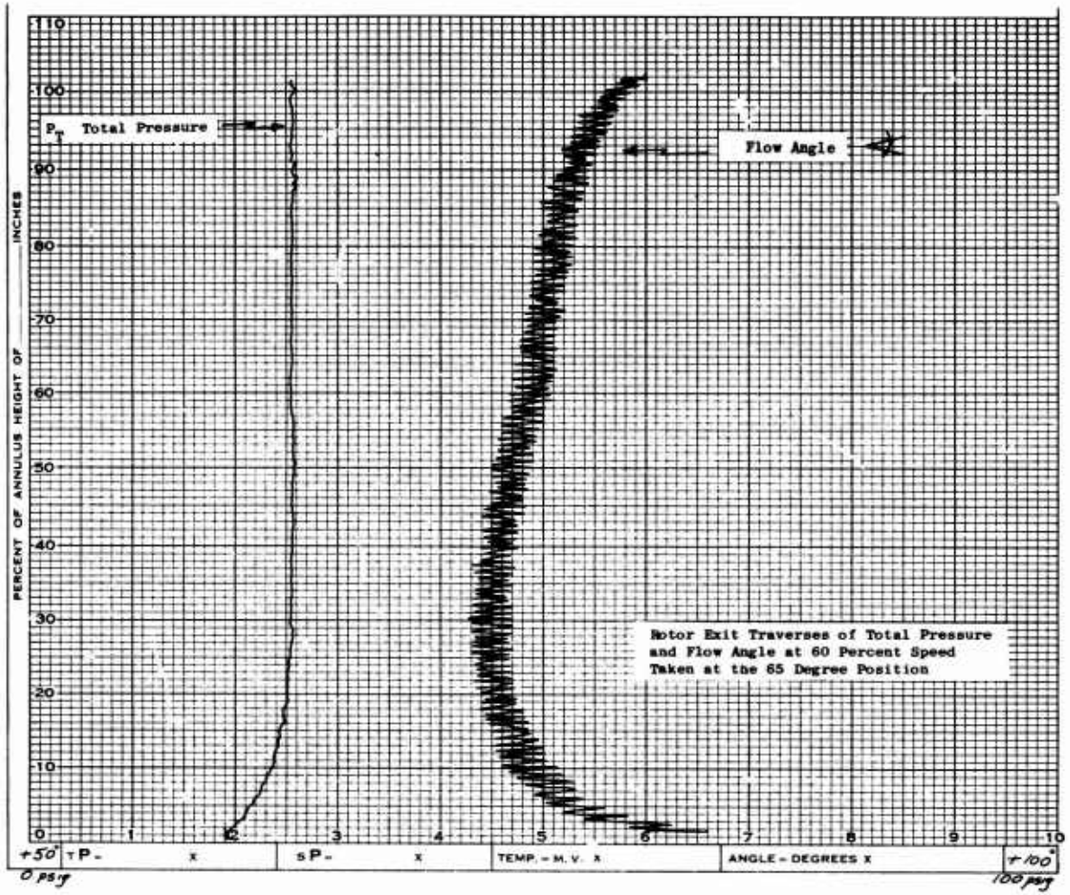

Figure 235. High-Speed ROC Flow Angle and Total Pressure Traverses for Run Number 17, Reading Number 52, With Circular Inlet Vane at 65 Degrees Position.

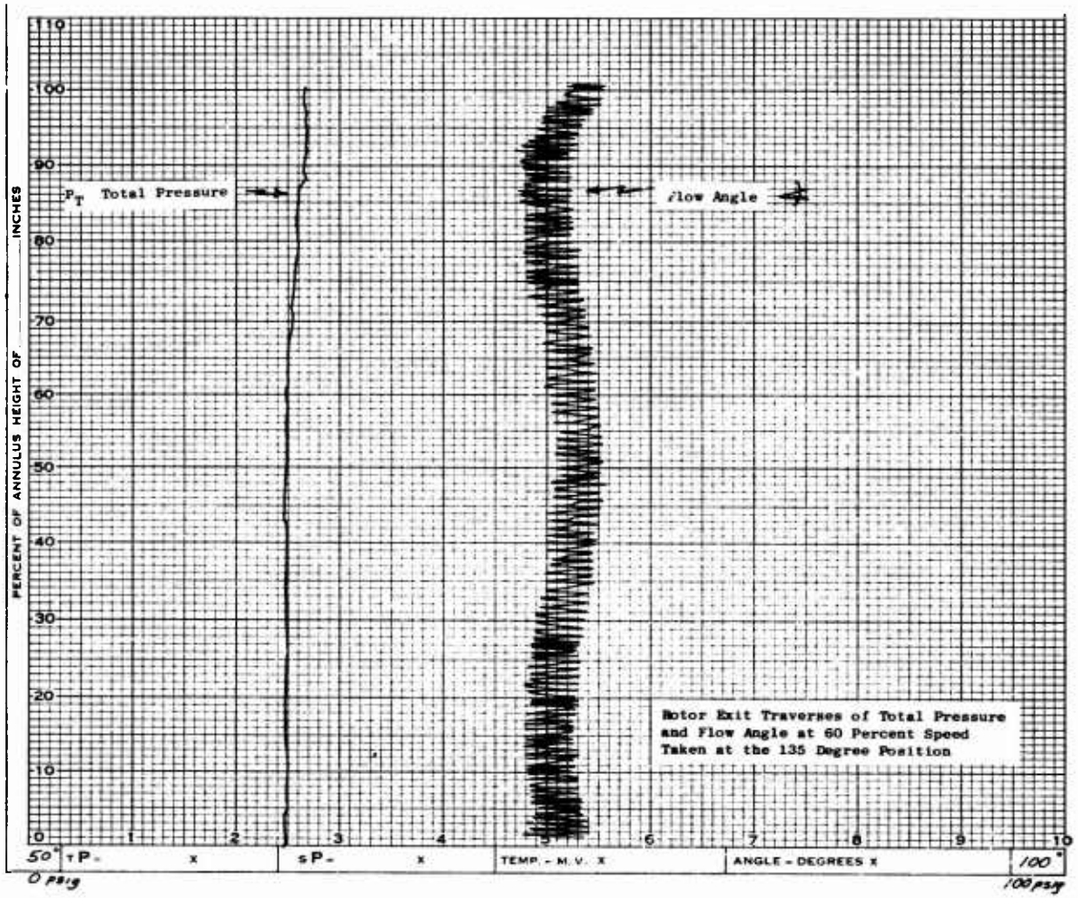

Figure 236. High-Speed ROC Flow Angle and Total Pressure Traverses for Run Number 17, Reading Number 52, With Circular Inlet Vane at 135 Degrees Position.

efficiency of 74.8 was obtained with a total pressure ratio of 4.39. A second point was taken with the stator vanes set an an angle of 82.2 degrees from radial. The rotor efficiency obtained at this reading was 76.4 percent with a total pressure ratio of 4.55. Although maximum performance was not necessarily obtained at 80 percent speed, all but 1 of the strain gages had been lost and none of the proximeters were functioning. For these reasons, it was felt unsafe to continue operating the compressor, so the run was discontinued, completing the test sequence of the Phase II investigation.

Following the final runs of the Phase II experimental investigation, the rotor was disassembled to make the blades available for use in the Phase III rotor buildup. Photographs of the rotor disc, shroud, stator, and seal were taken and are presented herein (Figures 237 through 244). The soot patterns on the rotor blades have been photographed to show close-up detail and are presented in Figures 249 through 252. During Run Numbers 17 and 18 of Buildup F, the outdoor temperatures were near freezing. In order to reduce the compressor inlet temperatures, ceiling vents and an outside door were opened to the test cell area. Probably as a result of this mode of operation, heavier soot deposits than usual occurred on the rotor blades during these runs. The dirt patterns on the rotor shroud indicated a continuous path from the rotor blades to the outer diameter of the shroud. There were no regions of dust deposit suggesting a zone of separated flow. Very prominent patterns like the letter V with the apex at the juncture of the rotor blade trailing edge and the shroud were apparent near each blade. One portion of the pattern appears tangent to the concave surface of each rotor blade, whereas the other leg of the pattern appears tangent to the primary stream patterns which occur as they progress outward becoming radial at the shroud outside diameter (Figures 237 and 238). A very similar pattern is visible on the disc (Figures 239 and 240). A complete understanding of these patterns is lacking, but it is believed that vortices are formed in the rotor blade passage and are being shed at the rotor blade trailing edge.

The rotor blades themselves show no deposit on the convex surface just as was the condition after previous buildups, but show a strong soot pattern on the concave surface. The pattern starts about 10 percent chord from the leading edge near the shroud and at about 15 percent chord near the disc. The pattern builds up in density from these locations to the trailing edge with only a narrow section about 10 percent of the exit width clear at the trailing edge. The clean zone is displaced from the center of the passage about 5 percent of the passage width toward the disc. The deposition is almost symmetrical about the center of the blade span in contrast to nonuniform deposits observed following Buildup C (Figure 202). Although the pattern is not fully understood, the radial nature of the clean zone suggests that an approach to two-dimensional flow was obtained in Buildup F of the Phase II investigation. Little or no depositions occurred on the convex surface of the rotor blades as shown in Figure 252.

Following disassembly of the ROC configuration Buildup F, photographs of the compressor casing (Figures 245 and 246) and of the main bearing housing (Figures 247 and 248) were taken. At this time, it was discovered that the spindle in which the Number 4 crystal was mounted protruded 0.25 inch into the flowpath. The dimensions of the special spindle holding the Number 4 crystal were such that the casing could not be assembled on the main bearing housing unless this spindle was driven forward into the airpath upon assembly. Positive interference of more than 1/8 inch occurred between the external portion of this spindle and the ring gear located on the rear side of the main bearing housing (Figures 247 and 248).

This finding means that during Runs 17 and 18 (which included the only running of Buildup F at 80 percent speed) the stator casing must have had this special spindle protruding 0.25 inch or 60 percent of the flowpath width into the airstream. The location of this spindle was approximately 3 inches upstream of the cobra probe used to survey flow angle and total pressure at the rotor exit. Certainly this large obstruction (about 0.90 inch in diameter) must have had a pronounced effect on the flow in the compressor and could be responsible for the decrease in performance observed during Run Numbers 17 and 18 of Buildup F at high speed.

Although very satisfactory rotor performance was obtained at 70 percent speed during Buildup F of the Phase II investigation, the Teflon seal used during that buildup was destroyed (Figure 253). It is likely that this Teflon seal was destroyed during runs at 80 percent speed. In addition to the protrusion of the crystal-containing-spindle, the seal failure helps to account for the significant decrease in rotor efficiency observed between 70 and 80 percent speeds with the Buildup F configuration.

Examination of the compressor on February 13, 1968, revealed that the Teflon seal had been separated into about 5 parts In addition, curling of the edges had occurred so the seal was completely ineffective. No damage to the rotor was apparent. The strain gage leads between the blade shank washers and the gages were missing. Apparently the adhesive had experienced greater temperatures than the material could withstand without losing strength.

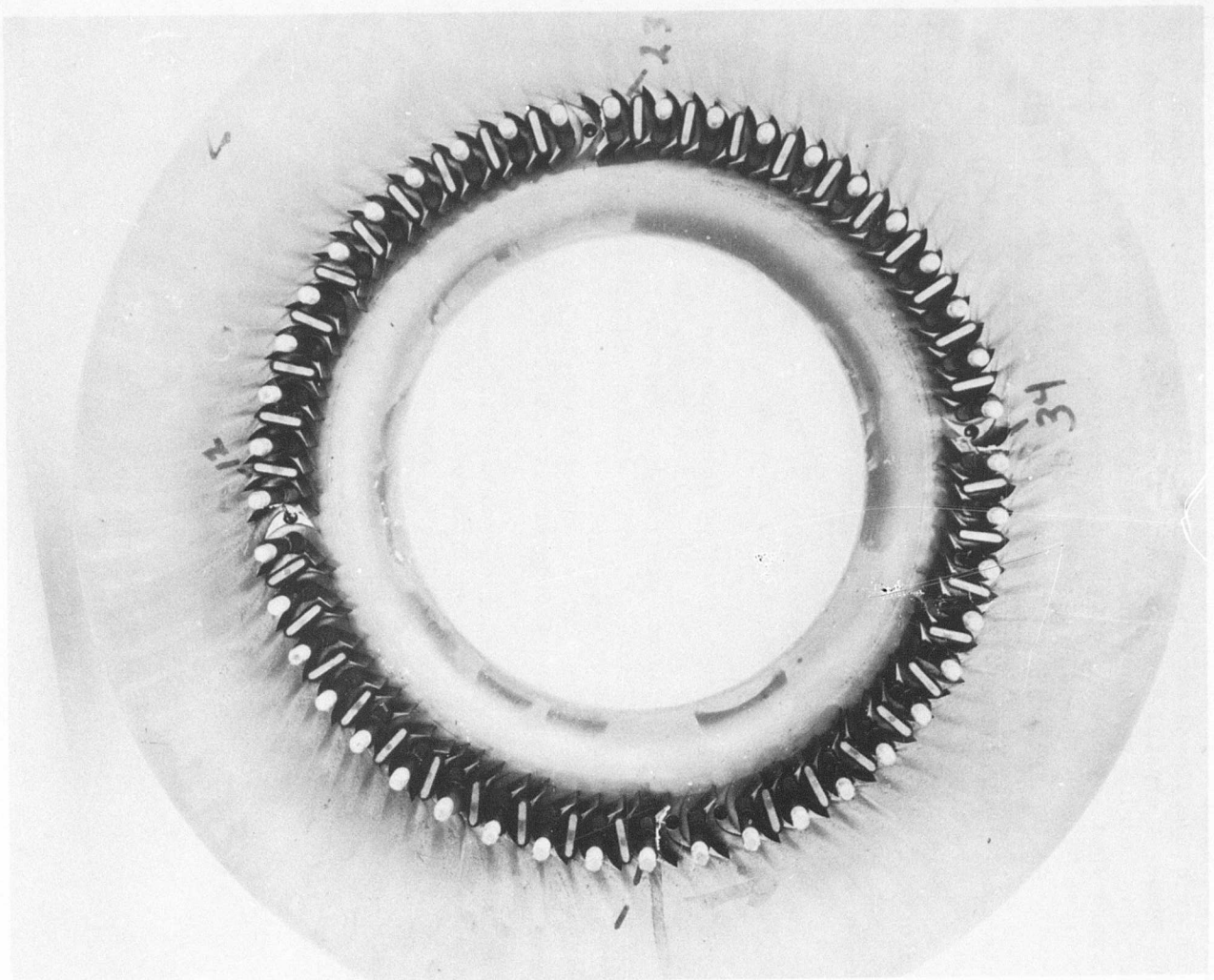

Figure 237. Soot Patterns on the Rotating Shroud Following Buildup F, Phase II Investigation.

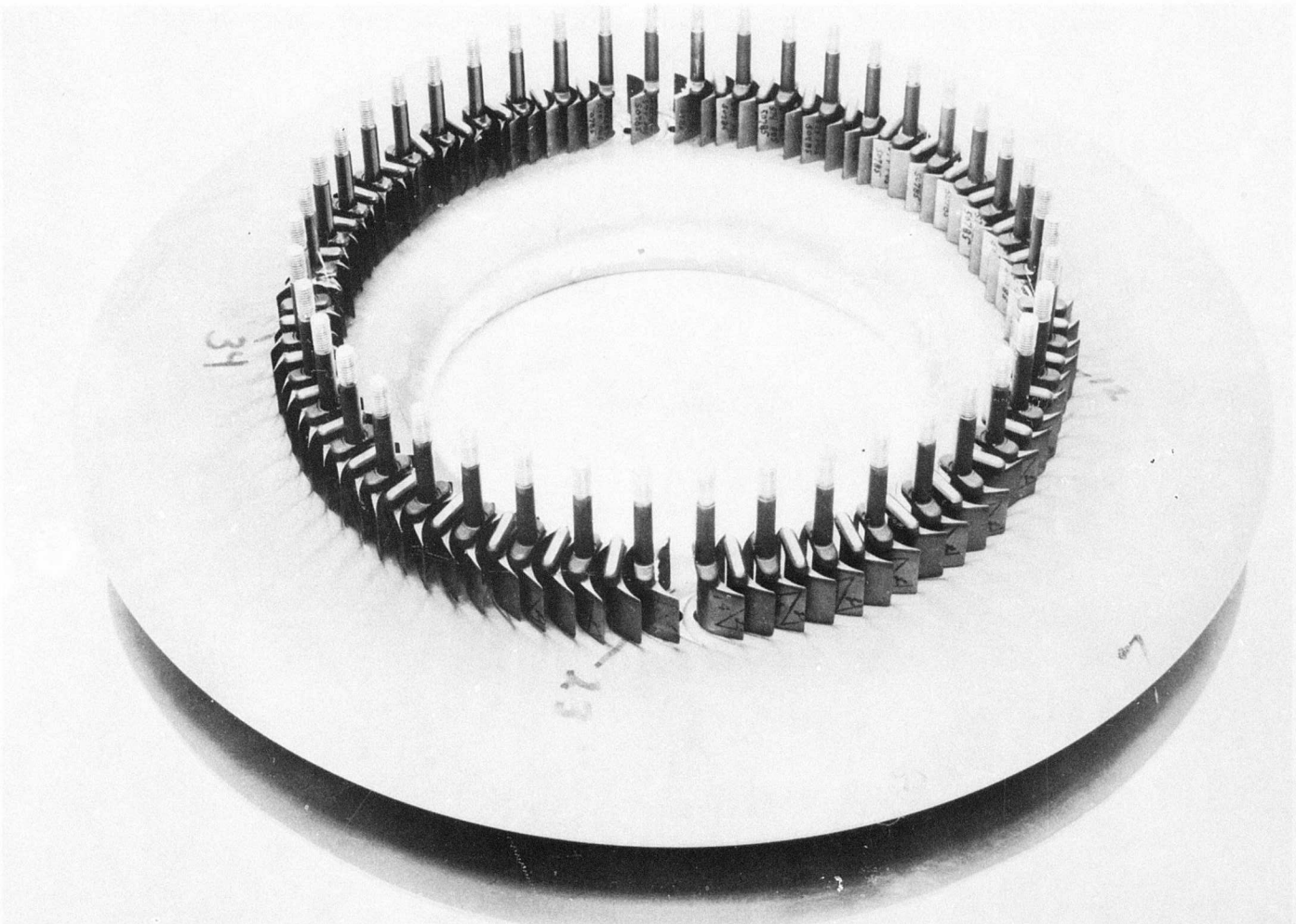

Figure 238. Soot Patterns on the Rotor Blades and Rotating Shroud Following Buildup F, Phase II Investigation.

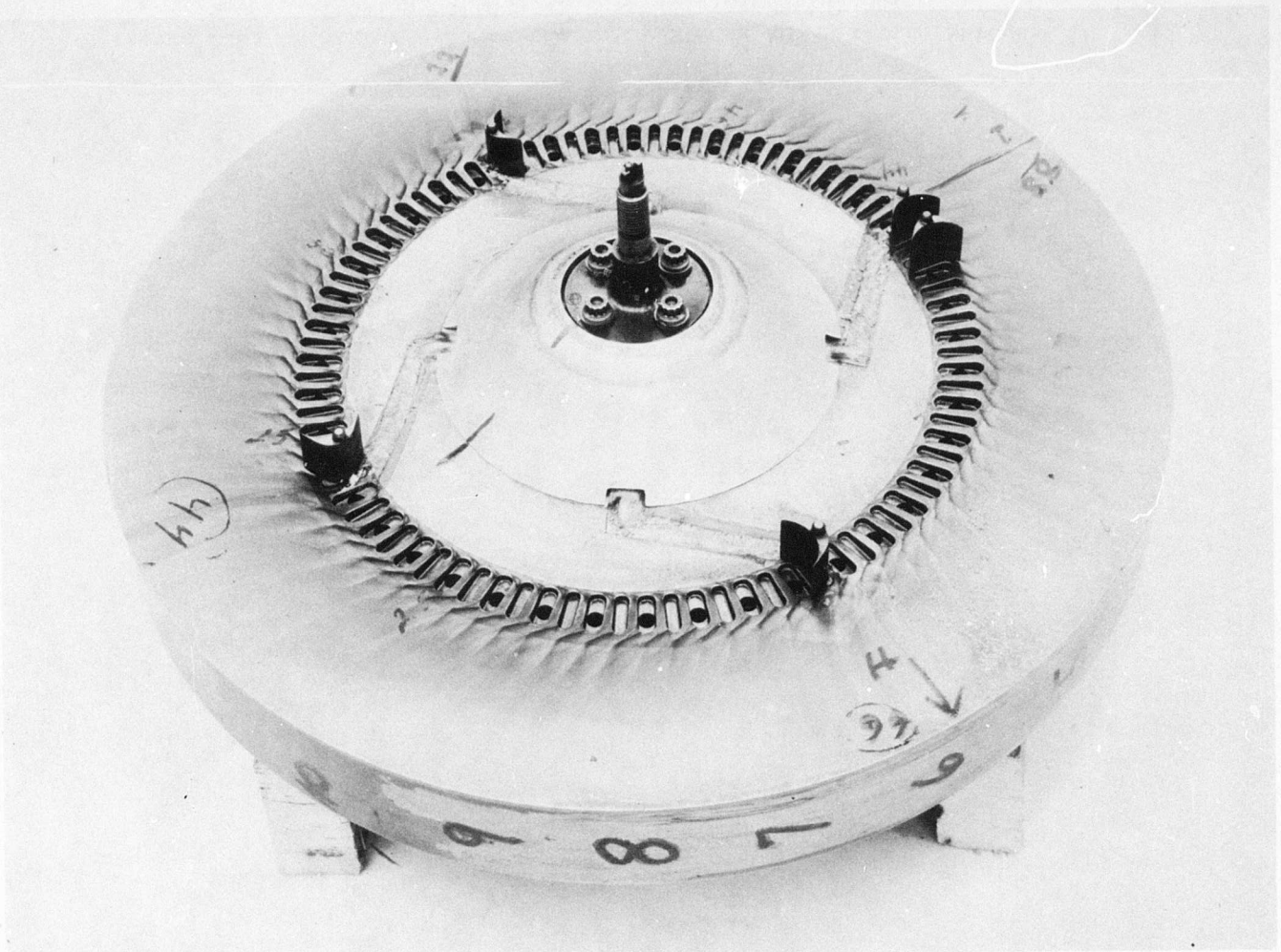

Figure 239. Soot Patterns on Rotor Disc Showing Variations Downstream of Strain Gage Leads.

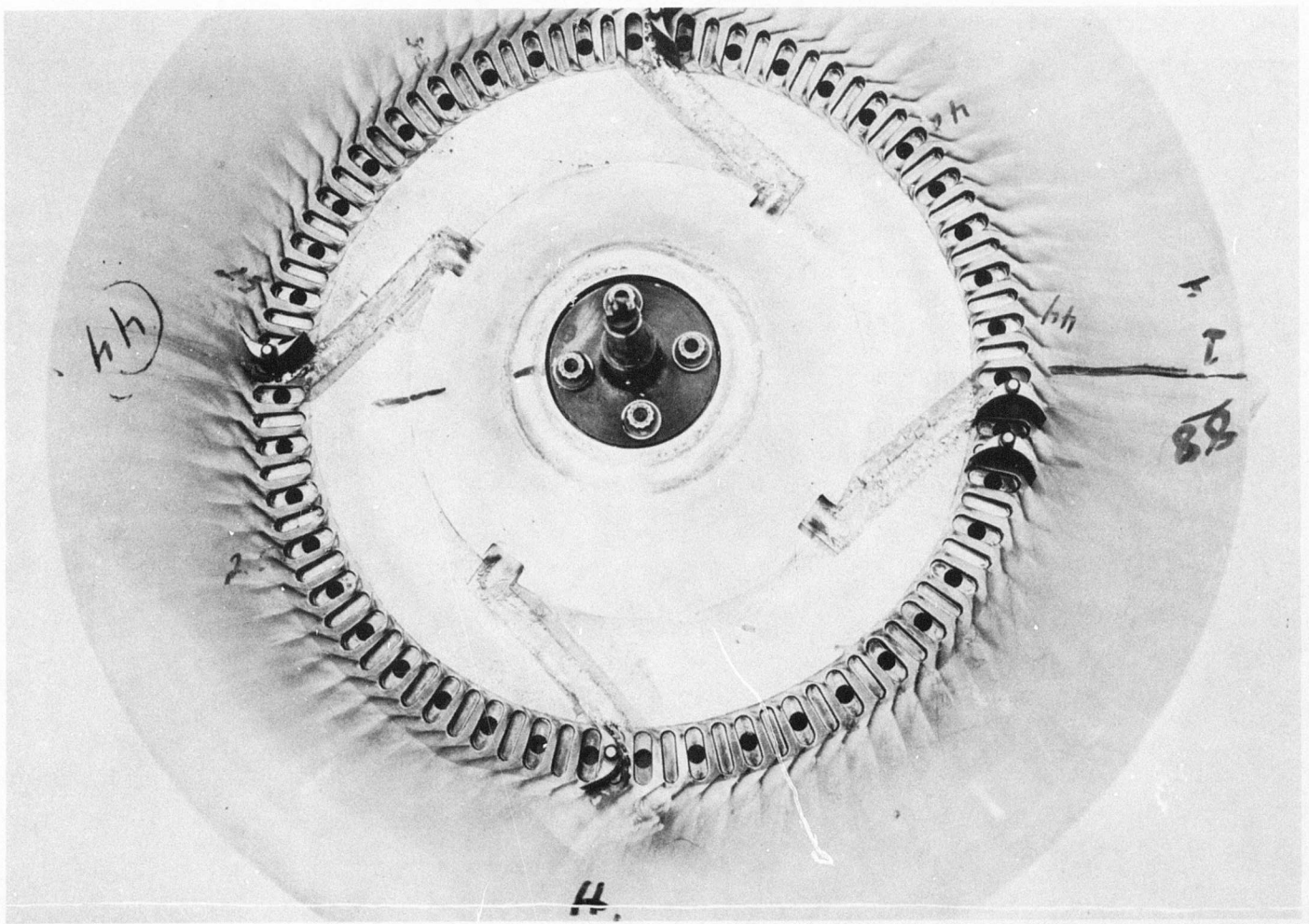

Figure 240. Soot Patterns on the Rotor Disc Following Buildup F, Phase II Investigation.

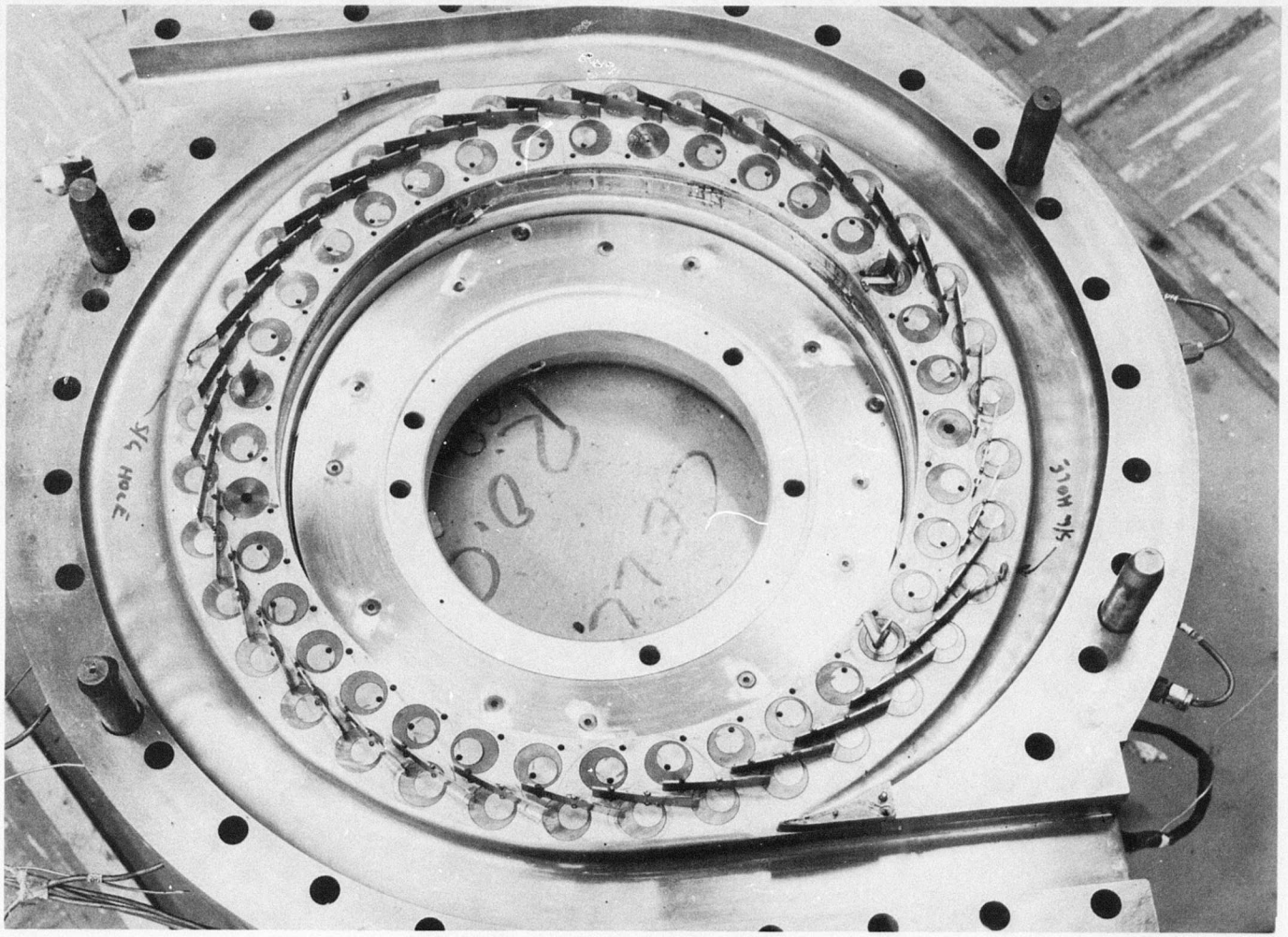

Figure 241. Stator Casing Illustrating Stator Vane, Instrumentation, and Scroll Configuration for Buildup F, Phase II Investigation.

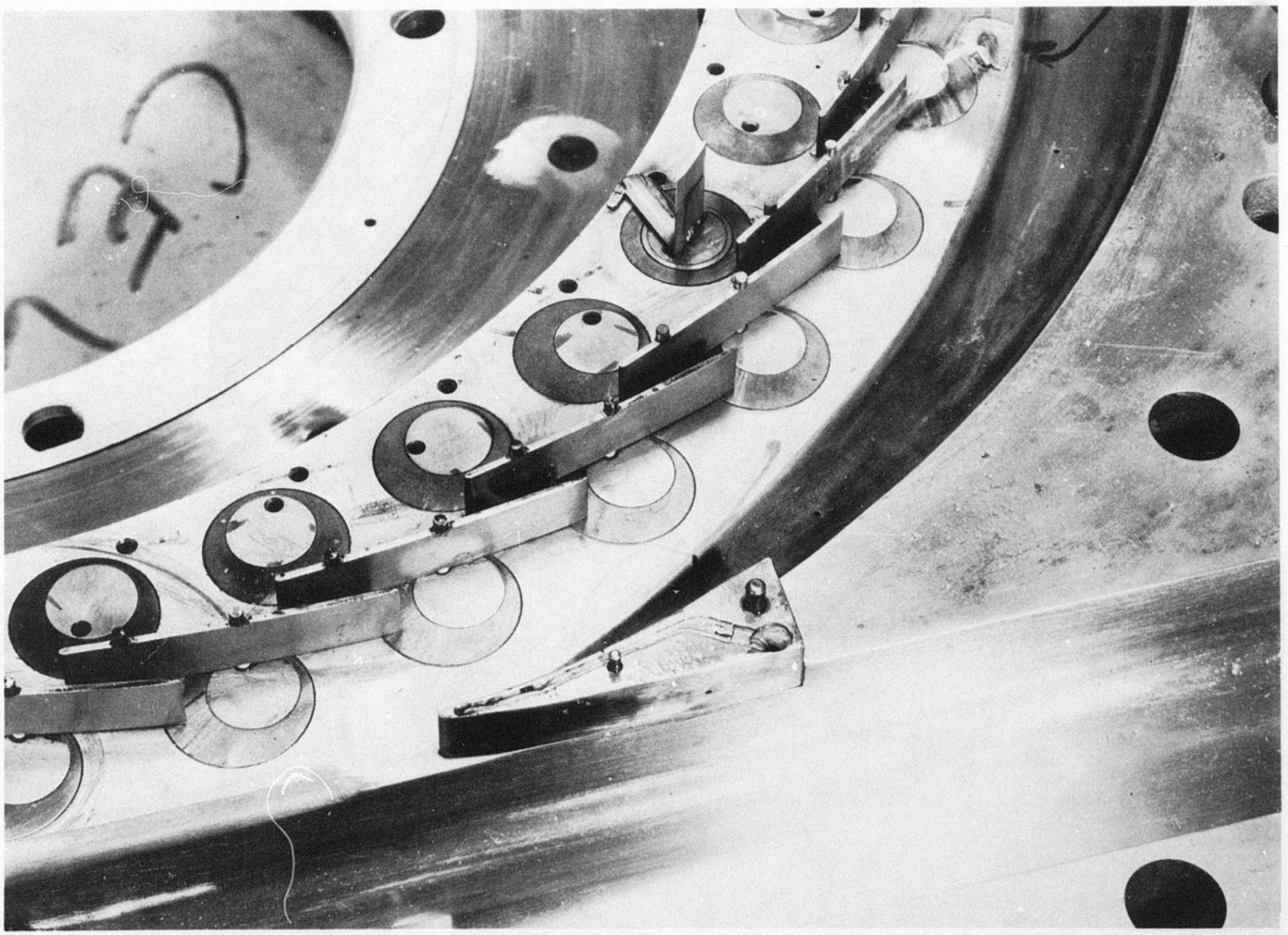

Figure 242. Close-up View of Scroll Splitter Lip, Subsonic Stators, and Cobra Probe for Buildup F, Phase II Investigation.

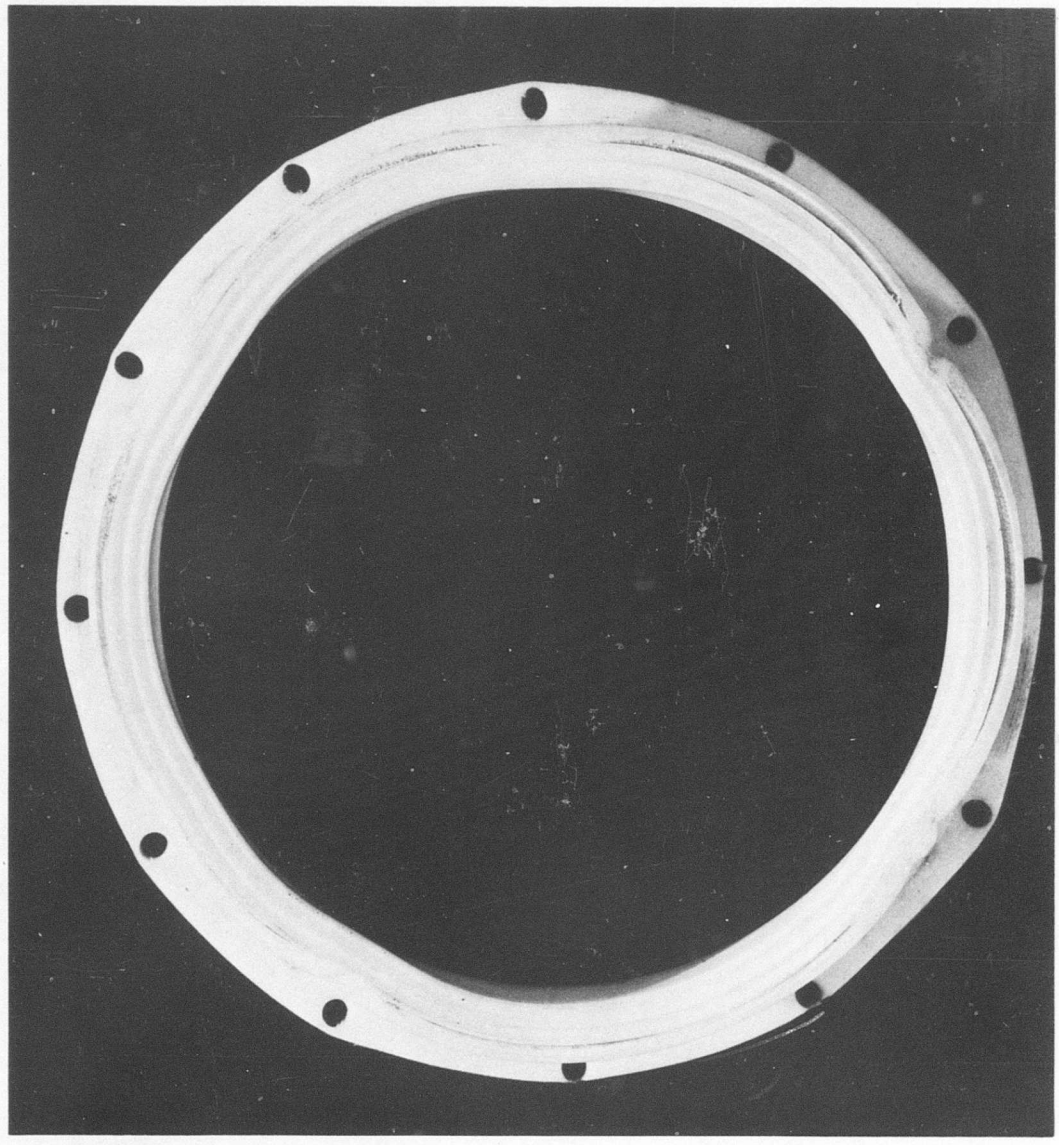

Figure 243. Teflon Seal Illustrating Warpage, Which Occurred During Run Numbers 15 and 16, Buildup F, Phase II Investigation.

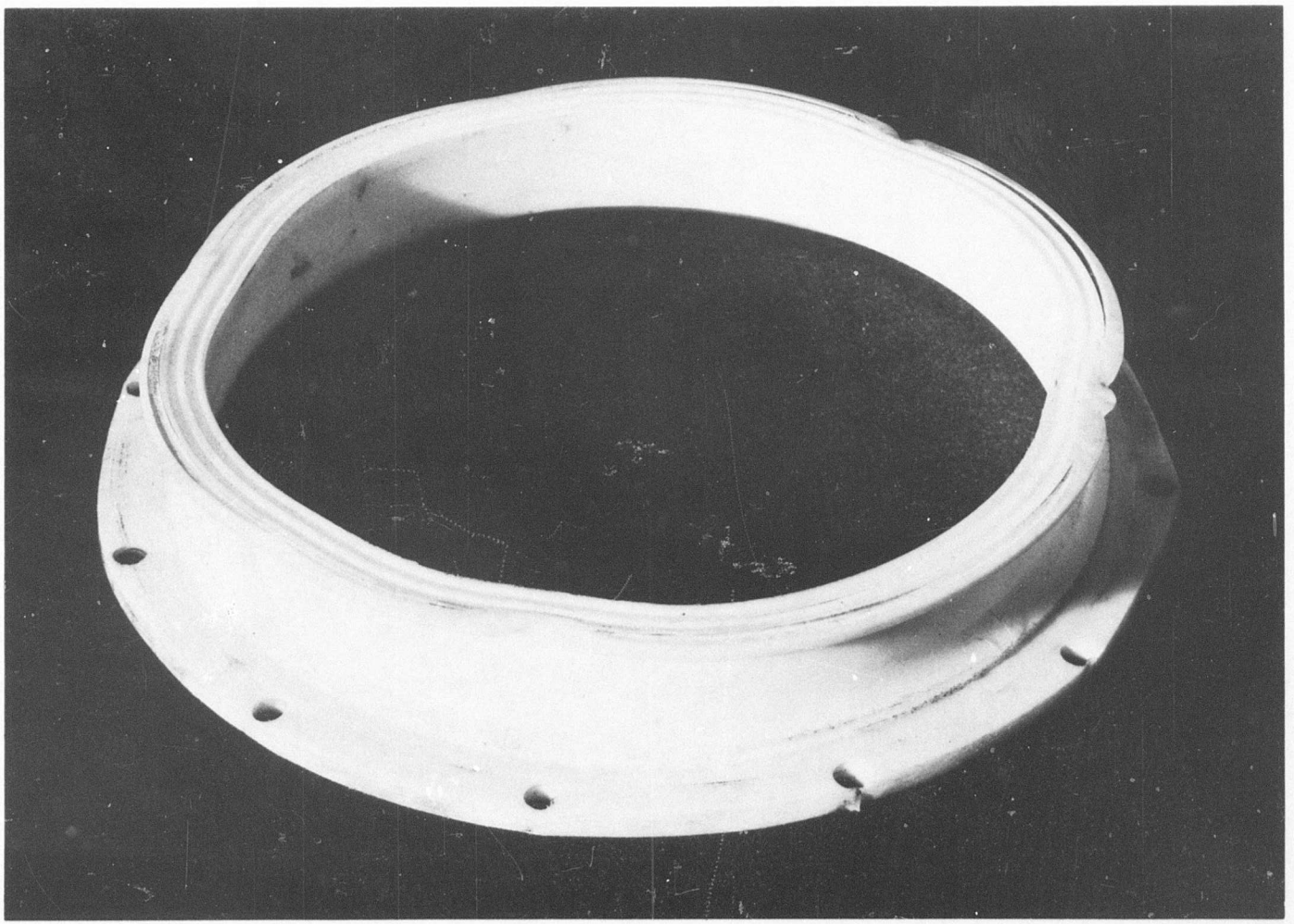

Figure 244. Side View of Teflon Seal Following Run Numbers 15 and 16, Buildup F, Phase II Investigation.

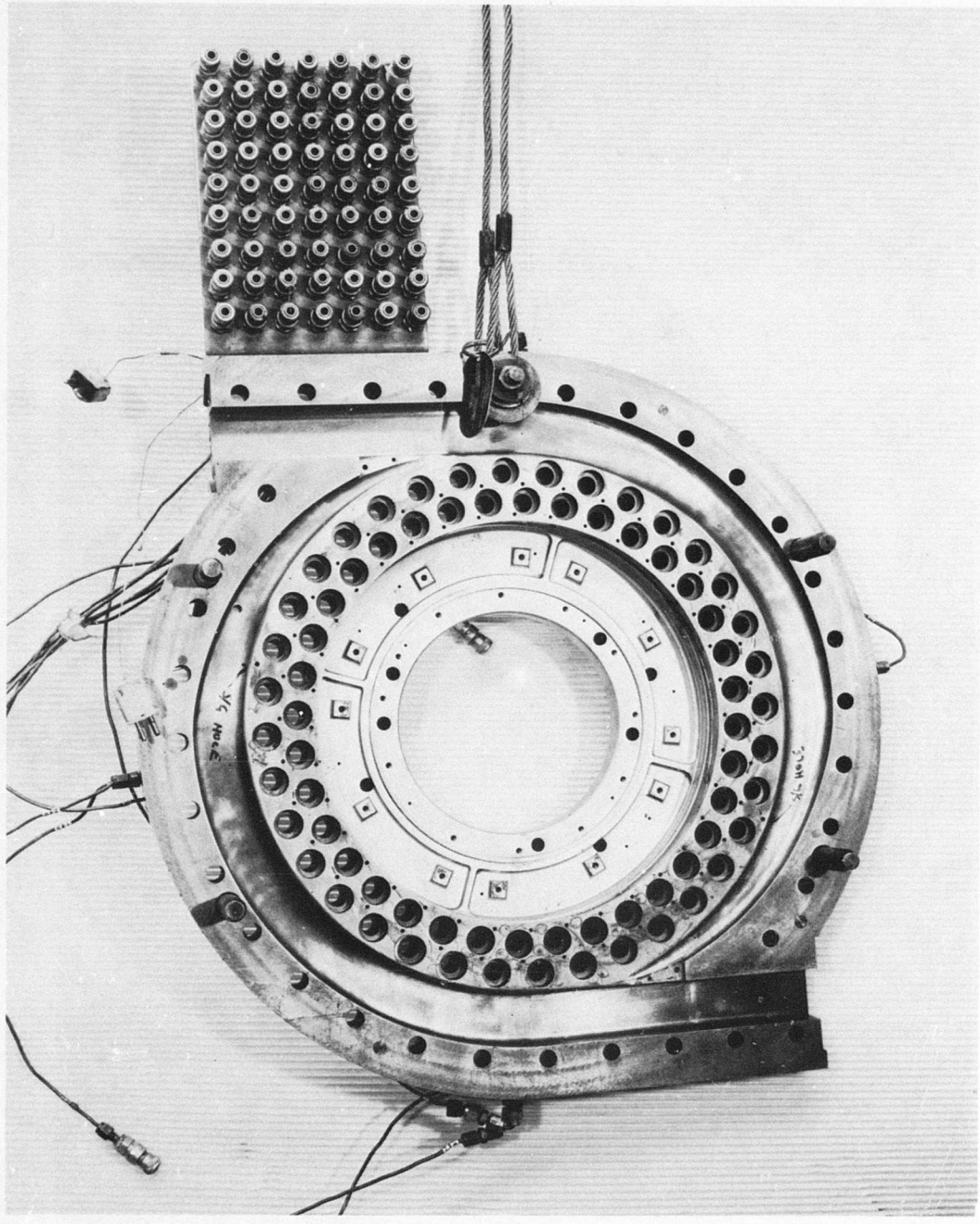

Figure 245. Internal View of Forward Compressor Casing Following Phase II Investigation.

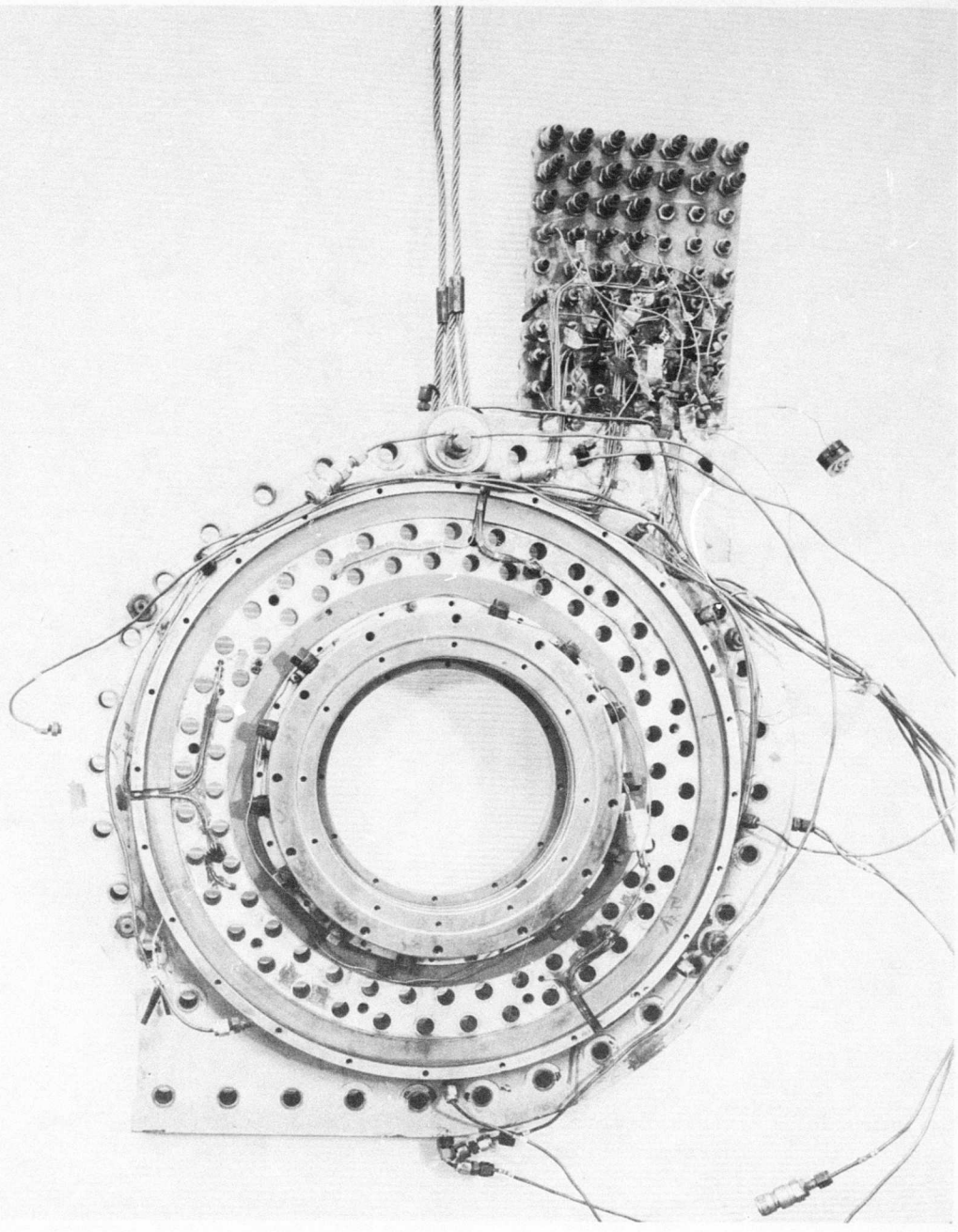

Figure 246. External View of Forward Compressor Casing Following Phase II Investigation.

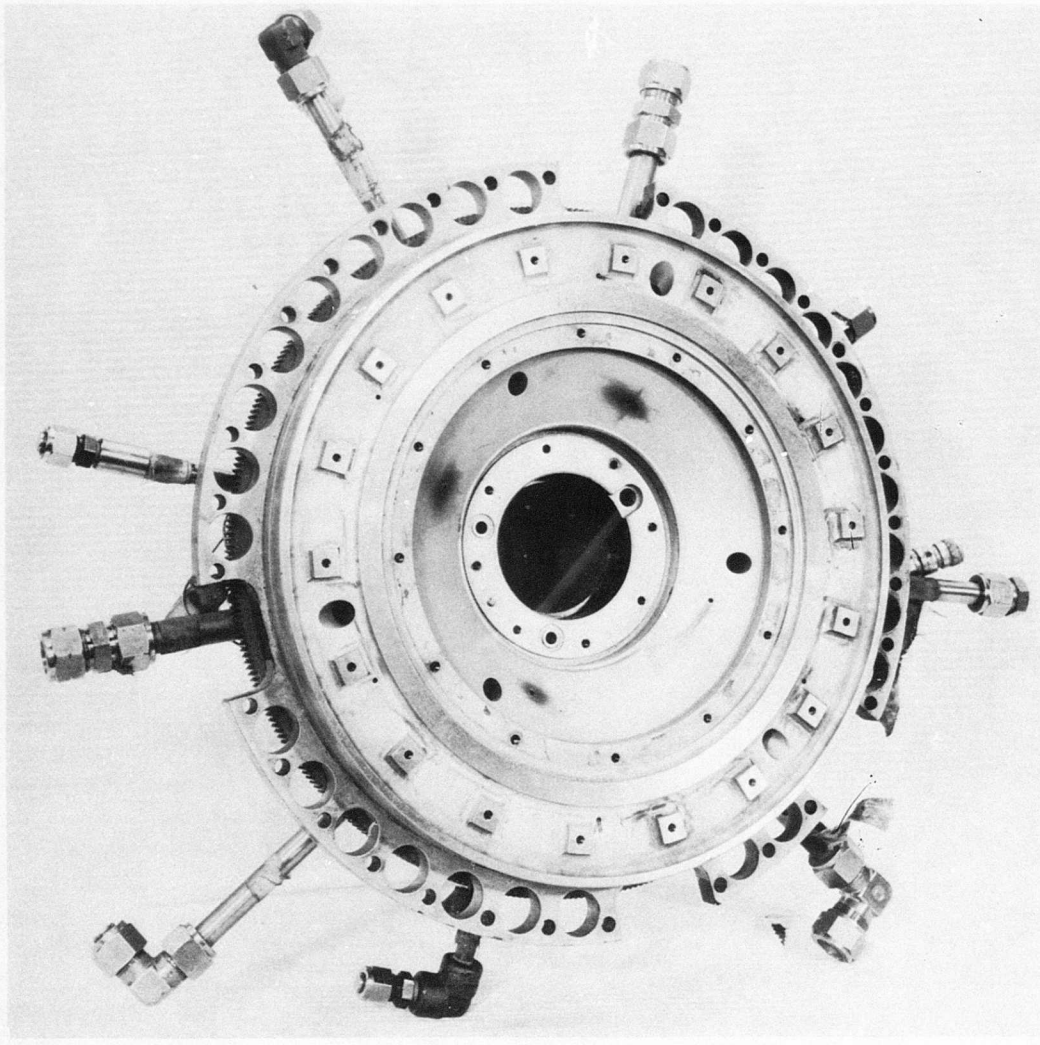

Figure 247. Internal View of Main Bearing Housing Following Phase II Investigation.

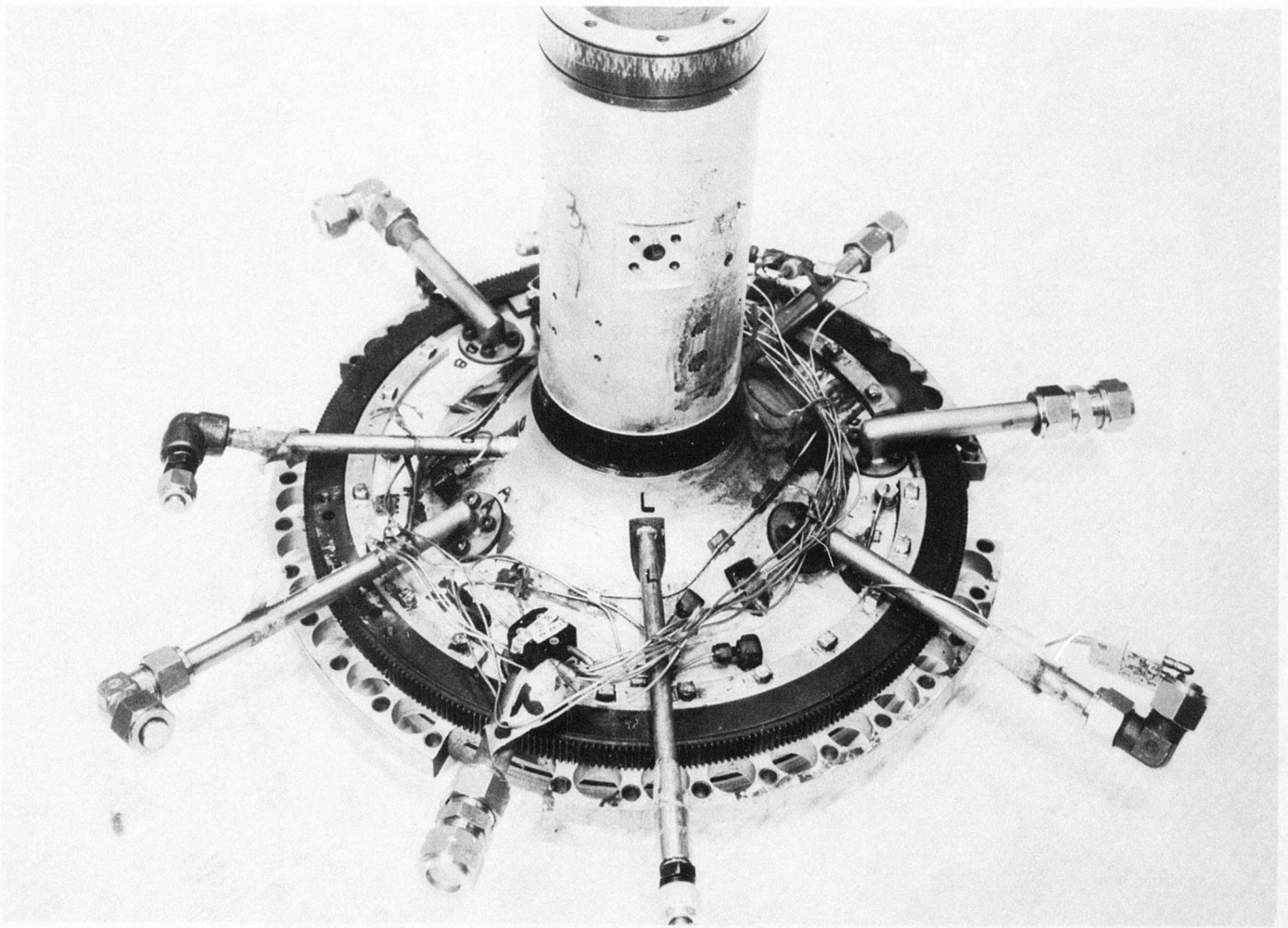

Figure 248. External View of Main Bearing Housing Following Phase II Investigation - Ring Gear in Position for Operating Supersonic Stators.

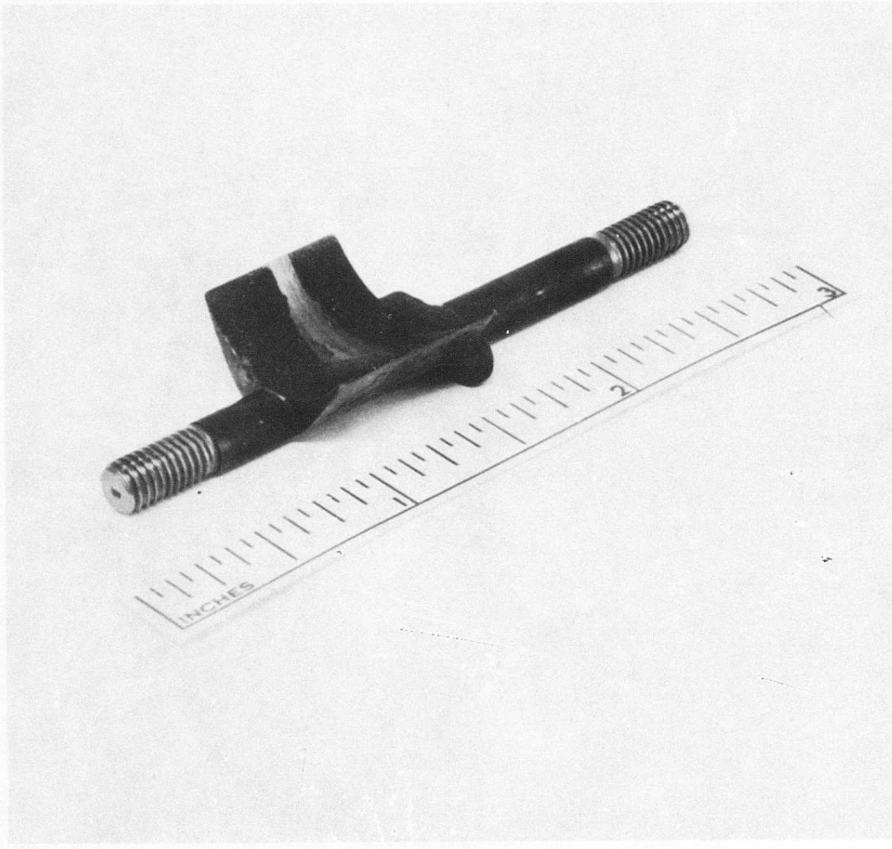

Figure 249. Overall View of Long Shank Rotor Blade Following Run Number 18 of Buildup F.

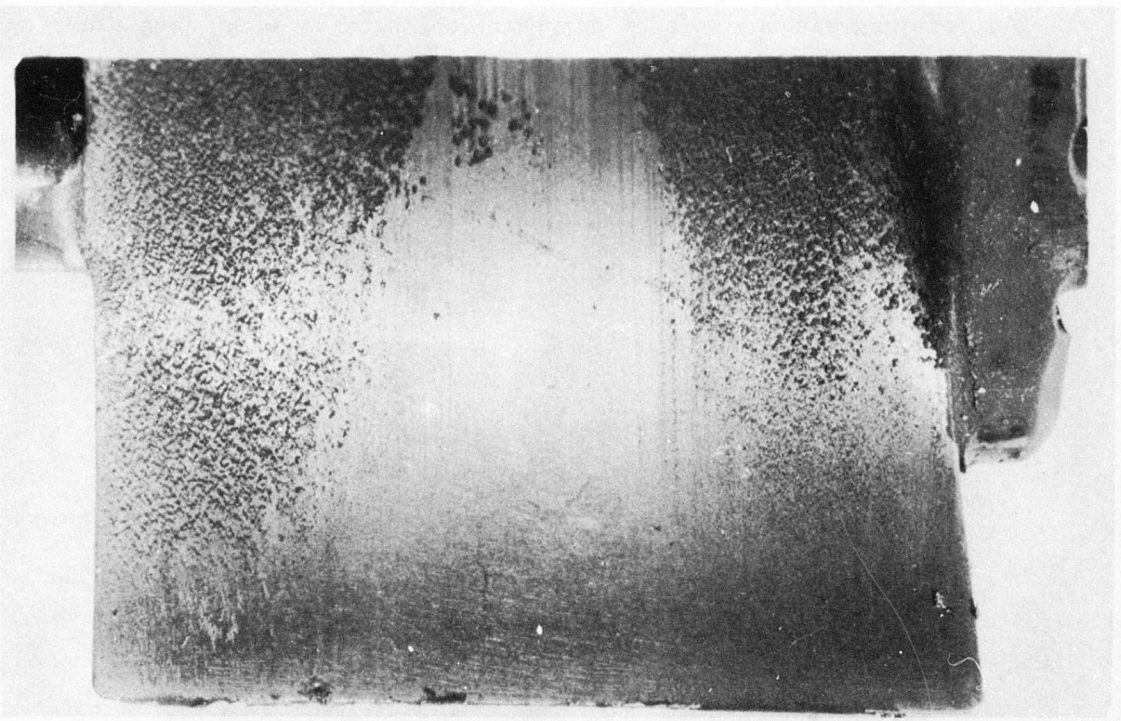

Figure 250. Detail of Soot Pattern Near Leading Edge on Concave Surface of Rotor Blade.

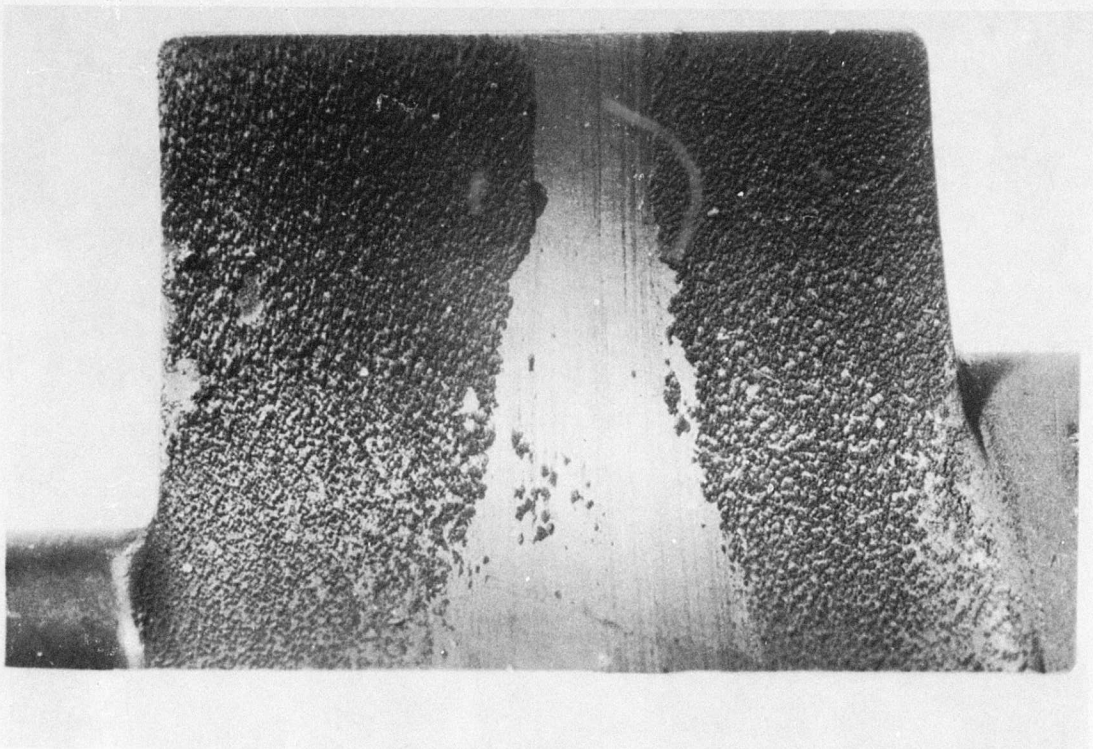

Figure 251. Soot Pattern Near Trailing Edge on Concave Surface of Rotor Blade.

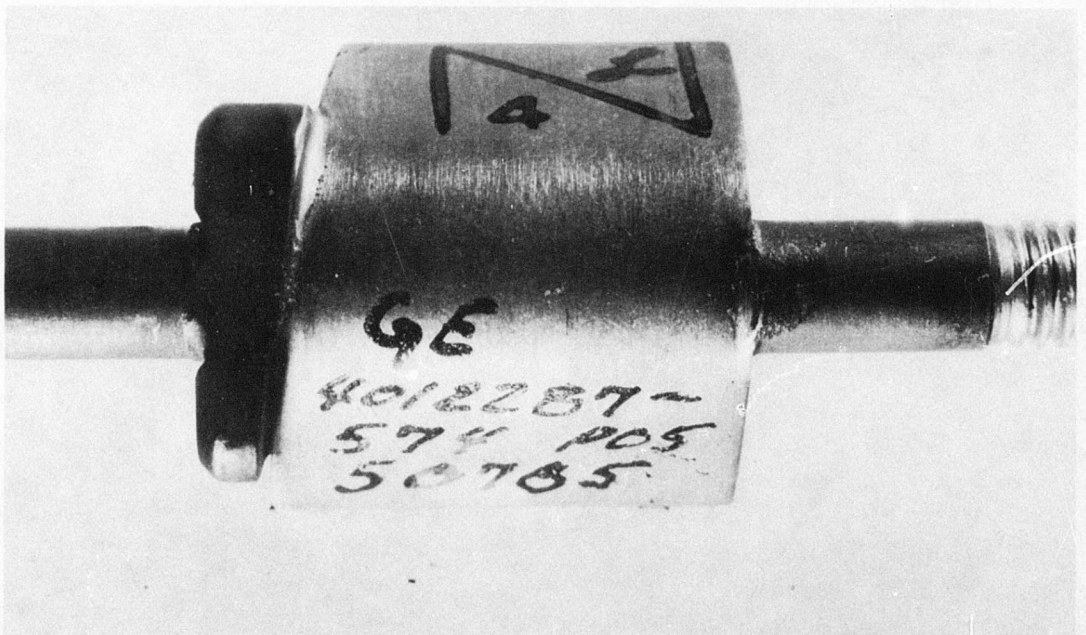

Figure 252. Convex Surface of Rotor Blade Following Run Number 18, Buildup F, Phase II Investigation.

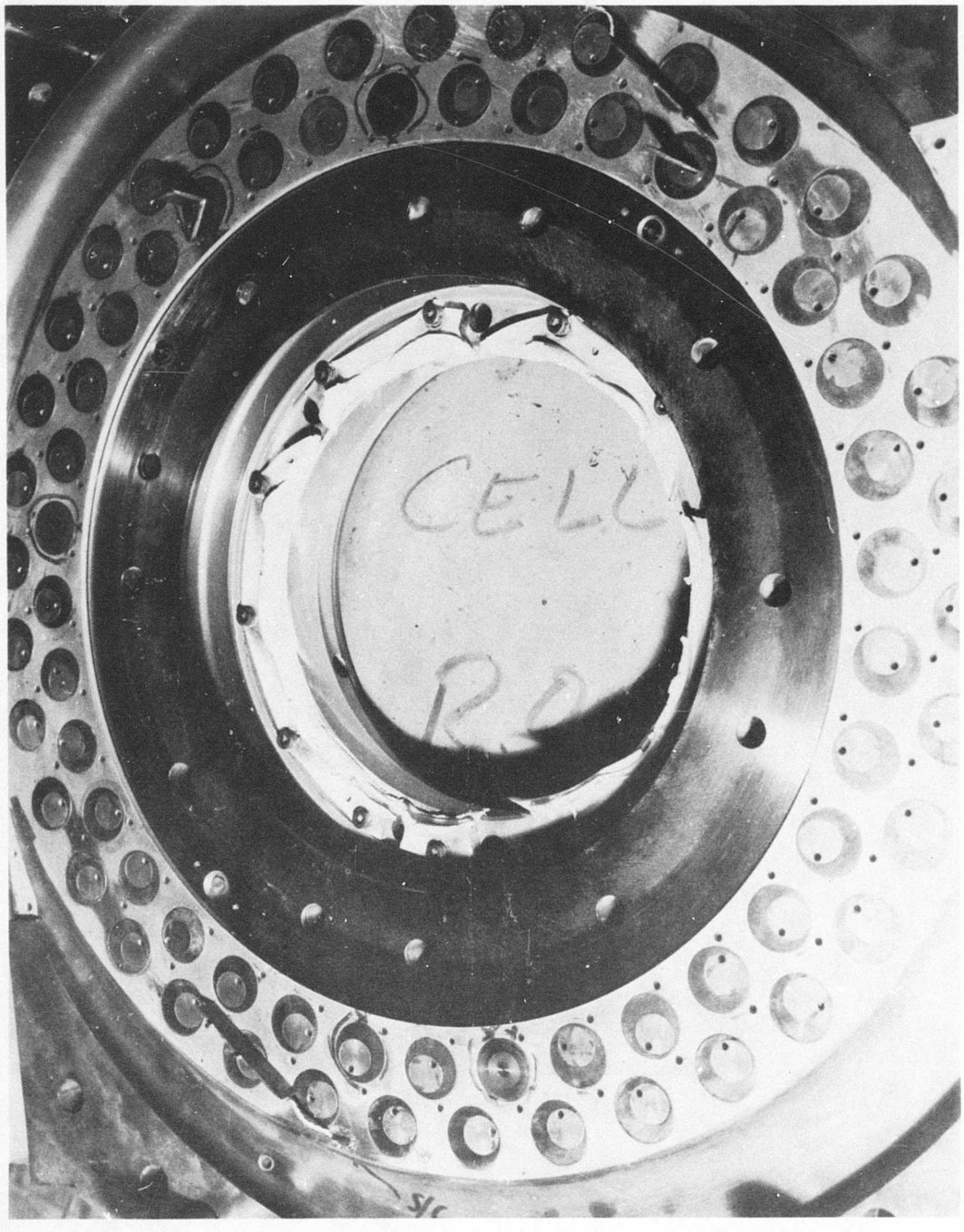

Figure 253. Remains of Teflon Seal Following Run Number 18, Buildup F, Phase II Investigation.

PHASE III COMPRESSOR DESIGN

STUDIES OF IMPROVED ROTORS

Increased Rotor Blade Chord

There are significant reasons for considering a decrease in the radius at which the leading edge of the rotor blades occurs. The primary reason is, of course, that the inlet Mach number decreases as the radius of the rotor blade leading edge decreases. Not only does the dynamic pressure entering the rotor blades decrease, but also the loss coefficient decreases. A decrease in the radius at which the leading edges are placed increases the difficulty of passing the airflow through the rotating shroud, since the radius of the opening must also become smaller. This change has the result of increasing the axial Mach number, and therefore, the local velocity around the lip of the rotating shroud. This problem might be alleviated by deviating from one of the ROC design principles: the use of two-dimensional flow through two-dimensional blading. By permitting the meridional streamlines to be curved to axial or partially to axial within the rotor blades, the entrance problem can be simplified. Since this configuration introduces a curvature of the flow in one plane (the radial-axial plane) while large flow curvatures are occurring in planes normal to the axis of rotation in the presence of nonuniform relative total pressure, strong secondary flows would be difficult if not impossible to avoid. For these reasons, it is presently believed that the optimum compressor will be achieved with only small changes in the radius at which the blade leading edges occur.

A few calculations of an ROC having a 1.4-inch rotor blade chord length have been made with the trailing edge placed at a 4.65-inch radius. This configuration reduces the radius at which the leading edges occur to 3.25 inches as compared to 3.6 inches in the original ROC. By this means, the center of the rotor blades is maintained at the original radius. With -18.5 degrees inlet flow turning, the inlet Mach number is reduced by this change to about 1.11. Due to the reduced inlet dynamic pressure and the reduced rotor blade loss coefficient, the rotor efficiency is increased by about 3 percent, and the total pressure calculated to occur at stator exit is 10 atmospheres. The diffuser contour used for this calculation is presented in Figure 254. A problem which remains with this rotor design is the high value of the effective pressure coefficient which occurs in the rotating diffuser at the blade trailing edge radius of 4.65 inches. Variation of the aerodynamic loading parameter G_2/r_2 shown in Figure 255 indicates a maximum of about 6.85, although the value decreases rapidly to about 4.3. Although a peak value of 6.85 can probably be sustained, particularly when the maximum is followed by a rapid decrease, difficulty may be encountered if the speed increase of 5 to 6 percent required to obtain target pressure ratio is attempted.

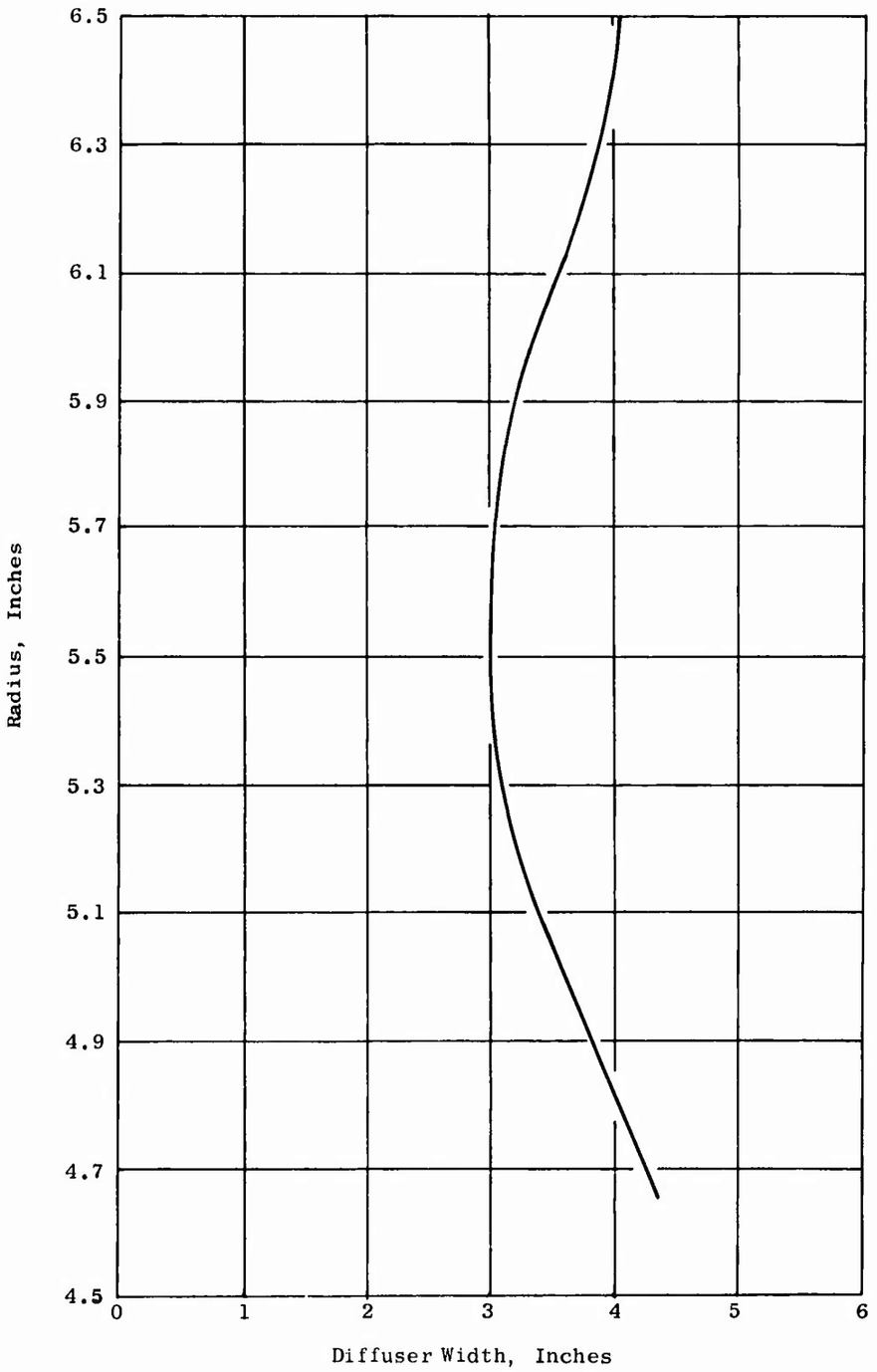

Figure 254. Variation of Diffuser Width With Radius for Contour Number 17.

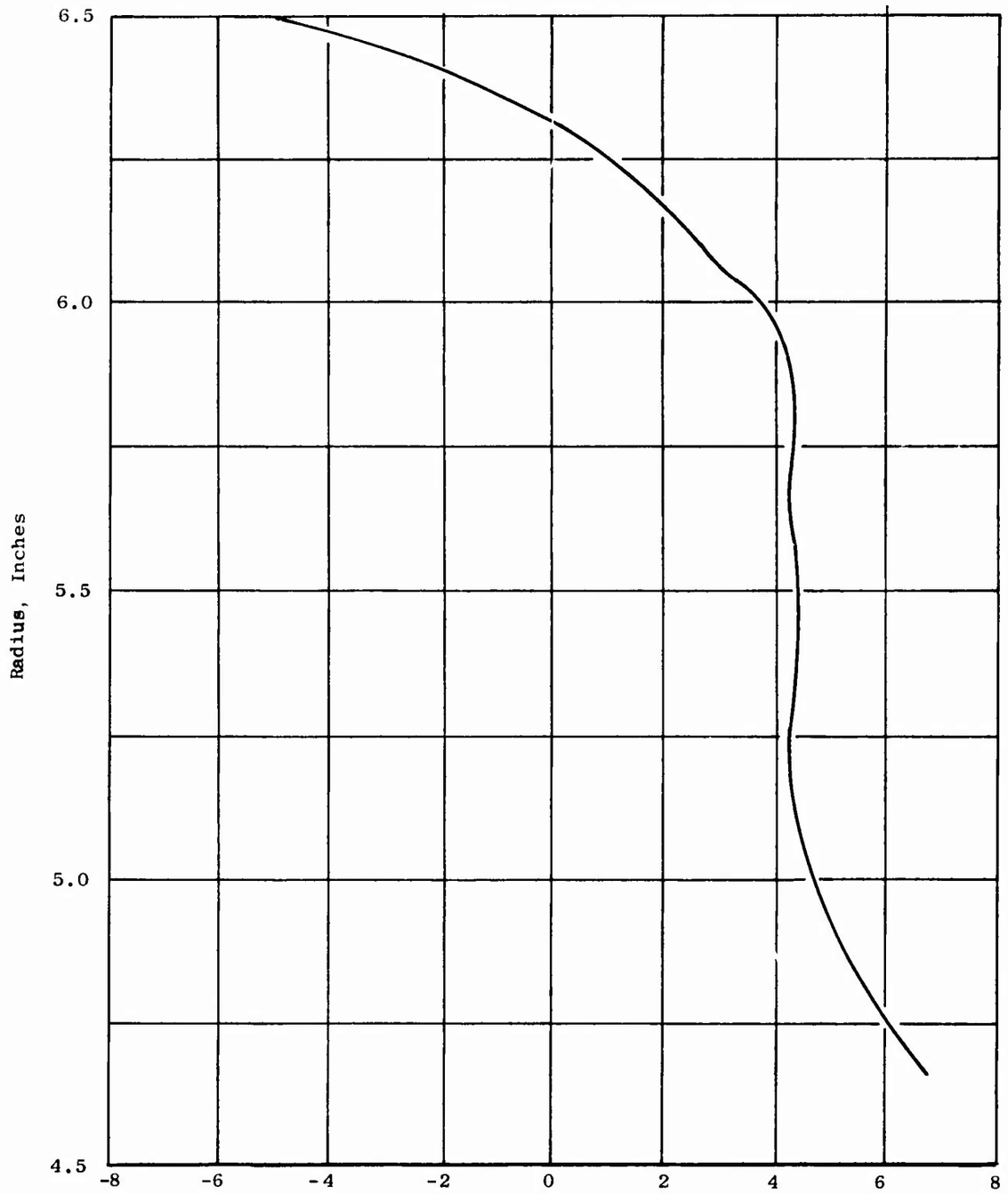

Figure 255. Distribution of the Diffuser Loading Parameter G_2/r_2 for Contour Number 17 at 100 Percent Speed With Design Swirl Angle at -18.4 Degrees.

Increased Rotor Blade Chord and Radius

There are several reasons for considering an increase in the radius at which the rotor blade trailing edges are located. As Figures 21 and 22 show, the largest effective pressure gradients occur at the smallest radius in the vaneless diffuser. This is due, of course, to the occurrence of the maximum free stream tangential velocity and the minimum boundary layer particle velocity (assumed to be equal to wheel speed) at the smallest radius. Thus, the design of a diffuser having reduced radial static pressure gradients to avoid separation is simplified by an increase in rotor blade trailing edge radius. To produce a given work input or total pressure ratio at constant rpm, the relative tangential velocity of the fluid is decreased as the rotor blade trailing edge radius is increased. Therefore, the friction loss in the diffuser is decreased due to the lower relative dynamic pressure and due to the shorter radial length of the diffuser which must be traversed. Higher compressor efficiency results, therefore.

A number of calculations have been made for different contours of the rotating vaneless diffuser for a rotor using blades of 1.4-inch chord (twice the original ROC rotor blade chord length). The leading edge conditions were kept the same, and the trailing edge was placed at 5.0-inch radius. For the same rotor rpm, the trailing edge rotational speed was increased from 1,300 to 1,500 fps, and the work input increased so that the absolute total pressure calculated at the rotor blade exit was 16.62 atmospheres. The exit flow angle from the rotor blades was decreased from 60 to 50 degrees for this design. At rotor exit, assuming a friction factor of 0.02, the total pressure P_t equals 13.98 atmospheres for a rotor efficiency of 86.8 percent. Using a stator loss coefficient of 0.25 to correspond with the stator inlet Mach number of 1.31 (compared to 1.16 with the present rotor), the stator exit total pressure equals 11.7 atmospheres with an efficiency of 79 percent. High inlet guide vane system losses are included in this calculation, and several points increase (3 to 5) should be obtained by inlet guide vane system improvement.

The initial calculation of this rotor assumed a straight-sided vaneless diffuser. The pressure gradients expressed in coefficient form are shown in Figures 256 and 257. The maximum value of the parameter G_2 using the Cos^2 term in the denominator is 6.0. Modifications to this contour, designed to reduce the maximum values are shown in Figure 258. The maximum value of G_2/r_2 has been reduced from 6.0 to about 4.9 with the maximum occurring about midway between the trailing edges of the rotor blades and the rotor exit radius (Figure 259). By contracting the passage slightly in the mid-region, Contour Number 7 was derived. The maximum value of the effective pressure coefficient of about 4.3 was calculated for this contour (Figure 260). When this value is compared to the maximum value which apparently can be sustained without separation from 6.3

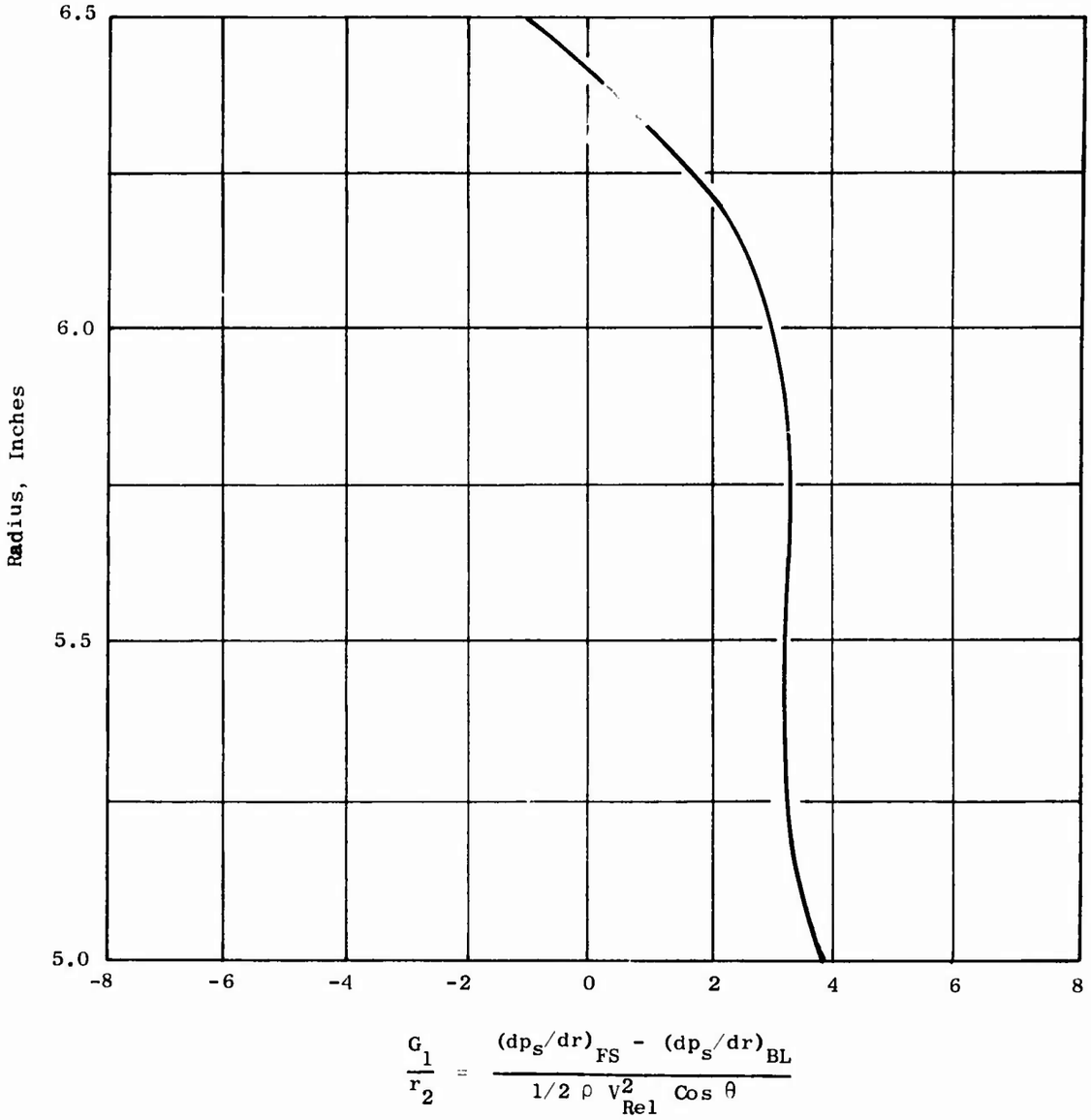

Figure 256. Distribution of the Diffuser Loading Parameter G_1/r_2 for Contour Number 6 at 100 Percent Speed With Design Inlet Swirl Angle of -18.4 Degrees.

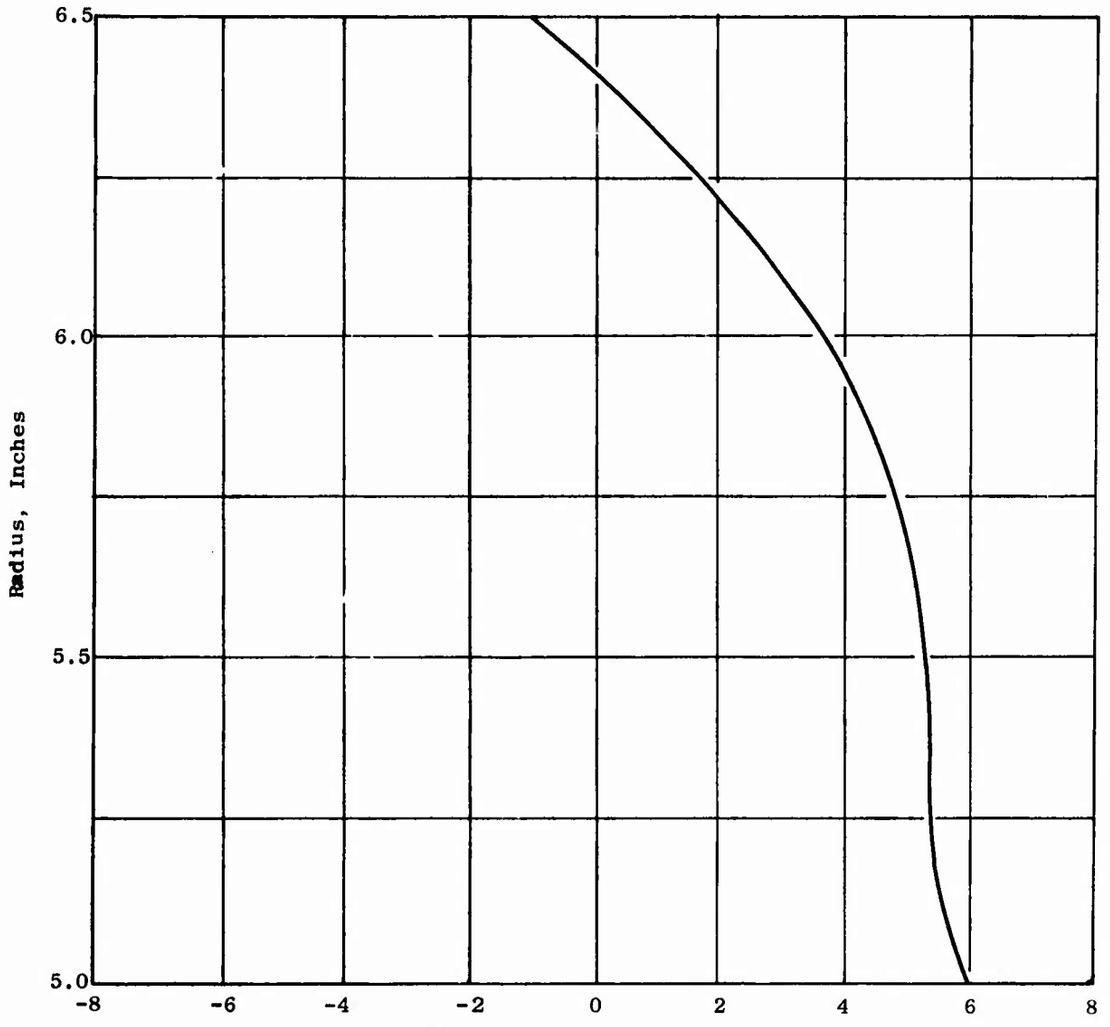

$$\frac{G_2}{r_2} = \frac{(dp_s/dr)_{FS} - (dp_s/dr)_{BL}}{1/2\ \rho\ V_{Rel}^2\ \cos^2\theta}$$

Figure 257. Distribution of the Diffuser Loading Parameter G_2/r_2 for Contour Number 6 at 100 Percent Speed With Design Inlet Swirl Angle of -18.4 Degrees.

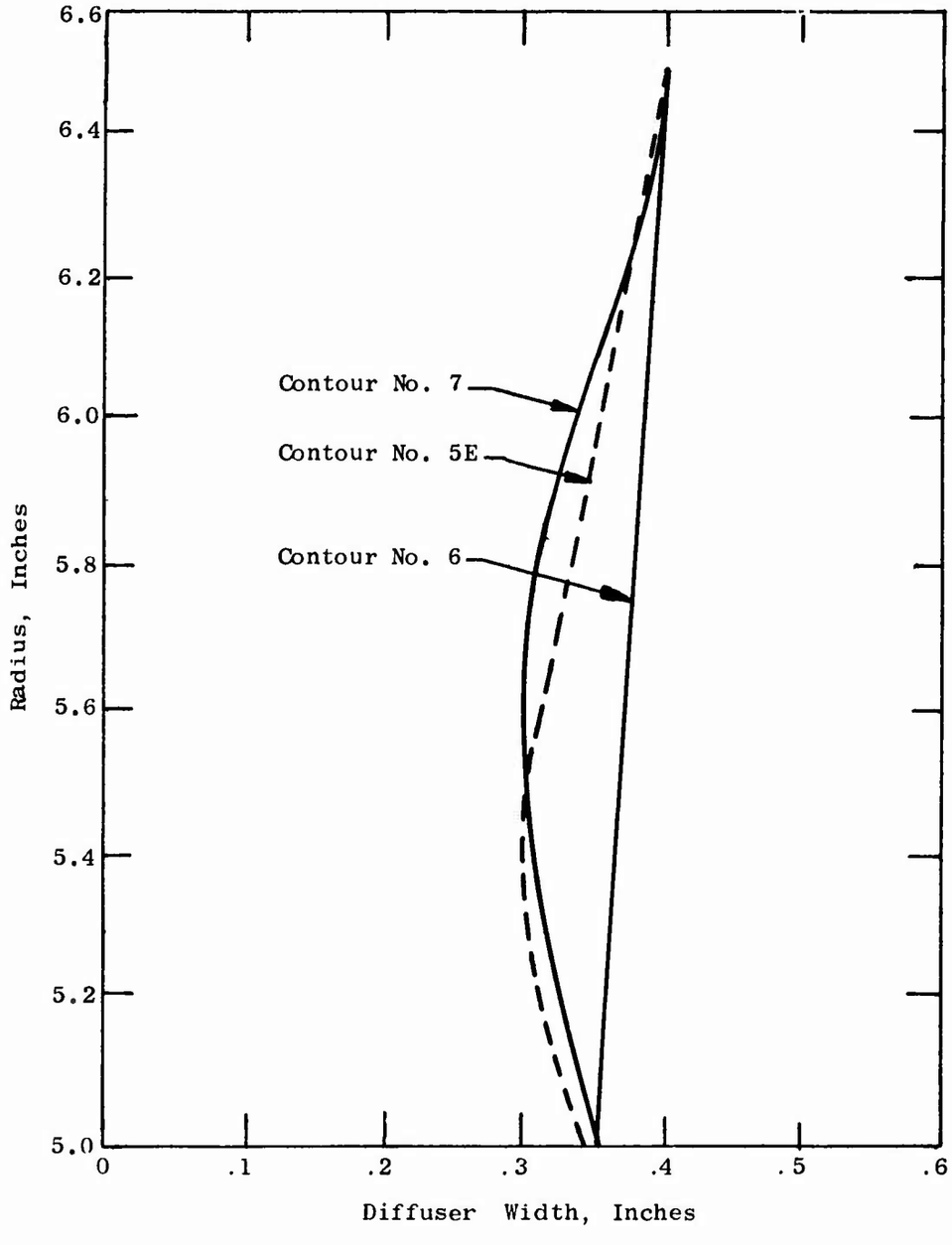

Figure 258. Variation of Diffuser Width With Radius for Contour Numbers 5E, 6, and 7.

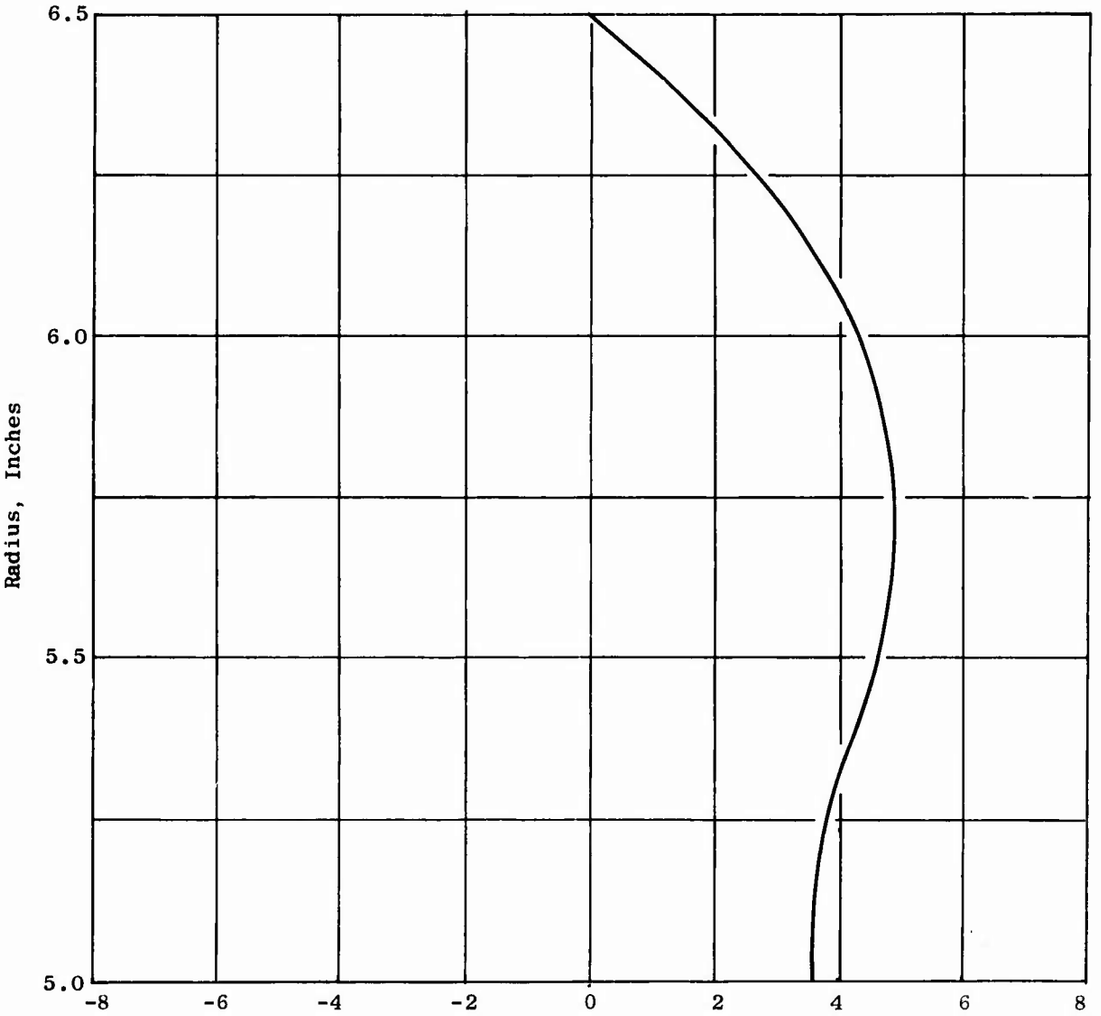

$$\frac{G_2}{r_2} = \frac{(dp_s/dr)_{FS} - (dp_s/dr)_{BL}}{1/2\ \rho\ V_{Rel}^2\ \cos^2\theta}$$

Figure 259. Distribution of the Diffuser Loading Parameter G_2/r_2 for Contour Number 5E at 100 Percent Speed With Design Inlet Swirl Angle at -18.4 Degrees.

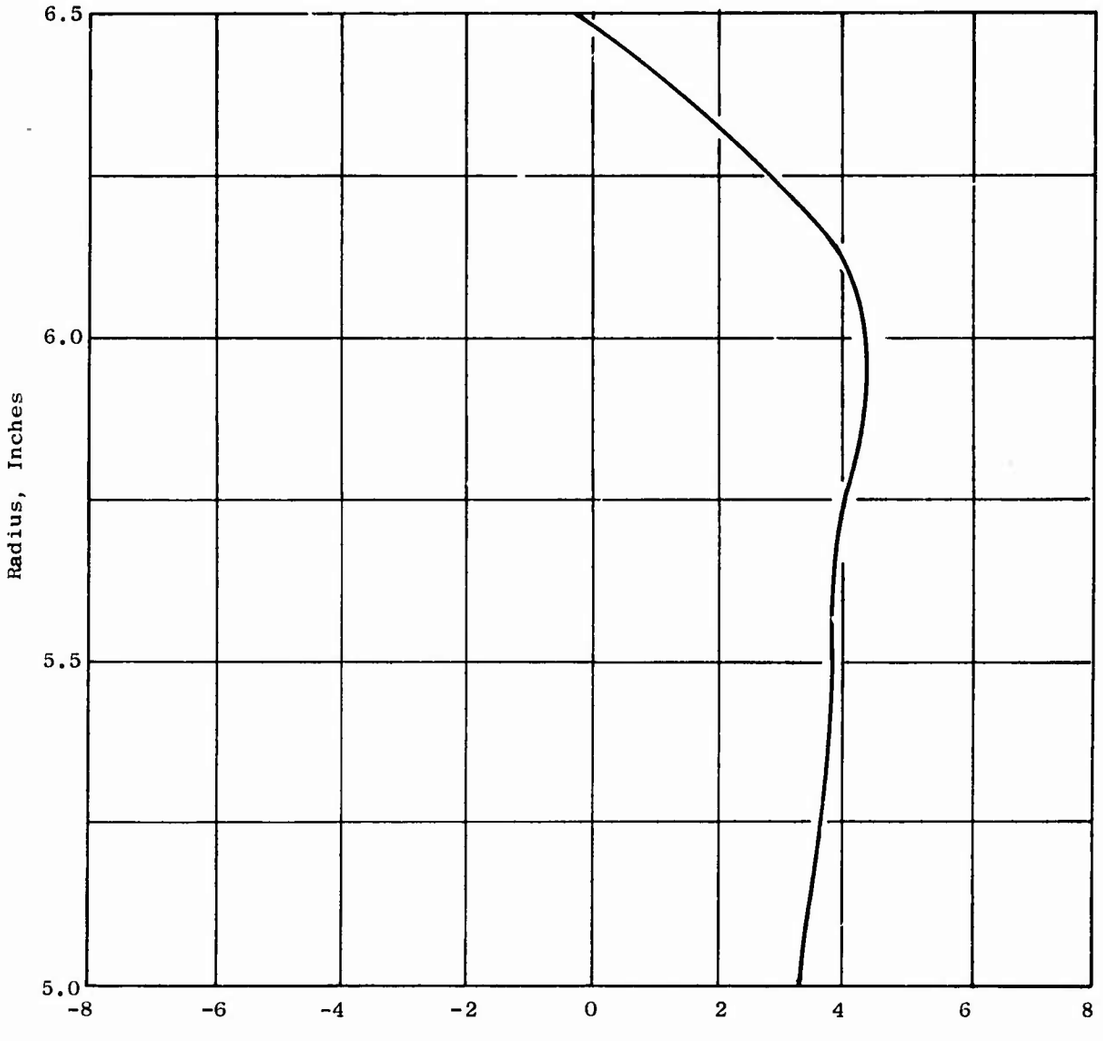

$$\frac{G_2}{r_2} = \frac{(dp_s/dr)_{FS} - (dp_s/dr)_{BL}}{1/2\ \rho\ V_{Rel}^2\ \cos^2\theta}$$

Figure 260. Distribution of the Diffuser Loading Parameter G_2/r_2 for Contour Number 7 at 100 Percent Speed With Design Inlet Swirl Angle at -18.4 Degrees.

to 6.9 (as noted previously from calculations of the rotating vaneless diffuser of the high-speed ROC running at 60 percent speed), a very significant reduction in aerodynamic loading of the vaneless diffuser can be achieved by increasing the rotational speed of the rotor blade trailing edges and by proper selection of diffuser area distribution.

ROTOR DESIGN

General

Agreement was reached on October 11, 1966, between representatives of General Electric and the U.S. Army that this Phase III rotor would constitute an evolutionary step toward target performance rather than a revolutionary jump having greater potential but less likelihood of succeeding. Rather than incorporate major changes in blade chord and number which would require complete aerodynamic and mechanical redesign and which would probably significantly increase cost and time, the decision was made to limit the modifications primarily to the rotating vaneless diffuser flow path. Performance within the contract target range might not be achieved, but more certain and steady progress toward the ultimate goal would be assured.

The rotating shroud mechanical design has been changed to a single stiffened rim. The purposes for these changes are to increase the fundamental frequency to 112 percent design speed to simplify test procedures and to permit the proximeters to detect vibrations of the blade-side rim in the event of strain gage system failure. These features, plus the use of a new shroud, blade, and disc, give greater assurance of reaching full speed safely.

In order to offset the imbalance resulting from the use of a single stiff rim, counterbalance weights were designed as the forward part of the rotating shroud. These counterbalance weights are indicated as the region forward of the dotted line shown in Figure 261. In order to achieve a close match of the radial growth of the disc and of the shroud, a reduction in the minimum diameter of the rotating shroud was required. The minimum diameter of the Phase II shroud was 4.9 inches. The bore of the Phase III shroud has been reduced to a minimum diameter of 4.52 inches. This means a reduction of the minimum flow area from about 19 to about 16 square inches or an increase in the average Mach number from 0.450 to 0.574 at the design weight flow of 4.5 pps. This increase in the average Mach number through the shroud inlet is certainly not desirable from the aerodynamic standpoint, but the maximum velocity on the shroud surface should not be increased because the flow area adjacent to the critical zone has not been changed. This critical zone occurs about 1.0 inch forward along the flow path from the rotor blade leading edge (Figure 262). These modifications permit the radial growth of the disc and shroud to match within 0.003 inch at full speed and result in an axial motion of the outer edge shroud rim of about 0.005 inch at full speed.

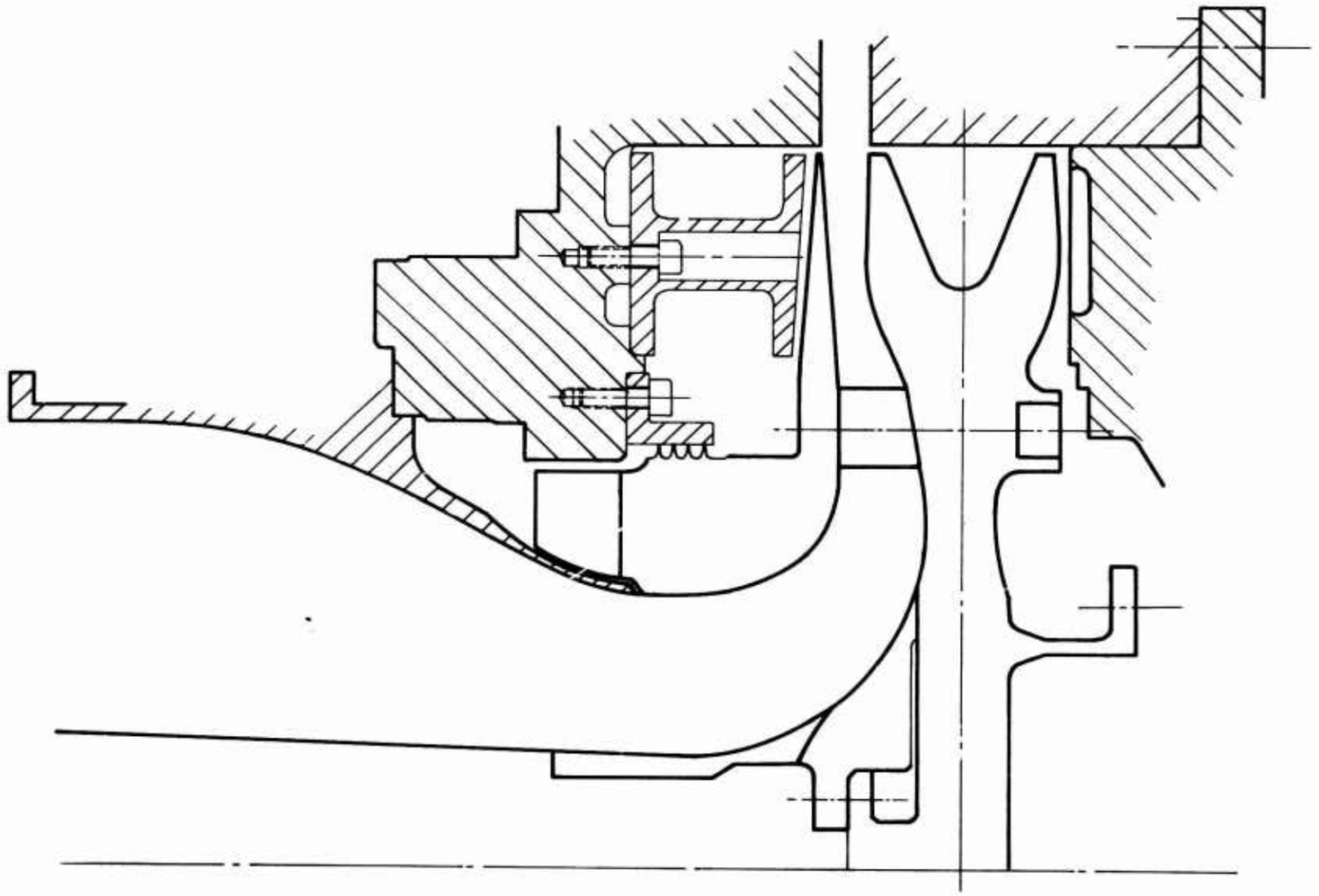

Figure 261. Configuration of the Rotor and Adjacent Parts for Buildup A of Phase III.

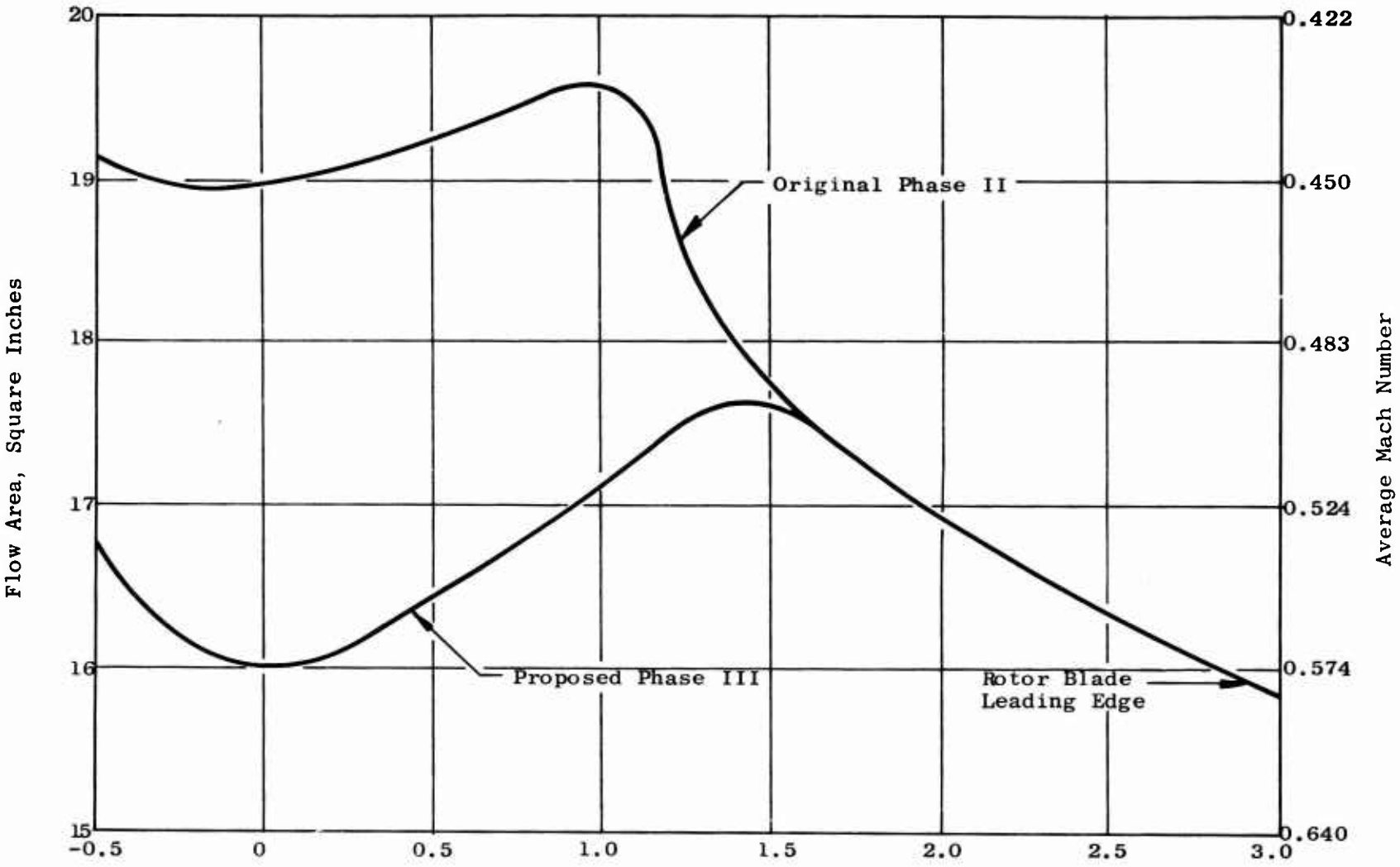

Figure 262. Flow Area and Mach Number Distribution for Original Phase II and Proposed Phase III ROC Inlet.

Stresses encountered in the rotor and shroud are well within the elastic limit of the titanium alloy at full speed with the possible exception of small regions of maximum stress concentration where the rotor has been drilled to accept the rotor blade shanks. Plastic flow of the material around these holes may occur during initial running at 100 percent speed.

Rotor Blade Design

As described in the Phase I report (Reference 1), the computer program used in designing the three-dimensional rotor blade sections used in the Phase II rotor did not permit including the effects of losses in the calculation of the characteristics network. Since a total pressure loss based on the two-dimensional rotor blade cascade tests was anticipated to take place in the rotor blades, an anomaly existed in the trailing edge region of the rotor blade design. An arbitrary trailing edge design that satisfied the exit flow direction required at the trailing edge and the minimum trailing edge angle which was feasible from the manufacturing standpoint was selected. Also, for manufacturing feasibility, the sharp leading and trailing edges of the calculated blade sections were rounded. This was accomplished by making the required leading edge radius tangent to the ideal characteristics layout. The result of this slight modification was to shorten the actual chord length of the rotor blades. In selecting the blade sections for the Phase III rotor, the trailing edge was extended to regain the chord length which had been lost in the rounding-off process. The same trailing edge radius was used, so the net effect was to thin out the trailing edge region of the sections. The concave surface was extended tangent to the original Phase II section, and the material was added to the convex surface (Figure 218). Slightly reduced rotor blade losses from the thinner trailing edge region and slightly more work input due to the extended chord length should result from these improvements. A titanium alloy having improved physical properties (see Appendix X) was selected as the best material available for the Phase III rotor blades.

These rotor blade sections became available prior to the assembly of the rotor for Buildup F of the Phase II investigation. The plan throughout this program has been to investigate the effect of only 1 major change in each buildup. Therefore, rather than test 2 different features during the first buildup of Phase III (new rotor blades and a new diffuser flow path), the decision was made to use the new rotor blades in the last tests of Phase II, Buildup F. Major improvements in rotor performance were observed during Buildup F, but whether the gains should be attributed to the circular inlet, the Phase III rotor blades, the use of subsonic stators, or some combination is not clear. The first buildup of the Phase III compressor will not use a circular inlet vane, although such a vane will be procured for use if necessary. The major change tested first in Phase III will be the modified rotor flow passage.

Rotor Disc

The change of the rotating diffuser flow path will be accomplished primarily by modifying the rotor disc (Figure 263). To minimize axial deflection, a radial centerline of the shroud rim has been selected, and symmetrical heavy rims have been incorporated in the disc design. The flow path shown in Figure 261 was obtained from the passage width distribution presented for Contour Number 5 (Figure 20).

The results obtained from the first 2 runs of Buildup F indicate that excellent rotor performance was obtained at 70 percent speed with the original rotating diffuser contour. The rotor modification to Contour Number 5 may be more conservative than necessary to accomplish efficient diffusion at full speed since the gradients calculated to occur at 60 percent speed in the original rotor were used as the criteria for selecting the particular contour for the Phase III rotor. The gradients thought to be limiting were exceeded close to the rotor blade trailing edges. The chosen diffuser passage shape may be conservative but, if so, can be modified by metal removal.

Compressor Stators and Casings

The major parts of the test vehicle will be the same as in Buildup F. The stator system will not be changed since both supersonic and subsonic stators have performed satisfactorily during the Phase II investigations.

A new liner for the inlet system will be procured to fit the Phase III rotor. The labyrinth seal will consist of rotating teeth integral with the shroud. The single-rim rotating shroud requires a new casing liner (Figure 261) to establish the desired axial clearance of 0.090 inch.

To reduce leakage between the labyrinth seal and the rotating shroud, the seal teeth will be machined as part of the shroud (Figure 261). The seal clearance will be set such that the teeth will intersect the Teflon seal ring at high speed, with the design intent of cutting grooves about 0.020 inch depth at full speed.

The circular inlet vane and the supersonic stators will be omitted for Buildup A of the Phase III investigation. The use of these parts will be determined through study of the results obtained from tests of Buildup A.

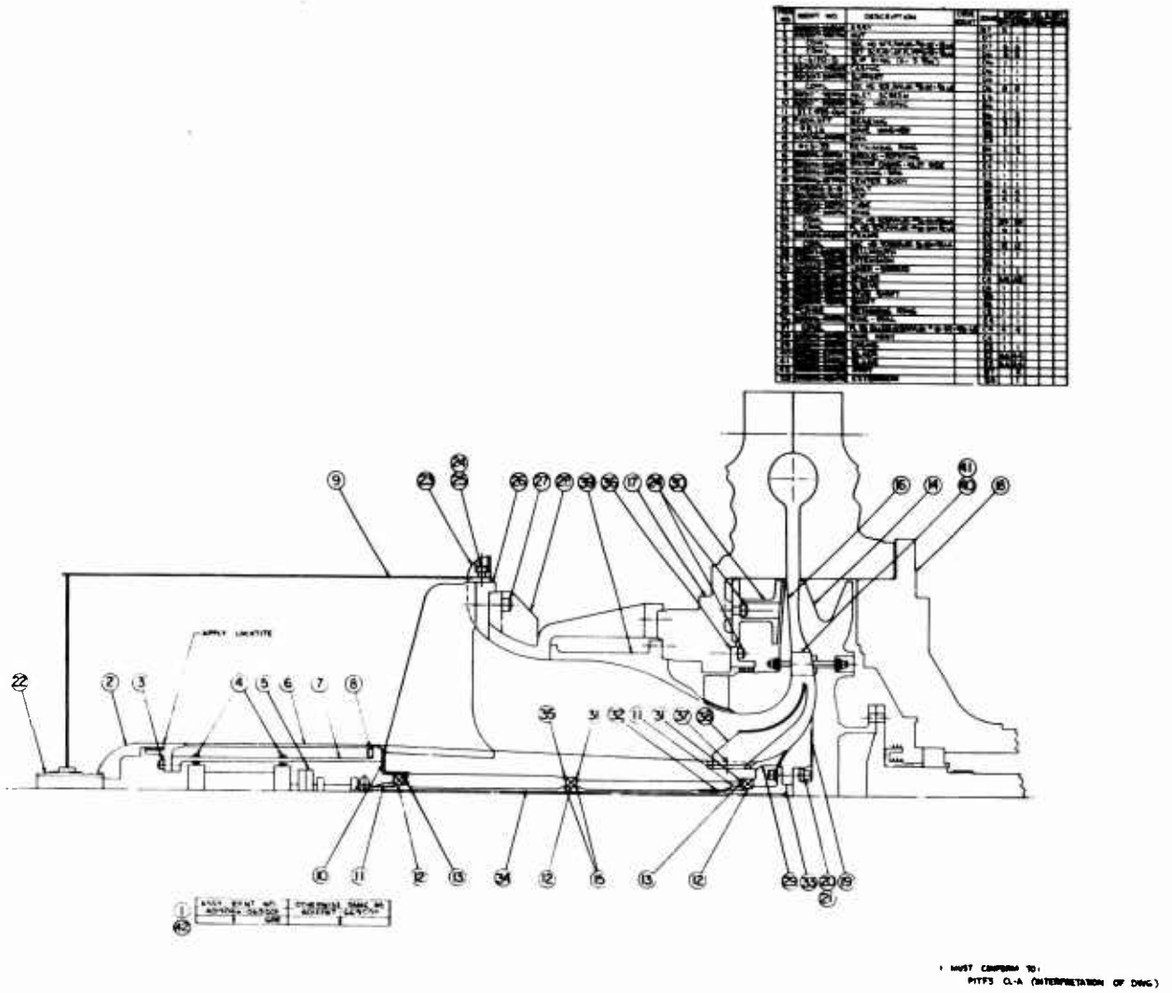

Figure 263. Configuration of the ROC for Phase III.

DISCUSSION

GENERAL

A series of 6 different test configurations or buildups has been investigated during the Phase II program. Each subsequent run has represented an attempt to improve conditions observed during previous runs and also to work toward demonstration of the target performance of the complete compressor. The attempt has been made to test the compressor components in a systematic manner so that rotor alone, rotor and supersonic stator, rotor and subsonic stator, and finally rotor with the tandem stator performance could be measured.

As frequently happens, following this ideal plan has not been possible. For example, in the early buildups in which the supersonic stators were not used, very strong circumferential static pressure gradients were found to exist in the scroll collector. These gradients projected radially inward and were observed to be quite strong at the rotor exit and certainly, therefore, within the rotor itself. This nonuniform pressure field would be expected to have an adverse effect on the rotor performance. For this reason, supersonic stators were installed to serve as an isolation barrier between the scroll collector and the rotor. Rotor alone tests were, therefore, not feasible with the existing exit system.

The first few runs were characterized by very slow and cautious accelerations to avoid those speeds at which shroud rim vibrations were expected or observed. It was found that the shroud rims were not only sensitive to rotational speed, but also could be caused to vibrate if excessive leakage flow was permitted across the rims either into the flow passage or outward from the flowpath. The operating problems were compounded by concern for the bearings and overall test vehicle vibrations. Although only after extended high speed running was any indication of bearing problems observed, and this was only through a gradual rise in the oil temperature to limiting values, a rather strict adherence to axial load limits as indicated by an analog computer was observed. The reason for the existence of the problem is the difference in projected area on the upstream side of the shroud as compared to the downstream side of the disc. At high speeds when a significant static pressure rise occurs in the rotor, a rather high axial thrust (about 800 pounds) is calculated to exist in the upstream direction. Since this force is larger than bearings are estimated to be capable of withstanding (for 100 hours), this expected aerodynamic loading was counteracted by a spring force in the downstream direction on the bearing farther from the rotor. This situation means that at some part speed (about 50 percent), the aerodynamic thrust would be about equal to the spring load on the bearing and, therefore, essentially no axial force would be acting on the thrust bearing located near the rotor. Angular contact bearings of this type require some axial load in order to function

properly. During the operation of the compressor at higher speeds, introducing higher pressure air on the rotating shroud than that in the disc cavity was believed necessary. These pressure differences were responsible for the presence of leakage flow across the shroud rims. Attempting to accelerate the compressor while avoiding critical rotational speeds, maintaining an acceptable axial thrust level on the bearings, and not permitting excessive leakage severely complicated the operation of the compressor.

BUILDUP A

During the first run of Buildup A the exit flow system from the compressor was discovered to be too small to permit obtaining design flow coefficient. The exit flow area had been selected on the basis of the static pressure rise coefficients obtained during high-speed cascade testing. The calculations at 60 percent speed assuming efficient stator performance indicated that the design flow coefficient could be obtained at 60 percent speed. For the early rotor alone tests, there was very little static pressure rise in the exit system beginning at the rotor exit. Design flow coefficients could not be obtained in the early tests. A large centrifugal compressor was installed as part of the facility wherein the ROC tests are conducted. This booster compressor was connected in a series at the ROC exit in an attempt to increase the weight flow to the test compressor. At low speeds, this procedure was quite effective, but at higher speeds, when the ROC compressor was producing a sufficient compression ratio to choke the exit system, the booster compressor had little or no effect.

A significant change to the exit system was required in order to permit obtaining design flow coefficient in the intermediate speed range; that is, at rotational speeds between 30 and 60 percent. The decision was made to install about 30 air relief tubes between the subsonic stator spindle holes and the flow measuring venturi meters. In the interim period while this modification was being manufactured, 2 runs were made in which the inlet guide vanes were closed 40 degrees to permit obtaining useful test information at the highest possible rotational speed.

BUILDUP B

The change of the compressor configuration from Buildup A to Buildup B was the addition of 27 air relief tubes which had the effect of more than doubling the flow exit area from the compressor. By this means, and by using the booster compressor, design flow coefficient could be obtained at all speeds. Testing at higher speeds and with higher flows introduced new combinations of mechanical and aerodynamic problems. During the second test sequence of Buildup B, high values of work input in the form of total temperature were observed at high speed. The static and total pressures measured were very low. Attempts to throttle the compressor were inhibited by indications of shroud and test vehicle vibrational

problems and, of course, by unfamiliarity with this new type of supersonic compressor. For the third test series of Buildup B (Run Number 6), the consistent indications of minor shroud vibrations were ignored and effective throttling of the compressor was achieved at high speed for the first time. The increase of total and static pressure obtained as compared to the previous run was quite significant. At a corrected speed of 76.5 percent, the maximum total pressure ratio measured during Run Number 5, was 2.83 while the maximum obtained during the next run using the same test configuration was 3.65, a value very close to that predicted. The first real progress toward development of ROC's was achieved.

BUILDUP C

The purpose of Buildup C was to determine whether the rotor performance could be improved by installing the supersonic stators and thus shielding the rotor from the strong circumferential pressure gradients observed in the scroll collector. Run Number 7, the first test of Buildup C, consisted of only high-speed tests. Because the supersonic stators are intentionally placed very close to the rotor exit for aerodynamic reasons, measurements of the rotor performance alone could not be made with the supersonic stators in place. Therefore, comparisons are only available between the rotor exit readings in Run Number 6 and the stator exit readings in Run Number 7. The best performance obtained prior to Run Number 6 at 58 percent corrected speed was a pressure ratio of 2.6 and a rotor efficiency of 84.8 percent. At this same speed, the total pressure ratio measured downstream of the stator was 2.64 with an efficiency of 77.4 percent. At 67.3 percent speed during Run Number 6, a total pressure ratio of 2.87 was observed with a rotor efficiency of 73.4 percent. During Run Number 7, the total pressure downstream of the supersonic stators was measured to be 3.07 with a stage efficiency measured at that station of 72.1 percent. These 2 comparisons tend to yield conclusions which are contradictory. For the lower speed points, the results suggest that the use of the supersonic stators may have improved the rotor performance since the total pressure measured downstream of the stators was higher, but also that the stators introduced high losses since the efficiency was reduced by more than 7 percent. The comparison at the higher speed also suggested that the rotor performance improved since total pressure ratio was higher downstream of the stators, but the fact that the efficiencies decreased by only about 1 percent with the stators installed suggests that the stators were performing very well.

The above comparisons are obviously not the whole story, and any conclusions must take into account the point at which the rotor was operating on its characteristic. The critical effect of being able to operate close to the optimum rotor back pressure will be discussed. This can best be seen by comparison of 2 points taken at 67.3 percent corrected speed. The use of the air relief tubes provided 2 separate exit

systems from the compressor. The original system employed remotely operated valves which were very convenient to use and could be accurately controlled. Manually operated valves were employed in the secondary relief system and were not only inconvenient to use, but were difficult to adjust with any degree of accuracy. In attempting to improve performance by changing the method of throttling, removing air from the stator spindle openings increased the observed pressure ratio from 3.43 with an efficiency of 71.1 percent to a pressure ratio of 3.85 with an efficiency of 74.6 percent. Small improvements in performance could be achieved with a few degrees change in stator angle. A setting of 75 degrees appeared to be optimum.

There were several indications at this time that the rotor performance was unsatisfactory at speeds of 60 percent and above. The particular evidence for this belief was the failure to obtain the calculated rotor exit total or static pressure at 67.5 percent speed. The total temperature measured at rotor exit was very close to the value calculated for supersonic exit flow from the rotor blades. The fact that the total pressure was significantly less than the value calculated using a friction coefficient of 0.03 suggested that the rotating vaneless diffuser contained regions of separated flow and was operating with high losses. The preliminary analysis of rotating vaneless diffusers indicated that the effective radial static pressure gradient increased rapidly with rotational speed. Therefore, improved performance was anticipated at speeds lower than 60 percent. For this reason, data were taken during Run Number 8 at 30, 40, and 50 percent. The overall result of this run was quite disappointing in that the efficiencies calculated from data taken during this run were not significantly better than those taken at 58 percent during Run Number 7.

BUILDUP D

During the Phase I low-speed investigation, the use of an inlet guide vane system other than a simple bellmouth resulted in a loss of efficiency of about 5 percent. The inlet guide vane system in the high-speed compressor was probably responsible for similar losses in efficiency. The possibility existed that poor flow conditions entering the rotor blades might be responsible for major flow distortion entering the rotating vaneless diffuser. To determine whether improving the inlet would improve the rotor performance significantly, an inlet representing an approach to the simple bellmouth used in the low-speed investigation was designed and fabricated for the high-speed compressor. For reasons of mechanical safety, strain gages are used on the rotor. In order to bring the strain leads to the slip rings, a central body of small diameter was required. The result of testing Buildup D using the rotor alone with the "open inlet" and the enlarged exit area in the scroll collector was a rather dramatic improvement in efficiency with a peak value of 92.3 percent measured at 40 percent corrected speed. At 30 percent speed, a maximum efficiency of about 89 percent was obtained

at the design flow coefficient. At 60 percent speed, however, the peak efficiency obtained was 79.3 percent, which was actually lower than that obtained in Buildup B, the previous test without stators. Therefore, the conclusion was reached that omitting the inlet guide vanes and permitting a rapid acceleration of the flow upstream of the rotor was definitely beneficial to the flow entering the rotor blades, but that the high-speed problem, believed to result from excessively high radial static pressure gradients in the rotating vaneless diffuser, was not helped by the improved inlet.

BUILDUP E

The enlarged scroll collector first used in Buildup D produced a stronger circumferential static pressure field than the original scroll. Since strong fluctuating static pressures were experienced by the rotor under this condition, the supersonic stator vanes were installed for Buildup E. Significant increases in performance were obtained at low speed as a result, but the high-speed performance did not improve. Attempts to help the rotor inlet conditions by blowing through the clearance upstream of the rotor did not achieve realistic gains when the blown air energy was charged to the compressor in a simple but conservative manner. Major modifications to the compressor appeared to be necessary to achieve major improvements in high-speed performance.

LOW-SPEED INVESTIGATION

Analyses of rotating vaneless diffusers, a detailed study of high-speed ROC data, and inspection of the rotor after extensive running indicated that high losses and insufficient diffusion were occurring in the vaneless rotating diffuser. Whether an aerodynamic loading limit was being exceeded within the diffuser or whether poor flow conditions entering the rotor were responsible could not be determined. To provide information on the behavior of vaneless diffusers in strong adverse pressure gradients, the low-speed compressor was modified to permit variation of the effective diffuser area by flow removal through 1 stationary wall. Under severe radial static pressure gradients approaching those calculated to occur in the rotor at full speed, the boundary layer on the rotating wall continued to be strong with no indication of approaching separation.

Leakage into the rotor from the upstream gap between rotor and bellmouth was found to have an extremely adverse effect on the flow leaving the rotor blades. A small amount of flow removal through this clearance was quite helpful in improving the rotor blade exit flow. A circular turning vane at rotor inlet produced the rather surprising result of an increase in total pressure across the entire span at rotor blade exit without a discernible wake from the inlet vane.

These low-speed tests were disappointing in that an aerodynamic limit could not be found with the equipment available; but in a larger sense they were very encouraging because of the evidence that severe radial static pressure gradients can be sustained by a rotating wall. The criticality of rotor inlet conditions, the value of boundary layer removal, and the advantage of using a circular inlet vane were established by these investigations.

BUILDUP F

The step-by-step process of changing only 1 variable at a time is strongly recommended when information concerning the effect of each variable is desired. In a sense, this process was not followed with respect to Buildup F, since 3 changes (a circular inlet vane, the Phase III rotor blades, and the subsonic stator vanes) were all used for the first time in this buildup. The major change was believed to be the use of the circular inlet vane, since the Phase III rotor blades were generally similar to the Phase II blades and the subsonic stators should isolate the rotor from the scroll as effectively as the supersonic stators.

The combination of the 3 modifications incorporated in Buildup F resulted in significant improvements in rotor performance. The total pressure ratios measured at corrected speeds of 30, 40, 50, 60, and 70 percent of design speed were greater than predicted values. The total temperature ratios were also higher. Perhaps even more significant and encouraging were the increased rotor static pressure ratios and efficiencies which were obtained. The fact that the rotor efficiencies exhibited a rising trend with increasing speed indicates that values higher than the maximum of 92.1 percent observed at 70 percent speed may be obtained. This trend and the rapid rise of rotor total pressure ratio with increasing speed lend strong encouragement to the belief that performance in the contract target range can be achieved by compressors of this type.

CONCLUSIONS

The results obtained from tests of the low-speed and high-speed ROC during this second phase investigation have led to the following conclusions.

The treatment of the airflow in the inlet system is critical in regard to obtaining satisfactory rotor performance. The original inlet guide vane system requiring inward turning of the swirling flow toward the axis of rotation and a long path length for high velocity flow was unsatisfactory. A simplified inlet, without inlet guide vanes and with a circular vane to assist in turning the airflow from the axial to the radial direction, proved to be satisfactory.

The rotor blades having an extended chord length and a more smoothly faired trailing edge region provided improved rotor performance.

The use of stator vanes, either the supersonic vanes placed adjacent to the rotor exit or the subsonic vanes spaced radially from the rotor exit, isolated the rotor from the strong circumferential static pressure gradient found to exist in the scroll collector.

Enlarging the cross-sectional area of the scroll collector by about 78 percent at all circumferential stations permitted a significant increase in the flow range over which the compressor could operate, particularly at low speeds. This modification increased the circumferential static pressure gradient found to exist rather than decreased this gradient as was expected.

The improved inlet system, the extended chord rotor blades, and the use of stator vanes permitted the rotating vaneless diffuser to operate effectively. An exit flow from the rotor that was quite uniform spanwise in total pressure and flow direction and circumferentially in static pressure was produced under these circumstances. Efficient stator performance is probable with such uniform entrance conditions, even with supersonic flow entering the stator system.

Performance in the range of efficiency and pressure ratio established as targets for the investigation is possible with compressors of the radial outflow type.

The design of a variable inlet guide vane system for compressors of this type is more difficult than anticipated due to the critical nature of the flow at inlet to the rotor.

The basic principles employed in the design of the ROC, two-dimensional radial flow, supersonic impulse-type rotor blades of high solidity and the use of a rotating vaneless diffuser have been demonstrated to be effective in producing efficient rotor performance. Final proof awaits full speed tests with the complete stator system installed.

RECOMMENDATIONS

It is recommended that the planned Phase IlI investigation of this program be conducted to provide demonstration of the principles applied in the design of the ROC and to determine the performance potential of this type of compressor.

REFERENCES

1. Erwin, J.R. and Vitale, N. G., RADIAL OUTFLOW COMPRESSOR COMPONENT DEVELOPMENT PROGRAM, VOLUME I - PHASE I, AERODYNAMIC AND MECHANICAL DESIGN ANALYSIS AND DIFFUSER TESTS, USAAVLABS Technical Report 68-38A, General Electric Company (in preparation).

2. Campbell, W., PROTECTION OF STEAM TURBINE DISC WHEELS FROM AXIAL VIBRATION, Transactions of ASME, Volume 46 (1924) page 31.

3. Campbell, W. and Heckman, W. C., TANGENTIAL VIBRATION OF STEAM TURBINE BUCKETS, ASME Paper Number 1975, 1924.

4. Keenan, J.H. and Kaye, J., GAS TABLES - THERMODYNAMIC PROPERTIES OF AIR PRODUCTS OF COMBUSTION AND COMPONENT GASES COMPRESSIBLE FLOW FUNCTIONS, Massachusetts Institute of Technology, May, 1960.

APPENDIX I
COMPRESSOR MAP CALCULATIONS

A compressor, like most devices, is a synthesis of components designed to operate in conjunction with one another to produce a desired end effect; i.e., in this case compression of a specified mass flow of fluid to a specified pressure at a specified efficiency. The Radial Outflow Compressor may, for example, be considered as a synthesis of the following components: an inlet, a rotor, a stationary diffuser, and a discharge system. Each of these elements in turn can be considered as being synthesized from other components as follows:

ROC Compressor

- Inlet
  - Bellmouth
  - Inlet Guide Vanes
  - Inlet Duct
- Rotor
  - Rotating Blade Row
  - Rotating Diffuser
- Stationary Diffuser
  - Supersonic Stators
  - Subsonic Stators
- Discharge System
  - Scroll
  - Elbow
  - Discharge Diffuser
  - Discharge Station

The calculations employed to achieve a synthesis of the above components may be loosely divided into 2 categories: design calculations and off-design calculations. The design calculations in turn may be considered to consist of preliminary design and detail design calculations. Basically, the preliminary design calculations begin with the specified inlet and discharge conditions, and by one means or another determine the number, type, size, and arrangement of compressor components required to attain these conditions. The preliminary calculations further determine the approximate flow conditions relevant to each component and the appropriate performance criteria. The detailed design calculations are concerned with the geometry, etc., of the components required to achieve the objectives which have been set by the preliminary design analysis. Essentially, design analysis is concerned with determining the geometry required to achieve specified flow conditions. Geometry is a generic term referring not only to the shapes of the compressor components, but also to any bleed, blowing or other techniques which may

have to be applied to achieve the flow objectives. Off-design calculations are essentially the inverse of design calculations. Here the geometry defined by the preliminary and detailed design work is considered as given, and the analysis objective is to determine the flow conditions (more specifically, the inlet and discharge conditions) which differ from the design conditions. Obviously, the differentiation between design and off-design, preliminary and detail design is not sharp. In fact, there is a constant interplay between all phases of the design procedure. The results of detail design can effect preliminary design, and the results of off-design analysis may require that modifications be made in detailed design. It may be noted in passing that the word analysis as used above refers not only to calculations, but also to cascade testing, artistic sketching, and a good deal of application of previous experience. In fact, the final word in both design and off-design analysis results from the testing of the actual hardware.

In any case, the net result of the design and off-design analysis is a compressor geometry and an associated compressor map. The compressor map, generally consisting of the mass flow versus pressure ratio curves for different compressor speeds, with superimposed efficiency contours, is a simple and clear means of presenting the gross performance of a very complicated mechanism. In addition to this information, the compressor map defines regions in which the compressor is unstable. The price for simplicity and clarity is detail, and the compressor map sacrifices much detail (some of which is quite significant). In particular, the compressor map does not provide information concerning the dynamic behavior of the machine, hysteresis properties, dependence on inlet conditions, or the quality of the discharge flow conditions. However, properly used, it contains much valuable information.

The preliminary and detailed design analysis of the ROC has been presented in the Phase I report. The Phase II report is basically concerned with the off-design analysis. The major portion of this analysis has been obtained by tests performed using the actual hardware. However, a good deal of effort has been expended in attempting to calculate the ROC off-design performance (in particular the compressor map) on the basis of the geometric structure.

The following material includes a description of the approach used in performing the analysis, some of the details of the calculations, and a discussion of the final results.

Despite the fact that the ROC can be considered as a synthesis of individual components, a compressor is in actuality an integral machine, and if an "exact" analysis were required, it would have to be treated as such. However, at present, this approach is not feasible, not only because of the enormous mathematical difficulties involved but because

of the lack of complete understanding of the physical processes involved (namely, turbulent flow). Even if this approach were feasible, it still would not necessarily be desirable, for in order to achieve the degree of detail necessary to specify a compressor map, much simpler approaches can successfully be employed over most of the regions of interest on the map. With this in mind, the approach used in calculating the ROC map has been to consider the individual components separately and in sequence, using modified one-dimensional flow theory.

The performance of an individual compressor component depends on its geometric design and on conditions of the flow field in which it is operating. Just what constitutes a sufficient specification of the flow depends on the individual component. For the purposes of this analysis, a one-dimensional specification generally consisting of Mach number, total temperature, total pressure, and flow angles was considered. Reynolds number effects, flow profile specification, etc., were either considered insignificant or were simply neglected. On the basis of this information, the modified one-dimensional flow theory was employed to calculate the behavior of the compressor components. The one-dimensional flow theory is of itself incapable of predicting such things as component losses, discharge profiles, deviation angles, etc.

The modified one-dimensional flow theory represents an attempt to reduce the deficiencies of the pure one-dimensional flow theory by introducing suitable parameters, such as loss coefficients, deviation rules, friction factors, blockage coefficients, etc., to compensate for many of the real flow effects. When suitably chosen, these parameters are intended to reflect not only the losses encountered under ideal operating conditions, but also the effects of nonuniform profiles, separation, etc. The freedom to vary these parameters adds sufficient flexibility into the calculation procedure to allow for reasonably good prediction of compressor behavior over most of the map. Obviously, a proper application of this technique requires experience with the appropriate components, as well as a constant checking between predicted and test results. A very important result of this cross checking is that by noting the values of the parameters necessary to achieve good correlations between test and calculation, one can obtain a good deal of insight into the behavior of the compressor components. It may be noted in passing that this particular procedure has been difficult in the ROC because of the impracticality of locating instrumentation at the crucial station just downstream of the rotor blades due to the presence of the rotating diffuser.

The major emphasis of the off-design calculations has been concerned with describing the behavior of the compressor flow from the compressor inlet (station 0) to the rotating diffuser discharge (station 3). Because of the complexity of these calculations, they were accomplished

with the aid of a digital computer. On the other hand, the extrapolation procedure used to go from station 3 to compressor discharge was comparatively simple and was performed manually. This extrapolation consisted of assigning a single loss coefficient to the components downstream of station 3 as a function of the Mach number at station 3. The loss coefficient was assumed to be independent of either station 3 flow angle, diffuser geometry (the supersonic and subsonic vanes are variable), or throttle valve setting. The implicit assumption here is that the throttle valve and stator geometries can always be set to achieve a loss coefficient for any Mach number and flow angle which is at least comparable in magnitude to the loss coefficient obtained at the same Mach number in the cascade tests of the tandem cascade. Whether this approach is adequate must await the results of further hardware testing. Detailed analysis of the stator-exit system of this compressor would be very difficult considering the high degree of variability of the system as well as the difficulty of predicting the behavior for even the simpler case of fixed geometry.

APPENDIX II
ROC ROTOR AND STATOR CASE DISPLACEMENTS

Figures 264 and 265 illustrate the calculated radial and axial adjustments of the ROC rotor and stator case.

Figure 265 is a summary of calculations upon which certain of the stackup settings on Figure 264 are based.

Figure 265 shows the relative cold to hot condition displacements of the rotor and stator case. These displacements are based on the assumption that the rotor is up to full speed and is generating the full design temperature rise. The stator case under this condition is assumed to have a metal temperature of $620^{\circ}F$ and an average coefficient of thermal expansion of 5.8×10^{-6}. The portion of the main bearing housing contributing to the total axial growth is assumed to be at a mean metal temperature of $270^{\circ}F$ with an average coefficient of 5.72×10^{-6}.

Figure 265 shows that a cold buildup offset of 0.018 will be set between the front face of the rotating disc and the face of the stator case. After reaching a stable operating condition, these 2 faces should align, with an 0.002 nominal offset on the opposite face.

For the first several buildups where maximum speed and design temperature rise will not be reached, it would be advisable to reduce the initial 0.018 cold offset somewhat to provide a better final centering of the rotor outlet flow path with respect to the stator case inlet flow path. At this time, we plan to establish an initial offset of 0.012/0.010 for the first buildup.

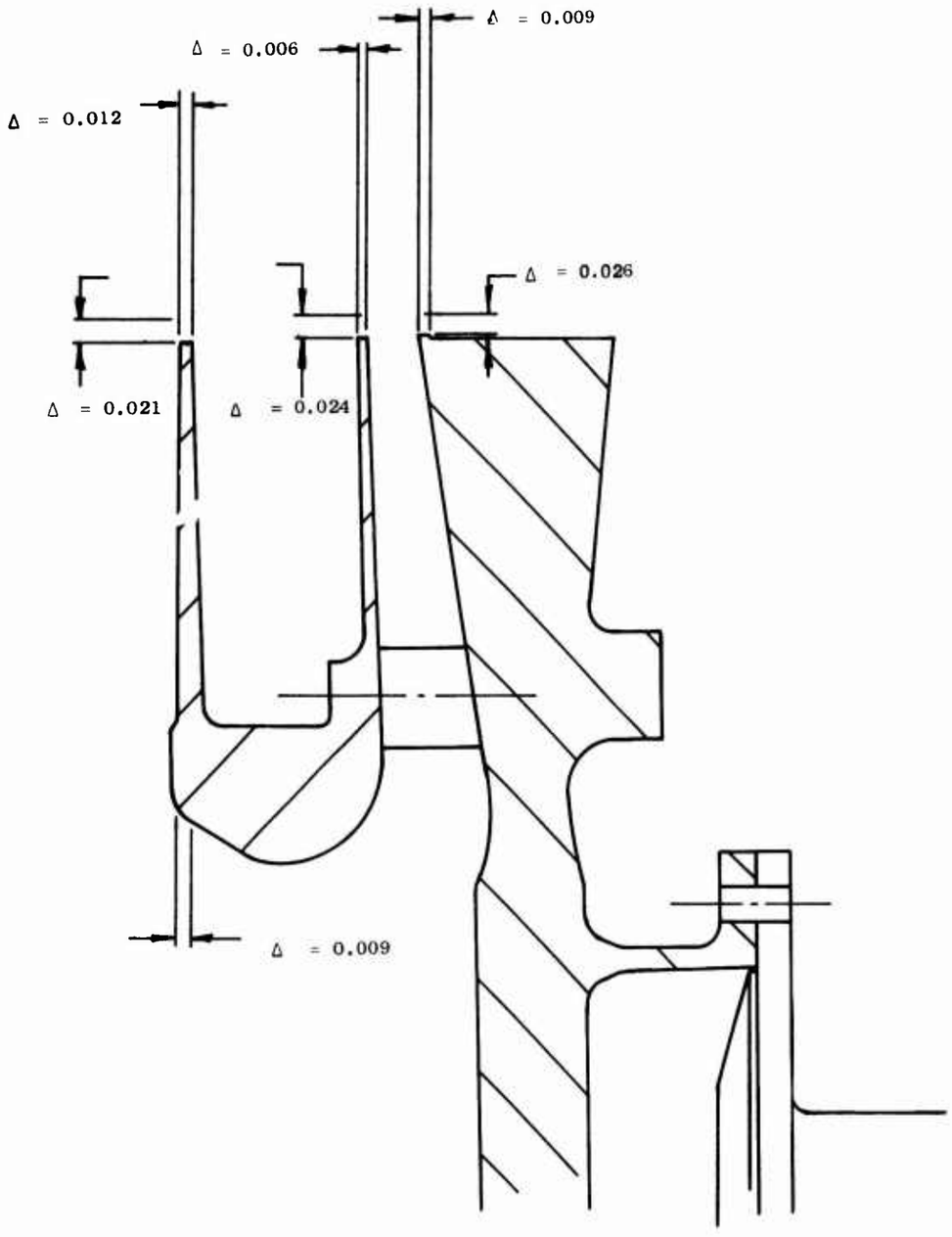

Figure 264. Calculated Net Terminal and Dynamic Displacement of the High-Speed ROC Shroud and Disc.

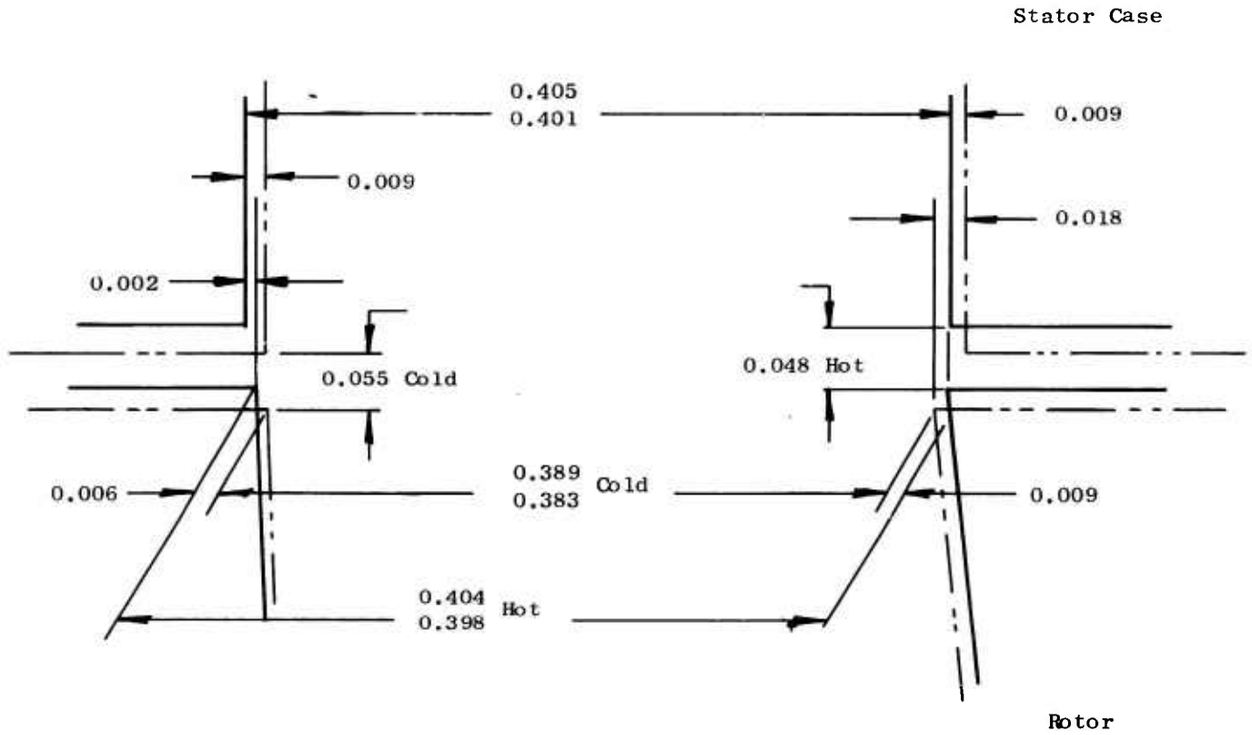

Figure 265. Calculated Relative Displacement of High-Speed ROC Rotor to Stator Case.

APPENDIX III
ROC ROTOR INSTRUMENTATION

The ROC rotor Buildup Number 1 was instrumented as follows:

INSTRUMENTATION REQUIRED

Shroud

No attached instrumentation.

Disc

Thermocouples only are required.

Type - Chromel-Alumel, grounded

Number - Two

Location - Attached to disc face as shown in Figure 269.

Attachment - Junction at localized area of flame-sprayed nichrome (FSN) on top of Metco 404 on disc face. Flame-sprayed area to be kept to a minimum and edges to be benched smooth prior to thermocouple attachment.

Blades

Strain gages only are required.

Type - Baldwin FAB-06-35-S9 (provides backing rated at 400°F, no temperature compensation, 0.0625-inch-square grid, 355-ohm resistance).

Number - Three gages per blade for 4 blades (9 each for 2 additional bench test blades).

Location - See Figures 266, 267, 268, and 269.

Attachment -

1) Dental abrasive, 50 micron maximum, to be used for blade surface preparation with minimum damage.

2) EPY 400 cement (good to +400°F) to be used for gage attachment.

Gage Pattern - Reference Figures 266, 267, 268, and 269.

Type Blade	Blade Number	Disc Slot Number	Gage Pattern
PO1	6	22	A
PO1	12	66	B
PO2	33	11	A
PO2	34	55	B
PO1	-	-	C
PO2	-	-	C

Lead Paths -

1) Lead paths on blades to be shortest distance from gage to side of blade unless noted otherwise in Figures 266, 267, and 268.

2) Lead paths beyond blades is defined by Figure 269.

Gage Switching -

Although all 12 blade strain gages cannot be monitored simultaneously because of the limited size of the slip ring, diode switching will allow half (or 6) of the gages to be read at any time. Thus, a grouping of gages will be made as follows:

Thermocouples 1 and 2 Blade Strain Gages	Thermocouples 1 and 2 Blade Strain Gages
06a22	33a11
06b22	33b11
06c22	33c11
12d66	34d55
12e66	34e55
12f66	34f55

The gage code numbers and instrument lead numbering are shown in Table XIII.

TABLE XIII. SWITCHING FOR STRAIN GAGES FOR SLIP RING HOOKUP

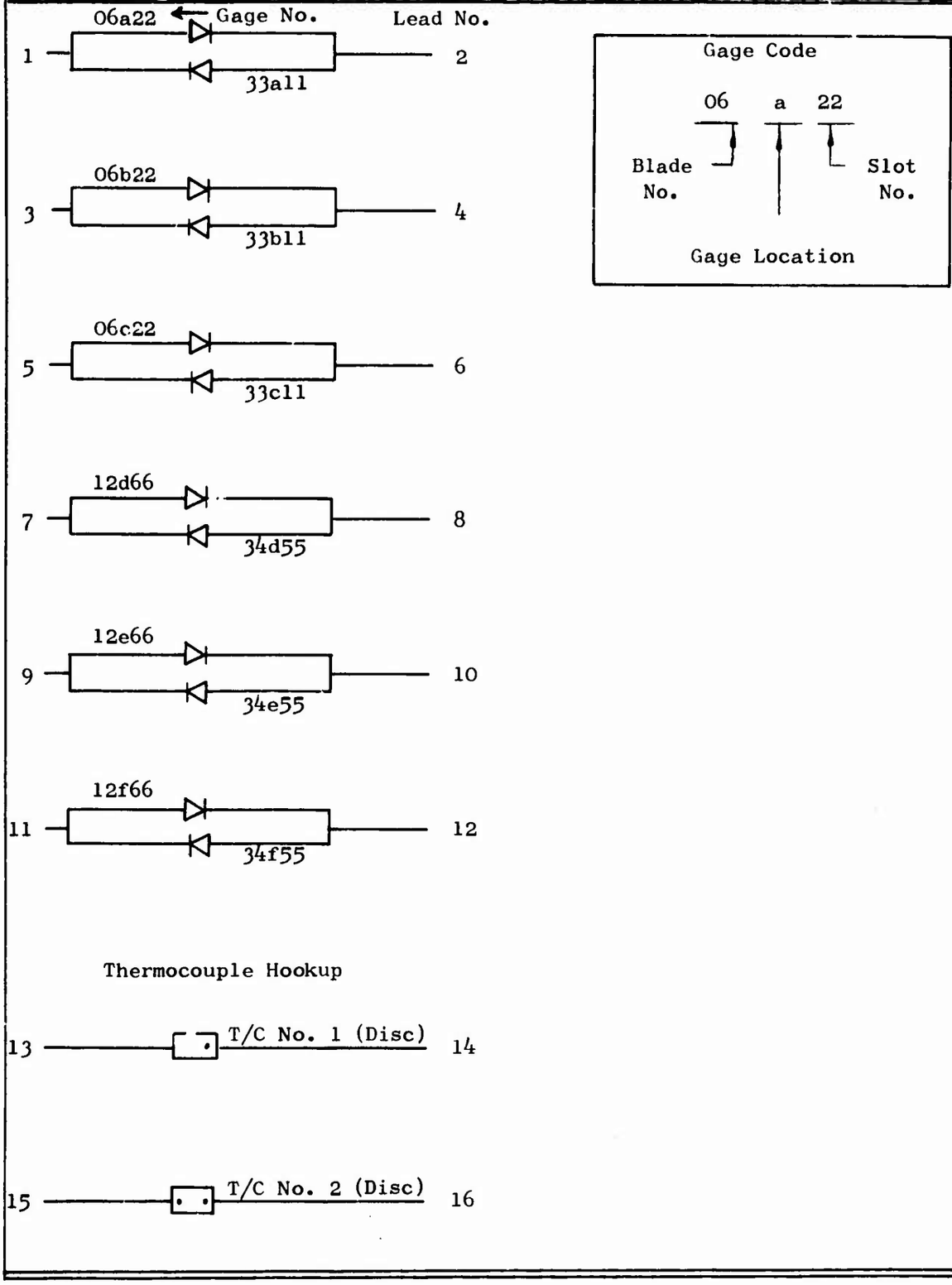

TABLE XIV. ROC BLADES - LOCATION LIST

P01 Blades				P02 Blades			
Slot Number	Blade Number	Slot Number	Blade Number	Slot Number	Blade Number	Slot Number	Blade Number
2	33	42	08	1	04	41	21
4	04	44	68	3	26	43	05
6	34	46	53	5	45	45	25
8	02	48	48	7	49	47	15
10	39	50	19	9	19	49	47
12	09	52	69	*11	33	51	24
14	32	54	54	13	50	53	29
16	40	56	51	15	06	**55	34
18	44	58	42	17	56	57	28
20	43	60	37	19	39	59	59
*22	06	62	26	21	16	61	37
24	07	64	18	23	54	63	55
26	16	66	12**	25	03	65	09
28	29	68	14	27	57	67	58
30	03	70	24	29	14	69	48
32	49	72	15	31	51	71	20
34	05	74	30	33	52	73	46
36	50	76	13	35	07	75	53
38	28	78	46	37	38	77	22
40	25	80	36	39	18	79	30
		82	22			81	32
		84	23			83	13
		86	58			85	08
		88	10			87	23

* Gage pattern for instrumented P01 Blades

** Gage pattern for instrumented P02 Blades

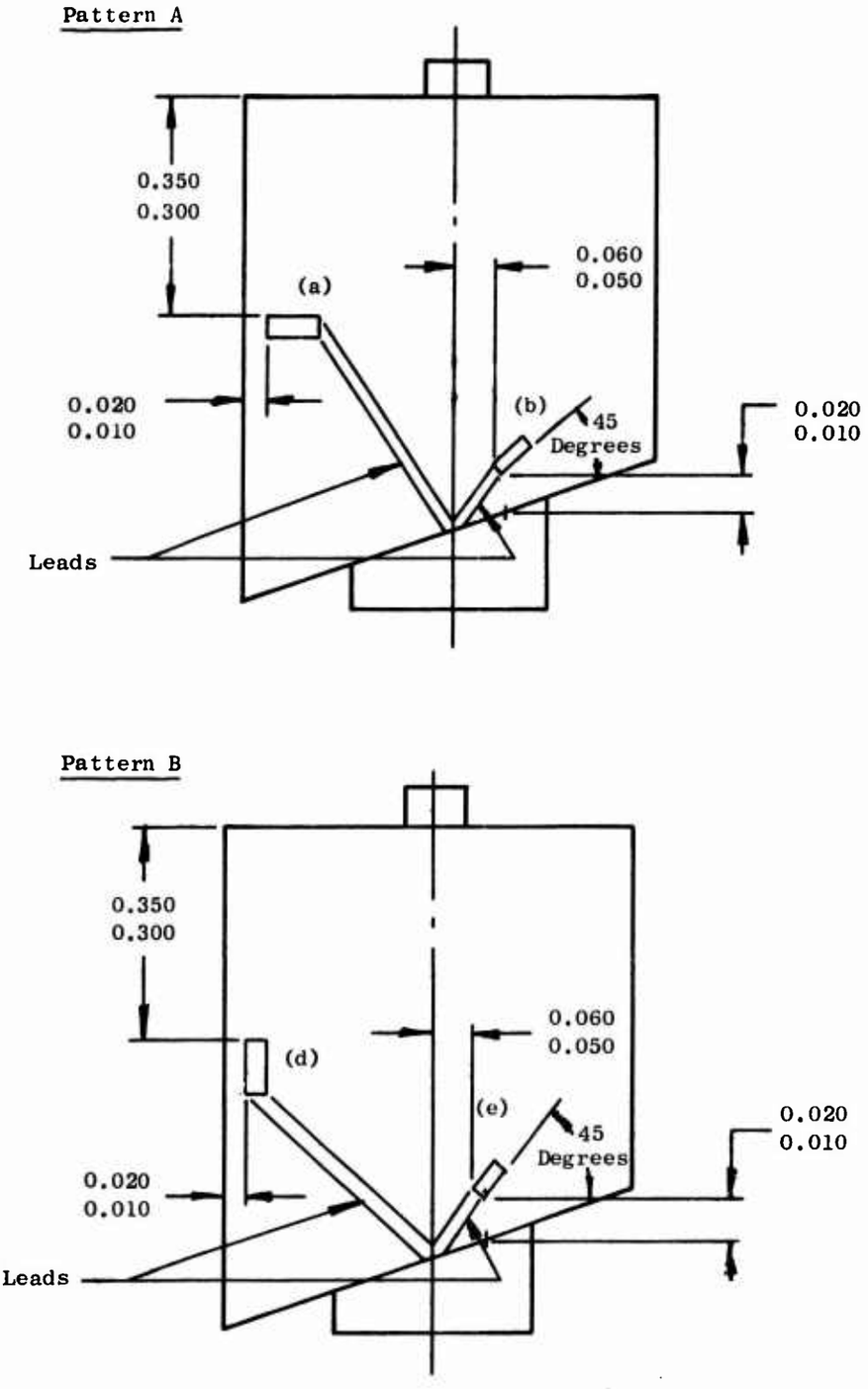

Figure 266. Strain Gage Locations Used on Concave Surface of Rotor Blades of High-Speed ROC.

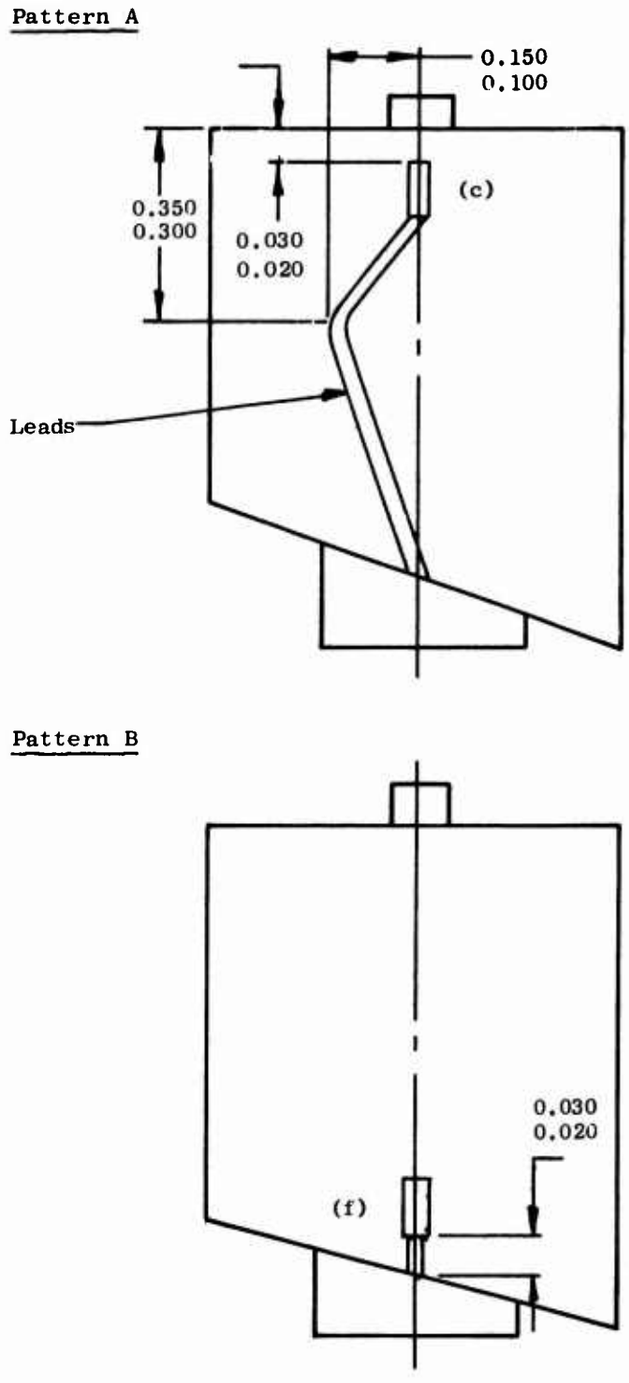

Figure 267. Strain Gage Locations Used on Convex Surface of Rotor Blades of High-Speed ROC.

Pattern C

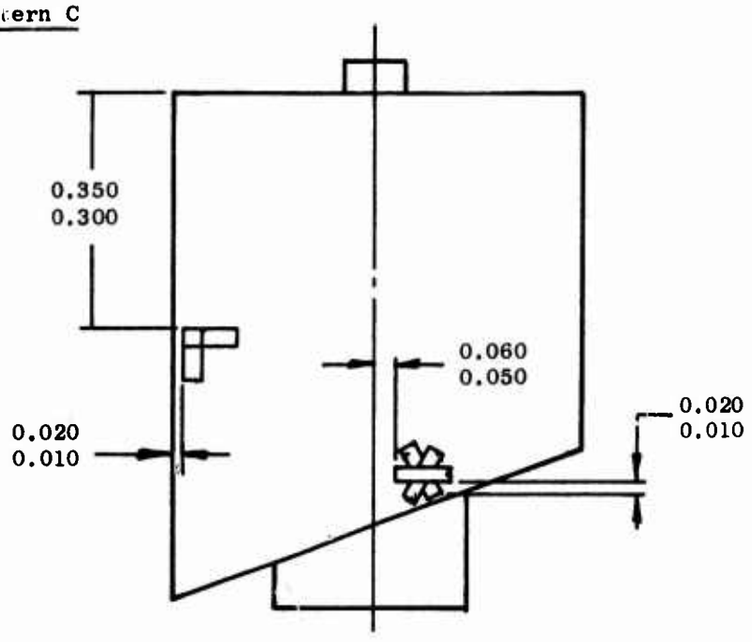

Concave Side

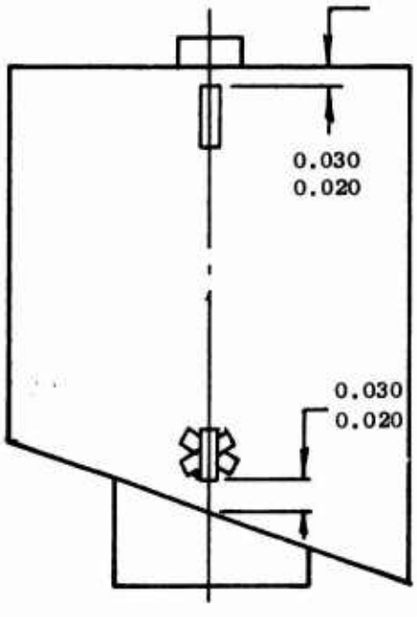

Convex Side

Figure 268. Strain Gage Location Used on Concave and Convex Surfaces of Rotor Blade of High-Speed ROC (for Bench Tests Only).

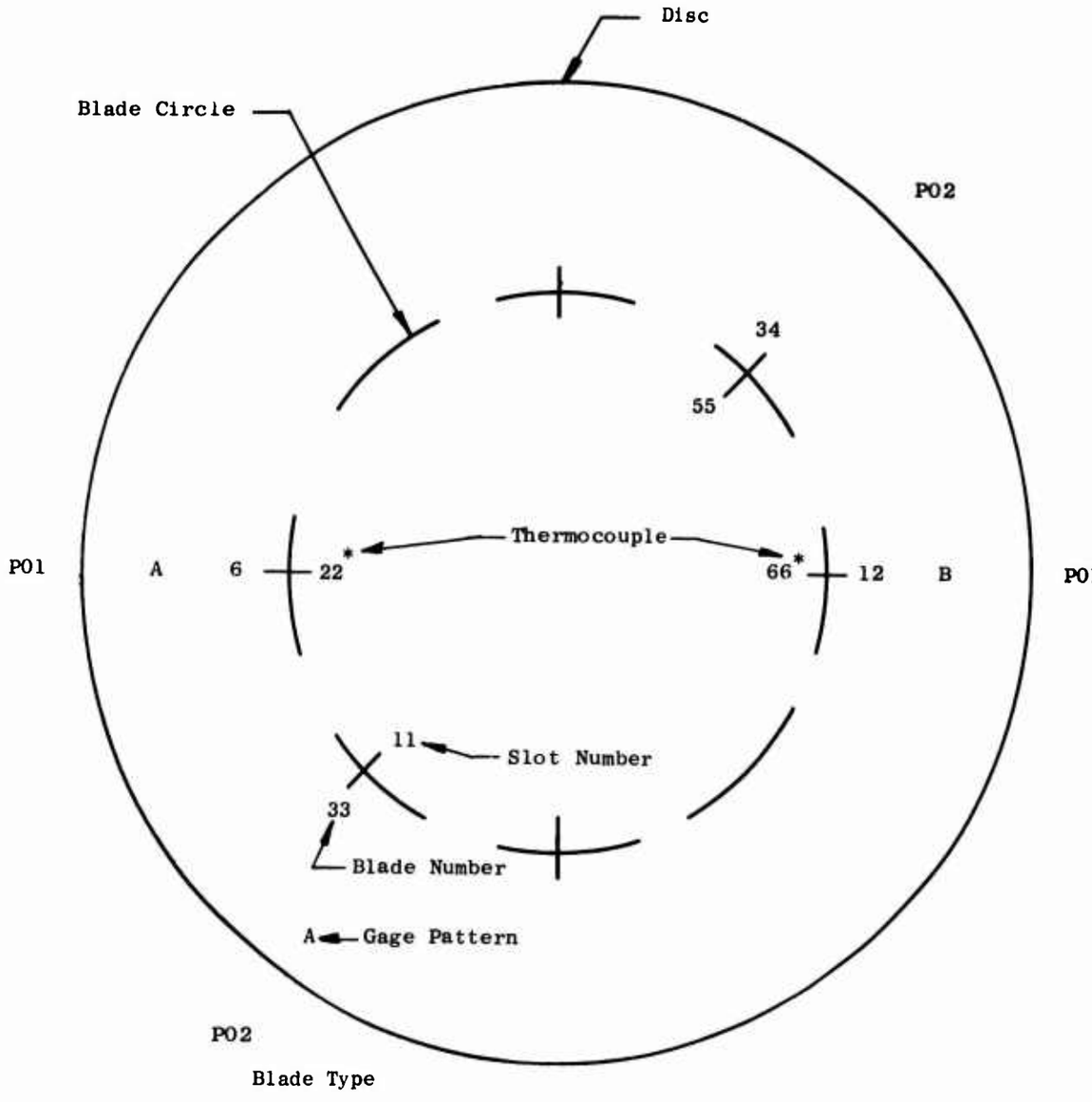

Figure 269. Circumferential Distribution of Strain Gages and Thermocouples Used in Buildup A of the High-Speed ROC.

APPENDIX IV
COMPONENT TEST - BELLEVILLE WASHER PRELOAD

PURPOSE

To evaluate the following:

1) Nut torque versus bolt tension versus Belleville deflection
2) Torque change versus load and deflection with reuse of nut
3) Failure load of nut-washer assembly

PARTS REQUIRED

Part	Number Required
1) Bolt, Number 4012186-573P2	5
2) Nut, ESNA Number LH8368-02	20
3) Nut Washer, ESNA Number 8368-0	20
4) Belleville Washer "A", Number 4013007-288	20
5) Belleville Washer "B", Number 010-M-35	20
6) Base	1
7) Load Cell(s) and attachment(s)	-
8) Titanium Surface Plate(s)	-

PROPOSED TEST SETUP

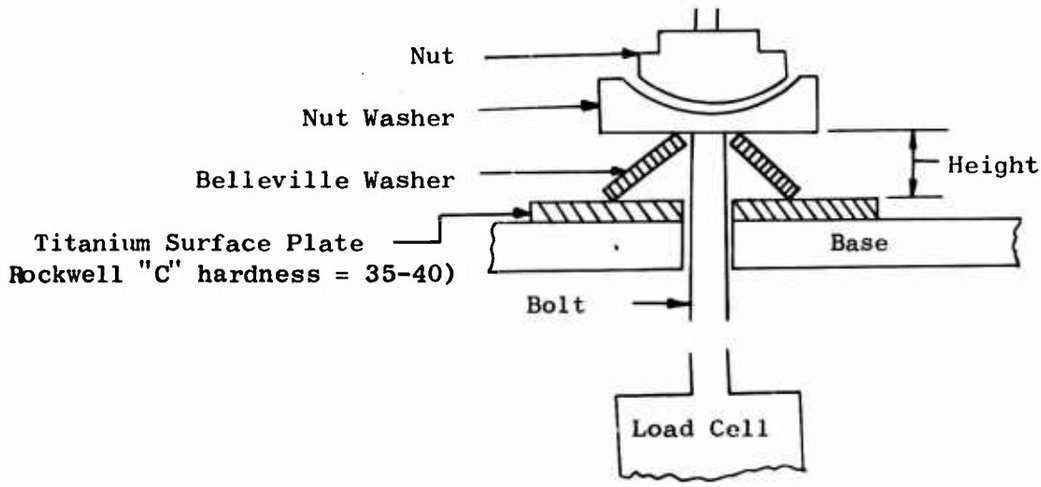

ESTIMATED BELLEVILLE LOADS IN FLATTENED CONDITION

Belleville Washer "A", 110 lbs
Belleville Washer "B", 375 lbs

RANGE OF BELLEVILLE WASHER HEIGHTS

Washer "A", estimate 0.030 inch maximum to 0.025 inch minimum
Washer "B", estimate 0.035 + 0.009 inch maximum to 0.035 inch minimum

REQUIRED ACCURACY

Results for tensile load, applied torque, and washer height have an accuracy of ±5 percent.

RESULTS DESIRED

Test setup description for each test:

Test	Bolt Number	Belleville Number	Nut Number	Nut Washer Number	Plate Number	Times Tested
A	1	A1	1	1	1	3
	1	A2	2	2	2	3
	1	A3	3	3	3	3
	1	A4	4	4	4	3
	1	A5	5	5	5	3
	2	B1	6	6	6	3
	2	B2	7	7	7	3
	2	B3	8	8	8	3
	2	B4	9	9	9	3
	2	B5	10	10	10	3
B	3	A6	11	11	11	1
	3	A7	12	12	12	1
	3	A8	13	13	13	1
	3	A9	14	14	14	1
	3	A10	15	15	15	1
	4	B6	16	16	16	1
	4	B7	17	17	17	1
	4	B8	18	18	18	1
	4	B9	19	19	19	1
	4	B10	20	20	20	1
C	5	B11	20	20	21	1

TEST PROCEDURE EXPLANATION

Test A - Load Curves

1) Load the assembly with washer "A" approximately 20 percent beyond flattened condition and plot applied torque, Belleville

deflection and bolt load for load increments of 10 pounds. Untorque nut and retorque 3 times, taking readings each time.

2) Repeat step number 1 four times with new parts each time (making 5 tests total).

3) Repeat step numbers 1 and 2 for washer "B" with new parts; plot for increments of 20 pounds.

4) Determine from load, torque, and deflection curves the nominal torque corresponding to desired bolt preload.

Test B - Simulated Assembly Torque

1) Make 5 separate torque tests of each type washer (10 tests total) using new parts for each test.

2) In each test, torque the nut to the nominal value determined in Test A. Tensile load and washer height shall be measured.

Test C - Load to Failure

With new parts (using washer "B"), torque nut to failure (nut or bolt breaking, or thread strippage) noting the yield point, if any, of the joint.

APPENDIX V
ROC TEST PHASES II AND III
FAILURE AREAS AND SAFETY ITEMS

Almost all the modes of failure will be either directly or indirectly related to rotation. Listed below are the various problems, the action taken to prevent the problem, and the control action taken to limit the damage in the event of a problem occurrence.

1) HIGH-SPEED RUB

a) Problem

A high-speed rub is always a cause for concern in any rotating piece of machinery. The major factors influencing the probability of a rub are initial clearances, thermal and centrifugal growth of related parts, axial play, pressure, temperature distortion or deflection, vibration displacement, and clearance closing as a result of foreign matter penetration.

b) Prevention

The best and most practical method of rub prevention is to allow maximum clearance between stationary and rotating parts. With enough clearance, other factors influencing a rub would be insignificant. Compensating for thermal and centrifugal growth and axial play, the vehicle will be assembled so that a minimum running clearance of 0.03 inch will exist at any location on the vehicle. A running clearance of 0.09 inch will be established between the rotor and the case liner. To prevent pressure and temperature distortion, limits will be established for all vehicle pressures and temperatures, and suitable readouts will be provided for constant monitoring. Vibration pickups have been placed on the stationary parts of the vehicle to provide indications of rotor vibration displacements. Limits will be provided for all vibration pickups, and suitable readouts will be provided for constant monitoring. A 10-micron filter will be installed in the west tank main air inlet and a 5-micron filter will be installed in the cooling air supply line.

c) Damage Control

Vehicle skin thermocouples and vibration pickups are the main sensor devices that will indicate a vehicle rub. A number of the skin thermocouples will have a readout provided with an overtemperature contact. Should the particular thermocouple exceed the established limit, the contact will automatically

trip out the compressor. Since a sudden change in vibration level may be a faster indication of vehicle rub, a tripout set at an established vibration displacement limit will also be used.

Furthermore, in order to extinguish a possible titanium fire, the following procedure will be effected:

1) Indication of rub.

2) Compressor tripout.

3) Energize "Emergency" contact which will shut off the cooling air supply and open the argon supply.

4) Manually bring tank down to maximum vacuum.

5) Manually close cooling exhaust lines.

6) When compressor wheel speed drops to 2,000 rpm or lower, manually close the throttle valve.

The above manual operations (3 through 6) will be executed when the cell operator or the test project engineer gives the command "Emergency".

2) BEARING FAILURE

a) Problem

A prolonged vehicle rotation during a bearing failure would increase the risk of extensive test vehicle damage. The failure of the bearing, like all other effects, is caused. The major factors influencing bearing failures are improper assembly, improper lubrication, too low or too high thrust loads, and running up to or beyond the rated bearing life.

b) Prevention

Bearing pressures and temperatures will be read out and monitored to insure an adequate lube supply for lubrication and heat dissipation. In the event of a decrease in the pressure supply, a pressure switch will automatically trip out the compressor. The pressure differentials for the thrust loads will be controlled at the cooling flow station. Established limits for the differential pressures and suitable readouts will be provided. In addition, the differential pressures will be input to the EASE analog computer which will compute the absolute wheel thrust value in pounds.

The EASE output will be traced on an X-Y recorder versus speed located at the cooling flow control station.

c) Damage Control

The bearing temperature meters will be provided with over-temperature contacts which will automatically trip out the compressor when the bearing temperature exceeds the established limit.

3) OVERSPEED

a) Problem

A rotor overspeed can occur at the Dynamatic Coupling if the current flow to the excitation coil is increased, if the output torque (compressor load) is increased, if the constant speed input (3,600 rpm motor) is increased, or if the coolant water flow is changed. An overspeed, of course, if great enough, would result in extreme loads and complete destruction of the vehicle.

b) Prevention

The ROC is an eddy-current coupling driven vehicle. The method we will use to prevent an overspeed will be to cut off the excitation current to the eddy-current generating coil and to cut off the coolant water supply at the instant of maximum rpm. This will cut off all power, and the vehicle acceleration rate will decrease. A small overspeed past the cutoff point will result depending on the time required to deenergize the coil, the acceleration at overspeed, the inertia of the rotating members, and the work absorption of the compressor.

c) Damage Control

The damage control will consist of the emergency procedure described in Item Number 1 (High-Speed Rub).

4) VIBRATIONS

a) Problem

Vibrations, depending on the frequency and the displacement, can produce extremely high loads and extensive damage to the vehicle. The amplitude of the vibrations will be proportional to the exciting force, which is normally the result of rotor

unbalance. In the resonant condition, the rotor unbalance force acts in the direction of the vibration velocity continuing to put work into the system. Such a resonant condition has been analyzed to occur in the ROC rotor assembly at a compressor speed of 8,500 rpm. The floor frame resonance is expected to occur at 10,500 and 25,000 rpm.

b) Prevention

The first steps in the prevention of vibration problems are to analyze and, if necessary, to modify the system so that a rotor critical does not exist at a design point speed. The compressor speed of 8,500 rpm is 24 percent and does not constitute a design point condition. A good balance is the second step in the elimination of vibration problems. The better the balance job, the lower the amplitudes that will be experienced either in the forced vibration areas or the resonant condition.

An increase in damping causes the vibration amplitude to die down, and also slightly changes the frequency. An adjustable friction damper bearing will be installed in the forward end of the compressor rotor. Problems that arise may be corrected by altering the friction force on this bearing.

c) Damage Control

Vibration meters are provided at the speed control area. In addition to constant monitoring, a variable overdisplacement tripout will be provided. This will be particularly useful on a fast acceleration attempt to break through a critical. Once the peak displacement limit is reached, the compressor will automatically trip out, saving the manual reaction time to effect this procedure. Should a rub indication occur, the "Emergency" procedure will be immediately effected.

5) STRESSES, SURGING OR STALL

a) Problem

A stall or a surge is a discontinuity of the flow through the compressor. The basic factors that can effect a flow discontinuity are a decrease in Reynolds number, a non-uniform flow, and an increase in a rotor or stator angle of attack by either increased rotor speed or decreased weight flow. As a result of the separation, a rotor blade

or vane will exhibit high dynamic stresses. Surging is the back and forth oscillation of unstable flow that is triggered by a flow discontinuity. The surge point and the description of surge were presented in Test Instruction Number 1.

b) Prevention

Strain gages to the rotor blades and stator vanes will be read out on scopes and continuously monitored. In addition, 4 Kistler high frequency pressure pickup probes will be installed at the subsonic stator exit plane and will also be read out on scopes and be continuously monitored. A throttle valve dump button, which will actuate both throttle valves to a prescribed open position, will be located at the stress area. In the event of a high stress or high frequency stress condition, the monitor will select 1 of 2 alternatives, depending on the variable that was being changed. One alternative will be to hit the throttle valve dump and the other will be to give the command "back off" indicating a speed reduction. This command will be immediately executed by the speed control operator.

c) Damage Control

A manual contact button designated "Tripout" will be provided to energize the tripout as discussed in Item Number 3 (Overspeed).

GENERAL

The tripout and emergency procedure will be discussed in detail in the Test Plan. Briefly, however, in the event of the tripout procedure, the cooling air control valves will remain as they were. The front and back side cavity pressures will simultaneously drop to a safe level as the effective exhaust area is increased with leakage into the compressor.

The tripout mentioned in all of the above items is the same. That is, the current to the eddy-current generating coil and the supply for the water coolant system is cut off.

This supplement takes precedence over any conflicting instructions issued in Test Instruction Number 1.

APPENDIX VI
DATA ANALYSIS METHODS

INTRODUCTION

The purpose of the ROC data analysis is to evaluate, from the measured test data, the significant compressor operational and performance parameters. The difference between operational and performance parameters is one of definition: the operational parameters are those which are considered as imposed on the compressor, and the performance parameters are those which are considered as resulting from operation under these imposed conditions.

The first test buildup of the ROC will require evaluation of the rotor-inlet combination without the supersonic or subsonic stators. The primary operational parameters for this buildup will be:

1) Rotor average relative inlet Mach number, $M_{1\,Rel}$

2) Rotor average relative inlet angle, β_1

3) Rotor average static pressure rise coefficient, C_p

4) Rotor average enthalpy equivalent static pressure rise coefficient, C_h

5) Rotor corrected rotational speed, $N/\sqrt{\theta}$

Due to the inability to instrument the compressor rotor inlet in the present configuration, no direct data concerning conditions at the rotor inlet will be available. It will be the task of data analysis to evaluate the first 4 parameters listed above by indirect means.

In addition to the 5 primary operational parameters, there are 3 secondary operational parameters. These parameters are qualitative rather than quantitative in nature:

1) Rotor inlet relative total pressure distortion

2) Rotor inlet relative angle distortion

3) Rotor exit circumferential static pressure distortion

Of the above 3 secondary operational parameters, only the last will be amenable to quantitative representation by data analysis.

The primary performance parameters for the first buildup are:

1) Compressor polytropic efficiency, η_p

2) Compressor isentropic efficiency, η_i

3) Compressor mechanical efficiency, η_M

4) Compressor pressure ratio based on isentropic work input, $(P/P)_i$

5) Compressor pressure ratio based on mass weighted discharge total pressure, $(P/P)_m$

6) Compressor mass flow $\frac{w\sqrt{\theta}}{\delta}$

7) Compressor polytropic work coefficient, ψ_p

8) Compressor isentropic work coefficient, ψ_i

9) Compressor inlet flow coefficient, $\phi_1 = \frac{\bar{V}_{r1}}{U_1}$

In addition, 3 secondary performance parameters will be evaluated as follows:

1) Rotor discharge absolute angle distortion

2) Rotor discharge relative angle distortion

3) Rotor discharge absolute total pressure distortion

Again, the 3 items listed above are qualitative in nature, but the data analysis will attempt to represent them quantitatively.

In addition to evaluation of the above parameters, it will be the task of data analysis to incorporate the results obtained from aerodynamic calibration of the measurement probes.

DATA ANALYSIS INPUT

The test measurements which will be required as input to data analysis are listed below. A brief description of the nature of each input is included.

1) Inlet total temperature ($0.05\ T_t$) - 16 unshielded thermocouples mounted on the compressor inlet screen. These thermocouples are arranged as 4 radial sets (4 thermocouples per set) spaced 90 degrees apart circumferentially.

2) IGV inlet total pressure ($0.25\ P_t$) - 8 unshielded total pressure tubes. Five of these tubes are arranged in a single radial rake. The remaining 3 tubes are located in the same axial-radial position as the rake center tube but are

displaced 90, 180, and 270 degrees from it circumferentially. The 5 rake elements are spaced on the basis of equal annulus area.

3) IGV inlet static pressure (0.25 P_s)-8 elements; 4 elements equally spaced circumferentially on the outer casing, and 4 similarly arranged taps on the centerbody.

4) IGV angle setting (α_o).

5) Compressor mass flow (w) - Obtained from main flow venturi readings.

6) Compressor leakage mass flow (w_1) - Obtained from leakage flow venturi readings.

7) Rotor discharge total temperature (4.5 T_t) - 5 elements set in an axial rake. This rake is located in the same radial position as the supersonic stator spindle. This rake has yaw capability.

8) Rotor discharge total pressure (3.0 P_t) - 3.0 P_t is obtained as an axial traverse of the single unshielded element. Proper orientation of the element is obtained by nulling the associated yaw element.

9) Rotor discharge static pressure (3.0 P_s) - 18 elements; 12 elements of 3.0 P_s are on the fore stator casing wall and are equally spaced circumferentially. The remaining 6 elements are on the aft stator casing wall and are equally spaced circumferentially.

10) Rotor discharge angle (α_3) - The α_3 reading is obtained as an axial traverse of a 2-element yaw probe. The readings are taken at the null position (3.0 P_t and α_3 actually from a single 3-element probe).

11) Compressor wheel speed (N).

12) Compressor torque (T).

CALCULATION OF PROPERTIES AT MEASUREMENT POINTS

Data measured by the following sensors will not be adjusted for aerodynamic calibration:

1) Static pressure taps

2) Inlet total pressure rake

3) Inlet screen thermocouple beads

The rotor exit total pressure will be measured with a single traversable total pressure tube nulled to 0 relative flow angle. A correction for total pressure across the element bow shock will be applied based on the upstream static pressure and the indicated total pressure P_{t3ind}, i.e.,

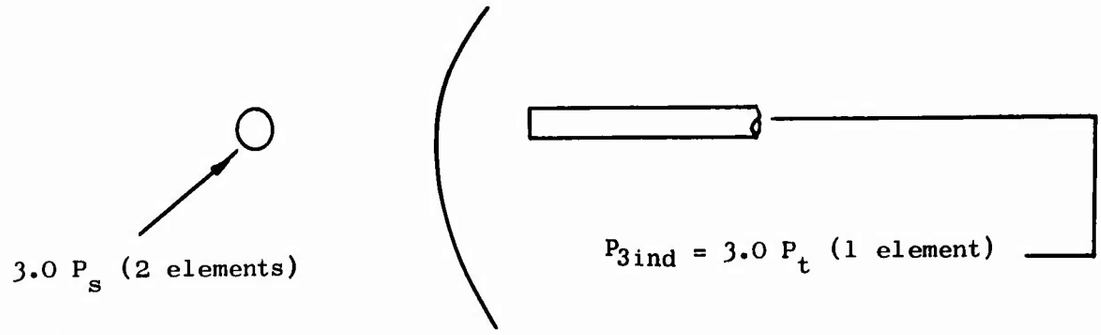

The element upstream static is obtained by averaging the two 3.0 P_s readings, and is denoted P_{s3}. The shock Mach number is given by

$$M_{sn}^2 = \frac{2}{\gamma-1}\left[\left(\frac{P_{s3}}{P_{t3}}\right)^{\frac{\gamma-1}{\gamma}} - 1\right] \tag{20}$$

The total pressure ratio across the shock is given by

$$\frac{P_{t3ind}}{P_{t3}} = \left(\frac{\frac{\gamma+1}{2} M_{sn}^2}{1 + \frac{\gamma-1}{2} M_{sn}^2}\right)^{\frac{\gamma}{\gamma-1}} \Bigg/ \left(\frac{2\gamma}{\gamma+1} M_{sn}^2 - \frac{\gamma-1}{\gamma+1}\right)^{\frac{1}{\gamma-1}} \tag{21}$$

and in addition,

$$\frac{P_3}{P_{3s}} = \frac{P_3}{P_{t3ind}} \cdot \frac{P_{t3ind}}{P_{3s}} \tag{22}$$

P_3/P_{3i} is solved for by iterating the above equations and then P_3 is obtained from

$$P_3 = P_{3ind} \cdot \frac{P_3}{P_{3ind}} \tag{23}$$

Angle measuring probes will be used to obtain flow angle as follows:

$$\alpha_3 = \alpha_{3ind} + \alpha_{corr} \tag{24}$$

where

α_3 = flow angle

α_{3ind} = indicated probe angle

α_{corr} = correction term obtained from low speed null test

Supersonic stator spindle total temperature readings, $T_{ind4.5}$, will be used to obtain total temperature, $T_{4.5}$, as follows:

$$T_{4.5} = \frac{T_{ind4.5}}{K_T} \tag{25}$$

where

$$K_T = \frac{T_{ind}}{T}$$

is the recovery ratio, which is obtained from calibration as a function of Mach number. K_T will be taken as an average value of the calibration results from all elements. The average value, determined as a function of Mach number, will be used for each element at the measurement plane. The same Mach number will be used for all elements at the measurement plane. The Mach number will be determined by a free vortex extension of the Mach number determined at the rotor exit from the average rotor exit total pressure and average rotor exit static pressure.

AVERAGING OF CORRECTED MEASUREMENTS

Compressor Inlet

The average inlet total temperature will be taken as the arithmetic average of the 16 data thermocouples mounted on the inlet screen:

$$\overset{\bullet\bullet}{T}_1 = \sum_{j=1}^{16} \frac{T_{0.1j}}{16} \tag{26}$$

The average inlet total pressure will be obtained by multiplying the mid-rake element of the radial inlet total pressure rake (5 elements) by a radial weighting function, X_r, and a circumferential weighting function, X_{cir}; i.e.,

$$\bar{P}_{t0.1} = X_r \, X_{cir} P_{tmid\text{-}rake} \tag{27}$$

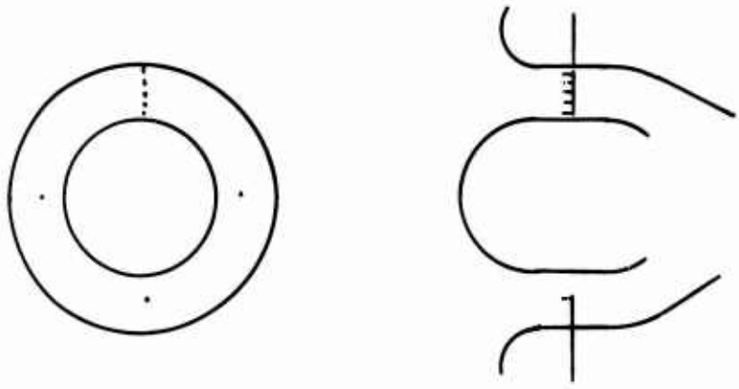

where

$$X_r = \frac{\sum_{j=1}^{5} P_{tr}}{5 \; P_{tmid\text{-}rake}}$$

$$X_{cir} = \frac{\sum_{j=1}^{4} P_{tcir}}{4 \; P_{tmid\text{-}rake}}$$

The inlet radial-rake has constant area element spacing.

The average inlet static pressure will be obtained from

$$\bar{P}_{sl} = \frac{1}{8} \sum_{j=1}^{8} P_{s \; 0.25} \tag{28}$$

Rotor Inlet

Due to lack of instrumentation at the rotor inlet, the average conditions at this station will have to be inferred from the conditions at other stations throughout the machine. In cases where average conditions at the rotor discharge are required, reference will be made to the appropriate equations in the rotor discharge section.

The loss in total pressure from compressor inlet to rotor inlet will be obtained from:

$$\Delta\bar{P}_L = \bar{\omega}_1 \quad (\bar{P}_t - \bar{P}_s)_{0.1} \tag{29}$$

where

$\bar{\omega}_1$ is an inlet total pressure loss coefficient defined as a function of IGV angle from the results of the low speed tests.

The average rotor inlet total pressure will then be estimated as:

$$\bar{P}_{t1} = \bar{P}_{t0.1} - \Delta\bar{P}_L \tag{30}$$

The mass average rotor inlet absolute tangential velocity component will be obtained from

$$\bar{V}_{u1} = \frac{r_3}{r_1} \bar{V}_{u3} - \frac{360}{\pi} g JC_p \frac{\left(T_{t3} - T_{t2}\right)}{(RPM)\ r_1} \tag{31}$$

For $\bar{V}_{u3}$, see equation 46.

For $\bar{T}_{t3}$, see equation 41.

The average rotor inlet radial velocity will be obtained from

$$\bar{V}_{r1} = \frac{W_1}{\rho_1 C_f A_1} \tag{32}$$

where

W_1 = the mass flow at station 1

ρ_1 = the average density at station 1

C_f = channel flow coefficient

A_1 = rotor inlet area

and

$$\rho_1 = \frac{144\ \bar{P}_{t1}}{R\ \bar{T}_{t1}} \left[1 - \frac{\gamma-1}{2} \left(\frac{\bar{V}_{r1}^2 + \bar{V}_{u1}^2}{a_t^2} \right) \right]^{\frac{1}{\gamma-1}} \qquad (33)$$

It is seen that the solution requires an iteration between equations (32) and (33). From $\bar{V}_{r1}$ and $\bar{V}_{u1}$, an average inlet angle will be obtained.

$$\bar{\alpha}_1 = \text{Arctan} \left(\frac{\bar{V}_{u1}}{\bar{V}_{r1}} \right) \qquad (34)$$

This average inlet angle should agree within $\pm$ 10 degrees with the IGV angle.

The average inlet velocity will be calculated from

$$\bar{V}_1 = \sqrt{\bar{V}_{r1}^2 + V_{u1}^2} \qquad (35)$$

The inlet average Mach number will be obtained from

$$\bar{M}_1 = \bar{M}_{t1} \Big/ \sqrt{1 - \frac{\gamma-1}{2}\ \bar{M}_{t1}^2} \qquad (36)$$

where

$$\bar{M}_{t1} = \frac{V_1}{A_{t1}}$$

$$A_{t1} = \sqrt{\gamma R g\ \bar{T}_{t1}}$$

The average relative inlet velocity will be obtained by

$$\bar{V}_{1R} = \sqrt{\bar{V}_{r1}^2 + \bar{V}_{uR1}^2} \qquad (37)$$

where

$$\bar{V}_{uR1} = \bar{V}_{u1} - U_1$$

The average relative inlet Mach number is

$$\bar{M}_{1R} = \left(\frac{\bar{V}_{1R}}{\bar{V}_1} \right) \bar{M}_1 \qquad (38)$$

The average relative inlet flow angle is

$$\bar{\beta}_1 = - \text{Arctan} \left(\frac{\bar{V}_{uR1}}{\bar{V}_{r1}} \right) \qquad (39)$$

Compressor Discharge

The property averages at the rotor discharge will be based on conditions at the center of 5 regions of equal axial width. The axial locations of the 5 axial data stations are:

Axial Data Station	Axial Station Location
1	0.040
2	0.120
3	0.200
4	0.280
5	0.360

The rotor discharge mass average total pressure will be obtained from

$$\bar{P}_{t3} = \frac{\Sigma \rho_{sj} V_{rj} P_{tj}}{\Sigma \rho_{sj} V_{rj}} \qquad (40)$$

The rotor discharge mass average total temperature will be assumed the same as at the supersonic stator measurement plane, hence,

$$\bar{T}_{t3} = \frac{\sum_{j=1}^{5} \rho_{sj} V_{rj} T_{t4.5j}}{\sum_{j=1}^{5} \rho_{sj} V_{rj}} \qquad (41)$$

Note: All terms subcripted "j" refer to the rotor discharge, station 3, unless otherwise specified.

In the preceding expressions, the following terms are defined:

$T_{t4.5j}$ = total temperatures at j immersion, station 4.5

P_{tj} = total pressure at j immersion, station 3

ρ_{sj} = static density at j immersion, station 3

V_{rj} = radial velocity at j immersion, station 3

The last 2 quantities will be obtained as follows: the static pressure will be assumed to vary linearly across the flow passage, and the static density at each immersion will be calculated from

$$\rho_{sj} = \frac{144\ P_{tj}}{R\ T_{t4.5j}} \left(\frac{P_{sj}}{P_{tj}}\right)^{\frac{1}{\gamma}} \tag{42}$$

The radial velocity at j immersion will be calculated from

$$V_{rj} = V_j \cos \alpha_j \tag{43}$$

where

α_j, the flow angle at j immersion, is obtained from the corrected yaw probe reading, and V_j, the fluid velocity at j immersion, is obtained from

$$V_j = \sqrt{2g\ J\ C_p\ T_{t4.5j} \left[\left(1 - \frac{P_{sj}}{P_{tj}}\right)^{\frac{\gamma-1}{\gamma}}\right]} \tag{44}$$

The rotor discharge absolute tangential velocity component at j immersion will be obtained from

$$V_{uj} = V_j \sin \alpha_j \tag{45}$$

Hence, the mass averaged tangential velocity component at rotor discharge is given by

$$\bar{V}_{u3} = \frac{\Sigma\, \rho_{sj}\, V_{rj}\, V_{uj}}{\Sigma\, \rho_{sj}\, V_{rj}} \tag{46}$$

The rotor discharge mass averaged radial velocity component will be obtained from

$$\bar{V}_{r3} = \frac{\Sigma\, \rho_{sj} V_{rj}^{\,2}}{\Sigma\, \rho_{sj}\, V_{rj}} \tag{47}$$

The average rotor discharge angle is then

$$\bar{\alpha}_3 = \text{Arctan}\left(\frac{\bar{V}_{u3}}{\bar{V}_{r3}}\right) \tag{48}$$

The rotor discharge relative tangential velocity at j immersion is

$$V_{uRj} = V_{uj} - U_3 \tag{49}$$

Hence the mass average relative tangential velocity will be obtained by

$$\bar{V}_{uR3} = \frac{\Sigma\, \rho_{sj}\, V_{rj}\, V_{uRj}}{\Sigma\, \rho_{sj}\, V_{rj}} \tag{50}$$

The average rotor discharge relative angle is given by

$$\bar{\beta}_3 = \text{Arctan}\ \frac{\bar{V}_{uR3}}{\bar{V}_{r3}} \tag{51}$$

CALCULATION OF OPERATIONAL AND PERFORMANCE PARAMETERS

Operational Parameters

Primary

1. Rotor average relative Mach number

   - see equation 38

2. Rotor average relative inlet angle

   - see equation 39

3. Rotor average static pressure rise coefficient

$$C_p = \frac{\bar{P}_{s3} - \bar{P}_{s1}}{\bar{P}_{t1R} - \bar{P}_{s1}} \tag{52}$$

where

$$\bar{P}_{s1} = \bar{P}_{t1}\left(1 + \frac{\gamma-1}{2}\ \bar{M}_1^{\,2}\right)^{-\frac{\gamma}{\gamma-1}}$$

$$P_{t1R} = \bar{P}_{s1}\left(1 + \frac{\gamma-1}{2}\ \bar{M}_{1R}^{\,2}\right)^{\frac{\gamma}{\gamma-1}}$$

$$\bar{P}_{s3} = \frac{1}{12}\sum_{j=1}^{12} P_j$$

The p_j above represents the 6 static pressure readings on the aft stator casing plus the 6 associate static pressure readings on the fore stator casing.

4. Rotor average enthalpy equivalent static pressure rise coefficient

$$C_h = \frac{2\,C_p\ \bar{T}_{t2}\left[\left(\frac{\bar{P}_{s3}}{\bar{P}_{s1}}\right)^{\frac{\gamma-1}{\gamma}} - 1\right]\ (U_3^{\,2} - U_1^{\,2})}{\bar{V}_{1R}^{\,2}} \tag{53}$$

Secondary

Rotor exit circumferential static pressure distortion, d_P

This parameter is qualitative in nature but will be represented quantitatively by 2 parameters defined as follows:

$$d_{P_{smax}} = \frac{P_{s_{3max}} - \bar{P}_{s3}}{\bar{P}_{t3} - \bar{P}_{s3}} \tag{54}$$

$$d_{P_{min}} = \frac{\overline{P}_{s3} - P_{s3\ min}}{\overline{P}_{t3} - \overline{P}_{s3}} \qquad (55)$$

where

$$\overline{P}_{s3} = \frac{1}{12} \sum_{j=1}^{12} P_{sj}$$

(The P_{sj} above represents the 12 taps on the fore stator casing).

Performance Parameters

Primary

1) Compressor pressure ratio based on isentropic work input

$$\overline{\Delta H_i} = \frac{\sum \rho_{sj} V_{rj} (\Delta H_i)_j}{\sum \rho_{sj} V_{rj}} \qquad (56)$$

where

$(\overline{\Delta H_i})_j$ is the isentropic enthalpy rise corresponding to an inlet total temperature (T_i) and pressure ratio (P_j/P_i). It will be obtained from Reference 4.

and

$(\overline{\Delta H})_i$ is the mass averaged isentropic enthalpy rise.

The isentropic work input equivalent pressure ratio $(P/P)_i$, is defined as the pressure ratio corresponding to an initial temperature T and an isentropic enthalpy rise $\overline{\Delta H_i}$. This value is also obtained from Reference 4.

2) Compressor pressure ratio based on mass weighted compressor discharge total pressure, $(P/P)_m$.

$$(P/P)_m = \frac{\sum \overline{P}_{t3} \rho_{sj} V_{rj}}{\overline{P}_{t1} \sum \rho_{sj} V_{rj}} \qquad (57)$$

3) Compressor or isentropic efficiency

$$\eta_A = \frac{\bar{H}_{3i} - \bar{H}_1}{\bar{H}_3 - \bar{H}_1} \tag{58}$$

The numerator may be obtained from Reference 4 using the compressor pressure ratio*.

The denominator may be obtained from the same source using the measured temperature rise.

4) Compressor polytropic efficiency

The compressor polytropic efficiency will be defined as

$$\eta_P = \frac{R \ln (P/P)_{i \text{ or } m}}{\phi_3 - \phi_1} \tag{59}$$

where

ϕ is a function of temperature in Reference 4.

5) Compressor mechanical efficiency

The mechanical efficiency will be defined as

$$\eta_M = \frac{\bar{H}_{3i} - \bar{H}_i}{\frac{2\pi N\tau}{60 J w}} \tag{60}$$

where

w = compressor mass flow (lb/sec)

N = compressor speed (rpm)

τ = compressor torque (ft lbs)

6) Compressor isentropic work coefficient

The isentropic work coefficient will be defined as

* All terms involving the compressor ratio will be evaluated for both $(P/P)_i$ and $(P/P)_m$.

$$\psi_i = \frac{g\left(\bar{H}_3 - \bar{H}_1\right)}{U_2^2} \tag{61}$$

7) Compressor polytropic work coefficient

$$\psi_p = \eta_p \psi_i \tag{62}$$

8) Compressor corrected mass flow

$$w_{corr} = \frac{\omega_c \sqrt{\theta}}{\delta} \tag{63}$$

where

$$\theta = T_i/T_{std}$$

$$\delta = P_i/P_{std}$$

$$T_{std} = 518.688^{\circ}\text{Rankine}$$

$$P_{std} = 14.696 \text{ lb/in.}^2$$

9) Compressor flow coefficient

$$\phi_1 = \frac{\bar{V}_{r1}}{U_1} \tag{64}$$

Secondary

The secondary performance parameters are qualitative in nature, but will be given quantitative representation as follows:

1) Rotor discharge absolute angle distortion

This parameter will be represented by a form factor defined as the percentage of flow with absolute discharge angle within plus or minus some angle of the average rotor discharge absolute angle ($\bar{\alpha}_3$).

2) Rotor discharge relative angle distortion

This parameter will be represented by a form factor defined as the percentage of flow with relative discharge angle within

plus or minus some angle of the average rotor discharge relative angle.

3) Rotor discharge absolute total pressure distortion

This parameter will be represented by a form factor defined as the difference between the maximum absolute discharge total pressure and the average discharge total pressure all divided by the difference between the average total discharge pressure and the average static discharge pressure

$$d_{P_t} = \frac{P_{t3\ max} - \bar{P}_{t3}}{\bar{P}_{t3} - \bar{P}_{s3}} \tag{65}$$

ACCURACY CHECKS

As a check on the accuracy of weighting procedures employed at the rotor discharge, the profile averaged mass flow will be checked against the venturi mass flow minus the leakage mass flow.

$$\bar{w} = \sum_{j=1} \rho_{rj} A_j \tag{66}$$

$$\Delta = \frac{\bar{w} - (w_v - w_l)}{(w_v - w_l)} \tag{67}$$

The deviation, Δ, will not be allowed to exceed 0.05 in absolute value without an investigation of the instrumentation to account for the discrepancy.

As a check on conditions at the rotor inlet, the rotor inlet average absolute angle will be checked against that predicted from the IGV setting. A difference of more than plus or minus 10 degrees will be investigated.

CONSTANTS

The following constants will be used in the calculations:

Standard pressure = 14.696 lb/in.^{2}

Standard temperature = 518.688°R

$R = 53.342$ ft-lb/lb - ^{o}R

$g = 32.174$ ft/sec^2

$J = 778.161$ ft-lb/Btu

Values of γ and C_p will be obtained from the Reference 4 data versus total temperature.

APPENDIX VII
EVALUATION OF LEBOW LIQUID COOLED SLIP RING

BACKGROUND

Testing of advanced components for flight propulsion systems at the Advanced Components Technology Department (ACTD) requires the measurement of strain and temperature on turbomachinery operating at high rotational speed. Reliable slip rings for transmission of these signals are a prerequisite for good data, and improved models are therefore always under consideration.

The Lebow slip ring, Model 6120-16, is a 16-ring unit which employs the concept of introducing liquid into direct contact with the brushes and rings for cooling, cleaning, and lubrication of the brush-ring interface. The brushes are cantilevered wire tufts, 2 of which contact each of the hard gold rings. The unit, not including the flexible coupling, is less than 4 inches long and weighs 171 grams.

This slip ring is manufactured by Lebow Associates under exclusive licensing agreement with The Boeing Company.

Serial Number 126, which was made for the Measurements Development Operation of the General Electric Company, was evaluated by Howard Willson of Lebow Associates on October 7, 1965. A description and the results of that evaluation are presented herein:

TEST CONDITIONS

Coolant:	Deionized water
Flow Rate:	2-3 gallons per hour
Rotation:	Clockwise looking at drive end
Current:	25 ma
Ambient Noise:	200 microvolts peak-to-peak while at zero rpm

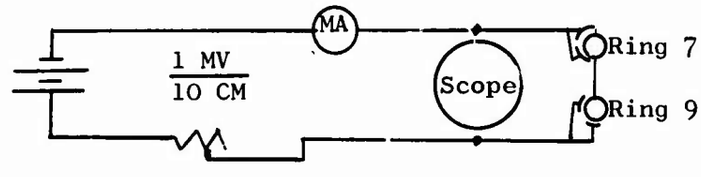

Coupling Runout: 0.0005 on drive end; 0.0015 on slip ring end

SLIP RING NOISE

During the first period of 5 minutes of operation, the noise level was read at 25,000, 30,000, and 35,000 rpm and speed was then held at 35,000 rpm for 2 minutes. During this time, the maximum peak excursion on the scope was about 300 microvolts, or net noise of 100 microvolts. The signal did not seem to vary as a function of speed.

After a short shutdown, the noise was checked at 36,500 rpm and total excursion was measured at 400 microvolts peak-to-peak. Shorting the slip ring out of the circuit revealed that ambient background noise had increased to 300 microvolts, so the net noise was still only 100 microvolts.

Speed was then increased to 42,000 rpm and held for about 5 minutes, during which time the noise had settled to somewhat less than 100 microvolts over ambient; it was more like 50 microvolts.

Because the ambient background noise had varied from 200 to 300 microvolts thus far, we reduced the speed to 25,000 rpm and attempted to reduce or stabilize the background noise by use of jumper cables, shields, etc. Although this was unsuccessful, we were able to confirm that it was the ambient noise that was varying and that the signal noise remained at no more than 100 microvolts peak-to-peak.

IMPEDENCE

While at 25,000 rpm, electrical leakage was measured from ring 9 to other rings and tabulated as follows:

9-1	1.1 meg
9-2	900 K
9-3	600 K
9-4	600 K
9-5	490 K
9-6	300 K
9-11	500 K
9-13	600 K
9-15	1.1 meg

It can be observed that the closer rings are together, the lower the resistance is between them, which is to be expected. Freon as the coolant is reportedly much better in this respect, but selecting suitable transmission lines for Freon is presently a problem.

After the slip ring was shut down, the electrical leakage to ground was measured on the first 5 rings with no flow of coolant, and then on all rings with coolant flowing at 3 gallons per hour. These values were recorded as follows:

No Flow		Flow of 3 Gallons per Hour	
Ring	Res	Ring	Res
Hub 1	120 K	Hub 1	250 K
Hub 2	220 K	Hub 2	550 K
Hub 3	300 K	Hub 3	760 K
Hub 4	380 K	Hub 4	950 K
Hub 5	400 K	Hub 5	1.1 meg
		Hub 6	1.1 meg
		Hub 7	1.1 meg
		Hub 8	1.2 meg
		Hub 9	1.1 meg
		Hub 10	1.2 meg
		Hub 11	1.3 meg
		Hub 12	1.3 meg
		Hub 13	1.2 meg
		Hub 14	1.1 meg
		Hub 15	900 K
		Hub 16	720 K

Two observations can be made from this tabulation:

1) Leakage is more severe when coolant is not flowing.

2) The closer a ring is to a hub, the lower its resistance to ground.

THERMOCOUPLE SIGNAL DISTORTION

For confirmation of accuracy in transmission of temperature signals through the slip ring, a thermocouple was installed in a sealed vial of lead that was coupled to the slip ring in such a way that the lead could be melted and frozen repeatedly while it was spinning. The recording of the arrest point as measured through the slip ring could then be compared to the reading obtained when the vial was removed from the slip ring and the thermocouple was connected directly to the recorder. Since repeatability was the chief concern rather than absolute value, no ice junction was used. With the slip ring and vial rotating at 22,000 rpm, the first time the lead was melted, it re-froze at 11.72 millivolts. On 3 subsequent melts, it re-froze at 11.91 millivolts. It has not been determined at the present time why the first-time freeze was indicated to be so much lower than the other. The difference in reading is the equivalent of $8^{o}F$.

After removing the vial from the slip ring and connecting the thermocouple directly to the recorder, the freeze point was recorded twice at 12.12 millivolts. Considering the possibility of the ring-to-ring leakage being accountable for the difference in indication, a resistance of 300 K was chopped between the thermocouple splices to simulate ring leakage. But the freeze point was still indicated to be 12.12 millivolts, which is $9^{o}F$ higher than the 11.9 millivolts recorded while running.

CONCLUSIONS

1) Throughout the speed range up to 42,000 rpm with a current flow of 25 milliamps, the noise levels did not exceed 100 microvolts peak-to-peak.

2) With deionized water used as a coolant, the ring-to-ring impedence may be as low as 300 K.

3) With deionized water used as a coolant, the ring-to-hub impedence may be as low as 250 K.

4) Error induced in thermocouple readings probably does not exceed 9°F.

5) Error in thermocouple readings is not due to ring-to-ring impedence.

FRACTURE ANALYSIS

Fracture examination was made of the Lebow slip ring flex connector used on the ROC.

The conclusion made was that the initial failure was due to bending fatigue of 1 thin flex web which occurred during slip ring operation. Possible contributing causes are:

1) Misalignment of connector ends

2) Poor surface finish of flex webs

3) Use of low fatigue strength material

Background

Examination was made of the flex connector used in ROC tests of June 17, 21, and 24, 1966. Three of the four flex webs at the pin connector end were broken (breaks were discovered upon inspection of ROC). One additional web was purposely broken and compared with the 3 earlier breaks under a 30X microscope.

Results

One of the breaks showed definite progressive failure under low rather than high stress conditions. Also observed were large amounts of fretting, indicating that the slip ring continued operating after this break. The break appeared fatigued initially at both inner diameter and outer diameter edges, indicating bending fatigue.

One of the remaining breaks showed some evidence of fatigue, large amounts of fretting, and a probable failure source at the inner diameter edge (possibly because of previous breakage of the web described above).

The web that was purposely broken showed large deformation and tearing, characteristic of the high stress failure that it was.

The remaining web break could not be definitely classified as either a fatigue or as a high stress failure.

APPENDIX VIII
ROC SCROLL COLLECTOR FLOW LIMITS

The following is a resumé of calculations made February 10, 1965, concerning the high-speed compressor scroll collector.

Determination of Mach number at scroll collector centerline at a point 90 degrees clockwise from start of semicircular collector:

Data: $r_{7.25}$ = Centerline of scroll = 8.475 inches

r_7 = scroll inlet = 7.6 inches

α = scroll inlet angle from tangential = 20 degrees

M_7 = assumed Mach number = 0.4

Answer: $M_{7.25}$ = 0.3185 Mach number with this design (original machine)

Determination of Mach number in scroll using results of computer and sonic flow function for case of 100 percent speed and -18.4 degrees inlet guide vane setting:

Data: Sonic flow function = 0.532

Area = 0.770 inch^2 located at 90 degrees clockwise from start of semicircular collector

P_t = 12.018 atmosphere

T_t = 1165.6 degrees Rankine

w = 4.5 lbs/sec

Answer: $M_{7.25}$ = 0.330

Determination of choke conditions and calculation of exit area necessary to unchoke exit for case of 60 percent speed and +10 degrees α:

Data: T_{t2} = 685.38

P_{t7}/P_{t1} = 2.4647

$\frac{w}{w_{des}}$ = 0.55691

Calculations:

$$\frac{w}{A}\frac{\sqrt{T_t}}{P_t} = 0.612 \text{ which chokes exit} \qquad (68)$$

Data:

$$\frac{w\sqrt{T_t R}}{A P_t} = 3.85 \text{ at } M = 0.9 \text{ (Unchoke to } M = 0.9) \qquad (69)$$

Answer:

A = 1.72 inches^2 = A for 50 percent flow (ROC uses double exit scroll)

M = 0.293 through this area

If the scroll collector area is increased to 1.766 square inches for each exit, which corresponds to a 1.5-inch exit diameter, the Mach number for the 100 percent speed and -18.4 degrees inlet guide vane setting condition is calculated to be 0.1355. For the 60 percent speed and +10 degrees inlet guide vane setting, the Mach number becomes 0.803.

Other operating conditions were investigated as follows:

Percent Speed	Inlet Guide Vane	Solution
100	0	Supersonic
60	0	Supersonic
60	+60	Supersonic
60	+60	Subsonic

It was found that these conditions were not critical.

Conclusion

The scroll exit diameter will be 1.50 inches. The area will increase linearly from the splitter lip to the scroll exit.

APPENDIX IX
ROC ROTOR INSTRUMENTATION FOR BUILDUP D

INSTRUMENTATION REQUIRED

Shroud

Only strain gages are required.

Type - Baldwin FAB-06-35-S9 (provides backing rated at 400°F, 0.0625-inch square grid, 355-ohm resistance).

Number - Four gages (2 on back of blade side, and 2 on back of seal side).

Location - See Figure 270.

Attachment -

1) Dental abrasive, 50 micron maximum, may be used for shroud surface preparation with minimum damage.

2) EPY 400 cement (good to 400°F) to be used for gage attachment.

Gage Pattern - See Figure 272.

Gage Number	Location
1S	Seal Side - Closest to Blade 6
2S	Seal Side - Closest to Blade 12
3B	Blade Side - Closest to Blade 6
4B	Blade Side - Closest to Blade 12

Lead Paths -

1) Lead paths should be the shortest distance from the gage to the blade. Blades 6 and 12 may be modified as shown in Figure 270 to allow for leads passage through shroud blade stem holes. The leads from the shroud gages will be extended to the stem holes of blades 6 and 12. Having mounted blades 6 and 12 on the disc, leads for the shroud gages will be attached to the disc and to the blade following the leads path indicated in Figure 271; these leads together with the blade stems will then be passed through the corresponding shroud holes and spliced to the shroud gage leads.

2) Lead paths beyond blades are defined by Figure 269.

Disc

Only thermocouples are required.

Type - chromel-alumel, grounded

Number - 2

Location - Attached to the disc face as shown in Figure 269 and Figure 272.

Attachment - Junction at location area of flame-sprayed nichrome (FSN) on top of Metco 404 on disc face. Flame-sprayed area to be kept to a minimum and edges to be benched smooth prior to thermocouple attachment.

Blades

Only strain gages are required.

Type - Baldwin FAB-06-36-S9 (provides backing rated at 400°F, 0.0625-inch square, 355-ohm resistance).

Number - One gage per blade for 2 blades.

Location - See Figure 271.

Attachment -

1) Dental abrasive, 50 micron maximum, to be used for blade surface preparation with minimum damage.

2) EPY 400 cement (good to 400°F) to be used for gage attachment.

Gage Pattern - Refer to Figure 272.

Type Blade	Blade Number	Disc Slot Number
P01	6	22
P01	12	66

Lead Paths -

1) Lead paths on blades to be shortest distance from gage to side of blade.

2) Lead paths beyond blades are defined by Figure 269.

Special Instructions

1) No diodes are required for instrumentation of this rotor buildup.

2) Extra lead length should be provided since the slip ring will be installed further away from the rotor than in original buildup (see new installation in Figure 204).

3) New centerbody will be modified with 2 radial grooves (similar to old centerbody) by Engineering Evaluation Operation in order to fit around the 2 lead paths on disc surface.

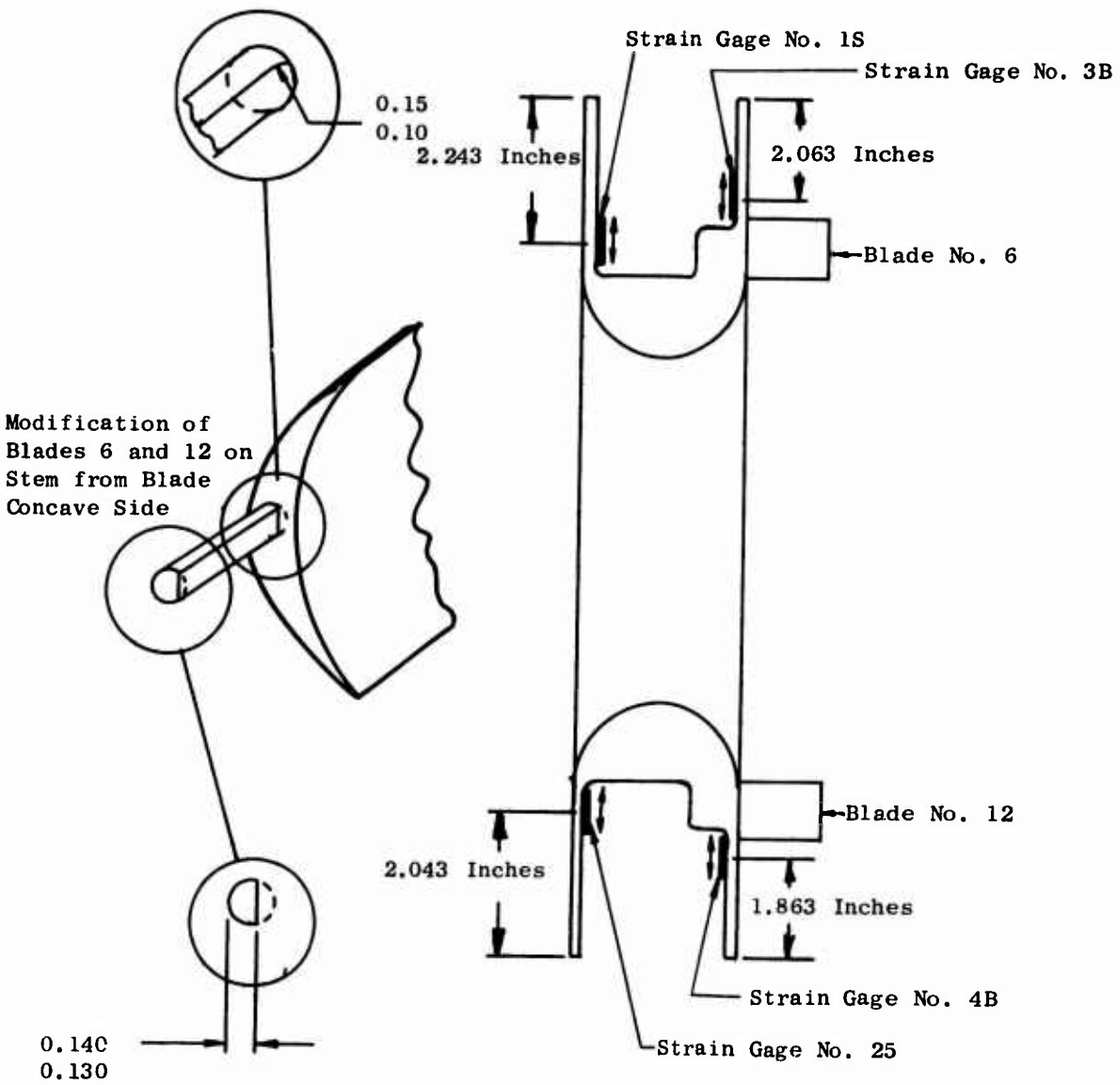

Figure 270. Location of Strain Gages on Rotating Shroud of High-Speed ROC.

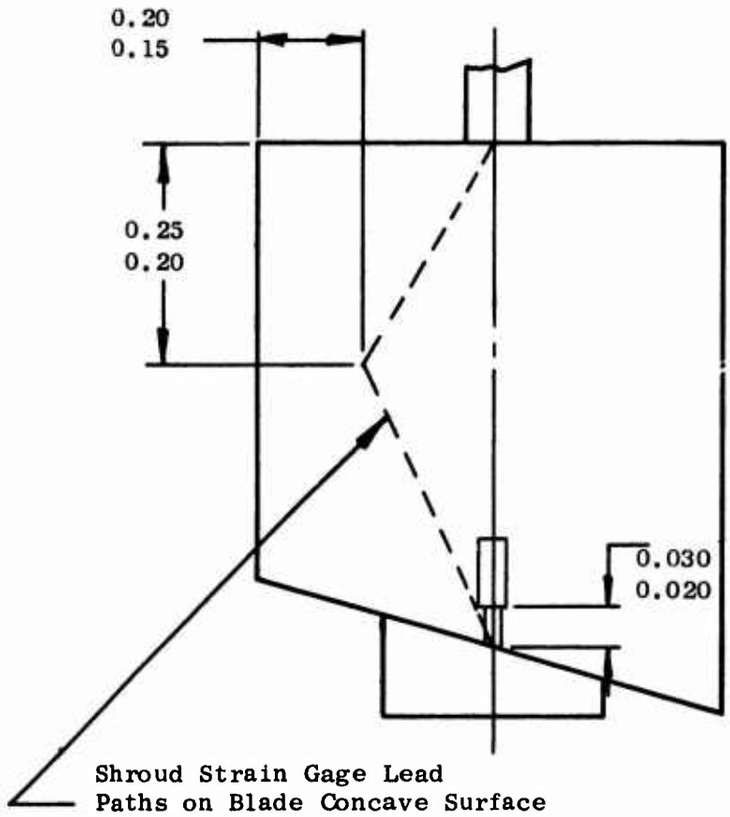

Figure 271. Strain Gage Location and Lead Path to Shroud Strain Gage on Convex Surface of High-Speed ROC Rotor Blade (for Buildup D Only).

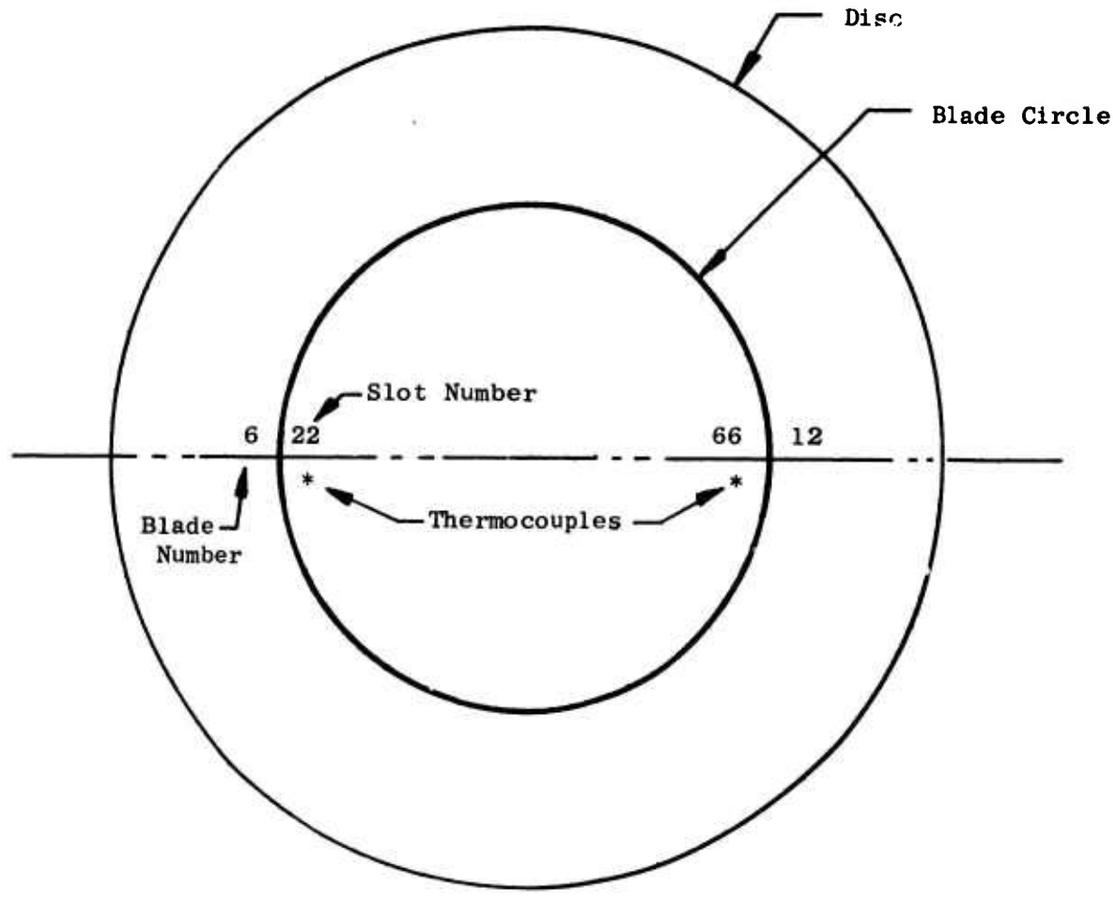

Figure 272. Circumferential Location of Thermocouples and Total Blades Having Shroud Strain Gage Leads.

APPENDIX X
MATERIAL INSPECTION OF PHASE III ROC BLADES

Results were received on tensile tests performed on Ti-6-6-2 bar stock planned for use on Phase III ROC blades. These tests were performed on 4 random samples chosen from the full material lot of 32 bars.

The results are as follows:

Sample Bar Number	Ultimate (ksi)	0.2 Yield (ksi)	Elongation (Percent)	Reduction of Area (Percent)
1	192	182	8	24
10	189	180	10	33
20	185	179	11	37
32	190	181	12	34
Average of 4 Samples	189	180.5	10.25	32
GE Spec C50TF1	180	170	10	20

APPENDIX XI
STATIC PRESSURE FLUCTUATIONS

During Run Number 17 of Buildup F, high frequency response crystal transducers were used to observe static pressure variations in the vaneless diffuser between the rotor exit and the subsonic stators. Four crystals were used, each being mounted in a supersonic stator spindle (Figure 211) on the spindle centerline. Three crystals were placed in the forward casing and Number 4 was placed in the rear casing. The Number 1 crystal was located 255 degrees in a clockwise direction from the top, the Number 2 was located 95 degrees from the top, and the Number 3 was located 15 degrees from the top (and therefore about 30 degrees from the splitter lip of the upper exit arm from the scroll). The Number 4 crystal was located in the rear casing opposite the Number 2 crystal.

The Number 2 and 4 crystal signals appeared to be in phase with each other and of similar amplitude. For this reason, the signals from crystals 1, 2, and 3 and a timing trace picked up from a rotating part were selected for display on the 4-channel oscilloscope. All 4, a timing trace from a 6-tooth gear and a timing trace from a 1/revolution indicator, were also recorded on magnetic tape during Run Number 17 readings. Photographs of typical oscilloscope traces are presented in Figures 273 and 274. The traces are shown in descending order with Number 1 at the top, Number 2 in the middle, and Number 3 next, with the 6/revolution or 1/revolution sweep rate timing trace at the bottom.

For the 40 percent speed trace (Figure 273), the display was compressed to show 10 revolutions of the rotor and thus illustrate a low frequency signal variation that was not apparent at high sweep rates. This low frequency signal rate occurs sufficiently close to 60 cps to be due to a spurious electrical pickup from line power. This possibility is being examined.

At 60 percent speed, multiple traces (MT) were displayed and photographed (Figure 274) to indicate the repeatability of the signal for many rotor revolutions. Since the rotor was rotating at about 345 turns per second, a 60 cps signal would require 6 rotor revolutions to complete 1 cycle. The traces shown for test point 60P3, Reading No. 55, exhibit about 8 cycles per revolution, many times more rapid than a 60 cps signal and less by a factor of 11 from the passing frequency of the rotor blades. Unstable, oscillating separation of the flow in the vaneless diffuser is a possible explanation of the 4 psi static pressure pulses seen, but the regularity over many rotor revolutions and the phase similarity between crystals Number 2 and 3 (which are 80 degrees apart) and between crystals Number 2 and 4 raise important questions concerning vaneless diffuser behavior.

At speeds higher than 60 percent, a similar pattern was observed, but with increasing amplitude. For the 80P8 test point, Reading No. 68, static pressure variations of over 1 atmosphere were recorded even though greatly reduced rotor shroud rim vibrations were indicated by strain gage readings. While this behavior has general significance for centrifugal compressors, the use of supersonic stators placed closely adjacent to the ROC rotor exit is anticipated to reduce or eliminate the static pressure fluctuations originating from this zone in the Radial Outflow Compressor.

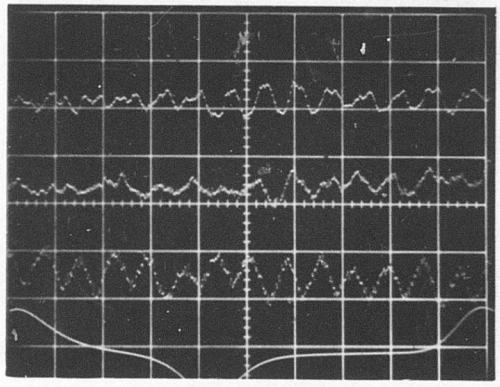

30 Percent Speed
Test Point - 30P1 Reading 48
0.5 psi per Vertical Division
Sweep Rate - 6 per Revolution

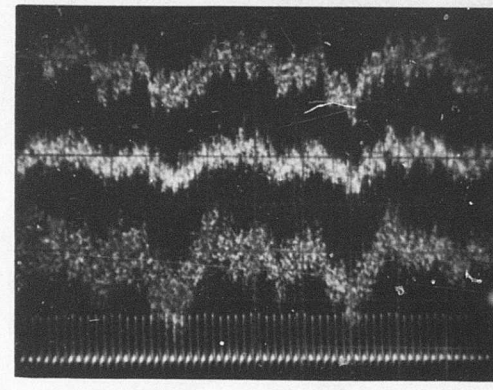

40 Percent Speed
Test Point - 40P2 Reading 50
0.5 psi per Vertical Division
Sweep Rate - 0.1 per Revolution

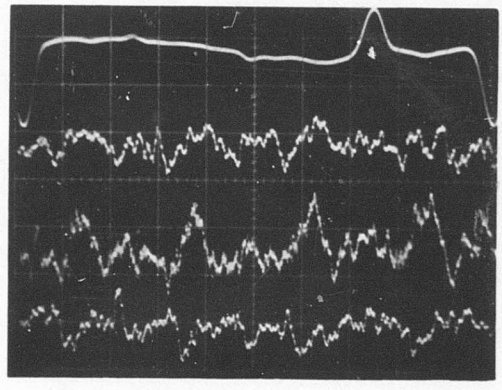

50 Percent Speed
Test Point - 50P1 Reading 51
1.0 psi per Vertical Division
Sweep Rate - 6 per Revolution

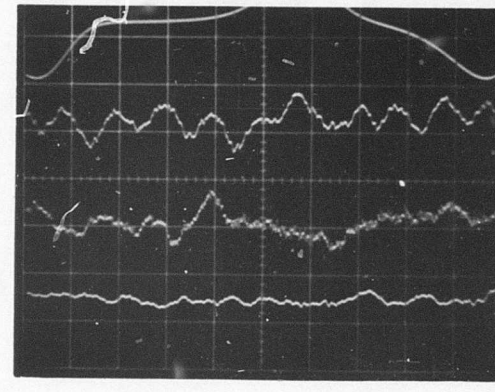

60 Percent Speed
Test Point - 60P3 Reading 55
2.0 psi per Vertical Division
Sweep Rate - 1 per Revolution

Figure 273. Oscilloscope Traces Obtained From High Frequency Response Static Pressure Crystals With Timing Trace Shown at Bottom.

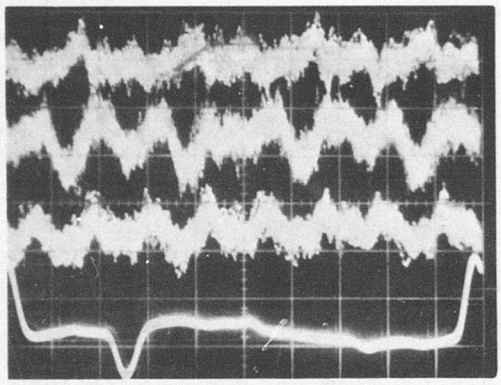

60 Percent Speed
Test Point - 60P3 Reading 55
2.0 psi per Vertical Division
Sweep Rate - 1 per Revolution (MT)

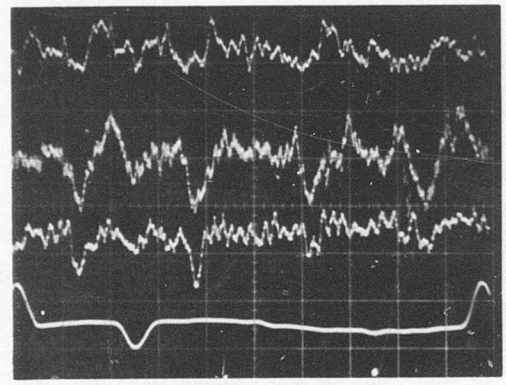

65 Percent Speed
Test Point - 65P1 Reading 53
2.0 psi per Vertical Division
Sweep Rate - 1 per Revolution

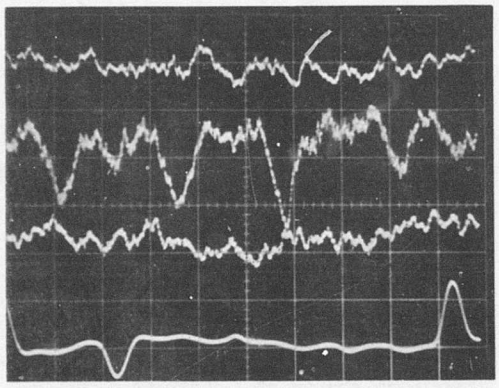

72 Percent Speed
Test Point - 72P2 Reading 64
5.0 psi per Vertical Division
Sweep Rate - 1 per Revolution

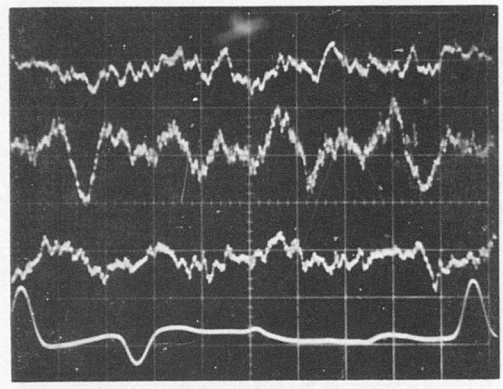

80 Percent Speed
Test Point - 80P8 Reading 68
10 psi per Vertical Division
Sweep Rate - 1 per Revolution

Figure 274. Oscilloscope Traces Obtained From High Frequency Response Static Pressure Crystals With Timing Trace Shown at Bottom.

APPENDIX XII
SUMMARY OF TEST RUNS

TABLE XV. SUMMARY OF TEST RUNS

Date	Buildup	Run	Points	(Percent)	IGV	Circular Vane	Supersonic Stators	Subsonic Stators	Description
4-30-66	A	1	11	30	Yes	No	No	No	Completed mechanical checkout to 30% speed - Aero test data showed insufficient discharge area - Booster used, but still unable to get required flow.
5-5-66	A	2	12	50	Yes	No	No	No	IGV closed to 40^{o} - Completed mechanical checkout to 50% speed - Obtained good aero data at 33% speed - At higher speeds airflow was restricted to values below that calculated for zero rotor blade incidence.
5-9-66	A	3	7	70	Yes	No	No	No	IGV $+40^{o}$
6-17-66	B	4	10	80	Yes	No	No	No	0^{o} IGV - Added exhaust bleed at stator spindles - 30 relief tubes - obtained flow requirements - Completed mechanical checkout to 80% speed - Cooling leakage continued to cloud dat Good zero leakage data at 33% speed.
6-21-66	B	5	13	80	Yes	No	No	No	0^{o} IGV - No stators, bleed exhaust - Obtained aero data at 70 and 80% speeds - Cooling leakage still a problem - Stators should help the problem - In-test data indicates poor efficiencies.
6-24-66	B	6	10	80	Yes	No	No	No	0^{o} IGV - No stators, bleed exhaust - Obtained further required points at 60, 70, and 80% speeds - More throttling improved efficiencies over that of Run Number 5. Still have leakage problems.
7-14-66	C	7	14	70	Yes	No	Yes	No	0^{o} IGV - Supersonic stators, bleed exhaust - Obtained aero data at 60 and 70% speeds. Efficiencies still low - Stator performance looks good.
8-4-66	C	8	18	50	Yes	No	Yes	No	0^{o} IGV - Supersonic stators, bleed exhaust - Obtained aero data at 30, 40, and 50% speeds with practically no leakage - Performance poor.
8-22-66	C	9	20	70	Yes	No	Yes	No	$+40^{o}$ IGV - Supersonic stators, bleed exhaust - Obtained aero data at 30, 50, 60, and 70% speeds with practically no leakage - No improvement in performance.
1-30-67	D	10	30	60	No	No	No	No	Inlet configuration 2 (IGV's removed, open inlet) - No stators, reworked discharge for open area, no bleed exhaust - Obtained good aero data at 30, 40, 50, and 60% speeds - Performance improved in subsonic points.
2-3-67	D	11	24	80	No	No	No	No	Inlet configuration 2 (open inlet) - No stators, reworked discharge for open area, no bleed exhaust - Obtained good aero data at speeds up to 80% - Performance very bad in supersonic points - Reworked exit system.

TABLE XV. CONTINUED

Date	Buildup	Run	Test Points	Speed Range (Percent)	IGV	Circular Vane	Supersonic Stators	Subsonic Stators	Description
3-27-67	E	12	12	50	No	No	Yes	No	Open inlet - Supersonic stators - Obtained aero data at 30, 40, and 50% speeds - Performance above 30% speed was poor.
3-28-67	E	13	17	70	No	No	Yes	No	Open inlet - Supersonic stators - Open exit - Obtained aero data at 40, 50, 53, 57, 60, and 70% speeds - Vibrations were a problem that prevented setting certain desired points particularly the subsonic high-speed (above 50%) points.
4-25-67	E	14	43	60	No	No	Yes	No	Open inlet - Supersonic stators - Inlet air injection - Obtained aero data at 30, 40, 49, 55, and 60% speeds - Vibrations continue to prevent setting high-speed (above 50%) subsonic points - Results indicate air injection had no significant effect on performance.
10-12-67	F	15	14	60	No	No	No	Yes	Data at 30, 40, 50, and 60% speed efficiency and P P higher than ever - Subsonic stators - Open inlet - Flow splitter - Inlet turning vane - Traversing probe.
10-17-67	F	16	32	70	No	No	No	Yes	Subsonic stators - Open inlet - Flow splitter - Data up to 70% speed - Performance very good - Unable to repeat low speed points, however, on inspection after run found 50 mills Teflon seal clearance and bad leak in rupture disc - Rotor instrumentation out except 2 proximeters.
12-28-67	F	17	21	80	No	No	No	Yes	Subsonic stators - Open inlet - Flow splitter - Data up to 80% speed - Closing vanes to as much as 80° increased efficiency 10 points, however, efficiency is low at 80% speed. Possible shroud fatigue damage.
12-29-67	F	18	4	80	No	No	No	Yes	Subsonic stators - Open inlet - Flow splitter - Took sound data from 30 to 80% speed - With stator vanes closed even more as far as 82.3°, performance data was taken at 70 and 80% speed - The efficiency at 80% improved another 10 points to 79% uncorrected, but efficiency was decreased at 70% speed.

Unclassified

Security Classification

DOCUMENT CONTROL DATA - R & D

(Security classification of title, body of abstract and indexing annotation must be entered when the overall report is classified)

1. ORIGINATING ACTIVITY *(Corporate author)* General Electric Company Cincinnati, Ohio	2a. REPORT SECURITY CLASSIFICATION Unclassified 2b. GROUP

3. REPORT TITLE

RADIAL OUTFLOW COMPRESSOR COMPONENT DEVELOPMENT, VOLUME II PHASE II - DESIGN, FABRICATION, AND TEST OF AN EXPERIMENTAL COMPRESSOR

4. DESCRIPTIVE NOTES *(Type of report and inclusive dates)*

Report of Phase II Investigation

5. AUTHOR(S) *(First name, middle initial, last name)*

John R. Erwin
Nickolas G. Vitale

6. REPORT DATE	7a. TOTAL NO. OF PAGES	7b. NO. OF REFS
March 1969	453	4

8a. CONTRACT OR GRANT NO.	9a. ORIGINATOR'S REPORT NUMBER(S)
DA 44-177-AMC-180(T) b. PROJECT NO. Task 1G121401D14413 c. d.	USAAVLABS Technical Report 68-38B 9b. OTHER REPORT NO(S) *(Any other numbers that may be assigned this report)* R68AEG361

10. DISTRIBUTION STATEMENT

This document is subject to special export controls and each transmittal to foreign governments or foreign nationals may be made only with prior approval of US Army Aviation Materiel Laboratories, Fort Eustis, Virginia 23604.

11. SUPPLEMENTARY NOTES	12. SPONSORING MILITARY ACTIVITY
Volume II of a 3-volume report	US Army Aviation Materiel Laboratories Fort Eustis, Virginia

13. ABSTRACT

This report describes the second phase of an investigation to develop a small, high-pressure-ratio radial outflow compressor (ROC). The first phase included aerodynamic and mechanical analyses, aerodynamic cascade tests, low-speed compressor tests, mechanical bench tests, machining, fabrication, and design studies which led to the configuration of a high-speed compressor. The second phase consisted of developmental testing of the high-speed compressor and further low-speed compressor testing to guide the design of an improved compressor.

DD FORM 1 NOV 68 1473 REPLACES DD FORM 1473, 1 JAN 64, WHICH IS OBSOLETE FOR ARMY USE.

Unclassified

Security Classification

14. KEY WORDS	LINK A		LINK B		LINK C	
	ROLE	WT	ROLE	WT	ROLE	WT
High-Pressure-Ratio Compressor						
Radial Flow Compressor						
Cascade Diffuser						
Variable Diffuser						
Rotating Diffuser						
Vaneless Diffuser						